Entwicklung und Anwendung von nichtadiabatischen Kopplungs-Matrixelementen für DFT/MRCI-Wellenfunktionen

---

Inaugural-Dissertation

zur

Erlangung des Doktorgrades der

Mathematisch-Naturwissenschaftlichen Fakultät

der Heinrich-Heine-Universität Düsseldorf

vorgelegt von

Mario Bracker

aus Haan

Düsseldorf, Februar 2022

Aus dem Institut für Theoretische Chemie und Computerchemie
der Heinrich-Heine-Universität Düsseldorf

Gedruckt mit der Genehmigung der
Mathematisch-Naturwissenschaftlichen Fakultät der
Heinrich-Heine-Universität Düsseldorf

Berichterstatter:
1. Univ.-Prof. Dr. Christel M. Marian
2. Univ.-Prof. Dr. Peter Gilch

Tag der mündlichen Prüfung: 02.05.2022

Eidesstattliche Erklärung

Ich versichere an Eides statt, dass die Dissertation von mir selbständig und ohne unzulässige fremde Hilfe unter Beachtung der „Grundsätze zur Sicherung guter wissenschaftlicher Praxis an der Heinrich-Heine-Universität“ erstellt worden ist. Aus Quellen direkt oder indirekt übernommene Gedanken sind als solche kenntlich gemacht. Die Arbeit hat in dieser oder vergleichbarer Form noch keinem anderem Prüfungsgremium vorgelegen. Es wurden keine früheren erfolglosen Promotionsversuche unternommen.

Düsseldorf, den 17.02.2022

Danksagung

An erster Stelle möchte ich mich bei Professorin Dr. Christel M. Marian bedanken. Sie hat mir die Möglichkeit gegeben zu diesem hochinteressanten Thema zu forschen. Gerade in schwierigen Situationen konnte ich von ihrem großen Erfahrungsschatz profitieren und lernen. Ein besonderer Dank gilt ebenso Dr. Martin Kleinschmidt für die immerwährende Hilfsbereitschaft und Unterstützung. Die zahlreichen Diskussionen haben maßgeblich zum Erfolg dieser Arbeit beigetragen. Professor Dr. Peter Gilch danke ich vielmals für die Bereitschaft, die Rolle als Mentor und das Korreferat zu übernehmen.

Ich danke PD Dr. Oliver Weingart für Hilfestellungen zu Beginn meiner Promotion. Darüber hinaus möchte ich mich bei Fabian Dinkelbach für Hilfestellungen bei meinen ersten Programmierversuchen und die gute Zusammenarbeit bedanken.

Ich danke dem gesamten Arbeitskreis der TC (und ehemaligen Mitgliedern) für die freundliche Arbeitsatmosphäre und anregende Gespräche im fachlichen sowie fachfremden Kontext. Vor allem danke ich meiner 'Laborpartnerin' Nora Lüdtke für die vielen interessanten Gespräche im Arbeitsalltag.

Den Initiatoren und Mitgliedern des Graduiertenkollegs 'ModISC' danke ich für das inspirierende Programm und die produktiven Kooperationen. Der deutschen Forschungsgesellschaft (DFG) danke ich für die finanzielle Unterstützung meiner Promotion (Projektnummer 396890929/GRK 2482).

Und nicht zuletzt danke ich meiner Familie und meinen Freunden. Ihr wart immer für mich da, wenn ich Ablenkung gesucht habe und habt stets Verständnis für mich gezeigt.

Kurzfassung

Die Born–Oppenheimer-Näherung ist einer der Eckpfeiler der Quantenchemie. Nichtadiabatische Kopplung stellt eine Korrektur der Näherung dar und wird benötigt, um strahlungslose Übergänge zwischen Zuständen mit derselben Spinmultiplizität zu modellieren (Interne Konversion, IC). Im Anschluss an die elektronische Anregung eines Moleküls ist das System bestrebt, die überschüssige Energie an die Umgebung abzugeben. IC stellt hierbei einen omnipräsenten Prozess dar, der letztlich zur Umwandlung von Anregungsenergie in thermische Energie führt.

DFT/MRCI ist eine etablierte semiempirische Methode zur Beschreibung elektronisch angeregter Zustände. Die ursprüngliche Idee und Umsetzung der Kombination von Dichtefunktionaltheorie (DFT) und Multireferenzkonfigurationswechselwirkung (MRCI) stammt von Stefan Grimme und Mirko Waletzke [J. Chem. Phys., 111, 5645 (1999)]. Die Methode wurde in der Folge am Institut für Theoretische Chemie und Computerchemie in Düsseldorf weiterentwickelt und eignet sich zur Modellierung komplexer chemischer Systeme, z. B. Übergangsmetall-Komplexe oder Donor-Akzeptor-Systeme. Der großen Flexibilität des semiempirischen Hamiltonoperators steht gegenüber, dass kein analytischer Gradient formuliert werden kann, sodass numerische Verfahren zur Beschreibung vibronischer Prozesse benötigt werden.

Zur Formulierung von nichtadiabatischen Kopplungs-Matrixelementen werden Ableitungen der elektronischen und Kern- Wellenfunktionen nach den Kernkoordinaten benötigt ('derivative couplings'). Für die elektronische Kopplung wurde im Rahmen dieser Arbeit das Programm Delta konzipiert. Dieses basiert auf der Bildung eines zentralen Differenzenquotienten von nichtorthogonalen Überlapps der Wellenfunktionen. Die Berechnung nichtorthogonaler Überlapps komplexer Wellenfunktionen stellt eine Herausforderung im Hinblick auf Rechenkapazitäten dar. Der implementierte Algorithmus basiert auf einem Verfahren von Plasser et al. [J. Chem. Theory Comput., 12, 1207 (2016)] und Schur's Determinanten Identität zur Wiederverwendung von Zwischenergebnissen sowie einem Selektionsverfahren nach Anregungsklassen. Zur Beschreibung der Kopplung von Kernwellenfunktionen wurde das Programm Vibes erweitert. Zur Quantifizierung von IC Ratenkonstanten wurde ein analytischer Ausdruck in Form einer Korrelationsfunktion hergeleitet und in den zeitabhängigen Zweig des Programms implementiert.

Im Rahmen dieser Arbeit wird demonstriert, dass das entwickelte Vorgehen zur Beschreibung interner Konversion basierend auf dem DFT/MRCI-Ansatz zuverlässige Ergebnisse für organische Moleküle liefert. Ein zentrales Projekt des anwendungsorientierten Teils dieser Arbeit ist die Modellierung der komplexen Kinetik des Xanthon Moleküls in wässrigem Medium sowie in apolarer Umgebung. Ein weiterer wichtiger Baustein ist das Design fluorierter Flavinderivate. Beispielsweise wird gezeigt, dass sich energetische Effekte gewisser Fluorierungen des Chromophors in guter Näherung additiv verhalten. Basierend auf dem Ansatz der Modulation von Übergängen von Singulett- in Triplettzustände (intersystem crossing, ISC), wurden vielversprechende Derivate konzipiert.

Abstract

The Born–Oppenheimer approximation forms a cornerstone of quantum chemistry. Nonadiabatic coupling is a correction of the approximation and is required to model nonradiative transitions between states with equal spin multiplicity (internal conversion, IC). Subsequent to electronic excitation of a molecule, the surplus energy is dissipated and transferred to the environment. IC is an omnipresent process which causes conversion of excitation energy into thermal energy.

DFT/MRCI is a well-established semiempirical method for the description of electronically excited states. The idea and first implementation of the combination of density functional theory (DFT) and multireference configuration interaction (MRCI) originates from Stefan Grimme and Mirko Waletzke [J. Chem. Phys., 111, 5645 (1999)]. The method was continuously refined at the Institute for Theoretical Chemistry and Computational Chemistry Düsseldorf and is suitable to describe complex chemical systems, e. g. transition metal complexes or donor–acceptor systems. The great flexibility of the semiempirical Hamilton operator is accompanied by the disadvantage that the method is not suitable for formulating an analytical gradient. For this reason, numerical approaches are required for modelling vibronic processes.

The formulation of nonadiabatic coupling matrix elements requires a description of derivatives of the electronic as well as nuclear wavefunctions with respect to nuclear coordinates ('derivative couplings'). For the electronic coupling, the program Delta was conceptualized as a part of this work. It is based on the calculation of central difference quotients of nonorthogonal overlaps of wavefunctions. The computation of nonorthogonal overlaps of complex wavefunctions represents a challenge with regard to computational capacity. The implemented algorithm is based on a procedure of Plasser et al. [J. Chem. Theory Comput., 12, 1207 (2016)] and Schur's determinant identity for reutilisation of intermediate results as well as a selection procedure by restriction of the excitation class. For describing the coupling of nuclear wavefunctions, the program Vibes was extended. For the quantification of IC rate constants, an analytic expression in the form of a correlation function was derived and implemented into the time-dependent branch of the program.

Within this work, it was demonstrated that the developed approach for the description of internal conversion based on the DFT/MRCI ansatz is suitable for organic compounds. A key project of the application-oriented part of this work is the modeling of the complex kinetics of the xanthone molecule in aqueous medium as well as apolar environment. Another important component is the design of fluorinated flavin derivatives. For example, it was shown that certain fluorinations of the chromophore can be described as linear effects on the energetics of the molecule. Based on the approach of modulation of transitions from singlet states to triplet states (intersystem crossing, ISC), promising derivatives were designed.

"*There is a theory which states that if ever anyone discovers exactly what the universe is for and why it is here, it will instantly disappear and be replaced by something even more bizarre and inexplicable. There is another theory which states that this has already happened.*"

– Douglas Adams

Inhaltsverzeichnis

Glossar

nichtadiabatisch:
Der Begriff ist griechischen Ursprungs und auf διαβαίνειν (diabaínein: hindurchgehen) sowie α (a: nicht) zurückzuführen. Die doppelte Negierung grenzt den Begriff von *diabatisch* ab und hebt hervor, dass es sich bei den nichatdiabatischen Termen um eine Korrektur des adiabatischen Bildes handelt. *Diabatisch* bedeutet im quantenchemischen Kontext die Wahl einer Basis, in welcher die nichtadiabatische Kopplung verschwindet bzw. reduziert wird.

AO **A**tom **O**rbital

BLUF **B**lue-**L**ight sensors **U**sing **F**AD

BO **B**orn–**O**ppenheimer

CASPT **C**omplete **A**ctive **S**pace **P**erturbation **T**heory

CASSCF **C**omplete **A**ctive **S**pace **S**elf-**C**onsistent **F**ield

CC **C**oupled **C**luster

conf **conf**iguration

ConIn **Con**ical **In**tersection

COSMO **CO**nductor-like **S**creening **MO**del

cry **cry**ptochrome

csf **c**onfiguration **s**tate **f**unction

(I)CT **I**nternal **C**harge **T**ransfer

(TD)DFT **T**ime-**D**ependent **D**ensity **F**unctional **T**heory

FAD **F**lavin **A**denine **D**inucleotide

FbFB **F**MN-**b**inding **F**luorescent **P**rotein

FC(WD) **F**ranck–**C**ondon[-**W**eighted **D**ensity (of states)]

FMN **F**lavin **M**ono-**N**ucleotide

FWHM **F**ull **W**idth at **H**alf **M**aximum

GFP **G**reen **F**luorescent **P**rotein

GGA **G**eneralized **G**radient **A**pproach

HF **H**artree–**F**ock

HOMO **H**ighest **O**ccupied **M**olecular **O**rbital

(r)IC (**r**everse) **I**nternal **C**onversion

(r)ISC (**r**everse) **I**nter**S**ystem **C**rossing

(I)ST (**I**nverted) **S**inglet–**T**riplet (gap)

IVR **I**nternal **V**ibrational **R**edistribution

LOV **L**ight-**O**xygen-**V**oltage(-sensing)

LU **L**ower–**U**pper

LUMO **L**owest **U**noccupied **M**olecular **O**rbital

MCTDH **M**ulti-**C**onfiguration **T**ime-**D**ependent **H**artree

MO **M**olecular **O**rbital

ModISC **Mod**ulation of **I**nter-**S**ystem **C**rossing

MP **M**øller–**P**lesset

(MR)CI (**M**ulti-**R**eference) **C**onfiguration **I**nteraction

NAC(ME) **N**on-**A**diabatic **C**oupling (**M**atrix **E**lement)

NADH **N**icotinamide **A**denine **D**inucleotide, **H**ydrogen

NOCI **N**on-**O**rthogonal **C**onfiguration **I**nteraction

NR **N**on-**R**adiative

NTO **N**atural **T**ransition **O**rbital

OLED **O**rganic **L**ight **E**mitting **D**iode

phot **phot**otropin

(MC)SCF (**M**ulti-**C**onfiguration) **S**elf-**C**onsistent **F**ield

SOC(ME) **S**pin–**O**rbit **C**oupling (**M**atrix **E**lement)

SVD **S**ingular **V**alue **D**ecomposition

TADF **T**hermally **A**ctivated **D**elayed **F**luorescence

TSH **T**rajectory **S**urface **H**opping

VER **V**ibrational **E**nergy **R**elaxation

HAP-3MF 2,5,8-Tris(4-fluoro-3-methylphenyl)-1,3,4,6,7,9,9*b*-heptaazaphenalene

MIA 10-Methylisoalloxazine

NMA-dF *N*-Methyl-difluoro-acridone

Liste der Veröffentlichungen

In dieser Arbeit enthalten:

1. *Internal conversion of singlet and triplet states employing numerical DFT/MRCI derivative couplings: Implementation, tests, and application to xanthone.*

   Mario Bracker, Christel M. Marian and Martin Kleinschmidt.
   J. Chem. Phys., 155:014102 (2021).

   Eigener Beitrag: Programmentwicklung und Implementierung, Herleitung und Darstellung der Formeln, Durchführung und Analyse der Rechnungen, Erstellung der Abbildungen und Tabellen für das Paper sowie die SI, Schreiben einer Zusammenfassung.

2. *Impact of fluorination on the photophysics of the flavin chromophore: a quantum chemical perspective.*

   Mario Bracker, Fabian Dinkelbach, Oliver Weingart and Martin Kleinschmidt.
   Phys. Chem. Chem. Phys., 21:9912 (2019).

   Eigener Beitrag: Anfertigung eines ersten Manuskripts und der SI. Durchführung und Analyse der Rechnungen, Erstellung von Abbildungen für das Paper und die SI.

3. *Computer-aided design of fluorinated flavin derivatives by modulation of intersystem crossing and fluorescence.*

   Mario Bracker, Mira K. Kubitz, Constantin Czekelius, Christel M. Marian and Martin Kleinschmidt.
   ChemPhotoChem, e202200040 (2022).

   Eigener Beitrag: Teil der Konzeptualisierung, Anfertigung eines ersten Manuskripts und der SI. Durchführung und Analyse der Rechnungen, Erstellung von Abbildungen für das Paper und die SI.

4. *Large inverted singlet–triplet energy gaps are not always favorable for triplet harvesting: Vibronic coupling drives the (reverse) intersystem crossing in heptazine derivatives.*

   Fabian Dinkelbach, Mario Bracker, Martin Kleinschmidt and Christel M. Marian.
   J. Phys. Chem. A, 125:10044 (2021).

   Eigener Beitrag: Setup für die Berechnung der Ratenkonstanten für interne Konversion, Durchführung und Analyse von Testrechnungen.

5. *Acridones: Strongly emissive HIGHrISC fluorophores.*

   Kristoffer Thom, Felix Wieser, Kevin Diestelhorst, Anna Reiffers, Constantin Czekelius, Martin Kleinschmidt, Mario Bracker, Christel M. Marian and Peter Gilch.
   J. Phys. Chem. Lett., 12:5703–5709 (2021).

   Eigener Beitrag: Setup für die Berechnung der Ratenkonstanten für interne Konversion.

Nicht in dieser Arbeit enthalten:

- *Visible light-induced homolytic cleavage of perfluoroalkyl iodides mediated by phosphines.*

  Mario Bracker, Lucas Helmecke, Martin Kleinschmidt, Constantin Czekelius and Christel M. Marian.
  Molecules, 25:1606 (2020).

  Eigener Beitrag: Durchführung und Analyse der Rechnungen, Erstellung von Abbildungen für das Paper und die SI.

Einleitung

Die Wechselwirkung von Molekülen mit Photonen ist der Startpunkt diverser Prozesse. Neben Streuung von Photonen und Schwingungsanregung der Kerne resultiert die Absorption von Photonen in elektronischer Anregung. Die Anregung der elektronischen Wellenfunktion ist von entscheidender Bedeutung für die Bereiche der Photochemie und Photophysik der Moleküle. Die Photochemie beschreibt, vergleichbar mit thermisch hervorgerufenen Reaktionen, die Reorganisation von inter- und intramolekularen Bindungen. Im Unterschied dazu beschäftigt sich die Forschung der Photophysik von Molekülen mit der Fragestellung, wie das angeregte Molekül ohne Umknüpfung chemischer Bindungen zurück zum Grundzustand gelangt. Im Allgemeinen gibt es hierfür drei Möglichkeiten konkurrierender Prozesse:

- nichtstrahlende Rückkehr zum Grundzustand,
- strahlende Rückkehr zum Grundzustand,
- Transfer von Anregungsenergie auf ein chemisches System in der unmittelbaren Umgebung.

Die Route der Photorelaxation hängt sowohl vom Chromophor als auch von externen Einflüssen ab. Bei den maßgeblichen Faktoren handelt es sich um:

- die energetische Lage der elektronischen Zustände und die damit verbundene Frage, welche Zustände thermodynamisch erreichbar sind,
- die Kopplungen zwischen den thermodynamisch erreichbaren vibronischen Zuständen,
- Umgebungseffekte (diese beeinflussen sowohl die Energien der elektronischen Zustände als auch die Stärke der Kopplungen),
- die Form der Anregung (Licht/Strom) des chemischen Systems.

Strahlende und nichtstrahlende Prozesse

Die elektronische Anregung durch Absorption von Photonen erfolgt auf der (sub-)Femtosekundenskala und ist um Größenordnungen schneller als strahlende sowie nichtstrahlende Übergänge, sodass die Anregung als instantan angenommen werden kann. Im Anschluss erfolgen die Reaktionen der elektronischen und Kern- Wellenfunktionen auf die Population des angeregten Zustands: Da Elektronen eine deutlich geringere Masse als Protonen aufweisen ($m^+/m^- \approx 1836$), erfolgt die Anpassung der Elektronenverteilung im Molekül deutlich schneller als die Änderung der Kernanordnung. Diese Unterscheidung der Zeitskalen ist die Grundlage des Franck–Condon-Prinzips [Con26, FD26, Con28]. Im Zuge der Anregung werden Schwingungszustände des angeregten elektronischen Zustands populiert und die Anregungsenergie wird auf verschiedenen Kanälen umverteilt: Zum einen erfolgt ein Übertrag von Schwingungsenergie an umgebende Moleküle (intermolekulares Wärmebad), die dadurch ihrerseits in angeregte Schwingungszustände übergehen [$\leq 10^{13}\,s^{-1}$ [KM95], vibrational energy relaxation (VER)]. Zum anderen geschieht durch die Kopplung von intramolekularen Schwingungsfreiheitsgraden eine intramolekulare Umverteilung der Schwingungsenergie (intramolekulares Wärmebad). Diese Nivellierung innerhalb der Mannigfaltigkeit von Schwingungsniveaus [$10^{10} - 10^{13}\,s^{-1}$ [UM91], intramolecular vibrational redistribution (IVR)] gewinnt an Bedeutung, falls sich das Molekül in der Gasphase befindet und Stoßrelaxation somit vernachlässigbar ist. Elektronische Übergänge von Molekülen sind grundsätzlich vibronischer Natur: Damit ein elektronischer Übergang erfolgen kann, müssen Schwingungsniveaus beider Zustände resonant sein und im Anschluss an den elektronischen Übergang erfolgen IVR sowie VER.

Tabelle 1.: Typische Ratenkonstanten k ausgewählter intramolekularer photophysikalischer Prozesse eines organischen, neutralen Chromophors.

Prozess	k / s^{-1}	Quelle
Absorption	10^{15}	[SHE11]
Molekulare Schwingung	$10^{12} - 10^{14}$	[Tur91]
Intramolekulare vibratorische Redistribution	$10^{11} - 10^{13}$	[UM91]
Intermolekulare Schwingungsrelaxation	$\leq 10^{13}$	[KM95]
Interne Konversion $S_n \rightsquigarrow S_1$	$10^{10} - 10^{14}$	[SHE11]
Interne Konversion $S_1 \rightsquigarrow S_0$	$10^{6} - 10^{7}$	[SHE11]
Interkombination $S_1 \rightsquigarrow T_1$	$10^{5} - 10^{8}$	[SHE11]
Fluoreszenz	$10^{7} - 10^{9}$	[SHE11]
Phosphoreszenz	$10^{-2} - 10^{3}$	[SHE11]
Infrarotemission	$\leq 10^{2}$	[Tur91]
Dielektrische Relaxation	$10^{11} - 10^{13}$	[Lak06]

Die Lebensdauer elektronisch angeregter Zustände ist stark abhängig vom Zustandsniveau. Übergänge zwischen angeregten elektronischen Zuständen innerhalb einer Multiplizität (interne Konversion, IC) finden typischerweise auf derselben Zeitskala wie molekulare Schwingungen und geometrische Relaxation statt ($10\,\mathrm{fs} - 1\,\mathrm{ps}$ [Tur91]). Aus dieser Eigenschaft folgt Kasha's Regel, die besagt, dass strahlende Übergänge innerhalb einer Multiplizität aus dem ersten angeregten Zustand stattfinden [Kas50]. Im Anschluss an die Population des ersten angeregten Zustands konkurrieren in der Regel diverse elektronische Prozesse mit Ratenkonstanten unterhalb von $10^{10}\,\mathrm{s}^{-1}$ [SHE11]. Fluoreszenz bezeichnet die spontane Emission von Photonen unter Erhalt der Multiplizität. Im Gegensatz zur stimulierten Emission, handelt es sich bei Fluoreszenz um einen zufälligen Prozess. Erstere wird durch die Wechselwirkung mit einem Photon identischer Energie ausgelöst, wohingegen spontane Emission ohne äußere Einwirkung von Vakuumfluktuationen ausgelöst wird [YU95]. Typische Ratenkonstanten betragen $10^7 - 10^9\,\mathrm{s}^{-1}$ [SHE11]. Aufgrund der vergleichsweise großen energetischen Separation des S_1 Zustands vom Grundzustand erfolgt $S_1 \rightsquigarrow S_0$ IC in der Regel um mehrere Größenordnungen langsamer ($10^6 - 10^7\,\mathrm{s}^{-1}$ [SHE11]) als IC zwischen angeregten Zuständen. Im Hinblick auf Anwendungen (z. B. OLEDs oder Sensibilisatoren) ist es im Allgemeinen wünschenswert die Umwandlung von Anregungsenergie in Wärme ausgehend vom S_1 Zustand möglichst gering zu halten. Ein weiterer konkurrierender Übergang ist Interkombination: Diese beschreibt den Übergang zwischen Domänen unterschiedlicher Multiplizität (inter-system crossing, ISC). In organischen Molekülen findet $S_1 \rightsquigarrow T_1$ ISC typischerweise mit Ratenkonstanten in der Größenordnung von $10^5 - 10^8\,\mathrm{s}^{-1}$ statt [SHE11].

Die Wahrscheinlichkeit von ISC ist abhängig von der Spin–Bahn-Kopplung. Diese bezeichnet die Wechselwirkung der Spindrehimpulse der Elektronen mit den Bahndrehimpulsen. Die Ausprägung der Wechselwirkung ist stark abhängig von der Elektronenverteilung der koppelnden Zustände sowie den Atomsorten. Beispielsweise nimmt die Kopplung tendenziell mit der Kernladungzahl zu (Schweratomeffekt). Gemäß den Auswahlregeln von El-Sayed [ES63] ist die direkte Kopplung nur dann groß, falls sich der Typus der Zustände ändert, beispielsweise für einen $^1(\pi\pi^*) \rightsquigarrow {}^3(n\pi^*)$-Übergang. Strahlende Rückkehr zum Grundzustand unter Spinumkehr wird als Phosphoreszenz bezeichnet. Analog zur ISC ist die Wahrscheinlichkeit von Phosphoreszenz abhängig von der Stärke der Spin–Bahn-Kopplung. Auf diese Weise borgt der Triplettzustand Übergangsmoment vom fluoreszenten Singulettzustand (intensity borrowing [Mar01]). Aufgrund dessen fallen typische Phosphoreszenzratenkonstanten organischer Moleküle ($10^{-2} - 10^3\,\mathrm{s}^{-1}$ [SHE11]) deutlich geringer aus als das spinerlaubte Pendant.

Die Anpassung des umgebenden Dielektrikums an angeregte elektronische Struktur erfolgt auf einer ähnlichen Zeitskala wie molekulare Schwingungen ($0{,}1 - 10\,\mathrm{ps}$ [Lak06]). Abgesehen von

intramolekularen Übergängen kann die Anregungsenergie durch Energietransferprozesse via Förster- [Fö48] oder Dexter-Mechanismus [Dex53] auf die Umgebung übertragen werden. Die Absorption mehrerer Photonen führt zu hochangeregten Molekülen und unter Umständen unerwünschten photochemischen Reaktionen (Photobleichung).

Zielsetzung dieser Arbeit

Im Hinblick auf die Kopplung von Zuständen gilt: Je stärker zwei Wellenfunktionen durch die Wirkung eines Operators wechselwirken, desto wahrscheinlicher ist der Übergang. Der Kopplung elektronischer Zustände durch molekulare Schwingungen kommt hierbei eine besondere Rolle zu: Die Bewegung des Kerngerüsts verursacht zum einen strahlungslose Übergänge innerhalb einer Multiplizität (interne Konversion, IC). Zum anderen führen Schwingungen zur Modulierung von elektronischen Kopplungen jeglicher Form, z. B. Spin–Bahn-Kopplung [Alb63, HS71, PGDM18, Mar21]. Dies ist insbesondere dann von Bedeutung, wenn die Kopplung zweier Zustände in erster Ordnung symmetrieverboten ist. Im Hinblick auf die Kopplung elektronischer Freiheitsgrade durch die Freiheitsgrade der Kerne muss an der Born–Oppenhemer-Näherung, einem der Eckpfeiler der quantenmechanischen Beschreibung chemischer Systeme, angesetzt werden. Sie besagt unter anderem, dass die elektronische Wellenfunktion für festgelegte Kernanordnungen generiert werden kann. Aus der Fixierung des Moleküls resultiert, dass der Einfluss der kinetischen Energie der Kerne auf die elektronischen Freiheitsgrade vernachlässigt wird. Aufbauend auf der Näherung ist es möglich sogenannte nichtadiabatische Kopplungsterme der elektronischen Freiheitsgrade sowie Freiheitsgrade der Kerne zu formulieren.

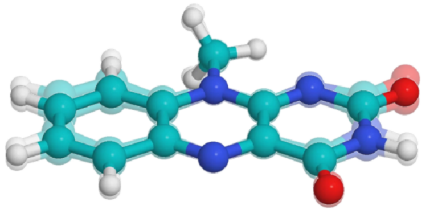

Abbildung 1.: Darstellung einer molekularen Schwingung von 10-Methylisoalloxazin.

Zur Beschreibung von nichtadiabatischen Kopplungs-Matrixelementen (nonadiabatic coupling matrix elements, NACMEs) kann auf diverse elektronische Strukturmethoden zurückgegriffen werden: Beispielsweise für zeitabhängige Dichtefunktionaltheorie (TD-DFT) [SF10, LL14, OFA$^+$14, ZH15], Coupled Cluster Methoden (CC) [Chr99, TS09, FMK18], Multikonfigurations-SCF (MCSCF) [LSY84, BJJ$^+$92, SHLM15, GDP$^+$16], complete-active space SCF mit störungstheoretischer Korrektur zweiter Ordnung (CASPT2) [PS17] und *ab-initio* Multireferenz-Konfi-

gurationswechselwirkung [MRCI(SD)] [LDS$^+$04, DLS$^+$04, KTH10] wurden analytische Ausdrücke formuliert und implementiert. Wellenfunktions-basierte Methoden eignen sich zwar zur präzisen Modellierung chemischer Systeme, allerdings beschränkt sich deren Anwendung auf vergleichsweise kleine Moleküle. Dichtefunktionaltheorie stellt eine günstige Alternative dar, eignet sich jedoch nicht zur Beschreibung von Zuständen mit Mehrfachanregungscharakter und Zustände mit charge-transfer-Charakter sowie Rydberg-Zustände werden qualitativ inkorrekt beschrieben [DH05].

Ziel dieser Arbeit ist es, eine Beschreibung für nichtadiabatische Kopplung und interne Konversion basierend auf dem DFT/MRCI Ansatz [GW99, MHK18] zu finden. DFT/MRCI-Wellenfunktionen stellen die Grundlage für viele Berechnungen von molekularen Eigenschaften dar und eignen sich zur Beschreibung großer chemischer Systeme. Die Methode stellt eine Kombination von Dichtefunktionaltheorie mit Wellenfunktions-basierter Methodik dar. Auf diese Weise konnten systematische Fehler von (TD)DFT korrigiert werden, während DFT/MRCI deutlich geringere Anforderungen an die Rechenkapazitäten stellt als *ab-initio* Methoden wie MRCI oder CCSD(T) (CC mit vollständiger Behandlung von Einfach- sowie Doppelanregungen und störungstheoretischer Behandlung von Dreifachanregungen).

Die besondere Herausforderung bei der Beschreibung von NACMEs für DFT/MRCI ist, dass für den semiempirschen Hamiltonoperator und folglich DFT/MRCI-Wellenfunktionen keine analytischen Gradienten definiert sind, sodass ein numerischer Ansatz verfolgt wird. Im Unterschied zu analytischen Implementierungen lassen sich numerische Verfahren grundsätzlich unabhängig von der gewählten elektronischen Strukturmethode anwenden. Der numerische Ansatz geht jedoch mit einem enormen Rechenaufwand / Speicherbedarf einher, sodass ein praktikabler Kompromiss gefunden werden muss.

Vor der Aufnahme meines Promotionsvorhabens haben Plasser et al. einen vergleichsweise effizienten Ansatz zur Berechnung von nichtorthogonalen Überlapps komplexer Wellenfunktionen veröffentlicht [PRM$^+$16]. Basierend auf diesem Ansatz wurde im Rahmen dieser Arbeit ein Algorithmus für DFT/MRCI-Wellenfunktionen entwickelt, welcher in der Konsequenz zur Berechnung von NACMEs mittels zentralem Differenzenquotienten eingesetzt werden kann. Im Laufe meiner Dissertation haben Neville et al. eine konkurrierende Implementierung für DFT/MRCI veröffentlicht [NSS20]. Diese entspricht in weiten Teilen jener von Plasser et al. und ist auf Molekulardynamik-Simulationen ausgelegt. Im Rahmen meiner Dissertation wurde die Beschreibung interner Konversion in einem statischen Bild verfolgt.

Zur Quantifizierung von Ratenkonstanten für IC wird des Weiteren die Kopplung der Kernwellenfunktionen benötigt. Diesbezüglich bietet es sich an den dynamischen Zweig zur Beschrei-

bung nichtstrahlender Ratenkonstanten des Programms VIBES [TGM07, ETM11, ETM14b, ETM14a] zu erweitern. Voraussetzung hierfür ist die Formulierung einer entsprechenden Korrelationsfunktion.

Die primären Anwendungsbereiche der resultierenden Programme/Routinen sind im Rahmen dieser Arbeit die

- interne Konversion in der Singulett- und Triplettdomäne von Xanthon,
- und das Design von fluorierten Flavinderivaten zur Modifikation der Fluoreszenz- und Triplettquantenausbeuten.

Die Photophysik von Xanthonen ist seit vielen Jahren Gegenstand experimenteller [DM74, LL80, AK86, MSLJ+99, BJ92, CPB96, LMSFJ00, SSR+04, HSR+06, AGV+10, VRRC+14, MVT+16] und quantenchemischer [RPSABJ06, RCKS+10, RCSM11, RCVR+14, MVT+16, ARdHR21] Untersuchungen, bislang konnte jedoch keine theoretische Beschreibung für interne Konversion beigetragen werden. Am Institut für Theoretische Chemie und Computerchemie Düsseldorf wurden unter anderem Studien zur Charakterisierung von Ratenkonstanten für Interkombination in wässrigem Medium sowie in apolarer Umgebung für das Molekül Xanthon angestellt [RCEM13]. Im Rahmen dieser Arbeit werden die kinetischen Schemata revidiert und vervollständigt.

Der Flavinchromophor ist von besonderem Interesse, da er als Cofaktor in Photorezeptoren [CJWL99, GK02, BB05, LG12, CBPS14] und Fluoreszenzproteinen [DEC+07, CFK+08, JG15, BPR+15] fungiert. Die Modifikation des Strukturmotivs durch die Einbringung des Elementes Fluor stellt einen Forschungsgegenstand des Graduiertenkollegs ModISC (Modulation of intersystem crossing) dar, in welches diese Promotion eingebettet ist. Im Zusammenhang mit ModISC sind weitere Kollaborationen zur Berechnung von IC Ratenkonstanten der Chromophore Heptazin, HAP-3MF [2,5,8-Tris(4-fluoro-3-methylphenyl)-1,3,4,6,7,9,9*b*-Heptaazaphenalen] sowie NMA-dF (*N*-Methyl-difluoro-Acridon) entstanden.

Teil I.

Theorie

1.1. Born–Oppenheimer- und adiabatische Näherung

Die Born–Oppenheimer-Näherung [BO27, DYK04] ist einer der Eckpfeiler der Quantenchemie. Da Protonen eine deutlich größere Masse als Elektronen aufweisen ($m^+/m^- \approx 1836$) und die Bewegung der Kerne somit sehr viel langsamer ausfällt als jene der Elektronen, werden elektronische und Kern- Wellenfunktion mittels Produktansatz separiert,

$$\Psi_a^{eN}(r, R) = \varphi_a^e(r; R)\chi_a^N(R) \ , \tag{1}$$

und iterativ bestimmt. Ψ beschreibt im Rahmen dieser Arbeit die Gesamtwellenfunktion. R repräsentiert die Kernkoordinaten und r die elektronischen Koordinaten. Die Wellenfunktion Ψ_a^{eN} des Basiszustands a setzt sich aus der Kernwellenfunktion χ_a (Index N: Nuklear) und dem adiabatischen elektronischen Zustand φ_a (Index e: elektronisch) zusammen. Letzterer hängt parametrisch von R ab. Die Lösung der Schrödingergleichung erfolgt in zwei Schritten:

1. Lösung der elektronischen Schrödingergleichung für parametrische Kernkoordinaten R.
2. Lösung der Schrödingergleichung der Kerne unter Verwendung des vorab berechneten elektronischen Potenzials $E^0(R)$.

Der Einfluss der Kernbewegung ($\mathcal{T}^N$: kinetische Energie-Operator der Kerne) auf die elektronischen Freiheitsgrade wird vernachlässigt. Der Unterschied zwischen adiabatischer und Born–Oppenheimer-Näherung liegt darin, dass Erstere die adiabatische Korrektur $\widetilde{K}$ (siehe Unterkapitel 1.2) berücksichtigt.

Born–Oppenheimer-Näherung:

$$\left[\mathcal{T}^N + E_a^0(R) - E\right] \chi_a^N(R) = 0 \tag{2}$$

Adiabatische Näherung:

$$\left[\mathcal{T}^N + E_a^0(R) + \widetilde{K}^{aa}(R) - E\right] \chi_a^N(R) = 0 \tag{3}$$

Typischerweise wird die adiabatische Korrektur vernachlässigt / die Born–Oppenheimer-Näherung angewandt.

1.2. Nichtadiabatische Kopplung

Die nichtadiabatische Kopplung beschreibt den Einfluss der kinetischen Energie der Kerne auf die Elektronenverteilung. Sowohl Born–Oppenheimer- als auch adiabatische Näherung vernachlässigen die nichtadiabatische Kopplung der Potenzialhyperflächen. In der Konsequenz werden die im Unterkapitel 1.1 beschriebenen entkoppelten Gleichungssysteme für die Kernwellenfunktionen erhalten. Im Folgenden wird das Matrixelement der nichtadiabatischen Kopplung (NACME, nonadiabatic coupling matrix element) hergeleitet. Die Herleitung basiert auf [Yar95, DYK04] und erfolgt unter Verwendung atomarer Einheiten sowie der in Abschnitt 1.1 eingeführten Nomenklatur.

$$\Psi^{eN}(r,R) = \sum_a \Psi_a^{eN}(r,R) = \sum_a \varphi_a^e(r;R)\chi_a^N(R) \tag{4}$$

Die Wellenfunktion Ψ^{eN} wird in der Basis der Wellenfunktionen aller Zustände entwickelt. Die elektronischen Zustände sind Eigenfunktionen des nichtrelativistischen Born–Oppenheimer-Hamiltonians $\mathcal{H}^0 = \mathcal{T}^e + \mathcal{V}^{ee} + \mathcal{V}^{eN} + \mathcal{V}^{NN}$:

$$\mathcal{H}^0(r;R)\varphi_a^e(r;R) = E_a^0(R)\varphi_a^e(r;R)\ . \tag{5}$$

Zusammen mit dem kinetischen Energieoperator der Kerne (κ: Freiheitsgrade) ergibt sich der gesamte Hamiltonoperator

$$\mathcal{H}^{eN}(r;R) = -\sum_\kappa (2M_\kappa)^{-1}\Delta_\kappa + \mathcal{H}^0(r;R) \equiv \mathcal{T}^N + \mathcal{H}^0(r;R)\ . \tag{6}$$

Wirkung von $\mathcal{H}^{eN}$ auf die Gesamtwellenfunktion Ψ_{eN} und Ausführen des Skalarprodukts mit dem elektronischen Basiszustand φ_a^e liefert folgendes Gleichungssystem für die Kernwellenfunktionen χ^N:

$$\begin{aligned}&\left[\mathcal{T}^N + E_a^0(R) + \widetilde{K}^{aa}(R) - E\right]\chi_a^N(R) \\ &= -\sum_{b\neq a}\left[\widetilde{H}^{ab}(R) + \sum_\kappa\left(-M_\kappa^{-1}f_\kappa^{ab}(R)\nabla_\kappa\right)\right]\chi_b^N(R)\ .\end{aligned} \tag{7}$$

Bei Gleichung 7 handelt sich um ein gekoppeltes Gleichungssystem, d. h. die Eigenfunktionen der Kernwellenfunktionen sind voneinander abhängig. Es treten zwei unterschiedliche elektronische Kopplungs-Matrixelemente auf, die sogenannten nichtadiabatischen Kopplungen:

1. Kopplung erster Ordnung f_κ^{ab},

2. Kopplung zweiter Ordnung $\widetilde{h}^{ab}$ (vgl. Gleichungen 11 und 12).

Diese Terme resultieren aus der Wirkung des kinetischen Energieoperators der Kerne $\mathcal{T}^N$ auf die Wellenfunktionen der Zustände Ψ_a^{eN}:

$$\begin{aligned}\mathcal{T}^N\Psi_a^{eN} &= -\sum_\kappa (2M_\kappa)^{-1}\Delta_\kappa\left(\varphi_a\chi_a\right) \\ &= -\sum_\kappa (2M_\kappa)^{-1}\nabla_\kappa\left[(\nabla_\kappa\varphi_a)\chi_a + \varphi_a\nabla_\kappa\chi_a\right] \\ &= -\sum_\kappa (2M_\kappa)^{-1}[(\Delta_\kappa\varphi_a)\chi_a + 2(\nabla_\kappa\varphi_a)\nabla_\kappa\chi_a + \varphi_a\Delta_\kappa\chi_a]\ .\end{aligned} \tag{8}$$

Ausführung des Skalarprodukts mit demselben elektronischen Zustand φ_a liefert

$$-\sum_\kappa (2M_\kappa)^{-1}\left\langle\varphi_a\,|\,\Delta_\kappa\,|\,\varphi_a\chi_a\right\rangle = -\sum_\kappa (2M_\kappa)^{-1}\left(\left\langle\varphi_a\,|\,\Delta_\kappa\,|\,\varphi_a\right\rangle + \Delta_\kappa\right)\chi_a\ . \tag{9}$$

Der Beitrag $-\sum_\kappa(2M_\kappa)^{-1}\Delta_\kappa\chi_a = \mathcal{T}^N\chi_a$ beschreibt die kinetische Energie der Kerne und das Diagonalelement ist in den Gleichungen 3 und 7 durch $\widetilde{K}^{aa}$ wiedergegeben. Das Matrixelement $\langle\varphi_a\,|\,\Delta_\kappa\,|\,\varphi_a\rangle$ ist die sogenannte adiabatische Korrektur der Born–Oppenheimer-Potenzialfläche. Das Matrixelement $\langle\varphi_a\,|\,\nabla_\kappa\,|\,\varphi_a\rangle = f^{aa}$ verschwindet aus Symmetriegründen (siehe Abschnitt 1.2.2).

Die Kopplungsterme werden analog durch das Skalarprodukt mit φ_b erhalten:

$$-\sum_\kappa (2M_\kappa)^{-1}\left\langle\varphi_a\,|\,\Delta_\kappa\,|\,\varphi_b\chi_b\right\rangle = -\sum_\kappa (2M_\kappa)^{-1}\left(\left\langle\varphi_a\,|\,\Delta_\kappa\,|\,\varphi_b\right\rangle + 2\left\langle\varphi_a\,|\,\nabla_\kappa\,|\,\varphi_b\right\rangle\nabla_\kappa\right)\chi_b\ . \tag{10}$$

Der erste Summand beschreibt die nichtadiabatische Kopplung zweiter Ordnung. Der Term ist der entsprechende Außerdiagonalbeitrag zu $\widetilde{K}^{aa}$. Die zugeordnete Abkürzung in Gleichung 7 lautet $\widetilde{H}^{ab}$:

$$\widetilde{H}^{ab}(R) = \sum_\kappa (-2M_\kappa)^{-1}\widetilde{h}^{ab}_{\kappa,\kappa}(R)\ , \tag{11}$$

mit

$$\widetilde{h}^{ab}_{\kappa,\gamma}(R) = \left\langle\varphi_a\,|\,\nabla_\kappa\nabla_\gamma\varphi_b\right\rangle\ . \tag{12}$$

Die Kreuzterme liefern die nichtadiabatische Kopplung erster Ordnung. Diese zeichnet sich dadurch aus, dass sowohl die elektronische Wellenfunktion als auch die Kernwellenfunktion einfach nach den Kernkoordinaten abgeleitet werden. Die Ordnung bezieht sich auf die elektronische Kopplung. Das Matrixelement wird typischerweise durch f^{ab} abgekürzt:

$$f^{ab}_\kappa(R) = \left\langle\varphi_a\,|\,\nabla_\kappa\varphi_b\right\rangle\ . \tag{13}$$

Beide Terme zweiter Ordnung ($\widetilde{H}^{ab}$ und $\widetilde{K}^{aa}$) werden üblicherweise vernachlässigt und in der Folge nicht weiter behandelt. Nichtadiabatische Kopplung vermittelt Übergänge zwischen Potenzialhyperflächen identischer Spinquantenzahl S und identischer magnetischer Spinquantenzahl M_S.

1.2.1. Singularität

Der Betrag von f_{ab} ist antiproportional zur vertikalen Energiedifferenz ΔE_{ab} der koppelnden Zustände. Im Falle entarteter Zustände / An konischen Durchschneidungen (siehe Abbildung 2) verhält sich die Kopplung singulär:

$$\lim_{\Delta E_{ab} \to 0} |f_{ab}| = \infty \ . \tag{14}$$

Mathematisch lässt sich dieses Verhalten durch eine andere Formulierung des Matrixelements nachvollziehen. Hierzu wird von der Eigenwertgleichung $\mathcal{H}\varphi_a = E_a\varphi_a$ ausgegangen [Dup81]. Räumliche Ableitung nach einer beliebigen Koordinate κ liefert:

$$\begin{aligned} &\Rightarrow \quad \nabla_\kappa \left(\mathcal{H}\varphi_a\right) = \nabla_\kappa \left(E_a\varphi_a\right) \\ &\Leftrightarrow \quad (\nabla_\kappa \mathcal{H})\varphi_a + \mathcal{H}\nabla_\kappa\varphi_a = (\nabla_\kappa E_a)\varphi_a + E_a\nabla_\kappa\varphi_a \ . \end{aligned} \tag{15}$$

Ausführung des Skalarprodukts mit der elektronischen Wellenfunktion φ_b vereinfacht den Ausdruck zu:

$$\Rightarrow \quad \langle \varphi_b \,|\, \nabla_\kappa \mathcal{H} \,|\, \varphi_a \rangle + \langle \varphi_b \,|\, \mathcal{H} \,|\, \nabla_\kappa \varphi_a \rangle = E_a \langle \varphi_b \,|\, \nabla_\kappa \varphi_a \rangle \ . \tag{16}$$

Unter Anwendung der Antisymmetrie von f_{ba} (siehe Abschnitt 1.2.2) und der Hermitizität des Hamiltonoperators lässt sich schlussendlich der gewünschte Ausdruck zur Beschreibung der Singularität nichtadiabatischer Kopplung für kreuzende Zustände formulieren:

$$\Rightarrow \quad f_{ab} = \langle \varphi_a \,|\, \nabla_\kappa \varphi_b \rangle = (E_b - E_a)^{-1} \langle \varphi_a \,|\, \nabla_\kappa \mathcal{H} \,|\, \varphi_b \rangle \ . \tag{17}$$

Die Auswertung des Hellmann–Feynman-Ausdrucks in Gleichung 17 erfordert die Auswertung von Einelektronenintegralen [HV80].

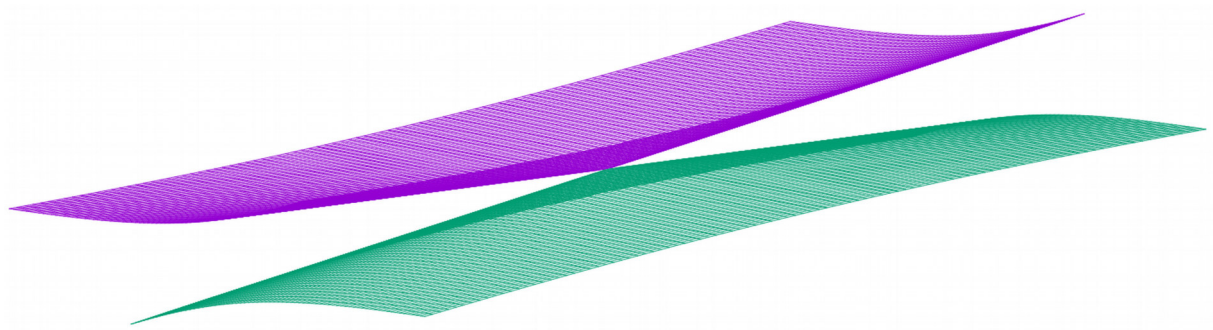

Abbildung 2.: Plot einer konischen Durchschneidung zweier Potenzialflächen eines Modellsystems mit zwei Schwingungsfreiheitsgraden. Die Darstellung ergibt sich gemäß der Gleichung $E_{1/2}(\vec{R}) = \tilde{E} + 1/2(h_1 + h_2)\vec{g}_{12} \pm 1/2[(h_1 - h_2)^2\vec{g}_{12}^2 + 4h_{12}^2\vec{c}_{12}^2]^{1/2}$ mit dem Gradienten der Energiedifferenz $\vec{g}_{12} = \frac{\partial(H_{11}-H_{22})}{\partial\vec{R}}$, dem interstate coupling vector $\vec{c}_{12} = \langle\varphi_1|\frac{\partial\hat{\mathcal{H}}}{\partial\vec{R}}|\varphi_2\rangle$ und $H_{11/22} = \tilde{E} + h_{1/2}\vec{g}_{12}$ [HLH63, Yar95].

1.2.2. Symmetrieverhalten von NACMEs

Ableitung eines beliebigen Überlapps elektronischer Zustände nach einer Koordinate κ liefert

$$\nabla_\kappa \langle\varphi_a \,|\, \varphi_b\rangle = \langle\nabla_\kappa\varphi_a \,|\, \varphi_b\rangle + \langle\varphi_a \,|\, \nabla_\kappa\varphi_b\rangle \ . \tag{18}$$

Für orthonormierte Zustände ($S_{ab} = \delta_{ab}$) gilt

$$\nabla_\kappa \langle\varphi_a \,|\, \varphi_b\rangle = \nabla_\kappa S_{ab} = 0 \ . \tag{19}$$

Somit verhalten sich NACMEs erster Ordnung antisymmetrisch bezüglich Vertauschung der Zustände a und b:

$$\begin{aligned} \langle\varphi_a \,|\, \nabla_\kappa\varphi_b\rangle &= -\langle\nabla_\kappa\varphi_a \,|\, \varphi_b\rangle \\ f_\kappa^{ab} &= -f_\kappa^{ba} \ . \end{aligned} \tag{20}$$

Der Ableitungsoperator transformiert sich entsprechend der Symmetrie der Koordinate κ. Für $f_\kappa^{ab} \neq 0$ muss das direkte Produkt der irreduziblen Darstellung der Koordinate und der irreduziblen Darstellungen der elektronischen Zustände die totalsymmetrische Darstellung enthalten:

$$\Gamma^a \otimes \Gamma^\kappa \otimes \Gamma^b \supset A \ . \tag{21}$$

1.3. Numerische Berechnung von NACMEs

Die numerische Berechnung nichtadiabatischer Kopplung erfolgt durch einen zentralen Differenzenquotienten [MW06]. Auf diese Weise kann die Ableitung der elektronischen Wellenfunktion nach den Freiheitsgraden der Kerne, $\nabla_R \varphi_b$, durch Auslenkungen entlang Normalkoordinaten Q_κ $[\Psi_b(\vec{R}_0 \pm \epsilon\vec{e}_\kappa)]$ beschrieben werden. Die elektronische Kopplung entlang einer Mode κ wird im Rahmen dieser Arbeit durch den Differenzenquotienten der Änderung des nichtorthogonalen Überlapps der Wellenfunktionen und der Schrittweite (2)ϵ erhalten. $\vec{e}_\kappa$ ist ein Einheitsvektor, der die Auslenkung entlang der Mode κ beschreibt.

$$
\begin{aligned}
f_{ab}(\vec{R}_0) &= \left\langle \varphi_a(\vec{R}) \,\middle|\, \nabla_R \varphi_b(\vec{R}) \right\rangle \Big|_{\vec{R}_0} \\
&= \nabla' \left\langle \varphi_a(\vec{R}) \,\middle|\, \varphi_b(\vec{R}') \right\rangle \Big|_{\vec{R}'=\vec{R}} \\
&= \nabla' S_{ab}(\vec{R}, \vec{R}')_{\vec{R}'=\vec{R}} \\
&= \sum_\kappa \frac{\partial}{\partial Q_\kappa} S_{ab}(\vec{R}_0; \vec{R}_0, Q_\kappa) \\
&= \lim_{\epsilon\to 0} \sum_\kappa \left[S_{ab}(\vec{R}_0, \vec{R}_0 + \epsilon\vec{e}_\kappa) - S_{ab}(\vec{R}_0, \vec{R}_0 - \epsilon\vec{e}_\kappa) \right] \frac{\vec{e}_\kappa}{2\epsilon}
\end{aligned}
\tag{22}
$$

1.3.1. Nicht-orthogonaler Überlapp

Der nichtorthogonale Überlapp zweier Slaterdeterminanten, Φ und Φ', lässt sich mit Hilfe der Definition der Slaterdeterminante (siehe Gleichung 23) beschreiben. Folgende Gleichungen für den Überlapp sind im Wesentlichen von Plasser et al. [PRM+16] übernommen und wurden ursprünglich von Per-Olov Löwdin hergeleitet [Löw55].

$$
|\Phi\rangle = \frac{1}{\sqrt{n!}} \sum_{\sigma\in S_n} \operatorname{sgn}(\sigma)\, \phi_{\sigma(1)}(r_1) \cdots \phi_{\sigma(n)}(r_n) \ . \tag{23}
$$

ϕ repräsentiert Molekülorbitale. Die symmetrische Gruppe S_n besteht aus allen Permutationen der n Elektronen innerhalb der Molekülorbitale und für die Signumfunktion $\operatorname{sgn}(\sigma)$ gilt:

$$
\operatorname{sgn}(\sigma) \coloneqq \begin{cases} +1, & \text{falls } \sigma \text{ gerade Permutation} \\ -1, & \text{falls } \sigma \text{ ungerade Permutation} \ . \end{cases} \tag{24}
$$

Der Überlapp von Φ und Φ' ist gegeben durch

$$\langle \Phi \,|\, \Phi' \rangle = \frac{1}{n!} \sum_{\sigma \in S_n} \mathrm{sgn}(\sigma) \sum_{\tau \in S_n} \mathrm{sgn}(\tau) \left\langle \phi_{\sigma(1)} \middle| \phi'_{\tau(1)} \right\rangle \cdots \left\langle \phi_{\sigma(n)} \middle| \phi'_{\tau(n)} \right\rangle \ . \tag{25}$$

Die Doppelsumme über die Signumfunktionen liefert $n! \times n!$ Summanden. Der Überlapp kann mit Hilfe der Leibniz-Formel als Determinante formuliert werden. Beide Signumfunktionen für die Permutationen der Vektoren lassen sich vor die Determinante ziehen:

$$\begin{aligned} \langle \Phi \,|\, \Phi' \rangle &= \frac{1}{n!} \sum_{\sigma \in S_n} \mathrm{sgn}(\sigma) \begin{vmatrix} \left\langle \phi_{\sigma(1)} \middle| \phi'_1 \right\rangle & \cdots & \left\langle \phi_{\sigma(1)} \middle| \phi'_n \right\rangle \\ \vdots & \ddots & \vdots \\ \left\langle \phi_{\sigma(n)} \middle| \phi'_1 \right\rangle & \cdots & \left\langle \phi_{\sigma(n)} \middle| \phi'_n \right\rangle \end{vmatrix} \\ &= \frac{1}{n!} \sum_{\sigma \in S_n} \mathrm{sgn}(\sigma)\mathrm{sgn}(\sigma) \det(\mathbf{S}) = \det(\mathbf{S}) \end{aligned} \tag{26}$$

mit

$$\mathbf{S} = \begin{pmatrix} \langle \phi_1 \,|\, \phi'_1 \rangle & \cdots & \langle \phi_1 \,|\, \phi'_n \rangle \\ \vdots & \ddots & \vdots \\ \langle \phi_n \,|\, \phi'_1 \rangle & \cdots & \langle \phi_n \,|\, \phi'_n \rangle \end{pmatrix} \ . \tag{27}$$

Somit kann der Überlapp zweier beliebiger[1] Slaterdeterminanten durch die Determinante einer Matrix mit Einträgen aller wechselseitigen Überlapps der Molekülorbitale beschrieben werden. Für orthogonale Wellenfunktionen reduziert sich das Problem auf das Produkt der Diagonaleinträge. Die Matrix $\mathbf{S}$ ist eine reguläre und damit invertierbare Matrix.

Eine beliebige elektronische Wellenfunktion φ_a kann als Linearkombination von Slaterdeterminanten geschrieben werden:

$$\varphi_a = \sum_k c_{a,k} \Phi_{a,k} \ . \tag{28}$$

Der Überlapp von $\varphi_a(R)$ mit $\varphi_b(R')$ lässt sich somit als Doppelsumme schreiben:

$$\langle \varphi_a \,|\, \varphi_b \rangle = \sum_{k,j} c_{a,k} c_{b,j} \langle \Phi_{a,k} \,|\, \Phi_{b,j} \rangle \ . \tag{29}$$

Gleichung 29 offenbart, dass Überlapps elektronischer Wellenfunktionen durch Linearkombinationen von Determinanten beschrieben werden.

[1] Gleichung 26 ist für Slaterdeterminanten mit der gleichen Anzahl an Elektronen definiert.

1.3.2. Berechnung von Determinanten

Aus Gleichung 29 geht hervor, dass die Vorgehensweise zur Auswertung von Determinanten von entscheidender Bedeutung für die Rechendauer nichtorthogonaler Überlapps elektronischer Wellenfunktionen ist. Zur Berechnung einer Determinante gibt es eine Vielzahl von Verfahren, die sich mitunter drastisch im Rechenaufwand unterscheiden. Das Scaling kann wesentlich von einer Zerlegung der $n \times n$-dimensionalen Überlappmatrix $\mathbf{S}$ profitieren. Im besten Fall wird die Matrix in zwei Dreiecksmatrizen (LU: 'lower–upper') zerlegt,

$$\mathbf{S} = \mathbf{LU} \ , \tag{30}$$

sodass lediglich die Produkte der Diagonalelemente in die Berechnung der Determinante eingehen, da alle Terme mit Außerdiagonalbeitrag verschwinden:

$$\Rightarrow \quad \det(\mathbf{S}) = \det(\mathbf{L}) \det(\mathbf{U}) = \prod_{i}^{n} \mathbf{L}_{ii} \prod_{i}^{n} \mathbf{U}_{ii} \ . \tag{31}$$

Die Dreieckszerlegung durch das gaußsche Eliminationsverfahren geht mit etwa $\frac{2}{3}n^3$ Rechenoperationen einher [TB97]. Im Vergleich dazu liefern die direkte Auswertung mit der Leibniz-Formel oder dem Laplaceschen Entwicklungssatz $n!$ Summanden. Lee et al. gehen für ihre Implementierung von nichtorthogonalen Überlapps von TDDFT-Wellenfunktionen von der Leibniz-Formel aus und führen Schemata zur Kürzung der Summe von Produkten von MO-Überlapps ein. Hierfür werden die Faktoren, nichtorthogonale MO-Überlapps, als Parameter für die Ordnung der Schemata verwendet [LKLC19]. Der Laplacesche Entwicklungssatz,

$$\det(\mathbf{S}) = \sum_{i}^{n} (-1)^{i+j} \ s_{ij} \ \det(\mathbf{S}_{ij}) = \sum_{j}^{n} (-1)^{i+j} \ s_{ij} \ \det(\mathbf{S}_{ij}) \ , \tag{32}$$

beschreibt die Determinante als Linearkombination von n $[(n-1) \times (n-1)]$-dimensionalen Unterdeterminanten/Minoren $\det(\mathbf{S}_{ij})$. Diese werden durch Streichen der i-ten Zeile sowie j-ten Spalte erhalten. Unter der Bedingung, dass Minoren wiederverwendet werden, eignet sich der Entwicklungssatz zur Vereinfachung des durch Gleichung 29 beschriebenen Problems. Entscheidend für den Nutzen dieser Strategie ist die Fragestellung, wie häufig die Minoren wiederverwendet werden können.

$$\frac{2}{3}xn^3 > \frac{2}{3}n(n-1)^3 + xn \tag{33}$$

1. Die linke Seite der Ungleichung beschreibt den Rechenaufwand für x Determinanten, die mit LU-Zerlegung berechnet werden.

2. Die rechte Seite der Ungleichung beschreibt den Rechenaufwand für x Determinanten, deren Unterdeterminanten mit LU-Zerlegung berechnet werden und gemäß dem Laplaceschen Entwicklungssatz wiederverwendet werden.

Fall 2 ist von Vorteil, falls x in etwa die Dimension der Determinante übersteigt (der lineare Term xn wird zur Vereinfachung vernachlässigt):

$$\begin{aligned} \frac{2}{3}xn^3 &> \frac{2}{3}n(n-1)^3 \\ x &> (n-1)^3/n^2 \\ x &> n - 3 + 3n^{-1} - n^{-2} \\ x &> n - 3 \ . \end{aligned} \tag{34}$$

Eine genäherte allgemeine Form der Ungleichung ist gegeben durch

$$x > n^u + \mathcal{O}\left(n^{u-1}\right) \ . \tag{35}$$

Hierbei beschreibt $u = 1$ die Wiederverwendung von Level 1 Minoren, $u = 2$ bezieht sich auf Level 2 Minoren, etc. Plasser et al. beschränken sich in ihrer Implementierung für nichtorthogonalen Überlapp auf die Kombination von LU-Zerlegung mit Level 1 Minoren [PRM$^+$16]. Die Erweiterung der Strategie auf $u = 2$ wurde von Sapunar et al. für CIS-artige Wellenfunktionen umgesetzt [SPDD19].

Eine alternative Herangehensweise an Gleichung 29 liefert das Determinanten Lemma:

$$\det(\mathbf{S} + \mathbf{u}\mathbf{v}^T) = \det(\mathbf{S})(1 + v^T\mathbf{S}^{-1}u) \ . \tag{36}$$

Setzt man $\mathbf{u}$ oder $\mathbf{v}$ als Einheitsvektor, so ergibt sich folgender Ausdruck:

$$\det(\mathbf{S} + \mathbf{X}) = \det(\mathbf{S})[1 + \mathrm{tr}(\mathbf{X}\mathbf{S}^{-1})] \ . \tag{37}$$

Hierbei beinhaltet die Matrix $\mathbf{X}$ lediglich einen Zeilen- bzw. Spaltenvektor mit Einträgen ungleich null [Rang($\mathbf{X}$) = 1]. Falls mehrere Vektoren der ursprünglichen Matrix $\mathbf{S}$ verändert werden sollen, so lässt sich das Lemma rekursiv anwenden. Die Inversen der intermediären Matrizen, $(\mathbf{S} + \mathbf{X})^{-1}$, lassen sich gemäß der Sherman–Morrison-Formel berechnen [Mil81]:

$$(\mathbf{S} + \mathbf{X})^{-1} = \frac{\mathbf{S}^{-1} - \mathbf{S}^{-1}\mathbf{X}\mathbf{S}^{-1}}{[1 + \mathrm{tr}(\mathbf{X}\mathbf{S}^{-1})]} \ . \tag{38}$$

Der Rechenaufwand dieses rekursiven Vorgehens ausgehend von det($\mathbf{S}$) und $\mathbf{S}^{-1}$ ist bestimmt durch die Matrizenmultiplikationen $\mathbf{S}^{-1}\mathbf{X}\mathbf{S}^{-1}$ [$\mathcal{O}\left(n^2\right)$].

1.3.3. Biorthogonalisierung

Eine triviale Überlegung zur Reduzierung des durch Gleichung 29 beschriebenen Rechenaufwands ist die Diagonalisierung der Überlappmatrizen, sodass der nichtorthogonale Überlapp durch das Produkt der Hauptdiagonaleinträge beschrieben wird. Hierbei gilt es zu beachten, dass Diagonalisierung nur dann vorteilhaft gegenüber LU-Zerlegung ist, falls die Überlappmatrix der MO Basen von $\varphi_a(R)$ und $\varphi_b(R')$ diagonalisiert wird. Diagonalisierung der einzelnen Determinanten in Gleichung 29 geht mit einem erhöhten Rechenaufwand einher ($\frac{4}{3}n^3$).

Bei den Matrizen, die aus der Berechnung des Überlapps von Slaterdeterminanten resultieren, handelt es sich zwangsläufig um asymmetrische Matrizen. Diagonalisierung durch die Behandlung als Eigenwertproblem liefert gemäß dem Spektralsatz jedoch nur für *normale* Matrizen orthonormale Eigenvektoren.

$$\mathbf{M}\mathbf{M}^\dagger = \mathbf{M}^\dagger\mathbf{M} \Leftrightarrow \mathbf{M}\ normal \tag{39}$$

Anschaulich bedeutet dies, dass für die betrachtete Problemstellung keine unitäre Transformation existiert, welche die MO Basen $\{\phi(R)\}$ und $\{\phi(R')\}$ biorthogonalisiert,

$$\sigma_i\delta_{ij} = \left\langle \tilde{\phi}_i(R) \,\middle|\, \tilde{\phi}_j(R') \right\rangle \ , \tag{40}$$

und gleichzeitig die Orthogonalität der einzelnen Basen erhält. Der Wert σ_i beschreibt den Überlapp der korrespondierenden Orbitale $\tilde{\phi}_i(R)$ und $\tilde{\phi}_i(R')$.

Alternativ kann nach zwei unterschiedlichen unitären Transformationen gesucht werden, welche zur gewünschten Biorthogonalisierung der Molekülorbitale führen und die Orthonormierung für die unterschiedlichen Geometrien aufrechterhalten. Die unitäre Transformation der symmetrischen Matrix $\mathbf{S}^\dagger\mathbf{S}$ beschreibt den ersten Satz orthonormaler Eigenvektoren:

$$\begin{aligned} \mathbf{S}^\dagger\mathbf{S} &= \mathbf{X}\mathbf{\Lambda}\mathbf{X}^\dagger \\ &= \mathbf{X}\sigma^\dagger\sigma\mathbf{X}^\dagger \ . \end{aligned} \tag{41}$$

Eine beliebige Diagonalmatrix $\mathbf{\Lambda}$ kann durch ein Produkt der Form $\sigma^\dagger\sigma$ beschrieben werden.

Für (reellwertige) Überlapps gilt $\sigma^\dagger = \sigma = \mathbf{\Lambda}^{\frac{1}{2}}$. Gesucht werden Transformationen,

$$\tilde{\phi}_i(R) = \sum_j \phi_j(R)\mathbf{Y}_{ji} \ , \tag{42}$$

$$\tilde{\phi}_i(R') = \sum_j \phi_j(R')\mathbf{X}_{ji} \ , \tag{43}$$

so dass Gleichung 40 erfüllt ist. Einführung der Matrizen $\mathbf{Y}^\dagger\mathbf{Y} = \mathbf{I_n}$ und Einfügen in Gleichung 41 liefert die gewünschte diagonalisierte Überlappmatrix mittels biorthogonalisierter, orthonormaler MO Basen:

$$\begin{aligned} \mathbf{S}^\dagger\mathbf{S} &= \mathbf{X}\sigma\mathbf{Y}^\dagger\mathbf{Y}\sigma\mathbf{X}^\dagger \\ \Rightarrow \quad \sigma &= \mathbf{Y}^\dagger\mathbf{S}\mathbf{X} \ . \end{aligned} \tag{44}$$

Die sogenannte Singulärwertzerlegung (singular value decomposition, SVD) stellt eine Verallgemeinerung der Eigenwertzerlegung für beliebige Matrizen dar. Bei den Diagonaleinträgen der Matrix σ handelt es sich um Singulärwerte. Diese entsprechen paarweisen Überlapps von Orbitalen der MO Basen $\{\tilde{\phi}(R)\}$ und $\{\tilde{\phi}(R')\}$ ('corresponding orbitals' [AH61], vgl. Gleichung 40). Durch Singulärwertzerlegung der Überlappmatrix $\mathbf{S}$ der MO Basen werden biorthogonale Molekülorbitale erhalten, die in der Konsequenz nur für Anregungen mit identischen Erzeugern und Vernichtern Beiträge zum Überlapp der Gesamtwellenfunktionen liefern. Dieses Vorgehen eignet sich jedoch nur für Methoden, deren Energie invariant bezüglich der Rotation der MOs ist (Gleichungen 42 und 43). Für DFT/MRCI ist dies nicht der Fall [PKEM12], die Parametrisierungen gelten für kanonische MOs [MHK18].

Für CIS-Wellenfunktionen ist SVD von besonderer Bedeutung: Die Zerlegung der CI Koeffizientenmatrix ($n_{\text{occ}} \times n_{\text{virt}}$) liefert die kompakteste Repräsentation der Wellenfunktion. Die Anwendung der resultierenden Transformationsmatrizen auf die n_{occ} besetzten bzw. n_{virt} virtuellen Orbitale liefert sogenannte 'natural transition orbitals' (NTOs) [Mar03, May07]. Neben der verbesserten Interpretierbarkeit von NTOs [PL12] eignen sich diese für eine effiziente Berechnung nichtorthogonaler Überlapps von CIS-artigen Wellenfunktionen [SPDD19]. SVD wird zudem für die effiziente Berechnung nichtorthogonaler Konfigurationswechselwirkung (NOCI) benötigt [KSK$^+$67, PTN$^+$84, BN88].

1.3.4. Zerlegung in Blockmatrizen

Die Slaterdeterminanten in Gleichung 29 unterscheiden sich mitunter in der Besetzung einzelner Orbitale. Diese Eigenschaft wirft die Frage auf, wie Bestandteile der Determinanten möglichst effizient wiederverwendet werden können. In Abschnitt 1.3.3 wurden Ansätze basierend auf dem Laplaceschen Entwicklungssatz (siehe Gleichung 32) und dem Determinanten Lemma (siehe Gleichung 36) dargelegt. Alternativ lassen sich die Matrizen in Blöcke aufteilen [$(n = q + p) \times (n = q + p)$, siehe Abbildung 3]. L(D)U-Zerlegung einer Blockmatrix liefert einen Ausdruck für die Determinante:

$$
\begin{aligned}
|\mathbf{S}| &= \begin{vmatrix} \mathbf{V} & \mathbf{P} \\ \mathbf{O} & \mathbf{F} \end{vmatrix} && (45) \\
&= \left| \begin{pmatrix} \mathrm{I}_\mathbf{p} & \mathbf{P}\mathbf{F}^{-1} \\ 0 & \mathrm{I}_\mathbf{q} \end{pmatrix} \begin{pmatrix} \mathbf{V} - \mathbf{P}\mathbf{F}^{-1}\mathbf{O} & 0 \\ 0 & \mathbf{F} \end{pmatrix} \begin{pmatrix} \mathrm{I}_\mathbf{p} & 0 \\ \mathbf{F}^{-1}\mathbf{O} & \mathrm{I}_\mathbf{q} \end{pmatrix} \right| \\
&= \begin{vmatrix} \mathbf{V} - \mathbf{P}\mathbf{F}^{-1}\mathbf{O} & 0 \\ 0 & \mathbf{F} \end{vmatrix} \\
&= |\mathbf{V} - \mathbf{P}\mathbf{F}^{-1}\mathbf{O}||\mathbf{F}| \\
&\coloneqq |\mathbf{S}/\mathbf{F}||\mathbf{F}| \ . && (46)
\end{aligned}
$$

Gleichung 46 ist Schur's Determinanten Identität [Sch17, BS83, Zi-09]. $\mathbf{S}/\mathbf{F}$ ist das sogenannte Schurkomplement. Die Determinante der gesamten Matrix kann somit als Produkt der Determinante des Blocks $\mathbf{F}$ und der Determinante des Schurkomplements geschrieben werden.

Der Rechenaufwand für dieses Vorgehen ist nur dann vorteilhaft, falls Teile der Identität wiederverwendet werden können. Der Aufwand für $\mathbf{F}^{-1}$ und $|\mathbf{F}|$ skaliert insgesamt mit $\frac{4}{3}(n-q)^3$, sodass deren Wiederverwendung vorausgesetzt ist. Der Rechenaufwand der Matrizenmultiplikationen skaliert mit $2(n-q)^2 q$ ($\mathbf{P}\mathbf{F}^{-1} = \mathbf{G}$) sowie $2(n-q)q^2$ ($\mathbf{G}\mathbf{O}$). Für den Fall, dass zusätzlich zu $\mathbf{F}^{-1}$ und $|\mathbf{F}|$ die Matrix $\mathbf{G}$ wiederverwendet wird, reduziert sich der Rechenaufwand pro Determinante $|\mathbf{S}|$ im Wesentlichen auf $2(n-q)q^2$ Operationen. Dieser ist unabhängig von den Dimensionen der Blöcke geringer als die Durchführung von $\frac{2}{3}n^3$ Operationen für eine LU-Zerlegung. Umso größer der konstante Block $\mathbf{F}$ ausfällt ($p > q$), desto größer ist die Ersparnis an Rechenoperationen.

Anschaulich bedeutet ein konstanter $\mathbf{F}$ Block, dass die Besetzung der enthaltenen MOs unverändert bleibt. Darauf aubauend bedeutet ein konstanter $\mathbf{P}$ Block, dass die Slaterdeterminante an der Referenzgeometrie Φ konstant bleibt und sich lediglich Φ' ändert (siehe Abbildung 3).

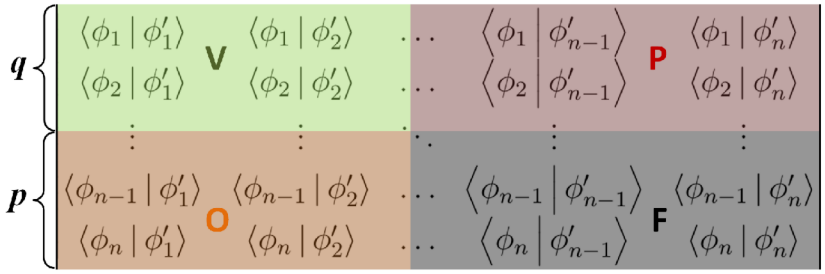

Abbildung 3.: Darstellung der Aufteilung einer Überlappmatrix beliebiger Slaterdeterminanten $|\phi_1\phi_2\dots\phi_{n-1}\phi_n|$ und $|\phi'_1\phi'_2\dots\phi'_{n-1}\phi'_n|$. Die Blöcke **V** $(q \times q)$ und **F** $(p \times p)$ sind quadratische Matrizen und die Dimensionen der Außerdiagonalblöcke sind dementsprechend $q \times p$ für **P** und $p \times q$ für **O**. Im Falle der HF-Referenzen beschreiben ϕ_1 und ϕ'_1 die HOMO (highest occupied molecular orbital) Orbitale. Der **F**-Block ist einer konstanten Orbitalbesetzung in beiden Slaterdeterminanten zugeordnet und die Orbitale des **V**-Blocks können durch virtuelle Orbitale ersetzt werden. Für den Fall, dass der **F**-Block konstant ist und die Slaterdeterminante an der Referenzgeometrie $|\phi_1\phi_2\dots\phi_{n-1}\phi_n|$ gleich bleibt, ist der **P**-Block ebenso konstant.

1.4. Fermis Goldene Regel

Fermis Goldene Regel stellt einen quantenmechanischen Formalismus zur Berechnung von Ratenkonstanten dar [Fer95]. Die Regel gilt für den Übergang in ein Quasikontinuum von Endzuständen. Die Herleitung erfolgte ursprünglich von Paul Dirac und basiert auf zeitabhängiger Störungstheorie [Dir27]. Ausgehend von der zeitabhängigen Schrödingergleichung,

$$i\hbar\frac{\partial\Psi(\vec{r},t)}{\partial t} = [\hat{\mathcal{H}} + \hat{\mathcal{V}}(\vec{r},t)]\Psi(\vec{r},t) \ , \tag{47}$$

und einem orthonormalen Satz an Eigenfunktionen von $\hat{\mathcal{H}}$ multipliziert mit einem Phasenfaktor $e^{-itE_k/\hbar}$,

$$\Psi(\vec{r},t) = \sum_k c_k(t)\Psi_k(\vec{r})e^{-itE_k/\hbar} \ , \tag{48}$$

wird ein Ausdruck für die zeitliche Entwicklung der Gesamtwellenfunktion Ψ unter Einfluss des Störoperators $\hat{\mathcal{V}}(\vec{r},t)$ erhalten

$$i\hbar\sum_k \frac{\partial c_k(t)}{\partial t}\Psi_k(\vec{r})e^{-itE_k/\hbar} = \sum_k \hat{\mathcal{V}}(\vec{r},t)c_k(t)\Psi_k(\vec{r})e^{-itE_k/\hbar} \ . \tag{49}$$

In der Folge wird von einer zeitlich konstanten, instantan angeschalteten Störung des Systems

$[\hat{\mathcal{V}}(\vec{r})]$ ausgegangen. Multiplikation mit dem Basiszustand $|\Psi_b\rangle$ und Zusammenfassen der Exponentialfunktionen liefert

$$i\hbar\frac{\partial c_b(t)}{\partial t} = \sum_k \left\langle \Psi_b \middle| \hat{\mathcal{V}} \middle| \Psi_k \right\rangle c_k(t) e^{it(E_b - E_k)/\hbar} \ . \tag{50}$$

$|c_b(t)|^2$ beschreibt die Aufenthaltswahrscheinlichkeit der Population in Zustand Ψ_b zum Zeitpunkt t. Gesucht wird ein Ausdruck zur Quantifizierung der Übergangswahrscheinlichkeit von einem Ausgangszustand $[c_a(0) = 1]$ in eine Mannigfaltigkeit von Endzuständen $[c_b(0) = 0]$. Für schwache Störungen des Systems kann $c_a \overset{!}{=} 1$ (Koeffizient nullter Ordnung) gesetzt werden, um die Korrektur erster Ordnung für $c_b(t)$ zu erhalten [Gri95]. Die Summe in Gleichung 50 wird somit auf den Ausgangszustand, Ψ_a, reduziert, und die Energiedifferenz bezieht sich folgerichtig auf Ψ_a und Ψ_b ($\Delta E = E_b - E_a$):

$$i\hbar\frac{\partial c_b(t)}{\partial t} = \left\langle \Psi_b \middle| \hat{\mathcal{V}} \middle| \Psi_a \right\rangle e^{it\Delta E/\hbar} \ . \tag{51}$$

Die Übergangswahrscheinlichkeit $\mathcal{P}_{ab}(t) = |c_b(t)|^2$ ist gegeben durch die Wahrscheinlichkeit das System zum Zeitpunkt t im Endzustand zu finden und wird durch Integration erhalten:

$$\mathcal{P}_{ab}(t) = 1/\hbar^2 \left| \left\langle \Psi_b \middle| \hat{\mathcal{V}} \middle| \Psi_a \right\rangle \right|^2 \left| \int_0^{t'} e^{it\Delta E/\hbar} dt' \right|^2 \tag{52}$$

$$= \left| \left\langle \Psi_b \middle| \hat{\mathcal{V}} \middle| \Psi_a \right\rangle \right|^2 |e^{it\Delta E} - 1|^2/\Delta E^2 \ . \tag{53}$$

Unter Anwendung der Eulerschen Formel für das Betragsquadrat der Exponentialfunktion wird Gleichung 54 erhalten.

$$\mathcal{P}_{ab}(t) = 4 \left| \left\langle \Psi_b \middle| \hat{\mathcal{V}} \middle| \Psi_a \right\rangle \right|^2 \sin^2(t\Delta E/2\hbar)/\Delta E^2 \ . \tag{54}$$

Die gesamte Funktion läuft aufgrund des Faktors $\sin^2(t\Delta E/2\hbar)/\Delta E^2$ für große Energiedifferenzen asymptotisch gegen null und weist ein ausgeprägtes globales Maximum für $\Delta E = 0$ auf. Mit zunehmender Zeit verschwinden die Nebenmaxima:

$$\lim_{t\to\infty} \frac{\sin^2(t\Delta E/2\hbar)}{(\Delta E/2\hbar)^2} = \pi t \delta(\Delta E/2\hbar) = 2\pi t\hbar\delta(\Delta E) \ . \tag{55}$$

Anschaulich bedeutet das Vorkommen von Nebenmaxima, dass Übergänge in Nachbarzustände mit ähnlicher Energie erlaubt sind. Die Unschärfe der Energie nimmt mit der Zeit ab. Mit Hilfe der Dirac-Funktion δ ergibt sich der finale Ausdruck für die zeitabhängige Wahrschein-

lichkeit des Übergangs $\Psi_a \rightsquigarrow \Psi_b$. Die Ratenkonstante ist definiert als die zeitliche Ableitung der Übergangswahrscheinlichkeit:

$$\dot{\mathcal{P}}_{ab}(t) = \frac{2\pi}{\hbar} \left| \left\langle \Psi_b \middle| \hat{\mathcal{V}} \middle| \Psi_a \right\rangle \right|^2 \delta(\Delta E) \ . \tag{56}$$

Gleichung 56 ist gültig für den Fall, dass der Übergang vom Ausgangszustand in ein Quasikontinuum von Endzuständen erfolgt. Zur Beschreibung strahlungsloser Übergänge ist es notwendig, die Kopplung der elektronischen sowie der Kern- Wellenfunktionen zu beschreiben. Die Ratenkonstante für einen vibronischen Ausgangszustand wird somit durch Summation über die vibronischen Sublevels des finalen Zustands erhalten:

$$k_{\mathrm{NR}} = \frac{2\pi}{\hbar} \sum_{\{\nu_b\}} \left| \hat{\mathcal{V}}_{ab} \right|^2 \delta(\Delta E) \ . \tag{57}$$

Gleichung 57 beschreibt Fermis Goldene Regel für irreversible strahlungslose Deaktivierung eines vibronischen Ausgangszustands, welcher durch den zeitunabhängigen Störoperator $\hat{\mathcal{V}}$ an eine Mannigfaltigkeit vibronischer Sublevels gekoppelt ist. Die Dirac-Funktion gewährleistet Energieerhaltung beim Übergang. Die Sublevels der Mannigfaltigkeit $\{\nu_b\}$ bilden für ausreichend große Energiedifferenzen ΔE ein Quasikontinuum, welches durch die energieabhängige Dichte der Niveaus von Ψ_b, $\rho_b(E)$, beschrieben wird.

Im Allgemeinen eignet sich Fermis Goldene Regel zur Beschreibung von Prozessen auf der μs–ps-Zeitskala. Ultraschnelle Übergänge auf der Femtosekundenskala werden durch starke vibronische Kopplung in der Nähe von konischen Durchschneidungen vermittelt und können deswegen nicht störungstheoretisch behandelt werden. Aufgrund der singulären Natur nichtadiabatischer Kopplung (siehe Abschnitt 1.2.1) gelangt die Population durch konische Durchschneidungen ("molekulare Tunnel", siehe Abbildung 2) unmittelbar zum energetisch tieferen Zustand. Entsprechende Übergänge stellen kohärente Prozesse dar: Der Übergang und die Schwingungsrelaxation finden auf der gleichen Zeitskala statt. Für entsprechende Geometrien bricht die Born–Oppenheimer-Näherung zusammen und zur Beschreibung der Dynamik des Übergangs muss in der Konsequenz die zeitabhängige Schrödingergleichung gelöst werden {z. B. mittels MCTDH (multi-configuration time-dependent Hartree) [MMC90, BJWM00, LKM17] oder TSH (trajectory surface hopping) [Tul90, CT14, DNG+19]}.

1.4.1. Korrelationsfunktion

Im Folgenden wird die Berechnung von Übergängen mittels Autokorrelationsfunktion motiviert. Es gilt hervorzuheben, dass sich die beschriebene Korrelation auf Kopplungen von Wellenfunktionen bezieht und von Elektronenkorrelation (siehe Abschnitt 1.5) abzugrenzen ist.

Die Anwendung Fermis Goldener Regel im Schrödinger-Bild ist mit großem Rechenaufwand verbunden. Die Berechnung von Überlappintegralen der Schwingungswellenfunktionen (Franck–Condon-Faktoren, siehe Abschnitt 1.4.2) ist bereits für kleine Systeme nur eingeschränkt praktikabel. Um eine weniger rechenaufwändige Herangehensweise zu formulieren, kann Fermis Goldene Regel vom Schrödinger- (S) in das Heisenberg-Bild (H) umgewandelt werden. Beide Modelle unterscheiden sich in der Behandlung von zeitabhängigen Problemen: Während im Schrödinger-Bild die zeitliche Entwicklung durch die Zustände beschrieben wird, erfolgt dies im Heisenberg-Bild durch die Operatoren. Im Heisenberg-Bild sind die Zustände somit stets zeitlich konstant, wohingegen im Schrödinger-Bild sowohl Operator als auch Eigenfunktion zeitlich variieren können. Beide Bilder lassen sich mit Hilfe eines unitären Zeitentwicklungsoperators $\hat{U}(t)$ ineinander überführen:

$$
\begin{aligned}
&\hat{\mathcal{O}}_S(t)|\Psi_S(t)\rangle = o|\Psi_S(t)\rangle \\
=&\left\langle \Psi_S(t) \,\middle|\, \hat{\mathcal{O}}_S(t) \,\middle|\, \Psi_S(t) \right\rangle = o \\
=&\left\langle \Psi_S(t) \,\middle|\, \hat{U}(t)\hat{U}^\dagger(t)\hat{\mathcal{O}}_S(t)\hat{U}(t)\hat{U}^\dagger(t) \,\middle|\, \Psi_S(t) \right\rangle \\
=&\left\langle \hat{U}^\dagger(t)\Psi_S(t) \,\middle|\, \hat{U}^\dagger(t)\hat{\mathcal{O}}_S(t)\hat{U}(t) \,\middle|\, \hat{U}^\dagger(t)\Psi_S(t) \right\rangle \\
=&\left\langle \Psi_S(0) \,\middle|\, \hat{U}^\dagger(t)\hat{\mathcal{O}}_S(t)\hat{U}(t) \,\middle|\, \Psi_S(0) \right\rangle \\
=&\left\langle \Psi_H \,\middle|\, \hat{\mathcal{O}}_H(t) \,\middle|\, \Psi_H \right\rangle \ .
\end{aligned}
\tag{58}
$$

Im Folgenden erfolgt die Transformation von Fermis Goldener Regel vom Schrödinger- in das Heisenberg-Bild. Zunächst wird die Resonanzbedingung in Gleichung 57 durch das Fourier Integral

$$
\delta(\Delta E)/\hbar = \delta(\Delta\omega) = \frac{1}{2\pi}\int_{-\infty}^{\infty} e^{it\Delta\omega}dt \tag{59}
$$

substituiert:

$$
k_{\mathrm{NR}} = \frac{1}{\hbar^2}\sum_{\{\nu_b\}} \left| \left\langle \Psi_b \,\middle|\, \hat{\mathcal{V}} \,\middle|\, \Psi_a \right\rangle \right|^2 \int_{-\infty}^{\infty} e^{it(E_b - E_a)/\hbar}dt \ . \tag{60}
$$

Mit dem Zeitentwicklungsoperator für einen zeitunabhängigen Hamiltonoperator,

$$
e^{-it\hat{\mathcal{H}}/\hbar}|\Psi_{a/b}(t)\rangle = e^{-itE_{a/b}/\hbar}|\Psi_{a/b}(t)\rangle \ , \tag{61}
$$

wird schließlich Fermis Goldene Regel im Heisenberg-Bild erhalten:

$$\begin{aligned} k_{\mathrm{NR}} &= \frac{1}{\hbar^2} \sum_{\{b\}} \int_{-\infty}^{\infty} \left\langle \Psi_a \middle| \hat{\mathcal{V}}_S \middle| \Psi_b \right\rangle \left\langle \Psi_b \middle| \hat{\mathcal{V}}_S \middle| \Psi_a \right\rangle e^{itE_b/\hbar} e^{-itE_a/\hbar} dt \\ &= \frac{1}{\hbar^2} \sum_{\{b\}} \int_{-\infty}^{\infty} \left\langle \Psi_a \middle| \hat{\mathcal{V}}_S \middle| \Psi_b \right\rangle \left\langle \Psi_b \middle| e^{it\hat{\mathcal{H}}/\hbar} \hat{\mathcal{V}}_S e^{-it\hat{\mathcal{H}}/\hbar} \middle| \Psi_a \right\rangle dt \\ &= \frac{1}{\hbar^2} \sum_{\{b\}} \int_{-\infty}^{\infty} \left\langle \Psi_a \middle| \hat{\mathcal{V}}_H(0) \middle| \Psi_b \right\rangle \left\langle \Psi_b \middle| \hat{\mathcal{V}}_H(t) \middle| \Psi_a \right\rangle dt \ . \end{aligned} \tag{62}$$

Der Integrand beschreibt die Korrelation der Störung des Systems zu Beginn des Übergangs ($t = 0$), wenn einzig der Ausgangszustand populiert ist, mit der Störung zu jedem späteren Zeitpunkt.

Der klassische Ausdruck für Autokorrelation einer Variable O ist gegeben durch [Cha87]

$$C_O(t, t') = \int \mathrm{d}\mathbf{q}\, \mathrm{d}\mathbf{p}\, O(\mathbf{q}, \mathbf{p}; t)\, O(\mathbf{q}, \mathbf{p}; t')\, \rho(\mathbf{q}, \mathbf{p}) \ . \tag{63}$$

Gleichung 63 folgt unmittelbar aus der Definition des Mittelwerts eines Ensembles im thermischen Gleichgewicht:

$$\langle O \rangle = \int \mathrm{d}\mathbf{q}\, \mathrm{d}\mathbf{p}\, O(\mathbf{q}, \mathbf{p}; t)\, \rho(\mathbf{q}, \mathbf{p}) \ . \tag{64}$$

Die Dichtefunktion $\rho(\mathbf{q}, \mathbf{p}) = Z^{-1} e^{-\beta E(\mathbf{q},\mathbf{p})}$ beschreibt die Verteilung der Mikrozustände im Phasenraum. Z ist die kanonische Zustandssumme und $\beta^{-1} = k_B T$ die thermische Energie. Mit Hilfe von $\sum_{\{b\}} |\Psi_b\rangle\langle\Psi_b| = 1$ lässt sich der quantenmechanische Ausdruck in Gleichung 62 in eine entsprechende Form bringen:

$$\begin{aligned} k_{\mathrm{NR}} &= \frac{1}{\hbar^2} \int_{-\infty}^{\infty} \left\langle \Psi_a \middle| \hat{\mathcal{V}}_H(0) \hat{\mathcal{V}}_H(t) \middle| \Psi_a \right\rangle dt \\ &= \frac{1}{\hbar^2} \int_{-\infty}^{\infty} dt\, \tilde{C}_{\hat{\mathcal{V}}}(0, t) \ . \end{aligned} \tag{65}$$

Die Berücksichtigung von Temperatureffekten ($T > 0\,K$) erfolgt analog: Unterschiedliche Ausgangszustände werden zugelassen und die Populationswahrscheinlichkeiten mittels Boltzmann-Verteilung festgelegt [IAWL93, ETM14a]:

$$\tilde{C}_{\hat{\mathcal{O}}}(t, t') = \sum_i Z^{-1} e^{-\beta E_i} \left\langle \Psi_a \middle| \hat{\mathcal{O}}_H(t) \hat{\mathcal{O}}_H(t') \middle| \Psi_a \right\rangle \ . \tag{66}$$

Die zeitabhängige Beschreibung von Übergängen mittels Korrelationsfunktion stellt eine vielseitig angewandte (z. B. Absorption [Lax52, MAYI85, Isl89, MHLL99], IC [HMLL98, IM07,

PYS07], ISC [ETM11, ETM14b], Elektronentransfer [LML$^+$03, IL91b, IL91a], etc. [O'R53, KT55, IDL00]) Methode dar.

1.4.2. Condon-Näherung und Franck–Condon-Faktoren

In der Condon-Näherung wird die Kopplung der elektronischen Wellenfunktionen als unabhängig von den Freiheitsgraden der Kerne angenommen. Dies ermöglicht die Vereinfachung der Integrale über die Gesamtwellenfunktionen $|\Psi\rangle = |\varphi\chi\rangle$ mittels Produktansatz:

$$\left\langle \varphi_a\chi_a \left| \hat{\mathcal{O}} \right| \varphi_b\chi_b \right\rangle = \left\langle \varphi_a \left| \hat{\mathcal{O}} \right| \varphi_b \right\rangle \langle \chi_a \,|\, \chi_b \rangle \ . \tag{67}$$

Dieses Vorgehen fußt analog zur Born–Oppenheimer-Näherung (siehe Unterkapitel 1.1) auf dem Unterschied der Massen von Elektronen und Protonen und der einhergehenden vergleichsweise großen Trägheit des Kerngerüsts. Das Franck–Condon-Prinzip [Con26, FD26, Con28] besagt, dass die molekularen Geometrien / Kernwellenfunktionen im Zuge eines elektronischen Übergangs gleich bleiben. Für den Fall, dass initial einzig das Sublevel $|\nu_{aj}\rangle$ populiert ist, ergibt sich der Franck–Condon-Überlapp gemäß:

$$\langle \chi_a \,|\, \chi_b \rangle = \sum_k \langle \nu_{aj} \,|\, \nu_{bk} \rangle \ . \tag{68}$$

In harmonischer Näherung werden die Schwingungsniveaus durch Hermite-Polynome beschrieben. Die Integrale über die Sublevels, $\langle \nu_{aj} \,|\, \nu_{bk} \rangle$, werden als Franck–Condon-Faktoren (FC-Faktoren) bezeichnet. Die explizite Summation über die FC-Faktoren ist aufgrund der hohen Dimensionalität der Problemstellung mit einem Rechenaufwand verbunden, der ohne Einschränkungen bereits für kleine Systeme nicht mehr zu stemmen ist [Eti10, Tat06, DG05].

Alternativ ermöglicht der Wechsel vom Schrödinger- in das Heisenberg-Bild (siehe Abschnitt 1.4.1) eine implizite Behandlung von FC-Faktoren. Im Hinblick auf Fermis Goldene Regel (siehe Unterkapitel 1.4) bedeutet dies, dass das Betragsquadrat des FC-Überlapps, $|\langle \chi_a \,|\, \chi_b \rangle|^2$, durch eine N-dimensionale Formulierung von Mehlers Formel [Meh66, Mar59] als Exponentialfunktion beschrieben wird.

$$\begin{aligned} &\sum_{\{b\}} \left| \hat{\mathcal{V}}_{ab} \right|^2 \delta(\Delta E) \\ =&\left| \left\langle \varphi_b \left| \hat{\mathcal{O}} \right| \varphi_a \right\rangle \right|^2 \sum_k |\langle \nu_{aj} \,|\, \nu_{bk} \rangle|^2 \delta(\Delta E) \\ =&\left| \left\langle \varphi_b \left| \hat{\mathcal{O}} \right| \varphi_a \right\rangle \right|^2 \rho^{\mathrm{FC}}(E_{aj}) \end{aligned} \tag{69}$$

Zusammen mit dem Fourier Integral (zeitabhängige Resonanzbedingung, siehe Gleichung 59) erhält man eine erzeugende Funktion für die FC-gewichtete Zustandsdichte ρ^{FC} (Franck–Condon-weighted density of states, FCWD) [Eti10, ETM11, ETM14b]:

$$\begin{aligned} G^{a\rightsquigarrow b}_{\mathrm{FCWD}}(t) = (2\pi)^{-N}\sqrt{\det(\boldsymbol{\mathcal{S}}_a^{-1}\boldsymbol{\mathcal{S}}_b^{-1}\boldsymbol{\Omega}_a\boldsymbol{\Omega}_b)} \\ \times \int\int e^{-\frac{1}{4}[(\mathbf{Q}_b+\bar{\mathbf{Q}}_b)^\dagger\boldsymbol{\Omega}_b\mathbf{B}_b(\mathbf{Q}_b+\bar{\mathbf{Q}}_b)+(\mathbf{Q}_b-\bar{\mathbf{Q}}_b)^\dagger\boldsymbol{\Omega}_b\mathbf{B}_b^{-1}(\mathbf{Q}_b-\bar{\mathbf{Q}}_b)]} \\ \times e^{-\frac{1}{4}[(\mathbf{Q}_a+\bar{\mathbf{Q}}_a)^\dagger\boldsymbol{\Omega}_a\mathbf{B}_a(\mathbf{Q}_a+\bar{\mathbf{Q}}_a)+(\mathbf{Q}_a-\bar{\mathbf{Q}}_a)^\dagger\boldsymbol{\Omega}_a\mathbf{B}_a^{-1}(\mathbf{Q}_a-\bar{\mathbf{Q}}_a)]}\, d^N\mathbf{Q}_a d^N\bar{\mathbf{Q}}_a \ . \end{aligned} \tag{70}$$

Hierbei stehen $\boldsymbol{\mathcal{S}}$, $\mathbf{B}$, $\boldsymbol{\Omega}$ für Diagonalmatrizen mit den Elementen $(\boldsymbol{\mathcal{S}}_a)_{ii} = \sinh[(\beta - it)\omega_{a,i}]$, $(\boldsymbol{\mathcal{S}}_b)_{ii} = \sinh(i\omega_{b,i}t)$, $(\mathbf{B}_a)_{ii} = \tanh[\omega_{a,i}(\beta - it)/2]$, $(\mathbf{B}_b)_{ii} = \tanh(i\omega_{b,i}t/2)$, $(\boldsymbol{\Omega}_a)_{ii} = \omega_{a,i}$, sowie $(\boldsymbol{\Omega}_b)_{ii} = \omega_{b,i}$. Die räumliche Integration in Gleichung 70 lässt sich im Anschluss an eine Duschinsky Transformation, $\mathbf{Q}_b = \mathbf{J}\mathbf{Q}_a + \mathbf{D}$, mit Hilfe von Gaußintegralen analytisch lösen und die zeitliche Integration erfolgt numerisch (siehe Unterkapitel 2.2). Die geschlossene Form der erzeugenden Funktion ist gegeben durch [ETM11]

$$\begin{aligned} G^{a\rightsquigarrow b}_{\mathrm{FCWD}}(t) = \sqrt{\frac{\det(\boldsymbol{\mathcal{S}}_a^{-1}\boldsymbol{\mathcal{S}}_b^{-1}\boldsymbol{\Omega}_a\boldsymbol{\Omega}_b)}{\det(\boldsymbol{\Omega}_a\mathbf{B}_a + \mathbf{J}^\dagger\boldsymbol{\Omega}_b\mathbf{B}_b\mathbf{J})\det(\boldsymbol{\Omega}_a\mathbf{B}_a^{-1} + \mathbf{J}^\dagger\boldsymbol{\Omega}_b\mathbf{B}_b^{-1}\mathbf{J})}} \\ \times e^{\mathbf{D}^\dagger(\boldsymbol{\Omega}_b\mathbf{B}_b\mathbf{J}(\boldsymbol{\Omega}_a\mathbf{B}_a+\mathbf{J}^\dagger\boldsymbol{\Omega}_b\mathbf{B}_b\mathbf{J})^{-1}\mathbf{J}^\dagger\boldsymbol{\Omega}_b\mathbf{B}_b-\boldsymbol{\Omega}_b\mathbf{B}_b)\mathbf{D}} \ . \end{aligned} \tag{71}$$

Für den Fall, dass die elektronische Kopplung klein ist oder symmetriebedingt verschwindet, ist es notwendig Korrekturterme für die Condon-Näherung einzuführen. Hierzu kann die funktionale Abhängigkeit der elektronischen Kopplung von den Kernkoordinaten durch eine Taylorreihe an der initialen Geometrie (Q_{a0}) beschrieben werden:

$$\begin{aligned} &\left\langle \varphi_a\chi_a \,\middle|\, \hat{\mathcal{O}} \,\middle|\, \varphi_b\chi_b \right\rangle \\ =&\left\langle \varphi_a \,\middle|\, \hat{\mathcal{O}} \,\middle|\, \varphi_b \right\rangle \langle \chi_a \,|\, \chi_b \rangle \\ &+ \sum_{\kappa}^{3N-6} \frac{\partial}{\partial Q_\kappa} \left\langle \varphi_a \,\middle|\, \hat{\mathcal{O}} \,\middle|\, \varphi_b \right\rangle \Big|_{Q_{a0}} \langle \chi_a \,|\, Q_\kappa \,|\, \chi_b \rangle \\ &+ \dots \ . \end{aligned} \tag{72}$$

Erzeugende Funktionen für die Korrektur erster Ordnung sowie durch die Quadratur der Kopplung entstehende gemischte Terme (Term 0. Ordnung mit Term 1. Ordnung) wurden von Mihaljo Etinski formuliert und in das Programm VIBES implementiert. Die beschriebene Korrektur wurde erstmals von Herzberg und Teller für Absorptionsspektren ($\hat{\mathcal{O}} = \hat{\mu}_{ab}$) berücksichtigt (Herzberg–Teller-Entwicklung [HT33]). Eine alternative Beschreibung der funktionalen Abhän-

gigkeit erfolgt störungstheoretisch in zweiter Ordnung. Hierfür wird der Störoperator als Summe $\hat{\mathcal{O}} + \sum_\kappa \frac{\partial \hat{\mathcal{H}}}{\partial Q_\kappa}$ aufgefasst [Alb63, HS71, PGDM18]. Auf diese Weise werden Kopplungsterme erhalten, die sowohl vom Störoperator $\hat{\mathcal{O}}$ abhängen als auch nichtadiabatische Terme berücksichtigen. Nichtadiabatische Kopplung stellt eine Korrektur der Born–Oppenheimer-Näherung dar und berücksichtigt definitionsgemäß die funktionale Abhängigkeit der Potenzialflächen von den Kernkoordinaten.

1.5. Elektronenkorrelation

In der Hartree–Fock-Theorie wird die elektronische Wellenfunktion $\Phi(\vec{r}_1, \vec{r}_2, \ldots, \vec{r}_n)$ in ein Produkt von n Einteilchenfunktionen (Molekülorbitale) aufgeteilt. Die Wechselwirkung eines Elektrons mit den restlichen Elektronen wird nicht explizit behandelt, sondern durch die Wechselwirkung mit einem gemittelten elektrostatischen Feld beschrieben. Die Differenz aus der resultierenden Gesamtenergie und der exakten Lösung ist die sogenannte Korrelationsenergie. Diese liegt typischerweise in der Größenordnung chemischer Bindungsenergien sowie spektraler Anregungsenergien von Valenzelektronen. Zur Beschreibung (photo-)chemischer Reaktionen sowie photophysikalischer Eigenschaften muss daher eine Korrektur für das zugrundeliegende Artefakt gefunden werden.

Die Wahrscheinlichkeit ein Elektron in einem bestimmten Volumenelement zu finden ist abhängig vom Aufenthaltsort der übrigen Elektronen. Mathematisch ausgedrückt und bezogen auf ein Molekülorbital weicht die Paardichte vom Produkt der Einzeldichten ab:

$$P_{Paar}(\vec{r}_1, \vec{r}_2) d\vec{r}_1 d\vec{r}_2 \neq p_1(\vec{r}_1) d\vec{r}_1 \cdot p_2(\vec{r}_2) d\vec{r}_2 \ . \tag{73}$$

Im Hinblick auf Elektronenkorrelation lässt sich zwischen Elektronen mit derselben und unterschiedlichen Spinquantenzahlen unterscheiden. Gemäß dem Pauli-Prinzip dürfen zwei Fermionen nicht in allen Quantenzahlen übereinstimmen, sodass $P^{\alpha\alpha}_{Paar}(\vec{r}_1 = \vec{r}_2) = P^{\beta\beta}_{Paar}(\vec{r}_1 = \vec{r}_2) = 0$ gelten muss. Durch die Antisymmetrisierung der Wellenfunktion im Rahmen der Hartree–Fock-Theorie wird diese Bedingung der Fermi-Korrelation erfüllt. Coulomb-Korrelation bezeichnet die Wechselwirkung von Elektronen mit unterschiedlichen Spinquantenzahlen. Im Allgemeinen lässt sich zwischen dynamischer und statischer Elektronenkorrelation unterscheiden. Dynamische Elektronenkorrelation beschreibt eine kurzreichweitige Wechselwirkung: Anschaulich bedeutet dies beispielsweise, dass sich Elektronen in einem Orbital abstoßen. Statische Elektronenkorrelation beschreibt im Umkehrschluss eine langreichweitige Wechselwirkung. Statisch korrelierte Elektronen sind räumlich tendenziell separiert. Zur Beschreibung des statischen An-

teils müssen daher weitere Slaterdeterminanten berücksichtigt werden. Hierfür existieren unterschiedliche Methoden, die auf der Hartree–Fock-Referenzdeterminante (Post-HF-Methoden, z. B. CI, CC, MP2) aufbauen. Diese Verfahren sind zu unterscheiden von Multireferenzmethoden, beispielsweise MRCI und MCSCF. Einen alternativen Ansatz zur Beschreibung der Gesamtenergie liefert die Dichtefunktionaltheorie (siehe Abschnitt 1.5.1).

1.5.1. Dichtefunktionaltheorie

Dichtefunktionaltheorie (DFT) unterscheidet sich im Ansatz grundlegend von Wellenfunktionsbasierter/*ab-initio* Methodik. Anstatt das Molekül als Vielteilchensystem mit $3N$ Dimensionen zu betrachten, basiert DFT auf einer ortsabhängigen Elektronendichte $\rho(\vec{r})$. Die zugrundeliegende Idee ist, dass diese Dichte eine eindeutige Beschreibung des Grundzustands darstellt und alle Eigenschaften des Sytems durch Funktionale beschrieben werden können. Die Grundzustandsenergie kann analog zur HF-Energie variationell erhalten werden. Das Funktional $E[\tilde{\rho}]$ für einen Testansatz der Elektronendichte $\tilde{\rho}$ liegt somit stets oberhalb der exakten Energie. Während in der HF-Theorie die bestmögliche Beschreibung der Energie durch das Limit $\mathrm{E_{HF}} = \mathrm{E_{exakt}} - \mathrm{E_{Korrelation}}$ gegeben ist, ermöglicht DFT eine Annäherung an die exakte Energie. Das Kernproblem von DFT besteht darin das entsprechende Funktional zu modellieren. Im quantenchemischen Kontext wird hierzu der Kohn–Sham-Formalismus angewandt: Es wird ein fiktives System bestehend aus N nicht-wechselwirkenden Fermionen definiert. Die Elektronendichte,

$$\rho = \sum_{i}^{N} |\phi_i(\vec{r})|^2 \ , \tag{74}$$

ist durch die Aufenthaltswahrscheinlichkeiten der Pseudo-Elektronen in sogenannten Kohn–Sham-Orbitalen bestimmt. Die Gesamtenergie des fiktiven Systems ergibt sich aus der kinetischen Energie der Pseudo-Elektronen und deren Wechselwirkung mit dem Kerngerüst. Zur Beschreibung der realen Elektronendichte wird das Funktional durch einen Term für die Wechselwirkung der Elektronen ergänzt: Dieser besteht aus der klassischen Coulomb-Wechselwirkung und einem Term $E_{xc}[\rho]$ zur Beschreibung der Austauschwechselwirkung (x, exchange) und Elektronenkorrelation (c, correlation) (sowie der Differenz der kinetischen Energie des fiktiven und realen Systems). DFT lässt sich in einem zeitabhängigen Ansatz für die Beschreibung angeregter Zustände erweitern. Hierbei wird die Antwort der Elektronendichte auf ein zeitabhängiges elektromagnetisches Feld untersucht. Die Anregungsenergien der Zustände ergeben sich als Polstellen der linearen Antwortfunktion und die angeregte Elektronendichte wird durch die Eigenvektoren/Amplituden einer nicht-hermiteschen Eigenwertgleichung beschrieben [DH05].

(TD)DFT ist eine Standardmethode der Quantenchemie. Es handelt es sich um ein größenkonsistentes Einfachreferenz-Verfahren, das insbesondere durch seine Effizienz besticht. Der Ansatz eignet sich am besten für Zustände, die lokalen Anregungscharakter aufweisen. TDDFT eignet sich nicht zur Beschreibung von Zuständen mit Mehrfachanregungscharakter. Zudem werden Zustände mit stark ausgeprägter Ladungsumverteilung (charge-transfer) und Rydberg-Zustände qualitativ inkorrekt beschrieben [DH05].

Im Rahmen dieser Arbeit wurden die Dichtefunktionale B3LYP [Bec88, LYP88], BHLYP [Bec93, LYP88] sowie PBE0 [AB99] zur Geometrieoptimierung und Berechnung der Kernwellenfunktionen mittels Born–Oppenheimer-Näherung (siehe Unterkapitel 1.1) verwendet. Bei diesen Funktionalen handelt es sich um Hybride: Die Beschreibung der kinetischen Energie E_{kin} erfolgt analog zur HF-Theorie ($E_{kin} \leftarrow \Psi$) und der Term E_{xc} beinhaltet Austauschwechselwirkung aus der HF-Methode sowie einen Anteil basierend auf der verallgemeinerten Gradientennäherung (generalized gradient approach, GGA), $E_{xc}^{GGA}[\rho]$ ($E_{xc} \leftarrow \Psi$, ρ). Letzterer liefert eine gute Beschreibung dynamischer Elektronenkorrelation.

1.5.2. Konfigurationswechselwirkung

Konfigurationswechselwirkung (configuration interaction, CI) ist eine Post-HF-Methode. Aufbauend auf der Grundzustandsdeterminante kann eine endliche Anzahl angeregter Slaterdeterminanten formuliert werden und jede einzelne beschreibt eine spezifische Verteilung der Elektronendichte im Molekül. Die Gesamtwellenfunktion wird als Linearkombination der resultierenden Determinanten und der HF-Referenz angesetzt. Die Anzahl möglicher Determinanten nimmt faktoriell mit der Anzahl an Elektronen zu, sodass vollständige CI-Entwicklungen (full-CI) praktisch nicht von Bedeutung sind. Stattdessen wird die Entwicklung systematisch auf sinnvolle Konfigurationen beschränkt. Ein Ansatz ist die Selektion ein- bis zweifach angeregter Slaterdeterminanten bezüglich der HF-Referenz (CISD). Höhere Anregungen tragen lediglich indirekt zur Energie bei, da durch die Ein- und Zweielektronenoperatoren des Hamiltonoperators keine Kopplung mit der Referenz möglich ist. Für eine ausgewogene Beschreibung angeregter Zustände sowie von Zuständen, deren Charakter auf mehrere Referenzen zurückzuführen ist, müssen angeregte Slaterdeterminanten in den Referenzraum aufgenommen werden. Multireference-CI (MRCI) stellt einen systematischen Ansatz zur Beschreibung angeregter Zustände dar.

Die Beschreibung statischer Elektronenkorrelation erfolgt durch nahezu entartete, schwach/moderat koppelnde Konfigurationen. Der Beitrag dynamischer Elektronenkorrelation zur Gesamtenergie ist auf starke Wechselwirkungen energetisch weit außeinander liegender Konfigurationen

zurückzuführen. Trotz der Einschränkung auf MRCISD stellt der schnell anwachsende CI-Raum ein Problem dar, das die Anwendungsmöglichkeiten der Methode stark einschränkt. Ein prinzipielles Problem von MRCI ist die fehlende Größenkonsistenz: Dies bedeutet, dass die separate Beschreibung von Fragmenten ungleich der CI-Entwicklung für das zusammengesetzte System ist. Dieser Fehler ist auf die Einschränkung erlaubter Anregungen zurückzuführen.

1.6. Die Kombination von DFT und MRCI

Die Idee hinter der DFT/MRCI-Methode [GW99, MHK18] ist die Kombination der Beschreibung dynamischer Elektronenkorrelation durch die DFT-Methode und die Beschreibung statischer Elektronenkorrelation durch die MRCI-Methodik. Im Rahmen von Post-HF- und Multireferenzmethoden wird dynamische Elektronenkorrelation durch stark wechselwirkende Konfigurationen beschrieben, die energetisch weit auseinander liegen. DFT liefert eine kostengünstige Beschreibung dieser Wechselwirkung, stellt jedoch keine ausreichende Beschreibung statischer Elektronenkorrelation dar. In DFT/MRCI wird die CI-Entwicklung in der Basis von Kohn–Sham-Orbitalen durchgeführt, wodurch die Dimension des CI-Raums deutlich verringert werden kann. Die Herausforderung besteht darin ein zuverlässiges Selektionsverfahren von Konfigurationen zu konstruieren und die resultierenden Coulomb- sowie Austauschintegrale zu skalieren, sodass die dynamische Elektronenkorrelation nicht doppelt gezählt wird und die Wechselwirkung der Konfigurationen in einem physikalisch sinnvollen Maße einkalkuliert wird. Analog zur semiempirischen DFT-Methodik wurden hierzu Parametersätze basierend auf dem BHLYP [Bec88, LYP88] Dichtefunktional entwickelt.

Der DFT/MRCI-Hamiltonoperator unterscheidet zwischen diagonalen und außerdiagonalen Matrixelementen und weist folgende Unterschiede zum exakten CI-Hamiltonoperator auf [WS75, SWW78] (w: Vektor der Besetzungszahlen der MOs, ω: Index der csf):

- Diagonalelemente $\langle \omega w|\mathcal{H}|\omega w\rangle$: Die Hartree-Fock-Energien werden durch die dichtefunktionaltheoretischen ersetzt und die Coulomb- sowie Austauschintegrale werden jeweils mittels globaler Parameter gewichtet.

- Außerdiagonalelemente mit gleichem Raumteil $\langle \omega w|\mathcal{H}|\omega' w\rangle$: Die Berechnung erfolgt in der ursprünglichen Formulierung des Operators analog zum exakten Hamiltonoperator und in den neu entwickelten Formulierungen wird der Beitrag skaliert.

- Außerdiagonalelemente mit unterschiedlichen Raumteilen $\langle \omega w|\mathcal{H}|\omega' w'\rangle$: Der Beitrag dynamischer Elektronenkorrelation via Konfigurationswechselwirkung wird durch ein Selekti-

onsverfahren und zwei globale Fitparameter eingeschränkt. Zu berücksichtigende Konfigurationen werden durch ein Energielücken-Kriterium selektiert und deren Wechselwirkung wird skaliert. Die Dämpfung des Beitrags nimmt mit der Energiedifferenz der betrachteten Konfigurationen zu.

Die ursprüngliche Formulierung des DFT/MRCI-Hamiltonoperators von Stefan Grimme und Mirko Waletzke [GW99] eignet sich für Singulett- und Triplettzustände von organischen Molekülen. Die Methode wurde am Institut für Theoretische und Computerchemie Düsseldorf zur Beschreibung von Donor-Akzeptor-Systemen, Dimeren, Übergangsmetall-Komplexen, sowie organischen Radikalen erweitert [LKM16, HM17, HKM18]. Zudem wurde der Code parallelisiert [KMWG09] und Programme zur Beschreibung relativistischer Effekte basierend auf DFT/MRCI-Wellenfunktionen wurden entwickelt [KTM02, KM05, KTM06]. Die große Flexibilität durch die Kombination beider Methoden gepaart mit einem Selektionsverfahren hat den Nachteil, dass kein analytischer Gradient formuliert werden kann, da die Unvollständigkeit der CI-Unterräume für Anregungsklassen dazu führt, dass die Energie nicht invariant bezüglich der Rotation der Orbitale ist. In der Konsequenz wurden numerische Ansätze zur Beschreibung von vibronischen Übergängen [TM06, TGM07, ETM14b, PGDM18, DM19] und zur Geometrieoptimierung [PKEM12] verfolgt.

Im Rahmen dieser Arbeit wurden Singulett- und Triplettzustände organischer Moleküle untersucht und zur Beschreibung der elektronischen Struktur wurde die DFT/MRCI-Methode mit der ursprünglichen Parametrisierung bzw. dem R2016 Hamiltonian [LKM16] verwendet.

1.7. Umgebungseffekte

Zur Beschreibung nichtadiabatischer Kopplung in Lösungsmittel ist es zwingend erforderlich die Verschiebungen der Potenzialflächen zu berücksichtigen. Gemäß Gleichung 17 verhält sich das Matrixelement antiproportional zur Energiedifferenz der koppelnden Zustände. ΔE bezieht sich hierbei auf die vertikale Energie. Unter der Annahme, dass sich die Elektronendichte im Zuge der Solvatisierung nicht grundlegend ändert, sodass

$$\langle \varphi_a \,|\, \nabla_\kappa \mathcal{H} \,|\, \varphi_b \rangle_{\text{solv}} \approx \langle \varphi_a \,|\, \nabla_\kappa \mathcal{H} \,|\, \varphi_b \rangle_{\text{vac}} \tag{75}$$

gilt, kann der Umgebungseffekt mit Hilfe zustandsspezifischer Verschiebungen im DFT/MRCI implementierten Davidson-Diagonalisierungsverfahren des CI-Raums behandelt werden. Die durch Gleichung 75 ausgedrückte Bedingung ist für Zustände mit schwach/moderat ausgeprä-

tem Übergangsdipolmoment hinreichend erfüllt. Die Annahme gilt folglich nicht für Übergänge mit stark ausgeprägter Ladungsumverteilung, beispielsweise charge-transfer Zustände. Zur Beschreibung der veränderten Wechselwirkung der Zustände werden die Diagonalelemente der Hamiltonmatrix

$$H_{ij}^{\text{solv}} = H_{ij}^{\text{vac}} + \sum_K \Delta E_K^{\text{solv}} |\Psi_K^{\text{vac}}\rangle\langle\Psi_K^{\text{vac}}| \tag{76}$$

modifiziert. Der Index K läuft über die betroffenen Zustände. Das Verfahren wurde von Dr. Martin Kleinschmidt implementiert und ist an eine entsprechende Prozedur für Spin–Bahn-CI angelehnt [RCSM98, SSBS10]. Die Energien ΔE_K^{solv} beschreiben den Umgebungseinfluss auf die Energien der koppelnden Zustände. Im Rahmen dieser Arbeit wurden Lösungsmitteleffekte auf die DFT/MRCI-Energien wie folgt generiert: Es wurden jeweils Grundzustandsgeometrien im Vakuum sowie der gewünschten Lösungsmittelumgebung optimiert und anschließend wurden die energetischen Verschiebungen berechnet. Die Behandlung des Lösungsmittels erfolgte hierfür im Allgemeinen implizit mittels COSMO [KS93] und für NMA-dF (*N*-Methyl-difluoro-Acridon, siehe Unterkapitel 3.4) sowie Xanthon (siehe Unterkapitel 3.1) wurden zusätzlich explizite Wechselwirkungen miteinbezogen (Xanthon in H_2O: siehe Abbildung 4). Im Rahmen meiner Masterarbeit [Bra17] wurde der Einfluss impliziter sowie expliziter Wechselwirkungen auf die Energien des Flavinchromophors ausführlich untersucht (siehe Unterkapitel 3.2). Die Zeitabhängigkeit der dielektrischen Relaxation wird im Rahmen des Modells nicht beschrieben.

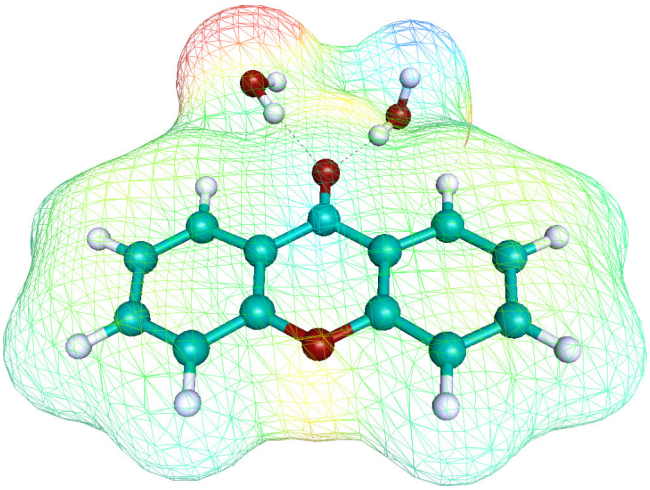

Abbildung 4.:
Darstellung des solvatisierten Grundzustandsminimums von Xanthon. Die Ausbildung von Wasserstoffbrückenbindungen mit der polaren Carbonylgruppe wurden durch explizite Wassermoleküle berücksichtigt. Die Färbung der Kavität (COSMO [KS93]) spiegelt die abschirmenden Ladungen wider [rot(+) → grün(0) → blau(−)]. Das Modell wurde von Rai-Constapel et al. übernommen [RCEM13].

Die Güte der Übertragung der Effekte der Lösungsmittelumgebung des Grundzustands auf angeregte Zustände ist abhängig vom Übergangsdipolmoment der koppelnden Zustände. Je ähnlicher die Ladungsverteilung des Grundzustands und der betrachteten angeregten Zustände ausfällt, desto besser eignet sich das Vorgehen.

Teil II.

Programmentwicklung

2.1. Das Programm DELTA

Die Berechnung nichtorthogonalen Überlapps stellt eine Herausforderung im Hinblick auf Rechenzeit dar. Die Anzahl an Kombinationen von Slaterdeterminanten skaliert mit den Dimensionen der CI-Entwicklungen. Zudem werden DFT/MRCI-Wellenfunktionen in der Basis von csfs entwickelt, sodass jeder Beitrag auf eine Linearkombination von Slaterdeterminanten zurückgeführt werden muss. Der Rechenaufwand für die resultierenden Determinanten skaliert mit der Anzahl an Elektronen n. Die Berechnung aller Beiträge ist für relevante Systeme nicht praktikabel, sodass effiziente Strategien zur Wiederverwendung von Zwischenergebnissen sowie Selektionskriterien für signifikante Beiträge entwickelt werden müssen. Zunächst lässt sich feststellen, dass die Dimension der Determinanten reduziert werden kann, indem die Orbitale der Slaterdeterminanten, z. B. $\Phi_k(R) = \Phi_k$ und $\Phi_l(R') = \Phi'_l$, nach den Spins sortiert werden. $\bar{\phi}$ kennzeichnet Elektronen mit β-Spin:

$$\begin{aligned} |\Phi_k\rangle &= |\phi_{k(1)} ... \phi_{k(n_\alpha)} \bar{\phi}_{k(n_\alpha+1)} ... \bar{\phi}_{k(n)}| \\ |\Phi'_l\rangle &= |\phi'_{l(1)} ... \phi'_{l(n_\alpha)} \bar{\phi}'_{l(n_\alpha+1)} ... \bar{\phi}'_{l(n)}| \ . \end{aligned}$$

Da $\langle\alpha|\beta\rangle = \langle\beta|\alpha\rangle = 0$ und $\langle\alpha|\alpha\rangle = \langle\beta|\beta\rangle = 1$ gilt, lässt sich die Determinante von $\langle\Phi'_k|\Phi_l\rangle$ in zwei Spinfaktoren, S^α_{kl} und S^β_{kl}, aufteilen [PRM+16]:

$$\begin{vmatrix} \left\langle \phi_{k(1)} \middle| \phi'_{l(1)} \right\rangle & \cdots & \left\langle \phi_{k(1)} \middle| \phi'_{l(n_\alpha)} \right\rangle & & & \\ \vdots & \ddots & \vdots & & 0 & \\ \left\langle \phi_{k(n_\alpha)} \middle| \phi'_{l(1)} \right\rangle & \cdots & \left\langle \phi_{k(n_\alpha)} \middle| \phi'_{l(n_\alpha)} \right\rangle & & & \\ & & & \left\langle \bar{\phi}_{k(n_{\alpha+1})} \middle| \bar{\phi}'_{l(n_\alpha+1)} \right\rangle & \cdots & \left\langle \bar{\phi}_{k(n_{\alpha+1})} \middle| \bar{\phi}'_{l(n)} \right\rangle \\ & 0 & & \vdots & \ddots & \vdots \\ & & & \left\langle \bar{\phi}_{k(n)} \middle| \bar{\phi}'_{l(n_\alpha+1)} \right\rangle & \cdots & \left\langle \bar{\phi}_{k(n)} \middle| \bar{\phi}'_{l(n)} \right\rangle \end{vmatrix}$$

$$=$$

$$\begin{vmatrix} \left\langle \phi_{k(1)} \middle| \phi'_{l(1)} \right\rangle & \cdots & \left\langle \phi_{k(1)} \middle| \phi'_{l(n_\alpha)} \right\rangle \\ \vdots & \ddots & \vdots \\ \left\langle \phi_{k(n_\alpha)} \middle| \phi'_{l(1)} \right\rangle & \cdots & \left\langle \phi_{k(n_\alpha)} \middle| \phi'_{l(n_\alpha)} \right\rangle \end{vmatrix} \times \begin{vmatrix} \left\langle \bar{\phi}_{k(n_{\alpha+1})} \middle| \bar{\phi}'_{l(n_\alpha+1)} \right\rangle & \cdots & \left\langle \bar{\phi}_{k(n_{\alpha+1})} \middle| \bar{\phi}'_{l(n)} \right\rangle \\ \vdots & \ddots & \vdots \\ \left\langle \bar{\phi}_{k(n)} \middle| \bar{\phi}'_{l(n_\alpha+1)} \right\rangle & \cdots & \left\langle \bar{\phi}_{k(n)} \middle| \bar{\phi}'_{l(n)} \right\rangle \end{vmatrix}$$

$$\hat{=}$$

$$S^\alpha_{kl} \times S^\beta_{kl} \ .$$

S^α_{kl} und S^β_{kl} sind unabhängig voneinander. Für den Fall, dass die α- oder β-Elektronen unterschiedlicher Slaterdeterminanten identische Molekülorbitale besetzen, kann der entsprechende

Spinfaktor somit wiederverwendet werden. Beispielsweise weisen die vier Kombinationen der Slaterdeterminanten

$$|\Phi_1\rangle = |\phi_1\phi_2\bar{\phi}_1\bar{\phi}_2|$$
$$|\Phi_2\rangle = |\phi_1\phi_2\bar{\phi}_2\bar{\phi}_1| \ ,$$

$\langle\Phi_1'|\Phi_1\rangle$, $\langle\Phi_2'|\Phi_2\rangle$, $\langle\Phi_1'|\Phi_2\rangle$, $\langle\Phi_2'|\Phi_1\rangle$, identische S^α Beiträge auf. Im Unterschied zu vorherigen Implementierungen (z. B. [MR89, PLB09]), nutzen Plasser et al. diese Eigenschaft aus und berechnen vorab alle benötigten Spinfaktoren und kontrahieren diese anschließend. Dieses Vorgehen führt zwar zu einer drastischen Reduktion des Rechenaufwands, erhöht dafür allerdings die Anforderungen an den Speicherbedarf [PRM+16]. Damit dieser nicht zum limitierenden Faktor für die Größe des Systems wird, wurde die Wiederverwendung von Spinfaktoren im Rahmen meiner Arbeit auf einfach angeregte Slaterdeterminanten eingeschränkt. Es gilt hervorzuheben, dass einfach angeregte Slaterdeterminanten Bestandteil höher angeregter csfs sind. Beispielsweise beschreibt eine zweifach angeregte csf acht einfach angeregte Beiträge in den beiden unabhängigen Spinräumen:

$$|\alpha\alpha\beta\beta\rangle$$
$$|\alpha\beta\alpha\beta\rangle$$
$$|\alpha\beta\beta\alpha\rangle$$
$$|\beta\alpha\alpha\beta\rangle$$
$$|\beta\alpha\beta\alpha\rangle$$
$$|\beta\beta\alpha\alpha\rangle \ .$$

Lediglich die Slaterdeterminanten $|\alpha\alpha\beta\beta\rangle$ und $|\beta\beta\alpha\alpha\rangle$ weisen jeweils zweifache Anregung in einem der beiden Spinräume auf. Zur optimalen Ausnutzung der Wiederverwendung von Spinfaktoren werden Triplettwellenfunktionen vom $M_S = 1$- in das $M_S = 0$-Sublevel transformiert. Dies hat den Vorteil, dass die Überlappmatrizen für beide Spinräume dieselbe Dimension aufweisen und resultierende Spinfaktoren somit unabhängig vom Spin wiederverwendet werden können.

Im Hinblick auf die csf-Basen lässt sich ausnutzen, dass die Slaterdeterminanten aller csfs bezüglich einer Konfiguration identisch sind und sich lediglich die Koeffizienten unterscheiden. Dadurch, kann die Dimension $n_{CI} \times n'_{CI}$ effektiv auf $n_{conf} \times n'_{conf}$ reduziert werden (conf: Konfiguration). Zudem kann der Rechenaufwand durch Ausnutzen der Spin-Symmetrieadaption

halbiert werden, z. B.

$$\begin{aligned}\langle\alpha\alpha\beta\beta\,|\,\alpha'\alpha'\beta'\beta'\rangle &= S^{\alpha}\times S^{\beta}\\ =\langle\beta\beta\alpha\alpha\,|\,\beta'\beta'\alpha'\alpha'\rangle &= S^{\beta}\times S^{\alpha}\ .\end{aligned}$$

Der Code des Programms DELTA ist in zwei verschachtelten Schleifen aufgebaut: Erstere durchläuft alle Konfigurationen an der Referenzgeometrie R und die innere Schleife durchläuft alle Konfigurationen an der verschobenen Geometrie R'. Zunächst werden für alle Slaterdeterminanten der Referenzkonfiguration Überlappmatrizen erzeugt: Hierzu werden die entsprechenden Erzeuger und Vernichter auf die Überlappmatrix der HF-Referenzen angwandt. In der Praxis bedeutet dies, dass jene Zeilen, die vernichteten Orbitalen zugeordnet sind, durch Zeilen der erzeugten MOs ersetzt werden. Dies erfolgt separat für die α- und β-Überlappmatrizen. Die resultierenden Matrizen sind in der Folge der Startpunkt für die Berechnung der Überlapps mit den Konfigurationen der Geometrie R'. Die Erzeuger- und Vernichter-Operatoren wirken für R' auf die Spaltenvektoren der intermediären Überlappmatrizen. Hierbei läuft eine Schleife über alle Slaterdeterminanten der jeweiligen Konfiguration bezüglich R'. Die Determinanten der resultierenden Überlappmatrizen sind die Spinfaktoren S^{α} und S^{β}. Diese werden folglich mit den entsprechenden CI- und csf-Koeffizienten gewichtet und aufsummiert.

An der Stelle der Erzeugung der intermediären Überlappmatrizen wurden weitere Zwischenschritte implementiert. Die Matrizen können in vier unterschiedliche Bereiche unterteilt werden (siehe Abbildung 3):

- Der Block **F** beschreibt die Überlapps energetisch niedrig liegender Molekülorbitale. Die Blockmatrix umfasst unter anderem den frozen core der DFT/MRCI-Rechnungen.
- Der **V**-Block beschreibt die Überlapps der übrigen, energetisch höherliegenden Molekülorbitale.
- Die Außerdiagonalblöcke **P** und **O** beschreiben die Überlapps der in den **F**- und **V**-Matrizen enthaltenen MOs. Die **O**-Matrix beschreibt die Überlapps der **F**-Orbitale der Referenz mit den **V**-Orbitalen der MOs von $\Psi(R')$ und für die **P**-Matrix verhält es sich umgekehrt.

Unter Anwendung von Schur's Determinanten Identität (siehe Abschnitt 1.3.4) kann die Determinante des **F**-Blocks wiederverwendet werden. Je größer die Dimension dieser Blockmatrix ausfällt ($p > q$, siehe Abbildung 3), desto größer ist die Ersparnis an Rechenoperationen.

Für die intermediären Überlappmatrizen werden folgende Schritte durchgeführt:

1. Es werden Determinanten $\det(\mathbf{F})$ und Inversen $\mathbf{F}^{-1}$ berechnet. Die Dimension der Matrix $\mathbf{F}$ wird schrittweise um eins heruntergesetzt bis der kleinste benötigte $\mathbf{F}$-Block erhalten wird. Die Dimension des kleinsten Blocks wird durch das unterste Orbital von $\Psi(R')$, aus welchem angeregt wird, festgelegt.

2. Anschließend wird für jede resultierende Inverse $\mathbf{F}^{-1}$ die Matrizenmultiplikation $\mathbf{PF}^{-1} = \mathbf{G}$ durchgeführt. Auf diese Weise wird jener Beitrag zur finalen Determinante, welcher lediglich von der Referenz ausgeht, vorab berechnet und zur Wiederverwendung für beliebige $\mathbf{O}$-Blöcke präpariert.

Das Prozedere erfolgt in einer Schleife über die Slaterdeterminanten der Referenzkonfiguration und die Zwischenergebnisse $\det(\mathbf{F})$, $\mathbf{F}^{-1}$ sowie $\mathbf{G}$ werden im Cache gehalten. Diese werden in der Schleife über die Konfigurationen der verschobenen Geometrie mit den resultierenden $\mathbf{O}$- und $\mathbf{V}$-Matrizen gemäß Schur's Determinanten Identität verrechnet. Die Anzahl zu berechnender Zwischenergebnisse $\det(\mathbf{F})$, $\mathbf{F}^{-1}$ und $\mathbf{G}$ ist deutlich geringer als die Anzahl zu berechnender Spinfaktoren.

Bis hierhin wurden keine Näherungs-/Selektionsverfahren eingeführt. Die Anzahl zu berechnender Determinanten kann weiter reduziert werden, indem der Beitrag einzelner Summanden abgeschätzt wird. Beispielsweise haben Neville et al. hierzu die Hadamard-Ungleichung eingeführt [NSS20]. Der Impuls der Kerne / Ableitungsoperator wirkt als Einelektronenoperator [HV80]. Formal betrachtet geht der Differenzenquotient für die numerische Berechnung von NACMEs (siehe Gleichung 22) für $(\lim \epsilon \to 0)$ in den analytischen Ausdruck über. In der Praxis lässt sich dies wie folgt nachvollziehen: Die Überlappmatrix der HF-Referenzen ist stark diagonaldominant. Die Überlapps einander korrespondierender Molekülorbitale sind Diagonalelemente. Erzeugung und Vernichtung von Orbitalen entspricht gegebenenfalls der Substitution eines Diagonalelements durch ein Außerdiagonalelement. Der größte Beitrag zur Determinante stammt für diagonaldominante Matrizen vom Produkt der Diagonalelemente, sodass der Überlapp in der Konsequenz stark reduziert ist. Der Effekt potenziert sich für mehrfache Substitution von Diagonalelementen, sodass Beiträge von Konfigurationen, die relativ zueinander zwei- oder mehrfach angeregt sind, um Größenordnungen kleiner ausfallen als Beiträge von Konfigurationen, die relativ zueinander lediglich einfach angeregt (oder identisch) sind.

Die Wahl der Auslenkung ϵ ist in der Praxis dadurch eingeschränkt, dass

1. der lineare Bereich für die Bildung eines Differenzenquotienten einen system- und richtungsabhängigen Maximalwert hat

2. und der Wert nicht beliebig klein gewählt werden kann, da die Überlapps sonst insignifikant werden.

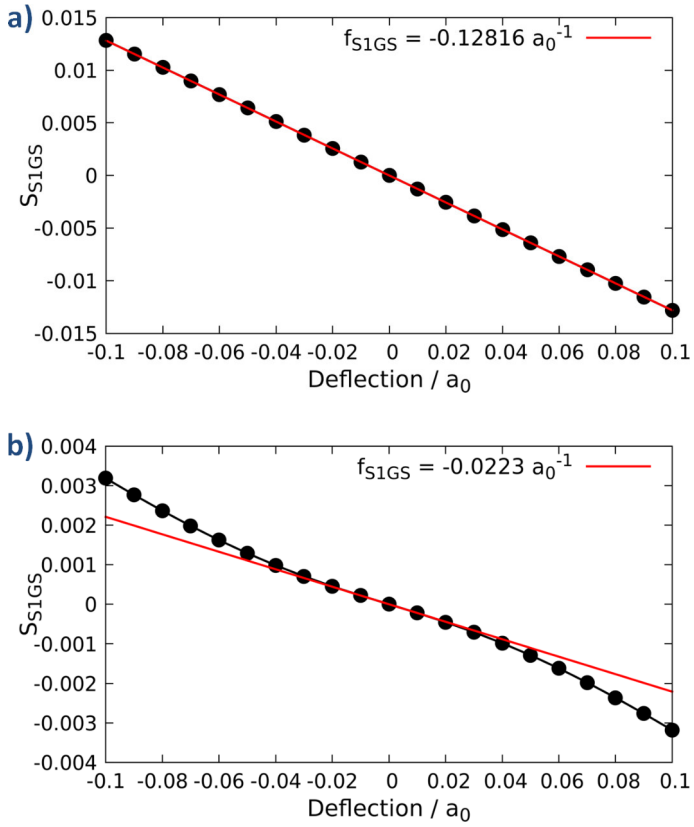

Abbildung 5.: Auftragung nichtorthogonaler Überlapps S_{S1GS} vom ersten angeregten Singulett und dem Grundzustand von Heptazin (siehe Unterkapitel 3.3) gegen die Schrittweite der Auslenkung ϵ entlang A_2'-symmetrischen Moden [a) $1652.45\,\mathrm{cm}^{-1}$, $\kappa = 39$; b) $1459.45\,\mathrm{cm}^{-1}$, $\kappa = 35$]. Die roten Geraden entsprechen den Steigungen für $\epsilon = 0.01$.

In Abbildung 5a) ist das Matrixelement der dominanten Kopplung des strahlungslosen $S_1 \rightsquigarrow S_0$ Übergangs von Heptazin (siehe Unterkapitel 3.3) dargestellt. Es zeigt sich, dass die Steigung der Tangente des maßgeblichen Beitrags praktisch unabhängig vom Parameter ϵ ist. Das zweite Beispiel beschreibt die nichtadiabatische Kopplung für das gleiche System entlang einer Mode, die vergleichsweise stark von der Wahl des Modulus abhängt. Im gegebenen Beispiel ist die resultierende Ratenkonstante nahezu unabhängig von der gewählten Auslenkung, da hauptäschlich das Matrixelement bezüglich $\kappa = 39$ den Übergang vermittelt. Im Allgemeinen empfiehlt sich ein Wert von $\epsilon = 0.01$. Auf diese Weise wird der Maximalwert nicht überschritten und auch für sehr schwach ausgeprägte Kopplungen ($< 0.01\,a_0^{-1}$) werden signifikante Überlapps erhalten.

Die Ableitungen nach den Normalmoden werden durch das in *Python* verfasste Skript *dd.py* gesteuert. Dieses setzt automatisch restart-Läufe ausgehend von einer Referenz-Rechnung an einer Gleichgewichtsgeometrie auf. Letztere wird durch das Skript vorab ausgeführt, sodass Artefakte durch Rotationen sowie Translationen der Geometrien vermieden werden. Die MO-Koeffizienten und Überlapps der Atomorbitale werden von Turbomole [Tur] erzeugt. Es ist empfehlenswert die Konvergenzkriterien von Turbomole für die Erzeugung der Kohn-Sham-Orbitale deutlich zu verschärfen. Unter Verwendung des Skripts *dd.py* werden die entsprechenden Kriterien standardmäßig auf `$scfconv=9` sowie `$denconv=1.0E-10` gesetzt. Der Einfluss des Konvergenzschwellwertes der Diagonalisierung der CI-Matrix ist relevant für die korrekte Beschreibung numerischer Nullen. Für den Standardwert des DFT/MRCI-Programms, `$prec=1`, werden im Allgemeinen fünf Nachkommastellen für symmetrieverbotene Kopplungen korrekt beschrieben. Zum Testen der Parameter wurden NACMEs vom Pyrazin Molekül verwendet. Die Validierung der Matrixelemente erfolgte durch den Vergleich mit analytischen Matrixelementen für CASSCF-Wellenfunktionen von Formaldehyd. Der entscheidende Parameter für die Effizienz der Berechnung numerischer NACMEs ist `$renorm`. Dieser ist ein Maß für die Anzahl an Konfigurationen, welche in die Berechnung des nichtorthogonalen Überlapps eingehen. Die Konfigurationen werden nach den größten Beträgen der CI-Koeffizienten der csfs sortiert und die DFT/MRCI-Wellenfunktionen anschließend entsprechend auf eine Norm $\geq 1-$`$renorm` gekürzt sowie renormiert. Aufgrund der Skalierung der Berechnung des nichtorthogonalen Überlapps mit der Anzahl an Konfigurationen beider Wellenfunktionen, $n_{conf} \times n'_{conf}$, führt etwa eine Halbierung der Länge beider CI-Entwicklungen zu einer Viertelung des gesamten Rechenaufwands. Zum Beispiel beträgt die Prozessorzeit für die Berechnung von einseitigen Ableitungen für die $1^3(n\pi^*)$ und $1^3(\pi\pi^*)$ Zustände des Xanthon Moleküls für ungekürzte Entwicklungen im Durchschnitt 2575 s. Die Anzahl einbezogener Konfigurationen beträgt 66952. Bereits für einen Schwellwert von `$renorm=1.0E-11` wird die Dauer der Rechnung auf 390 s gekürzt, die Anzahl an Konfigurationen beträgt 16341 für $\Psi(R)$ und 28798 für $\Psi(R')$. Der große Unterschied in den Anzahlen der Konfigurationen liegt darin begründet, dass im Zuge der Auslenkung die C_{2v}-Symmetrie des Minimums gebrochen wird. Für eine Konvergenz der NACMEs auf etwa fünf Nachkommastellen eignet sich der Default-Wert `$renorm=1.0E-8`. Die entsprechende Rechenzeit beträgt mit 272 s etwa 10 % der Zeit für die ungekürzten Wellenfunktionen. IC Ratenkonstanten verhalten sich robust bzgl. größerer Schwellwerte: Erhöhung von `$renorm` auf `1.0E-6` liefert etwa für den $^1(\pi\pi^*) \rightsquigarrow {}^1(n\pi^*)$ Übergang des Xanthon Moleküls im Vakuum eine Abweichung von 17 % ($3.9\times10^{11}\,s^{-1}$ und $3.2\times10^{11}\,s^{-1}$), die deutlich unterhalb der Fehlergrenzen des Ansatzes liegt. Für die entsprechende IC der wesentlich stärker gekoppelten Zustände in der Triplettdomäne fällt die Abweichung deutlich geringer aus (4 %, $2.2\times10^{14}\,s^{-1}$ und $2.1\times10^{14}\,s^{-1}$).

Im Vergleich mit vorherigen Implementierungen für nichtorthogonalen Überlapp zeichnet sich das im Rahmen dieser Arbeit entstandene Programm durch einen vorteilhaften Kompromiss aus Speicherbedarf und Rechenzeit aus. Das Programm für nichtorthogonalen Überlapp von Plasser et al. [PRM$^+$16], an welchem sich das Vorgehen grundsätzlich orientiert, ist darauf ausgelegt die Spinfaktoren vorab zu berechnen und anschließend zu kontrahieren. Dieses Vorgehen gewährleistet eine optimale Wiederverwendung von Spinfaktoren und führt zu vergleichsweise geringen Prozessorzeiten. Der Nachteil dieser Prozedur ist, dass das Abspeichern aller Spinfaktoren mit einem vergleichsweise großen Speicherbedarf einhergeht. Es wird ein schneller Anstieg des Bedarfs mit der Anzahl zu berechnender Spinfaktoren verzeichnet (siehe Abbildung 4 in [PRM$^+$16]). Zur Halbierung des notwendigen Arbeitsspeichers haben Plasser et al. einen weiteren Algorithmus implementiert, welcher die α-Spinfaktoren on-the-fly berechnet. Zudem wurde die Implementierung parallelisiert. Im Rahmen meiner Arbeit wurde die Wiederverwendung von Spinfaktoren auf Einfachanregungen bezüglich der HF-Referenzen beschränkt und Überlappmatrizen werden gegebenenfalls on-the-fly erneut generiert sowie ausgewertet. Alle im Rahmen dieser Arbeit durchgeführten Rechnungen kommen mit weniger als einem Gigabyte Arbeitsspeicher aus. Berechnungen numerischer NACMEs werden durch das Skript *dd.py* parallel für eine beliebige Anzahl von Schwingungsfreiheitsgraden durchgeführt. Die Determinanten werden im Algorithmus von Plasser et al. grundsätzlich durch LU-Zerlegung ausgewertet. Zusätzlich werden Level 1 Minoren durch die Anwendung des Laplaceschen Entwicklungssatzes wiederverwendet. Dieses Vorgehen ist insbesondere für MRCIS-Wellenfunktionen von Vorteil. Das Programm DELTA nutzt Schur's Determinanten Identität zur Berechnung der Spinfaktoren. Hierbei werden die Determinanten der Untermatrizen mittels LU-Zerlegung berechnet. Die im Laufe meiner Dissertation entstandene Implementierung von Neville et al. [NSS20] unterscheidet sich von jener von Plasser et al. im Wesentlichen dadurch, dass der Betrag einzelner Spinfaktoren vor der LU-Zerlegung abgeschätzt wird. Hierzu wird das sogenannte 'Hadamard screening' verwendet: Mittels Hadamard-Ungleichung werden obere Schranken für die Determinanten erhalten. Zur Selektion signifikanter Terme wurde im Rahmen meiner Arbeit zusätzlich ein Konfigurationsvergleich zur Selektion nach Anregungsklassen implementiert. Dieser führt zu einer drastischen Reduktion resultierender Determinanten ($<$1 %) und stellt eine effektivere Möglichkeit zur Selektion potentieller Beiträge zur Kopplung dar.

Das Programm DELTA ist zwar auf C_1-symmetrischen Input angewiesen, Symmetrie führt aber dennoch zu kürzeren Rechenzeiten, da CI-Koeffizienten symmetrieverbotener Irreps verschwindend gering sind und durch die Kürzung der Wellenfunktion wegfallen. Der Code ist in der Programmiersprache *Fortran* geschrieben.

Inputbeschreibung

Die Eingabedatei, **delta.in**, ist wie folgt aufgebaut:

```
$mult     1 ∨̇ 3
$roots    <int1> <int2>
$renorm   <real>
$ref      <Pfad zu φ(R)>
$dist     <Pfad zu φ(R')>
$end  .
```

Unter der Angabe `$mult` wird die Multiplizität spezifiziert. Die Integers bezüglich `$roots` spezifizieren die zu koppelnden Zustände. Die Reihenfolge der Wurzeln ist hierbei nicht von Bedeutung, da $f_{ab} = -f_{ba}$ (siehe Abschnitt 1.2.2). Der Parameter `$renorm` für die Kürzung und Renormierung der Wellenfunktionen kann einheitlich oder individuell gesetzt werden. In letzterem Falle bezieht sich `$renorm_ref` auf die Referenz und `$renorm_dist` auf die verschobene Geometrie. Der Parameter ist standardmäßig einheitlich auf `$renorm=1.0E-8` gesetzt. Hadamard-Screening lässt sich durch `$screening` ansteuern. Der Eingabewert (<real>) stellt einen Schwellwert für das Produkt $S^{\alpha} \times S^{\beta}$ dar. Die Pfade zu den DFT/MRCI-Rechnungen, `$ref` sowie `$dist`, werden vom Skript *dd.py* automatisch gesetzt.

Die Verwendung des Skripts *dd.py* ermöglicht zudem eine simple Umsetzung der stateshift-Prozedur (siehe Unterkapitel 1.7): Indem energetische Verschiebungen einzelner Zustände in der Eingabedatei **shift.dat** tabelliert werden, erfolgt die Berücksichtigung der Solvatationseffekte auf die Zustandsenergien im restart run. Der Input ist analog zum DFT/MRCI-Input aufgebaut:

<Wurzel> <Irrep> = a <Verschiebung> <Einheit>

z. B.

2 a −0.22 eV
3 a 0.11 eV .

Es ist ausreichend die beiden zu koppelnden Zustände zu verschieben. Hierbei gilt es zu beachten, dass sich die Zustandsnummern `$roots` in *delta.in* durch die Verschiebung der Zustände verändern können. Der Schwellwert für den Projektionsoperator der Zustandsverschiebung wird durch das Skript standardmäßig auf `$shiftthresh=1.0E-05` gesetzt.

2.2. Erzeugende Funktion

Zur Berechnung von IC Ratenkonstanten wurde das Programm VIBES erweitert. Ursprünglich wurde VIBES von Jörg Tatchen zur Berechnung von ISC Ratenkonstanten programmiert [Tat06, TGM07]. Die erste Version beruht auf der expliziten Berechnung von FC-Faktoren (siehe Abschnitt 1.4.2) in einem Energieintervall η. Aufbauend auf der zeitunabhängigen Implementierung erweiterte Mihaljo Etinski das Programm zur zeitabhängigen Beschreibung von Interkombination mit Hilfe von erzeugenden Funktionen [Eti10, ETM11, ETM14b]. Der zeitabhängige Ansatz hat den Vorteil, dass die FC-Faktoren implizit durch einen analytischen Ausdruck beschrieben werden. Der Rechenaufwand wird dadurch erheblich reduziert, sodass sich der zeitabhängige Ansatz auch für große Moleküle ohne Einschränkung von Moden/Schwingungsniveaus praktizieren lässt. Im Rahmen dieser Arbeit wurde eine entsprechende erzeugende Funktion für interne Konversion hergeleitet und in das Programm VIBES implementiert. Die Beschreibung von Ratenkonstanten nichtstrahlender Prozesse per Korrelationsfunktion erfolgt in atomaren Einheiten gemäß (vgl. Abschnitt 1.4.1)

$$k_{\mathrm{NR}}^{a\rightsquigarrow b} = Z^{-1} \int_{-\infty}^{\infty} G_{\mathrm{NR}}^{a\rightsquigarrow b}(t) e^{it\Delta E_{ab}} \ . \tag{77}$$

ΔE ist die adiabatische Energiedifferenz der beiden involvierten elektronischen Zustände. Ein weiterer Vorteil des zeitabhängigen Ansatzes ist die vergleichsweise einfache und kostengünstige Erweiterung für $T > 0\,K$ [ETM14a]. Temperatureffekte werden mittels Boltzmann-Verteilung berücksichtigt. Die kanonische Zustandssumme $Z = \sum_i e^{-\beta E_{a,i}}$ bezieht sich auf die Schwingungszustände des elektronischen Ausgangszustands a. β repräsentiert die inverse thermische Energie $(k_B T)^{-1}$ und $E_{a,i}$ beschreibt die Energie des vibronischen Sublevels ν_{ai}. Die erzeugende Funktion G_{NR} beschreibt die Prozess-spezifische Kopplung der Wellenfunktionen und unterscheidet sich von der im Abschnitt 1.4.1 hergeleiteten Korrelationsfunktion einzig durch den Exponentialterm für die adiabatische Energiedifferenz der elektronischen Zustände. Für interne Konversion kann die Funktion ausgehend vom Kopplungs-Matrixelement in Gleichung 7 hergeleitet werden:

$$\mathcal{H}_{ab} = \left\langle \Psi_b \middle| \hat{\mathcal{T}}^N \middle| \Psi_a \right\rangle = -\sum_{\kappa} M_{\kappa}^{-1} \left\langle \chi_b \middle| f_{ab}(\kappa) \nabla_{\kappa} \chi_a \right\rangle - \sum_{\kappa} (2M_{\kappa})^{-1} \tilde{h}_{ab}^{\kappa,\kappa} \left\langle \chi_a \middle| \chi_b \right\rangle \ . \tag{78}$$

Gleichung 78 beschreibt das gesamte nichtadiabatische Kopplungs-Matrixelement mit Termen erster und zweiter Ordnung. Eingesetzt in Fermis Goldene Regel erhält man einen Ausdruck für die Beschreibung der Ratenkonstante im Schrödinger-Bild. Die Ratenkonstante kann genähert

durch die Kopplung erster Ordnung beschrieben werden:

$$k_{\mathrm{IC}} = \frac{2\pi}{\hbar}\left|\sum_{\kappa}\langle\chi_b \,|\, f_{ab}(\kappa)\nabla_\kappa\chi_a\rangle + 1/2\tilde{h}_{ab}^{\kappa,\kappa}\,\langle\chi_b \,|\, \chi_a\rangle\right|^2\delta(\Delta E) \tag{79}$$
$$\simeq \frac{2\pi}{\hbar}\left|\sum_{\kappa}\langle\chi_b \,|\, f_{ab}(\kappa)\nabla_\kappa\chi_a\rangle\right|^2\delta(\Delta E)\ .$$

Das Argument der Deltafunktion bezieht sich auf beliebige Kombinationen von vibronischen Sublevels der Zustände a und b. Die Auswertung des Beitrags zweiter Ordnung erfolgt analog zur Interkombination via direkter Spin–Bahn-Kopplung. Die allgemeingültige Transformation von Fermis Goldener Regel in das zeitabhängige Heisenberg-Bild ist im Abschnitt 1.4.1 beschrieben und die implementierte erzeugende Funktion ist in Gleichung 80 wiedergegeben. Die Funktion unterscheidet sich von jener von Islampour und Miralinaghi [IM07] im Wesentlichen dadurch, dass die Normalkoordinaten des finalen Zustands in die Basis der Normalkoordinaten des Ausgangszustands entwickelt werden. Eine ausführliche Herleitung ausgehend von der erzeugenden Funktion für Franck–Condon-gewichtete Zustandsdichte mit Erläuterungen der Zwischenschritte und Matrizen ist im Unterkapitel 4.1 im Anhang aufgeführt.

$$\begin{aligned} G_{\mathrm{IC}}^{a\rightsquigarrow b}(t) = &\sqrt{\frac{\det(\boldsymbol{\mathcal{S}}_a^{-1}\boldsymbol{\mathcal{S}}_b^{-1}\boldsymbol{\Omega}_a\boldsymbol{\Omega}_b)}{\det(\boldsymbol{\Omega}_a\mathbf{B}_a+\mathbf{J}^\dagger\boldsymbol{\Omega}_b\mathbf{B}_b\mathbf{J})\det(\boldsymbol{\Omega}_a\mathbf{B}_a^{-1}+\mathbf{J}^\dagger\boldsymbol{\Omega}_b\mathbf{B}_b^{-1}\mathbf{J})}} \\ &\times\Big\{\frac{1}{2}tr[\boldsymbol{\mathcal{F}}(\boldsymbol{\Omega}_a^{-1}\mathbf{B}_a+\mathbf{J}^\dagger\boldsymbol{\Omega}_b^{-1}\mathbf{B}_b\mathbf{J})^{-1}]-\frac{1}{2}tr[\boldsymbol{\mathcal{F}}(\boldsymbol{\Omega}_a^{-1}\mathbf{B}_a^{-1}+\mathbf{J}^\dagger\boldsymbol{\Omega}_b^{-1}\mathbf{B}_b^{-1}\mathbf{J})^{-1}] \\ &+\mathbf{D}^\dagger\boldsymbol{\Omega}_b\mathbf{B}_b\mathbf{J}((\boldsymbol{\Omega}_a\mathbf{B}_a+\mathbf{J}^\dagger\boldsymbol{\Omega}_b\mathbf{B}_b\mathbf{J})^{-1})^\dagger\boldsymbol{\Omega}_a\mathbf{B}_a\boldsymbol{\mathcal{F}}\boldsymbol{\Omega}_a\mathbf{B}_a(\boldsymbol{\Omega}_a\mathbf{B}_a+\mathbf{J}^\dagger\boldsymbol{\Omega}_b\mathbf{B}_b\mathbf{J})^{-1}\mathbf{J}^\dagger\boldsymbol{\Omega}_b\mathbf{B}_b\mathbf{D}\Big\} \\ &\times e^{\mathbf{D}^\dagger(\boldsymbol{\Omega}_b\mathbf{B}_b\mathbf{J}(\boldsymbol{\Omega}_a\mathbf{B}_a+\mathbf{J}^\dagger\boldsymbol{\Omega}_b\mathbf{B}_b\mathbf{J})^{-1}\mathbf{J}^\dagger\boldsymbol{\Omega}_b\mathbf{B}_b-\boldsymbol{\Omega}_b\mathbf{B}_b)\mathbf{D}} \end{aligned} \tag{80}$$

Inputbeschreibung

Die im Rahmen dieser Arbeit entstandenen Routinen *intcon_gsl.c* und *intcon_t_gsl.c* sind analog zu der Erweiterung von Mihaljo Etinski in der Programmiersprache *C* verfasst und bilden ihrerseits eine Erweiterung des dynamischen Zweigs (`$method` dynamic) des Programms VIBES. Erstere Routine wird aufgerufen für den Fall $T = 0\,K$ und zweitere berechnet IC Ratenkonstanten für $T > 0\,K$. Unter Verwendung des dynamischen Zweigs wird eine Korrelationsfunktion (siehe Abschnitt 1.4.1) numerisch integriert. Hierfür wird vorab die Angabe des Zeitintervalls (in fs, `$interval`) und der Anzahl von Punkten (`$npoints`) für das Integrationsgitter benötigt. Das Intervall muss groß genug gewählt sein, sodass die gesamte Funktion

integriert wird. Zur Beschleunigung der Konvergenz ist es empfehlenswert die Korrelationsfunktion zu dämpfen. Der Parameter `$eta` spezifiziert die FWHM der Dämpfungsfunktion (in cm^{-1}). Physikalisch betrachtet beschreibt die Dämpfung die Dephasierung der Korrelationsfunktion durch VER bzw. IVR. Unabhängig vom verwendeten Zweig des Programms werden Daten für die Geometrien- und Normalmoden der Zustände (`$vibs` / `$coord-files`) sowie die adiabatische Energiedifferenz des rein elektronischen Übergangs (`$deltaE`) benötigt:

`$method`	dynamic
`$deltaE`	<real>
`$npoints`	<int>
`$interval`	<real>
`$eta`	<real>
`$temperature`	<real>
`$vibs`	gaufreq/mopac/molpro
<filename a>	
<filename b>	
`$coord-files`	
<filename a>	
<filename b> .	

Für die Berechnung von IC Ratenkonstanten müssen zudem NACMEs (in atomaren Einheiten) für alle vibratorischen Freiheitsgrade aufgelistet werden:

`$nac`	3N-6
1	f_1
2	f_2
3	f_3
⋮	⋮
3N-6	f_{3N-6}
`$end` .	

Teil III.

Anwendung

3.1. Xanthon

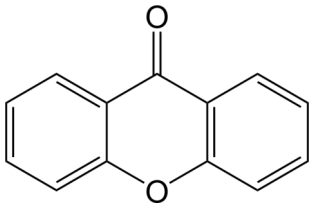

Abbildung 6.: Chemische Struktur von Xanthon.

Das Ziel dieses Projekts war die Modellierung von Übergängen zwischen angeregten Singulett- und Triplettzuständen des Xanthon Moleküls (siehe Abbildung 6) in Wasser sowie unpolarer Umgebung. Ein besonderes Augenmerk lag hierbei auf dem experimentellen Befund zeitversetzter Fluoreszenzkomponenten in wässriger Lösung. Im Kontrast dazu fällt die Fluoreszenzquantenausbeute in apolarem Medium deutlich geringer aus und das Molekül stellt einen guten Triplett-Sensibilisator dar [CPB96, LMSFJ00, SSR$^+$04, HSR$^+$06]. Ein zentraler Baustein zur Erklärung dieser Eigenschaften ist die Quantifizierung interner Konversion.

Xanthon ist ein Vertreter der aromatischen Ketone. Durch die charakteristische Carbonylgruppe kommt es für Xanthon und Derivate typischerweise zu stark ausgeprägter Spin–Bahn-Wechselwirkung von $n\pi^*$ und $\pi\pi^*$ Zuständen und effizienter Interkombination. Die Untersuchung der Photophysik von Xanthonen ist Gegenstand zahlreicher spektroskopischer [DM74, LL80, AK86, MSLJ$^+$99, BJ92, CPB96, LMSFJ00, SSR$^+$04, HSR$^+$06, AGV$^+$10, VRRC$^+$14, MVT$^+$16] und theoretischer Studien [RPSABJ06, RCKS$^+$10, RCSM11, RCVR$^+$14, MVT$^+$16, ARdHR21]. Die quantenchemische Beschreibung interner Konversion war bislang jedoch nicht erfolgt. Die durchgeführte Arbeit greift eine Studie von Rai-Constapel et al. [RCEM13] am Institut für Theoretische Chemie und Computerchemie Düsseldorf auf und liefert eine quantitative Beschreibung konkurrierender IC und ISC Übergänge.

Im Vakuum zeichnet sich nach Anregung des hellen $^1(\pi\pi^*)$ Zustands folgender Relaxationspfad ab (300 K): $^1(\pi\pi^*) \rightsquigarrow {}^1(n\pi^*)$ IC sowie Interkombination in die Triplettdomäne stellen konkurrierende Prozesse auf der Pikosekunden-Zeitskala dar. Im Anschluss an die Population des dunklen $n\pi^*$ Singuletts erfolgt ultraschnelle El-Sayed erlaubte ISC zum $\pi\pi^*$ Triplett. Beide Zustände liegen energetisch dicht beieinander, sodass sowohl ISC als auch rISC in der Größenordnung von $10^{12}\,\mathrm{s}^{-1}$ stattfinden. Der Rücktransfer von Population stellt jedoch keinen produktiven Kanal dar, da $^3(\pi\pi^*) \rightsquigarrow {}^3(n\pi^*)$ IC deutlich effizienter ausfällt ($\geq 10^{13}\,\mathrm{s}^{-1}$). Die adiabatische Energiedifferenz der Triplettzustände beträgt etwa 0.10 eV und die berechnete Ratenkonstante für rIC ist um zwei Größenordnungen kleiner als jene für den thermodynamisch

bevorzugten Übergang. Zusammenfassend lässt sich festhalten, dass der $^3(n\pi^*)$ T_1 Zustand ausgehend vom $^1(\pi\pi^*)$ S_2 Zustand auf konkurrierenden direkten sowie konsekutiven Pfaden auf der Pikosekunden-Zeitskala populiert wird. Hierbei stellen sowohl der $^1(n\pi^*)$ S_1 Zustand als auch der $^3(\pi\pi^*)$ T_2 Zustand Zwischenstadien dar. Die schwache Fluoreszenz des $n\pi^*$ Singuletts wird durch die ultraschnelle Kaskade von ISC gefolgt von IC gelöscht.

Zur Modellierung des kinetischen Schemas in Wasser wurden die Lösungsmitteleffekte an der Grundzustandsgeometrie auf die Geometrien der angeregten Zustände übertragen (siehe Unterkapitel 1.7). Die $\pi\pi^*$ Zustände werden moderat stabilisiert und die $n\pi^*$ Zustände werden stark blauverschoben, sodass es zur Umkehr der energetischen Reihenfolgen in den Domänen kommt. Das Lösungsmittelmodell führt zu einer Überschätzung der Blauverschiebung der $n\pi^*$ Zustände. Aufgrund dessen wurde die Abhängigkeit der Ratenkonstanten von den Energien der $n\pi^*$ Zustände untersucht. Das resultierende kinetische Schema für isoenergetische $^1(\pi\pi^*) \leftrightsquigarrow {}^3(n\pi^*)$ ISC liefert folgende Beschreibung für die Depopulation des hellen $^1(\pi\pi^*)$ Zustands (300 K): Die berechnete Ratenkonstante für $^1(\pi\pi^*) \rightsquigarrow {}^3(n\pi^*)$ ISC fällt um eine Größenordnung größer aus als jene für die direkte Population des energetisch isolierten ($\Delta E \approx 0.60\,eV$) $\pi\pi^*$ Tripletts. Sowohl ISC als auch rISC finden auf der Pikosekunden-Zeitskala statt, wobei der Rücktransfer bevorzugt wird. Die berechnete Ratenkonstante für $^1(\pi\pi^*) \leftsquigarrow {}^3(n\pi^*)$ rISC beträgt $3 \times 10^{10}\,s^{-1}$ und fällt damit ebenfalls größer aus als die Ratenkonstante für die konkurrierende IC in der Triplettdomäne ($8 \times 10^9\,s^{-1}$). Der bevorzugte Rücktransfer der Population zum fluoreszenten $^1(\pi\pi^*)$ Zustand ist im Einklang mit dem experimentellen Befund, dass für Xanthon in wässriger Umgebung sowohl direkte als auch verzögerte Fluoreszenzkomponenten beobachtet werden.

3.2. Fluorierte Flavine

Einen weiteren zentralen Gegenstand meiner Dissertation stellt die Modifikation des Flavinchromophpors dar (siehe Abbildung 7). Im Rahmen meiner Dissertation sind zwei Veröffentlichungen zu diversen Derivaten entstanden. An dieser Stelle werden sowohl die publizierten Verbindungen als auch Ergebnisse zu unveröffentlichten Derivaten diskutiert.

In der Natur ist das zugrundeliegende Strukturmotiv beispielsweise in Form von FMN (Flavinmononucleotid) und FAD (Flavin-Adenin-Dinukleotid) präsent. Zum einen als Coenzym in Oxidoreduktasen, z. B. für NADH-Dehydrogenase (NAD: Nicotinsäureamid-Adenin-Dinukleotid, H: Wasserstoff) im Komplex I der mitochondrialen Atmungskette oder für Succinat-Dehydrogenase

im Citratzyklus [CJ05]. Zum anderen sind diverse photoreaktive Proteine auf den Chromophor als Cofaktor angewiesen [PSS$^+$16, LG12, BB05, Bjö15, San03, MD15]. Aktuell sind drei Klassen Flavin-bindender Photorezeptoren bekannt: phot (Phototropine), cry (Cryptochrome) sowie BLUF (sensors of blue light using FAD) [CJWL99, GK02, BB05, LG12, CBPS14]. Im Zuge von Blaulicht-Absorption des Cofaktors wird ein Photozyklus eingeleitet, der im Falle von Phototropinen in der Ausbildung einer kovalenten Bindung zwischen Chromophor und einer Cysteineinheit der Proteintasche resultiert [SCC$^+$01, NS03, SSJTM09, NWM17]. Die Signaltransduktion wird durch die strukturelle Änderung im Apoprotein ausgelöst und dient der Steuerung diverser Prozesse. Dazu gehören beispielsweise die namensgebende Phototropie [LAL$^+$14], Photorelokation [SW07], Gametogenese [HB03] oder die Taktung der circadianen Rhythmik [San04]. Der Forschungsbereich der Optogenetik beschäftigt sich mit der Regulation zellulärer Aktivität durch Licht [FYD11]. In diesem Zusammenhang stellen Flavin-basierte Photorezeptoren vielversprechende Systeme zur biomimetischen Kontrolle dar: Zum Beispiel ist es gelungen, durch ein Rac Protein mit LOV [light-oxygen-voltage(-sensing)] Domäne, Einfluss auf die Beweglichkeit lebender Zellen zu nehmen [WFL$^+$09]. Weitere Anwendungsgebiete stellen die lichtinduzierte Erzeugung von Singulett Sauerstoff (oder anderer reaktiver Sauerstoffspezies) [SLRD$^+$11, TLS$^+$19] sowie in-vivo Fluoreszenzmikroskopie dar [DEC$^+$07, CFK$^+$08, JG15, BPR$^+$15]. Hierfür wird der Photozyklus durch Substitution der Cysteineinheit gegen Alanin oder Glycin auf den Cofaktor beschränkt [SSKV15]. LOV Domänen sind aufgrund ihrer geringen Größe von besonderem Interesse für das Design fluoreszenter Proteine (FMN-binding fluorescent protein, FbFP) [JG15]. Außerdem funktionieren FbFPs, anders als GFP (green fluorescent protein) und Derivate, unabhängig von molekularem Sauerstoff [BPR$^+$15]. Durch ungerichtete Mutagenese wurden die Photo-/Thermostabilität sowie Helligkeit verbessert. Die Fluoreszenzquantenausbeuten resultierender Fluoreszenzproteine liegen bei über 40 % [CFK$^+$08, KHN$^+$19] (freies FMN: 25 % [WPE$^+$14]).

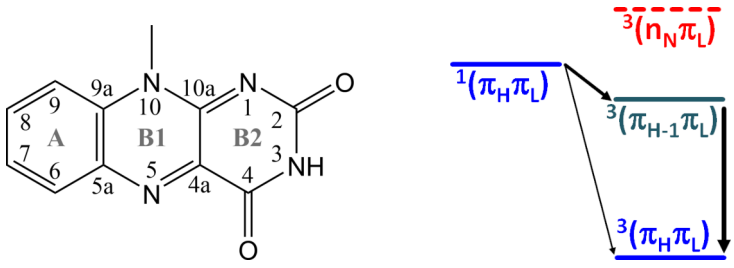

Abbildung 7.: Chemische Struktur von 10-Methylisoalloxazin (MIA) und Darstellung der adiabatischen Energien ausgewählter Zustände in wässrigem Medium.

Die Photophysik des zugrundeliegenden Chromophors, 10-Methylisoalloxazin (MIA, siehe Ab-

bildung 7), ist maßgeblich durch drei ISC Kanäle geprägt [STM08]. Im Anschluss an die Population des hellen $^1(\pi_H\pi_L)$ Zustands werden in polarer Umgebung zwei $\pi\pi^*$ Tripletts populiert: Sowohl der $^1(\pi_H\pi_L) \rightsquigarrow {}^3(\pi_H\pi_L)$ als auch der effektivere $^1(\pi_H\pi_L) \rightsquigarrow {}^3(\pi_{H-1}\pi_L)$ ISC Kanal sind spin-vibronisch angetrieben. Die $n\pi^*$ Zustände reagieren stark auf die Polarität und Protizität der Umgebung, sodass der El-Sayed erlaubte $^1(\pi_H\pi_L) \rightsquigarrow {}^3(n_N\pi_L)$ Kanal lediglich in unpolarem Medium zugänglich ist. Die Zielsetzung des Projekts im Rahmen des Graduiertenkollegs 'Modulation of ISC' (ModISC) besteht im Hinblick auf biomimetische Anwendungen von Photorezeptoren in der Erhöhung der Fluoreszenz- bzw. Triplettquantenausbeute. Dies soll primär dadurch erreicht werden, dass der $^1(\pi_H\pi_L) \rightsquigarrow {}^3(\pi_{H-1}\pi_L)$ Kanal deaktiviert / der El-Sayed erlaubte ISC Kanal aktiviert wird. Die modifizierten Chromophore wurden in wässrigem Medium untersucht. Die adiabatischen Energien [implizite Solvatation mittels COSMO Modell [KS93] und stateshift-Prozedur (Unterkapitel 1.7), siehe Abbildung 7 für eine maßstabsgerechte Darstellung] der ISC Übergänge betragen für die $^1(\pi_H\pi_L) \rightsquigarrow {}^3(\pi\pi^*)$ Kanäle 0.10 eV ($\pi_{H-1}\pi_L$) bzw. 0.56 eV ($\pi_H\pi_L$). Die berechnete adiabatische Barriere für den El-Sayed erlaubten Übergang beträgt 0.16 eV. Im Rahmen meiner Masterarbeit [Bra17] sowie der ersten Veröffentlichung wurde der Einfluss von Wasserstoffbrückenbindungen auf die Energien ausführlich untersucht. Unter Berücksichtigung expliziter Wassermoleküle ergibt sich eine zusätzliche Destabilisierung des $^3(n_N\pi_L)$ Zustands um 0.06 eV und der $^3(\pi_{H-1}\pi_L)$ ICT (internal charge-transfer) erfährt eine zusätzliche Stabilisierung um 0.11 eV.

Die untersuchten Modifikationen zielen darauf ab, die energetische Lage der elektronischen Zustände durch Fluorierung zu beeinflussen. Der methodische Ansatz ist eng mit der Wahl des Elementes Fluor verknüpft. Diese liegt zum einen darin begründet, dass es sich um das Element mit der höchsten Elektronegativität handelt. Somit ist zu erwarten, dass die Einführung von Fluor zu einer vergleichsweise starken Änderung der Verteilung von Elektronendichte und in der Konsequenz energetischen Verschiebung der elektronischen Zustände führt. Zum anderen ist Fluor ein vergleichsweise kompaktes Atom und weist nach Wasserstoff und Helium den drittkleinsten van-der-Waals-Radius auf ($r_F/r_H \approx 1.3$) [Bon64, RT96], sodass die Größe des Chromophors nur unwesentlich beeinflusst wird. Ein positiver Nebeneffekt ist die Stabilisierung der Verbindung bezüglich (Photo-)Oxidation [BFNR07, CVR+13]. MIA lässt sich in drei annelierte Ringe aufteilen und dementsprechend kann eine Unterscheidung der untersuchten Modifikationen getroffen werden:

1. Fluorierungen und Trifluoromethylierungen des Benzolrings [A-Ring: C(6)–C(9)], und
2. diverse Modifikationen der B1- und B2-Ringe, die mit Substitutionen der Stickstoff- bzw. Sauerstoffatome einhergehen.

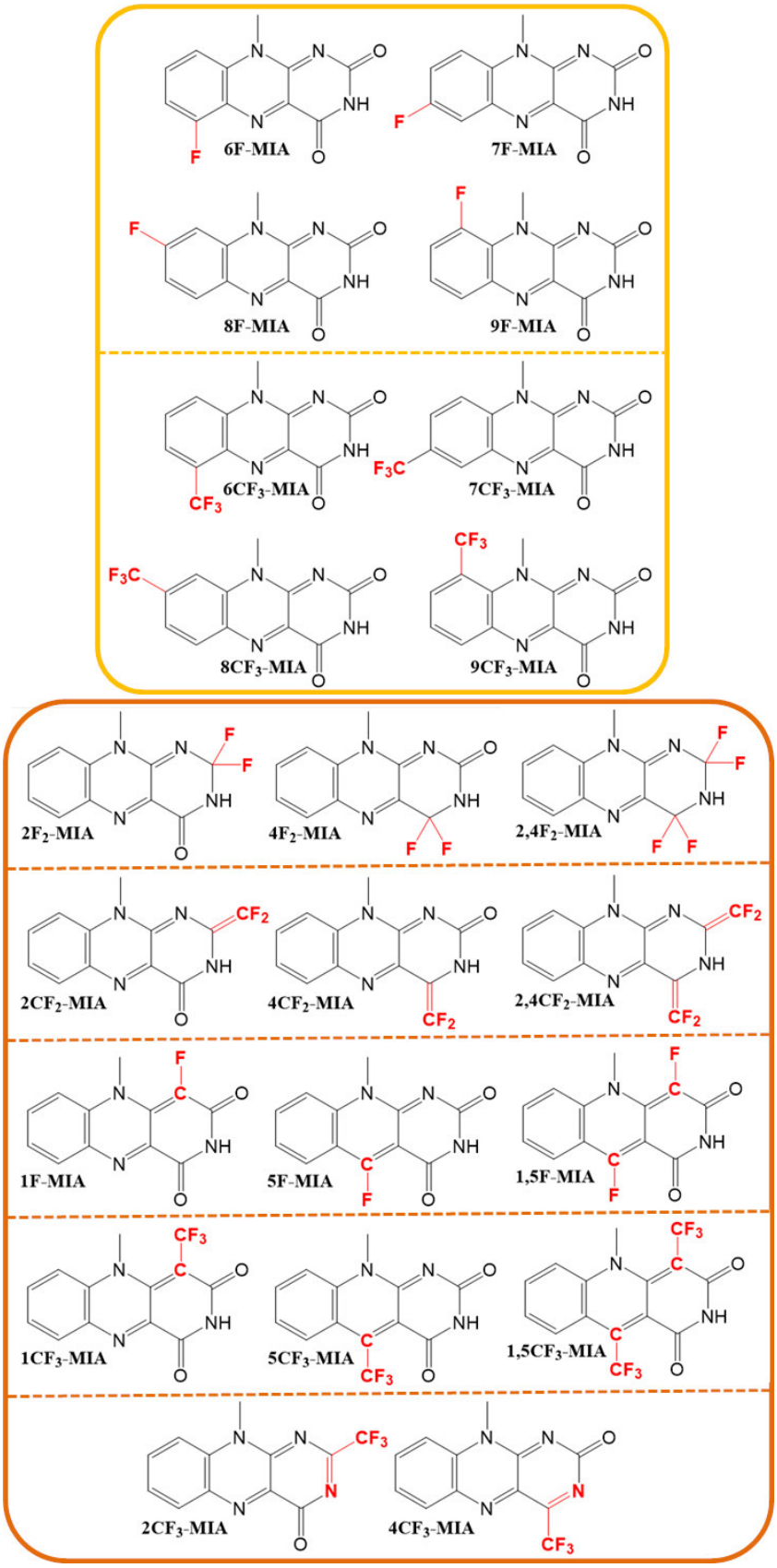

Abbildung 8.:

Abbildung der untersuchten fluorierten Flavinderivate mitsamt der zugeordneten Namen. Die gelbe Markierung umfasst die Substitutionen am A-Ring und die orange Markierung umfasst die Substitutionen an den B-Ringen. Die Änderungen am Chromophor sind rot hervorgehoben. Derivate mit mehrfachen Substitutionen am A-Ring sind nicht dargestellt.

Die erste Veröffentlichung behandelt die Fluorierung des Benzolrings. Der Einfluss auf die Energien der S1–2 und T1–3 Zustände fällt vergleichsweise klein aus ($< 0.10\,\text{eV}$, siehe Abbildung 9). Die Effekte verursachen keine grundlegende Änderung der Photophysik des Chromophors [RTE+18] und sind eher als Feinabstimmung der Energien zu verstehen. Neben den einfach fluorierten Derivaten wurden zudem mehrfache Fluorierungen des A-Rings untersucht. Es konnte festgestellt werden, dass sich die energetischen Verschiebungen in guter Näherung additiv verhalten. Der Einfluss von Trifluoromethylierung in den Positionen 6–9 ist mit $\leq 0.17\,\text{eV}$ (siehe Abbildung 9) ähnlich schwach ausgeprägt. Der $n\pi^*$ Triplettzustand wird durch die CF_3 Gruppen systematisch stabilisiert, wohingegen der $^3(\pi_{H-1}\pi_L)$ Zustand systematisch destabilisiert wird. Der Vergleich mit Fluorierung des Benzolrings zeigt, dass der $^3(\pi_{H-1}\pi_L)$ Zustand für die Derivate 6F- und 9F-MIA destabilisiert wird und die Energie des $^3(n_N\pi_L)$ Zustands nahezu gleich bleibt. Die Substituenten unterscheiden sich im Wesentlichen dadurch, dass das Fluoratom Elektronendichte im out-of-plane p Orbital aufnimmt und es dadurch zu einer Vergrößerung des π-Systems kommt, wohingegen der Effekt der CF_3 Gruppe auf Hyperkonjugation

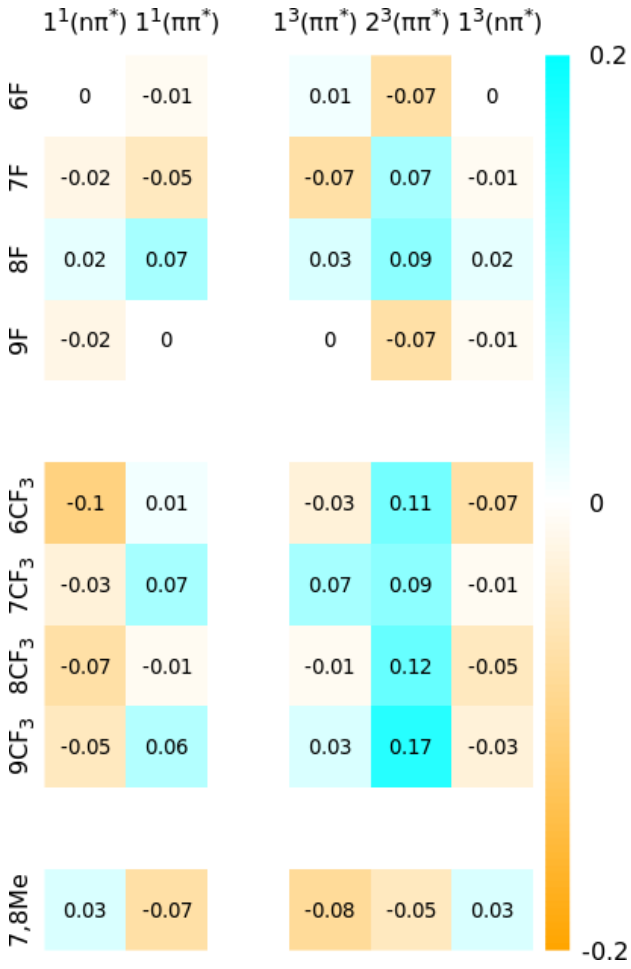

Abbildung 9.:
Darstellung der Verschiebungen vertikaler elektronischer Energien durch Fluorierung sowie Trifluoromethylierung am Benzolring (A-Ring, Positionen 6–9). Die Effekte sind relativ zu den Zustandsenergien des Stammmoleküls MIA an der Grundzustandsgeometrie in wässriger Lösung. Bei den ausgewählten Zuständen handelt es sich um die $^1(n_N\pi_L)$, $^1(\pi_H\pi_L)$ Singuletts sowie die $^3(\pi_H\pi_L)$, $^3(\pi_{H-1}\pi_L)$, $^3(n_N\pi_L)$ Tripletts (in entsprechender Reihenfolge). Die Skala umfasst $\pm 0.2\,\text{eV}$. Die ensprechenden chemischen Strukturen sind in Abbildung 8 dargestellt. Zusätzlich zu den fluorierten Derivaten sind energetische Unterschiede zwischen MIA und Lumiflavin dargestellt (unterste Zeile).

und einen größeren negativen induktiven Effekt zurückzuführen ist. Die einzelnen energetischen Verschiebungen hängen von der Elektronendichte am jeweiligen Zentrum im Stammmolekül MIA sowie Änderungen der CI-Koeffizienten ab und sind stark positionsabhängig. Die Rot-/Blauverschiebungen durch die CF_3 Gruppe sind einzeln betrachtet zu schwach, um den $^1(\pi_H\pi_L) \rightsquigarrow {}^3(\pi_{H-1}\pi_L)$ Kanal zu deaktivieren / den $^1(\pi_H\pi_L) \rightsquigarrow {}^3(n_N\pi_L)$ Kanal zu aktivieren und mehrfache Trifluoromethylierung führt teilweise zu starken sterischen Verzerrungen des Chromophors.[2] Aufgrund dessen wurden für die zweite Veröffentlichung Änderungen an den B-Ringen in Betracht gezogen.

Da es sich bei der zweiten Gruppe von Flavinderivaten um wesentlich größere Eingriffe in die elektronische Struktur des Chromophors handelt, ergeben sich für die entsprechenden Verbindungen weitaus größere Effekte (siehe Abbildung 12). Die Konsequenzen sind mitunter weitreichend und umfassen sowohl die angestrebte Deaktivierung des geschwindigkeitsbestimmenden ISC Kanals als auch die Aktivierung El-Sayed erlaubter ISC Kanäle. Für $2CF_2$- sowie 1F- und $1CF_3$-MIA ergibt sich eine stark ausgeprägte Rotverschiebung der $\pi_H\pi_L$-Übergänge von einem viertel bis zu einem halben Elektronenvolt, die neben der Deaktivierung des zweiten ISC Kanals auch zur Änderung des Farbeindrucks der Fluoreszenz ($2CF_2$- und 1F-MIA: rot, $1CF_3$-MIA: gelb) führt. Substitution des N(1) Atoms resultiert in sterischer Wechselwirkung der Methylgruppe mit dem zusätzlichen Bindungspartner des C(1) Zentrums. Während der Effekt für 1F-MIA mit einer Barriere von 0.05 eV gering ausfällt, zwingt Trifluoromethylierung das Molekül, die CF_3 Gruppen in entgegengesetzten Richtungen aus der Ebene zu heben (siehe Abb. 10).

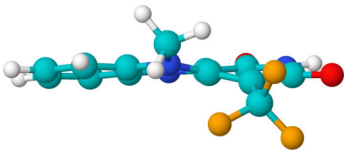

Abbildung 10.: Abbildung der S_0 Geometrie von $1CF_3$-MIA.

Die Barriere zwischen den einhergehenden Isomeren beläuft sich auf etwa 0.5 eV, sodass eine Isomerisierung ausgeschlossen ist. Aufgrund der Verzerrung der Verbindung und der einhergehenden Problematik für die Synthese wurde von einer detaillierten Charakterisierung von $1CF_3$-MIA Abstand genommen. Für 1F- und $2CF_2$-MIA geht die starke Rotverschiebung der S1 und T1 Zustände mit erhöhten Ratenkonstanten für $S_1 \rightsquigarrow S_0$ interne Konversion einher, sodass geringe Fluoreszenzquantenausbeuten zu erwarten sind. Bezüglich einer Erhöhung der Triplettquantenausbeute weisen die Derivate $2CF_3$- und $4CF_3$-MIA interessante Eigenschaften auf: Entfernung des Wasserstoffatoms in Position 3 resultiert in einer starken Stabilisierung der $n\pi^*$ Zustände und Aktivierung El-Sayed erlaubter ISC mit gesteigerter SOC. Im Rahmen der zweiten Veröffentlichung wurden detaillierte kinetische Schemata für die vier selektierten Derivate aufgestellt.

[2] Eine Ausnahmen ist das Derivat $6,8CF_3$-MIA. Im Falle von Position 9 führt bereits einfache Substitution zur Entplanarisierung.

Abbildung 12 enthält zusätzlich zu den veröffentlichten Substitutionen sowie den Derivaten 1CF_3- und 5CF_3-MIA auch Kombinationen von Modifikationen. Die Blauverschiebungen sind für 2,4F_2-MIA deutlich stärker ausgeprägt als für 2F_2-MIA sowie 4F_2-MIA und lassen sich analog zur Fluorierung des A-Rings durch Addition der einzelnen Effekte beschreiben. Für 2,4CF_2-, 1,5F- sowie 1,5CF_3-MIA bricht diese Näherung zusammen. Neben sterischen Effekten kann dies darauf zurückgeführt werden, dass eine Korrespondenz von elektronischen Zuständen nur noch bedingt gegeben ist: Beispielsweise stellen die $1\,^3(\pi\pi^*)$ und $2\,^3(\pi\pi^*)$ Zustände für 2,4CF_2-MIA ähnliche Anregungen von den CF_2 Fragmenten in das π_L Orbital dar. Beide Zustände sind Linearkombinationen der $\pi_H\pi_L$ und $\pi_{H-1}\pi_L$ Anregungen und liegen energetisch 0.28 eV auseinander. Die π_H und π_{H-1} Orbitale weisen vorwiegend Elektronendichte auf einem der beiden Fragmente auf:

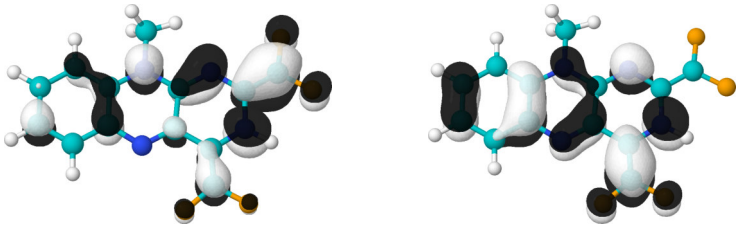

Abbildung 11.: Darstellung der π_H (links) sowie π_{H-1} (rechts) Orbitale von 2,4CF_2-MIA.

Zusammenfassend lässt sich festhalten, dass durch Fluorierung am Benzolring keine grundlegende Änderung der Photophysik des Flavinchromophors erwartet werden kann. Die Effekte durch Trifluoromethylierung in den Positionen 6–9 fallen zwar größer aus, allerdings führt mehrfache Substitution, mit Ausnahme von 6,8CF_3-MIA, zur Entplanarisierung des Chromophors. Deutlich größere Effekte auf die elektronischen Energien und in der Konsequenz Eigenschaften des Moleküls werden durch Modifikationen der Pteridindion-Einheit berechnet. Im Hinblick auf eine Erhöhung der Triplettquantenausbeute konnten zwei vielversprechende Derivate gefunden werden: Für 2CF_3- und 4CF_3-MIA werden El-Sayed erlaubte ISC Kanäle in polarer Umgebung aktiviert. Die Fluoreszenz wird gelöscht und strahlungslose Deaktivierung ist deutlich langsamer als ISC (4CF_3-MIA) bzw. steht in Konkurrenz zur ISC (2CF_3-MIA). Für eine Erhöhung der Fluoreszenzquantenausbeute ist die verfolgte Strategie, den S_1 Zustand von den T_2 und T_3 Zuständen durch Rotverschiebung zu separieren, zu kurz gegriffen, da die Stabilisierung des S_1 Zustands für die untersuchten Flavinderivate mit einer Steigerung der Geschwindigkeit der strahlungslosen Deaktivierung einhergeht. Für die Derivate 1F- sowie 2CF_2-MIA wird zwar die Interkombination verlangsamt, allerdings sind die berechneten IC Ratenkonstanten deutlich größer als für die Stammverbindung. In der Konsequenz müssen alternative Strategien verfolgt werden, die mit geringeren IC Ratenkonstanten einhergehen.

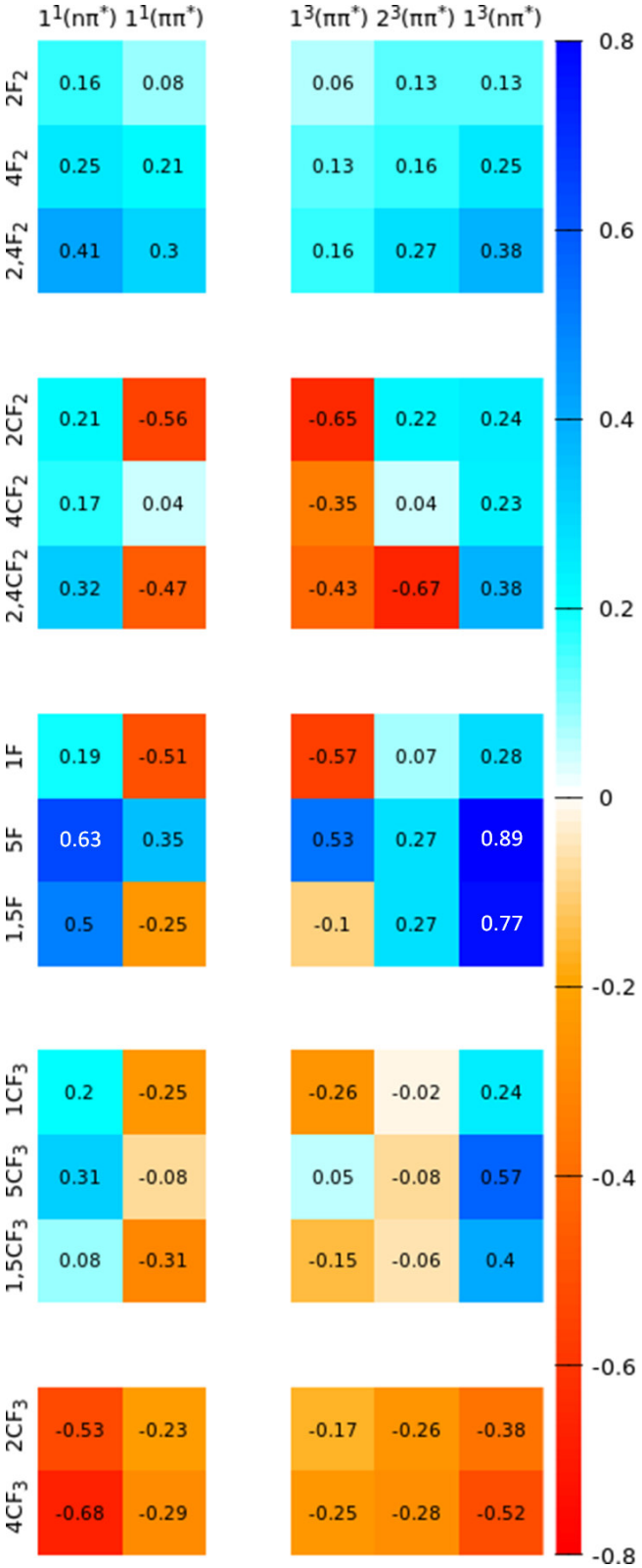

Abbildung 12.:

Darstellung der Verschiebungen vertikaler elektronischer Energien durch diverse Substitutionen an den B-Ringen (Positionen 1–5). Die Effekte sind relativ zu den Zustandsenergien des Stammmoleküls MIA an der Grundzustansgeometrie in wässriger Lösung. Bei den ausgewählten Zuständen handelt es sich um das erste $n\pi^*$ Singulett, den $^1(\pi_H\pi_L)$ Zustand sowie die $^3(\pi_H\pi_L)$, $^3(\pi_{H-1}\pi_L)$ Zustände und das erste $n\pi^*$ Triplett (in entsprechender Reihenfolge). Die Skala umfasst $\pm 0.8\,\mathrm{eV}$ und ist somit um Faktor vier größer als jene für Modifikation am A-Ring (vgl. Abb. 9). Die ensprechenden chemischen Strukturen sind in Abbildung 8 dargestellt.

3.3. Heptazin und HAP-3MF

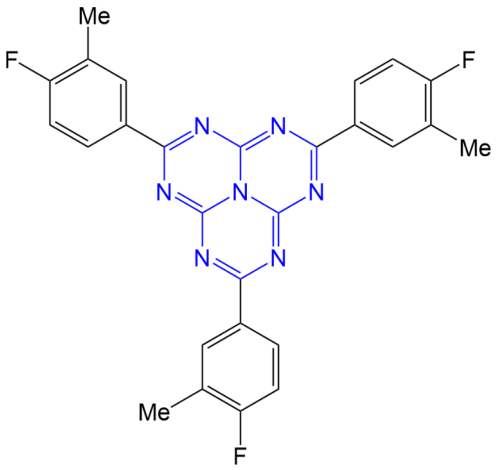

Abbildung 13.: Chemische Struktur von HAP-3MF [2,5,8-Tris(4-fluoro-3-methylphenyl)-1,3,4,6,7,9,9*b*-Heptaazaphenalen]. Die blau eingefärbte Struktur ist der zugrundeliegende Heptazin Chromophor.

Der Heptazin Chromophor (siehe Abbildung 13) stellt grundsätzlich ein vielversprechendes Strukturmotiv für den Einsatz als Emitter in OLEDs dar. Der erste angeregte Singulett- und der analoge Triplettzustand sind nahezu isoenergetisch, sodass sowohl ISC als auch rISC effizient ablaufen können und eine gegenseitige Umwandlung von Singulett- und Triplettexzitonen möglich ist. Üblicherweise wird die Singulett–Triplett-Energielücke, ΔE_{ST}, und dementsprechend die Austauschwechselwirkung durch räumliche Separation einer Donor- und einer Akzeptoreinheit (charge-transfer, CT) gering gehalten [MFKE18]. Im Falle von Heptazin liegt die geringe Aufspaltung der beiden $\pi_H\pi_L$ Zustände darin begründet, dass die Orbitale π_H und π_L disjunkt sind. Die tatsächliche Aufspaltung sowie Reihenfolge der beiden Zustände ist abhängig von der elektronischen Strukturmethode [ERP$^+$19, PFL$^+$21] und daher nicht eindeutig geklärt. Im Falle von DFT/MRCI führt Spinpolarisierung [KS78, aTNT85] dazu, dass der Triplettzustand energetisch unterhalb des korrespondierenden Singulettzustands liegt [inverted singlet–triplet (IST) gap].

Im Rahmen der Veröffentlichung wird geschlussfolgert, dass die Effizienz des $S_1 \leftsquigarrow T_1$ Rücktransfers für Heptazin und das Derivat 2,5,8-Tris(4-fluoro-3-methylphenyl)-1,3,4,6,7,9,9*b*-Heptaazaphenalen (HAP-3MF, siehe Abbildung 13) nicht etwa dadurch bestimmt ist, dass die Energielücke groß ausfällt [ERP$^+$19, PFL$^+$21, SD21], sondern vielmehr die Effizienz der Spin–Bahn-Kopplung und eine geringe energetische Aufspaltung der Zustände den Prozess begünstigt. Da es sich bei den $S_1 \leftrightsquigarrow T_1$ sowie $S_1 \rightsquigarrow S_0$ Übergängen um symmetrieverbotene Prozesse han-

delt, sind sowohl (r)ISC als auch Fluoreszenz auf vibronische Kopplung angewiesen. $S_1 \rightsquigarrow S_0$ interne Konversion wird symmetriebedingt einzig von $A'_{(2)}$-Moden (Heptazin: D_{3h}, HAP-3MF: C_{3h}) vermittelt. Im Falle von Heptazin in vacuo ist die berechnete IC Ratenkonstante deutlich größer ($\sim 10^8\,s^{-1}$) als die Ratenkonstanten für Interkonversion ($\sim 10^{6-7}\,s^{-1}$) und Fluoreszenz ($\sim 10^5\,s^{-1}$). Im Einklang mit dem experimentellen Befund, dass HAP-3MF in Toluol TADF auf der μs-Zeitskala aufweist [LZN+14], wurden für das Vakuum Ratenkonstanten in der gleichen Größenordnung erhalten: $k_{IC} = k_F = 9 \times 10^5\,s^{-1}$, $k_{rISC} = 3 \times 10^5\,s^{-1}$ und $k_{ISC} = 7 \times 10^7\,s^{-1}$. Die deutlich weniger effiziente IC für das Derivat kann auf die Substitution der Wasserstoffatome durch 4-Fluoro-3-methylphenyl-Gruppen zurückgeführt werden: Die Kopplungen der elektronischen und vibratorischen Wellenfunktionen skalieren mit der inversen molekularen Masse (siehe Gleichung 78).

3.4. NMA-dF

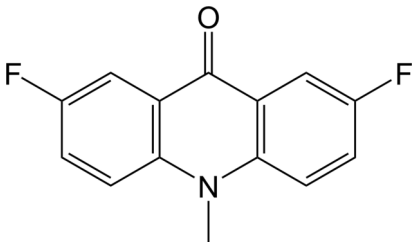

Abbildung 14.: Chemische Struktur von NMA-dF (*N*-Methyl-difluoro-Acridon).

Zur Maximierung der Elektrolumineszenz in OLEDs werden unterschiedliche Strategien zum Design effizienter Emitter verfolgt. In der Praxis kommen aktuell vor allem Iridium- und Platin-Komplexe zum Einsatz [VWF+15]: In Folge stark ausgeprägter Spin–Bahn-Kopplung werden effektiv sowohl die 3/4 Triplett- als auch die 1/4 Singulettexzitonen durch Phosphoreszenz strahlend emittiert [BOY+98]. Der Nachteil dieser Strategie ('triplet harvesting') sind vergleichsweise lange Lebensdauern (μs-Zeitskala) der Lumineszenz sowie hohe Kosten der verwendeten Übergangsmetalle. Die Lebensdauern stellen insbesondere für entsprechende Emitter im blauen Bereich des Spektrums ein Problem dar: Der hohe Energiegehalt in Kombination mit der Population des Triplettzustands geht mit gesteigerter chemischer Reaktivität einher. Der Kostenfaktor kann durch die Verwendung vergleichsweise günstiger Metalle (etwa Kupfer oder Zink) reduziert werden [FGSM19, LaCMM20, HBT+21, Dum14]. Ein alternativer Ansatz mit organischen Verbindungen basiert auf der Idee Triplettexzitonen durch eine geringe Singulett–Triplett-Aufspaltung ($\Delta E_{ST} \approx k_B T$) in Population des fluoreszenten Singuletts umzuwandeln

('singlet harvesting'). Beim Design sogenannter TADF (thermally activated delayed fluorescence [EOT+09]) Moleküle wird der Chromophor typischerweise in eine Emitter- und eine Akzeptoreinheit aufgeteilt, wodurch die Austauschwechselwirkung minimiert werden kann [MFKE18]. Eine weitere Möglichkeit stellt der elektronische Übergang zwischen disjunkten Elektronendichteverteilungen dar (siehe Unterkapitel 3.3). Intrinsische Nachteile der TADF Strategie sind vergleichsweise breite Emissionsspektren und langsame Fluoreszenzraten, welche die Helligkeit limitieren und in ähnlichen Lebensdauern wie für Emitter mit Metallzentren resultieren. Prinzipiell lassen sich die Nachteile von TADF Emittern durch eine alternative intramolekulare Strategie eliminieren: Die Umwandlung von Triplettexzitonen eines T_n Zustands ($n > 1$) in Singulettexzitonen. Voraussetzung für ein solches System ist, dass die ISC Ratenkonstante vom T_n Zustand in die Singulettdomäne mit der IC Ratenkonstante $T_n \rightsquigarrow T_1$ konkurrieren kann ('high re-ISC' / 'hot exciton' [XXHM21]) und die Fluoreszenzquantenausbeute nahe eins ist.

Im Rahmen dieser Veröffentlichung stehen die experimentellen Befunde stark im Vordergrund und den quantenchemischen Ergebnissen kommt eine unterstützende Rolle zu. NMA-dF (*N*-Methyl-difluoro-Acridon, siehe Abbildung 14) in Methanol emittiert im blauen Wellenlängenbereich und weist eine Fluoreszenzquantenausbeute nahe eins ($\Phi_F \approx 0.9$) auf. Im Rahmen der angestellten Studie konnte gezeigt werden, dass das untersuchte fluorierte Acridonderivat Triplettexzitonen anteilig in Fluoreszenz umwandelt. Für $^3(n\pi^*) \rightsquigarrow S_1$ Interkombination wurde eine Ratenkonstante von $7 \times 10^{10}\,s^{-1}$ berechnet. Die theoretisch ermittelte Ratenkonstante für $^3(n\pi^*) \rightsquigarrow T_1$ interne Konversion beläuft sich auf $4 \times 10^{10}\,s^{-1}$ und liegt somit in der gleichen Größenordnung wie die konkurrierende ISC in die Singulettdomäne. Die S_1 und T_1 Zustände weisen $\pi\pi^*$ Charakter auf. Die direkte Population des T_1 Zustands ausgehend vom nächsthöheren $^3(\pi\pi^*)$ Zustand, welcher energetisch in der Nähe liegt, wurde aufgrund einer deutlich größeren $2\,^3(\pi\pi^*) \rightsquigarrow 1\,^3(\pi\pi^*)$ Ratenkonstante ausgeschlossen. Zur Modellierung des Lösungsmitteleffekts von Methanol wurden die Effekte an der Grundzustandsgeometrie auf die Geometrien der angeregten Zustände übertragen (siehe Unterkapitel 1.7). Zusätzlich zur impliziten Solvatation mittels COSMO wurden Wasserstoffbrückenbindungen zur Carbonylgruppe durch zwei explizite Methanolmoleküle berücksichtigt.

Zusammenfassung

Das zentrale Ergebnis dieser Dissertation ist eine Methode zur Quantifizierung von Ratenkonstanten für interne Konversion. Zur Berechnung nichtadiabatischer Kopplung wurde ein numerisches Verfahren basierend auf nichtorthogonalen Überlapps umgesetzt. Zur effizienten Berechnung der Überlapps von DFT/MRCI-Wellenfunktionen wurde das Programm Delta entwickelt. Der implementierte Algorithmus basiert auf der Herangehensweise von Plasser et al. [PRM$^+$16] in Kombination mit Schur's Determinanten Identität und einem Selektionsverfahren nach Anregungsklassen. Zur Berechnung des nichtorthogonalen Überlapps der elektronischen Wellenfunktionen ist es notwendig, paarweise Überlapps von Slaterdeterminanten auszuwerten. Die Verwendung der Identität fußt auf der Erkenntnis, dass die anfallenden Überlappmatrizen blockweise variieren, sodass Zwischenergebnisse der Identität wiederverwendet werden können. Die von Plasser et al. eingeführte Wiederverwendung von Spinfaktoren wurde auf einfach angeregte Slaterdeterminanten beschränkt. Das Programm Delta generiert Überlappmatrizen on-the-fly. Der Algorithmus zeichnet sich durch einen vorteilhaften Kompromiss bezüglich Rechenzeit und Speicherbedarf aus. DFT/MRCI berechnet aus Symmetriegründen $M_S = 1$-Komponenten von Triplettwellenfunktionen. Es wurde gezeigt, dass für die Berechnung der Überlapps von $M_S = 0$-Komponenten eine geringere Anzahl an Determinanten von Überlappmatrizen anfällt, sodass Triplettwellenfunktionen in die $M_S = 0$-Komponente transformiert werden.

Zur Berechnung von IC Ratenkonstanten mittels Fermis Goldener Regel werden NACMEs entlang aller Normalmoden des initialen Zustands benötigt. Die Matrixelemente werden durch Bildung eines zentralen Differenzenquotienten erhalten: Der Zähler wird durch die nichtorthogonalen Überlapps für positive und negative Auslenkungen entlang der jeweiligen Mode gebildet und der Nenner ist durch die Schrittweite der Auslenkungen gegeben. Letztere stellt einen technischen Parameter dar. Es wurde gezeigt, dass sich für massegewichtete Normalkoordinaten ein Wert von $\epsilon = 0.01$ eignet. Die Koordination der SCF-, DFT/MRCI-, sowie Delta-Rechnungen erfolgte im Rahmen dieser Arbeit durch das Skript *dd.py*. Dieses steuert sämtliche Schritte ausgehend von einer initialen DFT/MRCI-Rechnung an der Referenzgeometrie. Entsprechende Rechnungen für ausgelenkte Geometrien werden als restart-Läufe aufgesetzt.

Zur Beschreibung der Kopplung der Kernwellenfunktionen wurde eine implizite Beschreibung von Franck–Condon-Faktoren verfolgt. Der zeitabhängige Zweig des Programms VIBES basiert auf der Formulierung von Fermis Goldener Regel im Heisenberg-Bild und beschreibt die Wechselwirkung der initialen und finalen Wellenfunktionen mittels Korrelationsfunktionen. Im Rahmen dieser Arbeit wurde eine entsprechende Korrelationsfunktion für die temperaturabhängige Quantifizierung interner Konversion hergeleitet und implementiert.

Die erfolgte Methodenentwicklung geht mit Anwendungsbeispielen einher: Zum besseren Verständnis des Xanthon Moleküls wurden kinetische Schemata für wässriges Medium sowie apolare Lösungsmittel aufgestellt. Diese umfassen ISC und IC Ratenkonstanten für die ersten $\pi\pi^*$ und nπ^* Zustände in den Singulett- und Triplettdomänen. Nichtadiabatische Kopplung verhält sich antiproportional zur vertikalen Energiedifferenz wechselwirkender Zustände. Zur Beschreibung der NACMEs und SOCMEs in wässrigem Medium wurden die Rotverschiebungen der $\pi\pi^*$ Zustände und Blauverschiebungen der $n\pi^*$ Zustände an der Grundzustandsgeometrie auf die entsprechenden Zustände an den angeregten Geometrien übertragen. Experimentell weist Xanthon in apolarer Umgebung eine verschwindend geringe Fluoreszenzquantenausbeute auf, wohingegen in wässrigem Medium eine deutliche Steigerung festgestellt wurde. Es wurden sowohl direkte als auch verzögerte Fluoreszenzkomponenten detektiert. Das kinetische Modell für wässriges Medium steht im Einklang mit diesem Befund: Die $^1(\pi\pi^*) \leftsquigarrow {}^3(n\pi^*)$ reverse ISC Ratenkonstante zum fluoreszenten Singulettzustand ist größer als jene für die strahlungslose Deaktivierung innerhalb der Triplettdomäne. In apolarer Umgebung wird die Singulettdomäne auf der ps-Zeitskala depopuliert.

Im Rahmen der Veröffentlichung [J. Chem. Phys., 155, 014102 (2021)] wurde das numerische Vorgehen zur Berechnung von NACMEs durch Vergleiche mit analytischen Matrixelementen validiert. Hierfür wurden Kopplungen von CASSCF-Wellenfunktionen von Formaldehyd ausgewertet. Des Weiteren wurde die Abhängigkeit des Programms DELTA von technischen Parametern untersucht. Der Einfluss des Konvergenzschwellwertes der Diagonalisierung der CI-Matrix ist bedeutsam für die korrekte Beschreibung numerischer Nullen. Für das Testmolekül Pyrazin wurden für den Default-Wert des DFT/MRCI-Programms fünf korrekte Nachkommastellen für symmetrieverbotene Kopplungen erhalten. Es stellt sich heraus, dass die Default-Konvergenzschwellwerte von Turbomole für die Molekülorbitale zu gering ausfallen. Das Skript *dd.py* setzt die entsprechenden Parameter standardmäßig auf `$scfconv=9` sowie `$denconv=1.0E-10`. Von entscheidender Bedeutung für die Effizienz der numerischen Berechnung von NACMEs ist der Parameter `$renorm` für die Kürzung und Renormierung der Wellenfunktionen. Es wird gezeigt, dass sich ein Schwellwert von `$renorm=1.0E-8` für Konvergenz der

NACMEs auf 5 Nachkommastellen eignet. Die berechneten IC Ratenkonstanten für Xanthon ändern sich für Werte $\leq$ `1.0E-6` nur unwesentlich.

Ein weiteres Anwendungsbeispiel ist das Acridonderivat NMA-dF in Methanol. Bei diesem Molekül handelt es sich um einen effizienten Fluorophor im blauen Wellenlängenbereich. Im Rahmen einer experimentell geprägten Studie wurde die Eignung von NMA-dF als Emitter von T_n ($n > 1$) Triplettexzitonen via $T_n \rightsquigarrow S_1$ Interkombination untersucht. Im Experiment wurde ein Triplettsensibilisator zur Population der Triplettdomäne des Fluorophors eingesetzt. Die berechneten IC Ratenkonstanten für die Triplettdomäne tragen im Rahmen dieser Studie zur Interpretation der experimentellen Quantenausbeuten bei.

Das komplexeste Projekt des Anwendungsteils dieser Dissertation stellt das Design fluorierter Flavinderivate dar. In einer ersten Veröffentlichung wurden Fluorierungen des A-Rings untersucht. Es wurde gezeigt, dass sich die Effekte der Fluorierungen auf die elektronischen Energien in guter Näherung additiv verhalten. Die kinetischen Modelle für 6–9F-MIA verdeutlichen, dass durch Fluorierungen des A-Rings keine grundlegende Änderung der Photophysik des Chromophors erwartet werden kann. Der Einfluss von Trifluoromethylierung fällt zwar größer aus, aufgrund sterischer Hinderungen können die Effekte allerdings nicht auf analoge Weise potenziert werden. Aufgrund dessen wurden für die zweite Veröffentlichung Modifikationen an der Pteridindion-Einheit vorgenommen. Die Effekte auf die elektronischen Energien fallen um ein Vielfaches größer aus als für die untersuchten Modifikationen der Benzol-Einheit. Im Hinblick auf den thematischen Schwerpunkt des Graduiertenkollegs 'Modulation of ISC', wurde folgende Idee für das Design von Derivaten mit erhöhter Triplett- (Φ_T) bzw. Fluoreszenzquantenausbeute (Φ_F) verfolgt: Die ISC vom Stammmolekül MIA in apolarem Medium ist durch den El-Sayed erlaubten $^1(\pi\pi^*) \rightsquigarrow {}^3(n\pi^*)$ Übergang bestimmt. In polarer Umgebung erfährt der $^3(n\pi^*)$ Zustand eine ausgeprägte Blauverschiebung und in der Konsequenz bleiben lediglich El-Sayed verbotene Kanäle bestehen. Das Design der Derivate beruht auf der Annahme, dass Φ_T in polarer Umgebung gesteigert werden kann, falls der El-Sayed erlaubte Übergang thermodynamisch erlaubt ist. Im Umkehrschluss wird angenommen, dass die Deaktivierung des geschwindigkeitsbestimmenden $^1(\pi\pi^*) \rightsquigarrow {}^3(\pi\pi^*)$ Kanals von MIA in einer Erhöhung von Φ_F resultiert. Basierend auf einem Screening-Verfahren wurden im Rahmen der zweiten Veröffentlichung vier fluorierte Flavinderivate mit adäquaten elektronischen Energien detailliert untersucht. Die kinetischen Schemata beinhalten ISC, Fluoreszenz, sowie interne Konversion. IC Ratenkonstanten wurden sowohl für Übergänge zwischen angeregten Zuständen als auch für strahlungslose Deaktivierung des hellen $^1(\pi\pi^*)$ Zustands berechnet. Für die Derivate mit dem aktivierten $^1(\pi\pi^*) \rightsquigarrow {}^3(n\pi^*)$ Kanal wird eine gesteigerte Φ_T prognostiziert. Für die vermeint-

lichen Fluorophore zeigt sich hingegen, dass starke Stabilisierung des S_1 Zustands mit einer deutlichen Beschleunigung strahlungsloser Deaktivierung einhergeht.
Im Falle von Heptazin und dem Derivat HAP-3MF wurden $S_1 \rightsquigarrow S_0$ IC Ratenkonstanten berechnet. Das Strukturmotiv ist aufgrund disjunkter Elektronendichteverteilungen der π_H und π_L Orbitale von besonderem Interesse für das Design von IST- bzw. TADF-Emittern. Das Substitutionsmuster von HAP-3MF führt zu einer vergleichsweise langsamen strahlungslosen Deaktivierung des fluoreszenten S_1 Zustands. Die berechneten Ratenkonstanten sind im Einklang mit dem experimentellen Befund direkter sowie verzögerter Fluoreszenzkomponenten in apolarer Umgebung.

Die zahlreichen Anwendungsbeispiele zeigen, dass die entwickelte Methode ein zuverlässiges Vorgehen zur Beschreibung interner Konversion darstellt. Für zukünftige Anwendungen gilt es zu klären, unter welchen Bedingungen sich die statische Herangehensweise in harmonischer Näherung für $S_1 \rightsquigarrow S_0$ IC eignet. Diese stellt aufgrund der vergleichsweise großen energetischen Separation der Zustände eine besondere Herausforderung für die Beschreibung der Franck–Condon-gewichteten Zustandsdichte sowie der Ableitungen von Kernwellenfunktionen dar.

Literaturverzeichnis

[AB99] C. Adamo and V. Barone. Toward reliable density functional methods without adjustable parameters: The PBE0 model. *J. Chem. Phys.*, 110:6158, 1999.

[AGV+10] G. Angulo, J. Grilj, E. Vauthey, L. Serrano-Andrés, Ò. Rubio-Pons, and P. Jacques. Ultrafast Decay of the Excited Singlet States of Thioxanthone by Internal Conversion and Intersystem Crossing. *ChemPhysChem*, 11:480, 2010.

[AH61] A. T. Amos and G. G. Hall. Single determinant wave functions. *Proc. R. Soc. A*, 263:483, 1961.

[AK86] K. A. Abdullah and T. J. Kemp. Solvatochromic effects in the fluorescence and triplet–triplet absorption spectra of xanthone, thioxanthone and N-methylacridone. *J. Photochem.*, 32:49, 1986.

[Alb63] A. C. Albrecht. Vibronic–Spin–Orbit Perturbations and the Assignment of the Lowest Triplet State of Benzene. *J. Chem. Phys.*, 38:354, 1963.

[ARdHR21] M. Alias-Rodríguez, C. de Graaf, and M. Huix-Rotllant. Ultrafast Intersystem Crossing in Xanthone from Wavepacket Dynamics. *J. Am. Chem. Soc.*, 143:21474, 2021.

[aTNT85] S. Koseki an T. Nakajima and A. Toyota. Violation of Hund's multiplicity rule in the electronically excited states of conjugated hydrocarbons. *Can. J. Chem.*, 63:1572, 1985.

[BB05] R. Banerjee and A. Batschauer. Plant blue-light receptors. *Planta*, 220:498, 2005.

[BDWK19] M. Bracker, F. Dinkelbach, O. Weingart, and M. Kleinschmidt. Impact of fluorination on the photophysics of the flavin chromophore: a quantum chemical perspective. *Phys. Chem. Chem. Phys.*, 21:9912, 2019.

[Bec88] Becke-1988. Density-functional exchange-energy approximation with correct asymptotic behavior. *Phys. Rev. A*, 38:3089, 1988.

[Bec93] A. D. Becke. A new mixing of Hartree-Fock and local density-functional theories. *J. Chem. Phys.*, 98:1372, 1993.

[BFNR07] F. Babudri, G. M. Farinola, F. Naso, and R. Ragni. Fluorinated organic materials for electronic and optoelectronic applications: the role of the fluorine atom. *Chem. Commun.*, page 1003, 2007.

[BJ68] M. Bixon and J. Jortner. Intramolecular Radiationless Transitions. *J. Chem. Phys.*, 48:715, 1968.

[BJ92] D. Burget and P. Jacques. Dramatic solvent effects on thioxanthone fluorescence lifetime. *J. Lumin.*, 54:177, 1992.

[BJJ+92] K. L. Bak, P. Jørgensen, H. J. A. Jensen, J. Olsen, and T. Helgaker. First-order nonadiabatic coupling matrix elements from multiconfigurational self-consistent-field response theory. *J. Chem. Phys.*, 97:7573, 1992.

[Bjö15] L. O. Björn (Hrsg.). Photobiology: The Science of Light and Life. New York: Springer, 2015.

[BJWM00] M. H. Beck, A. Jäckle, G. A. Worth, and H.-D. Meyer. The multiconfigurational time-dependent Hartree (MCTDH) method: a highly efficient algorithm for propagating wavepackets. *Phys. Rep.*, 324:1, 2000.

[BMK21] M. Bracker, C. M. Marian, and M. Kleinschmidt. Internal conversion of singlet and triplet states employing numerical DFT/MRCI derivative couplings: Implementation, tests, and application to xanthone. *J. Chem. Phys.*, 155:014102, 2021.

[BN88] R. Broer and W. Nieuwpoort. Broken orbital symmetry and the description of valence hole states in the tetrahedral $[CrO_4]^{2-}$ anion. *Theor. Chim. Acta*, 73:405, 1988.

[BO27] M. Born and R. Oppenheimer. Zur Quantentheorie der Molekeln. *Ann. Phys.*, 84:457, 1927.

[Bon64] A. Bondi. van der Waals Volumes and Radii. *J. Phys. Chem.*, 68:441, 1964.

[BOY+98] M. A. Baldo, D. F. O'Brien, Y. You, A. Shoustikov, S. Sibley, M. E. Thompson, and S. R. Forrest. Highly Efficient Phosphorescent Emission from Organic Electroluminescent Devices. *Nature*, 395:151, 1998.

[BPR+15] A. M. Buckley, J. Petersen, A. J. Roe, G. R. Douce, and J. M. Christie. LOV-based reporters for fluorescence imaging. *Curr. Opin. Chem. Biol.*, 27:39, 2015.

[Bra17] M. Bracker. Photophysik fluorierter Flavine aus quantenchemischer Sicht. Master thesis, Heinrich-Heine-Universität Düsseldorf, 2017.

[BS83] R. A. Brualdi and H. Schneider. Determinantal Identities: Gauss, Schur, Cauchy, Sylvester, Kronecker, Jacobi, Binet, Laplace, Muir, and Cayley. *Lin. Alg. Appl.*, 52/53:769, 1983.

[CBPS14] J. M. Christie, L. Blackwood, J. Petersen, and S. Sullivan. Plant Flavoprotein Photoreceptors. *Plant Cell Physiol*, 56:401, 2014.

[CFK+08] S. Chapman, C. Faulkner, E. Kaiserli, C. Garcia-Mata, E. I. Savenkov, A. G. Roberts, K. J. Oparka, and J. M. Christie. The photoreversible fluorescent protein iLOV outperforms GFP as a reporter of plant virus infection. *Proc. Natl. Acad. Sci. USA*, 105:20038, 2008.

[Cha87] D. Chandler. Introduction to Modern Statistical Mechanics. New York: Oxford University Press, 1987.

[Chr99] O. Christiansen. First-order nonadiabatic coupling matrix elements using coupled cluster methods. I. Theory. *J. Chem. Phys.*, 110:711, 1999.

[CJ05] P. Christen and R. Jaussi. Biochemie: Eine Einführung. Berlin Heidelberg: Springer, 2005.

[CJWL99] A. R. Cashmore, J. A. Jarillo, Y.-J. Wu, and D. Liu. Cryptochromes: Blue Light Receptors for Plants and Animals. *Science*, 284:760, 1999.

[Con26] E. U. Condon. A Theory of Intensity Distribution in Band Systems. *Phys. Rev.*, 28:1182, 1926.

[Con28] E. U. Condon. Nuclear Motions Associated with Electron Transitions in Diatomic Molecules. *Phys. Rev.*, 32:858, 1928.

[CPB96] J. H. Cavaleri, K. Prater, and R. M. Bowman. An investigation of the solvent dependence on the ultrafast intersystem crossing kinetics of xanthone. *Chem. Phys. Lett.*, 259:195, 1996.

[CT14] G. Cui and W. Thiel. Generalized trajectory surface-hopping method for internal conversion and intersystem crossing. *J. Chem. Phys.*, 141:124101, 2014.

[CVR+13] A. Calzolari, B. Vercelli, A. Ruini, T. Virgili, and M. Pasini. Fluorine-Induced Enhancement of the Oxidation Stability and Deep-Blue Optical Activity in Conductive Polyfluorene Derivatives. *J. Phys. Chem. C*, 117:26760, 2013.

[DBKM21] F. Dinkelbach, M. Bracker, M. Kleinschmidt, and C. M. Marian. Large Inverted Singlet–Triplet Energy Gaps Are Not Always Favorable for Triplet Harvesting: Vibronic Coupling Drives the (Reverse) Intersystem Crossing in Heptazine Derivatives. *J. Phys. Chem. A*, 125:10044, 2021.

[DEC+07] T. Drepper, T. Eggert, F. Circolone, A. Heck, U. Krauß, J.-K. Guterl, M. Wendorff, A. Losi, W. Gärtner, and K.-E. Jaeger. Reporter proteins for *in vivo* fluorescence without oxygen. *Nat. Biotechnol.*, 25:443, 2007.

[Dex53] D. L. Dexter. A Theory of Sensitized Luminescence in Solids. *J. Chem. Phys.*, 21:836, 1953.

[DG05] M. Dierksen and S. Grimme. An efficient approach for the calculation of Franck–Condon integrals of large molecules. *J. Chem. Phys.*, 122:244101, 2005.

[DH05] A. Dreuw and M. Head-Gordon. Single-Reference ab Initio Methods for the Calculation of Excited States of Large Molecules. *Chem. Rev.*, 105:4009, 2005.

[Dir27] P. A. M. Dirac. The Quantum Theory of the Emission and Absorption of Radiation band 114, 1927, s. 243. *Proc. R. Soc. A*, 114:243, 1927.

[DLS+04] M. Dallos, H. Lischka, R. Shepard, D. R. Yarkony, and P. G. Szalay. Analytic evaluation of nonadiabatic coupling terms at the MR-CI level. II. Minima on the crossing seam: Formaldehyde and the photodimerization of ethylene. *J. Chem. Phys.*, 120:7330, 2004.

[DM74] J. C. Dalton and F. C. Montgomery. Solvent Effects on Thioxanthone Fluorescence. *J. Am. Chem. Soc*, 96:6230, 1974.

[DM19] F. Dinkelbach and C. M. Marian. Vibronic and spin–orbit coupling effects in the absorption spectra of pyrazine: A quantum chemical approach. *J. Serb. Chem. Soc.*, 84:819, 2019.

[DNG+19] I. Dokukina, A. Nenov, M. Garavelli, C. M. Marian, and O. Weingart. QM/MM Photodynamics of Retinal in the Channelrhodopsin Chimera C1C2 with OM3/MRCI. *ChemPhotoChem*, 3:107, 2019.

[Dum14] F. Dumur. Zinc complexes in OLEDs: An overview. *Synth. Met.*, 195:241, 2014.

[Dup81] M. Dupuis. Energy derivatives for configuration interaction wave functions. *J. Chem. Phys.*, 74:5758, 1981.

[DYK04] W. Domcke, D. R. Yarkony und H. Köppel (Hrsg.). Conical Intersections: Electronic Structure, Dynamics & Spectroscopy. Singapore: World Scientific Publishing (Advanced Series in Physical Chemistry – Vol. 15), 2004.

[EOT+09] A. Endo, M. Ogasawara, A. Takahashi, D. Yokoyama, Y. Kato, and C. Adachi. Thermally Activated Delayed Fluorescence from Sn^{4+}–Porphyrin Complexes and Their Application to Organic Light Emitting Diodes — A Novel Mechanism for Electroluminescence. *Adv. Mater.*, 21:4802, 2009.

[ERP+19] J. Ehrmaier, E. J. Rabe, S. R. Pristash, K. L. Corp, C. W. Schlenker, A. L. Sobolewski, and W. Domcke. Singlet–Triplet Inversion in Heptazine and in Polymeric Carbon Nitrides. *J. Phys. Chem. A*, 123:8099, 2019.

[ES63] M. El-Sayed. Spin–orbit Coupling and the Radiationless Processes in Nitrogen Heterocyclics. *J. Chem. Phys.*, 38:2834, 1963.

[Eti10] M. Etinski. Comparison between time-dependent and time-independent methods for the calculation of inter-system crossing rates: Application to uracil and its derivatives. PhD dissertation, Heinrich-Heine-Universität Düsseldorf, 2010.

[ETM11] M. Etinski, J. Tatchen, and C. M. Marian. Time-dependent approaches for the calculation of intersystem crossing rates. *J. Chem. Phys.*, 134:154105, 2011.

[ETM14a] M. Etinski, J. Tatchen, and C. M. Marian. Thermal and solvent effects on the triplet formation in cinnoline. *Phys.Chem.Chem.Phys.*, 16:4740, 2014.

[ETM14b] M. Etinski, J. Tatchen, and C. M. Marian. Time-dependent approach to spin–vibronic coupling: Implementation and assessment. *J. Chem. Phys.*, 140:114104, 2014.

[Fö48] T. Förster. Zwischenmolekulare Energiewanderung und Fluoreszenz. *Ann. Phys.*, 437:55, 1948.

[FD26] J. Franck and E. G. Dymond. Elementary Processes of Photochemical Reactions. *Trans. Faraday Soc.*, 21:536, 1926.

[Fer95] E. Fermi. Nuclear Physics. University of Chicago Press, 1995.

[FGSM19] J. Föller, C. Ganter, A. Steffen, and C. M. Marian. Computer-Aided Design of Luminescent Linear N-Heterocyclic Carbene Copper(I) Pyridine Complexes. *Inorg. Chem.*, 58:5446, 2019.

[FMK18] S. Faraji, S. Matsika, and A. I. Krylov. Calculations of non-adiabatic couplings within equation-of-motion coupled-cluster framework: Theory, implementation, and validation against multi-reference methods. *J. Chem. Phys.*, 148:044103, 2018.

[FYD11] L. Fenno, O. Yizhar, and K. Deisseroth. The Development and Application of Optogenetics. *Annu. Rev. Neurosci.*, 34:389, 2011.

[GDP+16] I. F. Galván, M. G. Delcey, T. B. Pedersen, F. Aquilante, and R. Lindh. Analytical State-Average Complete-Active-Space Self-Consistent Field Nonadiabatic Coupling Vectors: Implementation with Density-Fitted Two-Electron Integrals and Application to Conical Intersections. *J. Chem. Theory Comput.*, 12:3636, 2016.

[GK02] M. Gomelsky and G. Klug. BLUF: a novel FAD-binding domain involved in sensory transduction in microorganisms. *Trends Biochem. Sci.*, 27:497, 2002.

[Gri95] D. J. Griffiths. Introduction to Quantum Mechanics. Prentice Hall, 1995.

[GW99] S. Grimme and M. Waletzke. A combination of Kohn–Sham density functional theory and multi-reference configuration interaction methods. *J. Chem. Phys.*, 111:5645, 1999.

[HB03] K. Huang and C. F. Beck. Phototropin is the blue-light receptor that controls multiple steps in the sexual life cycle of the green alga *Chlamydomonas reinhardtii*. *Proc. Natl. Acad. Sci. U.S.A.*, 100:6269, 2003.

[HBT+21] T. Hölzel, A. Belyaev, M. Terzi, L. Stenzel, M. Gernert, C. M. Marian, A. Steffen, and C. Ganter. Linear Carbene Pyridine Copper Complexes with Sterically Demanding *N,N´*-Bis(trityl)imidazolylidene: Syntheses, Molecular Structures, and Photophysical Properties. *Inorg. Chem.*, 60:18529, 2021.

[HKM18] A. Heil, M. Kleinschmidt, and C. M. Marian. On the performance of DFT/MRCI Hamiltonians for electronic excitations in transition metal complexes: The role of the damping function. *J. Chem. Phys.*, 149:164106, 2018.

[HLH63] G. Herzberg and H. C. Longuet-Higgins. Intersection of Potential Energy Surfaces in Polyatomic Molecules. *Discuss. Faraday Soc.*, 35:77, 1963.

[HM17] A. Heil and C. M. Marian. DFT/MRCI Hamiltonian for odd and even numbers of electrons. *J. Chem. Phys.*, 147:194104, 2017.

[HMLL98] M. Hayashi, A. M. Mebel, K. K. Liang, and S. H. Lin. *Ab initio* calculations of radiationless transitions between excited and ground singlet electronic states of ethylene. *J. Chem. Phys.*, 108:2044, 1998.

[HS71] B. R. Henry and W. Siebrand. Spin–Orbit Coupling in Aromatic Hydrocarbons. Analysis of Nonradiative Transitions between Singlet and Triplet States in Benzene and Naphthalene. *J. Chem. Phys.*, 54:1072, 1971.

[HSR+06] B. Heinz, B. Schmidt, C. Root, H. Satzger, F. Milota, B. Fierz, T. Kiefhaber, W. Zinth, and P. Gilch. On the unusual fluorescence properties of xanthone in water. *Phys.Chem.Chem.Phys.*, 8:3432, 2006.

[HT33] G. Herzberg and E. Teller. Schwingungsstruktur der Elektronenübergänge bei mehratomigen Molekülen. *Z. Phys. Chem.*, 21:410, 1933.

[HV80] P. Habitz and C. Votava. The Hellmann–Feynman theorem for approximate wave functions and its application to nonadiabatic coupling matrix elements with the aid of a coupled Hartree–Fock method. *J. Chem. Phys.*, 72:5532, 1980.

[IAWL93] R. Islampour, R. G. Alden, G. Y. C. Wu, and S. H. Lin. Effect of Temperature, Energy Gap, and Distortion of Potential Surfaces on Photoinduced Intramolecular Electron Transfer. *J. Phys. Chem.*, 97:6793, 1993.

[IDL00] R. Islampour, M. Dehestani, and S. H. Lin. Calculation of resonance Raman excitation profiles. *Mol. Phys.*, 98:101, 2000.

[IL91a] R. Islampour and S. H. Lin. Effects of anharmonicity on intramolecular electron transfer rates. *Chem. Phys. Lett.*, 179:147, 1991.

[IL91b] R. Islampour and S. H. Lin. On the Theory of Photoinduced Intramolecular Electron Transfer. *J. Phys. Chem.*, 95:10261, 1991.

[IM07] R. Islampour and M. Miralinaghi. Dynamics of Radiationless Transitions: Effects of Displacement–Distortion–Rotation of Potential Energy Surfaces on Internal Conversion Decay Rate Constants. *J. Phys. Chem. A*, 111:9454, 2007.

[Isl89] R. Islampour. Electronic spectral line shape of a polyatomic molecule. *Chem. Phys.*, 133:425, 1989.

[JG15] L. Jullien and A. Gautier. Fluorogen-based reporters for fluorescence imaging: a review. *Methods Appl. Fluoresc.*, 3:042007, 2015.

[Kas50] M. Kasha. Characterization of Electronic Transitions in Complex Molecules. *Discuss. Faraday Soc.*, 9:14, 1950.

[KHN+19] S. Ko, B. Hwang, J.-H. Na, J. Lee, and S. T. Jung. Engineered *Arabidopsis* Blue Light Receptor LOV Domain Variants with Improved Quantum Yield, Brightness, and Thermostability. *J. Agric. Food Chem.*, 67:12037, 2019.

[KM95] M. Klessinger and J. Michl. Excited states and photochemistry of organic molecules. Wiley-VCH, Weinheim, 1995.

[KM05] M. Kleinschmidt and C. M. Marian. Efficient generation of matrix elements for one-electron spin–orbit operators. *Chem. Phys.*, 311:71, 2005.

[KMWG09] M. Kleinschmidt, C. M. Marian, M. Waletzke, and S. Grimme. Parallel multireference configuration interaction calculations on mini-β-carotenes and β-carotene. *J. Chem. Phys.*, 130:044708, 2009.

[KS78] H. Kollmar and V. Staemmler. Violation of Hund's Rule by Spin Polarization in Molecules. *Theoret. Chim. Acta*, 48:223, 1978.

[KS93] A. Klamt and G. Schüürmann. COSMO: A New Approach to Dielectric Screening in Solvents with Explicit Expressions for the Screening Energy and its Gradient. *J. Chem. Soc., Perkin Trans. 2*, page 799, 1993.

[KSK+67] H. F. King, R. E. Stanton, H. Kim, R. E. Wyatt, and R. G. Parr. Corresponding Orbitals and the Nonorthogonality Problem in Molecular Quantum Mechanics. *J. Chem. Phys. 47, 1936 (1967)*, 47:1936, 1967.

[KT55] R. Kubo and Y. Toyozawa. Application of the Method of Generating Function to Radiative and Non-Radiative Transitions of a Trapped Electron in a Crystal. *Prog. Theor. Phys.*, 13:160, 1955.

[KTH10] Y. G. Khait, D. Theis, and M. R. Hoffmann. Lagrangian approach for geometrical derivatives and nonadiabatic coupling terms in MRCISD. *Mol. Phys.*, 108:2703, 2010.

[KTM02] M. Kleinschmidt, J. Tatchen, and C. M. Marian. Spin–orbit Coupling of DFT/MRCI Wavefunctions: Method, Test Calculations and Application to Thiophene. *J. Comp. Chem.*, 23:824, 2002.

[KTM06] M. Kleinschmidt, J. Tatchen, and C. M. Marian. SPOCK.CI: A multireference spin–orbit configuration interaction method for large molecules. *J. Chem. Phys.*, 124:124101, 2006.

[LaCMM20] N. Lüdtke and J. Föller an C. M. Marian. Understanding the luminescence properties of Cu(I) complexes: a quantum chemical perusal. *Phys. Chem. Chem. Phys.*, 22:23530, 2020.

[Lak06] J. R. Lakowicz. Principles of Fluorescence Spectroscopy. Boston: Springer, 2006.

[LAL+14] E. Liscum, S. K. Askinosie, D. L. Leuchtman, J. Morrow, K. T. Willenburg, and D. R. Coats. Phototropism: Growing towards an Understanding of Plant Movement. *Plant Cell*, 26:38, 2014.

[Lax52] M. Lax. The Franck–Condon Principle and Its Application to Crystals. *J. Chem. Phys*, 20:1752, 1952.

[LDS+04] H. Lischka, M. Dallos, P. G. Szalay, D. R. Yarkony, and R. Shepard. Analytic evaluation of nonadiabatic coupling terms at the MR-CI level. I. Formalism. *J. Chem. Phys.*, 120:7322, 2004.

[LG12] A. Losi and W. Gärtner. The Evolution of Flavin-Binding Photoreceptors: An Ancient Chromophore Serving Trendy Blue-Light Sensors. *Annu. Rev. Plant Biol.*, 63:49, 2012.

[LKLC19] S. Lee, E. Kim, S. Lee, and C. H. Choi. Fast Overlap Evaluations for Nonadiabatic Molecular Dynamics Simulations: Applications to SF-TDDFT and TDDFT. *J. Chem. Theory Comput.*, 15:882, 2019.

[LKM16] I. Lyskov, M. Kleinschmidt, and C. M. Marian. Redesign of the DFT/MRCI Hamiltonian. *J. Chem. Phys.*, 144:034104, 2016.

[LKM17] I. Lyskov, H. Köppel, and C. M. Marian. Nonadiabatic photodynamics and UV absorption spectrum of all-*trans*-octatetraene. *Phys. Chem. Chem. Phys.*, 19:3937, 2017.

[LL80] T. Lai and E. Lim. Photophysical behavior of aromatic carbonyl compounds related to proximity effect: thioxanthone. *Chem. Phys. Lett.*, 73:244, 1980.

[LL14] Z. Li and W. Liu. First-order nonadiabatic coupling matrix elements between excited states: A Lagrangian formulation at the CIS, RPA, TDHF, and TD-DFT levels. *J. Chem. Phys.*, 141:014110, 2014.

[LML+03] K. K. Liang, A. M. Mebel, S. H. Lin, M. Hayashi, H. L. Selzle, E. W. Schlag, and M. Tachiya. Influence of distortion and Duschinsky effects on Marcus-type theories of electron transfer rate. *Phys. Chem. Chem. Phys.*, 5:4656, 2003.

[LMSFJ00] C. Ley, F. Morlet-Savary, J. P. Fouassier, and P. Jaques. The spectral shape dependence of xanthone triplet–triplet absorption on solvent polarity. *J. Photochem. Photobiol. A*, 137:87, 2000.

[Löw55] P.-O. Löwdin. Quantum Theory of Many-Particle Systems. I. Physical Interpretations by Means of Density Matrices, Natural Spin-Orbitals, and Convergence Problems in the Method of Configurational Interaction. *Phys. Rev.*, 97:1474, 1955.

[LSY84] B. H. Lengsfield III, P. Saxe, and D. R. Yarkony. On the evaluation of nonadiabatic coupling matrix elements using SA-MCSCF/CI wave functions and analytic gradient methods. I. *J. Chem. Phys.*, 81:4549, 1984.

[LYP88] C. Lee, W. Yang, and R. G. Parr. Development of the Colle-Salvetti correlation-energy formula into a functional of the electron. *Phys. Rev. B*, 37:785, 1988.

[LZN+14] J. Li, Q. Zhang, H. Nomura, H. Miyazaki, and C. Adachi. Thermally activated delayed fluorescence from $^3n\pi^*$ to $^1n\pi^*$ up-conversion and its application to organic light-emitting diodes. *Appl. Phys. Lett.*, 105:013301, 2014.

[Mar59] J. J. Markham. Interaction of Normal Modes with Electron Traps. *Rev. Mod. Phys.*, 31:956, 1959.

[Mar01] C. M. Marian. Spin–orbit coupling in molecules. In: K. Lipkowitz und D. Boyd (Hrsg.): Reviews in Computational Chemistry, 17:99–204, Wiley-VCH, Weinheim, 2001.

[Mar03] R. L. Martin. Natural transition orbitals. *J. Chem. Phys.*, 118:4775, 2003.

[Mar21] C. M. Marian. Understanding and controlling intersystem crossing in molecules. *Annu. Rev. Phys. Chem.*, 72:617, 2021.

[May07] I. Mayer. Using singular value decomposition for a compact presentation and improved interpretation of the CIS wave functions. *Chem. Phys. Lett.*, 437:284, 2007.

[MAYI85] S. Mukamel, S. Abe, Y. J. Yan, and R. Islampour. Generating Function for Electronic Spectra of Polyatomic Molecules. *J. Phys. Chem.*, 89:201, 1985.

[MD15] Q. Mei and V. Dvornyk. Evolutionary History of the Photolyase/Cryptochrome Superfamily in Eukaryotes. *PLoS ONE*, 10:e0135940, 2015.

[Meh66] F. G. Mehler. Ueber die Entwicklung einer Function von beliebig vielen Variablen nach Laplaceschen Functionen höherer Ordnung. *J. Reine Angew. Math.*, 1866:161, 1866.

[MFKE18] C. M. Marian, J. Föller, M. Kleinschmidt, and M. Etinski. Intersystem crossing processes in TADF emitters. In: H. Yersin (Hrsg.): Highly Efficient OLEDs, Materials Based on Thermally Activated Delayed Fluorescence, 257–296, Wiley-VCH, Weinheim, 2018.

[MHK18] C. M. Marian, A. Heil, and M. Kleinschmidt. The DFT/MRCI method. *Wiley Interdiscip. Rev. Comput. Mol. Sci.*, 9:e1394, 2018.

[MHLL99] A. M. Mebel, M. Hayashi, K. K. Liang, and S. H. Li. Ab Initio Calculations of Vibronic Spectra and Dynamics for Small Polyatomic Molecules: Role of Duschinsky Effect. *J. Phys. Chem. A*, 103:10674, 199.

[Mil81] K. S. Miller. On the Inverse of the Sum of Matrices. *Math. Mag.*, 54:67, 1981.

[MMC90] H.-D. Meyer, U. Manthe, and L. S. Cederbaum. The multi-configurational time-dependent Hartree approach. *Chem. Phys. Lett.*, 165:73, 1990.

[MR89] P.-Å. Malmqvist and B. O. Roos. The CASSCF state interaction method. *Chem. Phys. Lett.*, 24:189, 1989.

[MSLJ+99] F. Morlet-Savary, C. Ley, P. Jacques, F. Wieder, and J. P. Fouassier. Time dependent solvent effects on the T_1–T_n absorption spectra of thioxanthone: a picosecond investigation. *J. Photochem. Photobiol. A*, 126:7, 1999.

[MVT+16] R. Mundt, T. Villnow, C. Torres Ziegenbein, P. Gilch, C. M. Marian, and V. Rai-Constapel. Thioxanthone in apolar solvents: ultrafast internal conversion precedes fast intersystem crossing. *Phys. Chem. Chem. Phys.*, 18:6637, 2016.

[MW06] C.-D. Muntz and T. Westermann. Differenzenverfahren. In: Numerische Behandlung gewöhnlicher und partieller Differenzialgleichungen, 231–283, Springer, Berlin Heidelberg, 2006.

[NS03] C. Neiß and P. Saalfrank. *Ab Initio* Quantum Chemical Investigation of the First Steps of the Photocycle of Phototropin: A Model Study. *Photochem. Photobiol.*, 77:101, 2003.

[NSS20] S. P. Neville, I. Seidu, and M. S. Schuurman. Propagative block diagonalization diabatization of DFT/MRCI electronic states. *J. Chem. Phys.*, 152:114110, 2020.

[NWM17] S. Nakagawa, O. Weingart, and C. M. Marian. Dual Photochemical Reaction Pathway in Flavin-Based Photoreceptor LOV Domain: A Combined Quantum-Mechanics/Molecular-Mechanics Investigation. *J. Phys. Chem. B*, 121:9583, 2017.

[OFA+14] Q. Ou, S. Fatehi, E. Alguire, Y. Shao, and J. E. Subotnik. Derivative couplings between TDDFT excited states obtained by direct differentiation in the Tamm-Dancoff approximation. *J. Chem. Phys.*, 141:024114, 2014.

[O'R53] R. C. O'Rourke. Absorption of Light by Trapped Electrons. *Phys. Rev.*, 91:165, 1953.

[PFL+21] R. Pollice, P. Friederich, C. Lavigne, G. dos Passos Gomes, and A. Aspuru- Guzik. Organic Molecules with Inverted Gaps between First Excited Singlet and Triplet States and Appreciable Fluorescence Rates. *Matter*, 4:1654, 2021.

[PGDM18] T. J. Penfold, E. Gindensperger, C. Daniel, and C. M. Marian. Spin–vibronic mechanism for intersystem crossing. *Chem. Rev.*, 118:6975, 2018.

[PKEM12] L. Pohler, M. Kleinschmidt, M. Etinski, and C. M. Marian. In search of the dark state of 5-methyl-2-hydroxypyrimidine using a numerical DFT/MRCI gradient. *Mol. Phys.*, 110:2429, 2012.

[PL12] F. Plasser and H. Lischka. Analysis of Excitonic and Charge Transfer Interactions from Quantum Chemical Calculations. *J. Chem. Theory Comput.*, 8:2777, 2012.

[PLB09] J. Pittner, H. Lischka, and M. Barbatti. Optimization of mixed quantum-classical dynamics: Time-derivative coupling terms and selected couplings. *Chem. Phys.*, 356:147, 2009.

[PRM+16] F. Plasser, M. Ruckenbauer, S. Mai, M. Oppel, P. Marquetand, and Leticia González. Efficient and Flexible Computation of Many-Electron Wave Function Overlaps. *J. Chem. Theory Comput.*, 12:1207, 2016.

[PS17] J. W. Park and T. Shiozaki. Analytical Derivative Coupling for Multistate CASPT2 Theory. *J. Chem. Theory Comput.*, 13:2561, 2017.

[PSS+16] P. Parihar, R. Singh, S. Singh, D. K. Tripathi, D. K. Chauhan, V. P. Singh, and S. M. Prasad. Photoreceptors mapping from past history till date. *J. Photochem. Photobiol. B*, 162:223, 2016.

[PTN+84] I. D. Petsalakis, G. Theodorakopoulos, C. A. Nicolaides, R. J. Buenker, and S. D. Peyerimhoff. Nonorthonormal CI for molecular excited states. I. The sudden polarization effect in 90° twisted ethylene. *J. Chem. Phys.*, 81:3161, 1984.

[PYS07] Q. Peng, Y. Yi, and Z. Shuai. Excited state radiationless decay process with Duschinsky rotation effect: Formalism and implementation. *J. Chem. Phys.*, 126:114302, 2007.

[RCEM13] V. Rai-Constapel, M. Etinski, and C. M. Marian. Photophysics of Xanthone: A Quantum Chemical Perusal. *J. Phys. Chem. A*, 117:3935, 2013.

[RCKS+10] V. Rai-Constapel, M. Kleinschmidt, S. Salzmann, L. Serrano-Andrés, and C. M. Marian. Thioxanthone: on the shape of the first absorption band. *Phys. Chem. Chem. Phys.*, 12:9320, 2010.

[RCSM98] F. Rakowitz, M. Casarrubios, L. Seijo, and C. M. Marian. *Ab initio* spin-free-state-shifted spin–orbit configuration interaction calculations on singly ionized iridium. *J. Chem. Phys.*, 108:7980, 1998.

[RCSM11] V. Rai-Constapel, S. Salzmann, and C. M. Marian. Isolated and Solvated Thioxanthone: A Photophysical Study. *J. Phys. Chem. A*, 115:8589, 2011.

[RCVR+14] V. Rai-Constapel, T. Villnow, G. Ryseck, P. Gilch, and C. M. Marian. Chimeric Behavior of Excited Thioxanthone in Protic Solvents: II. Theory. *J. Phys. Chem. A*, 118:11708, 2014.

[RPSABJ06] Ò. Rubio-Pons, L. Serrano-Andrés, D. Burget, and P. Jacques. A butterfly like motion as a clue to the photophysics of thioxanthone. *J. Photochem. Photobiol. A*, 179:298, 2006.

[RT96] R. S. Rowland and R. Taylor. Intermolecular Nonbonded Contact Distances in Organic Crystal Structures: Comparison with Distances Expected from van der Waals Radii. *J. Phys. Chem.*, 100:7384, 1996.

[RTE+18] A. Reiffers, C. Torres Ziegenbein, A. Engelhardt, R. Kühnemuth, P. Gilch, and C. Czekelius. Impact of Mono-Fluorination on the Photophysics of the Flavin Chromophore. *Photochem. Photobiol.*, 94:667, 2018.

[San03] A. Sancar. Structure and Function of DNA Photolyase and Cryptochrome Blue-Light Photoreceptors. *Chem. Rev.*, 103:2203, 2003.

[San04] A. Sancar. Regulation of the Mammalian Circadian Clock by Cryptochrome. *J. Biol. Chem.*, 279:34079, 2004.

[SCC+01] T. E. Swartz, S. B. Corchnoy, J. M. Christie, J. W. Lewis, I. Szundi, W. R. Briggs, and R. A. Bogomolni. The Photocycle of a Flavin-binding Domain of the Blue Light Photoreceptor Phototropin. *J. Biol. Chem.*, 276:36493, 2001.

[Sch17] J. Schur. Über Potenzreihen, die im Innern des Einheitskreises beschränkt sind. *J. Reine Angew. Math.*, 147:205, 1917.

[SD21] A. L. Sobolewski and W. Domcke. Are Heptazine-Based Organic Light-Emitting Diode Chromophores Thermally Activated Delayed Fluorescence or Inverted Singlet–Triplet Systems? *J. Phys. Chem. Lett.*, 12:6852, 2021.

[SF10] R. Send and F. Furche. First-order nonadiabatic couplings from time-dependent hybrid density functional response theory: Consistent formalism, implementation, and performance. *J. Chem. Phys.*, 132:044107, 2010.

[SHE11] M. Sauer, J. Hofkens, and J. E. Enderlein. Handbook of Fluorescence Spectroscopy and Imaging. Wiley-VCH, Weinheim, 2011.

[SHLM15] J. W. Snyder, E. G. Hohenstein, N. Luehr, and T. J. Martínez. An atomic orbital-based formulation of analytical gradients and nonadiabatic coupling vector elements for the stateav-eraged complete active space self-consistent field method on graphical processing units. *J. Chem. Phys.*, 143:154107, 2015.

[SLRD+11] X. Shu, V. Lev-Ram, T. J. Deerinck, Y. Qi, E. B. Ramko, M. W. Davidson, Y. Jin, M. H. Ellisman, and R. Y. Tsien. A Genetically Encoded Tag for Correlated Light and Electron Microscopy of Intact Cells, Tissues, and Organisms. *PLoS Biol.*, 9:e100104, 2011.

[SPDD19] M. Sapunar, T. Piteša, D. Davidović, and N. Došlić. Highly Efficient Algorithms for CIS Type Excited State Wave Function Overlaps. *J. Chem. Theory Comput.*, 15:3461, 2019.

[SSBS10] G. Sánchez-Sanz, Z. Barandiarán, and L. Seijo. Energy level shifts in two-step spin–orbit coupling *ab initio* calculations. *Chem. Phys. Lett.*, 498:226, 2010.

[SSJTM09] S. Salzmann, M. R. Silva-Junior, W. Thiel, and C. M. Marian. Influence of the LOV Domain on Low-Lying Excited States of Flavin: A Combined Quantum-Mechanics/Molecular-Mechanics Investigation. *J. Phys. Chem. B*, 113:15610, 2009.

[SSKV15] D. M. Shcherbakova, A. A. Shemetov, A. A. Kaberniuk, and V. V. Verkhusha. Natural Photoreceptors as a Source of Fluorescent Proteins, Biosensors, and Optogenetic Tools. *Annu. Rev. Biochem.*, 84:519, 2015.

[SSR+04] H. Satzger, B. Schmidt, C. Root, W. Zinth, B. Fierz, F. Krieger, T. Kiefhaber, and P. Gilch. Ultrafast Quenching of the Xanthone Triplet by Energy Transfer: New Insight into the Intersystem Crossing Kinetics. *J. Phys. Chem. A*, 108:10072, 2004.

[STM08] S. Salzmann, J. Tatchen, and C. M. Marian. The photophysics of flavins: What makes the difference between gas phase and aqueous solution? *J. Photochem. Photobiol. A*, 198:221, 2008.

[SW07] N. Suetsugu and M. Wada. Chloroplast photorelocation movement mediated by phototropin family proteins in green plants. *Biol. Chem.*, 388:927, 2007.

[SWW78] G. A. Segal, R. W. Wetmore, and K. Wolf. Efficient methods for configuration interaction calculations. *Chem. Phys.*, 30:269, 1978.

[Tat06] J. Tatchen. Spin-verbotene photophysikalische Prozesse in organischen Molekülen: Entwicklung quantenchemischer Methoden und Anwendung auf Psoralene. PhD dissertation, Heinrich-Heine-Universität Düsseldorf, 2006.

[TB97] L. N. Trefethen and D. Bau. Numerical Linear Algebra. Philadelphia: Society for Industrial and Applied Mathematics, 1997.

[TGM07] J. Tatchen, N. Gilka, and C. M. Marian. Intersystem crossing driven by vibronic spin–orbit coupling: a case study on psoralen. *Phys. Chem. Chem. Phys.*, 9:5209, 2007.

[TLS+19] J. Torra, C. Lafaye, L. Signor, S. Aumonier, C. Flors, X. Shu, G. Gotthard, and A. Royant. Tailing miniSOG: structural bases of the complex photophysics of a flavin-binding singlet oxygen photosensitizing protein. *Sci. Rep.*, 9:2428, 2019.

[TM06] J. Tatchen and C. M. Marian. Vibronic absorption, fluorescence, and phosphorescence spectra of psoralen: a quantum chemical investigation. *Phys. Chem. Chem. Phys.*, 8:2133, 2006.

[TS09] A. Tajti and P. G. Szalay. Analytic evaluation of the nonadiabatic coupling vector between excited states using equation-of-motion coupled-cluster theory. *J. Chem. Phys.*, 131:124104, 2009.

[Tul90] J. C. Tully. Molecular dynamics with electronic transitions. *J. Chem. Phys.*, 93:1061, 1990.

[Tur] TURBOMOLE V7.3 2018, a development of University of Karlsruhe and Forschungszentrum Karlsruhe GmbH, 1989–2007, TURBOMOLE GmbH, since 2007; available from
`http://www.turbomole.com`.

[Tur91] N. J. Turro. Modern Molecular Photochemistry. University Science Books, Sausalito, CA, 1991.

[TWD+21] K. A. Thom, F. Wieser, K. Diestelhorst, A. Reiffers, C. Czekelius, M. Kleinschmidt, M. Bracker, C. M. Marian, and P. Gilch. Acridones: Strongly Emissive HIGHrISC Fluorophores. *J. Phys. Chem. Lett.*, 12:5703, 2021.

[UM91] T. Uzer and W. H. Miller. Theories of Intramolecular Vibrational Energy Transfer. *Phys. Rep.*, 199:73, 1991.

[VRRC+14] T. Villnow, G. Ryseck, V. Rai-Constapel, C. M. Marian, and P. Gilch. Chimeric Behavior of Excited Thioxanthone in Protic Solvents: I. Experiments. *J. Phys. Chem. A*, 118:11696, 2014.

[VWF+15] D. Volz, M. Wallesch, C. Fléchon, M. Danz, A. Verma, J. M. Navarro, D. M. Zink, S. Bräse, and T. Baumann. From iridium and platinum to copper and carbon: new avenues for more sustainability in organic light-emitting diodes. *Green Chem.*, 17:1988, 2015.

[WFL+09] Y. I. Wu, D. Frey, O. I. Lungu, A. Jaehrig, I. Schlichting, B. Kuhlmann, and K. M. Hahn. A genetically-encoded photoactivatable Rac controls the motility of living cells. *Nature*, 461:104, 2009.

[WPE+14] M. Wingen, J. Potzkei, S. Endres, G. Casini, C. Rupprecht, C. Fahlke, U. Krauss, K.-E. Jaeger, T. Drepper, and T. Gensch. The photophysics of LOV-based fluorescent proteins – new tools for cell biology. *Photochem. Photobiol. Sci.*, 13:875, 2014.

[WS75] R. W. Wetmore and G. A. Segal. Efficient generation of configuration interaction matrix elements. *Chem. Phys. Lett.*, 36:478, 1975.

[XXHM21] Y. Xu, P. Xu, D. Hu, and Y. Ma. Recent progress in hot exciton materials for organic light-emitting diodes. *Chem. Soc. Rev.*, 50:1030, 2021.

[Yar95] D. R. Yarkony (Hrsg.). Modern Electronic Structure Theory (Part I, II). Singapore: World Scientific Publishing (Advanced Series in Physical Chemistry – Vol. 2), 1995.

[YU95] H. Yokoyama and K. Ujihara (Hrsg.). Spontaneous Emission and Laser Oscillation in Microcavities. Boca Raton: CRC Press, 1995.

[ZH15] X. Zhang and J. M. Herbert. Analytic derivative couplings in time-dependent density functional theory: Quadratic response theory versus pseudo-wavefunction approach. *J. Chem. Phys.*, 142:064109, 2015.

[Zi-09] Y. Zi-Zong. Schur Complements and Determinant Inequalities. *J. Math. Inequal.*, 3:161, 2009.

Abbildungsverzeichnis

Teil IV.

Anhang

4.1. Herleitung der erzeugenden Funktion

Die erzeugende Funktion für Franck–Condon-gewichtete Zustandsdichte unter Verwendung massegewichteter Normalkoordinaten $Q_\kappa = \sqrt{\mu_\kappa} R_\kappa$ (R: kartesische Normalkoordinaten, μ: reduzierte Masse) [TGM07] hat folgende Form [Eti10, ETM11, ETM14b]:

$$\begin{aligned} G_{\mathrm{FCWD}}^{a\rightsquigarrow b}(t) = (2\pi)^{-N} \sqrt{\det(\boldsymbol{\mathcal{S}}_a^{-1}\boldsymbol{\mathcal{S}}_b^{-1}\boldsymbol{\Omega}_a\boldsymbol{\Omega}_b)} \\ \times \int\int e^{-\frac{1}{4}[(\mathbf{Q}_b+\bar{\mathbf{Q}}_b)^\dagger \boldsymbol{\Omega}_b \mathbf{B}_b (\mathbf{Q}_b+\bar{\mathbf{Q}}_b) + (\mathbf{Q}_b-\bar{\mathbf{Q}}_b)^\dagger \boldsymbol{\Omega}_b \mathbf{B}_b^{-1} (\mathbf{Q}_b-\bar{\mathbf{Q}}_b)]} \\ \times e^{-\frac{1}{4}[(\mathbf{Q}_a+\bar{\mathbf{Q}}_a)^\dagger \boldsymbol{\Omega}_a \mathbf{B}_a (\mathbf{Q}_a+\bar{\mathbf{Q}}_a) + (\mathbf{Q}_a-\bar{\mathbf{Q}}_a)^\dagger \boldsymbol{\Omega}_a \mathbf{B}_a^{-1} (\mathbf{Q}_a-\bar{\mathbf{Q}}_a)]} \; d^N\mathbf{Q}_a d^N\bar{\mathbf{Q}}_a \; . \end{aligned} \tag{81}$$

† kennzeichnet Transposition und $\boldsymbol{\mathcal{S}}$, $\mathbf{B}$, $\boldsymbol{\Omega}$ stehen für folgende Diagonalmatrizen:

- $(\boldsymbol{\mathcal{S}}_a)_{ii} = \sinh[(\beta - it)\omega_{a,i}]$,
- $(\boldsymbol{\mathcal{S}}_b)_{ii} = \sinh(i\omega_{b,i}t)$,
- $(\mathbf{B}_a)_{ii} = \tanh[\omega_{a,i}(\beta - it)/2]$,
- $(\mathbf{B}_b)_{ii} = \tanh(i\omega_{b,i}t/2)$,
- $(\boldsymbol{\Omega}_a)_{ii} = \omega_{a,i}$,
- $(\boldsymbol{\Omega}_b)_{ii} = \omega_{b,i}$.

Gesucht wird eine erzeugende Funktion, die Integrale der Form $\langle\chi_b|\nabla_\kappa\chi_a\rangle$ implizit beschreibt. Die Ableitungen nach den $3N-6$ Normalkoordinaten κ wirken auf die Schwingungswellenfunktion des Ausgangszustands. Aufgrund der Berechnung des Betragsquadrats der Terme $\sum_\kappa \langle\chi_b \,|\, f_{ab}(\kappa)\nabla_\kappa\chi_a\rangle$ (vgl. Gleichung 79) wirken zwei voneinander unabhängige Ableitungen auf die Exponentialfunktion mit den Normalkoordinaten des Ausgangszustands im Exponenten [IM07]. Dementsprechend werden zwei Indices, κ und $\bar{\kappa}$, eingeführt. In der Konsequenz resultieren sowohl außerdiagonale Beiträge als auch zweite Ableitungen nach einer Mode. Die Kopplungen der Kernwellenfunktionen müssen gemäß Gleichung 79 mit den entsprechenden elektronischen Kopplungen gewichtet werden [BJ68].

Durch beide Modifikationen ergibt sich die gewünschte erzeugende Funktion für interne Konversion in ihrer Ausgangsform:

$$
\begin{aligned}
G_{\mathrm{IC}}^{a\rightsquigarrow b}(t) = (2\pi)^{-N}\sqrt{\det(\boldsymbol{\mathcal{S}}_a^{-1}\boldsymbol{\mathcal{S}}_b^{-1}\boldsymbol{\Omega}_a\boldsymbol{\Omega}_b)}\sum_{\kappa}\sum_{\bar{\kappa}} f_{ab}(\kappa)f_{ab}(\bar{\kappa}) \qquad (82)\\
\times\int\int e^{-\frac{1}{4}[(\mathbf{Q}_b+\bar{\mathbf{Q}}_b)^{\dagger}\boldsymbol{\Omega}_b\mathbf{B}_b(\mathbf{Q}_b+\bar{\mathbf{Q}}_b)+(\mathbf{Q}_b-\bar{\mathbf{Q}}_b)^{\dagger}\boldsymbol{\Omega}_b\mathbf{B}_b^{-1}(\mathbf{Q}_b-\bar{\mathbf{Q}}_b)]}\\
\times\frac{\partial^2}{\partial Q_{a,\kappa}\partial\bar{Q}_{a,\bar{\kappa}}}e^{-\frac{1}{4}[(\mathbf{Q}_a+\bar{\mathbf{Q}}_a)^{\dagger}\boldsymbol{\Omega}_a\mathbf{B}_a(\mathbf{Q}_a+\bar{\mathbf{Q}}_a)+(\mathbf{Q}_a-\bar{\mathbf{Q}}_a)^{\dagger}\boldsymbol{\Omega}_a\mathbf{B}_a^{-1}(\mathbf{Q}_a-\bar{\mathbf{Q}}_a)]}\; d^N\mathbf{Q}_a d^N\bar{\mathbf{Q}}_a\ .
\end{aligned}
$$

Der Satz an Normalkoordinaten des finalen Zustands $\mathbf{Q}_b$ wird mittels Duschinsky Transformation durch die Normalkoordinaten des initialen Zustands $\mathbf{Q}_a$ ausgedrückt. Hierbei beschreibt $\mathbf{J}$ die Duschinsky Rotationsmatrix und $\mathbf{D}$ beinhaltet die Verschiebung der Koordinaten

$$
\begin{aligned}
G_{\mathrm{IC}}^{a\rightsquigarrow b}(t) = (2\pi)^{-N}\sqrt{\det(\boldsymbol{\mathcal{S}}_a^{-1}\boldsymbol{\mathcal{S}}_b^{-1}\boldsymbol{\Omega}_a\boldsymbol{\Omega}_b)}\sum_{\kappa}\sum_{\bar{\kappa}} f_{ab}(\kappa)f_{ab}(\bar{\kappa}) \qquad (83)\\
\times\int\int e^{-\frac{1}{4}[(\mathbf{J}\mathbf{Q}_a+\mathbf{D}+\mathbf{J}\bar{\mathbf{Q}}_a+\mathbf{D})^{\dagger}\boldsymbol{\Omega}_b\mathbf{B}_b(\mathbf{J}\mathbf{Q}_a+\mathbf{D}+\mathbf{J}\bar{\mathbf{Q}}_a+\mathbf{D})+(\mathbf{J}\mathbf{Q}_a+\mathbf{D}-\mathbf{J}\bar{\mathbf{Q}}_a-\mathbf{D})^{\dagger}\boldsymbol{\Omega}_b\mathbf{B}_b^{-1}(\mathbf{J}\mathbf{Q}_a+\mathbf{D}-\mathbf{J}\bar{\mathbf{Q}}_a-\mathbf{D})]}\\
\times\frac{\partial^2}{\partial Q_{a,\kappa}\partial\bar{Q}_{a,\bar{\kappa}}}e^{-\frac{1}{4}[(\mathbf{Q}_a+\bar{\mathbf{Q}}_a)^{\dagger}\boldsymbol{\Omega}_a\mathbf{B}_a(\mathbf{Q}_a+\bar{\mathbf{Q}}_a)+(\mathbf{Q}_a-\bar{\mathbf{Q}}_a)^{\dagger}\boldsymbol{\Omega}_a\mathbf{B}_a^{-1}(\mathbf{Q}_a-\bar{\mathbf{Q}}_a)]}\; d^N\mathbf{Q}_a d^N\bar{\mathbf{Q}}_a\ .
\end{aligned}
$$

Zunächst wird die Ableitung der Exponentialfunktion nach den Normalkoordinaten bestimmt. Der resultierende Vorfaktor beschreibt die zeitabhängige Modulierung des Franck–Condon-Überlapps durch die Wirkung der Ableitungsoperatoren. Die Indices $\kappa/\bar{\kappa}$ kennzeichnen die jeweilige Position des Eintrags der abgeleiteten Mode im Vektor der Normalkoordinaten, z. B.:

$$
\frac{\partial}{\partial Q_a^N}\mathbf{Q}_a^{\dagger} = \frac{\partial}{\partial Q_a^N}(Q_a^1\ Q_a^2\cdots Q_a^N) = (0\ 0\cdots 1)\ . \qquad (84)
$$

Ausführung der ersten Ableitung liefert:

$$
\begin{aligned}
&\frac{\partial^2}{\partial Q_{a,\kappa}\partial\bar{Q}_{a,\bar{\kappa}}} e^{-\frac{1}{4}[(\mathbf{Q}_a+\bar{\mathbf{Q}}_a)^\dagger \mathbf{\Omega}_a\mathbf{B}_a(\mathbf{Q}_a+\bar{\mathbf{Q}}_a)+(\mathbf{Q}_a-\bar{\mathbf{Q}}_a)^\dagger \mathbf{\Omega}_a\mathbf{B}_a^{-1}(\mathbf{Q}_a-\bar{\mathbf{Q}}_a)]} \qquad (85)\\
&= \frac{\partial^2}{\partial Q_{a,\kappa}\partial\bar{Q}_{a,\bar{\kappa}}}\Big(e^{-\frac{1}{4}(\mathbf{Q}_a^\dagger \mathbf{\Omega}_a\mathbf{B}_a\mathbf{Q}_a+\mathbf{Q}_a^\dagger \mathbf{\Omega}_a\mathbf{B}_a\bar{\mathbf{Q}}_a+\bar{\mathbf{Q}}_a^\dagger \mathbf{\Omega}_a\mathbf{B}_a\mathbf{Q}_a+\bar{\mathbf{Q}}_a^\dagger \mathbf{\Omega}_a\mathbf{B}_a\bar{\mathbf{Q}}_a)}\\
&\qquad\qquad \times e^{-\frac{1}{4}(\mathbf{Q}_a^\dagger \mathbf{\Omega}_a\mathbf{B}_a^{-1}\mathbf{Q}_a-\mathbf{Q}_a^\dagger \mathbf{\Omega}_a\mathbf{B}_a^{-1}\bar{\mathbf{Q}}_a-\bar{\mathbf{Q}}_a^\dagger \mathbf{\Omega}_a\mathbf{B}_a^{-1}\mathbf{Q}_a+\bar{\mathbf{Q}}_a^\dagger \mathbf{\Omega}_a\mathbf{B}_a^{-1}\bar{\mathbf{Q}}_a)}\Big)\\
&= -\frac{1}{4}\frac{\partial}{\partial\bar{Q}_{a,\bar{\kappa}}}\Big[(\mathbf{Q}_a^\dagger \mathbf{\Omega}_a\mathbf{B}_a+\mathbf{\Omega}_a\mathbf{B}_a\mathbf{Q}_a+\mathbf{\Omega}_a\mathbf{B}_a\bar{\mathbf{Q}}_a+\bar{\mathbf{Q}}_a^\dagger \mathbf{\Omega}_a\mathbf{B}_a\\
&\qquad\qquad +\mathbf{Q}_a^\dagger \mathbf{\Omega}_a\mathbf{B}_a^{-1}+\mathbf{\Omega}_a\mathbf{B}_a^{-1}\mathbf{Q}_a-\mathbf{\Omega}_a\mathbf{B}_a^{-1}\bar{\mathbf{Q}}_a-\bar{\mathbf{Q}}_a^\dagger \mathbf{\Omega}_a\mathbf{B}_a^{-1})_\kappa\\
&\qquad\qquad \times e^{-\frac{1}{4}(\mathbf{Q}_a^\dagger \mathbf{\Omega}_a\mathbf{B}_a\mathbf{Q}_a+\mathbf{Q}_a^\dagger \mathbf{\Omega}_a\mathbf{B}_a\bar{\mathbf{Q}}_a+\bar{\mathbf{Q}}_a^\dagger \mathbf{\Omega}_a\mathbf{B}_a\mathbf{Q}_a+\bar{\mathbf{Q}}_a^\dagger \mathbf{\Omega}_a\mathbf{B}_a\bar{\mathbf{Q}}_a)}\\
&\qquad\qquad \times e^{-\frac{1}{4}(\mathbf{Q}_a^\dagger \mathbf{\Omega}_a\mathbf{B}_a^{-1}\mathbf{Q}_a-\mathbf{Q}_a^\dagger \mathbf{\Omega}_a\mathbf{B}_a^{-1}\bar{\mathbf{Q}}_a-\bar{\mathbf{Q}}_a^\dagger \mathbf{\Omega}_a\mathbf{B}_a^{-1}\mathbf{Q}_a+\bar{\mathbf{Q}}_a^\dagger \mathbf{\Omega}_a\mathbf{B}_a^{-1}\bar{\mathbf{Q}}_a)}\Big]\ .
\end{aligned}
$$

Im Zuge der zweiten Ableitung werden Diagonalterme erhalten. Diese sind durch das Kroneckerdelta $\delta_{\kappa\bar{\kappa}}$ gekennzeichnet

$$
\begin{aligned}
&\frac{\partial^2}{\partial Q_{a,\kappa}\partial\bar{Q}_{a,\bar{\kappa}}} e^{-\frac{1}{4}[(\mathbf{Q}_a+\bar{\mathbf{Q}}_a)^\dagger \mathbf{\Omega}_a\mathbf{B}_a(\mathbf{Q}_a+\bar{\mathbf{Q}}_a)+(\mathbf{Q}_a-\bar{\mathbf{Q}}_a)^\dagger \mathbf{\Omega}_a\mathbf{B}_a^{-1}(\mathbf{Q}_a-\bar{\mathbf{Q}}_a)]} \qquad (86)\\
&= -\frac{1}{4}(\mathbf{\Omega}_a\mathbf{B}_a+\mathbf{\Omega}_a\mathbf{B}_a-\mathbf{\Omega}_a\mathbf{B}_a^{-1}-\mathbf{\Omega}_a\mathbf{B}_a^{-1})_{\kappa\kappa}\delta_{\kappa\bar{\kappa}}\\
&\quad +\Big[-\frac{1}{4}(\mathbf{Q}_a^\dagger \mathbf{\Omega}_a\mathbf{B}_a+\mathbf{\Omega}_a\mathbf{B}_a\mathbf{Q}+\mathbf{\Omega}_a\mathbf{B}_a\bar{\mathbf{Q}}_a+\bar{\mathbf{Q}}_a^\dagger \mathbf{\Omega}_a\mathbf{B}_a\\
&\qquad +\mathbf{Q}_a^\dagger \mathbf{\Omega}_a\mathbf{B}_a^{-1}+\mathbf{\Omega}_a\mathbf{B}_a^{-1}\mathbf{Q}_a-\mathbf{\Omega}_a\mathbf{B}_a^{-1}\bar{\mathbf{Q}}_a-\bar{\mathbf{Q}}_a^\dagger \mathbf{\Omega}_a\mathbf{B}_a^{-1})_\kappa\\
&\quad \times -\frac{1}{4}(\mathbf{Q}_a^\dagger \mathbf{\Omega}_a\mathbf{B}_a+\mathbf{\Omega}_a\mathbf{B}_a\mathbf{Q}_a+\bar{\mathbf{Q}}_a^\dagger \mathbf{\Omega}_a\mathbf{B}_a+\mathbf{\Omega}_a\mathbf{B}_a\bar{\mathbf{Q}}_a\\
&\qquad -\mathbf{Q}_a^\dagger \mathbf{\Omega}_a\mathbf{B}_a^{-1}-\mathbf{\Omega}_a\mathbf{B}_a^{-1}\mathbf{Q}_a+\bar{\mathbf{Q}}_a^\dagger \mathbf{\Omega}_a\mathbf{B}_a^{-1}+\mathbf{\Omega}_a\mathbf{B}_a^{-1}\bar{\mathbf{Q}}_a)_{\bar{\kappa}}\Big]\\
&\quad \times e^{-\frac{1}{4}(\mathbf{Q}_a^\dagger \mathbf{\Omega}_a\mathbf{B}_a\mathbf{Q}_a+\mathbf{Q}_a^\dagger \mathbf{\Omega}_a\mathbf{B}_a\bar{\mathbf{Q}}_a+\bar{\mathbf{Q}}_a^\dagger \mathbf{\Omega}_a\mathbf{B}_a\mathbf{Q}_a+\bar{\mathbf{Q}}_a^\dagger \mathbf{\Omega}_a\mathbf{B}_a\bar{\mathbf{Q}}_a)}\\
&\quad \times e^{-\frac{1}{4}(\mathbf{Q}_a^\dagger \mathbf{\Omega}_a\mathbf{B}_a^{-1}\mathbf{Q}_a-\mathbf{Q}_a^\dagger \mathbf{\Omega}_a\mathbf{B}_a^{-1}\bar{\mathbf{Q}}_a-\bar{\mathbf{Q}}_a^\dagger \mathbf{\Omega}_a\mathbf{B}_a^{-1}\mathbf{Q}_a+\bar{\mathbf{Q}}_a^\dagger \mathbf{\Omega}_a\mathbf{B}_a^{-1}\bar{\mathbf{Q}}_a)}\ .
\end{aligned}
$$

An dieser Stelle werden die übrigen Terme ($\kappa = \bar{\kappa} \wedge \kappa \neq \bar{\kappa}$) separat behandelt:

$$
\begin{aligned}
& -\frac{1}{4}(\mathbf{Q}_a^\dagger \mathbf{\Omega}_a \mathbf{B}_a + \mathbf{\Omega}_a \mathbf{B}_a \mathbf{Q}_a + \mathbf{\Omega}_a \mathbf{B}_a \bar{\mathbf{Q}}_a + \bar{\mathbf{Q}}_a^\dagger \mathbf{\Omega}_a \mathbf{B}_a \\
& \quad + \mathbf{Q}_a^\dagger \mathbf{\Omega}_a \mathbf{B}_a^{-1} + \mathbf{\Omega}_a \mathbf{B}_a^{-1} \mathbf{Q}_a - \mathbf{\Omega}_a \mathbf{B}_a^{-1} \bar{\mathbf{Q}}_a - \bar{\mathbf{Q}}_a^\dagger \mathbf{\Omega}_a \mathbf{B}_a^{-1})_\kappa \\
\times & -\frac{1}{4}(\mathbf{Q}_a^\dagger \mathbf{\Omega}_a \mathbf{B}_a + \mathbf{\Omega}_a \mathbf{B}_a \mathbf{Q}_a + \bar{\mathbf{Q}}_a^\dagger \mathbf{\Omega}_a \mathbf{B}_a + \mathbf{\Omega}_a \mathbf{B}_a \bar{\mathbf{Q}}_a \\
& \quad - \mathbf{Q}_a^\dagger \mathbf{\Omega}_a \mathbf{B}_a^{-1} - \mathbf{\Omega}_a \mathbf{B}_a^{-1} \mathbf{Q}_a + \bar{\mathbf{Q}}_a^\dagger \mathbf{\Omega}_a \mathbf{B}_a^{-1} + \mathbf{\Omega}_a \mathbf{B}_a^{-1} \bar{\mathbf{Q}}_a)_{\bar{\kappa}} \\
= \quad & -\frac{1}{4}[(\mathbf{Q}_a + \bar{\mathbf{Q}}_a)^\dagger \mathbf{\Omega}_a \mathbf{B}_a + \mathbf{\Omega}_a \mathbf{B}_a (\mathbf{Q}_a + \bar{\mathbf{Q}}_a) + (\mathbf{Q}_a - \bar{\mathbf{Q}}_a)^\dagger \mathbf{\Omega}_a \mathbf{B}_a^{-1} + \mathbf{\Omega}_a \mathbf{B}_a^{-1} (\mathbf{Q}_a - \bar{\mathbf{Q}}_a)]_\kappa \\
\times & -\frac{1}{4}[(\mathbf{Q}_a + \bar{\mathbf{Q}}_a)^\dagger \mathbf{\Omega}_a \mathbf{B}_a + \mathbf{\Omega}_a \mathbf{B}_a (\mathbf{Q}_a + \bar{\mathbf{Q}}_a) - (\mathbf{Q}_a - \bar{\mathbf{Q}}_a)^\dagger \mathbf{\Omega}_a \mathbf{B}_a^{-1} - \mathbf{\Omega}_a \mathbf{B}_a^{-1} (\mathbf{Q}_a - \bar{\mathbf{Q}}_a)]_{\bar{\kappa}} \ .
\end{aligned} \tag{87}
$$

Zur Vereinfachung der räumlichen Integration werden die Integrationsvariablen substituiert. Die positive Linearkombination $\mathbf{Q}_a + \bar{\mathbf{Q}}_a$ wird als $\mathbf{X}$ bezeichnet und die negative Linearkombination $\mathbf{Q}_a - \bar{\mathbf{Q}}_a$ ist gleich $\mathbf{Y}$. Ausmultiplizieren liefert:

$$
\begin{aligned}
& \frac{1}{16}[\mathbf{X}^\dagger \mathbf{\Omega}_a \mathbf{B}_a + \mathbf{\Omega}_a \mathbf{B}_a \mathbf{X} + \mathbf{Y}^\dagger \mathbf{\Omega}_a \mathbf{B}_a^{-1} + \mathbf{\Omega}_a \mathbf{B}_a^{-1} \mathbf{Y}]_\kappa \\
& \quad \times [\mathbf{X}^\dagger \mathbf{\Omega}_a \mathbf{B}_a + \mathbf{\Omega}_a \mathbf{B}_a \mathbf{X} - \mathbf{Y}^\dagger \mathbf{\Omega}_a \mathbf{B}_a^{-1} - \mathbf{\Omega}_a \mathbf{B}_a^{-1} \mathbf{Y}]_{\bar{\kappa}} \\
= \quad & [\mathbf{X}_\kappa^\dagger (\mathbf{\Omega}_a \mathbf{B}_a)_{\kappa\kappa} \mathbf{X}_{\bar{\kappa}}^\dagger (\mathbf{\Omega}_a \mathbf{B}_a)_{\bar{\kappa}\bar{\kappa}} \\
& + \mathbf{X}_\kappa^\dagger (\mathbf{\Omega}_a \mathbf{B}_a)_{\kappa\kappa} (\mathbf{\Omega}_a \mathbf{B}_a)_{\bar{\kappa}\bar{\kappa}} \mathbf{X}_{\bar{\kappa}} \\
& - \mathbf{X}_\kappa^\dagger (\mathbf{\Omega}_a \mathbf{B}_a)_{\kappa\kappa} \mathbf{Y}_{\bar{\kappa}}^\dagger (\mathbf{\Omega}_a \mathbf{B}_a^{-1})_{\bar{\kappa}\bar{\kappa}} \\
& - \mathbf{X}_\kappa^\dagger (\mathbf{\Omega}_a \mathbf{B}_a)_{\kappa\kappa} (\mathbf{\Omega}_a \mathbf{B}_a^{-1})_{\bar{\kappa}\bar{\kappa}} \mathbf{Y}_{\bar{\kappa}} \\
& + (\mathbf{\Omega}_a \mathbf{B}_a)_{\kappa\kappa} \mathbf{X}_\kappa \mathbf{X}_{\bar{\kappa}}^\dagger (\mathbf{\Omega}_a \mathbf{B}_a)_{\bar{\kappa}\bar{\kappa}} \\
& + (\mathbf{\Omega}_a \mathbf{B}_a)_{\kappa\kappa} \mathbf{X}_\kappa (\mathbf{\Omega}_a \mathbf{B}_a)_{\bar{\kappa}\bar{\kappa}} \mathbf{X}_{\bar{\kappa}} \\
& - (\mathbf{\Omega}_a \mathbf{B}_a)_{\kappa\kappa} \mathbf{X}_\kappa \mathbf{Y}_{\bar{\kappa}}^\dagger (\mathbf{\Omega}_a \mathbf{B}_a^{-1})_{\bar{\kappa}\bar{\kappa}} \\
& - (\mathbf{\Omega}_a \mathbf{B}_a)_{\kappa\kappa} \mathbf{X}_\kappa (\mathbf{\Omega}_a \mathbf{B}_a^{-1})_{\bar{\kappa}\bar{\kappa}} \mathbf{Y}_{\bar{\kappa}}
\end{aligned} \tag{88}
$$

$$
\begin{aligned}
&+\mathbf{Y}^\dagger_\kappa(\mathbf{\Omega}_a\mathbf{B}_a^{-1})_{\kappa\kappa}\mathbf{X}^\dagger_{\bar\kappa}(\mathbf{\Omega}_a\mathbf{B}_a)_{\bar\kappa\bar\kappa}\\
&+\mathbf{Y}^\dagger_\kappa(\mathbf{\Omega}_a\mathbf{B}_a^{-1})_{\kappa\kappa}(\mathbf{\Omega}_a\mathbf{B}_a)_{\bar\kappa\bar\kappa}\mathbf{X}_{\bar\kappa}\\
&-\mathbf{Y}^\dagger_\kappa(\mathbf{\Omega}_a\mathbf{B}_a^{-1})_{\kappa\kappa}\mathbf{Y}^\dagger_{\bar\kappa}(\mathbf{\Omega}_a\mathbf{B}_a^{-1})_{\bar\kappa\bar\kappa}\\
&-\mathbf{Y}^\dagger_\kappa(\mathbf{\Omega}_a\mathbf{B}_a^{-1})_{\kappa\kappa}(\mathbf{\Omega}_a\mathbf{B}_a^{-1})_{\bar\kappa\bar\kappa}\mathbf{Y}_{\bar\kappa}\\
&+(\mathbf{\Omega}_a\mathbf{B}_a^{-1})_{\kappa\kappa}\mathbf{Y}_\kappa\mathbf{X}^\dagger_{\bar\kappa}(\mathbf{\Omega}_a\mathbf{B}_a)_{\bar\kappa\bar\kappa}\\
&+(\mathbf{\Omega}_a\mathbf{B}_a^{-1})_{\kappa\kappa}\mathbf{Y}_\kappa(\mathbf{\Omega}_a\mathbf{B}_a)_{\bar\kappa\bar\kappa}\mathbf{X}_{\bar\kappa}\\
&-(\mathbf{\Omega}_a\mathbf{B}_a^{-1})_{\kappa\kappa}\mathbf{Y}_\kappa\mathbf{Y}^\dagger_{\bar\kappa}(\mathbf{\Omega}_a\mathbf{B}_a^{-1})_{\bar\kappa\bar\kappa}\\
&-(\mathbf{\Omega}_a\mathbf{B}_a^{-1})_{\kappa\kappa}\mathbf{Y}_\kappa(\mathbf{\Omega}_a\mathbf{B}_a^{-1})_{\bar\kappa\bar\kappa}\mathbf{Y}_{\bar\kappa}]/16\ .
\end{aligned}
$$

Jeweils 4 Beiträge sind identisch und somit ergibt sich:

$$
\begin{aligned}
&\frac{1}{16}[\mathbf{X}^\dagger\mathbf{\Omega}_a\mathbf{B}_a+\mathbf{\Omega}_a\mathbf{B}_a\mathbf{X}+\mathbf{Y}^\dagger\mathbf{\Omega}_a\mathbf{B}_a^{-1}+\mathbf{\Omega}_a\mathbf{B}_a^{-1}\mathbf{Y}]_\kappa \qquad (89)\\
&\quad\times[\mathbf{X}^\dagger\mathbf{\Omega}_a\mathbf{B}_a+\mathbf{\Omega}_a\mathbf{B}_a\mathbf{X}-\mathbf{Y}^\dagger\mathbf{\Omega}_a\mathbf{B}_a^{-1}-\mathbf{\Omega}_a\mathbf{B}_a^{-1}\mathbf{Y}]_{\bar\kappa}\\
=\ &\frac{1}{16}[4(\mathbf{\Omega}_a\mathbf{B}_a)_{\kappa\kappa}(\mathbf{\Omega}_a\mathbf{B}_a)_{\bar\kappa\bar\kappa}\mathbf{X}_\kappa\mathbf{X}_{\bar\kappa}-4(\mathbf{\Omega}_a\mathbf{B}_a)_{\kappa\kappa}(\mathbf{\Omega}_a\mathbf{B}_a^{-1})_{\bar\kappa\bar\kappa}\mathbf{X}_\kappa\mathbf{Y}_{\bar\kappa}\\
&\quad+4(\mathbf{\Omega}_a\mathbf{B}_a^{-1})_{\kappa\kappa}(\mathbf{\Omega}_a\mathbf{B}_a)_{\bar\kappa\bar\kappa}\mathbf{Y}_\kappa\mathbf{X}_{\bar\kappa}-4(\mathbf{\Omega}_a\mathbf{B}_a^{-1})_{\kappa\kappa}(\mathbf{\Omega}_a\mathbf{B}_a^{-1})_{\bar\kappa\bar\kappa}\mathbf{Y}_\kappa\mathbf{Y}_{\bar\kappa}]\\
=\ &\frac{1}{4}[(\mathbf{\Omega}_a\mathbf{B}_a)_{\kappa\kappa}(\mathbf{\Omega}_a\mathbf{B}_a)_{\bar\kappa\bar\kappa}\mathbf{X}_\kappa\mathbf{X}_{\bar\kappa}-(\mathbf{\Omega}_a\mathbf{B}_a)_{\kappa\kappa}(\mathbf{\Omega}_a\mathbf{B}_a^{-1})_{\bar\kappa\bar\kappa}\mathbf{X}_\kappa\mathbf{Y}_{\bar\kappa}\\
&\quad+(\mathbf{\Omega}_a\mathbf{B}_a^{-1})_{\kappa\kappa}(\mathbf{\Omega}_a\mathbf{B}_a)_{\bar\kappa\bar\kappa}\mathbf{Y}_\kappa\mathbf{X}_{\bar\kappa}-(\mathbf{\Omega}_a\mathbf{B}_a^{-1})_{\kappa\kappa}(\mathbf{\Omega}_a\mathbf{B}_a^{-1})_{\bar\kappa\bar\kappa}\mathbf{Y}_\kappa\mathbf{Y}_{\bar\kappa}]\ .
\end{aligned}
$$

Die erhaltenen Terme sind Skalare. Die Indices kennzeichnen die Einträge in den Diagonalmatrizen, welche in das Produkt eingehen. Diese sind durch die nichtverschwindenden Einträge in $\mathbf{X}$ bzw. $\mathbf{Y}$ festgelegt. Letztlich werden alle Terme zuammengefasst.

Der gesamte Ausdruck für die Ableitung der Exponentialfunktion nach den Normalkoordinaten lautet:

$$
\begin{aligned}
&\frac{\partial^2}{\partial Q_{a,\kappa}\partial \bar{Q}_{a,\bar{\kappa}}} e^{-\frac{1}{4}[(\mathbf{Q}_a+\bar{\mathbf{Q}}_a)^\dagger \mathbf{\Omega}_a \mathbf{B}_a (\mathbf{Q}_a+\bar{\mathbf{Q}}_a)+(\mathbf{Q}_a-\bar{\mathbf{Q}}_a)^\dagger \mathbf{\Omega}_a \mathbf{B}_a^{-1} (\mathbf{Q}_a-\bar{\mathbf{Q}}_a)]} \\
= \;& \frac{1}{2}\{[(\mathbf{\Omega}_a\mathbf{B}_a^{-1})_{\kappa\kappa} - (\mathbf{\Omega}_a\mathbf{B}_a)_{\kappa\kappa}]\delta_{\kappa\bar{\kappa}} \\
&+\frac{1}{2}[(\mathbf{\Omega}_a\mathbf{B}_a)_{\kappa\kappa}(\mathbf{\Omega}_a\mathbf{B}_a)_{\bar{\kappa}\bar{\kappa}}\mathbf{X}_\kappa\mathbf{X}_{\bar{\kappa}} - (\mathbf{\Omega}_a\mathbf{B}_a)_{\kappa\kappa}(\mathbf{\Omega}_a\mathbf{B}_a^{-1})_{\bar{\kappa}\bar{\kappa}}\mathbf{X}_\kappa\mathbf{Y}_{\bar{\kappa}} \\
&\quad +(\mathbf{\Omega}_a\mathbf{B}_a^{-1})_{\kappa\kappa}(\mathbf{\Omega}_a\mathbf{B}_a)_{\bar{\kappa}\bar{\kappa}}\mathbf{Y}_\kappa\mathbf{X}_{\bar{\kappa}} - (\mathbf{\Omega}_a\mathbf{B}_a^{-1})_{\kappa\kappa}(\mathbf{\Omega}_a\mathbf{B}_a^{-1})_{\bar{\kappa}\bar{\kappa}}\mathbf{Y}_\kappa\mathbf{Y}_{\bar{\kappa}}]\} \\
&\times e^{-\frac{1}{4}(\mathbf{X}^\dagger\mathbf{\Omega}_a\mathbf{B}_a\mathbf{X}+\mathbf{Y}^\dagger\mathbf{\Omega}_a\mathbf{B}_a^{-1}\mathbf{Y})} \,.
\end{aligned}
\tag{90}
$$

Bevor die Ableitung in den vorangegangenen Ausdruck für die erzeugende Funktion eingefügt wird, ist es nötig die Exponentialfunktion zur Beschreibung der finalen Schwingungsniveaus umzuformulieren. Erneut werden die Substitutionen $\mathbf{Q}_a + \bar{\mathbf{Q}}_a = \mathbf{X}$ und $\mathbf{Q}_a - \bar{\mathbf{Q}}_a = \mathbf{Y}$ durchgeführt. Die Exponentialfunktion kann in drei Funktionen aufgeteilt werden, sodass keine Exponenten mit Abhängigkeiten von beiden Integrationsvariablen entstehen. Mit der Umstellung $\mathbf{D}^\dagger\mathbf{\Omega}_b\mathbf{B}_b\mathbf{J}(\mathbf{Q}_a+\bar{\mathbf{Q}}_a) = [(\mathbf{Q}_a+\bar{\mathbf{Q}}_a)^\dagger\mathbf{J}^\dagger\mathbf{\Omega}_b\mathbf{B}_b\mathbf{D}]^\dagger = (\mathbf{Q}_a+\bar{\mathbf{Q}}_a)^\dagger\mathbf{J}^\dagger\mathbf{\Omega}_b\mathbf{B}_b\mathbf{D}$ ergibt sich:

$$
\begin{aligned}
&e^{-\frac{1}{4}[(\mathbf{J}\mathbf{Q}_a+\mathbf{D}+\mathbf{J}\bar{\mathbf{Q}}_a+\mathbf{D})^\dagger\mathbf{\Omega}_b\mathbf{B}_b(\mathbf{J}\mathbf{Q}_a+\mathbf{D}+\mathbf{J}\bar{\mathbf{Q}}_a+\mathbf{D})+(\mathbf{J}\mathbf{Q}_a+\mathbf{D}-\mathbf{J}\bar{\mathbf{Q}}_a-\mathbf{D})^\dagger\mathbf{\Omega}_b\mathbf{B}_b^{-1}(\mathbf{J}\mathbf{Q}_a+\mathbf{D}-\mathbf{J}\bar{\mathbf{Q}}_a-\mathbf{D})]} \\
= \;& e^{-\frac{1}{4}(\mathbf{Q}_a+\bar{\mathbf{Q}}_a)^\dagger\mathbf{J}^\dagger\mathbf{\Omega}_b\mathbf{B}_b\mathbf{J}(\mathbf{Q}_a+\bar{\mathbf{Q}}_a)} \\
&\times e^{-(\mathbf{Q}_a+\bar{\mathbf{Q}}_a)^\dagger\mathbf{J}^\dagger\mathbf{\Omega}_b\mathbf{B}_b\mathbf{D}} \\
&\times e^{-\mathbf{D}^\dagger\mathbf{\Omega}_b\mathbf{B}_b\mathbf{D}} \\
&\times e^{-\frac{1}{4}[(\mathbf{Q}_a-\bar{\mathbf{Q}}_a)^\dagger\mathbf{J}^\dagger\mathbf{\Omega}_b\mathbf{B}_b^{-1}\mathbf{J}(\mathbf{Q}_a-\bar{\mathbf{Q}}_a)]} \\
= \;& e^{-\frac{1}{4}\mathbf{X}^\dagger\mathbf{J}^\dagger\mathbf{\Omega}_b\mathbf{B}_b\mathbf{J}\mathbf{X}-\mathbf{X}^\dagger\mathbf{J}^\dagger\mathbf{\Omega}_b\mathbf{B}_b\mathbf{D}} \times e^{-\frac{1}{4}\mathbf{Y}^\dagger\mathbf{J}^\dagger\mathbf{\Omega}_b\mathbf{B}_b^{-1}\mathbf{J}\mathbf{Y}} \times e^{-\mathbf{D}^\dagger\mathbf{\Omega}_b\mathbf{B}_b\mathbf{D}} \,.
\end{aligned}
\tag{91}
$$

In der Folge werden der Ausdruck für die abgeleitete Exponentialfunktion sowie Gleichung 91 zusammengeführt. Die resultierende Formulierung von G_{IC} stellt einen handlichen Ausdruck für die räumliche Integration dar, da diese mit Hilfe von analytischen Formeln für Gaußfunktionen durchgeführt werden kann. Der Grund für den eingeführten Faktor 2^{-N} liegt in der Änderung der Integrationsvariablen. Die Transformation der räumlichen Integration wird durch den Betrag der Determinante der Jacobi-Matrix

$$\left|\det\left[\frac{\partial(\mathbf{Q}_a,\bar{\mathbf{Q}}_a)}{\partial(\mathbf{X},\mathbf{Y})}\right]\right| = \left|\mathbf{I}_N\mathbf{I}_N + \mathbf{I}_N\mathbf{I}_N\right|^{-1} = 2^{-N}\left|\mathbf{I}_N\right|^{-1} = 2^{-N} \tag{92}$$

berücksichtigt. Zusammengesetzt ergibt sich

$$\begin{aligned} G_{\mathrm{IC}}^{a\rightsquigarrow b}(t) = (4\pi)^{-N}\sqrt{\det(\boldsymbol{\mathcal{S}}_a^{-1}\boldsymbol{\mathcal{S}}_b^{-1}\boldsymbol{\Omega}_a\boldsymbol{\Omega}_b)}e^{-\mathbf{D}^\dagger\boldsymbol{\Omega}_b\mathbf{B}_b\mathbf{D}}\sum_{\kappa}\sum_{\bar{\kappa}} f_{ab}(\kappa)f_{ab}(\bar{\kappa}) \\ \times\int\int\frac{1}{2}\{[(\boldsymbol{\Omega}_a\mathbf{B}_a^{-1})_{\kappa\kappa} - (\boldsymbol{\Omega}_a\mathbf{B}_a)_{\kappa\kappa}]\delta_{\kappa\bar{\kappa}} \\ +\frac{1}{2}[(\boldsymbol{\Omega}_a\mathbf{B}_a)_{\kappa\kappa}(\boldsymbol{\Omega}_a\mathbf{B}_a)_{\bar{\kappa}\bar{\kappa}}\mathbf{X}_\kappa\mathbf{X}_{\bar{\kappa}} - (\boldsymbol{\Omega}_a\mathbf{B}_a)_{\kappa\kappa}(\boldsymbol{\Omega}_a\mathbf{B}_a^{-1})_{\bar{\kappa}\bar{\kappa}}\mathbf{X}_\kappa\mathbf{Y}_{\bar{\kappa}} \\ +(\boldsymbol{\Omega}_a\mathbf{B}_a^{-1})_{\kappa\kappa}(\boldsymbol{\Omega}_a\mathbf{B}_a)_{\bar{\kappa}\bar{\kappa}}\mathbf{Y}_\kappa\mathbf{X}_{\bar{\kappa}} - (\boldsymbol{\Omega}_a\mathbf{B}_a^{-1})_{\kappa\kappa}(\boldsymbol{\Omega}_a\mathbf{B}_a^{-1})_{\bar{\kappa}\bar{\kappa}}\mathbf{Y}_\kappa\mathbf{Y}_{\bar{\kappa}}]\} \\ \times e^{-\frac{1}{4}\mathbf{X}^\dagger(\boldsymbol{\Omega}_a\mathbf{B}_a+\mathbf{J}^\dagger\boldsymbol{\Omega}_b\mathbf{B}_b\mathbf{J})\mathbf{X}-\mathbf{X}^\dagger\mathbf{J}^\dagger\boldsymbol{\Omega}_b\mathbf{B}_b\mathbf{D}} \\ \times e^{-\frac{1}{4}\mathbf{Y}^\dagger(\boldsymbol{\Omega}_a\mathbf{B}_a^{-1}+\mathbf{J}^\dagger\boldsymbol{\Omega}_b\mathbf{B}_b^{-1}\mathbf{J})\mathbf{Y}}\, d\mathbf{X}^N d\mathbf{Y}^N \ . \end{aligned} \tag{93}$$

Räumliche Integration über $\mathbf{X}^N$ and $\mathbf{Y}^N$

Die resultierenden N-dimensionalen Integrale können mit Hilfe folgender Gaußintegrale gelöst werden [IM07]:

I.

$$\int e^{-\mathbf{z}^\dagger\mathbf{p}\mathbf{z}+2\mathbf{z}^\dagger\mathbf{q}}d\mathbf{z} = \pi^{\frac{N}{2}}\sqrt{\det(\mathbf{p}^{-1})}e^{\mathbf{q}^\dagger\mathbf{p}^{-1}\mathbf{q}} \ , \tag{94}$$

II.

$$\int \mathbf{z}_k e^{-\mathbf{z}^\dagger\mathbf{p}\mathbf{z}+2\mathbf{z}^\dagger\mathbf{q}}d\mathbf{z} = \pi^{\frac{N}{2}}(\mathbf{p}^{-1}\mathbf{q})_k\sqrt{\det(\mathbf{p}^{-1})}e^{\mathbf{q}^\dagger\mathbf{p}^{-1}\mathbf{q}} \ , \tag{95}$$

III.

$$\int \mathbf{z}_k\mathbf{z}_l e^{-\mathbf{z}^\dagger\mathbf{p}\mathbf{z}+2\mathbf{z}^\dagger\mathbf{q}}d\mathbf{z} = \pi^{\frac{N}{2}}\left[\frac{1}{2}(\mathbf{p}^{-1})_{kl} + (\mathbf{p}^{-1}\mathbf{q})_k(\mathbf{p}^{-1}\mathbf{q})_l\right]\sqrt{\det(\mathbf{p}^{-1})}e^{\mathbf{q}^\dagger\mathbf{p}^{-1}\mathbf{q}} \ , \tag{96}$$

mit

- $d\mathbf{z} = \prod_j^N dz_j$,
- $\mathbf{z}, \mathbf{q}$: N-dimensionale Vektoren,
- $\mathbf{p}$: $N \times N$ symmetrische Matrix.

Gemäß I.:

$$\begin{aligned}&\int e^{-\frac{1}{4}\mathbf{Y}^\dagger(\mathbf{\Omega}_a\mathbf{B}_a^{-1}+\mathbf{J}^\dagger\mathbf{\Omega}_b\mathbf{B}_b^{-1}\mathbf{J})\mathbf{Y}}\ d\mathbf{Y}^N \\ &= 2^N\pi^{\frac{N}{2}}\sqrt{\det[(\mathbf{\Omega}_a\mathbf{B}_a^{-1}+\mathbf{J}^\dagger\mathbf{\Omega}_b\mathbf{B}_b^{-1}\mathbf{J})^{-1}]}\ ,\end{aligned} \tag{97}$$

$$\begin{aligned}&\int e^{-\frac{1}{4}\mathbf{X}^\dagger(\mathbf{\Omega}_a\mathbf{B}_a+\mathbf{J}^\dagger\mathbf{\Omega}_b\mathbf{B}_b\mathbf{J})\mathbf{X}-\mathbf{X}^\dagger\mathbf{J}^\dagger\mathbf{\Omega}_b\mathbf{B}_b\mathbf{D}}\ d\mathbf{X}^N \\ &= 2^N\pi^{\frac{N}{2}}\sqrt{\det[(\mathbf{\Omega}_a\mathbf{B}_a+\mathbf{J}^\dagger\mathbf{\Omega}_b\mathbf{B}_b\mathbf{J})^{-1}]}e^{\mathbf{D}^\dagger\mathbf{\Omega}_b\mathbf{B}_b\mathbf{J}(\mathbf{\Omega}_a\mathbf{B}_a+\mathbf{J}^\dagger\mathbf{\Omega}_b\mathbf{B}_b\mathbf{J})^{-1}\mathbf{J}^\dagger\mathbf{\Omega}_b\mathbf{B}_b\mathbf{D}}\ .\end{aligned} \tag{98}$$

Gemäß II.:

$$\begin{aligned}&\int \mathbf{Y}_\kappa e^{-\frac{1}{4}\mathbf{Y}^\dagger(\mathbf{\Omega}_a\mathbf{B}_a^{-1}+\mathbf{J}^\dagger\mathbf{\Omega}_b\mathbf{B}_b^{-1}\mathbf{J})\mathbf{Y}}\ d\mathbf{Y}^N \\ &= 0\times 2^N\pi^{\frac{N}{2}}\sqrt{\det[(\mathbf{\Omega}_a\mathbf{B}_a^{-1}+\mathbf{J}^\dagger\mathbf{\Omega}_b\mathbf{B}_b^{-1}\mathbf{J})^{-1}]}=0\ ,\end{aligned} \tag{99}$$

$$\begin{aligned}&\int \mathbf{X}_\kappa e^{-\frac{1}{4}\mathbf{X}^\dagger(\mathbf{\Omega}_a\mathbf{B}_a+\mathbf{J}^\dagger\mathbf{\Omega}_b\mathbf{B}_b\mathbf{J})\mathbf{X}-\mathbf{X}^\dagger\mathbf{J}^\dagger\mathbf{\Omega}_b\mathbf{B}_b\mathbf{D}}\ d\mathbf{X}^N \\ &= -2[(\mathbf{\Omega}_a\mathbf{B}_a+\mathbf{J}^\dagger\mathbf{\Omega}_b\mathbf{B}_b\mathbf{J})^{-1}\mathbf{J}^\dagger\mathbf{\Omega}_b\mathbf{B}_b\mathbf{D}]_\kappa\times 2^N\pi^{\frac{N}{2}}\sqrt{\det[(\mathbf{\Omega}_a\mathbf{B}_a+\mathbf{J}^\dagger\mathbf{\Omega}_b\mathbf{B}_b\mathbf{J})^{-1}]} \\ &\quad\times e^{\mathbf{D}^\dagger\mathbf{\Omega}_b\mathbf{B}_b\mathbf{J}(\mathbf{\Omega}_a\mathbf{B}_a+\mathbf{J}^\dagger\mathbf{\Omega}_b\mathbf{B}_b\mathbf{J})^{-1}\mathbf{J}^\dagger\mathbf{\Omega}_b\mathbf{B}_b\mathbf{D}}\ .\end{aligned} \tag{100}$$

Gemäß III.:

$$\begin{aligned}&\int \mathbf{Y}_\kappa\mathbf{Y}_{\bar\kappa}e^{-\frac{1}{4}\mathbf{Y}^\dagger(\mathbf{\Omega}_a\mathbf{B}_a^{-1}+\mathbf{J}^\dagger\mathbf{\Omega}_b\mathbf{B}_b^{-1}\mathbf{J})\mathbf{Y}}\ d\mathbf{Y}^N \\ &= 2(\mathbf{\Omega}_a\mathbf{B}_a^{-1}+\mathbf{J}^\dagger\mathbf{\Omega}_b\mathbf{B}_b^{-1}\mathbf{J})^{-1}_{\kappa\bar\kappa}\times 2^N\pi^{\frac{N}{2}}\sqrt{\det[(\mathbf{\Omega}_a\mathbf{B}_a^{-1}+\mathbf{J}^\dagger\mathbf{\Omega}_b\mathbf{B}_b^{-1}\mathbf{J})^{-1}]}\ ,\end{aligned} \tag{101}$$

$$\begin{aligned}&\int \mathbf{X}_\kappa\mathbf{X}_{\bar\kappa}e^{-\frac{1}{4}\mathbf{X}^\dagger(\mathbf{\Omega}_a\mathbf{B}_a+\mathbf{J}^\dagger\mathbf{\Omega}_b\mathbf{B}_b\mathbf{J})\mathbf{X}-\mathbf{X}^\dagger\mathbf{J}^\dagger\mathbf{\Omega}_b\mathbf{B}_b\mathbf{D}}\ d\mathbf{X}^N \\ &= \Big\{2(\mathbf{\Omega}_a\mathbf{B}_a+\mathbf{J}^\dagger\mathbf{\Omega}_b\mathbf{B}_b\mathbf{J})^{-1}_{\kappa\bar\kappa}+4[(\mathbf{\Omega}_a\mathbf{B}_a+\mathbf{J}^\dagger\mathbf{\Omega}_b\mathbf{B}_b\mathbf{J})^{-1}\mathbf{J}^\dagger\mathbf{\Omega}_b\mathbf{B}_b\mathbf{D}]_\kappa \\ &\quad[(\mathbf{\Omega}_a\mathbf{B}_a+\mathbf{J}^\dagger\mathbf{\Omega}_b\mathbf{B}_b\mathbf{J})^{-1}\mathbf{J}^\dagger\mathbf{\Omega}_b\mathbf{B}_b\mathbf{D}]_{\bar\kappa}\Big\}\times 2^N\pi^{\frac{N}{2}}\sqrt{\det[(\mathbf{\Omega}_a\mathbf{B}_a+\mathbf{J}^\dagger\mathbf{\Omega}_b\mathbf{B}_b\mathbf{J})^{-1}]} \\ &\quad\times e^{\mathbf{D}^\dagger\mathbf{\Omega}_b\mathbf{B}_b\mathbf{J}(\mathbf{\Omega}_a\mathbf{B}_a+\mathbf{J}^\dagger\mathbf{\Omega}_b\mathbf{B}_b\mathbf{J})^{-1}\mathbf{J}^\dagger\mathbf{\Omega}_b\mathbf{B}_b\mathbf{D}}\ .\end{aligned} \tag{102}$$

Im Folgenden werden die Integrale über $\mathbf{X}$ und $\mathbf{Y}$ für die Fälle I und III zusammengefasst. Kreuzterme (Fall II) liefern keinen Beitrag zur erzeugenden Funktion, da das Integral über $\mathbf{Y}^N$ verschwindet.

Fall I - Modulus unabhängig von den Integrationsvariablen:

$$\begin{aligned} & \frac{1}{2}[(\mathbf{\Omega}_a\mathbf{B}_a^{-1})_{\kappa\kappa} - (\mathbf{\Omega}_a\mathbf{B}_a)_{\kappa\kappa}]\delta_{\kappa\bar{\kappa}} \times 2^N\pi^{\frac{N}{2}}\sqrt{\det[(\mathbf{\Omega}_a\mathbf{B}_a^{-1} + \mathbf{J}^\dagger\mathbf{\Omega}_b\mathbf{B}_b^{-1}\mathbf{J})^{-1}]} \\ & \times 2^N\pi^{\frac{N}{2}}\sqrt{\det[(\mathbf{\Omega}_a\mathbf{B}_a + \mathbf{J}^\dagger\mathbf{\Omega}_b\mathbf{B}_b\mathbf{J})^{-1}]}e^{\mathbf{D}^\dagger\mathbf{\Omega}_b\mathbf{B}_b\mathbf{J}(\mathbf{\Omega}_a\mathbf{B}_a+\mathbf{J}^\dagger\mathbf{\Omega}_b\mathbf{B}_b\mathbf{J})^{-1}\mathbf{J}^\dagger\mathbf{\Omega}_b\mathbf{B}_b\mathbf{D}} \\ = \quad & \frac{1}{2}[(\mathbf{\Omega}_a\mathbf{B}_a^{-1})_{\kappa\kappa} - (\mathbf{\Omega}_a\mathbf{B}_a)_{\kappa\kappa}]\delta_{\kappa\bar{\kappa}} \\ & \times(4\pi)^N\sqrt{\det[(\mathbf{\Omega}_a\mathbf{B}_a + \mathbf{J}^\dagger\mathbf{\Omega}_b\mathbf{B}_b\mathbf{J})^{-1}]\det[(\mathbf{\Omega}_a\mathbf{B}_a^{-1} + \mathbf{J}^\dagger\mathbf{\Omega}_b\mathbf{B}_b^{-1}\mathbf{J})^{-1}]} \\ & \times e^{\mathbf{D}^\dagger\mathbf{\Omega}_b\mathbf{B}_b\mathbf{J}(\mathbf{\Omega}_a\mathbf{B}_a+\mathbf{J}^\dagger\mathbf{\Omega}_b\mathbf{B}_b\mathbf{J})^{-1}\mathbf{J}^\dagger\mathbf{\Omega}_b\mathbf{B}_b\mathbf{D}} \,. \end{aligned} \tag{103}$$

Fall III - Modulus mit quadratischer Abhängigkeit von den Integrationsvariablen:

$$\begin{aligned} & \Big\{ -\frac{1}{4}(\mathbf{\Omega}_a\mathbf{B}_a^{-1})_{\kappa\kappa}(\mathbf{\Omega}_a\mathbf{B}_a^{-1})_{\bar{\kappa}\bar{\kappa}} \\ & \times 2(\mathbf{\Omega}_a\mathbf{B}_a^{-1} + \mathbf{J}^\dagger\mathbf{\Omega}_b\mathbf{B}_b^{-1}\mathbf{J})^{-1}_{\kappa\bar{\kappa}} \\ & \quad + \frac{1}{4}(\mathbf{\Omega}_a\mathbf{B}_a)_{\kappa\kappa}(\mathbf{\Omega}_a\mathbf{B}_a)_{\bar{\kappa}\bar{\kappa}} \\ & \times \Big\{2(\mathbf{\Omega}_a\mathbf{B}_a + \mathbf{J}^\dagger\mathbf{\Omega}_b\mathbf{B}_b\mathbf{J})^{-1}_{\kappa\bar{\kappa}} + 4[(\mathbf{\Omega}_a\mathbf{B}_a + \mathbf{J}^\dagger\mathbf{\Omega}_b\mathbf{B}_b\mathbf{J})^{-1}\mathbf{J}^\dagger\mathbf{\Omega}_b\mathbf{B}_b\mathbf{D}]_\kappa \\ & \quad [(\mathbf{\Omega}_a\mathbf{B}_a + \mathbf{J}^\dagger\mathbf{\Omega}_b\mathbf{B}_b\mathbf{J})^{-1}\mathbf{J}^\dagger\mathbf{\Omega}_b\mathbf{B}_b\mathbf{D}]_{\bar{\kappa}}\Big\}\Big\} \\ & \times (4\pi)^N\sqrt{\det[(\mathbf{\Omega}_a\mathbf{B}_a + \mathbf{J}^\dagger\mathbf{\Omega}_b\mathbf{B}_b\mathbf{J})^{-1}]\det[(\mathbf{\Omega}_a\mathbf{B}_a^{-1} + \mathbf{J}^\dagger\mathbf{\Omega}_b\mathbf{B}_b^{-1}\mathbf{J})^{-1}]} \\ & \times e^{\mathbf{D}^\dagger\mathbf{\Omega}_b\mathbf{B}_b\mathbf{J}(\mathbf{\Omega}_a\mathbf{B}_a+\mathbf{J}^\dagger\mathbf{\Omega}_b\mathbf{B}_b\mathbf{J})^{-1}\mathbf{J}^\dagger\mathbf{\Omega}_b\mathbf{B}_b\mathbf{D}} \,. \end{aligned} \tag{104}$$

Im nächsten Schritt müssen die erhaltenen Lösungen für die Integrale in Gleichung 93 eingesetzt werden.

Das Zwischenergebnis ist gegeben durch:

$$
\begin{aligned}
G_{\mathrm{IC}}^{a\rightsquigarrow b}(t) = & \sqrt{\frac{\det(\boldsymbol{\mathcal{S}}_a^{-1}\boldsymbol{\mathcal{S}}_b^{-1}\boldsymbol{\Omega}_a\boldsymbol{\Omega}_b)}{\det(\boldsymbol{\Omega}_a\mathbf{B}_a+\mathbf{J}^\dagger\boldsymbol{\Omega}_b\mathbf{B}_b\mathbf{J})\det(\boldsymbol{\Omega}_a\mathbf{B}_a^{-1}+\mathbf{J}^\dagger\boldsymbol{\Omega}_b\mathbf{B}_b^{-1}\mathbf{J})}} \\
& \times e^{-\mathbf{D}^\dagger\boldsymbol{\Omega}_b\mathbf{B}_b\mathbf{D}}\sum_\kappa\sum_{\bar\kappa} f_{ab}(\kappa)f_{ab}(\bar\kappa) \\
& \times \Big\{[(\boldsymbol{\Omega}_a\mathbf{B}_a^{-1})_{\kappa\kappa}-(\boldsymbol{\Omega}_a\mathbf{B}_a)_{\kappa\kappa}]\delta_{\kappa\bar\kappa}/2 \\
& + (\boldsymbol{\Omega}_a\mathbf{B}_a)_{\kappa\kappa}(\boldsymbol{\Omega}_a\mathbf{B}_a+\mathbf{J}^\dagger\boldsymbol{\Omega}_b\mathbf{B}_b\mathbf{J})^{-1}_{\kappa\bar\kappa}(\boldsymbol{\Omega}_a\mathbf{B}_a)_{\bar\kappa\bar\kappa}/2 \\
& - (\boldsymbol{\Omega}_a\mathbf{B}_a^{-1})_{\kappa\kappa}(\boldsymbol{\Omega}_a\mathbf{B}_a^{-1}+\mathbf{J}^\dagger\boldsymbol{\Omega}_b\mathbf{B}_b^{-1}\mathbf{J})^{-1}_{\kappa\bar\kappa}(\boldsymbol{\Omega}_a\mathbf{B}_a^{-1})_{\bar\kappa\bar\kappa}/2 \\
& + (\boldsymbol{\Omega}_a\mathbf{B}_a)_{\kappa\kappa}[(\boldsymbol{\Omega}_a\mathbf{B}_a+\mathbf{J}^\dagger\boldsymbol{\Omega}_b\mathbf{B}_b\mathbf{J})^{-1}\mathbf{J}^\dagger\boldsymbol{\Omega}_b\mathbf{B}_b\mathbf{D}]_\kappa \\
& \times (\boldsymbol{\Omega}_a\mathbf{B}_a)_{\bar\kappa\bar\kappa}[(\boldsymbol{\Omega}_a\mathbf{B}_a+\mathbf{J}^\dagger\boldsymbol{\Omega}_b\mathbf{B}_b\mathbf{J})^{-1}\mathbf{J}^\dagger\boldsymbol{\Omega}_b\mathbf{B}_b\mathbf{D}]_{\bar\kappa}\Big\} \\
& \times e^{\mathbf{D}^\dagger\boldsymbol{\Omega}_b\mathbf{B}_b\mathbf{J}(\boldsymbol{\Omega}_a\mathbf{B}_a+\mathbf{J}^\dagger\boldsymbol{\Omega}_b\mathbf{B}_b\mathbf{J})^{-1}\mathbf{J}^\dagger\boldsymbol{\Omega}_b\mathbf{B}_b\mathbf{D}} \ .
\end{aligned}
\tag{105}
$$

Zur Vereinfachung der halbierten Terme wird folgende Matrizenidentität angewandt:

$$
\begin{aligned}
& \mathbf{B}+\mathbf{A} = \mathbf{B}+\mathbf{A} \\
\Leftrightarrow\ & \mathbf{E}+\mathbf{B}^{-1}\mathbf{A} = \mathbf{B}^{-1}(\mathbf{B}+\mathbf{A}) \\
\Leftrightarrow\ & \mathbf{A}^{-1}+\mathbf{B}^{-1} = \mathbf{B}^{-1}(\mathbf{B}+\mathbf{A})\mathbf{A}^{-1} \\
\Leftrightarrow\ & (\mathbf{A}^{-1}+\mathbf{B}^{-1})^{-1} = \mathbf{A}(\mathbf{B}+\mathbf{A})^{-1}\mathbf{B} \\
\Leftrightarrow\ & \mathbf{A}^{-1}(\mathbf{A}^{-1}+\mathbf{B}^{-1})^{-1} = (\mathbf{B}+\mathbf{A})^{-1}\mathbf{B} \ .
\end{aligned}
\tag{106}
$$

In einem Zwischenschritt wird der zweite Term umgeformt ($\mathbf{B}=\boldsymbol{\Omega}_a\mathbf{B}_a$ und $\mathbf{A}=\mathbf{J}^\dagger\boldsymbol{\Omega}_b\mathbf{B}_b\mathbf{J}$):

$$
\begin{aligned}
& -\boldsymbol{\Omega}_a\mathbf{B}_a+\boldsymbol{\Omega}_a\mathbf{B}_a(\boldsymbol{\Omega}_a\mathbf{B}_a+\mathbf{J}^\dagger\boldsymbol{\Omega}_b\mathbf{B}_b\mathbf{J})^{-1}\boldsymbol{\Omega}_a\mathbf{B}_a \\
= & -\boldsymbol{\Omega}_a\mathbf{B}_a+\boldsymbol{\Omega}_a\mathbf{B}_a\mathbf{J}^\dagger\boldsymbol{\Omega}_b^{-1}\mathbf{B}_b^{-1}\mathbf{J}(\boldsymbol{\Omega}_a^{-1}\mathbf{B}_a^{-1}+\mathbf{J}^\dagger\boldsymbol{\Omega}_b^{-1}\mathbf{B}_b^{-1}\mathbf{J})^{-1} \ .
\end{aligned}
\tag{107}
$$

Des Weiteren ergibt sich aus der Identität:

$$\begin{aligned} \mathbf{A}^{-1} + \mathbf{B}^{-1} &= \mathbf{B}^{-1}(\mathbf{B} + \mathbf{A})\mathbf{A}^{-1} \\ \Leftrightarrow\ \mathbf{A}^{-1} &= -\mathbf{B}^{-1} + \mathbf{B}^{-1}(\mathbf{B} + \mathbf{A})\mathbf{A}^{-1}\ . \end{aligned} \tag{108}$$

Mit $\mathbf{B} = \mathbf{\Omega}_a^{-1}\mathbf{B}_a^{-1}$ und $\mathbf{A} = -(\mathbf{\Omega}_a^{-1}\mathbf{B}_a^{-1} + \mathbf{J}^\dagger\mathbf{\Omega}_b^{-1}\mathbf{B}_b^{-1}\mathbf{J})$ vereinfacht sich der Ausdruck zu:

$$\begin{aligned} &- \mathbf{\Omega}_a\mathbf{B}_a + \mathbf{\Omega}_a\mathbf{B}_a\mathbf{J}^\dagger\mathbf{\Omega}_b^{-1}\mathbf{B}_b^{-1}\mathbf{J}(\mathbf{\Omega}_a^{-1}\mathbf{B}_a^{-1} + \mathbf{J}^\dagger\mathbf{\Omega}_b^{-1}\mathbf{B}_b^{-1}\mathbf{J})^{-1} \\ =& - (\mathbf{\Omega}_a^{-1}\mathbf{B}_a^{-1} + \mathbf{J}^\dagger\mathbf{\Omega}_b^{-1}\mathbf{B}_b^{-1}\mathbf{J})^{-1}\ . \end{aligned} \tag{109}$$

Die halbierten Terme des Modulus in Gleichung 105 lassen sich unter Verwendung des finalen Ausdrucks zu zwei Termen vereinfachen. Aus Gleichung 105 folgt somit Gleichung 110:

$$\begin{aligned} G_{\mathrm{IC}}^{a\rightsquigarrow b}(t) = &\sqrt{\frac{\det(\boldsymbol{\mathcal{S}}_a^{-1}\boldsymbol{\mathcal{S}}_b^{-1}\mathbf{\Omega}_a\mathbf{\Omega}_b)}{\det(\mathbf{\Omega}_a\mathbf{B}_a + \mathbf{J}^\dagger\mathbf{\Omega}_b\mathbf{B}_b\mathbf{J})\det(\mathbf{\Omega}_a\mathbf{B}_a^{-1} + \mathbf{J}^\dagger\mathbf{\Omega}_b\mathbf{B}_b^{-1}\mathbf{J})}} \\ &\times e^{-\mathbf{D}^\dagger\mathbf{\Omega}_b\mathbf{B}_b\mathbf{D}}\sum_\kappa\sum_{\bar\kappa} f_{ab}(\kappa)f_{ab}(\bar\kappa) \\ &\times \Big\{\frac{1}{2}[(\mathbf{\Omega}_a^{-1}\mathbf{B}_a + \mathbf{J}^\dagger\mathbf{\Omega}_b^{-1}\mathbf{B}_b\mathbf{J})^{-1} - (\mathbf{\Omega}_a^{-1}\mathbf{B}_a^{-1} + \mathbf{J}^\dagger\mathbf{\Omega}_b^{-1}\mathbf{B}_b^{-1}\mathbf{J})^{-1}]_{\kappa\bar\kappa} \\ &+ (\mathbf{\Omega}_a\mathbf{B}_a)_{\kappa\kappa}[(\mathbf{\Omega}_a\mathbf{B}_a + \mathbf{J}^\dagger\mathbf{\Omega}_b\mathbf{B}_b\mathbf{J})^{-1}\mathbf{J}^\dagger\mathbf{\Omega}_b\mathbf{B}_b\mathbf{D}]_\kappa \\ &\times (\mathbf{\Omega}_a\mathbf{B}_a)_{\bar\kappa\bar\kappa}[(\mathbf{\Omega}_a\mathbf{B}_a + \mathbf{J}^\dagger\mathbf{\Omega}_b\mathbf{B}_b\mathbf{J})^{-1}\mathbf{J}^\dagger\mathbf{\Omega}_b\mathbf{B}_b\mathbf{D}]_{\bar\kappa}\Big\} \\ &\times e^{\mathbf{D}^\dagger\mathbf{\Omega}_b\mathbf{B}_b\mathbf{J}(\mathbf{\Omega}_a\mathbf{B}_a + \mathbf{J}^\dagger\mathbf{\Omega}_b\mathbf{B}_b\mathbf{J})^{-1}\mathbf{J}^\dagger\mathbf{\Omega}_b\mathbf{B}_b\mathbf{D}}\ . \end{aligned} \tag{110}$$

Zur weiteren Vereinfachung werden die Indices $\kappa, \bar{\kappa}$ zusammengezogen:

$$
\begin{aligned}
G_{\mathrm{IC}}^{a\rightsquigarrow b}(t) = & \sqrt{\frac{\det(\boldsymbol{\mathcal{S}}_a^{-1}\boldsymbol{\mathcal{S}}_b^{-1}\boldsymbol{\Omega}_a\boldsymbol{\Omega}_b)}{\det(\boldsymbol{\Omega}_a\mathbf{B}_a + \mathbf{J}^\dagger\boldsymbol{\Omega}_b\mathbf{B}_b\mathbf{J})\det(\boldsymbol{\Omega}_a\mathbf{B}_a^{-1} + \mathbf{J}^\dagger\boldsymbol{\Omega}_b\mathbf{B}_b^{-1}\mathbf{J})}} \\
& \times e^{-\mathbf{D}^\dagger\boldsymbol{\Omega}_b\mathbf{B}_b\mathbf{D}} \sum_\kappa \sum_{\bar{\kappa}} f_{ab}(\kappa) f_{ab}(\bar{\kappa}) \\
& \times \Big\{ \frac{1}{2}[(\boldsymbol{\Omega}_a^{-1}\mathbf{B}_a + \mathbf{J}^\dagger\boldsymbol{\Omega}_b^{-1}\mathbf{B}_b\mathbf{J})^{-1} - (\boldsymbol{\Omega}_a^{-1}\mathbf{B}_a^{-1} + \mathbf{J}^\dagger\boldsymbol{\Omega}_b^{-1}\mathbf{B}_b^{-1}\mathbf{J})^{-1}]_{\kappa\bar{\kappa}} \\
& + [\boldsymbol{\Omega}_a\mathbf{B}_a(\boldsymbol{\Omega}_a\mathbf{B}_a + \mathbf{J}^\dagger\boldsymbol{\Omega}_b\mathbf{B}_b\mathbf{J})^{-1}\mathbf{J}^\dagger\boldsymbol{\Omega}_b\mathbf{B}_b\mathbf{D}]_\kappa [\boldsymbol{\Omega}_a\mathbf{B}_a(\boldsymbol{\Omega}_a\mathbf{B}_a + \mathbf{J}^\dagger\boldsymbol{\Omega}_b\mathbf{B}_b\mathbf{J})^{-1}\mathbf{J}^\dagger\boldsymbol{\Omega}_b\mathbf{B}_b\mathbf{D}]_{\bar{\kappa}} \Big\} \\
& \times e^{\mathbf{D}^\dagger\boldsymbol{\Omega}_b\mathbf{B}_b\mathbf{J}(\boldsymbol{\Omega}_a\mathbf{B}_a + \mathbf{J}^\dagger\boldsymbol{\Omega}_b\mathbf{B}_b\mathbf{J})^{-1}\mathbf{J}^\dagger\boldsymbol{\Omega}_b\mathbf{B}_b\mathbf{D}} \, .
\end{aligned}
\tag{111}
$$

In einem Zwischenschritt werden die separaten Terme gemischt $[(\kappa, \bar{\kappa}) \mapsto c_{\kappa\bar{\kappa}}]$:

$$
\begin{aligned}
G_{\mathrm{IC}}^{a\rightsquigarrow b}(t) = & \sqrt{\frac{\det(\boldsymbol{\mathcal{S}}_a^{-1}\boldsymbol{\mathcal{S}}_b^{-1}\boldsymbol{\Omega}_a\boldsymbol{\Omega}_b)}{\det(\boldsymbol{\Omega}_a\mathbf{B}_a + \mathbf{J}^\dagger\boldsymbol{\Omega}_b\mathbf{B}_b\mathbf{J})\det(\boldsymbol{\Omega}_a\mathbf{B}_a^{-1} + \mathbf{J}^\dagger\boldsymbol{\Omega}_b\mathbf{B}_b^{-1}\mathbf{J})}} \\
& \times e^{-\mathbf{D}^\dagger\boldsymbol{\Omega}_b\mathbf{B}_b\mathbf{D}} \sum_\kappa \sum_{\bar{\kappa}} f_{ab}(\kappa) f_{ab}(\bar{\kappa}) \\
& \times \Big\{ \frac{1}{2}[(\boldsymbol{\Omega}_a^{-1}\mathbf{B}_a + \mathbf{J}^\dagger\boldsymbol{\Omega}_b^{-1}\mathbf{B}_b\mathbf{J})^{-1} - (\boldsymbol{\Omega}_a^{-1}\mathbf{B}_a^{-1} + \mathbf{J}^\dagger\boldsymbol{\Omega}_b^{-1}\mathbf{B}_b^{-1}\mathbf{J})^{-1}]_{\kappa\bar{\kappa}} \\
& + [\boldsymbol{\Omega}_a\mathbf{B}_a(\boldsymbol{\Omega}_a\mathbf{B}_a + \mathbf{J}^\dagger\boldsymbol{\Omega}_b\mathbf{B}_b\mathbf{J})^{-1}\mathbf{J}^\dagger\boldsymbol{\Omega}_b\mathbf{B}_b\mathbf{D}\mathbf{D}^\dagger\boldsymbol{\Omega}_b\mathbf{B}_b\mathbf{J}((\boldsymbol{\Omega}_a\mathbf{B}_a + \mathbf{J}^\dagger\boldsymbol{\Omega}_b\mathbf{B}_b\mathbf{J})^{-1})^\dagger\boldsymbol{\Omega}_a\mathbf{B}_a]_{\kappa\bar{\kappa}} \Big\} \\
& \times e^{\mathbf{D}^\dagger\boldsymbol{\Omega}_b\mathbf{B}_b\mathbf{J}(\boldsymbol{\Omega}_a\mathbf{B}_a + \mathbf{J}^\dagger\boldsymbol{\Omega}_b\mathbf{B}_b\mathbf{J})^{-1}\mathbf{J}^\dagger\boldsymbol{\Omega}_b\mathbf{B}_b\mathbf{D}} \, .
\end{aligned}
\tag{112}
$$

Die Doppelsumme lässt sich als Matrizenmultiplikation formulieren. Mit der nichtadiabatischen Kopplung in Vektorschreibweise, $\mathbf{f} \equiv f_{ab}(\kappa);\ \kappa = 1, ..., N$, werden gemischte Terme $\kappa\bar{\kappa}$ gemäß $\sum_\kappa \sum_{\bar{\kappa}} \mathbf{c}_\kappa \mathbf{M}_{\kappa\bar{\kappa}} \mathbf{c}_{\bar{\kappa}} = \sum_\kappa \sum_{\bar{\kappa}} \mathbf{c}_{1\kappa} \mathbf{M}_{\kappa\bar{\kappa}} \mathbf{c}_{\bar{\kappa}1} = \mathbf{c}^\dagger\mathbf{M}\mathbf{c}$ umformuliert:

$$
\begin{aligned}
G_{\mathrm{IC}}^{a\rightsquigarrow b}(t) = & \sqrt{\frac{\det(\boldsymbol{\mathcal{S}}_a^{-1}\boldsymbol{\mathcal{S}}_b^{-1}\boldsymbol{\Omega}_a\boldsymbol{\Omega}_b)}{\det(\boldsymbol{\Omega}_a\mathbf{B}_a + \mathbf{J}^\dagger\boldsymbol{\Omega}_b\mathbf{B}_b\mathbf{J})\det(\boldsymbol{\Omega}_a\mathbf{B}_a^{-1} + \mathbf{J}^\dagger\boldsymbol{\Omega}_b\mathbf{B}_b^{-1}\mathbf{J})}} \\
& \times \Big\{ \frac{1}{2} f^\dagger[(\boldsymbol{\Omega}_a^{-1}\mathbf{B}_a + \mathbf{J}^\dagger\boldsymbol{\Omega}_b^{-1}\mathbf{B}_b\mathbf{J})^{-1} - (\boldsymbol{\Omega}_a^{-1}\mathbf{B}_a^{-1} + \mathbf{J}^\dagger\boldsymbol{\Omega}_b^{-1}\mathbf{B}_b^{-1}\mathbf{J})^{-1}] f \\
& + f^\dagger\boldsymbol{\Omega}_a\mathbf{B}_a(\boldsymbol{\Omega}_a\mathbf{B}_a + \mathbf{J}^\dagger\boldsymbol{\Omega}_b\mathbf{B}_b\mathbf{J})^{-1}\mathbf{J}^\dagger\boldsymbol{\Omega}_b\mathbf{B}_b\mathbf{D}\mathbf{D}^\dagger\boldsymbol{\Omega}_b\mathbf{B}_b\mathbf{J}((\boldsymbol{\Omega}_a\mathbf{B}_a + \mathbf{J}^\dagger\boldsymbol{\Omega}_b\mathbf{B}_b\mathbf{J})^{-1})^\dagger\boldsymbol{\Omega}_a\mathbf{B}_a f \Big\} \\
& \times e^{\mathbf{D}^\dagger(\boldsymbol{\Omega}_b\mathbf{B}_b\mathbf{J}(\boldsymbol{\Omega}_a\mathbf{B}_a + \mathbf{J}^\dagger\boldsymbol{\Omega}_b\mathbf{B}_b\mathbf{J})^{-1}\mathbf{J}^\dagger\boldsymbol{\Omega}_b\mathbf{B}_b - \boldsymbol{\Omega}_b\mathbf{B}_b)\mathbf{D}} \, .
\end{aligned}
\tag{113}
$$

Mit dem äußeren Produkt $\mathbf{f}\mathbf{f}^\dagger = \boldsymbol{\mathcal{F}}$ und $\mathbf{f}^\dagger\mathbf{W}\mathbf{f} = \mathrm{tr}(\mathbf{f}^\dagger\mathbf{W}\mathbf{f}) = \mathrm{tr}(\boldsymbol{\mathcal{F}}\mathbf{W})$ ergibt sich schlussendlich die im Programm VIBES implementierte erzeugende Funktion interner Konversion G_{IC}:

$$
\begin{aligned}
G_{\mathrm{IC}}^{a\rightsquigarrow b}(t) = & \sqrt{\frac{\det(\boldsymbol{\mathcal{S}}_a^{-1}\boldsymbol{\mathcal{S}}_b^{-1}\boldsymbol{\Omega}_a\boldsymbol{\Omega}_b)}{\det(\boldsymbol{\Omega}_a\mathbf{B}_a + \mathbf{J}^\dagger\boldsymbol{\Omega}_b\mathbf{B}_b\mathbf{J})\det(\boldsymbol{\Omega}_a\mathbf{B}_a^{-1} + \mathbf{J}^\dagger\boldsymbol{\Omega}_b\mathbf{B}_b^{-1}\mathbf{J})}} \\
& \times \Big\{\frac{1}{2}tr[\boldsymbol{\mathcal{F}}(\boldsymbol{\Omega}_a^{-1}\mathbf{B}_a + \mathbf{J}^\dagger\boldsymbol{\Omega}_b^{-1}\mathbf{B}_b\mathbf{J})^{-1}] - \frac{1}{2}tr[\boldsymbol{\mathcal{F}}(\boldsymbol{\Omega}_a^{-1}\mathbf{B}_a^{-1} + \mathbf{J}^\dagger\boldsymbol{\Omega}_b^{-1}\mathbf{B}_b^{-1}\mathbf{J})^{-1}] \\
& + \mathbf{D}^\dagger\boldsymbol{\Omega}_b\mathbf{B}_b\mathbf{J}((\boldsymbol{\Omega}_a\mathbf{B}_a + \mathbf{J}^\dagger\boldsymbol{\Omega}_b\mathbf{B}_b\mathbf{J})^{-1})^\dagger\boldsymbol{\Omega}_a\mathbf{B}_a\boldsymbol{\mathcal{F}}\boldsymbol{\Omega}_a\mathbf{B}_a(\boldsymbol{\Omega}_a\mathbf{B}_a + \mathbf{J}^\dagger\boldsymbol{\Omega}_b\mathbf{B}_b\mathbf{J})^{-1}\mathbf{J}^\dagger\boldsymbol{\Omega}_b\mathbf{B}_b\mathbf{D}\Big\} \\
& \times e^{\mathbf{D}^\dagger(\boldsymbol{\Omega}_b\mathbf{B}_b\mathbf{J}(\boldsymbol{\Omega}_a\mathbf{B}_a + \mathbf{J}^\dagger\boldsymbol{\Omega}_b\mathbf{B}_b\mathbf{J})^{-1}\mathbf{J}^\dagger\boldsymbol{\Omega}_b\mathbf{B}_b - \boldsymbol{\Omega}_b\mathbf{B}_b)\mathbf{D}} \,.
\end{aligned}
\tag{114}
$$

The Journal of Chemical Physics ARTICLE scitation.org/journal/jcp

Internal conversion of singlet and triplet states employing numerical DFT/MRCI derivative couplings: Implementation, tests, and application to xanthone

Cite as: J. Chem. Phys. 155, 014102 (2021); doi: 10.1063/5.0056182
Submitted: 7 May 2021 • Accepted: 16 June 2021 •
Published Online: 2 July 2021

Mario Bracker, Christel M. Marian, and Martin Kleinschmidt[a]

AFFILIATIONS

Institute of Theoretical and Computational Chemistry, Heinrich-Heine-University Düsseldorf, Universitätsstraße 1, 40225 Düsseldorf, Germany

[a]Author to whom correspondence should be addressed: Martin.Kleinschmidt@hhu.de

ABSTRACT

We present an efficient implementation of nonadiabatic coupling matrix elements (NACMEs) for density functional theory/multireference configuration interaction (DFT/MRCI) wave functions of singlet and triplet multiplicity and an extension of the VIBES program that allows us to determine rate constants for internal conversion (IC) in addition to intersystem crossing (ISC) nonradiative transitions. Following the suggestion of Plasser *et al.* [J. Chem. Theory Comput. **12**, 1207 (2016)], the derivative couplings are computed as finite differences of wave function overlaps. Several measures have been taken to speed up the calculation of the NACMEs. Schur's determinant complement is employed to build up the determinant of the full matrix of spin-blocked orbital overlaps from precomputed spin factors with fixed orbital occupation. Test calculations on formaldehyde, pyrazine, and xanthone show that the mutual excitation level of the configurations at the reference and displaced geometries can be restricted to 1. In combination with a cutoff parameter of $t_{norm} = 10^{-8}$ for the DFT/MRCI wave function expansion, this approximation leads to substantial savings of cpu time without essential loss of precision. With regard to applications, the photoexcitation decay kinetics of xanthone in apolar media and in aqueous solution is in the focus of the present work. The results of our computational study substantiate the conjecture that $S_1 \leftsquigarrow T_2$ reverse ISC outcompetes the $T_2 \rightsquigarrow T_1$ IC in aqueous solution, thus explaining the occurrence of delayed fluorescence in addition to prompt fluorescence.

I. INTRODUCTION

Density functional theory/multireference configuration interaction (DFT/MRCI) is a very efficient method for computing electronically excited states of extended molecular systems.[1–3] It combines density functional theory (DFT), which is well suited for describing dynamic electron correlation, with multireference configuration interaction (MRCI), which provides non-dynamic correlation. To avoid double counting of electron correlation contributions, the Hamiltonian is parameterized against experimental excitation energies, and the configuration space is subjected to extensive selection procedures. The combination of these measures results in high computational efficiency in conjunction with root mean square deviations from experiment typically smaller than 0.2 eV for organic molecules and metal organic complexes with a closed-shell electronic ground state.[1,3–7] The related spin–orbit coupling kit, SPOCK,[8–10] forms the basis for computing spin-dependent properties, such as rate constants for phosphorescence, inter-system crossing (ISC), and its reverse (rISC), with good accuracy.[11–14] So far, the ability to compute rate constants for internal conversion (IC) of arbitrary multiplicity states at the DFT/MRCI level of theory is missing. This work aims to fill this gap.

Derivative couplings, also addressed as nonadiabatic coupling matrix elements (NACMEs), play an essential role in studying spin-allowed excited-state decay kinetics. Analytical approaches for computing NACMEs are available, e.g., for time-dependent density functional theory (TD-DFT),[15–18] coupled-cluster (CC) methods,[19–21] multiconfiguration self-consistent field (MCSCF) approaches,[22–26] complete active space self-consistent field with perturbative second-order correction (CASPT2) methods,[27] and

The Journal of Chemical Physics ARTICLE scitation.org/journal/jcp

ab initio multi-reference configuration interaction singles and doubles (MRCISD) schemes.[28–30] Among these methods, only TD-DFT and MCSCF with small active spaces are applicable to extended molecular systems. The individual configuration selection inherent to the DFT/MRCI method destroys the invariance of the energy with respect to orbital rotations and thus prevents an easy formulation of analytic energy gradients and derivative couplings. Hence, a numerical ansatz for evaluating NACMEs appears more appropriate in conjunction with the DFT/MRCI.

In principle, there are the following three major routes that can be pursued for obtaining numerical derivative couplings between two wave functions $\Psi_a(R)$ and $\Psi_b(R)$,

1. indirect calculation making use of the Hellmann–Feynman theorem
$$f_{ab} = \langle \Psi_b | \nabla \mathcal{H} | \Psi_a \rangle (E_a - E_b)^{-1};$$
2. indirect calculation by application of an approximate diabatization procedure; and
3. direct calculation of the desired overlap matrix element
$$f_{ab} = \langle \Psi_b(R) | \nabla \Psi_a(R) \rangle.$$

The Hellmann–Feynman-type expression[31] (route 1) appears to be rather straightforward, but it requires the evaluation of additional one-electron potential energy derivatives in static approaches. This route has been followed, e.g., by Peng *et al.* for computing IC rate constants at the TDDFT level of theory.[32] In fewest-switches surface-hopping molecular dynamics simulations, the nonadiabatic coupling has been approximated numerically using a finite difference method to evaluate the derivative of the wave function with respect to time.[33–35] Iterative block diabatization (route 2) is typically pursued in quantum dynamics calculations where precomputed adiabatic potentials along selected coordinates are available.[36] In conjunction with DFT/MRCI, the latter approach has been applied, e.g., to study the nonadiabatic excited-state dynamics of the ISC and rISC of a spiro-conjugated donor–acceptor emitter with multi configuration time-dependent Hartree (MCTDH) methods.[37] Recently, Plasser *et al.*[38] suggested a simple ansatz for approximating the NACMEs in a direct approach (route 3) by computing finite differences of wave function overlaps,

$$f_{ab}(\vec{R}_0) = \left\langle \Psi_b(\vec{R}) \middle| \nabla_R \Psi_a(\vec{R}) \right\rangle \Big|_{\vec{R}_0} = \lim_{\epsilon \to 0} \sum_\kappa \frac{S_{ba}(\vec{R}_0, \vec{R}_0 + \epsilon \vec{e}_\kappa) - S_{ba}(\vec{R}_0, \vec{R}_0 - \epsilon \vec{e}_\kappa)}{2\epsilon} \vec{e}_\kappa. \quad (1)$$

Herein, $\vec{e}_\kappa$ is a unit displacement vector in the κ direction, and ϵ is the modulus of the displacement. The challenge lies in the efficient computation of a large number of overlaps between configurations in terms of nonorthogonal sets of molecular orbitals. In their paper, Plasser *et al.*[38] reported benchmark studies and applications at the CASSCF and MR-CIS(D) levels of theory. An implementation for DFT/MRCI wave functions was presented lately by Neville *et al.*[39] who basically followed Plasser's algorithm. These authors used the overlaps of the electronic wave functions at neighboring nuclear geometries in MCTDH quantum dynamics calculations for a propagative block diagonalization diabatization.

The aim of the present work is to extend this approach to DFT/MRCI wave functions of higher multiplicity and to apply the method after careful validation to compute IC rate constants in xanthone. In this aromatic ketone, $T_2 \rightsquigarrow S_1$ ISC followed by delayed fluorescence is observed in aqueous solution.[40,41] The reason why this spin-forbidden transition outcompetes the spin-allowed $T_2 \rightsquigarrow T_1$ IC is not known so far and will be elucidated in this work.

II. THEORY

A. IC and ISC rate constants

Following Henry and Siebrand,[42–44] pure spin Born–Oppenheimer molecular states are chosen as starting points for all further considerations. In the harmonic oscillator approximation, they are given by

$$\Xi_{a,S,M_S,\mathbf{v}}(\mathbf{r}, \mathbf{Q}_a) = \Psi_{a,S,M_S}(\mathbf{r}, \tilde{\mathbf{Q}}_a) \prod_\iota^{3N-6} v_{a,\iota}(Q_{a,\iota}), \quad (2)$$

where a labels the electronic state, S is its total spin quantum number, M_S is its magnetic spin quantum number, and $\mathbf{r}$ and $\mathbf{Q}_a$ represent the electronic and mass-weighted vibrational normal coordinates, respectively. The tilde in $\tilde{\mathbf{Q}}_a$ indicates a parametric dependence of the electronic wave functions on the nuclear coordinates. In this basis, the perturbation causing IC and ISC transitions is given by the perturbation operator

$$\hat{\mathcal{V}} = \hat{\mathcal{T}}_N + \hat{\mathcal{H}}_{\mathrm{SO}} = -\frac{\hbar^2}{2} \nabla_{\mathbf{Q}}^\dagger \nabla_{\mathbf{Q}} + \hat{\mathcal{H}}_{\mathrm{SO}}(\mathbf{r}, \tilde{\mathbf{Q}}). \quad (3)$$

While ultrafast nonradiative transitions at the subpicosecond time scale are best modeled by nonadiabatic dynamics computations, slower processes may be treated perturbatively employing the Fermi's golden rule approximation. In the statistical limit, the probability of a nonradiative transition from a manifold of thermally populated initial vibronic states to a quasi-continuum of final vibronic states subject to a perturbation $\hat{\mathcal{V}}$ can be characterized by a rate constant. To simplify the resulting expressions, we omit the coordinate dependencies of the electronic and vibrational wave functions in the following and label the manifolds of vibrational states, $\{v_{aj}\}$ and $\{v_{bk}\}$, respectively, by an index symbolizing the related electronic state and a common vibrational index irrespective of the normal coordinate. Wherever needed, the coordinate dependencies will be reintroduced. According to Fermi's golden rule, a Boltzmann population of the initial vibrational states corresponding to the temperature T gives rise to an expression for the rate constant of the nonradiative transition (in atomic units),

$$k_{ab}^{\mathrm{NR}} = \frac{2\pi}{Z} \sum_j \sum_k e^{-E_{aj}/k_B T} \times \left| \left\langle \Psi_{b,S',M_S'}, \{v_{bk}\} \middle| \hat{\mathcal{V}} \middle| \Psi_{a,S,M_S}, \{v_{aj}\} \right\rangle \right|^2 \times \delta(\Delta E_{ab} + E_{aj} - E_{bk}), \quad (4)$$

where $Z = \sum_j e^{-E_{aj}/k_B T}$ is the canonical partition function for vibrational motion in the initial electronic state, k_B is the Boltzmann constant, and E_{aj} is the energy of the vibrational level j in the electronic state Ψ_{a,S,M_S}. The Dirac delta function ensures that only isoenergetic transitions are allowed, i.e., the vibrational energy in the final electronic state $\Psi_{b,S',M_S'}$, E_{bk}, must match the adiabatic energy

The Journal of Chemical Physics ARTICLE scitation.org/journal/jcp

difference between the electronic states ΔE_{ab} plus the vibrational energy in the initial state.

In first order, perturbations due to $\hat{\mathcal{T}}_N$ and $\hat{\mathcal{H}}_{\mathrm{SO}}$ do not give mixed terms. Hence, the selection rules $\delta_{S,S'}\delta_{M_S,M'_S}$ apply for IC in this order. The major perturbations driving the IC are the nonadiabatic coupling terms,

$$V_{ab}^{IC} = \left\langle \Psi_{b,S',M'_S}, \{v_{b\,k}\} \left| \nabla^{\dagger}_{\mathbf{Q}_a} \nabla_{\mathbf{Q}_a} \right| \Psi_{a,S,M_S}, \{v_{a\,j}\} \right\rangle \times \delta_{S,S'}\delta_{M_S,M'_S} \tag{5}$$

$$\approx \sum_{\kappa}^{3N-6} \left\langle \{v_{b\,k}\} \left| \left\langle \Psi_b \left| \frac{\partial}{\partial Q_{a,\kappa}} \right| \Psi_a \right\rangle \frac{\partial}{\partial Q_{a,\kappa}} \right| \{v_{a\,j}\} \right\rangle \tag{6}$$

$$= \sum_{\kappa}^{3N-6} \left\langle \{v_{b\,k}\} \left| f_{ab}(\kappa) \frac{\partial}{\partial Q_{a,\kappa}} \right| \{v_{a\,j}\} \right\rangle. \tag{7}$$

In the latter expression, diagonal nonadiabatic corrections have been omitted, retaining only the linear derivative coupling terms $f_{ab}(\kappa)$.

The symmetry properties of $\hat{\mathcal{H}}_{\mathrm{SO}}$ allow ISC between states of different spin multiplicities, namely, $S' - S = 0, \pm 1$ for $S' + S \geq 1$, and different spin magnetic quantum numbers, namely, $M'_S - M_S = 0, \pm 1$ unless for $M_S = 0$ where matrix elements vanish for components with $\Delta M_S = 0$. Hence, spin–orbit coupling matrix elements (SOCMEs) are preferentially evaluated for $M_s = S$ wave functions, and SOCMEs for all symmetry allowed combinations of M_S quantum numbers are then generated by means of the Wigner–Eckart theorem.[45] $\hat{\mathcal{H}}_{\mathrm{SO}}$ depends parametrically on $\mathbf{Q}$ and does not act directly on the vibrational wave functions. The dependence of the SOCME on the nuclear coordinates is therefore often expanded in a Taylor series about a fixed nuclear arrangement, typically the equilibrium geometry of the initial state ($\mathbf{Q}_0$). Because this expansion closely resembles the Herzberg–Teller (HT) expansion of the radiative electric dipole transition, the $\mathbf{Q}$-dependent SOC terms have been dubbed Herzberg–Teller spin–orbit coupling (HT SOC) terms,[13,14,46]

$$V_{a,S,M_S,b,S',M'_S}^{ISC} = \left\langle \Psi_{b,S',M'_S}, \{v_{b\,k}\} \left| \hat{\mathcal{H}}_{\mathrm{SO}} \right| \Psi_{a,S,M_S}, \{v_{a\,j}\} \right\rangle \tag{8}$$

$$\approx \left\langle \Psi_{b,S',M'_S} \left| \hat{\mathcal{H}}_{\mathrm{SO}} \right| \Psi_{a,S,M_S}, \right\rangle \Big|_{\mathbf{Q}_{a0}} \times \langle \{v_{b\,k}\} | \{v_{a\,j}\} \rangle \tag{9}$$

$$+ \sum_{\kappa}^{3N-6} \frac{\partial \left\langle \Psi_{b,S',M'_S} \left| \hat{\mathcal{H}}_{\mathrm{SO}} \right| \Psi_{a,S,M_S} \right\rangle}{\partial Q_{a,\kappa}} \Bigg|_{\mathbf{Q}_{a0}} \times \langle \{v_{b\,k}\} | Q_{a,\kappa} | \{v_{a\,j}\} \rangle + \cdots . \tag{10}$$

Note that the HT SOC terms indirectly account for admixtures of other electronic structures upon nuclear displacements and are not easily told apart from spin–vibronic terms arising from second-order couplings involving $\hat{\mathcal{T}}_N$ as well as $\hat{\mathcal{H}}_{\mathrm{SO}}$.[14] In the linear HT SOC approximation, the ISC rate is a sum of three contributions due to (1) a Franck–Condon term $k_{ab}^{\mathrm{ISC,\,FC}}$, (2) a mixed FC/HT term $k_{ab}^{\mathrm{ISC,\,FC/HT}}$, and (3) a quadratic HT/HT term $k_{ab}^{\mathrm{ISC,\,HT/HT}}$.[13]

Vibes is an in-house computer program that determines rate constants for nonradiative ISC transitions in harmonic approximation according to Fermi's golden rule. In addition to FC terms, HT-type expressions can be evaluated. While the original implementation was based on the computation of discrete vibrational overlaps,[46,47] later versions make use of a generating function approach.[13,48,49] Generating function approaches for the calculation of the transition rate constants are based on a transformation of the Fermi golden rule approximation into the Heisenberg picture.[50] They are particularly attractive for multidimensional molecular systems because they completely avoid the explicit summation over the vibrational states in Eq. (4). Analytic expressions for time-correlation functions that depend on two sets of normal coordinates $\mathbf{Q}_a$ and $\mathbf{Q}_b$ can be derived employing Mehler's formula.[51,52] Formulas for computing thermal ISC rate constants in FC and HT approximations using the generating function approach in conjunction with a Duschinsky transformation

$$\mathbf{Q}_b = \mathbf{J}\mathbf{Q}_a + \mathbf{D} \tag{11}$$

between the normal coordinates $\mathbf{Q}_b$ of the final state and $\mathbf{Q}_a$ of the initial state had been implemented in the Vibes program before.[13,49] Herein, $\mathbf{J}$ is the Duschinsky rotation matrix, and $\mathbf{D}$ is the coordinate displacement. The generating function approach did not only extend the application range of the Vibes program to larger molecules but also allowed the inclusion of temperature effects on the calculated properties. The latter feature turned out to be extremely valuable for computing rate constants of thermally activated reverse ISC (rISC) processes that play a key role in modern TADF OLEDs.[14]

In the present work, formulas for IC rate constants have been worked out in analogy. Once, the NACMEs $f_{ab}(\kappa)$ with respect to all normal mode coordinates $Q_{a,\kappa}$ of the initial electronic state Ψ_a [cp. Eq. (7)] are known, the generating function of the transition can be set up in the time domain,

$$G_{IC}^{a\rightsquigarrow b}(t) = (2\pi)^{-N} \sqrt{\det(\boldsymbol{\mathcal{S}}_a^{-1}\boldsymbol{\mathcal{S}}_b^{-1}\boldsymbol{\Omega}_a\boldsymbol{\Omega}_b)} \sum_{\kappa=1}^{N}\sum_{\bar{\kappa}=1}^{N} f_{ab}(\kappa) f_{ab}^{*}(\bar{\kappa}) \int e^{-\frac{1}{4}[(\mathbf{Q}_b+\bar{\mathbf{Q}}_b)^{\dagger}\boldsymbol{\Omega}_b\mathbf{B}_b(\mathbf{Q}_b+\bar{\mathbf{Q}}_b)+(\mathbf{Q}_b-\bar{\mathbf{Q}}_b)^{\dagger}\boldsymbol{\Omega}_b\mathbf{B}_b^{-1}(\mathbf{Q}_b-\bar{\mathbf{Q}}_b)]}$$

$$\times \frac{\partial^2}{\partial Q_{a,\kappa}\partial \bar{Q}_{a,\bar{\kappa}}} e^{-\frac{1}{4}[(\mathbf{Q}_a+\bar{\mathbf{Q}}_a)^{\dagger}\boldsymbol{\Omega}_a\mathbf{B}_a(\mathbf{Q}_a+\bar{\mathbf{Q}}_a)+(\mathbf{Q}_a-\bar{\mathbf{Q}}_a)^{\dagger}\boldsymbol{\Omega}_a\mathbf{B}_a^{-1}(\mathbf{Q}_a-\bar{\mathbf{Q}}_a)]}\, d^N\mathbf{Q}_a d^N\bar{\mathbf{Q}}_a, \tag{12}$$

The Journal of Chemical Physics ARTICLE scitation.org/journal/jcp

Herein, $\mathbf{Q}_a$ denominates the set of normal coordinates of state Ψ_a with harmonic vibrational frequencies $\{\omega_{a,\kappa}\}$, and $\mathbf{Q}_b$ and $\{\omega_{b,\kappa}\}$ are the corresponding entities in the electronic state Ψ_b. Barred symbols have been introduced in accordance with the nomenclature of Islampour and Miralinaghi[53] to stress that the quadrature of the coupling matrix elements V_{ab}^{IC} [Eq. (7)] produces diagonal as well as off-diagonal terms, and hence, the sums over κ and $\bar{\kappa}$ run independently. $\boldsymbol{\mathcal{S}}$, $\mathbf{B}$, and $\boldsymbol{\Omega}$ are diagonal matrices with elements $(\boldsymbol{\mathcal{S}}_a)_{\kappa\kappa} = \sinh[(\beta - it)\omega_{a,\kappa}]$, $(\boldsymbol{\mathcal{S}}_b)_{\kappa\kappa} = \sinh(i\omega_{b,\kappa}t)$, $(\mathbf{B}_a)_{\kappa\kappa} = \tanh[\omega_{a,\kappa}(\beta - it)/2]$, $(\mathbf{B}_b)_{\kappa\kappa} = \tanh(i\omega_{b,\kappa}t/2)$, $(\boldsymbol{\Omega}_a)_{\kappa\kappa} = \omega_{a,\kappa}$, and $(\boldsymbol{\Omega}_b)_{\kappa\kappa} = \omega_{b,\kappa}$, $\beta = 1/k_BT$ is the inverse temperature, i is the imaginary unit, and t is the time. Expressing the set of normal mode coordinates of the final state, $\mathbf{Q}_b$, in the basis of the initial state normal coordinates, $\mathbf{Q}_a$, by means of the Duschinsky transformation (11) results in

$$G_{IC}^{a\rightsquigarrow b}(t) = (2\pi)^{-N}\sqrt{\det(\boldsymbol{\mathcal{S}}_a^{-1}\boldsymbol{\mathcal{S}}_b^{-1}\boldsymbol{\Omega}_a\boldsymbol{\Omega}_b)}\sum_{\kappa=1}^{N}\sum_{\bar{\kappa}=1}^{N} f_{ab}(\kappa)f_{ab}^{*}(\bar{\kappa}) \times \int e^{-\frac{1}{4}[(\mathbf{J}\mathbf{Q}_a+\mathbf{D}+\mathbf{J}\bar{\mathbf{Q}}_a+\mathbf{D})^{\dagger}\boldsymbol{\Omega}_b\mathbf{B}_b(\mathbf{J}\mathbf{Q}_a+\mathbf{D}+\mathbf{J}\bar{\mathbf{Q}}_a+\mathbf{D})+(\mathbf{J}\mathbf{Q}_a+\mathbf{D}-\mathbf{J}\bar{\mathbf{Q}}_a-\mathbf{D})^{\dagger}\boldsymbol{\Omega}_b\mathbf{B}_b^{-1}(\mathbf{J}\mathbf{Q}_a+\mathbf{D}-\mathbf{J}\bar{\mathbf{Q}}_a-\mathbf{D})]}$$
$$\times \frac{\partial^2}{\partial Q_{a,\kappa}\partial\bar{Q}_{a,\bar{\kappa}}} e^{-\frac{1}{4}[(\mathbf{Q}_a+\bar{\mathbf{Q}}_a)^{\dagger}\boldsymbol{\Omega}_a\mathbf{B}_a(\mathbf{Q}_a+\bar{\mathbf{Q}}_a)+(\mathbf{Q}_a-\bar{\mathbf{Q}}_a)^{\dagger}\boldsymbol{\Omega}_a\mathbf{B}_a^{-1}(\mathbf{Q}_a-\bar{\mathbf{Q}}_a)]}\, d^N\mathbf{Q}_a d^N\bar{\mathbf{Q}}_a. \tag{13}$$

We now can carry out the differentiation of the exponential function. Employing coordinate transformations $\mathbf{X} = \mathbf{Q}_a + \bar{\mathbf{Q}}_a$ as well as $\mathbf{Y} = \mathbf{Q}_a - \bar{\mathbf{Q}}_a$, as proposed by Islampour and Miralinaghi,[53] yields

$$G_{IC}^{a\rightsquigarrow b}(t) = (4\pi)^{-N}\sqrt{\det(\boldsymbol{\mathcal{S}}_a^{-1}\boldsymbol{\mathcal{S}}_b^{-1}\boldsymbol{\Omega}_a\boldsymbol{\Omega}_b)}\, e^{-\mathbf{D}^{\dagger}\boldsymbol{\Omega}_b\mathbf{B}_b\mathbf{D}}\sum_{\kappa=1}^{N}\sum_{\bar{\kappa}=1}^{N} f_{ab}(\kappa)f_{ab}^{*}(\bar{\kappa})\frac{1}{2}\int\Big\{[(\boldsymbol{\Omega}_a\mathbf{B}_a^{-1})_{\kappa\kappa} - (\boldsymbol{\Omega}_a\mathbf{B}_a)_{\kappa\kappa}]\delta_{\kappa\bar{\kappa}} + (\boldsymbol{\Omega}_a\mathbf{B}_a)_{\kappa\kappa}(\boldsymbol{\Omega}_a\mathbf{B}_a)_{\bar{\kappa}\bar{\kappa}}\mathbf{X}_{\kappa}\mathbf{X}_{\bar{\kappa}}$$
$$- (\boldsymbol{\Omega}_a\mathbf{B}_a)_{\kappa\kappa}(\boldsymbol{\Omega}_a\mathbf{B}_a^{-1})_{\bar{\kappa}\bar{\kappa}}\mathbf{X}_{\kappa}\mathbf{Y}_{\kappa'} + (\boldsymbol{\Omega}_a\mathbf{B}_a^{-1})_{\kappa\kappa}(\boldsymbol{\Omega}_a\mathbf{B}_a)_{\bar{\kappa}\bar{\kappa}}\mathbf{Y}_{\kappa}\mathbf{X}_{\bar{\kappa}} - (\boldsymbol{\Omega}_a\mathbf{B}_a^{-1})_{\kappa\kappa}(\boldsymbol{\Omega}_a\mathbf{B}_a^{-1})_{\bar{\kappa}\bar{\kappa}}\mathbf{Y}_{\kappa}\mathbf{Y}_{\bar{\kappa}}\Big\}$$
$$\times e^{-\frac{1}{4}\mathbf{X}^{\dagger}(\boldsymbol{\Omega}_a\mathbf{B}_a+\mathbf{J}^{\dagger}\boldsymbol{\Omega}_b\mathbf{B}_b\mathbf{J})\mathbf{X}-\mathbf{X}^{\dagger}\mathbf{J}^{\dagger}\boldsymbol{\Omega}_b\mathbf{B}_b\mathbf{D}} e^{-\frac{1}{4}\mathbf{Y}^{\dagger}(\boldsymbol{\Omega}_a\mathbf{B}_a^{-1}+\mathbf{J}^{\dagger}\boldsymbol{\Omega}_b\mathbf{B}_b^{-1}\mathbf{J})\mathbf{Y}}\, d\mathbf{X}^N d\mathbf{Y}^N. \tag{14}$$

At this point, the evaluation of the generating function is reduced to N-dimensional Gaussian integrals, which can be determined analytically. Finally, the double sum over κ and $\bar{\kappa}$ is rewritten in terms of vector–matrix–vector products, and Eq. (14) is cast into a form that is closely related to the quadratic HT/HT term of ISC,[13]

$$G_{IC}^{a\rightsquigarrow b}(t) = \sqrt{\frac{\det(\boldsymbol{\mathcal{S}}_a^{-1}\boldsymbol{\mathcal{S}}_b^{-1}\boldsymbol{\Omega}_a\boldsymbol{\Omega}_b)}{\det(\boldsymbol{\Omega}_a\mathbf{B}_a + \mathbf{J}^{\dagger}\boldsymbol{\Omega}_b\mathbf{B}_b\mathbf{J})\det(\boldsymbol{\Omega}_a\mathbf{B}_a^{-1} + \mathbf{J}^{\dagger}\boldsymbol{\Omega}_b\mathbf{B}_b^{-1}\mathbf{J})}}\Big\{\frac{1}{2}tr[\boldsymbol{\mathcal{F}}(\boldsymbol{\Omega}_a^{-1}\mathbf{B}_a + \mathbf{J}^{\dagger}\boldsymbol{\Omega}_b^{-1}\mathbf{B}_b\mathbf{J})^{-1}] - \frac{1}{2}tr[\boldsymbol{\mathcal{F}}(\boldsymbol{\Omega}_a^{-1}\mathbf{B}_a^{-1} + \mathbf{J}^{\dagger}\boldsymbol{\Omega}_b^{-1}\mathbf{B}_b^{-1}\mathbf{J})^{-1}]$$
$$+ \mathbf{D}^{\dagger}\boldsymbol{\Omega}_b\mathbf{B}_b\mathbf{J}((\boldsymbol{\Omega}_a\mathbf{B}_a + \mathbf{J}^{\dagger}\boldsymbol{\Omega}_b\mathbf{B}_b\mathbf{J})^{-1})^{\dagger}\boldsymbol{\Omega}_a\mathbf{B}_a\boldsymbol{\mathcal{F}}\boldsymbol{\Omega}_a\mathbf{B}_a(\boldsymbol{\Omega}_a\mathbf{B}_a + \mathbf{J}^{\dagger}\boldsymbol{\Omega}_b\mathbf{B}_b\mathbf{J})^{-1}\mathbf{J}^{\dagger}\boldsymbol{\Omega}_b\mathbf{B}_b\mathbf{D}\Big\}$$
$$\times e^{\mathbf{D}^{\dagger}(\boldsymbol{\Omega}_b\mathbf{B}_b\mathbf{J}(\boldsymbol{\Omega}_a\mathbf{B}_a+\mathbf{J}^{\dagger}\boldsymbol{\Omega}_b\mathbf{B}_b\mathbf{J})^{-1}\mathbf{J}^{\dagger}\boldsymbol{\Omega}_b\mathbf{B}_b-\boldsymbol{\Omega}_b\mathbf{B}_b)\mathbf{D}}, \tag{15}$$

where $\boldsymbol{\mathcal{F}}$ contains products corresponding to all possible combinations of NACMEs $f_{ab}(\kappa)$ and $f_{ab}(\bar{\kappa})$.

B. Numerical determination of nonadiabatic derivative couplings

Computing the wave function overlaps in a straightforward manner without further approximations would require massive amounts of computational power. The MO overlap determinant of every Slater determinant of the reference state with every Slater determinant of the distorted state has to be evaluated. It is therefore mandatory to reduce this enormous cost to a reasonable amount, especially as we are aiming at larger molecules than xanthone. This can be achieved by

1. reducing the number of overlap determinants to be calculated and
2. speeding up the computation of individual overlap determinants.

A reduction in the number of overlap determinants to be calculated has been achieved by

1. exploiting the spin blocking when computing all Slater determinants of a given pair of configurations (see Secs. II B 1 and II B 3),
2. estimating the value of the determinant by Hadamard's inequality (Sec. II B 6),
3. identifying small determinants by excitation class (Sec. II B 5), and
4. using the fact that the value of the determinant will be multiplied by two CI coefficients, which may be very small (Sec. II B 4).

Other authors reduce the number of determinants by expanding CIS-type wave functions in terms of natural transition orbitals.[54] This strategy is not transferable to our case because the DFT/MRCI method, at least in its current formulation, strictly requires the use of canonical Kohn–Sham MOs as one-particle basis.[1,3]

The Journal of Chemical Physics ARTICLE scitation.org/journal/jcp

The calculation of the remaining overlap determinants is accelerated by

1. applying a caching strategy for spin blocks, as the same spin blocks may occur in multiple pairs of configurations (Sec. II C),
2. using the Schur's complement method for generating spin factors in open-shell cases (Sec. II B 2), and
3. precomputing some of the entities in Schur's identity (Sec. II C).

1. Spin blocking of the determinants

In the case that the Hamiltonian is spin-independent and the CI expansion is given in a basis of Slater determinants, the overlap matrix can be block diagonalized because their α and β spin parts do not interact.[38] Let the unbarred entities ϕ and ϕ' denote spin orbitals occupied by one of the n_α electrons with α spin and the barred entities $\bar{\phi}$ and $\bar{\phi}'$ denote those occupied by one of the $n_\beta = n - n_\alpha$ electrons with β spin.

The overlap of two Slater determinants $\langle\Phi_k|$ and $|\Phi'_l\rangle$, defined in the basis of the spin orbitals $\{\phi, \bar{\phi}\}$

$$\langle\Phi_k| = |\phi_{k(1)} \cdots \phi_{k(n_\alpha)} \bar{\phi}_{k(n_\alpha+1)} \cdots \bar{\phi}_{k(n)}| \tag{16}$$

and $\{\phi', \bar{\phi}'\}$

$$|\Phi'_l\rangle = |\phi'_{l(1)} \cdots \phi'_{l(n_\alpha)} \bar{\phi}'_{l(n_\alpha+1)} \cdots \bar{\phi}'_{l(n)}|\,, \tag{17}$$

respectively, is then given by[38]

$$\begin{aligned}\langle\Phi_k|\Phi'_l\rangle = &\begin{vmatrix} \langle\phi_{k(1)}|\phi'_{l(1)}\rangle & \cdots & \langle\phi_{k(1)}|\phi'_{l(n_\alpha)}\rangle \\ \vdots & \ddots & \vdots \\ \langle\phi_{k(n_\alpha)}|\phi'_{l(1)}\rangle & \cdots & \langle\phi_{k(n_\alpha)}|\phi'_{l(n_\alpha)}\rangle \end{vmatrix} \\ &\times \begin{vmatrix} \langle\bar{\phi}_{k(n_{\alpha+1})}|\bar{\phi}'_{l(n_\alpha+1)}\rangle & \cdots & \langle\bar{\phi}_{k(n_{\alpha+1})}|\bar{\phi}'_{l(n)}\rangle \\ \vdots & \ddots & \vdots \\ \langle\bar{\phi}_{k(n)}|\bar{\phi}'_{l(n_\alpha+1)}\rangle & \cdots & \langle\bar{\phi}_{k(n)}|\bar{\phi}'_{l(n)}\rangle \end{vmatrix} \\ \equiv\ & S^\alpha_{kl} \times S^\beta_{kl}. \end{aligned} \tag{18}$$

As already noted by Plasser *et al.*,[38] these spin determinantal factors are not unique to a specific combination of Slater determinants $\langle\Phi_k|$ and $|\Phi'_l\rangle$ but can be reused for all pairs of determinants with an equal occupation pattern either in the S^α block or in the S^β block. Note further that this factorization scheme does not require the two spin blocks to be of equal dimension, i.e., it is applicable to determinants with an arbitrary M_s quantum number. For corresponding orbital occupations of spin restricted wave functions, the work load can be additionally reduced by exchanging the factors S^α and S^β. For example, in the two-open-shell case with equal numbers of α and β spin electrons ($M_S = 0$),

$$\langle\phi_i\bar{\phi}_j|\phi'_i\bar{\phi}'_j\rangle = \langle\bar{\phi}_i\phi_j|\bar{\phi}'_i\phi'_j\rangle, \tag{19}$$

$$\langle\phi_i\bar{\phi}_j|\bar{\phi}'_i\phi'_j\rangle = \langle\bar{\phi}_i\phi_j|\phi'_i\bar{\phi}'_j\rangle. \tag{20}$$

2. Reuse of the fixed spin determinantal subblocks

As shown in Sec. II B 1, the computation of numerical derivative couplings of DFT/MRCI wave functions essentially reduces to the calculation of very many spin-blocked determinants of orbital overlaps. The efficient evaluation of these determinants is therefore crucial for keeping the task manageable. As described in more detail in the following, we employ a combination of LU decomposition and the Schur's complement method for this purpose.

Given an $n \times n$-dimensional matrix $\mathbf{A} = (a_{ij})$, one possibility to calculate its determinant $|\mathbf{A}|$ is to carry out a Laplace expansion,

$$\det\mathbf{A} = \sum_{i=1}^{n} (-1)^{i+j} a_{ij} A_{ij} = \sum_{j=1}^{n} (-1)^{i+j} a_{ij} A_{ij}, \tag{21}$$

where A_{ij} is the determinant of the $(n-1) \times (n-1)$ submatrix, obtained by removing row i and column j from $\mathbf{A}$. Problematic about the Laplace expansion is its factorial scaling $[\mathcal{O}(n!)]$, which makes it impossible to be applied straightforwardly to DFT/MRCI wave functions. A Laplace expansion can be useful, however, in conjunction with other techniques. If, e.g., only a single MO is exchanged in a Slater determinant, precomputed and stored cofactors $\tilde{a}_{ij} = (-1)^{i+j} A_{ij}$ could be reused to calculate the determinant of the full matrix at the cost of a scalar product of two n dimensional vectors.[38] Note that an extension to level 2 minors, as introduced by Sapunar *et al.*[54] for CIS-type wave functions, requires the precomputation and storage of $n^2(n-1)^2/4$ unique level 2 minors, which can become very demanding. As outlined in more detail below, we employ the Schur's determinant complement method instead.

For computing the initial determinants, an LU decomposition is performed because of its advantageous $\frac{2}{3}n^3 + \mathcal{O}(n^2)$ scaling.[55] The principle idea of an LU decomposition is to factorize a matrix into a lower $\mathbf{L}$ and an upper $\mathbf{U}$ triangular matrix,

$$\mathbf{A} = \mathbf{LU}. \tag{22}$$

Due to the vanishing off-diagonal elements, computing the corresponding determinant $\det\mathbf{A}$ consequently reduces to products of main diagonal entries of the matrices $\mathbf{L}$ and $\mathbf{U}$,

$$\det\mathbf{A} = \det\mathbf{L}\det\mathbf{U} = \prod_i l_{ii} \prod_i u_{ii}. \tag{23}$$

Although the number of active orbitals is not a limiting factor in DFT/MRCI calculations, in practical applications, many electrons reside in frozen or inactive orbitals that are common to all Slater determinants of the CI expansion. Hence, large parts of the overlap matrices S^α and S^β are independent of the specific determinant pair under consideration. Let $\mathbf{F}$ be an $f \times f$ square matrix corresponding to the fixed part and $\mathbf{V}$ be the $v \times v$ square matrix corresponding to variable part of the overlap matrix. Let further $\mathbf{P}$ and $\mathbf{O}$ denote off-diagonal blocks with dimension $v \times f$ and $f \times v$, respectively. The contribution of the fixed part to the determinant $\det(\mathbf{S})$ can then be precomputed and reused in the evaluation of every determinant pair employing the Schur's determinant identity

$$\det\mathbf{S} = \begin{vmatrix} \mathbf{V} & \mathbf{P} \\ \mathbf{O} & \mathbf{F} \end{vmatrix} = \det\mathbf{F}\det(\underbrace{\mathbf{V} - \mathbf{P}\mathbf{F}^{-1}\mathbf{O}}_{\mathbf{S/F}}), \tag{24}$$

where $\mathbf{S/F}$ denotes the Schur complement.

The Journal of Chemical Physics ARTICLE scitation.org/journal/jcp

In open shell cases, several determinants share the same spatial occupation numbers and differ only in the spin parts of the open shells. Here, the matrix **F** can be extended to include all doubly occupied orbitals of this configuration. The inversion of the matrix **F**, an extra step scaling like $\frac{2}{3}f^3 + \mathcal{O}(f^2)$, pays off already if the number of unique determinantal pairs to be evaluated exceeds two, i.e., for configurations with more than two open shells.

3. Choice of the magnetic spin quantum number

DFT/MRCI variationally determines wave function coefficients for configuration state functions (CSFs) built up from Slater determinants with a maximal spin magnetic quantum number, i.e., $M_S = S$. In this way, the number of determinants is kept minimal. For example, the $M_S = 1$ CSF of a two-open-shell triplet configuration consists of a single Slater determinant, whereas two Slater determinants are required to form an $M_S = 0$ triplet wave function. Another argument in favor of an $M_S = 1$ triplet wave function is the fact that SOCMEs of two triplet states can be determined in subsequent Spock calculations, whereas the corresponding matrix elements of the $M_S = 0$ sublevels vanish by symmetry. The eigenvalues of a spin-free Hamiltonian do not depend on the M_S quantum number. Therefore, ladder or tensor operators can be applied to the eigenvectors of the CI matrix with $M_S = 1$ to generate solutions with the $M_S = 0$ quantum number. In the example given above, calculation of the nonorthogonal overlap of the configurations in a determinantal basis requires the evaluation of a single pair of $M_S = 1$ determinants as opposed to four pairs in an $M_S = 0$ expansion. The number of pairs grows rapidly with an increasing number of open shells. For a configuration with four open shells, six determinants with $M_S = 0$ are obtained, yielding 36 determinant pairs in contrast to $4 \times 4 = 16$ pairs for $M_S = 1$ wave functions. A six-open-shell triplet will produce 225 determinant pairs in the $M_S = 1$ case as opposed to 400 pairs in the $M_S = 0$ case.

On the other hand, the spin symmetry blocking of determinant overlaps [Eq. (18)] is optimal only when the number of α and β spin electrons is equal, i.e., in the $M_S = 0$ case. As shown in Eqs. (19) and (20), only two of the four pairs in a triplet configuration with two open shells have unique determinantal overlaps. Likewise, the 36 pairs of a four-open-shell wave function can be reduced to 18 unique pairs, and the 400 pairs of the six-open-shell case can be contracted to 200 unique expressions.

Right from the beginning, it is therefore not clear which of the following routes is more efficient:

1. Application of ladder operators on the two triplet wave functions to down shift their M_S values from 1 to 0, followed by the computation of overlaps between many pairs of determinants with optimal use of symmetry relations between S^α and S^β blocks.
2. Evaluation of the minimal number of determinant overlaps while accepting that for each pair of determinants, the use of spin blocking symmetry relations is suboptimal.

Similar considerations hold true for quintet states. Among other parameters, the preference for either route will depend on the weights of configurations with many open shells in the wave function. If their contributions can be neglected, the choice $M_S = S$ is expected to be more favorable. If, on the other hand, the reuse of precomputed information is decisive, things could be different. A comparison of the timings for evaluating triplet derivative couplings will be presented in Sec. III B 3.

4. Truncation of the wave function expansion

An obvious approach to save computing time is the truncation of the CI expansion.[38,39] This is accomplished by introducing a threshold t_{norm} for the desired residual norm of the truncated CI vector

$$\left\|\tilde{\Psi}_a\right\|^2 = \left\langle\tilde{\Psi}_a|\tilde{\Psi}_a\right\rangle = \sum_{k=1}^{k_t} d_{ak}^2 \geq 1 - t_{norm}. \tag{25}$$

Herein, k_t is the smallest index of the sorted CI vector that fulfills the inequality [Eq. (25)]. Alternatively, the magnitude of the individual CSF coefficients can be used as a selection criterion t_{cutoff}. To conserve spin multiplicity, all determinants of a given configuration are included irrespective of their individual contributions. The norm of the truncated CI vector typically is smaller than 1, and therefore, the truncation of the CI expansion will, in general, lead to an underestimation of the overlap. Assuming that the direction of the derivative coupling is approximately conserved, i.e.,

$$\frac{\left\langle\tilde{\Psi}_b|\tilde{\Psi}'_a\right\rangle}{\left\|\tilde{\Psi}_b\right\|\left\|\tilde{\Psi}'_a\right\|} \approx \frac{\langle\Psi_b|\Psi'_a\rangle}{\|\Psi_b\|\|\Psi'_a\|}, \tag{26}$$

the overlap S_{ab} can be approximated as

$$S_{ab} \approx \tilde{S}_{ab} = \frac{\left\langle\tilde{\Psi}_b|\tilde{\Psi}'_a\right\rangle}{\left\|\tilde{\Psi}_b\right\|\left\|\tilde{\Psi}'_a\right\|}. \tag{27}$$

In Sec. III C, extensive tests and timings regarding the choice of the wave function truncation parameters will be presented.

5. Restriction of the excitation class

The kinetic energy operator of the nuclei, $\hat{T}_N$, acts only on the one-electron terms of the electronic Hamiltonian. Nonvanishing linear derivative coupling terms $f_{ab}(\kappa)$ are therefore obtained only if Ψ_a and Ψ_b in Eq. (7) are singly excited with respect to one another. This property transfers to a certain extent to approximate expressions for $f_{ab}(\kappa)$ as well.

For small displacements ϵ, there is usually a good correspondence between the MOs at the reference and displaced geometries. This relation implies that $\langle\Phi_i|\Phi'_j\rangle \approx \delta_{ij}$. The analysis of numerous test calculations has shown that every orbital replacement typically reduces the nonorthogonal overlap of the Slater determinants at the reference and displaced geometries approximately by two orders of magnitude, irrespective of their CI coefficients. A double replacement of orbitals therefore generates nonorthogonal determinant overlaps of the order of 10^{-4}, etc. Given a close correspondence between the MO sets $\{\Phi_i\}$ and $\{\Phi'_i\}$, it might therefore be possible to restrict the mutual excitation between Ψ_a and Ψ'_b to at most one replacement in the orbital occupation vector (1-exc. approximation) without significant loss of precision. Note that this selection criterion does not necessarily mean that these configurations are singly excited with respect to the ground-state configuration. It is their mutual excitation level that counts.

A similar approach was pursued by Lee *et al.*[56] to speed up the evaluation of the determinants. They proposed to introduce an

The Journal of Chemical Physics ARTICLE scitation.org/journal/jcp

order parameter λ representing the relative magnitudes of orbital overlaps and to truncate the direct determinant evaluation by the Leibniz formula according to this order parameter. In combination with determinant factorization, improvements of the performance up to five orders were achieved for spin flip-TDDFT and linear response-TDDFT in that work.

6. Hadamard's inequality

Neville *et al.*[39] suggested estimating the size of det **S** by Hadamard's inequality

$$\| \det \mathbf{S} \|^2 \leq \prod_{i=1}^{s} \| x_i \|^2 \tag{28}$$

as a means for reducing the number of S^α and S^β factors to be evaluated. Here, x_i represent the column vectors of the matrix **S** with dimension s. They proposed to set the screening threshold δ_H for the vector norms in Eq. (28) to values between 10^{-6} and 10^{-4}. In their pyrazine test case, even the relatively loose screening threshold of 10^{-4} led to a negligible degradation of the accuracy while saving about 70% of the computation time. As we will see below, Hadamard screening is less efficient when applied in combination with the 1-exc. approximation (Sec. II B 5) because the latter filters out already many small spin factors.

C. Implementation strategies: The program Delta

Unlike the procedure in MD simulations, where the computation of wave function overlaps at neighboring points of the trajectory is required at every time step t,[38,39,57] the number of points for an IC rate constant in the Fermi's golden rule approximation is limited to the number of symmetry-allowed vibrational coupling modes in the harmonic oscillator model. Under these particular conditions, the computational effort of evaluating nonorthogonal DFT/MRCI wave function overlaps can be significantly reduced with respect to more general cases.

In the current version of the DFT/MRCI program, all excitations are defined with respect to the so-called anchor determinant, which therefore plays a prominent role for understanding the algorithm implemented in Delta. For electronic states with an even number of electrons (singlets, triplets, ...), the anchor determinant is the closed-shell determinant used for generating the restricted Kohn–Sham (RKS) DFT orbital basis. In that case, the fixed subblocks **F** of **S** are identical for α and β electrons, i.e., $\mathbf{F}^\beta = \mathbf{F}^\alpha$. Therefore, only the α blocks of the matrices **F** and the corresponding inverse matrices $(\mathbf{F}^\alpha)^{-1}$ need to be processed explicitly. In principle, the program branch for computing overlaps of determinants with the magnetic spin quantum number $M_S = S$ (*vide infra*) could be employed equally well for radicals with an odd number of electrons (doublets, quartets, ...). In that case, the anchor determinant would be a restricted open-shell Kohn–Sham (ROKS) determinant with one unpaired electron.

The workflow of our current implementation is sketched in Fig. 1. To speed up the computation of the nonorthogonal overlaps, the expansion lengths of the wave functions can be reduced in a preparatory step. Application of the selection criterion [Eq. (25)] to Ψ_a and Ψ'_b in conjunction with the user-defined cutoff threshold t_{norm} yields the truncated expansions $\tilde{\Psi}_a$ and $\tilde{\Psi}'_b$, respectively. For triplet states, the spin-symmetry adapted expansions of Slater

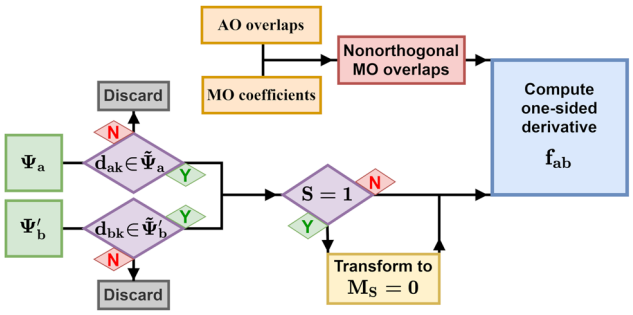

FIG. 1. Workflow of the algorithm implemented in the Delta program for computing nonorthogonal overlaps of DFT/MRCI wave functions.

determinants with the magnetic spin quantum number $M_S = 1$ are transformed to $M_S = 0$.

For each normal mode, the outermost loop runs over configurations m of the wave function $\tilde{\Psi}_a$ at the reference geometry (unprimed symbols). At this level, the annihilation and creation operators become known, which are needed for generating a configuration of the (truncated and renormalized) DFT/MRCI wave function from the RKS anchor determinant at the reference point. Their application exchanges rows in the overlap determinant. Later, application of the annihilators in the displaced configurations will exchange columns and thereby define the size of the **F** block for use in conjunction with the Schur's complement method [Eq. (24)]. As a large number of displaced configurations will use the same **F** block, it is advantageous to determine all **F** blocks already at this point. To this end, for $\mathbf{F}^{f\times f}$ blocks of decreasing size ($f = n_\alpha - i$), the inverses $(\mathbf{F}^{(n_\alpha-i)\times(n_\alpha-i)})^{-1}$, the determinants $\det \mathbf{F}^{(n_\alpha-i)\times(n_\alpha-i)}$, and the products $\mathbf{P}^{i\times(n_\alpha-i)}(\mathbf{F}^{(n_\alpha-i)\times(n_\alpha-i)})^{-1}$ are precomputed and stored. Subsequently, the loop over the configurations n of the displaced wave function $\tilde{\Psi}'_b$ is processed. In case the configurations m and n differ by more than a mutual single excitation, the displaced configuration n is skipped (1-exc. approximation). In the implementations of numerical derivative couplings by Plasser *et al.*[38] and Neville *et al.*,[39] all spin factors S^α and S^β are precomputed and cached. This caching substantially accelerates the computations of the wave function overlaps in the nonadiabatic dynamics simulations, on the one hand, but leads to huge memory requirements, on the other hand. We tried to find some middle ground and store only spin factors that correspond to single excitations with respect to the anchor determinant. As the single excitation may take place independently in the S^α and S^β subblocks, partially even spin factors for higher excited Slater determinants can be retrieved from memory. Due to the high memory demand, we refrained from storing the spin factors for all possible combinations of double and higher excitations. These determinants have to be (re)constructed on-the-fly. Before the Schur complement $\mathbf{S/F} = \mathbf{V} - \mathbf{P}(\mathbf{F})^{-1}\mathbf{O}$ is actually formed, Hadamard's inequality [Eq. (28)] can be applied piecewise to estimate the size of det **S**,

$$\| \det \mathbf{S} \|^2 \leq \prod_{i=1}^{s} \| x_i \|^2 = \prod_{i=1}^{s-f} \| x_i \|^2 \prod_{i=s-f+1}^{s} \| x_i \|^2. \tag{29}$$

The Journal of Chemical Physics ARTICLE scitation.org/journal/jcp

Herein, f is the dimension of the **F** block. Once, the blocks **P** and **F** are known in the outer reference loop, the product of their row vector norms can be precomputed and stored. When the much smaller **V** block and the **O** block, both carrying information about the excitations at the displaced geometry, become available in the inner loop, the precomputed product needs to be extended by just a few terms corresponding to the rank of **V**. The threshold δ_H for the upper bound of Hadamard's estimate can be set by the user. Values of the order of 10^{-6} were found to be sufficient for determining derivative couplings with a precision of five decimal places. Finally, the product of the resulting spin factors, $S^{\alpha}S^{\beta}$, is weighted by the CSF coefficients of the DFT/MRCI wave functions and by the expansion coefficients of the Slater determinants within the respective CSFs.

III. VALIDATION OF THE ALGORITHM AND THE IMPLEMENTATION

The present version of the DELTA program is executed sequentially, and all reported cpu times were measured on a single core of a 2.8 GHz AMD EPYC "ROME" 7402 CPU.

A. Comparison with analytic MCSCF derivative couplings

To validate the implementation of our finite-difference algorithm, we computed analytic CASSCF derivative couplings of small model systems by means of the Columbus package.[58–60] Two different *ab initio* CASSCF setups were prepared for investigating NAMCEs within the triplet manifold of the formaldehyde molecule. To ensure that the technical parameters and wave function characteristics match as closely as possible, a double zeta (DZ) basis without *d* functions was chosen to avoid normalization and phase issues when using the Columbus-generated CASSCF MOs in subsequent Turbomole one- and two-electron integral routines. Analytic NACMEs were determined at the C_{2v}-symmetric ground-state geometry with all nuclei lying in the XZ plane. For technical details, see Sec. S1 A of the supplementary material. The first test case comprises the coupling between the A_1-symmetric $T_2(\pi_{HOMO} \rightarrow \pi^*_{LUMO})$ and the A_2-symmetric $T_1(n \rightarrow \pi^*_{LUMO})$ pair of states in a CAS(4,4) setup with MOs optimized for state-averaged electron densities of these two states. The second test case is purely artificial and was chosen because the NACME between the A_2-symmetric $T_8(\pi_{HOMO} \rightarrow \sigma^*)$ and the B_2-symmetric $T_6(\pi_{HOMO} \rightarrow \sigma^{*\prime})$ states of the CAS(6,6) space has a very large value although the wave functions contain non-negligible contributions of multiply excited determinants. In this case, a state-averaging of six triplet densities was performed in the orbital optimization step.

Ab initio MRCI calculations were performed such that the inactive orbitals were frozen, and a full CI expansion was obtained in the respective reference space while all excitations to external orbitals were prohibited. Energies and wave function coefficients of the corresponding triplet states from Columbus and MRCI are listed in Tables S2–S6 of the supplementary material. The entries closely resemble one another, but they are not exactly equal because the MRCI program employs two-electron integrals in the resolution-of-the-identity (RI) approximation,[1,61,62] whereas Columbus uses the full four-index two-electron integrals.

The displacement of one H-atom in the Y-direction (perpendicular to the molecular plane) is capable of coupling the $T_2(\pi_H \rightarrow \pi^*_L)$ and $T_1(n \rightarrow \pi^*_L)$ pair of states. A step size of 0.01 a_0 was chosen for evaluating the numerical derivative. Its $\langle T_2 \,|\, \vec{\nabla}_{Y(H1)} \,|\, T_1 \rangle$ component (0.225 867 a_0^{-1}) agrees with the analytical reference value (0.225 591 a_0^{-1}) within 3 decimal places (see Table S7 of the supplementary material for details). In this particular case, the leading terms alone give rise to a NAMCE that overshoots the full value by less than 1%. It should be noted, however, that the CI expansions comprise merely 15 CSFs.

The CI expansion lengths of the $T_8(\pi_{HOMO} \rightarrow \sigma^*)$ and $T_6(\pi_{HOMO} \rightarrow \sigma^{*\prime})$ states amounts to 189 CSFs without symmetry blocking. In their case, an in-plane distortion of the carbon atom in the X direction (perpendicular to the C_2 axis) was chosen for comparison with the corresponding component of the analytical NACME (3.851 424 a_0^{-1}). The numerical procedure yields a slightly larger value of 3.853 828 a_0^{-1} for the derivative coupling. Because of the higher percentage of multiple excitations in their electronic wave functions, the magnitude of this NACME is more sensitive with respect to the truncation of the CI expansion. Restricting the computation of the non-orthogonal overlap to configurations that are singly excited with respect to the anchor configuration yields a coupling of 4.058 911 a_0^{-1}. Admixture of doubly excited configurations (3.842 277 a_0^{-1}) brings the analytical and numerical couplings into agreement within 0.2%. If the modulus of the CI coefficients ($\|d_i\|$) is chosen as a truncation criterion, the cutoff has to be set to values lower than 0.01 to reach an accuracy of better than 1%.

With regard to timings, truncation of the MRCI wave function leads to substantial speed-ups. As may be anticipated, the cpu time required for calculating the NACME correlates nearly linearly with the number of spin factors because their computation is the time determining step.

B. The pyrazine test cases

Pyrazine [Fig. 2(a)] is a D_{2h}-symmetric molecule in the electronic ground state. Due to its moderate size and strong vibronic coupling effects in the singlet excited state manifold, it has ever since been a guinea pig of the theoretical chemistry community for testing the validity of their vibronic coupling methods and algorithms.[39,63–69] The much lower vibronic activity in the $T_1 \leftarrow S_0$ absorption spectrum has been explained by the fact that this spin-forbidden transition borrows its intensity from optically bright singlet transitions by a direct spin–orbit mechanism without the necessity to invoke spin–vibronic coupling.[69,70]

Due to its high molecular symmetry, pyrazine is an ideal test case for verifying the proper implementation of our numerical

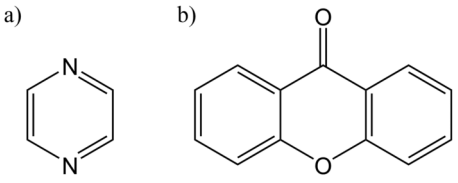

FIG. 2. The pyrazine (a) and xanthone (b) molecules.

The Journal of Chemical Physics ARTICLE scitation.org/journal/jcp

algorithm for computing DFT/MRCI NACMEs as well. The precision of numerical zeros for symmetry-forbidden couplings and of the NACMEs for symmetry-allowed couplings offers the possibility to check the dependence of the derivative couplings on various wave function parameters, such as the convergence thresholds of the underlying KS calculation and of the iterative Davidson diagonalization in the DFT/MRCI step. These parameters set aside, the computational protocol for generating molecular orbitals and DFT/MRCI wave functions of pyrazine proceeds along the lines of previous work performed in our laboratory, which focused on vibronic traces in the $S_1 \leftarrow S_0$ and $T_1 \leftarrow S_0$ absorption spectra caused by HT-type couplings.[69] Technical details may be found in Sec. S1 of the supplementary material.

The wave function of the first excited singlet state of pyrazine, $S_1(n\pi^*)$, transforms according to the B_{3u} irreducible representation (irrep) at the ground-state geometry. Energetically, the $S_1(n\pi^*)$ state is well separated from the B_{2u} symmetric $S_2(\pi\pi^*)$ state. According to the symmetry selection rules, the derivatives along all normal coordinates must vanish, save for b_{1g} modes. There is only one mode of the appropriate symmetry type, namely, mode 7 ($\tilde{\nu} = 941$ cm^{-1}), which corresponds to ν_{10a} in the common nomenclature introduced by Innes *et al.*[63] The situation is slightly more complicated in the triplet manifold. The spacing between the T_1 $^3(n\pi^*)$ excitation (B_{3u} symmetry) and the $T_2(\pi\pi^*)$ state is much smaller than for their singlet counterparts. Moreover, the T_2 and T_3 states swap order upon geometry relaxation.[69] In the FC region, which is relevant in the present case study, the B_{2u} symmetric $T_2(\pi\pi^*)$ is energetically favored, and its nonadiabatic coupling with T_1 will be investigated here as the second test example. In the following, unprimed state designations refer to DFT/MRCI wave functions at the S_0 reference geometry $\vec{R}$ of pyrazine, whereas primed entities symbolize wave functions calculated at a displaced geometry $\vec{R}'$.

1. Dependence on orbital and wave function convergence parameters

When the usual SCF convergence thresholds (10^{-8} E$_h$ for the SCF energy and 10^{-7} for the SCF density matrix), recommended for subsequent DFT/MRCI computations, are employed in the dscf iterative eigenvalue solver of the Turbomole program,[71] a value for the only symmetry-allowed $\langle T_2 | \frac{\partial}{\partial Q_{10a}} | T_1 \rangle \big|_{S_{0,\min}}$ NACME is obtained, which is ~2% lower than the fully converged value (Table S9 of the supplementary material). This means that the standard SCF convergence thresholds are too sloppy for computing this DFT/MRCI NACME with a higher precision than the first decimal place. Reducing the convergence thresholds by a factor of 10 yields a NACME for the coupling of the T_1 and T_2 states by $\partial/\partial \mathbf{Q}_{10a}$ that agrees with the value obtained for an even tighter convergence threshold in the third decimal place. We therefore recommend to set the convergence thresholds in the KS orbital optimization step to at least 10^{-10} E$_h$ for the SCF energy and 10^{-9} for the SCF density matrix in conjunction with the numerical determination of DFT/MRCI derivative couplings. In contrast, minuscule variations of the NACME are encountered when the default convergence threshold (0.5×10^{-5} E$_h$) of the iterative Davidson solver of the DFT/MRCI secular equation is tightened (Table S9 of the supplementary material). However, the quality of the numerical zeros for the symmetry-forbidden derivative couplings improves in this case. While a value of $\approx 1.3 \times 10^{-5}$ is obtained for the $\langle T_2(\vec{R}) | T_1'(\vec{R}') \rangle$ overlap for a displacement in the direction of mode 4 when the standard convergence threshold of 0.5×10^{-5} E$_h$ is used in the Davidson procedure, the numerically determined value of this symmetry-forbidden coupling drops to $\approx 1.9 \times 10^{-7}$ when a threshold of 0.5×10^{-7} E$_h$ is employed instead. For all other 22 symmetry-forbidden coupling modes, the precision of the numerical zero is higher than for mode 4 (Table S10 of the supplementary material). Summarizing, we find the impact of the orbital convergence parameters on the precision of the computed derivative couplings to be more pronounced than the influence of the Davidson convergence parameter. Nevertheless, we recommend tightening the SCF and CI convergence thresholds by a factor of 0.01 in relation to the default values.

2. Step size of the normal mode displacement

The second set of test calculations on pyrazine investigated the range of deflections for which the magnitude of the nonorthogonal overlaps of the $^3B_{2u}$ T_2 DFT/MRCI wave function of pyrazine at the S_0 reference geometry $\vec{R}$ and the $^3B_{3u}$ T_1' wave function at a displaced geometry $\vec{R}' = \vec{R} + \epsilon\, \vec{e}_{Q10a}$ scales approximately linearly with the step size ϵ. The ν_{Q10a} mode is the only out-of-plane vibration that has the proper b_{1g} symmetry for coupling these states. The results as well as the overlaps of the corresponding singlet wave functions $\langle S_2(\vec{R}) | S_1(\vec{R}') \rangle$ are depicted graphically in Fig. 3. The confidence interval for which the nonorthogonal overlap may be considered to increase linearly with increasing displacement is approximately $\epsilon = \pm 0.01$, in agreement with observations for other molecules. Unless noted otherwise, all finite difference calculations [Eq. (1)] have been carried out using this ϵ value.

3. Performance of the Delta program for different triplet sublevels

Test calculations for comparing the outcomes and timings of $M_S = 0$ and $M_S = 1$ triplet wave functions were performed for the $\langle T_2(\vec{R}) | T_1(\vec{R}') \rangle$ overlap of the pyrazine molecule where

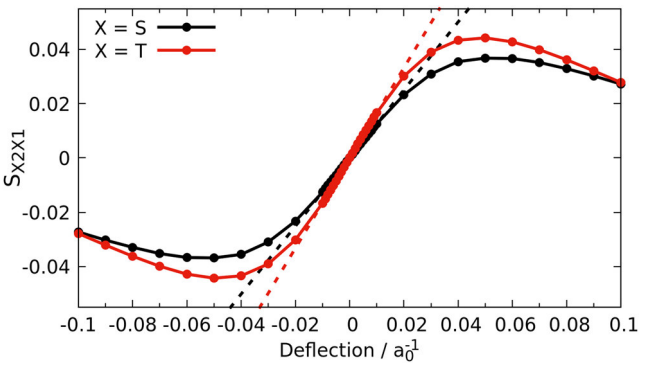

FIG. 3. Nonorthogonal overlaps of the $^1B_{3u}$ $S_1'(\vec{R}')$ and the $^1B_{2u}$ $S_2(\vec{R})$ pair of states (black) as well as of the $^3B_{3u}$ $T_1'(\vec{R}')$ and $^3B_{2u}$ $T_2(\vec{R})$ (red) pair of states in pyrazine determined for varying displacements along the mass-weighted normal coordinate of the $\nu_{10a}(b_{1g})$ vibrational mode. $\vec{R}$ denotes the S_0 reference geometry, $\vec{R}' = \vec{R} + \epsilon\, \vec{e}_{Q10a}$ denotes the displaced geometry.

The Journal of Chemical Physics ARTICLE scitation.org/journal/jcp

$\vec{R}' = \vec{R} + 0.1\vec{e}_{Q10a}$ and the unit vector $\vec{e}_{Q10a}$ points along the normal coordinate of the only symmetry-allowed vibrational coupling mode ν_{10a}. At the ground state geometry ($\vec{R}$), the T_1 and T_2 DFT/MRCI wave functions are composed of 6663 CSFs corresponding 3065 configurations. Further computational details may be found in Sec. S1 B of the supplementary material.

Two conclusions may be drawn from the data entries in Table S11. First, corresponding matrix elements employing either $M_S = 0$ or $M_S = 1$ are identical to at least 14 decimal places. As different parts of the program are addressed in either case, we consider this agreement a confirmation that the down shift of the M_S quantum number and the computation of the spin factors $\mathbf{S}_{kl}$ [Eq. (18)] are coded properly. Second, convergence of the $\langle T_2(\vec{R}) \,|\, T_1(\vec{R}')\rangle$ matrix element up to 10^{-4} is reached for a cutoff parameter $t_{cutoff} = 10^{-3}$. This parameter steers the length of the DFT/MRCI wave function and is chosen such that configurations are discarded if none of its CSF coefficients d_i fulfills the condition $|d_i| \geq t_{cutoff}$. To converge the coupling matrix element to $\pm 10^{-5}$ a_0^{-1} requires the wave function cutoff parameter to be reduced to $t_{cutoff} = 10^{-6}$ at least.

Table S12 displays the number of spin factors $\mathbf{S}_{kl}$ [Eq. (18)] and the timings for the two approaches and a series of cutoff parameters t_{cutoff}. Because of the smaller number of Slater determinants, the total number of spin factors $\mathbf{S}_{kl}$ needed for computing $\langle T_2(\vec{R}) \,|\, T_1(\vec{R}')\rangle$ is, of course, smaller in the $M_S = 1$ case in comparison with $M_S = 0$. Counterintuitively, however, the timings tell a different story. Because the percentage of cached spin factors that can be retrieved from memory and reused instead of being computed on-the-fly is much larger if the number of α and β electrons is identical, the $M_S = 0$ setup has a clear advantage, in particular, when the number of open-shell configurations increases.

C. Truncation of the wave function expansion: Precision and timings

Various actions can be taken to speed up the computation of the numerical derivatives. Aside from making use of symmetry selection rules, the most obvious one is the truncation of the MRCI expansion because the timings increase quadratically with the number of Slater determinants to be processed. As described in detail in Sec. II B 4, we defined a cutoff parameter for the residual norm of the truncated wave function [Eq. (25)]. Alternatively, the magnitude of individual CSF coefficients was used as a criterion. Moreover, we have investigated the performance of the numerical procedure with regard to precision and timings for cases in which only the overlaps of singly excited pairs of configurations are evaluated (1-exc. approximation, Sec. II B 5), either as a stand-alone criterion or in combination with truncated wave function expansions. Finally, Hadamard's inequality [Eq. (28)] has been used in addition to the 1-exc. approximation to speed up the numerical evaluation of NACMEs.

Many of the tests have been performed for the spin-allowed derivative couplings between the lowest $^{1,3}(n_O\pi_L^*)$ and $^{1,3}(\pi_H\pi_L^*)$ states of xanthone in vacuum. The physical relevance of these couplings will be discussed at length in Sec. IV. Here, we focus on the technical aspects of the NACME evaluation. Using C_{2v} point-group symmetry, the $(\pi_H\pi_L^*)$ states transform according to the totally symmetric irreducible representation A_1, whereas the $(n_O\pi_L^*)$ are A_2 symmetric. For this reason, only the 9 a_2-symmetric normal coordinates exhibit the appropriate point-group symmetry to produce nonvanishing NACMEs.

The 1-exc. approximation results in a substantial speed-up of the calculation without essential loss of precision. As shown in Table S13 of the supplementary material, the NACMEs of the full DFT/MRCI expansion and the 1-exc. approximation agree to within 3–4 decimal places while cpu times are reduced on the average from about 24 h to 7 min per mode in the triplet case and from about 48 h to 11 min per mode in the singlet case. A further reduction in computation time can be achieved if the wave function expansions are truncated. Setting the cutoff parameter t_{norm} to 10^{-11} yields essentially the same IC rate constant as the full expansion in 1-exc. approximation but diminishes the cpu time by another factor of 6 (Tables S14 and S15 of the supplementary material). The entries of these tables and the graphs in Figs. S1 and S3 of the supplementary material suggest that setting t_{norm} to values $> 10^{-7}$ is not meaningful due to loss of precision. Application of the Hadamard screening as an additional measure for reducing the computation time appears to be less effective in comparison to the truncation of the wave function expansion, at least in our implementation. A Hadamard screening parameter of 10^{-5} for the overlap of the spin factors leads to a saving of merely 20% in comparison to employing all overlaps in the 1-exc. approximation (Tables S16 and S17 of the supplementary material).

Summarizing the trade-off between precision and timing, we recommend to restrict the mutual excitation level of the configurations at the reference and displaced geometries to 1 (1-exc. approximation) in combination with a cutoff parameter of $t_{norm} = 10^{-8}$ for the DFT/MRCI wave function expansion.

IV. APPLICATION TO EXCITED-STATE PROCESSES IN XANTHONE

Xanthone [Fig. 2(b)] is a good triplet sensitizer in apolar and mildly polar environments, whereas it is fluorescent in water.[40,41,72,73] In apolar media such as hexane, the lowest triplet state exhibits $^3(n_O\pi_L^*)$ character, whereas this changes to $^3(\pi_H\pi_L^*)$ character in polar environments such as acetonitrile. In the singlet manifold, this transition occurs at much higher dielectric permittivities.[12,74,75] While the S_1 state retains its $^1(n_O\pi_L^*)$ character in acetonitrile and methanol, a strongly polar protic solvent, such as water, reverses the energetic order of the $^1(n_O\pi_L^*)$ and $^1(\pi_H\pi_L^*)$ electronic structures. In the following, we will investigate the probabilities of IC vs ISC decay in two different environments: gas phase and aqueous solution.

A. Gas phase and in apolar media

In hexane, a biphasic rise of triplet–triplet absorption was observed experimentally after photoexcitation of the S_2 $^1(\pi_H\pi_L^*)$ state. Cavaleri *et al.*[72] assigned the fast component with a time constant of 0.70 ps to the El-Sayed allowed S_2 $^1(\pi_H\pi_L^*) \rightsquigarrow T_1$ $^3(n_O\pi_L^*)$ ISC and the slower process with a time constant of 10 ps to the alternative decay cascade S_1 $^1(n_O\pi_L^*) \rightsquigarrow T_2$ $^3(\pi_H\pi_L^*)$ ISC, including the subsequent T_2 $^3(\pi_H\pi_L^*) \rightsquigarrow T_1$ $^3(n_O\pi_L^*)$ IC. For the S_2 $^1(\pi_H\pi_L^*) \rightsquigarrow S_1$ $^1(n_O\pi_L^*)$ IC, a time constant of 2.3 ps was determined in that solvent. These findings and their interpretation raise the question why the spin-forbidden $S_2 \rightsquigarrow T_1$ channel and not the spin-allowed

The Journal of Chemical Physics ARTICLE scitation.org/journal/jcp

$S_2 \rightsquigarrow S_1$ dominates the decay of the S_2 population of xanthone in non-polar solvents. DFT/MRCI calculations in our laboratory confirmed the assumed energetic scheme but found the vibronically induced $S_2\ ^1(\pi_H\pi_L^*) \rightsquigarrow T_2\ ^3(\pi_H\pi_L^*)$ ISC to be about two orders of magnitude faster than the direct $S_2\ ^1(\pi_H\pi_L^*) \rightsquigarrow T_1\ ^3(n_O\pi_L^*)$ ISC in Condon approximation.[12] It should be noted, however, that the geometry optimization of the $S_2\ ^1(\pi_H\pi_L^*)$ state using TDDFT leads to a very shallow C_2-symmetric double minimum potential connected by a planar C_{2v}-symmetric saddle point. At the DFT/MRCI level of theory, the C_{2v}-symmetric structure is lower in energy and represents the minimum along this reaction coordinate. The artificial occurrence of symmetry breaking deformations at the TDDFT level has been observed in various aromatic ketones[46,76] and flavin derivatives.[77,78] In these cases, we typically use the vibrational coordinates of the saddle point and replace the imaginary frequency by a reasonable real value corresponding to the curvature of the outer branches of the TDDFT profile. Peculiar in the case of the xanthone $S_2\ ^1(\pi_H\pi_L^*)$ is that the $T_2\ ^3(\pi_H\pi_L^*)$ and $T_1\ ^3(n_O\pi_L^*)$ states are energetically almost degenerate ($\Delta E \approx 0.01$ eV) at the C_2-symmetric $S_2\ ^1(\pi_H\pi_L^*)$ structure and exhibit strongly mixed wave functions. Even small coordinate displacements can and do lead to a reversal of the order of triplet states. The determination of HT-SOC terms by a finite difference procedure at this point in coordinate space is therefore extremely error-prone and needs close monitoring of the dominant wave function characteristics. In our earlier work,[12] the rate constant of the El-Sayed allowed $S_2\ ^1(\pi_H\pi_L^*) \rightsquigarrow T_1\ ^3(n_O\pi_L^*)$ transition was determined in the Condon approximation at the C_2-symmetric minimum geometry of the S_2 state, which appears inappropriate in a retrospective analysis. Moreover, due to the lack of nonadiabatic derivative couplings, IC rate constants could not be determined at the DFT/MRCI level at that time, and therefore, the kinetic model remained fragmentary.

Here, we include vibronic terms and employ the C_{2v}-symmetric structure of the $S_2\ ^1(\pi_H\pi_L^*)$ state as the reference point for our (re-)investigation of the S_2 ISC and IC processes while carefully testing the sensitivity of the computed rate constants with respect to the vibrational frequency of the A_2-symmetric deformation mode. The adiabatic energy difference between the C_{2v}-symmetric $S_2\ ^1(\pi_H\pi_L^*)$ structure and the $S_1\ ^1(n_O\pi_L^*)$ minimum amounts to 0.71 eV at the DFT/MRCI level of theory. Zero-point vibrational energy (ZPVE) corrections (Table S18 of the supplementary material) are automatically accounted for in the VIBES program. Varying the vibrational frequency of the A_2-symmetric deformation mode between 50 and 500 cm^{-1} yields rate constants of $k^{IC}_{S_2S_1} = 3 - 4 \times 10^{11}\ s^{-1}$ for the $S_2\ ^1(\pi_H\pi_L^*) \rightsquigarrow S_1\ ^1(n_O\pi_L^*)$ IC in vacuum (Table S19 of the supplementary material). These values agree very well with the time constant of 2.3 ps observed by Cavaleri *et al.*[72] in hexane solution. (Choosing the C_2-symmetric structure as reference point instead gives a rate constant of $k^{IC}_{S_2S_1} = 4.3 \times 10^{11}\ s^{-1}$ for this process, which fortuitously exactly matches the experimental time constant.) The comparatively slow IC in the singlet manifold is considered a consequence of the substantial energy separation between the adiabatic S_1 and S_2 states and a lack of an energetically accessible conical intersection between them.

Both low-lying triplet states, $T_2\ ^3(\pi_H\pi_L^*)$ and $T_1\ ^3(n_O\pi_L^*)$, have planar minimum geometries at the DFT/MRCI level of theory. In contrast, TDDFT finds one imaginary frequency at the C_{2v}-symmetric T_1 structure, which is why we followed Rai-Constapel *et al.*[12] in employing the nuclear arrangement and vibrational modes of the $S_1\ ^1(n_O\pi_L^*)$ state as a proxy for the corresponding triplet state properties. Because of the much smaller energy gap between the two triplet states (0.14 eV), the rate constant for the $T_2\ ^3(\pi_H\pi_L^*) \rightsquigarrow T_1\ ^3(n_O\pi_L^*)$ IC is significantly larger ($k^{IC}_{T_2T_1} > \times 10^{13}\ s^{-1}$) than for the corresponding singlet transition. We may therefore conclude that the $T_2\ ^3(\pi_H\pi_L^*) \rightsquigarrow T_1\ ^3(n_O\pi_L^*)$ IC is not the rate determining step for the population of the $T_1\ ^3(n_O\pi_L^*)$ state, monitored experimentally through time-resolved triplet excited-state absorption spectroscopy. Combining the knowledge on IC and ISC rate constants acquired in our present study with the experimental information provided by Cavaleri *et al.*,[72] the following schematic picture emerges for the decay kinetics following photoexcitation of xanthone to the $S_2\ ^1(\pi_H\pi_L^*)$ state in apolar media [Fig. 4(a)].

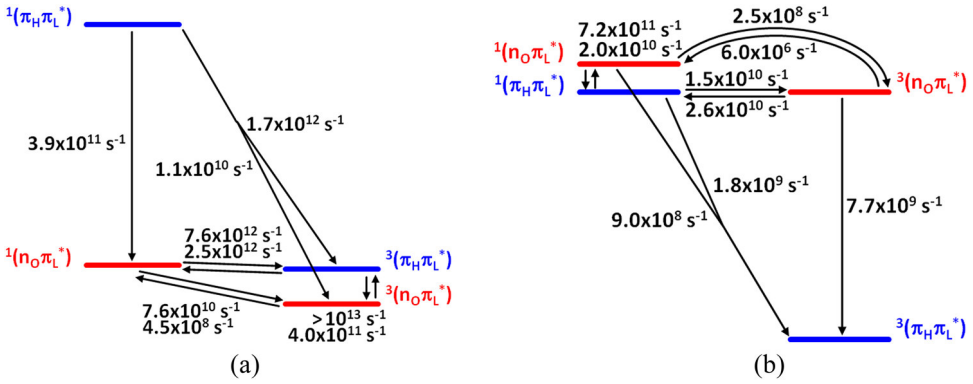

FIG. 4. Theoretically determined energy level scheme and rate constants (300 K) for IC and ISC transitions following the photoexcitation of xanthone in vacuum (a) and aqueous solution (b). In vacuum, ZPVE-corrected adiabatic transition energies amount to 0.63 eV for IC in the singlet domain, 0.09 eV for IC in the triplet domain, and 0.01 eV for the $S_1 \rightsquigarrow T_2$ ISC. In aqueous solution, the $(n_O\pi_L^*)$ states are blue shifted relative to the $(\pi_H\pi_L^*)$ states. To better match with experimental data, their solvent shifts were reduced by 0.11 eV in comparison to the hybrid model employed by Rai-Constapel *et al.*[12] In this way, the vibrational ground states of the T_2 and S_1 potentials become isoenergetic in aqueous solution while energy separations of 0.07 eV between S_2 and S_1 and of 0.61 eV between T_2 and T_1 are obtained.

The Journal of Chemical Physics ARTICLE scitation.org/journal/jcp

S_2 can be considered the starting point for two spin-forbidden and one spin-allowed nonradiative transitions. The direct $S_2\,{}^1(\pi_H\pi_L^*) \rightsquigarrow T_1\,{}^3(n_O\pi_L^*)$ ISC is an El-Sayed-allowed process, but the adiabatic energy separation between these states is substantial. The two-step process involving the $T_2\,{}^3(\pi_H\pi_L^*)$ state as an intermediate is El-Sayed forbidden and appears unattractive at first sight. Nevertheless, both ISC channels are investigated here because a conical intersection of the T_2 and T_1 potentials lies close to the S_2 minimum. While intuitively the one-step process is expected to prevail, the calculations actually find the cascade $S_2\,{}^1(\pi_H\pi_L^*) \rightsquigarrow T_2\,{}^1(\pi_H\pi_L^*)$ ISC followed by $T_2\,{}^3(\pi_H\pi_L^*) \rightsquigarrow T_1\,{}^3(n_O\pi_L^*)$ IC to be much more effective than the direct $S_2\,{}^1(\pi_H\pi_L^*) \rightsquigarrow T_1\,{}^3(n_O\pi_L^*)$ process when spin–vibronic interactions are included.

A further productive channel for populating the T_1 state on the picosecond time scale is a cascade starting with the spin-allowed $S_2\,{}^1(\pi_H\pi_L^*) \rightsquigarrow S_1\,{}^1(n_O\pi_L^*)$ IC. Due to the energetic proximity of the S_1 and T_2 states and their substantial mutual SOC ($\langle T_2\,{}^3(\pi_H\pi_L^*)|\hat{\mathcal{H}}_{SO}|S_1\,{}^1(n_O\pi_L^*)\rangle = -50.75\ cm^{-1}$ at the S_1 minimum), the $S_1\,{}^1(n_O\pi_L^*) \rightsquigarrow T_2\,{}^1(\pi_H\pi_L^*)$ ISC is ultrafast. This ISC step is followed by an even faster $T_2\,{}^3(\pi_H\pi_L^*) \rightsquigarrow T_1\,{}^3(n_O\pi_L^*)$ IC. Thus, the rate determining step in this cascade is the $S_2 \rightsquigarrow S_1$ IC.

In summary, the photoexcitation decay of xanthone in apolar media is best described by a unified kinetics model comprising branched and consecutive pathways involving the $S_1\,{}^1(n_O\pi_L^*)$ and $T_2\,{}^1(\pi_H\pi_L^*)$ states as intermediates [Fig. 4(a)]. Note further that the equilibration between S_1, T_2, and T_1 by ISC and thermally activated rISC processes, on the one hand, and by IC and the rIC upconversion from $T_2 \leftsquigarrow T_1$, on the other hand, are much faster than the prompt $S_1\,{}^1(n_O\pi_L^*) \rightarrow S_0$ fluorescence in apolar media, which is therefore quenched.

B. Water solution

In addition to prompt fluorescence, xanthone emits delayed fluorescence in aqueous solution. Heinz *et al.* concluded that the $T_2\,{}^3(n_O\pi_L^*)$ state rapidly equilibrates with the near degenerate bright $S_1\,{}^1(\pi_H\pi_L^*)$ state and that the backtransfer of population via the El-Sayed-allowed $T_2 \rightsquigarrow S_1$ ISC is the origin of this delayed fluorescence.[41] This interpretation implies that the spin-allowed $T_2 \rightsquigarrow T_1$ IC cannot compete against the spin-forbidden $T_2 \rightsquigarrow S_1$ nonradiative transition in aqueous solution. Because $T_1\,{}^3(\pi_H\pi_L^*)$ and S_1 have similar electronic structures and are separated by about 0.60 eV, thermally activated $T_1 \rightsquigarrow S_1$ rISC was considered highly improbable. The quantum chemical investigation by Rai-Constapel *et al.*[12] corroborated the near degeneracy of the S_1 and T_2 states in water and reported a $S_1 \rightsquigarrow T_2$ rate constant of $2.5 \times 10^8\ s^{-1}$ in Condon approximation, but the rate constant neither for the $T_2 \rightsquigarrow S_1$ rISC process nor for the $T_2 \rightsquigarrow T_1$ IC was computed. Here, we use a similar computational setup as described before and set out for determining the missing rate constants.

A complication arises due to the flexibility of the solvent environment. In polar solvents, $n\pi^*$ excited states typically experience strong blue shifts, while $\pi\pi^*$ excited states are moderately red shifted.[77] The electrostatic solvent–solute interaction can be well described by continuum models, such as COSMO. In contrast, the shifts brought about by hydrogen bond formation in protic solvents require a hybrid model including explicit solvent molecules and an electrostatic surrounding. To mimic an aqueous medium, Rai-Constapel *et al.*[12] used a hybrid model consisting of a hydrogen-bonded complex of xanthone and two water molecules surrounded by a COSMO electrostatic field. Reorientation of the loosely bonded water molecules upon geometry relaxation in the excited states leads to large amplitude displacements of the corresponding normal coordinates, thus preventing a meaningful Duschinsky transformation (11) of the normal coordinates. To account for solvent–solute interactions, we use here an ansatz that closely resembles the energy level shift procedures in two-step spin–orbit coupling calculations.[79,80] The impact of the aqueous solution is taken care of implicitly by introducing state-specific energy shifts in the Davidson diagonalization procedure of the DFT/MRCI program. To this end, the diagonal elements of the Hamiltonian matrix

$$H_{ij}^{solv} = H_{ij}^{vac} + \sum_{K=1}^{nroots} \Delta E_K^{solv} |\,\Psi_K^{vac}\,\rangle\langle\,\Psi_K^{vac}\,| \tag{30}$$

are modified. In accord with the results of previous work,[12] the energy shifts ΔE_K^{solv} tabulated in Table S21 of the supplementary material were employed for the states under consideration. Test calculations reveal that truncated DFT/MRCI vectors including only terms with $\|d_i\| > 10^{-5}$ can be used to construct the projection operators without loss of accuracy but speeding up the Davidson diagonalization of the modified Hamiltonian matrix significantly.

Including spin–vibronic interactions in the computation of rate constants for the El-Sayed allowed processes $^1(\pi_H\pi_L^*) \leftsquigarrow {}^3(n_O\pi_L^*)$ do not change lot. While the reverse ISC is predicted to proceed at a rate constant of about $2.3 \times 10^{10}\ s^{-1}$, the computed rate constant of $1.8 \times 10^8\ s^{-1}$ for the forward ISC is too small to explain the fast $S_1 \leftsquigarrow T_2$ equilibration observed experimentally by Heinz *et al.*[41] For an ISC process that is dominated by direct SOC, the electronic SOCME and the Franck–Condon weighted density of vibrational states at the energy of the initial state determine the transition probability. Because of the close energetic proximity of the $^1(\pi_H\pi_L^*)$ and $^3(n_O\pi_L^*)$ states in water, already small changes of the relative energy separation of their vibrational ground states (ΔE_0) can have large impact on the magnitude of the vibrational overlaps and hence on the transition rates. Considering that our rather crude solvent model might overestimate the blue shifts of the $(n_O\pi_L^*)$ state energies, we therefore varied this parameter. The entries of Table S22 in the supplementary material reveal that a reduction in their solvent shift by 0.11 eV, which makes the S_1 and T_2 states nearly degenerate, increases the rate constant of the thermally activated $S_1 \rightsquigarrow T_2$ transition by a factor of about 80 while changing the rate constant of the reverse $S_1 \leftsquigarrow T_2$ process only slightly. This solvent model appears to give a more balanced description of the forward and backward $S_1 \leftrightsquigarrow T_2$ ISC kinetics of xanthone in aqueous solution. For this reason, we applied the same shift to the $^1(n_O\pi_L^*)$ state potential and investigated the sensitivity of the calculated $S_2 \rightsquigarrow S_1$ and $T_2 \rightsquigarrow T_1$ IC rate constants with respect to the applied shift as well. An overview of the kinetic constants obtained for this model is shown in Fig. 4(b).

At first sight, it is surprising that the $S_2 \rightsquigarrow S_1$ IC rate constant is reduced from about $8 \times 10^{12}\ s^{-1}$ to about $7 \times 10^{11}\ s^{-1}$ when their ΔE_0 separation changes from 0.18 to 0.07 eV (Table S26 of the supplementary material). To understand the variation of the IC rate constants with the applied shift, we have to be aware that two

The Journal of Chemical Physics ARTICLE scitation.org/journal/jcp

factors influence the magnitude of the nonradiative transition rate constants if vibronic coupling is accounted for. In addition to the FC overlaps, the NACME itself is sensitive with respect to the energy separation between the coupling states. In principle, both factors can increase or decrease with diminishing ΔE_0. In the weak coupling limit, characterized by nested potentials, the FC overlaps drop exponentially with growing adiabatic energy gap, whereas an inverse energy gap relation is expected for strong coupling cases characterized by large displacements of the minimum geometry parameters.[81] In contrast, the magnitude of the NACME is primarily related to the vertical energy difference of the interacting states $\Delta E_{\text{vertical}}$, which is easily seen when inspecting the Hellmann–Feynman-type expression[31] $f_{ab} = \langle \Psi_b | \nabla \mathcal{H} | \Psi_a \rangle (E_a - E_b)^{-1}$. While the $^1(\pi_H \pi_L^*)$ state is adiabatically the lowest excited singlet state of xanthone in water, it lies vertically above the $^1(n_O \pi_L^*)$ state at the $^1(n_O \pi_L^*)$ minimum geometry. Counterintuitively, therefore, a global red shift of the $^1(n_O \pi_L^*)$ potential by small amounts leads to an increase in the vertical energy separation $\Delta E_{\text{vertical}}$ between these states and a strong reduction of the NACME (Fig. S5 of the supplementary material), leading, in turn, to a decrease in the IC rate constant (Table S26 of the supplementary material) by a factor of about 10. The contrary is true for the reverse IC process because the $^1(\pi_H \pi_L^*)$ lies below the $^1(n_O \pi_L^*)$ state at the $^1(\pi_H \pi_L^*)$ minimum. An additional red shift of the $^1(n_O \pi_L^*)$ state therefore brings the two states into closer proximity and increases the rIC rate constant by two orders of magnitude. The IC in the triplet manifold is less affected by small variations of the relative $^3(\pi_H \pi_L^*)$–$^3(n_O \pi_L^*)$ energy separation because these states lie further apart in aqueous solution.

V. CONCLUSIONS AND OUTLOOK

In this paper, we have presented a new program for computing numerical NACMEs for DFT/MRCI wave functions of triplet and singlet multiplicity. The implementation makes extensive use of the Schur's determinant identity to improve the scaling of the computation of spin factors. To keep the task manageable with respect to memory demand, only the spin factors of singly excited determinants are cached, while those of double and higher excitations with respect to the ground-state determinant are generated on-the-fly. This flexibility and the application of suitable selection schemes allow the computation of NACMEs even for large molecules. Although the current implementation is restricted to singlet and triplet states, the foundation has been laid to extend our approach to states of arbitrary multiplicity.

The recommended value for the step size in numerical calculations of derivative couplings is $\epsilon = \pm 0.01$ in units of dimensionless mass weighted normal coordinates. The derivative couplings are found to be quite sensitive to the convergence of the SCF procedure. To obtain numerically stable results, the convergence thresholds should be set to at least $10^{-10} E_h$ for the KS energy and to 10^{-9} for the SCF density. Restriction of the mutual excitation class of configurations at the reference and displaced geometries to single replacements (1-exc. approximation) in combination with a truncation of the wave function expansion ($t_{\text{norm}} = 10^{-8}$) substantially accelerates the numerical evaluation of nonorthogonal DFT/MRCI wave function overlaps without significant loss of precision. On-top application of Hadamard's inequality for estimating the contribution of spin factors does not lead to marked additional savings of computation time.

Formulas for computing IC rate constants in a generating function approach including Dushinsky transformations have been worked out and implemented into the Vibes program. This new program version has been used in conjunction with DFT/MRCI NACMEs to provide a better understanding of the complex photoexcitation decay kinetics of the xanthone chromophore in vacuum as well as aqueous solution.

SUPPLEMENTARY MATERIAL

See the supplementary material for technical parameters of the calculations and data supporting the analyses and conclusions presented in this work.

ACKNOWLEDGMENTS

This research was funded by the Deutsche Forschungsgemeinschaft (DFG, German Research Foundation)—No. 396890929/GRK 2482.

DATA AVAILABILITY

The data that support the findings of this study are available from the corresponding author upon reasonable request.

REFERENCES

[1] S. Grimme and M. Waletzke, J. Chem. Phys. **111**, 5645 (1999).
[2] M. Kleinschmidt, C. M. Marian, M. Waletzke, and S. Grimme, J. Chem. Phys. **130**, 044708 (2009).
[3] C. M. Marian, A. Heil, and M. Kleinschmidt, Wiley Interdiscip. Rev.: Comput. Mol. Sci. **9**, e1394 (2019).
[4] M. R. Silva-Junior, M. Schreiber, S. P. A. Sauer, and W. Thiel, J. Chem. Phys. **129**, 104103 (2008).
[5] C. M. Marian and N. Gilka, J. Chem. Theory Comput. **4**, 1501 (2008).
[6] I. Lyskov, M. Kleinschmidt, and C. M. Marian, J. Chem. Phys. **144**, 034104 (2016).
[7] A. Heil, M. Kleinschmidt, and C. M. Marian, J. Chem. Phys. **149**, 164106 (2018).
[8] M. Kleinschmidt, J. Tatchen, and C. M. Marian, J. Comput. Chem. **23**, 824 (2002).
[9] M. Kleinschmidt and C. M. Marian, Chem. Phys. **311**, 71 (2005).
[10] M. Kleinschmidt, J. Tatchen, and C. M. Marian, J. Chem. Phys. **124**, 124101 (2006).
[11] C. M. Marian, Wiley Interdiscip. Rev.: Comput. Mol. Sci. **2**, 187 (2012).
[12] V. Rai-Constapel, M. Etinski, and C. M. Marian, J. Phys. Chem. A **117**, 3935 (2013).
[13] M. Etinski, V. Rai-Constapel, and C. M. Marian, J. Chem. Phys. **140**, 114104 (2014).
[14] T. J. Penfold, E. Gindensperger, C. Daniel, and C. M. Marian, Chem. Rev. **118**, 6975 (2018).
[15] R. Send and F. Furche, J. Chem. Phys. **132**, 044107 (2010).
[16] Z. Li and W. Liu, J. Chem. Phys. **141**, 014110 (2014).
[17] Q. Ou, S. Fatehi, E. Alguire, Y. Shao, and J. E. Subotnik, J. Chem. Phys. **141**, 024114 (2014).
[18] X. Zhang and J. M. Herbert, J. Chem. Phys. **142**, 064109 (2015).
[19] O. Christiansen, J. Chem. Phys. **110**, 711 (1999).
[20] A. Tajti and P. G. Szalay, J. Chem. Phys. **131**, 124104 (2009).
[21] S. Faraji, S. Matsika, and A. I. Krylov, J. Chem. Phys. **148**, 044103 (2018).

The Journal of Chemical Physics ARTICLE scitation.org/journal/jcp

[22]B. H. Lengsfield, P. Saxe, and D. R. Yarkony, J. Chem. Phys. **81**, 4549 (1984).
[23]P. Saxe, B. H. Lengsfield III, and D. R. Yarkony, Chem. Phys. Lett. **113**, 159 (1984).
[24]K. L. Bak, P. Jorgensen, H. J. A. Jensen, J. Olsen, and T. Helgaker, J. Chem. Phys. **97**, 7573 (1992).
[25]J. W. Snyder, E. G. Hohenstein, N. Luehr, and T. J. Martínez, J. Chem. Phys. **143**, 154107 (2015).
[26]I. F. Galván, M. G. Delcey, T. B. Pedersen, F. Aquilante, and R. Lindh, J. Chem. Theory Comput. **12**, 3636 (2016).
[27]J. W. Park and T. Shiozaki, J. Chem. Theory Comput. **13**, 2561 (2017).
[28]H. Lischka, M. Dallos, P. G. Szalay, D. R. Yarkony, and R. Shepard, J. Chem. Phys. **120**, 7322 (2004).
[29]M. Dallos, H. Lischka, R. Shepard, D. R. Yarkony, and P. G. Szalay, J. Chem. Phys. **120**, 7330 (2004).
[30]Y. G. Khait, D. Theis, and M. R. Hoffmann, Mol. Phys. **108**, 2703 (2010).
[31]P. Habitz and C. Votava, J. Chem. Phys. **72**, 5532 (1980).
[32]Q. Peng, Y. Niu, Q. Shi, X. Gao, and Z. Shuai, J. Chem. Theory Comput. **9**, 1132 (2013).
[33]S. Hammes-Schiffer and J. C. Tully, J. Chem. Phys. **101**, 4657 (1994).
[34]E. Tapavicza, I. Tavernelli, and U. Rothlisberger, Phys. Rev. Lett. **98**, 023001 (2007).
[35]J. Pittner, H. Lischka, and M. Barbatti, Chem. Phys. **356**, 147 (2009).
[36]H. Köppel, W. Domcke, and L. S. Cederbaum, Adv. Chem. Phys. **57**, 59 (1984).
[37]I. Lyskov and C. M. Marian, J. Phys. Chem. C **121**, 21145 (2017).
[38]F. Plasser, M. Ruckenbauer, S. Mai, M. Oppel, P. Marquetand, and L. González, J. Chem. Theory Comput. **12**, 1207 (2016).
[39]S. P. Neville, I. Seidu, and M. S. Schuurman, J. Chem. Phys. **152**, 114110 (2020).
[40]H. Satzger, B. Schmidt, C. Root, W. Zinth, B. Fierz, F. Krieger, T. Kiefhaber, and P. Gilch, J. Phys. Chem. A **108**, 10072 (2004).
[41]B. Heinz, B. Schmidt, C. Root, H. Satzger, F. Milota, B. Fierz, T. Kiefhaber, W. Zinth, and P. Gilch, Phys. Chem. Chem. Phys. **8**, 3432 (2006).
[42]B. R. Henry and M. Kasha, Annu. Rev. Phys. Chem. **19**, 161 (1968).
[43]B. R. Henry and W. Siebrand, J. Chem. Phys. **54**, 1072 (1971).
[44]B. R. Henry and W. Siebrand, in *Organic Molecular Photophysics*, edited by J. B. Birks (John Wiley & Sons, London; New York, 1973), Vol. 1, pp. 153–237.
[45]C. M. Marian, in *Reviews in Computational Chemistry*, edited by K. Lipkowitz and D. Boyd (Wiley; Wiley-VCH, Weinheim, 1999; 2001), Vol. 17, pp. 99–204.
[46]J. Tatchen, N. Gilka, and C. M. Marian, Phys. Chem. Chem. Phys. **9**, 5209 (2007).
[47]J. Tatchen and C. M. Marian, Phys. Chem. Chem. Phys. **8**, 2133 (2006).
[48]M. Etinski, J. Tatchen, and C. M. Marian, J. Chem. Phys. **134**, 154105 (2011).
[49]M. Etinski, J. Tatchen, and C. M. Marian, Phys. Chem. Chem. Phys. **16**, 4740 (2014).
[50]D. J. Tannor, *Introduction to Quantum Mechanics: A Time-Dependent Perspective* (University Science Books, 2006).
[51]F. G. Mehler, J. Reine Angew. Math. **66**, 161 (1866).
[52]J. J. Markham, Rev. Mod. Phys. **31**, 956 (1959).
[53]R. Islampour and M. Miralinaghi, J. Phys. Chem. A **111**, 9454 (2007).
[54]M. Sapunar, T. Piteša, D. Davidović, and N. Došlić, J. Chem. Theory Comput. **15**, 3461 (2019).
[55]L. N. Trefethen and D. Bau, *Numerical Linear Algebra* (Society for Industrial and Applied Mathematics, Philadelphia, 1997).
[56]S. Lee, E. Kim, S. Lee, and C. H. Choi, J. Chem. Theory Comput. **15**, 882 (2019).
[57]S. Mai, P. Marquetand, and L. Gonzaléz, Wiley Interdiscip. Rev.: Comput. Mol. Sci. **8**, e1370 (2018).
[58]H. Lischka, T. Müller, P. G. Szalay, I. Shavitt, R. M. Pitzer, and R. Shepard, Wiley Interdiscip. Rev.: Comput. Mol. Sci. **1**, 191 (2011).
[59]H. Lischka, R. Shepard, R. M. Pitzer, I. Shavitt, M. Dallos, T. Müller, P. G. Szalay, M. Seth, G. S. Kedziora, S. Yabushita, and Z. Zhang, Phys. Chem. Chem. Phys. **3**, 664 (2001).
[60]H. Lischka, R. Shepard, I. Shavitt, R. M. Pitzer, M. Dallos, T. Müller, P. G. Szalay, F. B. Brown, R. Ahlrichs, H. J. Böhm, A. Chang, D. C. Comeau, R. Gdanitz, H. Dachsel, C. Ehrhardt, M. Ernzerhof, P. Höchtl, S. Irle, G. Kedziora, T. Kovar, V. Parasuk, M. J. M. Pepper, P. Scharf, H. Schiffer, M. Schindler, M. Schüler, M. Seth, E. A. Stahlberg, S. Y. J.-G. Zhao, Z. Zhang, M. Barbatti, S. Matsika, M. Schuurmann, D. R. Yarkony, S. R. Brozell, E. V. Beck, J.-P. Blaudeau, M. Ruckenbauer, B. Sellner, F. Plasser, J. J. Szymczak, R. F. K. Spada, and A. Das, COLUMBUS, an *ab initio* electronic structure program, release 7.0, 2017.
[61]O. Vahtras, J. Almlöf, and M. W. Feyereisen, Chem. Phys. Lett. **213**, 514 (1993).
[62]F. Weigend, M. Häser, H. Patzelt, and R. Ahlrichs, Chem. Phys. Lett. **294**, 143 (1998).
[63]K. K. Innes, I. G. Ross, and W. R. Moomaw, J. Mol. Spectrosc. **132**, 492 (1988).
[64]L. Seidner, G. Stock, A. L. Sobolewski, and W. Domcke, J. Chem. Phys. **96**, 5298 (1992).
[65]C. Woywod, W. Domcke, A. L. Sobolewski, and H. J. Werner, J. Chem. Phys. **100**, 1400 (1994).
[66]G. A. Worth, H.-D. Meyer, and L. S. Cederbaum, J. Chem. Phys. **105**, 4412 (1996).
[67]A. Raab, G. A. Worth, H.-D. Meyer, and L. S. Cederbaum, J. Chem. Phys. **110**, 936 (1999).
[68]R. Berger, C. Fischer, and M. Klessinger, J. Phys. Chem. A **102**, 7157 (1998).
[69]F. Dinkelbach and C. M. Marian, J. Serb. Chem. Soc. **84**, 819 (2019).
[70]G. Fischer, Can. J. Chem. **71**, 1537 (1993).
[71]TURBOMOLE, A Development of University of Karlsruhe and Forschungszentrum Karlsruhe GmbH, 1989–2007, TURBOMOLE GmbH, since 2007; available from http://www.turbomole.com.
[72]J. J. Cavaleri, K. Prater, and R. M. Bowman, Chem. Phys. Lett. **259**, 495 (1996).
[73]C. Ley, F. Morlet-Savary, J. P. Fouassier, and P. Jacques, J. Photochem. Photobiol., A **137**, 87 (2000).
[74]H. J. Pownall and J. R. Huber, J. Am. Chem. Soc. **93**, 6429 (1971).
[75]V. Ravi Kumar and S. Umapathy, J. Raman Spectrosc. **47**, 1220 (2016).
[76]J. T. K. Tomić and C. M. Marian, J. Phys. Chem. A **109**, 8410 (2005).
[77]S. Salzmann, J. Tatchen, and C. M. Marian, J. Photochem. Photobiol., A **198**, 221 (2008).
[78]M. Bracker, F. Dinkelbach, O. Weingart, and M. Kleinschmidt, Phys. Chem. Chem. Phys. **21**, 9912 (2019).
[79]F. Rakowitz, M. Casarrubios, L. Seijo, and C. M. Marian, J. Chem. Phys. **108**, 7980 (1998).
[80]G. Sánchez-Sanz, Z. Barandiarán, and L. Seijo, Chem. Phys. Lett. **498**, 226 (2010).
[81]C. M. Marian, Annu. Rev. Phys. Chem. **72**, 616 (2021).

Supplementary Material for Internal conversion of singlet and triplet states employing numerical DFT/MRCI derivative couplings: Implementation, tests and application to xanthone

Mario Bracker, Christel M. Marian, Martin Kleinschmidt*

Institute of Theoretical and Computational Chemistry,

Heinrich-Heine-University Düsseldorf,

Universitätsstraße 1, 40225 Düsseldorf, Germany

*Electronic address: Martin.Kleinschmidt@hhu.de

S1. DATA RELATED TO TEST AND VALIDATION RUNS

The present version of the DELTA program is executed sequentially and all reported cpu times were measured on a single core of a 2.8 GHz AMD EPYC "ROME" 7402 CPU.

A. Formaldehyde

All calculations on formaldehyde were performed at the ground state geometry. The analytic NACME was computed with the Columbus package [1–3] using a 6-31G basis [4] and state averaging of the CASSCF wave function over 2 roots in the CAS(4,4) or 6 roots in the CAS(6,6) setup. For the computation of the numerical coupling, the molecular orbital coefficients generated by Columbus were used as input for the MRCI program used in our laboratories. The latter performs a resolution-of-the-identity (RI) approximation of the two-electron integrals [5, 6]. For this purpose, the TZVP auxiliary basis [7] was utilized. No symmetry constraints were imposed.

The step size ϵ for the numerical determination of the NACMEs by our finite-differences technique was set to 0.01 a_0. The sensitivity of the derivative coupling was examined w.r.t. various wave function cutoff parameters as well as the contribution of excitation classes.

Table S1: Coordinates (a_0) of formaldehyde at the ground state minimum.

atom	x	y	z
C	0.000000000	0.000000000	0.043563280
O	0.000000000	0.000000000	2.342632440
H	1.765925050	0.000000000	-1.057375190
H	-1.765925050	0.000000000	-1.057375200

Table S2: Absolute energies (E_h) of various triplet states at the S_0 geometry of formaldehyde.

State	Columbus	MRCI
T_1/CAS(4,4)	–113.723922	–113.723749
T_2/CAS(4,4)	–113.665322	–113.665144
T_6/CAS(6,6)	–113.381086	–113.380986
T_8/CAS(6,6)	–113.312917	–113.312841

Table S3: Leading CSF coefficients and respective annihilators (ann) and creators (cre) of the $T_2(A_1)$ and $T_1(A_2)$ CASSCF(4,4) wave functions as determined by the Columbus package.

$T_2(A_1)$			$T_1(A_2)$		
coefficient	ann	cre	coefficient	ann	cre
0.9974067243	1	3	0.9985954446	2	3
0.0665475584	1 2 2	3 4 4	-0.0449357381	1 2 2	3 3 4
-0.0238584229	1 2	3 4	-0.0246225308	2 2	3 4
0.0111685237	2	4	-0.0082995997	1 1	3 4
0.0049196846	1 1 2	3 4 3	0.0082745043	1	4
0.0041841030	1 2	3 4	-0.0061597011	1 1 2	3 4 4
-0.0039469655	1 2	3 4	0.0022074796	1 2	4 4

Table S4: Leading CSF coefficients of the $T_2(A_1)$ and $T_1(A_2)$ wave functions (MRCI code) alongside the respective annihilators (ann) and creators (cre) with regard to the HF anchor determinant.

$T_2(A_1)$			$T_1(A_2)$		
coefficient	ann	cre	coefficient	ann	cre
-0.9974086	1	3	0.9985936	2	3
0.0665314	1 2 2	3 4 4	0.0449314	1 2 2	3 3 4
-0.0238914	1 2	3 4	-0.0247030	2 2 3	4
0.0110574	2	4	-0.0083097	1 1	3 4
-0.0049042	1 1 2	3 4 3	-0.0082717	1	4
-0.0040528	1 2	3 4	-0.0061399	1 1 2	3 4 4
-0.0040190	1 2	3 4	0.0022298	1 2	4 4

Table S5: Leading CSF coefficients and respective annihilators (ann) and creators (cre) of the $T_8(A_2)$ and $T_6(B_2)$ CASSCF(6,6) wave functions as determined by the Columbus package.

$T_8(A_2)$			$T_6(B_2)$		
coefficient	ann	cre	coefficient	ann	cre
-0.9732756823	2	6	0.9900009188	2	5
-0.2044448014	2 3	4 4	0.0960143105	3 3	4 5
-0.0532155236	2 3	5 5	0.0564766885	2 3	5 6
-0.0377295474	3 3	4 6	0.0389207378	2 3	5 6
0.0347926373	3	4	-0.0371882299	2 2	4 5
-0.0337228550	1 1	4 6	0.0299079096	1 1	4 5
0.0271383607	2 2	4 6	-0.0232793974	2 3 3	4 4 5
-0.0254917693	2 3	6 6	0.0231006674	1	4
-0.0243183761	1 2	5 6	0.0230687528	2 3 3	5 6 6
0.0208757356	2 3 3	4 4 6	-0.0196040856	2 2 3	4 5 6
0.0185876597	2 2 3	4 6 6	0.0187835733	1 2	6 6
-0.0182961269	1 1 2	4 4 6	0.0162803691	1 1 2	4 4 5
-0.0172513580	1 3	4 5	-0.0161550551	2 3	5 6
0.0163021937	2 3 3	5 5 6	-0.0127760723	2 2 3	4 5 6
0.0130307655	1 2 2	4 5 6	0.0127138688	2 2 3	4 5 6

Table S6: Leading CSF coefficients of the $T_8(A_2)$ and $T_6(B_2)$ wave functions (MRCI code) alongside the respective annihilators (ann) and creators (cre) with regard to the HF anchor determinant.

$T_8(A_2)$			$T_6(B_2)$		
coefficient	ann	cre	coefficient	ann	cre
0.9732215	2	6	0.9899650	2	5
-0.2044878	2 3	4 4	-0.0962947	3 3	4 5
-0.0534254	2 3	5 5	-0.0566450	2 3	5 6
-0.0378480	3 3	4 6	0.0388173	2 3	5 6
0.0348139	3	4	0.0373235	2 2	4 5
-0.0339175	1 1	4 6	-0.0299348	1 1	4 5
0.0274747	2 2	4 6	-0.0232134	2 3 3	4 4 5
-0.0258725	2 3	6 6	-0.0231119	1	4
-0.0244151	1 2	5 6	-0.0229566	2 3 3	5 6 6
-0.0208305	2 3 3	4 4 6	0.0195592	2 2 3	4 5 6
0.0186698	2 2 3	4 6 6	-0.0187736	1 2	6 6
-0.0183725	1 1 2	4 4 6	-0.0162998	1 1 2	4 4 5
0.0171822	1 3	4 5	0.0162426	2 3	5 6
-0.0163565	2 3 3	5 5 6	0.0128417	2 2 3	4 5 6
0.0130397	1 2 2	4 5 6	0.0127168	2 2 3	4 5 6

Table S7: Non-adiabatic coupling matrix elements (a_0^{-1}) of various formaldehyde test cases at the ground-state geometry. Truncated MRCI wave functions were not renormalized.

$\langle T_2 \vert \vec{\nabla}_{Y(H1)} \vert T_1 \rangle$		norm of the MRCI wave function		# of spin	selection
analytical	numerical	T_2	T_1'	factors	criterion[a]
	0.227264	0.9974085810	0.9985933464	4	$\vert\vert d_i \vert\vert > 0.9$
	0.227130	0.9999879732	0.9999091362	72	$\vert\vert d_i \vert\vert > 0.01$
	0.225278	0.9974698713	0.9986276060	64	all S
	0.225629	0.9977722800	0.9989712395	484	all SD
	0.225769			564	1-exc.
0.225591	0.225867	1.0000000000	1.0000000000	900	no truncation
$\langle T_8 \vert \vec{\nabla}_{X(C)} \vert T_6 \rangle$		norm of the MRCI wave function		# of spin	selection
analytical	numerical	T_8	T_6'	factors	criterion[a]
	2.511387	0.9732214912	0.9897638680	4	$\vert\vert d_i \vert\vert > 0.9$
	2.514265	0.9959064236	0.9969124338	60	$\vert\vert d_i \vert\vert > 0.05$
	2.528650	0.9990586919	0.9987941755	480	$\vert\vert d_i \vert\vert > 0.02$
	4.080482	0.9998018953	0.9995664179	1152	$\vert\vert d_i \vert\vert > 0.015$
	3.803030	0.9999073833	0.9996584655	1428	$\vert\vert d_i \vert\vert > 0.0125$
	3.855966	0.9999999992	0.9999999866	16168	$\vert\vert d_i \vert\vert > 0.0001$
	4.058911	0.9738439708	0.9901634971	324	all S
	3.842277	0.9991077385	0.9988374053	11664	all SD
	3.853595	0.9999909899	0.9999816300	73984	all SDT
	3.852203			51016	1-exc.
3.851424	3.853828	1.0000000000	1.0000000000	144400	no truncation

[a]The $\vert\vert d_i \vert\vert$ criterion refers to the modulus of the indivudual CSF coefficient.

S, D, T stand for single, double, triple excitations w.r.t. the anchor configuration.

1-exc.: Only pairs of configurations contribute to the NACME which differ by a mutual single excitation.

B. Pyrazine

All calculations on pyrazine were performed at the D_{2h}-symmetric ground state geometry optimized in previous work. [8] The RKS orbitals used as one-particle basis for the DFT/MRCI run were generated with Turbomole [9] using the TZVP basis set [10] and the BH-LYP functional. Unless noted otherwise, an integration grid size `m4` and SCF convergence thresholds of `$scfconv=7` and `$denconv=1.0E-8` were employed in the orbital optimization step. The TZVP auxiliary basis [7] was utilized for the RI approximation of the two-electron integrals. In the MRCI runs, we employed the original DFT/MRCI Hamiltonian by Grimme and Waletzke [6] with standard parameters and a selector threshold of $\delta E_{sel} = 1.0 E_h$. No symmetry constraints were imposed in these calculations. The MRCI reference space was generated iteratively starting with all single and double excitations of 10 electrons in 13 active orbitals. In a second step, all configurations with CI coefficients larger than 0.003 in one of the 5 lowest roots of the initial step were included in the reference space. Unless noted otherwise, the default convergence threshold ($0.5 \times 10^{-5} E_h$) was employed in the iterative Davidson solver of the DFT/MRCI secular equation.

Table S8: Coordinates of pyrazine at the ground state minimum.

atom	x	y	z
C	-2.12802545844861	1.31260676977036	0.00000000000000
C	-2.12802545844861	-1.31260676977036	0.00000000000000
N	0.00000000000000	-2.64411084402921	0.00000000000000
C	2.12802545844861	-1.31260676977036	0.00000000000000
C	2.12802545844861	1.31260676977036	0.00000000000000
N	0.00000000000000	2.64411084402921	0.00000000000000
H	-3.88944320982055	2.36594252195867	0.00000000000000
H	-3.88944320982055	-2.36594252195867	0.00000000000000
H	3.88944320982055	-2.36594252195867	0.00000000000000
H	3.88944320982055	2.36594252195867	0.00000000000000

1. SCF and CI convergence parameters

Setting a SCF convergence parameter `$scfconv=<integer>` in the Turbomole input means that the SCF energy is converged to at least $10^{-\texttt{integer}}$ E_h in the dscf iterative eigenvalue solver. The parameter `$denconv=<real>` refers to the convergence threshold of the SCF density matrix. The standard convergence threshold of the Davidson diagonalization of the DFT/MRCI Hamiltonian matrix is 0.5×10^{-5} E_h. The parameter `$prec=<real>` is used as a scaling factor for setting a tighter threshold in the Davidson procedure.

Table S9: Dependence of the derivative coupling $\langle T_2 \,|\, \frac{\partial}{\partial Q_{10a}} \,|\, T_1 \rangle \Big|_{S_{0,min}}$ of pyrazine on parameters `$scfconv`, `$denconv` and `$prec`. Nonorthogonal overlaps $\langle T_2(\vec{R}) \,|\, T_1'(\vec{R}') \rangle$ are computed for displacements $\vec{R}' = \vec{R} \pm 0.01 \; \vec{e}_{Q10a}$ along the dimensionless normal mode coordinates of the ν_{10a} vibrational mode.

	Parameter		
NACME	`$scfconv`	`$denconv`	`$prec`
1.62944238662562	7	1.0E-08	1
1.65567822155470	8	1.0E-08	1
1.66133063265500	9	1.0E-08	1
1.66148448902611	10	1.0E-08	1
1.62959550803048	7	1.0E-09	1
1.65223458780458	7	1.0E-10	1
1.66169977427017	7	1.0E-11	1
1.62940810111565	7	1.0E-08	0.1
1.62939489215459	7	1.0E-08	0.01
1.62940047227138	7	1.0E-08	0.001
1.66180114282537	10	1.0E-11	1
1.66176242577145	10	1.0E-11	0.001

Table S10: Derivative couplings $\langle \mathrm{T}_2 \,|\, \frac{\partial}{\partial Q} \,|\, \mathrm{T}_1 \rangle$ of the $\mathrm{T}_2\,(^3B_{2u})$ and $\mathrm{T}_1\,(^3B_{3u})$ wave functions of pyrazine at the S_0 reference geometry $\vec{R}$ obtained numerically by computing nonorthogonal overlaps $\langle \mathrm{T}_2(\vec{R}) \,|\, \mathrm{T}_1'(\vec{R}') \rangle$ for displacements $\vec{R}' = \vec{R} + 0.01\ \vec{e}_{Q\kappa}$ along all 24 normal modes.

Normal	Davidson Diagonalization Threshold in DFT/MRCI [$\mathrm{E_h}$]		
Mode	0.5×10^{-5}	0.5×10^{-6}	0.5×10^{-7}
1	–0.00000547287318	–0.00000035478698	–0.00000004496192
2	–0.00000170447907	–0.00000052138671	–0.00000008960016
3	0.00000012203163	–0.00000010126089	0.00000000271410
4	–0.00001270438702	–0.00000299575714	–0.00000018675052
5	0.00000091211561	–0.00000028850739	0.00000030037834
6	–0.00000308890141	–0.00000021740598	–0.00000001999311
7	1.62944238662562	1.62940810111565	1.62939489215459
8	–0.00000739441362	–0.00000047405545	–0.00000005633274
9	–0.00000457498771	–0.00000029917729	0.00000004975296
10	0.00000554203036	0.00000039143871	0.00000003973005
11	–0.00000117950360	–0.00000016598735	–0.00000001223329
12	0.00000721555002	0.00000045274767	0.00000005354430
13	–0.00000756762700	–0.00000048718473	–0.00000005075210
14	–0.00000539490714	–0.00000040739735	–0.00000005935211
15	–0.00000028948185	–0.00000001709860	–0.00000001238558
16	0.00000582610744	0.00000032208063	0.00000004601051
17	0.00000552410718	0.00000038397235	0.00000002904622
18	–0.00000761643915	–0.00000049066617	–0.00000005097822
19	–0.00000536139963	0.00000054489880	–0.00000000643513
20	–0.00000868163183	0.00000092053747	0.00000017409758
21	0.00000859713531	0.00000098032543	0.00000006328628
22	0.00000767253200	0.00000050038051	0.00000005542700
23	0.00000718500584	0.00000046900995	0.00000005246747
24	–0.00000018737233	–0.00000012740282	0.00000001317866

2. Choice of magnetic spin quantum number

Table S11: Overlap of the renormalized T_2 ($^3B_{2u}$) DFT/MRCI wave function of pyrazine at the S_0 reference geometry $\vec{R}$ and the T_1' ($^3B_{3u}$) wave function at $\vec{R}' = \vec{R} + 0.1\vec{e}_{Q10a}$ for different values of the magnetic spin quantum number M_S and of the cutoff parameter t_{cutoff}. A configuration is included in the evaluation of the NACME, if at least one of its CSF coefficients d_i fulfills the condition $||d_i|| \geq t_{\text{cutoff}}$.

Cutoff	Wave Function Norm		$\langle T_2(\vec{R}) \,\vert\, T_1'(\vec{R}')\rangle \times 10^2$	
t_{cutoff}	T_2	T_1'	$M_S = 0$	$M_S = 1$
10^{-01}	0.985689451264332	0.982698699497338	2.595272096429573	2.595272096429570
10^{-02}	0.999408225400078	0.998883888758683	2.670835341542079	2.670835341542078
10^{-03}	0.999976555714491	0.999960576946983	2.781472110299374	2.781472110299386
10^{-04}	0.999999903995773	0.999999613077459	2.783852857948308	2.783852857948347
10^{-05}	0.999999998355061	0.999999998303963	2.783983000111110	2.783983000111135
10^{-06}	0.999999999923356	0.999999999983635	2.784200269425108	2.784200269425129
10^{-07}	0.999999999995544	0.999999999997158	2.784202095336776	2.784202095336849
10^{-08}	0.999999999999999	0.999999999999998	2.784246031573553	2.784246031573617
10^{-09}	0.999999999999999	0.999999999999999	2.785547948023917	2.785547948023979
10^{-10}	1.000000000000000	1.000000000000000	2.785061122623378	2.785061122623440

Table S12: Number of spin factors and cpu time required for determining the overlap of the wave functions described in Table S11. Only spin factors corresponding to single excitations were stored and reused.

Cutoff	Computed		Reused		Total		CPU Time [s]	
t_{cutoff}	$M_S = 0$	$M_S = 1$	$M_S = 0$	$M_S = 1$	$M_S = 0$	$M_S = 1$	$M_S = 0$	$M_S = 1$
10^{-01}	18	12	14	4	32	16	0.1	0.1
10^{-02}	3386	3218	6038	3774	9424	6992	0.1	0.2
10^{-03}	163868	168644	289692	199876	453560	368520	2.0	2.3
10^{-04}	789392	1005842	1656352	1001328	2445744	2007170	10.3	12.1
10^{-05}	1498657	2094143	3396051	1881317	4894708	3975460	18.7	23.3
10^{-06}	2053880	2920230	4943320	2671854	6997200	5592084	27.5	32.8
10^{-07}	12638702	16701121	27950946	16456315	40589648	33157436	145.1	194.6
10^{-08}	52481854	75972141	125964898	68769359	178446752	144741500	615.2	802.3
10^{-09}	53008676	76826381	128147548	69639225	181156224	146465606	621.2	810.1
10^{-10}	53047938	76903610	128350894	69716242	181398832	146619852	622.6	814.1

C. Xanthone test cases

1. *Truncation of the Wave Function Expansion*

Table S13: Test of the single excitation approximation for DFT/MRCI NACMEs (a_0^{-1}) of xanthone in vacuum.

Normal	$\langle {}^3(n\pi^*) \vert \vec{\nabla}_{Qa_2} \vert {}^3(\pi\pi^*)\rangle$		$\langle {}^1(n\pi^*) \vert \vec{\nabla}_{Qa_2} \vert {}^1(\pi\pi^*)\rangle$	
mode	full expansion	1-exc.[a]	full expansion	1-exc.[a]
1	0.47984	0.48003	0.03795	0.03791
2	0.44710	0.44708	0.03138	0.03151
3	-1.13539	-1.13548	0.00976	0.00972
4	0.15439	0.15447	0.02716	0.02723
5	-0.12641	-0.12653	-0.03988	-0.03982
6	0.27375	0.27377	0.00073	0.00073
7	0.29702	0.29702	0.05077	0.05055
8	-0.26733	-0.26732	-0.01393	-0.01384
9	0.09564	0.09566	-0.05152	-0.05145
# spin factors[b]	$\approx 18 \times 10^9$	$\approx 50 \times 10^6$	$\approx 35 \times 10^9$	$\approx 80 \times 10^6$
cpu times[b]	$\approx$ 24 h	$\approx$ 7 min	$\approx$ 48 h	$\approx$ 11 min

[a] Only pairs of configurations contribute to the NACME which differby a mutual single excitation.

[b] Average values per mode

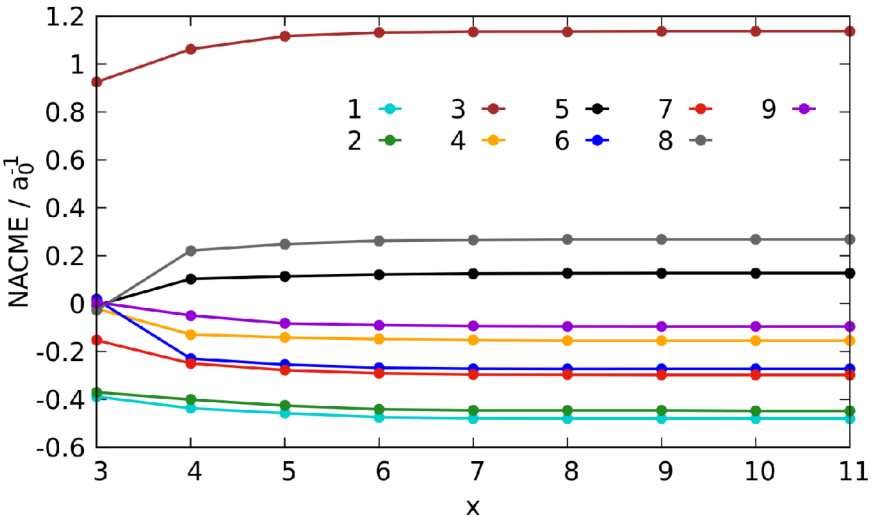

Figure S1: Influence of the wave function cutoff parameter t_{norm} ($= 10^{-x}$) on the magnitude of the NACMEs $\langle {}^3(n\pi^*) \,|\, \vec{\nabla}_{Q_\kappa} \,|\, {}^3(\pi\pi^*) \rangle$ for the a_2-symmetric normal modes at the equilibrium geometry of the ${}^3(\pi\pi^*)$ state of xanthone in vacuum. The indices κ are assigned to different colors and the corresponding displacement vectors are visualized in Figure S2.

Table S14: Average single-processor cpu times (s) for one-sided derivatives $\langle {}^3(n\pi^*)[\vec{R}] \,|\, \vec{\nabla}_{Qa_2} \,|\, {}^3(\pi\pi^*)[\vec{R}'] \rangle$ of xanthone at the equilibrium geometry of ${}^3(\pi\pi^*)$ in vacuum, wave function expansion lengths (averaged over all displacements $\vec{R}'$) and corresponding ${}^3(\pi\pi^*) \rightsquigarrow {}^3(n\pi^*)$ IC rate constants (s^{-1}). Note that the coefficient-based configuration selection has been performed in addition to applying the 1-exc. approximation.

t_{norm}	cpu time	confs ${}^3(n\pi^*)[\vec{R}]$	confs ${}^3(\pi\pi^*)[\vec{R}']$	IC rate constant
1E-05	89	6795	3965	1.92358e+14
1E-06	153	10386	7200	2.09611e+14
1E-07	213	12949	11282	2.15595e+14
1E-08	272	14571	15905	2.16950e+14
1E-09	323	15525	21015	2.17200e+14
1E-10	362	16051	25390	2.17241e+14
1E-11	390	16341	28798	2.17243e+14
-	2575	66952	66952	2.17243e+14

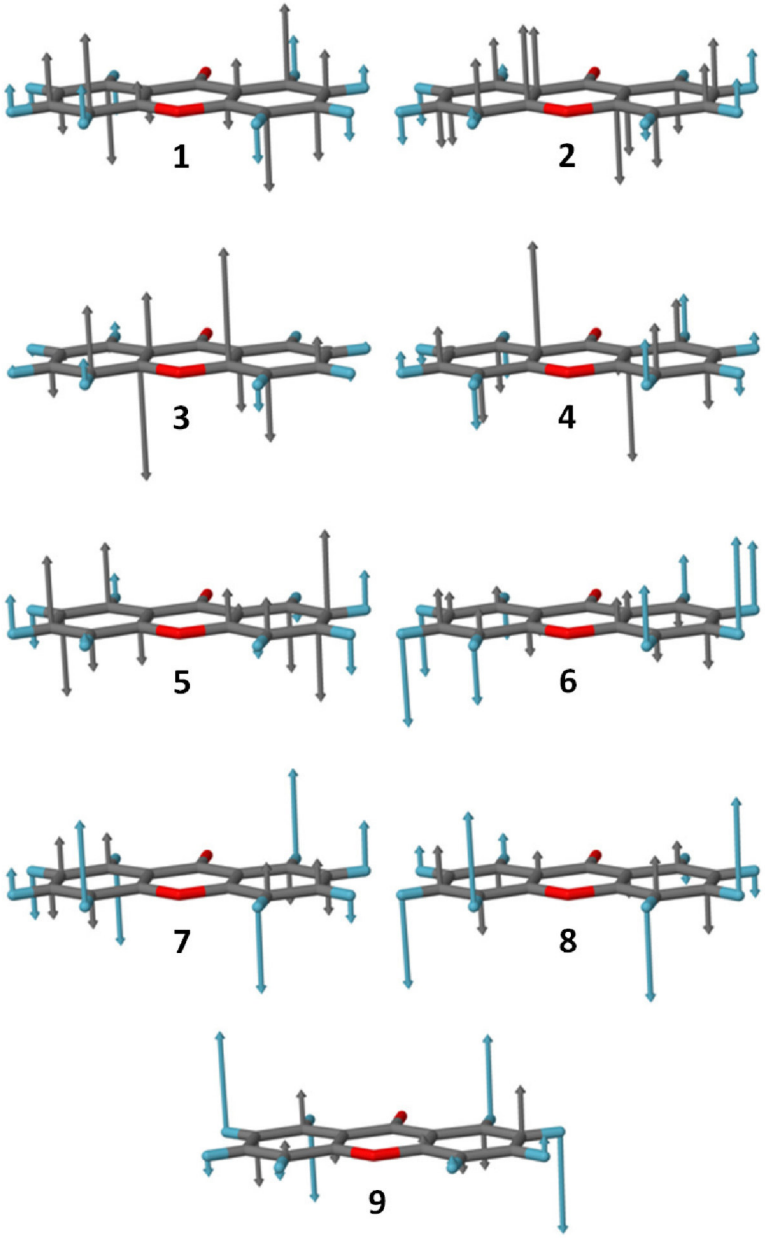

Figure S2: Displacement vectors of the a_2-symmetric normal modes at the equilibrium geometry of the $^3(\pi\pi^*)$ state of xanthone in vacuum.

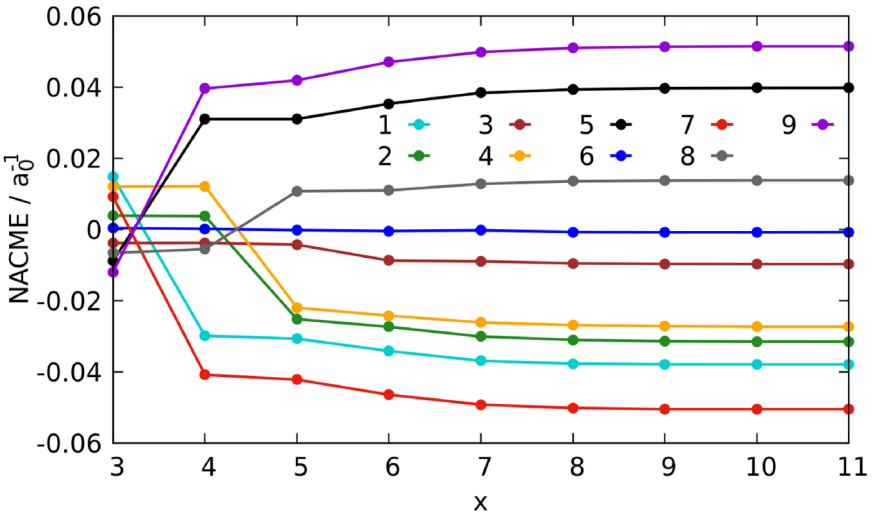

Figure S3: Influence of the wave function cutoff parameter t_{norm} ($= 10^{-x}$) on the magnitude of the NACMEs $\langle {}^1(n\pi^*) \,|\, \vec{\nabla}_{Q_\kappa} \,|\, {}^1(\pi\pi^*) \rangle$ for the a_2-symmetric normal modes at the equilibrium geometry of the ${}^1(\pi\pi^*)$ state of xanthone in vacuum. The indices κ are assigned to different colors and the corresponding displacement vectors are visualized in Figure S4. Note that the magnitude of the coupling in the singlet domain is much smaller in comparison to the triplet domain (see Figure S1).

Table S15: Average single-processor cpu times (s) for one-sided derivatives $\langle {}^1(n\pi^*)[\vec{R}] \,|\, \vec{\nabla}_{Qa_2} \,|\, {}^1(\pi\pi^*)[\vec{R}'] \rangle$ of xanthone at the equilibrium geometry of ${}^1(\pi\pi^*)$ in vacuum, wave function expansion lengths (averaged over all displacements $\vec{R}'$) and corresponding ${}^1(\pi\pi^*) \rightsquigarrow {}^1(n\pi^*)$ IC rate constants (s^{-1}). Note that the coefficient-based configuration selection has been performed in addition to applying the 1-exc. approximation.

t_{norm}	cpu time	confs ${}^1(n\pi^*)[\vec{R}]$	confs ${}^1(\pi\pi^*)[\vec{R}']$	IC rate constant
1E-05	168	10676	5615	2.61859e+11
1E-06	267	15836	10150	3.23989e+11
1E-07	360	19669	15383	3.67810e+11
1E-08	437	21803	20843	3.850761+11
1E-09	502	22805	26183	3.90408e+11
1E-10	536	23241	31362	3.91469e+11
1E-11	628	23445	36717	3.91631e+11
-	4145	92920	92920	3.91640e+11

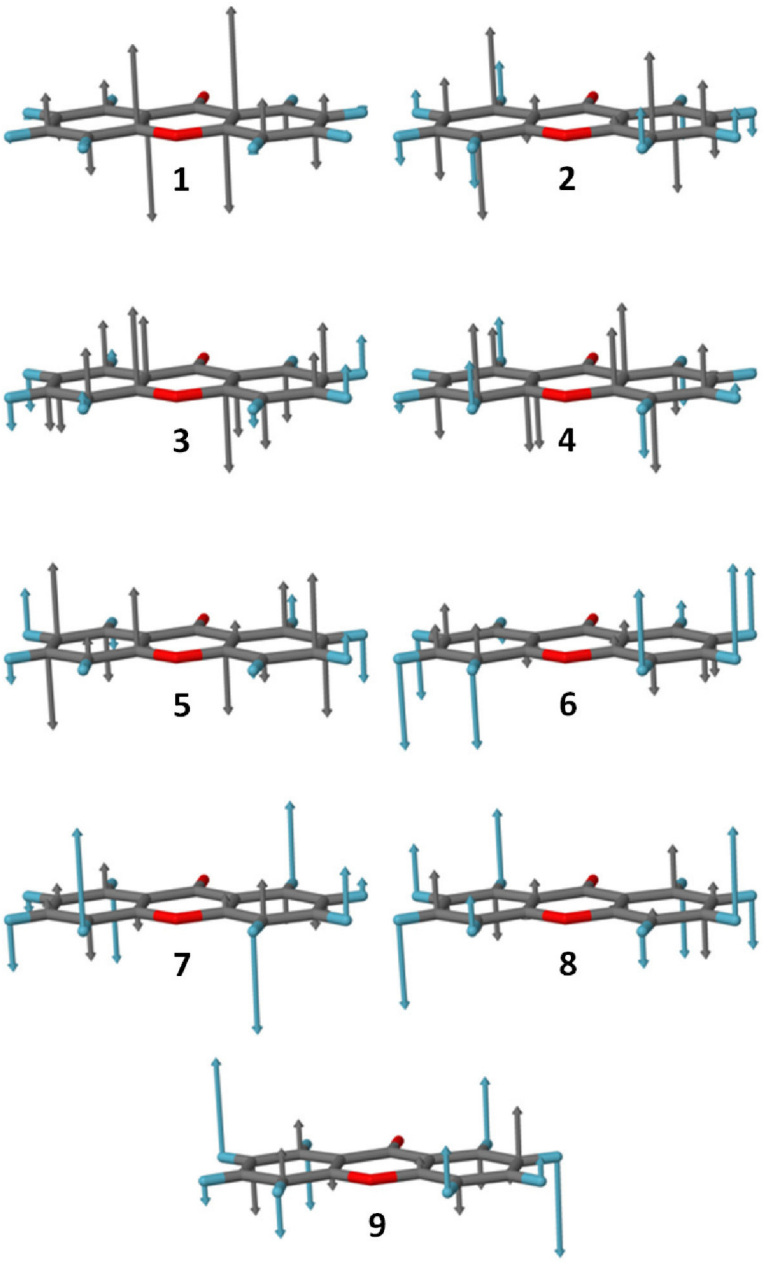

Figure S4: Displacement vectors of the a_2-symmetric normal modes at the equilibrium geometry of the $^1(\pi\pi^*)$ state of xanthone in vacuum.

Table S16: Numerical NACMEs $\langle {}^3(n\pi^*) \,|\, \vec{\nabla}_{Qa_2} \,|\, {}^3(\pi\pi^*)\rangle$ (a_0^{-1}) of xanthone at the equilibrium geometry of ${}^3(n\pi^*)$ in vacuum and cpu times (s) for selected thresholds δ_H of the Hadamard screening, applied on top of the 1-exc. approximation.

	$\langle {}^3(n\pi^*) \,\vert\, \vec{\nabla}_{Qa_2} \,\vert\, {}^3(\pi\pi^*)\rangle$									cpu
δ_H / mode	1	2	3	4	5	6	7	8	9	time
1E-05	-0.48003	-0.44710	1.13546	-0.15447	0.12644	-0.27376	-0.29702	0.26732	-0.09567	2079
1E-06	-0.48003	-0.44708	1.13548	-0.15447	0.12653	-0.27377	-0.29702	0.26732	-0.09566	2137
1E-10	-0.48003	-0.44708	1.13548	-0.15447	0.12653	-0.27377	-0.29702	0.26732	-0.09566	2159
-	-0.48003	-0.44708	1.13548	-0.15447	0.12653	-0.27377	-0.29702	0.26732	-0.09566	2575

Table S17: Numerical NACMEs $\langle {}^1(n\pi^*) \,|\, \vec{\nabla}_{Qa_2} \,|\, {}^1(\pi\pi^*)\rangle$ (a_0^{-1}) of xanthone at the equilibrium geometry of ${}^1(n\pi^*)$ in vacuum and cpu times (s) for selected thresholds δ_H of the Hadamard screening, applied on top of the 1-exc. approximation.

	$\langle {}^1(n\pi^*) \,\vert\, \vec{\nabla}_{Qa_2} \,\vert\, {}^1(\pi\pi^*)\rangle$									cpu
δ_H / mode	1	2	3	4	5	6	7	8	9	time
1E-05	-0.03793	-0.03152	-0.00973	-0.02722	0.03982	-0.00073	-0.05055	0.01386	0.05144	3277
1E-06	-0.03791	-0.03151	-0.00972	-0.02723	0.03982	-0.00073	-0.05055	0.01384	0.05145	3296
1E-10	-0.03791	-0.03151	-0.00972	-0.02723	0.03982	-0.00073	-0.05055	0.01384	0.05145	3391
-	-0.03791	-0.03151	-0.00972	-0.02723	0.03982	-0.00073	-0.05055	0.01384	0.05145	4145

S2. RATE CONSTANT CALCULATIONS FOR XANTHONE

All DFT, DFT/MRCI and SPOCK calculations on xanthone were performed with the same basis sets, density functionals and DFT/MRCI wave function parameters as in previous work. [11] NACMEs and SOCMEs were based on DFT/MRCI calculations for five excited singlet and triplet states, respectively. Phase factors for derivatives of SOCMEs, employed in conjunction with HT-Type calculations, were determined from DFT/MRCI runs for ten roots of singlet and triplet multiplity. State shifts to mimic the solvent environment were applied to the lowest five excited states in the singlet and triplet manifolds.

Rate constants for IC and ISC were determined using the following integration and damping parameters in the VIBES calculations:

- `$interval = 3000`
- `$npoints = 60000`
- `$eta = 10`

A. Calculations in Vacuum

Table S18: ZPVE corrections (eV) on low-lying excited states of xanthone in vacuum (C_{2v}-symmetry).

State	ZPVE correction
$^1(\pi\pi^*)$	-0.20
$^1(n\pi^*)$	-0.12
$^3(\pi\pi^*)$	-0.17
$^3(n\pi^*)$	-0.12

Table S19: Variation of the $^1(\pi\pi^*) \rightsquigarrow {}^1(n\pi^*)$ IC rate constant (s^{-1}) of xanthone with regard to the frequency (cm^{-1}) of the a_2-symmetric deformation mode. A value of $\nu_{a_2} = 310.36514$ cm^{-1} corresponds to the frequency of the analogous normal mode of the C_2-symmetric $^1(\pi\pi^*)$ state.

ν_{a_2}/cm^{-1}	k_{IC} / s
50	3.08198e+11
100	4.37229e+11
150	4.43113e+11
200	4.21291e+11
250	4.033770+11
300	3.93076e+11
310.36514	3.91640e+11
350	3.85935e+11
400	3.80272e+11
450	3.76693e+11
500	3.72771e+11

Table S20: NACMEs (a_0^{-1}) of low-lying xanthone states in vacuum. Only a_2-symmetric normal modes exhibit nonvanishing matrix elements.

	NACME		
Mode	$^1(\pi\pi^*) \rightsquigarrow {}^1(n\pi^*)$	$^3(\pi\pi^*) \rightsquigarrow {}^3(n\pi^*)$	$^3(n\pi^*) \rightsquigarrow {}^3(\pi\pi^*)$
1	-0.03791	-0.48003	0.09181
2	-0.03151	-0.44708	0.00953
3	-0.00972	1.13548	-0.29959
4	-0.02723	-0.15447	0.21516
5	0.03982	0.12653	-0.03040
6	-0.00073	-0.27377	0.08979
7	-0.05055	-0.29702	0.08122
8	0.01384	0.26732	-0.05917
9	0.05145	-0.09566	0.02756

B. Aqueous Solution

Table S21: Applied state shifts (eV) on xanthone states to mimic an aqueous solution environment with two hydrogen-bonded water molecules and a COSMO electrostatic field.

State		Shift
$^1(\pi\pi^*)$	2^1A1	-0.21
	3^1A1	-0.18
$^1(n\pi^*)$	1^1A2	+0.59
	1^1B1	-0.15
	2^1B1	-0.31
$^3(\pi\pi^*)$	1^3A1	-0.19
	2^3A1	-0.02
$^3(n\pi^*)$	1^3A2	+0.62
	1^3B1	-0.10
	2^3B1	-0.16

Table S22: Scan of the (reverse) ISC rate constants (s^{-1}) of El-Sayed-allowed transitions of xanthone in aqueous solution with respect to small variations of the energy separation. An additional red shift of the ($n\pi^*$) state energies by 0.11 eV makes the ZPVE corrected minima of the $^1(\pi\pi^*)$ and $^3(n\pi^*)$ isoenergetic.

Red shift	(Re-)ISC rate constant		
/ eV	$^1(\pi\pi^*) \rightsquigarrow {}^3(n\pi^*)$	$^3(n\pi^*) \rightsquigarrow {}^1(\pi\pi^*)$	$^1(n\pi^*) \rightsquigarrow {}^3(\pi\pi^*)$
0	1.83633e+08	2.33237e+10	2.02647e+08
0.01	2.20787e+08	1.90858e+10	2.23724e+08
0.02	3.83666e+08	2.24669e+10	2.57301e+08
0.03	6.52806e+08	2.60638e+10	2.96538e+08
0.04	7.02763e+08	1.90373e+10	3.44287e+08
0.05	1.23276e+09	2.26894e+10	3.97714e+08
0.06	1.87608e+09	2.34914e+10	4.50380e+08
0.07	1.95327e+09	1.65697e+10	5.12534e+08
0.08	3.67581e+09	2.10163e+10	5.86756e+08
0.09	5.90172e+09	2.31923e+10	6.64664e+08
0.10	5.99053e+09	1.59090e+10	7.74638e+08
0.11	1.45684e+10	2.60551e+10	8.95355e+08
0.12	1.44165e+10	1.77881e+10	1.01732e+09

Table S23: (Reverse) ISC rate constants (s^{-1}) of El-Sayed allowed transitions of xanthone in aqueous solution for temperatures ranging from 280 K to 340 K in HT approximation. The ZPVE corrected minima of $^1(\pi\pi^*)$ and $^3(n\pi^*)$ were set to be isoenergetic.

T	(Re-)ISC rate constant		
/ K	$^1(\pi\pi^*) \rightsquigarrow {}^3(n\pi^*)$	$^3(n\pi^*) \rightsquigarrow {}^1(\pi\pi^*)$	$^1(n\pi^*) \rightsquigarrow {}^3(\pi\pi^*)$
280	1.82022e+10	3.08947e+10	8.66945e+08
290	1.62038e+10	2.82397e+10	8.80804e+08
300	1.45684e+10	2.60551e+10	8.95355e+08
310	1.32275e+10	2.42627e+10	9.10626e+08
320	1.21247e+10	2.27952e+10	9.26649e+08
330	1.12134e+10	2.15948e+10	9.43455e+08
340	1.04561e+10	2.06131e+10	9.61073e+08

Table S24: Scan of the (reverse) ISC rate constants (s^{-1}) of El-Sayed-forbidden transitions of xanthone in aqueous solution with respect to small variations of the energy separation. An additional red shift of the $(n\pi^*)$ state energies by 0.11 eV makes the ZPVE corrected minima of the $^1(\pi\pi^*)$ and $^3(n\pi^*)$ isoenergetic.

Red shift	(Re-)ISC rate constant		
/ eV	$^1(\pi\pi^*) \rightsquigarrow {}^3(\pi\pi^*)$	$^1(n\pi^*) \rightsquigarrow {}^3(n\pi^*)$	$^3(n\pi^*) \rightsquigarrow {}^1(n\pi^*)$
0	1.06833e+09	3.05309e+09	7.28643e+07
0.01	1.11056e+09	2.41201e+09	5.75710e+07
0.02	1.15579e+09	1.91509e+09	4.57173e+07
0.03	1.20434e+09	1.52614e+09	3.64393e+07
0.04	1.25652e+09	1.21921e+09	2.91178e+07
0.05	1.31273e+09	9.75359e+08	2.33008e+07
0.06	1.37338e+09	7.80543e+08	1.86533e+07
0.07	1.43897e+09	6.24211e+08	1.49235e+07
0.08	1.51006e+09	4.98335e+08	1.19201e+07
0.09	1.58727e+09	3.96745e+08	9.49587e+06
0.10	1.67136e+09	3.14647e+08	7.53643e+06
0.11	1.76315e+09	2.48285e+08	5.95230e+06
0.12	1.86364e+09	1.94693e+08	4.67273e+06

Table S25: (Reverse) ISC rate constants (s^{-1}) of El-Sayed forbidden transitions of xanthone in aqueous solution for temperatures ranging from 280 K to 340 K in HT approximation. The ZPVE corrected minima of $^1(\pi\pi^*)$ and $^3(n\pi^*)$ were set to be isoenergetic.

T	(Re-)ISC rate constant		
/ K	$^1(\pi\pi^*) \rightsquigarrow {}^3(\pi\pi^*)$	$^1(n\pi^*) \rightsquigarrow {}^3(n\pi^*)$	$^3(n\pi^*) \rightsquigarrow {}^1(n\pi^*)$
280	1.68451e+09	2.45031e+08	4.86753e+06
290	1.72355e+09	2.46627e+08	5.39957e+06
300	1.76315e+09	2.48285e+08	5.95230e+06
310	1.80325e+09	2.50002e+08	6.52457e+06
320	1.84379e+09	2.51773e+08	7.11520e+06
330	1.88472e+09	2.53597e+08	7.72317e+06
340	1.92599e+09	2.55469e+08	8.34743e+06

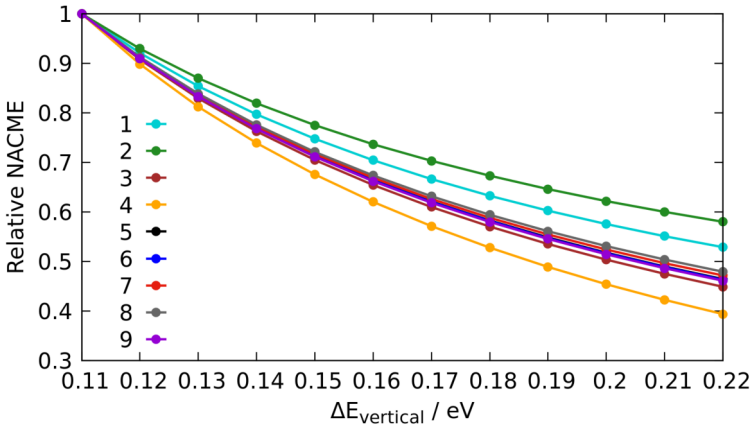

Figure S5: Influence of the state shift on the NACMEs $\langle {}^1(\pi\pi^*) \,|\, \vec{\nabla}_{Q_\kappa} \,|\, {}^1(n\pi^*) \rangle$ at the ${}^1(n\pi^*)$ equilibrium geometry. The indices κ of the nine a_2-symmetric coupling modes are assigned to different colors. Relative NACMEs have been obtained by dividing the NACME at a given vertical energy separation by the NACME at $\Delta E_{vertical} = 0.11\,eV$ corresponding to the original solvent shift introduced by Rai-Constapel et al. [11]. $\Delta E_{vertical} = 0.22\,eV$ refers to a model in which the vibrational ground states of the ${}^1(\pi\pi^*)$ and ${}^3(n\pi^*)$ states are isoenergetic.

Table S26: Scan of the (reverse) IC rate constants (s^{-1}) of xanthone in aqueous solution at 300 K with respect to small variations of the energy separation. An additional red shift was applied to the $n\pi^*$ states. Highlighted rate constants relate to a situation in which the ZPVE corrected adiabatic energies of the $^1(\pi\pi^*)$ and $^3(n\pi^*)$ states are identical.

Red shift	(Re-)IC rate constant		
/ eV	$^3(n\pi^*) \rightsquigarrow {}^3(\pi\pi^*)$	$^1(n\pi^*) \rightsquigarrow {}^1(\pi\pi^*)$	$^1(\pi\pi^*) \rightsquigarrow {}^1(n\pi^*)$
0	1.51030e+09	8.24452e+12	3.78519e+08
0.01	1.77582e+09	8.24590e+12	6.46857e+08
0.02	2.03660e+09	5.58314e+12	8.91046e+08
0.03	2.32733e+09	4.73420e+12	1.28232e+09
0.04	2.68490e+09	5.29306e+12	2.39101e+09
0.05	3.13329e+09	3.58260e+12	3.38921e+09
0.06	3.71767e+09	2.92615e+12	4.34858e+09
0.07	4.36051e+09	3.21608e+12	7.99496e+09
0.08	5.06402e+09	2.07224e+12	1.07722e+10
0.09	5.80348e+09	1.34732e+12	1.11681e+10
0.10	6.70062e+09	1.14649e+12	1.57402e+10
0.11	7.67720e+09	7.22242e+11	1.94829e+10
0.12	9.01071e+09	4.87681e+11	2.10996e+10

Table S27: (Reverse) IC rate constants (s^{-1}) of xanthone in aqueous solution for temperatures ranging from 280 K to 340 K. An additional red shift of 0.11 eV was applied to the $n\pi^*$ states.

T	(Re-)IC rate constant		
/ K	$^3(n\pi^*) \rightsquigarrow {}^3(\pi\pi^*)$	$^1(n\pi^*) \rightsquigarrow {}^1(\pi\pi^*)$	$^1(\pi\pi^*) \rightsquigarrow {}^1(n\pi^*)$
280	7.34084e+09	6.50231e+11	1.55859e+10
290	7.50534e+09	6.86520e+11	1.75060e+10
300	7.67720e+09	7.22242e+11	1.94829e+10
310	7.85665e+09	7.57368e+11	2.15094e+10
320	8.04396e+09	7.91869e+11	2.35794e+10
330	8.23939e+09	8.25721e+11	2.56876e+10
340	8.44323e+09	8.58906e+11	2.78290e+10

Table S28: NACMEs (a_0^{-1}) of xanthone in aqueous solution. An additional red shift of 0.11 eV was applied to the ($n\pi^*$) states to make the ZPVE corrected minima of the $^1(\pi_H\pi_L^*)$ and $^3(n_O\pi_L^*)$ state isoenergetic. Only a_2-symmetric normal modes exhibit nonvanishing matrix elements.

Mode	NACME		
	$^3(n\pi^*) \rightsquigarrow {}^3(\pi\pi^*)$	$^1(n\pi^*) \rightsquigarrow {}^1(\pi\pi^*)$	$^1(\pi\pi^*) \rightsquigarrow {}^1(n\pi^*)$
1	0.05352	-0.02223	0.07548
2	-0.01809	0.02083	0.04013
3	-0.13401	-0.08182	0.00210
4	0.05953	-0.01812	0.05549
5	-0.00919	-0.08739	-0.05926
6	0.03403	0.01882	0.00252
7	0.01564	0.07884	0.07143
8	-0.03962	0.07387	-0.02809
9	0.01238	0.08270	-0.07948

[1] H. Lischka, T. Müller, P. G. Szalay, I. Shavitt, R. M. Pitzer, and R. Shepard. COLUMBUS – a program system for advanced multireference theory calculations. *WIREs 2011*, 1:191–199, 2011.

[2] H. Lischka, R. Shepard, R. M. Pitzer, I. Shavitt, M. Dallos, T. Müller, P. G. Szalay, M. Seth, G. S. Kedziora, S. Yabushita, and Z. Zhang. High-level multireference methods in the quantum-chemistry program system COLUMBUS: Analytic MR-CISD and MR-AQCC gradients and MR-AQCC-LRT for excited states, GUGA spin–orbit CI and parallel CI density. *Phys. Chem. Chem. Phys.*, 3:664–673, 2001.

[3] H. Lischka, R. Shepard, I. Shavitt, R. M. Pitzer, M. Dallos, T. Müller, P. G. Szalay, F. B. Brown, R. Ahlrichs, H. J. Böhm, A. Chang, D. C. Comeau, R. Gdanitz, H. Dachsel, C. Ehrhardt, M. Ernzerhof, P. Höchtl, S. Irle, G. Kedziora, T. Kovar, V. Parasuk, M. J. M. Pepper, P. Scharf, H. Schiffer, M. Schindler, M. Schüler, M. Seth, E. A. Stahlberg, S. Yabushita J.-G. Zhao, Z. Zhang, M. Barbatti, S. Matsika, M. Schuurmann, D. R. Yarkony, S. R. Brozell, E. V. Beck, , J.-P. Blaudeau, M. Ruckenbauer, B. Sellner, F. Plasser, J. J. Szymczak, R. F. K. Spada, and A. Das. COLUMBUS, an *ab initio* electronic structure program, release 7.0, 2017.

[4] W. J. Hehre, R. Ditchfield, and J. A. Pople. Self–Consistent Molecular Orbital Methods. XII. Further Extensions of Gaussian–Type Basis Sets for Use in Molecular Orbital Studies of Organic Molecules. *J. Chem. Phys.*, 56:2257, 1972.

[5] O. Vahtras, J. Almlöf, and M.W. Feyereisen. Integral approximations for LCAO-SCF calculations. *Chem. Phys. Lett.*, 213:514 – 518, 1993.

[6] Stefan Grimme and Mirko Waletzke. A combination of Kohn–Sham density functional theory and multi-reference configuration interaction methods. *J. Chem. Phys.*, 111:5645–5655, 1999.

[7] Florian Weigend, Marco Häser, Holger Patzelt, and Reinhart Ahlrichs. RI-MP2: optimized auxiliary basis sets and demonstration of efficiency. *Chem. Phys. Lett.*, 294:143–152, 1998.

[8] Fabian Dinkelbach and Christel M. Marian. Vibronic and spin–orbit coupling effects in the absorption spectra of pyrazine: A quantum chemical approach. *J. Serb. Chem. Soc.*, 84:819–836, 2019.

[9] TURBOMOLE, a development of University of Karlsruhe and Forschungszentrum Karlsruhe GmbH, 1989-2007, TURBOMOLE GmbH, since 2007; available from

http://www.turbomole.com.

[10] Ansgar Schäfer, Christian Huber, and Reinhart Ahlrichs. Fully optimized contracted gaussian basis sets of triple zeta valence quality for atoms Li to Kr. *J. Chem. Phys.*, 100(8):5829–5835, 1994.

[11] V Rai-Constapel, M Etinski, and C M Marian. Photophysics of xanthone: A quantum chemical perusal. *J. Phys. Chem. A*, 117:3935–3944, 2013.

PCCP

PAPER

View Article Online
View Journal | View Issue

Cite this: *Phys. Chem. Chem. Phys.*, 2019, **21**, 9912

Impact of fluorination on the photophysics of the flavin chromophore: a quantum chemical perspective†

Mario Bracker, Fabian Dinkelbach, Oliver Weingart and Martin Kleinschmidt *

Received 8th February 2019,
Accepted 15th April 2019

DOI: 10.1039/c9cp00805e

rsc.li/pccp

10-Methylisoalloxazine (MIA) and its mono-fluorinated derivatives (6-9F-MIA) were investigated by means of quantum chemistry, looking into the influence of fluorination on fluorescence, absorption and inter-system crossing (ISC). A maximized fluorescence quantum yield (Φ_{Fl}) of this chromophore is desirable for application as a potential fluorescence marker in biodiagnostics/photobiological studies. An enhanced triplet quantum yield Φ_T on the other hand may open a perspective for photodynamic therapies (PDT) in cancer treatment. Determination of equilibrium geometries was carried out employing (time-dependent) Kohn–Sham density functional theory and electronic properties were obtained using a combined density functional theory and multi-reference configuration interaction (DFT/MRCI) method. In the gas phase, El-Sayed-favored $^1(\pi\pi^*) \rightsquigarrow {}^3(n\pi^*)$-ISC enables population transfer to the triplet domain on a timescale of 10^9 s^{-1}, *i.e.* significantly faster than fluorescence ($k_{Fl} \approx 10^7$ s^{-1}). Two different models were applied to investigate the influence of aqueous medium on absorption and relaxation: the implicit solvation model A is the well-established conductor-like screening model (COSMO) and hybrid model B combines quantum mechanical micro-hydration and conductor-like screening. A polar, protic environment leads to a significant blue-shift of the $n\pi^*$ potentials, slowing down the ISC process to 10^7–10^8 s^{-1}, now enabled by vibronic spin–orbit coupling. Simple principles are derived that demonstrate the effect of fluorination at different positions on the spectroscopic properties. These principles can be utilized with respect to multiply fluorinated derivatives and even further substitution to enlarge effects on the population decay and quantum yields.

1 Introduction

Flavins (Fig. 1) play an important role in biological photoreception.[1] They work uniformly as light-mediated signal transductors and take part as cofactors in a variety of processes. BLUF (blue light sensors using flavin adenine dinucleotide (FAD)) and cry (cryptochromes) use FAD as a chromophore. These systems take part as blue light-photosensors in the circadian rhythm,[2] and in magnetoreception[3] (cry) and operate several signal transductions in microorganisms[4] (BLUF). Phototropin-receptors (phot) are based on the mononucleotide FMN, as *e.g.*, the light-oxygen-voltage (LOV) domain that senses environmental conditions in plants, procaryotes and eucaryotes.[1] Phots are involved in eponymous phototropism,[5,6] chloroplast movement,[7] stomata opening,[8] inhibition of cell growth[9] and gametogenesis.[10]

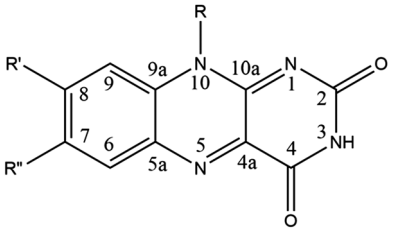

Fig. 1 General structural motif of flavins. The chromophore, isoalloxazin (IA), results from R = H. By definition, flavins are equipped with methyl groups for R′ and R″ as well as a specific residue linked to N(10).

The ubiquity of flavins in biological systems suggests interesting photophysical properties. Chemical modification may enable sensitive change of the photophysical behavior to create potent systems for application in fluorescence microscopy or in photodynamic therapy (PDT). Usage as a fluorescence marker requires maximization of the fluorescence yield (Φ_{Fl}), whereas for PDT accumulation of the triplet domain (Φ_T) is necessary. As fluorescence and triplet sensitisation are competing processes,

Institut für Theoretische Chemie und Computerchemie, Heinrich-Heine-Universität Düsseldorf, 40225 Düsseldorf, Germany. E-mail: Martin.Kleinschmidt@hhu.de; Fax: +49 211 81 13466; Tel: +49 211 81 13212

† Electronic supplementary information (ESI) available: Molecular orbitals, geometry parameters, details of computations, spin–orbit couplings, state energies in vacuum and solvent. See DOI: 10.1039/c9cp00805e

only one capacity can be optimized. Further application has already been tested in the field of photo-redox catalysis.[11–13]

This study focuses on the change in electronic structure of the parent compound 10-methylisoalloxazine (MIA, see Fig. 1) induced by fluorination. The primary motivation is to understand the influence of fluorination on the electronic properties of the flavin chromophore. Secondarily it is desirable to determine potential derivatives for optical imaging applications (maximizing Φ_{Fl}) or chromophores for maximizing singlet oxygen generation[14] (maximizing Φ_T). We investigate in detail the fluorination of the attached benzene (C6–9) core, as these positions may have significant impact on the photophysically relevant second $\pi\pi^*$ triplet state with internal charge transfer character (ICT). In polar solvents, this state comes close in energy to the S1-state and therefore participates in the deactivation process of photo-excited flavin.[15–18] With its inductive effect, fluorine might effectively hinder charge relocation in this state and thus enable tuning of its energy gap with S1. These positions furthermore play a passive role in photobiology – the benzene ring is positioned in a hydrophobic pocket of the respective apoprotein[17] and fluorine is expected to have a negligible steric influence.

The unmodified isoalloxazine chromophore exhibits three bands in the absorption spectrum up to 5.5 eV.[19–21] The energetically lowest band is barely influenced by the polarity and proticity of the solvent, whereas the second band is highly solvatochromic.[16,22,23] Investigations on the photophysics of fluorinated flavins have not been available until recently. Reiffers *et al.*[24] published an extensive steady-state as well as time-resolved examination finding shifts of the adiabatic excitation energy of the lowest allowed transition up to 500 cm^{-1}. For 7F-MIA they report a 50% increase of the fluorescence quantum yield as well as a 50% decrease of Φ_T. For 9F-MIA to the best of our knowledge neither experimental nor theoretical studies have been performed. The isoalloxazine chromophore is well characterized by quantum chemists[16,25–28] and photophysicists.[22,24] Aside from mono-fluorination, 8-bromo- and 8-trifluoromethyl-substituted derivatives have been characterized quantum chemically and experimentally.[29] For the bromine derivative, a triplet quantum yield of 0.97 was achieved.[29] Moreover, triplet quantum yields close to unity were predicted for the respective thioflavins.[30] Further publications regarding various substituted flavins focus on the electrochemical properties of the chromophore rather than photophysics.[31–33] Regarding FMN as a prosthetic group of the phototropin YtvA (of *Bacillus subtilis*), spin–orbit coupling has been taken into account for the mechanism of blue-light photoreception in the LOV-domain (light, oxygen and voltage sensitive).[17,26,34] In the present investigation, MIA and its fluorinated derivatives 6F-MIA, 7F-MIA, 8F-MIA and 9F-MIA are characterized quantum chemically. The absorption behavior and relaxation pathways are analyzed in the gas phase and in solution. For comparison with the experiment and validation of our calculations, a sophisticated solvation model has been applied to mimick the absorption process in aqueous medium. A similar model has been used by Salzmann *et al.* to study solvation effects on the MIA system.[17] Based on the analysis of the resulting energetics of the fluorinated derivatives, the effect of fluorination becomes transparent and general rules are derived.

2 Methods and computational details

For each analyzed flavin, the three lowest-lying singlet and triplet structures were optimized at the density functional theory (DFT) level utilizing the Turbomole 7.1 program package.[37] For the optimizations and all further calculations the TZVP basis set was employed. For geometry optimizations we chose the B3LYP functional[35,36] as implemented in Turbomole 7.1. Electronically excited states were optimized employing the time-dependent variant of density functional theory (TDDFT). All optimizations in the gas phase were conducted under C_s-symmetry constraints. To verify that these planar structures correspond to true minima of the potential energy hypersurfaces (PEHs), harmonic vibrational frequencies were calculated numerically using the program SNF.[38] Resulting zero-point vibrational energy (ZPVE) corrections were scaled by a factor of 0.9614 as recommended for the B3LYP functional.[39] For geometry optimizations in aqueous medium the C_s-symmetry-constraint was removed.

Vertical excitation energies and (transition) dipole moments were calculated from subsequent single-point calculations using the combined density functional theory/multi-reference configuration interaction (DFT/MRCI) method developed by Grimme and Waletzke.[40] DFT/MRCI is based on BHLYP-Kohn–Sham[36,41] orbitals as a single-particle basis. Up to 20 roots were calculated for each singlet and triplet manifold, 10 belonging to each irreducible representation (A′/A″).

Using the resulting DFT/MRCI wavefunctions, we calculated spin–orbit matrix elements (SOMEs) with the spin–orbit coupling kit (SPOCK) developed in our group.[42,43] The coupling is described by the Breit–Pauli Hamiltonian; the calculation is based on the spin–orbit-mean-field-approximation (SOMF).[44,45] For efficiency reasons, the atomic-mean-field-approximation (AMFI) is applied. This implementation makes the calculation drastically less costly, losing only 5% of the accuracy of the full treatment.[46,47]

Solvation effects were covered in two different models: model A employs screening charges generated by the conductor-like screening model (COSMO)[48] as implemented in Turbomole 7.1. The relative permittivity ε_r was set to 80 corresponding to water at ambient temperature. The COSMO-model was included for ground state optimization. For the excited states, the structures were first optimized with TD-DFT *in vacuo*. Thereafter, the BH-LYP orbitals were computed including the COSMO cavity, corresponding to the charge distribution in the electronic ground state. These orbitals were used as a one-particle basis for subsequent DFT/MRCI computations. Model B consists of a combination of explicit water molecules treated quantum mechanically and a COSMO cavity. The explicit solvation shell is used to include the covalent character of the bound water molecules in addition to purely electrostatic effects. For a systematic positioning of water molecules, for each flavin derivative 200 ps of molecular dynamics simulations were performed using the Amber14 software.[49] Two force fields were applied: TIP3P for water[50] molecules

and the generalized amber force field (GAFF)[51] for the chromophores. Point charges for interaction of the respective flavin derivative with water in the force field were generated using the Merz–Singh–Kollmann scheme.[52] First, the pseudo-stochastic arrangement of water in an octahedron (r = 25 Å) with the respective flavin centered in it was relaxed using the steepest descent and conjugate gradient method algorithms as implemented in Amber14. Periodic boundary conditions were used and the particle-mesh-Ewald summation method was applied to compute electrostatic interactions beyond a cutoff of 12 Å. Before the final propagation by means of the Verlet-algorithm (Amber14), the kinetic energy was scaled utilizing a Langevin thermostat as implemented in Amber14. The pressure was regulated to 1 bar using a Berendsen-barostat[53] and scaled isotropically during the simulation. Finally, from each trajectory, 10 snapshots were extracted and QM/MM-optimized using COBRAMM 2.0.[54] Therefore, a spherical droplet was created from the central octahedron, including the chromophore and the nearest 1000 water molecules. The chromophore (QM) and water molecules (MM) within a distance of 4 Å were allowed to move during optimization; the rest of the water molecules were kept fixed. Hydrogen bonded atoms of the chromophore were identified for each snapshot. The final number of hydrogen bonded water molecules (six in our case) was evaluated statistically by computing average occupation numbers for each atom (see the ESI† for further details). For the positioning of these water molecules, a representative snapshot with six bound water molecules was selected. To enable comparability among the systems, we used the same water-bonded network (see Fig. 5) for all calculations. In the course of this study, rate constants of fluorescence and intersystem crossing (ISC) were calculated. The former were obtained according to

$$k_{\mathrm{Fl}} = \frac{1}{3\pi\varepsilon_0\hbar^4c^3}(E_{\mathrm{i}} - E_{\mathrm{f}})^3\left|\left\langle \Psi_{\mathrm{f}}\left|\hat{\vec{\mu}}\right|\Psi_{\mathrm{i}}\right\rangle\right|^2 \quad (1)$$

The energy gap and transition dipole moment $\vec{\mu}_{\mathrm{fi}}$ were taken from the corresponding DFT/MRCI calculations at S1 equilibrium geometries.

ISC rate constants were calculated for two different kinds of electronic couplings based on the Fermi golden rule neglecting explicit non-adiabatic coupling. $\hat{\mathscr{H}}_{\mathrm{SO}}$ can be expanded into a power series around a reference configuration, for example the S1-optimum, to describe vibronically induced spin–orbit coupling.[55] For an El-Sayed-favored transition direct spin–orbit coupling is the dominant electronic contribution to the non-radiative process. The corresponding expression for the rate constant[56] is as follows:

$$k_{\mathrm{ISC}}^{\mathrm{dir},\alpha} = \frac{2\pi}{Z\hbar}\left|\left\langle S_{\mathrm{a}}\left|\hat{\mathscr{H}}_{\mathrm{SO}}\right|T_{\mathrm{b}}^{\alpha}\right\rangle\right|_{q_0}^2 \times \sum_{j,k} \mathrm{e}^{-\beta E_j}\left|\left\langle\{\nu_{aj}\}\middle|\{\nu_{bk}\}\right\rangle\right|^2\delta(E_{aj} - E_{bk}) \quad (2)$$

$Z = \sum_j \mathrm{e}^{-\beta E_j}$ is the partition function, α are fine-structure components, and β is the inverse temperature. It can be evaluated using a time-dependent approach employing a Fourier transform representation of the delta function.[57] According to El-Sayed, $^1\pi\pi^* \nrightarrow {}^3\pi\pi^*$ ISC is expected to be linked to small spin–orbit matrix elements. For these types of transitions, Herzberg–Teller type expansions about the minimized S1 geometries were carried out yielding vibronic first-order derivatives/spin–orbit coupling[58,59] (explicit derivatives are presented in the ESI†):

$$k_{\mathrm{ISC}}^{\mathrm{vib},\alpha} = \frac{2\pi}{Z\hbar}\sum_{j,k} \mathrm{e}^{-\beta E_j}\left|\left\langle\{\nu_{aj}\}\middle|b^{\mathrm{T}}Q_{\mathrm{S}}\middle|\{\nu_{bk}\}\right\rangle\right|^2\delta(E_{aj} - E_{bk}) \quad (3)$$

Q_{S} contains normal mode coordinates of the singlet electronic state; b is the vector that contains the first-order derivative couplings:

$$b_m = \left.\frac{\partial\left\langle S_{\mathrm{a}}\left|\hat{\mathscr{H}}_{\mathrm{SO}}\right|T_{\mathrm{b}}^{\alpha}\right\rangle}{\partial(Q_{\mathrm{S}})_m}\right|_{q_0} \quad (4)$$

To account for temperature effects, we applied a Boltzmann population of vibrational states at 298 K. The calculations of final rate constants were performed using the VIBES program[57] with the respective electronic coupling generated by SPOCK and normal modes/frequencies received from SNF used as the input. The first-order derivatives of the SOMEs were calculated using finite difference techniques. Rate constants in water were obtained applying model A.

3 Results and discussion

In the following sections, excited-state energies and properties are discussed extensively. Because states with a given electronic structure change order in the course of structural changes, different nomenclatures have to be introduced:

- Order of electronic states at the ground-state geometry in vacuum: S1...*SN* with respect to MIA
- Actual order of electronic states for a given geometry: $S_1...S_N$

Furthermore, for the sake of comparability, the electronic ground state energy at the ground state geometry has been chosen as the common origin.

3.1 Properties in the gas phase

Bond lengths. For the reference molecule MIA, Wang *et al.* carried out X-ray diffraction experiments.[60] The comparison with the calculated values (see the ESI†) shows very good agreement with a maximal error of 2.5 pm and a mean average error of 0.8 pm. The bond lengths in the pteridine-based core are basically unaffected by fluorination, whereas the values for the benzene ring show small changes depending on the position of fluorination.

Absorption. The absorption characteristics and the nature of orbitals in the unsubstitued MIA chromophore have been discussed in earlier work.[16] The fluorinated F-MIA compounds show very similar behaviour in this respect.

Fig. 2 depicts DFT/MRCI computed absorption spectra for F-MIA and MIA. Yet, no experimental gas phase spectra are available for comparison. The orbitals involved in characteristic excitations are shown in Fig. 3, taking the 7F-MIA compound as an example. The frontier orbitals of the fluorinated species do

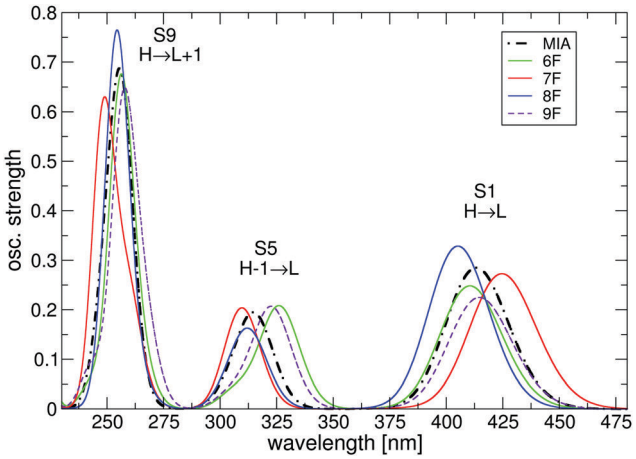

Fig. 2 DFT/MRCI computed absorption spectra of MIA and F-MIA *in vacuo*. Line spectra were convoluted in the eV regime using a Gaussian function with a full-width at half maximum (FWHM) of 0.1 eV and then converted to nm.

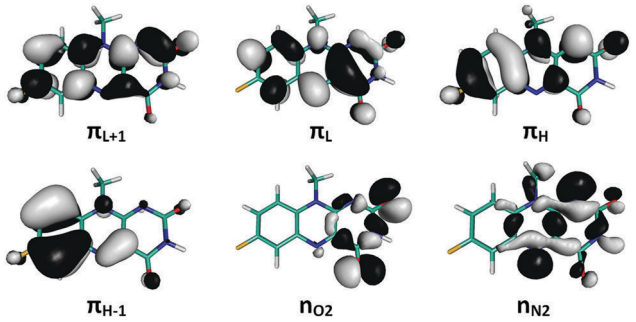

Fig. 3 Illustration of selected frontier orbitals (isovalue = 0.03) of 7F-MIA.

not differ visually from the ones illustrated for MIA (see also Fig. 4 in ref. 16), except for a small shift of density from the fluorinated carbon atoms to the respective fluorine atoms.

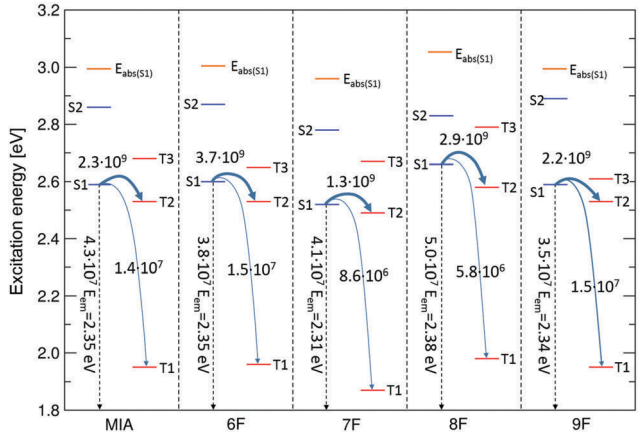

Fig. 4 ZPVE corrected adiabatic state energies in eV (DFT/MRCI) and calculated rate constants for fluorescence (k_{Fl}, vertical arrows) and ISC rate constants (k_{ISC}, curved arrows) in the gas phase. The arrow thickness indicates the magnitude of the corresponding rate constant.

The fluorine atom introduces an additional nodal plane at the corresponding position in the π_H, π_L and π_{L+1} orbitals.

Also, the character of the states does not differ significantly from the parent compound. The energies of the 10 lowest singlet and four lowest triplet states of 7F-MIA are summarized in Table 1. The changes in the excitation of the bright states and the first three triplet states in the other fluorinated compounds are documented in the ESI.†

In agreement with several theoretical studies of flavins (SAC-CI,[25] CASPT2,[26] TDDFT[22,27,28,34]) our calculations describe three dominant $^1(\pi\pi^*)$ transitions assembling the absorption spectra of MIA and F-MIA (Fig. 2). The main contributor to the first visible band (f = 0.23–0.35) is the redistribution of charge described by the $\pi_H \rightarrow \pi_L$ transition with *ca.* 80% for MIA and F-MIA (see Table 1 and ref. 16). With respect to MIA, 7F-MIA shows the largest red-shift of this absorption. 9F-MIA stays at the same value with a slightly lower oscillator strength; 6F- and 8F-MIA are blue-shifted.

The next visible band is due to excitation to the close lying S5 and S6 states with oscillator strengths of *ca.* 0.15 and 0.07. These excitations involve transitions from π_{H-1} and π_{H-2} to the π_L orbital. In 7F-MIA, these states are mixed (see also Table 1) – the redistribution of charge caused by the internal charge transfer (ICT) induces the relatively high oscillator strength. The largest red-shift for this band with respect to MIA is observed in 6F-MIA, right after 9F-MIA. 8F- and 7F-MIA are blue-shifted.

Excitation to the S9 state yields the highest oscillator strength in the energy regime up to 5 eV (200 nm). The high oscillator strength can be mainly related to the $\pi_H \rightarrow \pi_{L+1}$ excitation, which describes a slight redistribution of charge into the benzene core. We note small red-shifts of 6F- and 9F-MIA. 8F-MIA stays at the same value as MIA but gains some oscillator strength. 7F-MIA is blue-shifted.

Fluorination apparently has a different effect on the absorption bands of S1, S5 and S9. 8F-MIA *e.g.* results in a moderate blue-shift of S1, and slight blue-shifts of S5 and S9. 7F-MIA shows a red-shift of the S1 band, while S5 and S9 are blue-shifted. 6F-MIA has a notable blue-shift in S1, a moderate red-shift in S5 and a slight red-shift in S9. 9F-MIA finally red-shifts all absorption bands, with the largest effect on S5.

Table 1 gives information on the nature of the dark states energetically below the (bright) S9/S10 states, using 7F-MIA as an example. The three states following the S1 excitation are $n \rightarrow \pi_L^*$ excitations with negligible oscillator strengths, involving orbitals located at the oxygen or nitrogen centers. S7 is of similar character. S8 is a $\pi\pi^*$ state with very low oscillator strength. Also the S10 state involves $\pi\pi^*$ transitions. For 7F-MIA, this state is switched in energy with respect to MIA. Due to contributions from π_H to π_{L+1} and π_{L+2} with ICT character, it has a moderate oscillator strength.

The T1 state in all computed compounds (see the ESI†) is the counterpart to the S1 (2A′) excitation with dominant $\pi_H \rightarrow \pi_L$ character. From an energetic point of view, the first triplet state is stabilized by the large exchange interaction between π_H and π_L. It lies more than half an eV below the next higher state (T2). T2 has strong $n\pi^*$ character. The T3 state is the counterpart to

Table 1 Vertical excitation energies [eV], oscillator strengths $f(r)$, irreducible representations and electronic structure information (DFT/MRCI) for the first ten singlet and first four triplet states of 7F-MIA at the ground state geometry *in vacuo*. State labels are with respect to the corresponding excitations in MIA.[16] Only contributions $|c|^2 \geq 0.1$ are shown

State		Electronic structure ($\lvert c\rvert^2$)	ΔE/eV	$f(r)$
S0	1A′	Ground state (0.95)	—	—
S1	2A′	$\pi_H \rightarrow \pi_L(0.84)$	2.92	0.272
S2	1A″	$n_{O_2} \rightarrow \pi_L(0.49) + n_{N_2} \rightarrow \pi_L(0.27)$	3.15	0.002
S3	2A″	$n_{N_2} \rightarrow \pi_L(0.48) + n_{O_2} \rightarrow \pi_L(0.21)$	3.29	0.001
S4	3A″	$n_{O_2} \rightarrow \pi_L(0.60)$	3.85	0.000
S5	3A′	$\pi_{H-2} \rightarrow \pi_L(0.48) + \pi_{H-1} \rightarrow \pi_L(0.25)$	3.99	0.133
S6	4A’	$\pi_{H-1} \rightarrow \pi_L(0.48) + \pi_{H-2} \rightarrow \pi_L(0.27)$	4.03	0.075
S7	4A″	$n_{N_1} \rightarrow \pi_L(0.62)$	4.48	0.000
S8	5A′	$\pi_{H-3} \rightarrow \pi_L(0.54) + \pi_{H-1} \rightarrow \pi_{L+1}(0.12)$	4.64	0.013
S10	6A′	$\pi_H \rightarrow \pi_{L+2}(0.34) + \pi_H \rightarrow \pi_{L+1}(0.27)$	4.78	0.224
S9	7A′	$\pi_H \rightarrow \pi_{L+1}(0.43) + \pi_H \rightarrow \pi_{L+2}(0.24)$	4.99	0.603
T1	1A′	$\pi_H \rightarrow \pi_L(0.86)$	2.23	—
T2	1A″	$n_{N_2} \rightarrow \pi_L(0.60) + n_{O_2} \rightarrow \pi_L(0.13) + n_{N_1} \rightarrow \pi_L(0.10)$	2.86	—
T3	2A′	$\pi_{H-1} \rightarrow \pi_L(0.75)$	3.11	—
T4	2A″	$n_{O_2} \rightarrow \pi_L(0.55)$	3.14	—

the bright S5 transition with leading $\pi_{H-1} \rightarrow \pi_L$-configuration. It is a possible candidate for ISC, as it lies close in energy to S1 in all molecules. The T4 state with strong $n\pi^*$ character plays a minor role for relaxation processes, because it is energetically not accessible from the respective S1-minima.

3.2 Excited-state geometries

For all S1 geometries an imaginary frequency corresponding to an a″-symmetric normal mode was obtained. The observed phenomenon is considered an artifact of the TDDFT/B3LYP method and has been encountered previously (cytosine, thiophene, psoralen, and flavins[16,61–63]). To obtain real-value frequencies we carried out least square fits for TDDFT scans along the respective modes. Using the fitted parabolas, the second derivative at the vertex was calculated to obtain the related force constants and frequencies respectively (see the ESI† for details).

Geometrical changes (see the ESI† and ref. 16) primarily arise from the dominant excitations contributing to the respective state; the trends are barely influenced by fluorination. As expected, the geometrical changes in the S1 and T1 states are very similar (see the ESI† for structural changes in other excited state geometries). The $\pi_H \rightarrow \pi_L$ transitions in S1 and T1 result in elongated C(4a)–N(5) and shortened C(2)–N(3)- and C(4a)–C(10a)-bonds.

Induced by the geometrical changes, the order of states changes as well (see ref. 16 and the ESI†). As a consequence we expect that, except for T1, various crossings occur between the low-lying states.

3.3 Relaxation channels *in vacuo*

After absorption of the bright states S1, S5 and S9, the population follows a path back to the ground state. The S1 state plays an important role in this process, as it represents the longest-lived singlet state. Energetically higher singlet excitations preferably dissipate the surplus energy *via* internal conversion (IC) followed by vibrational relaxation (VR) as well as vibrational energy redistribution (VER) and consequentially populate the S1 state. From there, the molecules can either decay non-radiatively *via* IC or fluoresce (Kasha’s rule). Another concurring process is ISC between singlet and triplet states. Typically, internal conversion of higher states is significantly faster than ISC ($S_n \rightsquigarrow S_1$: 10^{12}–10^{14} s^{-1}; $S_1 \rightsquigarrow T_1$: 10^6–10^{11} s^{-1}).[64] Thus, the S1 state will finally be populated and all other possible decay paths are initiated from this state.

Fig. 4 shows the DFT/MRCI computed adiabatic energies of all compounds *in vacuo*. Additionally, the longest wavelength absorption ($E_{abs(S1)}$) and computed rate constants for fluorescence and ISC are shown. The adiabatic state energies are ZPVE-corrected; emission energies are purely electronic. Numerical values are reported in the ESI.† The energetic ordering of the adiabatic states is similar in all computed molecules. The largest blue-shift for S1 (*ca.* 0.07 eV) wrt. MIA is observed for 8F-MIA; 7F-MIA has the largest red-shift by about the same amount. Larger influence due to fluorination is observed for the S2 and T3 states; the T2 energies are only moderately shifted with respect to MIA. 9F-MIA shows the largest separation between S1 and S2 (*ca.* 0.31 eV). For 6F-MIA and 9F-MIA the S1 and T3 states come very close in energy; in 9F-MIA they are almost degenerate. Starting from the adiabatic S1 state, there are four possible deactivation paths, three toward the triplet states *via* ISC, and fluorescence to the ground state. For the latter process, which depends on the energy gap and the transition dipole moment, we compute rate constants on the order of *ca.* 3.5–5 $\times$ 10^7 s^{-1}.

Transitions to the El-Sayed forbidden triplet states with $\pi\pi^*$ character can be enhanced by vibronic spin–orbit coupling. The S1 $\rightsquigarrow$ T3 transition additionally requires thermal activation for MIA, 6F, 7F- and 8F-MIA; it has a low thermodynamic barrier for 9F-MIA. The reverse process back to S1, however, is expected to be considerably faster. Therefore, this channel is neglected in the following. The El-Sayed favored transition to the T2 state with $n\pi^*$ character is thermally allowed. For all molecules, we find the highest rate constants for this process *via* direct spin–orbit coupling (ranging from 1.3–3.7 $\times$ 10^9 s^{-1}). The rate constants for S1 $\rightsquigarrow$ T1 deactivation are *ca.* two orders of magnitude smaller. From the performed computations we conclude that the main deactivation path for the flavin compounds *in vacuo* is conversion toward T2 *via* direct spin–orbit coupling.

The main effects of fluorination on the adiabatic states can be summarized as follows: 6F has only a marginal effect on the T3 state, which is slightly lowered in energy. 7F mainly lowers the S1, S2 and T1 states and brings S1 and T2 closer in energy. In 8F, the S1, T1 and T3 states are upshifted in energy. 9F behaves essentially as 6F, with a smaller separation of T2 and T3 states.

3.4 Properties in aqueous medium

Solvent modeling. Recently, Reiffers *et al.* published an in-depth spectroscopic study of MIA and the derivatives 6F, 7F- and 8F-MIA in aqueous solution.[24] For comparison with these data, we applied two solvation models to mimick aqueous surroundings.

As described in Section 2, model A consists of screening charges generated by COSMO. In model B, explicit water molecules are added to the chromophore to include the effect of hydrogen bridge linkages into our description of the medium. The position and number of water molecules were determined systematically by molecular dynamics simulations for each flavin (see the ESI†). Based on the relative occupations $f_{rel.}$, on average 6.13 hydrogen bond linkages influence the chromophore. Rounding up/down results in one hydrogen bond to N(1), N(3), N(5), and O(4) and two bonds regarding O(2). The actual orientation of the water molecules corresponds to a snapshot with six hydrogen bonds on the deduced, "desired" positions and was applied to all analyzed flavins prior to the geometry optimizations.

Solvent effects on the vertical excitations. The effect of the solvation shells on the electronic state energies is illustrated for 7F-MIA in Fig. 6. In the singlet manifold we additionally include the S3 $n_{N_2}\pi^*$-state due to a strong blue-shift of the S2 $n_{O_2}\pi^*$-state in water, and the S10 state due to strong mixing with S9 in 7F-MIA. It is immediately visible that the $n\pi^*$ transitions are profoundly blue-shifted. The same effect was also observed in MIA[16] and by Hasegawa *et al.* for the similar lumiflavin.[25] The nitrogen-centered S3-transition is lifted by 0.17 eV (model A), plus another 0.06 eV when considering explicit water molecules. The oxygen-centered S2 state undergoes a much larger blue-shift of 0.55 eV (model A). This state is not further influenced by inclusion of explicit water in model B. For the S1 state, our calculations result in a small energetic red-shift of 0.05 eV. Contrary to the aforementioned $\pi\pi^*$ transitions, the S5 $\pi\pi^*$ state is strongly affected by the polarized environment. For model A we obtain a red-shift of 0.24 eV; the explicit water molecules in model B shift the absorption by another 0.12 eV. This is in accordance with the observations of Sikorska *et al.*, stating that the proticity of the solvent has a decisive impact on the solvatochromism of flavins.[22] The shifts in model B are more pronounced for the $n\pi^*$- (S2, S3 and T2) and ICT-states (S5 and T3) than for the $\pi\pi^*$-states (S1, S9 and T1).

The solvent effects in the triplet domain can be explained qualitatively in the same manner as for the singlet states: the T_1 state corresponds to the S1 transition and experiences a small shift (+0.04 eV for model B). The T2 state is related to the dark S3 state and experiences a blue-shift by electrostatic interactions as well as hydrogen bonds. The ICT-state T3 is related to the S5 transition (see Table 1) and similarly stabilized by the polar solvent environment.

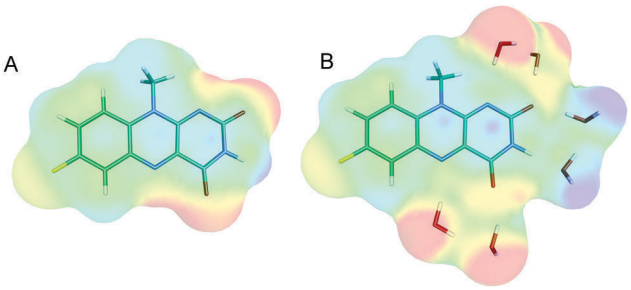

Fig. 5 Illustration of solution model A (left), which represents a cavity of screening charges generated by COSMO and solution model B (right) with explicit water molecules. The coloring of the cavities reflects the screening charges as follows: red (+) → yellow → green (0) → turquoise → blue (−). The molecule displayed is 7F-MIA.

The calculated vertical transition energies for the bright transitions in MIA and F-MIA (S1, S5 and S9) can be directly compared to experimental excitation energies to validate our method. Fig. 7 depicts computed absorption spectra for solvent models A and B and available experimental spectra. Computed values for the fluorinated compounds are summarized in Table 2, together with experimental values for the first two absorptions. 9F-MIA has not been studied experimentally yet. For our example 7F-MIA, Reiffers *et al.* report an absorption band maximum at 2.88 eV[24] for the first visible band (S1), and 3.75 eV for the second (S5). Our purely electronic computations yield 2.92 eV for S1 and 3.71 eV for S5, *i.e.* we obtain only small deviations of *ca.* 0.04 eV. Similar deviations apply for the other compounds. Generally, S1 and S9 absorptions are slightly blue-shifted in our calculations, while the

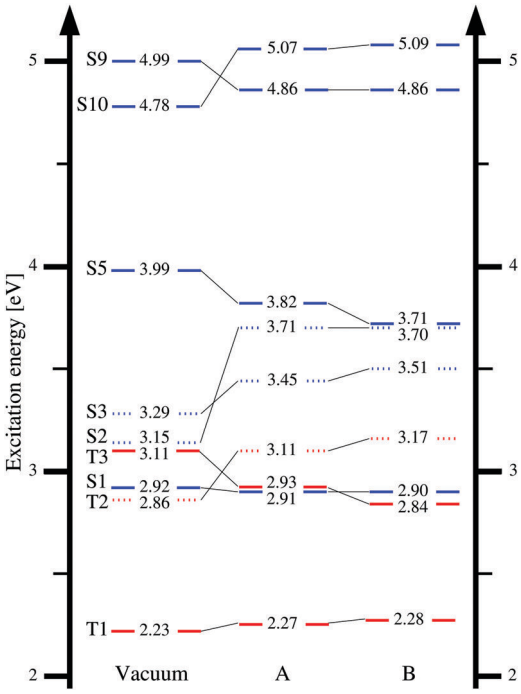

Fig. 6 Solvation effects on the vertical excitation energies (eV) of 7F-MIA at the ground state geometry (left: gas phase, middle: solvation model A, right: solvation model B). Singlets are shown in blue, triplets in red. The line styles depict the character of the states, broken lines: $n\pi^*$, solid lines: $\pi\pi^*$.

View Article Online

PCCP Paper

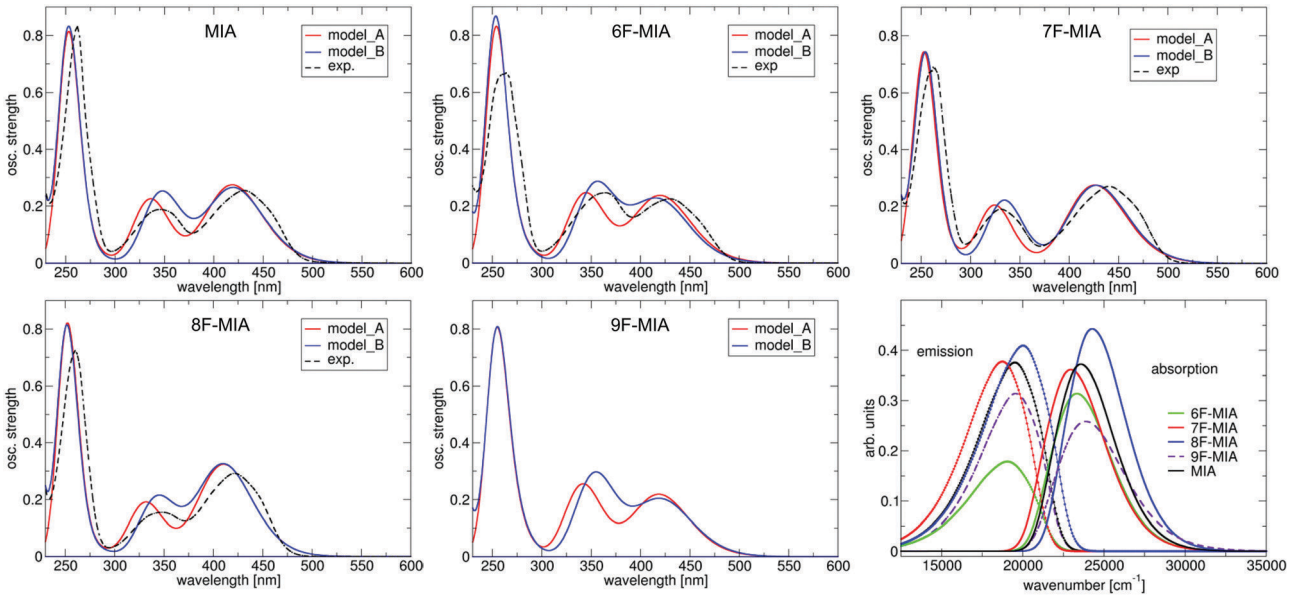

Fig. 7 DFT/MRCI computed and experimental[65] spectra in aqueous medium. Line spectra were convoluted in the eV regime using a Gaussian function with a full-width at half maximum (FWHM) of 0.1 eV and then converted to nm. The lower right graph shows the computed emission bands obtained from model A, together with the S1-absorption in a wavenumber representation. Both bands include explicit vibrational broadening. The height of the emission and absorption bands is solely influenced by the magnitude of the corresponding transition dipole moment. Emission bands were scaled to match the height of the absorption band for MIA (see the text).

Table 2 Vertical excitation energies (eV) for 6-9F-MIA at the ground state geometries *in vacuo* and for solvation models A and B. Oscillator strengths are included in bold for bright states. Experimental values of the absorption maxima are taken from Reiffers *et al.*[24,65]

	Excitation energy/eV														
	6F-MIA				7F-MIA				8F-MIA				9F-MIA		
State	Vac.	A	B	*Exp.*	Vac.	A	B	*Exp.*	Vac.	A	B	*Exp.*	Vac.	A	B
S1	3.02	2.95	2.96	*2.88*	2.92	2.91	2.90	*2.81*	3.06	3.02	3.02	*2.94*	2.99	2.96	2.94
Vib. cor.		*2.88*				*2.83*				*2.99*				*2.94*	
	0.25	**0.24**	**0.22**		**0.27**	**0.28**	**0.27**		**0.33**	**0.32**	**0.32**		**0.23**	**0.22**	**0.20**
S2	3.14	3.72	3.73		3.15	3.71	3.70		3.21	3.76	3.75		3.18	3.72	3.72
S3	3.31	3.47	3.52		3.29	3.45	3.51		3.35	3.50	3.55		3.30	3.46	3.53
S5	3.80	3.60	3.49	*3.41*	3.99	3.82	3.71	*3.75*	3.96	3.74	3.61	*3.56*	3.84	3.63	3.50
	0.21	**0.24**	**0.28**		**0.13**	**0.20**	**0.21**		**0.14**	**0.19**	**0.20**		**0.20**	**0.25**	**0.29**
S9	4.84	4.88	4.89	*4.71*	4.99	4.86	4.86	*4.73*	4.87	4.91	4.92	*4.77*	4.82	4.87	4.86
	0.66	**0.78**	**0.80**		**0.60**	**0.59**	**0.65**		**0.73**	**0.78**	**0.75**		**0.61**	**0.73**	**0.72**
T1	2.31	2.34	2.38		2.23	2.27	2.28		2.32	2.37	2.38		2.30	2.34	2.35
T2	2.85	3.12	3.16		2.86	3.11	3.17		2.91	3.14	3.21		2.89	3.11	3.18
T3	3.00	2.78	2.68		3.11	2.93	2.84		3.15	2.94	2.84		2.99	2.79	2.68

S5 excitation is always red-shifted. 7F-MIA is an exception; here the S9 state is red-shifted. At least for the S1-band this can be explained by the lack of vibrational intensity distributions (see also ref. 18). Both solvation models show valuable agreement with the experiment for the first three bright absorptions. Model B yields an overall better description of the S5 state, with slight enhancement of its oscillator strength. Comparison with the reference molecule MIA reveals that, due to relatively small interactions of fluorine with the screening charges (see the ESI†), fluorination does not have a distinct impact on the solvation shifts.

Excited state geometry optimizations of model B lead, in many cases, to an artificial deprotonation of the bound water molecules, consequently delivering unreliable structures. We therefore restrict the discussion of ISC and fluorescence rate constants in the following sections to computations using the implicitly solvated model A that showed good agreement for vertical excitations, despite the fact that COSMO only considers a ground state charge distribution.

Solvent effects on relaxation paths. Surrounded by aqueous medium, the following effects on the relaxation mechanism are expected:

- Fluorescence: solvation with water changes the energetics of the S1 state only marginally, hence the rate constants are expected to be similar to those for the gas phase.
- ISC: the relaxation channel of ISC undergoes a profound change: The $^3(n\pi^*)$ state T2 is strongly blue-shifted in aqueous

medium, so that it is only accessible by thermal activation. Instead, the $^3(\pi\pi^*)$ state (T3) is strongly stabilized and becomes accessible for all investigated flavins. This means that direct spin–orbit coupling is less involved in the overall rate determining process, and vibrational spin–orbit-coupling becomes decisive. Following the same argumentation as for fluorescence, the rates of the S1 ⇝ T1 channels are expected to be similar to those in gas phase.

3.4.1 Radiative depopulation of the S1 state. Table 3 summarizes the DFT/MRCI-computed emission energies and fluorescence rate constants in aqueous environment (model A), compared to the corresponding experimental values. For direct comparison, we have removed the frequency dependence of the emission wavelengths (ν^3), as also reported in the work of Reiffers *et al.* We find a good overall agreement between experimental and computed emission maxima; the largest deviation (0.04 eV) is obtained for MIA. The computed emission spectra are, together with the highest wavelength absorption, also depicted in Fig. 8. This figure may be directly compared to the corresponding plot (Fig. 2) in ref. 24, considering the fact that our computed emission bands do not include information on the obtained quantum yields. The height of our computed bands (all in arbitrary units) only depends on the magnitude of the transition dipole moment. For a better view, the height of the MIA emission band was scaled to match the corresponding S1 absorption. The bands for F-MIA were scaled by the same factor.

The energy of the emitted photons corresponds to emission of green light (λ_{comp} = 504–539 nm). In accordance with the experiment, the emission energy barely changes when fluorine is introduced at the C6 position. The same trend is also observed for fluorination at C9. 7F-MIA is slightly red-shifted in emission with respect to MIA, while 8F-MIA exhibits a small blue-shift.

The computed fluorescence rates are all of the same order of magnitude (10^7 s^{-1}) and slightly higher than the experimental values (max. deviation *ca.* 9% for 6F-MIA). The relative trends are, however, well reproduced. 8F-MIA has the largest value, and, within the experimental rate constants, 6F-MIA has the smallest. Due to its relatively small transition dipole moment, the predicted rate constant for 9F-MIA is even lower.

Reiffers *et al.* report the highest fluorescence quantum yield (0.33) for 7F-MIA, while 6F-MIA has the lowest quantum yield. The value for ϕ_{Fl}, however, depends on several factors, also on the rate constant for IC, which is not accessible in our current model.

3.4.2 Non-radiative depopulation. Non-radiative relaxation from S1 involves IC and also ISC in a competitive manner. As already explained, the former cannot be obtained quantitively. Fig. 8 depicts the situation for MIA and F-MIA in aqueous medium by means of ZPVE-corrected adiabatic state energies. The computed rate constants for ISC and fluorescence are also given in this graph. Transition dipole moments and spin–orbit couplings are given in the ESI.†

In solution, all nπ* transitions are strongly blue-shifted. The El-Sayed allowed $^1(\pi\pi^*)$ ⇝ $^3(n\pi^*)$-ISC channel from S1 to T2 found in vacuum is therefore no longer accessible (Fig. 8). ISC can, however, occur *via* the El-Sayed-forbidden $^1(\pi\pi^*)$ ⇝ $^3(\pi\pi^*)$ transitions involving the T3 and T1 states. These states are accessible due to vibronic spin–orbit coupling.[58] A Herzberg–Teller type expansion about the S1 minimum (see the ESI†) shows that mainly out-of-plane modes of a″ character induce the interaction between the ππ*(a′) and nπ* states (a″). As a consequence, the mixed n + π → π* state (a″/a′) can depopulate to the respective ππ* triplet state (a′) due to the partial change of orbital type (intensity borrowing). As the T3–T2 distance is still smaller than T1–T2, T3 can borrow the a″-character of T2 more efficiently, and the spin–vibronic coupling mechanism[55] is more effective in the S1 ⇝ T3 path.

This is also apparent from the computed rate constants (Fig. 8 and Table 4). For S1 ⇝ T1, we obtain values around 10^6 s^{-1}, *i.e.* two orders of magnitude smaller than those for S1 ⇝ T3 ISC. This process takes place on the nanosecond timescale (10^8 s^{-1}). The rate constant of fluorescence (10^7 s^{-1}) is about one order of magnitude smaller. For the El-Sayed allowed S1 ⇝ T2 process, thermal activation is required. Just as in the gas phase, the reverse T2 ⇝ S1 reaction is expected to be faster and thus this channel is neglected.

Values around 10^8 s^{-1} for ISC that match our computed S1 ⇝ T3 rate constant are also reported by Reiffers *et al.* using transient absorption spectroscopy.[24] The only deviation has been measured for 7F-MIA: The observed timescale for ISC of

Table 3 Calculated/experimental[24] fluorescence rate constants k_{Fl}·10^7/s^{-1} and emission energies E_{Em} in eV for MIA and its fluorinated derivatives 6F-, 7F-, 8F- and 9F-MIA in aqueous medium. All values are ZPVE corrected. For direct comparison with the reported experimental values, the frequency dependence of the emission wavelength was omitted

Flavin	k_{Fl}	$k_{Fl(exp.)}$	E_{Em}	$E_{Em(exp.)}$
MIA	5.09	4.45	2.40	2.36
6F-MIA	4.28	3.94	2.34	2.33
7F-MIA	5.01	4.66	2.30	2.32
8F-MIA	6.06	5.94	2.46	2.43
9F-MIA	4.01	—	2.41	—

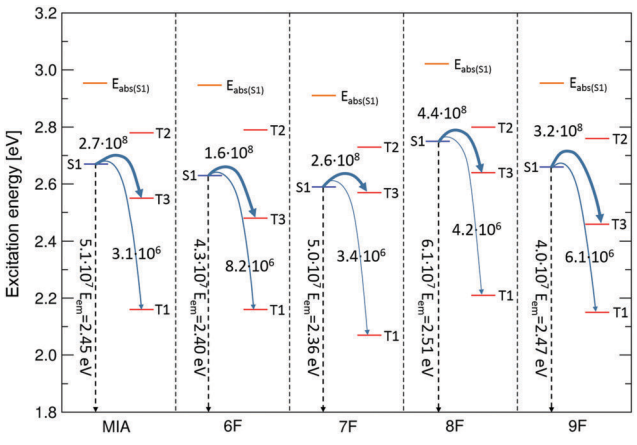

Fig. 8 Adiabatic state energies in eV (DFT/MRCI) and calculated rate constants for fluorescence (k_{Fl}, vertical arrows) and ISC rate constants (k_{ISC}, curved arrows) in aqueous medium (model A). The arrow thickness indicates the magnitude of the corresponding rate constant.

Table 4 Calculated ISC rate constants at 298 K in aqueous medium (model A). For all triplets vibronic spin–orbit coupling was applied. Experimental rate constants in aqueous medium are taken from Reiffers *et al.*[24]

	k_{ISC}/s^{-1}		
Flavin	S1 ⇝ T1	S1 ⇝ T3	$k_{ISC(exp.)}$
MIA	3.1×10^6	2.7×10^8	1.3×10^8
6F-MIA	8.2×10^6	1.6×10^8	1.5×10^8
7F-MIA	3.4×10^6	2.6×10^8	0.3×10^8
8F-MIA	4.2×10^6	4.4×10^8	1.3×10^8
9F-MIA	6.1×10^6	3.2×10^8	—

10^7 s^{-1} could not be reproduced using the energy gap obtained by DFT/MRCI. However, 7F-MIA is the derivate with the lowest energetic release for the S1 ⇝ T3 channel with almost isoenergetic minima (see the ESI†). The rate constant for this molecule is very sensitive to the energy gap between S1 and T3. Raising the T3 energy by only 0.05 eV (*i.e.* by approximately the error in our computed values) results in a lowering of the rate constant by one order of magnitude (10^7 s^{-1}, see the ESI†). We have tested this behaviour also for the other computed compounds. They prove to be less sensitive to shifts of T3, as long as the sign of the adiabatic S1–T3 energy does not change.

In summary, we observe the following effects of fluorination in aqueous medium wrt. the unsusbtituted MIA chromophore. Like in vacuum, 6F mainly lowers the energy of T3. In the same way, 7F has a significantly lower S1 and T1 energy; T3 is slightly upshifted and brings S1 and T3 into close proximity. 8F acts on all ππ*-states and increases their energy. Except for a larger S1–T3 gap, 9F behaves similarly to 6F.

3.5 Additivity of fluorination effects

To predict the effect of di-, tri-, and tetra-fluorination on the excited state properties in solution, we have optimized ground state geometries in aqueous environment (model A) with various substitution patterns and computed the corresponding vertical excitation energies with DFT/MRCI. We find that the relative shifts for poly-fluorination with respect to the unsubstituted MIA-chromophore can be directly obtained by adding the shifts of the mono-fluorinated derivatives. The upper section of Fig. 9 summarizes the relative effects of mono-fluorination on the vertical excitation energies for the low lying singlet and triplet states. Energy differences in eV are reported with respect to MIA. Following this line, fluorination at the C7 position lowers the S1-state energy by 0.05 eV, while for 8F-MIA we obtain a rise in

mono	S1	S3	T1	T2	T3
6F	-0.01	0.00	0.01	0.00	-0.07
7F	-0.05	-0.02	-0.07	-0.01	0.07
8F	0.07	0.02	0.03	0.02	0.09
9F	0.00	-0.02	0.00	-0.01	-0.07

poly	S1	S3	T1	T2	T3
6,7F	-0.05 *(-0.06)*	-0.02 *(-0.03)*	-0.05 *(-0.06)*	0.01 *(-0.01)*	-0.01 *(0.00)*
6,8F	0.07 *(0.06)*	0.02 *(0.02)*	0.04 *(0.04)*	0.03 *(0.03)*	0.03 *(0.02)*
6,9F	-0.01 *(-0.01)*	-0.02 *(-0.02)*	0.02 *(0.01)*	0.02 *(0.00)*	-0.12 *(-0.14)*
7,8F	0.01 *(0.02)*	0.00 *(0.00)*	-0.03 *(-0.04)*	0.02 *(0.01)*	0.15 *(0.16)*
7,9F	-0.05 *(-0.05)*	-0.05 *(-0.04)*	-0.06 *(-0.06)*	-0.02 *(-0.02)*	0.02 *(0.00)*
8,9F	0.07 *(0.07)*	0.00 *(0.00)*	0.04 *(0.03)*	0.01 *(0.01)*	-0.01 ***(0.02)***
6,7,8F	0.02 *(0.01)*	0.01 *(-0.01)*	-0.01 *(-0.03)*	0.03 *(0.02)*	0.08 *(0.09)*
6,7,9F	-0.06 *(-0.06)*	-0.04 *(-0.05)*	-0.05 *(-0.06)*	-0.01 *(-0.01)*	-0.07 *(-0.07)*
6,8,9F	0.07 *(0.06)*	0.00 *(0.00)*	0.04 *(0.04)*	0.01 *(0.02)*	-0.06 *(-0.05)*
7,8,9F	0.02 *(0.01)*	-0.03 *(-0.02)*	-0.01 *(-0.03)*	0.00 *(0.00)*	0.06 ***(0.09)***
6,7,8,9F	0.02 *(0.01)*	-0.01 *(-0.02)*	0.00 ***(-0.03)***	-0.01 *(-0.01)*	0.00 *(-0.02)*

Fig. 9 DFT/MRCI computed shifts of vertical excitation energies wrt. MIA in eV for mono-fluorination (upper part) and poly-fluorination (lower part) in implicit water (model A). The color code indicates whether the respective substitution induces a red- or a blue-shift of the excitation energy. The values in brackets denote direct sums of the values for mono-fluorination. Deviations from the computed value by more than 0.02 eV are marked in red.

the S1 energy by 0.07 eV. The color code behind the values indicates whether the corresponding fluorination delivers a red- or blue-shift for the associated state. As is apparent, the S3 and T2 states with nπ*-character are only marginally affected by mono-fluorination, while the ππ*-states S1, T1 and T3 experience somewhat larger shifts.

In the lower section of Fig. 9 we display the quantum mechanically computed relative shifts for di-, tri- and also tetra-fluorination in implicit water (model A). The values in brackets were obtained by directly adding the shifts of the mono-fluorinated derivatives, *i.e.*, to obtain the value for 6,7F-MIA in S1 (−0.06), the mono 6F (−0.01) and 7F values (−0.05) were summed. The deviations between the quantum-mechanically computed values and those obtained by just adding the mono-fluorination shifts are remarkably small, with just three outliers above 0.02 eV (marked in red in Fig. 9). Thus, the expected shift in the vertical excitation can, with a very tiny error, be directly obtained from the mono-fluorination shifts. This provides an interesting perspective to design substitution patterns for a specific property of the system without the actual need to model all possible permutations and optimize their geometries. Although the matching is remarkable and consistent for all fluorinations and calculations within model A, we must state that the energy differences in these systems are small compared to the error bars of our computed data (*ca.* 0.1–0.2 eV for absorption energies when using implicit solvent modelling), and interpretation thus requires some caution.

Leaving the error bars aside, we find that the potential modifications through poly-fluorination are rather limited and may not significantly outperform those of mono-fluorination. The reason is that mainly ππ* states can be addressed by this substitution technique, and the computed shifts are rather small. Consequently, constructive modification of the system requires substituents with a larger influence on the electronic states.

4 Summary and conclusions

In this work, we have presented optimized geometries for the ground states of MIA and its fluorinated derivatives 6F-, 7F-, 8F- and 9F-MIA. With these geometries we have illustrated vertical absorption spectra in the gas phase for all investigated flavins. Furthermore, oscillator strengths and electronic structures have been analyzed. To include surrounding effects we have applied two solvation models: Model A represents the well-established conductor-like screening model (COSMO) and model B is a more sophisticated ansatz including explicit hydrogen bridge linkages. The respective positions and count of water molecules attached to the chromophores have been deduced systematically from overall 50 molecular-mechanics simulations. This procedure has enabled us to validate our calculated electronic information: An extensive comparison with experimental spectra clarifies that our methodological approach is capable of reproducing electronic properties well in addition to structural parameters.

To investigate possible relaxation channels, we have optimized S1, S2 and the three energetically lowest triplet states and determined vibrational frequencies. The pathways for the competing processes of fluorescence and ISC were evaluated quantitatively. The latter one includes two mechanisms depending on the surroundings of the flavins: for $^1(\pi\pi^*) \rightsquigarrow {}^3(n\pi^*)$-ISC (T2) direct electronic coupling has been considered and for $^1(\pi\pi^*) \rightsquigarrow {}^3(\pi\pi^*)$ transitions (T1 and T3) vibronic spin–orbit coupling by a Herzberg–Teller type expansion has been applied.

Overall, we have outlined the following relaxation model for the photoreaction of MIA and F-MIA: Subsequent to absorption of the states S9, S5 or directly S1, a major part of the population arrives in the S1 state. From here it can either deplete *via* IC, be emitted radiatively (fluorescence) or pass over to the triplet domain. For ISC in vacuum the dominating process is the El-Sayed allowed $^1(\pi\pi^*) \rightsquigarrow {}^3(n\pi^*)$ transition toward the T2 state on a timescale of 10^9 s^{-1}. In aqueous medium there is a fundamental change in the deactivation channel to the triplet domain: T2 is blue-shifted and the $^1(\pi\pi^*) \rightsquigarrow {}^3(n\pi^*)$ transition toward the T3 state becomes thermodynamically accessible. This process now dominates the ISC-timescale in water (10^8 s^{-1}) through spin–vibronic coupling. Fluorescence, on the contrary, generally occurs on a timescale of 10^7 s^{-1}. The largest increase of the fluorescence rate has been computed for 8F-MIA (+16%); the smallest rate constant results for 9F-MIA (−21%). Comparison with experimental values[24] for the solvated systems reveals good agreement of our theoretical values, supporting the described insights into the mechanism of deactivation.

We have also gained insight into the effect of fluorination and could identify trends that depend on the position of substitution. Except for the switch in T2/T3 state ordering, the effects in vacuum and solvent show some similarities. 6F substitution mainly affects the T3 state energy. The lowering of this state is, however, more pronounced in solution. In both vacuum and water, the energy of S1 and T1 in 7F-MIA is lower than in MIA, and the T3 state is slightly upshifted. In solvent, this leads to a small S1/T3 energy gap. Even slight modification of this gap toward smaller values significantly reduces the ISC S1 $\rightsquigarrow$ T3 ISC rate, thus favoring fluorescence. 8F upshifts all ππ* state energies in both surroundings, and finally 9F behaves similarly to 6F.

The influence of fluorine substitution on the excitation energies is additive, *i.e.* the properties of poly-fluorinated systems can, with a small error, be derived from the mono-fluorinated ones. This opens a perspective for targeted control and optimization of dyes toward applications as fluorescence markers or as efficient generators of singlet oxygen[14] for photodynamic therapy. The effects of poly-fluorination for the molecules under study are, however, small, and computational inaccuracies must be considered in this analysis.

In a much less polar protein environment ($\varepsilon \approx 3$), the nπ* states experience a considerably smaller blue-shift. Modifications for fluorescence optimization must therefore aim at preventing the El-Sayed allowed ISC to the ^{3}nπ* state. The FMN core is a viable target for such modifications. 1-Deaza-FMN and 5-deaza-FMN particularly influence the nπ* energies by deleting one nitrogen lone pair.[66] For the latter, even a higher fluorescence yield in aqueous solution and an alternative reaction pathway in YtvA

were reported. In combination with fluorination, such strategies may deliver promising results.

Conflicts of interest

There are no conflicts of interest to declare.

Acknowledgements

We cordially thank Prof. Christel M. Marian and Prof. Peter Gilch (both from HHU Düsseldorf) for helpful discussion and Anna Reiffers (HHU Düsseldorf) for providing experimental UV spectra. Financial support by Deutsche Forschungsgemeinschaft (DFG) through funds (INST 208/704-1 FUGG) to purchase the hybrid computer cluster used in this study is gratefully acknowledged.

References

1 A. Losi and W. Gärtner, *Annu. Rev. Plant Biol.*, 2012, **63**, 49–72.
2 M. A. van der Horst and K. J. Hellingwerf, *Acc. Chem. Res.*, 2004, **37**, 13–20.
3 A. Möller, S. Sagasser, W. Wiltschko and B. Schierwater, *J. Nat. Sci.*, 2004, **91**, 585–588.
4 M. Gomelsky and G. Klug, *Trends Biochem. Sci.*, 2002, **27**, 497–500.
5 E. Demarsy and C. Fankhauser, *Curr. Opin. Plant Biol.*, 2009, **12**, 69–74.
6 W. R. Briggs, C. F. Beck, A. R. Cashmore, J. M. Christie, J. Hughes, J. A. Jarillo, T. Kagawa, H. Kanegae, E. Liscum, A. Nagatani, K. Okada, M. Salomon, W. Rüdiger, T. Sakai, M. Takano, M. Wada and J. C. Watson, *Plant Cell*, 2001, **13**, 993–997.
7 N. Suetsugu and M. Wada, *J. Biol. Chem.*, 2007, **388**, 927–935.
8 S. Inoue, A. Takemiya and K. Shimazaki, *Curr. Opin. Plant Biol.*, 2010, **13**, 587–593.
9 B. M. Parks, K. M. Parks and E. P. Spalding, *Curr. Opin. Plant Biol.*, 2001, **4**, 436–440.
10 K. Huang and C. F. Beck, *Proc. Natl. Acad. Sci. U. S. A.*, 2003, **100**(10), 6269–6274.
11 J. Svoboda, H. Schmaderer and B. Konig, *Chem. – Eur. J.*, 2008, **14**(6), 1854–1865.
12 N. A. Romero and D. A. Nicewicz, *Chem. Rev.*, 2016, **116**, 10075–10166.
13 S. Fukuzumi, K. Tanii and T. Tanaka, *J. Chem. Soc., Perkin Trans. 2*, 1989, 2103–2108.
14 X. Shu, V. Lev-Ram, T. J. Deerinck, Y. Qi, E. B. Ramko, M. W. Davidson, Y. Jin, M. H. Ellisman and R. Y. Tsien, *PLoS Biol.*, 2011, **9**, e1001041.
15 E. Sikorska, I. V. Khmelinskii, W. Prukała, S. L. Williams, M. Patel, D. R. Worrall, J. L. Bourdelande, J. Koput and M. Sikorski, *J. Phys. Chem. A*, 2004, **108**, 1501–1508.
16 S. Salzmann, J. Tatchen and C. M. Marian, *J. Photochem. Photobiol., A*, 2008, **198**, 221–231.
17 S. Salzmann, M. R. Silva-Junior, W. Thiel and C. M. Marian, *J. Phys. Chem. B*, 2009, **113**, 15610–15618.
18 S. Salzmann, V. Martinez-Junza, S. E. Braslavsky, M. Mansurova, C. M. Marian and W. Gärtner, *J. Phys. Chem. A*, 2009, **113**, 9365–9375.
19 M. Sung, T. A. Moore and P. Song, *J. Am. Chem. Soc.*, 1972, **94**, 1730–1740.
20 J. T. M. Kennis, S. Crosson, M. Gauden, I. H. M. van Stokkum, K. Moffat and R. van Grondelle, *Biochemistry*, 2003, **42**, 3385–3392.
21 W. Holzer, A. Penzkofer and P. Hegemann, *Chem. Phys.*, 2005, **308**, 79–91.
22 E. Sikorska, I. V. Khmelinskii, D. R. Worrall, J. Koput and M. Sikorski, *J. Fluoresc.*, 2004, **14**, 57–64.
23 B. Klaumünzer, D. Kröner and P. Saalfrank, *J. Phys. Chem. B*, 2010, **114**, 10826–10834.
24 A. Reiffers, C. Torres Ziegenbein, A. Engelhardt, R. Kühnemuth, P. Gilch and C. Czekelius, *Photochem. Photobiol.*, 2018, **94**, 667–676.
25 J. Hasegawa, S. Bureekaew and H. Nakatsuji, *J. Photochem. Photobiol., A*, 2007, **189**, 205–210.
26 T. Climent, R. González-Luque, M. Merchán and L. Serrano-Andrés, *J. Phys. Chem. A*, 2006, **110**, 13584–13590.
27 C. Neiss, P. Saalfrank, M. Parac and S. Grimme, *J. Phys. Chem. A*, 2003, **107**, 140–147.
28 E. Sikorska, I. V. Khmelinskii, J. Koput, J. L. Bourdelande and M. Sikorski, *J. Mol. Struct.*, 2004, **697**, 137–141.
29 M. Mansurova, J. Simon, S. Salzmann, C. M. Marian and W. Gärtner, *ChemBioChem*, 2013, **14**, 645–654.
30 C. M. Marian, S. Nakagawa, V. Rai-Constapel, B. Karasulu and W. Thiel, *J. Phys. Chem. B*, 2014, **118**, 1743–1753.
31 M. A. North, S. Bhattacharyya and D. G. Truhlar, *J. Phys. Chem. B*, 2010, **114**, 14907–14915.
32 X. Li and Y. Fu, *THEOCHEM*, 2008, **856**, 112–118.
33 W. A. Francisco, H. M. Abu-Soud, R. Topgi, T. O. Baldwin and F. M. Raushel, *J. Biol. Chem.*, 1997, **272**, 10982.
34 K. Zenichowski, M. Gothe and P. Saalfrank, *J. Photochem. Photobiol., A*, 2007, **190**, 290–300.
35 A. D. Becke, *J. Chem. Phys.*, 1993, **98**, 5648–5652.
36 C. Lee, W. Yang and R. G. Parr, *Phys. Rev. B: Condens. Matter Mater. Phys.*, 1988, **37**, 785–789.
37 TURBOMOLE V7.1 2017, a development of University of Karlsruhe and Forschungszentrum Karlsruhe GmbH, 1989-2007, TURBOMOLE GmbH, since 2007, available from http://www.turbomole.com.
38 J. Neugebauer, M. Reiher, C. Kind and B. A. Hess, *J. Comput Chem.*, 2002, **23**(9), 895–910.
39 A. P. Scott and L. Radom, *J. Phys. Chem.*, 1996, **100**, 16502–16513.
40 S. Grimme and M. Waletzke, *J. Chem. Phys.*, 1999, **111**, 5645.
41 A. D. Becke, *J. Chem. Phys.*, 1993, **98**, 1372–1377.
42 M. Kleinschmidt, J. Tatchen and C. M. Marian, *J. Comput. Chem.*, 2002, **23**, 824–833.
43 M. Kleinschmidt and C. M. Marian, *Chem. Phys.*, 2005, **311**, 71–79.
44 B. A. Heß, C. M. Marian, U. Wahlgren and O. Gropen, *Chem. Phys. Lett.*, 1996, **251**, 365–371.

45 B. Schimmelpfennig, *AMFI, an atomic mean-field spin-orbit integral program*, Stockholm University, 1996.
46 J. Tatchen and C. M. Marian, *Chem. Phys. Lett.*, 1999, **313**, 351–357.
47 D. Danovich, C. M. Marian, T. Neuheuser, S. D. Peyerimhoff and S. Shaik, *J. Phys. Chem. A*, 1998, **102**, 5923–5936.
48 A. Klamt and G. Schüürmann, *J. Chem. Soc., Perkin Trans. 2*, 1993, 799–805.
49 D. A. Case, V. Babin, J. T. Berryman, R. M. Betz, Q. Cai, D. S. Cerutti, T. E. Cheatham, III, T. A. Darden, R. E. Duke, H. Gohlke, A. W. Goetz, S. Gusarov, N. Homeyer, P. Janowski, J. Kaus, I. Kolossváry, A. Kovalenko, T. S. Lee, S. LeGrand, T. Luchko, R. Luo, B. Madej, K. M. Merz, F. Paesani, D. R. Roe, A. Roitberg, C. Sagui, R. Salomon-Ferrer, G. Seabra, C. L. Simmerling, W. Smith, J. Swails, R. C. Walker, J. Wang, R. M. Wolf, X. Wu and P. A. Kollman, *AMBER 14*, University of California, San Francisco, 2014.
50 W. L. Jorgensen, J. Chandrasekhar, J. D. Madura, R. W. Impey and I. Klein, *J. Chem. Phys.*, 1983, **79**, 926–935.
51 J. Wang, R. M. Wolf, J. W. Caldwell, P. A. Kollman and D. A. Case, *J. Comput. Chem.*, 2004, **25**, 1157–1174.
52 U. C. Singh and P. A. Kollmann, *J. Comput. Chem.*, 1984, **5**, 129–145.
53 H. J. C. Berendsen, J. P. M. Postma, W. F. van Gunsteren, A. DiNola and J. R. Haak, *J. Chem. Phys.*, 1984, **81**, 3684.
54 O. Weingart, A. Nenov, P. Altoè, I. Rivalta, J. Segarra-Martí, I. Dokukina and M. Garavelli, *J. Mol. Model.*, 2018, **24**, 271.
55 T. Penfold, E. Gindensperger, C. Daniel and C. M. Marian, *Chem. Rev.*, 2018, **118**, 6975–7025.
56 M. Etinski, J. Tatchen and C. M. Marian, *Phys. Chem. Chem. Phys.*, 2014, **16**, 4740–4751.
57 M. Etinski, J. Tatchen and C. M. Marian, *J. Chem. Phys.*, 2011, **134**, 154105.
58 J. Tatchen, N. Gilka and C. M. Marian, *Phys. Chem. Chem. Phys.*, 2007, **9**, 5209–5221.
59 M. Etinski, V. Rai-Constapel and C. M. Marian, *J. Chem. Phys.*, 2014, **140**, 114104.
60 M. Wang and C. J. Fritchie Jr., *Acta Crystallogr., Sect. B: Struct. Crystallogr. Cryst. Chem.*, 1973, **29**, 2040–2045.
61 K. Tomić, J. Tatchen and C. M. Marian, *J. Phys. Chem. A*, 2005, **109**, 8410–8418.
62 S. Salzmann, M. Kleinschmidt, J. Tatchen, R. Weinkauf and C. M. Marian, *Phys. Chem. Chem. Phys.*, 2008, **10**, 380–392.
63 J. Tatchen and C. M. Marian, *Phys. Chem. Chem. Phys.*, 2006, **8**, 2133–2144.
64 M. Klessinger and J. Michl, *Excited states and photochemistry of organic molecules*, Wiley VCH, New York, 1995.
65 P. Gilch and A. Reiffers, private communication.
66 M. R. Silva-Junior, M. Mansurova, W. Gärtner and W. Thiel, *ChemBioChem*, 2013, **14**, 1648–1661.

Impact of Mono-Fluorination on the Photophysics of the Flavin Chromophore: A Quantum Chemical Perspective (Electronic Supplementary information)

*Mario Bracker, Fabian Dinkelbach, Oliver Weingart, Martin Kleinschmidt**

Institute of Theoretical and Computational Chemistry, Heinrich Heine University Düsseldorf, Universitätsstr. 1,
D-40225 Düsseldorf, Germany

Corresponding author

*Tel.: +49 211 8113209; fax: +49 211 8113466.
E-mail address: Martin.Kleinschmidt@uni-duesseldorf.de (M. Kleinschmidt).
URL: http://www.theochem.uni-duesseldorf.de (M. Kleinschmidt).

1 Molecular orbitals

At the ground state geometries the energetic order of orbitals in general is as follows:

1. π_{L+2}
2. π_{L+1}
3. π_{L}
4. π_{H}
5. π_{H-1}
6. n_{O2}
7. π_{H-2}
8. n_{N2}
9. n_{O1}
10. π_{H-3}
11. n_{N1}

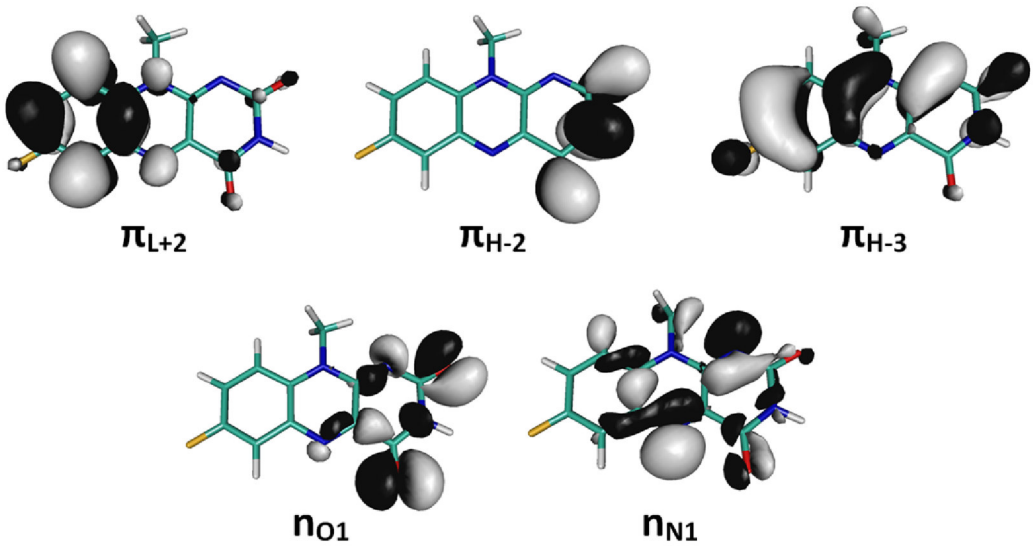

The remaining orbitals of 7F-MIA are depicted in the main paper. With respect to the O/N2 orbitals, the O/N1 orbitals in large part represent the opposite linear combinations of the respective in-plane lone pairs.

2 Geometries

2.1 Ground state

Table S1: Calculated bond lengths in picometres (pm) for the ground state of MIA and its fluorinated derivatives 6-9F-MIA. Experimental values originate from X-ray diffraction [M. Wang, C. J. Fritchie Jr., Acta Crystallogr. (1973) 2040-2045].

Bond	Length / pm					
	MIA	exp.	6F-MIA	7F-MIA	8F-MIA	9F-MIA
N(1)–C(2)	138.1	136.0(5)	138.3	138.2	138.3	138.2
C(2)–N(3)	141.4	140.8(5)	141.3	141.5	141.3	141.4
N(3)–C(4)	137.9	135.4(5)	138.0	137.8	137.9	137.7
C(4)–C(4a)	150.2	148.5(5)	150.3	150.4	150.1	150.4
C(4a)–N(5)	129.0	129.5(5)	129.0	129.0	129.1	128.8
N(5)–C(5a)	136.9	136.6(5)	136.3	137.0	136.6	136.9
C(5a)–C(6)	140.6	141.8(5)	141.1	140.5	140.6	140.5
C(6)–C(7)	137.8	136.8(6)	137.5	137.2	137.7	137.6
C(7)–C(8)	140.1	139.5(6)	139.8	139.4	139.5	139.8
C(8)–C(9)	138.4	138.8(6)	138.4	138.3	137.9	137.7
C(9)–C(9a)	140.3	139.2(5)	140.3	140.4	140.2	140.8
C(9a)–N(10)	138.6	139.0(5)	138.4	138.6	138.2	138.8
N(10)–C(10a)	138.2	136.9(5)	138.4	138.1	138.5	138.6
C(10a)–N(1)	130.0	131.9(5)	129.8	129.9	129.8	129.9
C(5a)–N(9a)	141.9	141.8(5)	142.0	141.8	141.7	142.4
C(4a)–N(10a)	146.2	146.6(5)	146.2	146.3	146.1	146.1
C(10)–R	146.8	148.8(5)	146.8	146.8	146.8	147.9
C(2)–O	121.1	121.6(5)	121.0	121.1	121.0	121.0
C(4)–O	121.0	121.7(5)	120.9	121.0	121.0	121.0
C(6/7/8/9)–F	-	-	133.4	134.8	134.5	135.4

2.2 Excited states

Table S2: Calculated bond lengths in picometres (pm) for the excited states (S1, S2, T1-3) of 7F-MIA.

Bond	Length / pm				
	S1	S2	T1	T2	T3
N(1)–C(2)	140.2	130.5	139.3	137.7	138.1
C(2)–N(3)	137.7	135.9	138.4	140.3	140.9
N(3)–C(4)	141.5	143.3	139.9	138.8	138.7
C(4)–C(4a)	145.6	145.2	147.3	146.2	147.0
C(4a)–N(5)	135.2	135.5	136.2	132.2	136.8
N(5)–C(5a)	134.1	133.6	133.5	134.5	132.5
C(5a)–C(6)	140.8	142.0	141.6	139.9	144.1
C(6)–C(7)	138.0	136.9	136.8	137.9	142.9
C(7)–C(8)	139.9	139.5	140.6	138.5	135.3
C(8)–C(9)	138.6	139.0	138.3	139.4	144.5
C(9)–C(9a)	140.3	139.4	140.1	139.3	139.7
C(9a)–N(10)	138.8	140.2	138.6	140.1	138.0
N(10)–C(10a)	137.2	136.4	140.2	138.5	141.1
C(10a)–N(1)	133.2	135.5	132.5	130.0	130.3
C(5a)–N(9a)	144.7	143.6	145.7	142.8	142.8
C(4a)–N(10a)	142.9	141.1	141.0	144.5	142.8
C(10)–R	147.1	146.5	146.4	146.4	146.5
C(2)–O	121.8	129.3	121.9	121.2	121.4
C(4)–O	121.5	121.0	121.3	121.8	121.9
C(7)–F	134.1	135.1	134.3	134.8	133.9

3 Solvent modeling

Table S3 summarizes statistics derived from overall 50 molecular dynamics simulations, which were conducted to ensure a systematic approach for including explicit interactions of the investigated flavins with water (solvation model B).

Table S3: Count of hydrogen bridge linkages per oxygen/nitrogen/fluorine atom for MIA and its fluorinated (positions 6-9) derivatives. In the last two columns the counts C and relative frequencies $f_{rel.}$ are specified. The results stem from QM/MM-optimized snapshots of molecular dynamics simulations at 298 K and 1 bar, each lasting for 200 ps.

Atom	Count of hydrogen bridge linkages						
	MIA	6F-MIA	7F-MIA	8F-MIA	9F-MIA	C	$f_{rel.}$
N(1)	8	8	10	6	9	41	0.82
O(11)	20	19	20	21	19	99	1.98
N(3)	11	9	9	10	9	48	0.96
O(13)	15	17	12	15	13	72	1.44
N(5)	4	5	6	4	6	25	0.50
F(6/7/8/9)	-	3	5	4	5	17	0.43

4 Vibronic absorption spectra

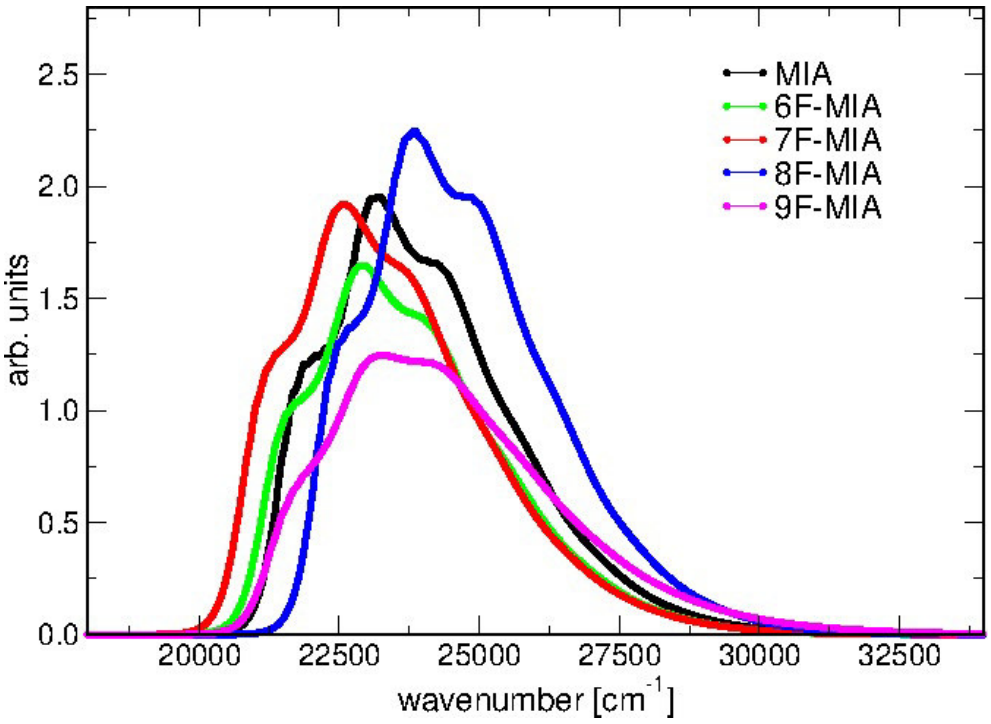

Figure S1: DFT/MRCI computed (model A) vibronic absorption spectra highlighting vibrational finestructure.

5 Artificial imaginary frequencies

To obtain real-valued values for artificial imaginary frequencies we carried out least square fits for TDDFT scans along the respective modes – the convoluted potential stemming from the artifact

herefore was excluded. In practice we neglected the inner region of the respective parabola: Beginning at the artificial maximum points were neglected consecutively until a threshold for the coefficient of determination fulfilled a criterion of $R^2 > 0.9999$. To validate this approach, the same procedure was tested for normal modes delivering real-valued frequencies with respect to normal mode analysis – the resulting frequencies were reproduced well for fitted parabolas neglecting the inner region of the fitted curves.

6 Adiabatic transition energies

Gas phase

To construct potential relaxation paths after photoexcitation, adiabatic transition energies are indispensable. Table S4 summarizes those for the S1 minima to the respective triplet minima T1, T2 and T3 of MIA and its derivatives 6F-, 7F, 8F- and 9F-MIA in gas phase. This selection is due to the preferential population of the comparatively long-lived S1 state with regard to the absorption-relaxation-cycle.

Table S4: Summarized adiabatic transition energies in gas phase. The values include zero-point vibrational energy (ZPVE) corrections for the equilibrium geometries. Computed ISC rate constants are given in brackets.

Flavin	Energy difference / eV; (rate constant / s^{-1}) adiabatic transition				
	S1 $\rightsquigarrow$ T1	S1 $\rightsquigarrow$ T2	S1 $\rightsquigarrow$ T3	S1 $\rightsquigarrow$ S0	S1 $\rightsquigarrow$ S2
MIA	-0.64 ($1.4 \cdot 10^7$)	-0.06 ($2.3 \cdot 10^9$)	0.09	-2.59	0.27
6F-MIA	-0.64 ($1.5 \cdot 10^7$)	-0.06 ($3.7 \cdot 10^9$)	0.06	-2.60	0.28
7F-MIA	-0.65 ($8.6 \cdot 10^6$)	-0.02 ($1.3 \cdot 10^9$)	0.15	-2.52	0.27
8F-MIA	-0.68 ($5.8 \cdot 10^6$)	-0.08 ($2.9 \cdot 10^9$)	0.13	-2.66	0.17
9F-MIA	-0.63 ($1.5 \cdot 10^7$)	-0.06 ($2.2 \cdot 10^9$)	0.00	-2.57	0.31

Aqueous medium

For the solvated flavins the energetics of the S1 and T1 states and as a consequence S1 $\rightsquigarrow$ T1 transition energies barely change. Due to strong stabilization of the T3 state in water, the S1 $\rightsquigarrow$ T3 channel becomes thermodynamically allowed for all vibrational states. Reversely, the T2 state is strongly blue shifted and consequentially can be neglected. Similarly, $(n\pi^*)^1$-states are strongly blue shifted in aqueous medium, so that interaction with the S1 potential is excluded from the investigation.

Table S5: Summarized adiabatic transition energies in aqueous solution. The values include zero-point vibrational energy (ZPVE) corrections for the equilibrium geometries. Computed ISC rate constants are given in brackets.

Flavin	Energy difference / eV; (rate constant / s^{-1}) adiabatic transition			
	S1 $\rightsquigarrow$ T1	S1 $\rightsquigarrow$ T2	S1 $\rightsquigarrow$ T3	S1 $\rightsquigarrow$ S0
MIA	-0.50 ($3.1 \cdot 10^6$)	0.11	-0.12 ($2.7 \cdot 10^8$)	-2.67
6F-MIA	-0.47 ($8.2 \cdot 10^6$)	0.15	-0.15 ($1.6 \cdot 10^8$)	-2.63
7F-MIA	-0.52 ($3.4 \cdot 10^6$)	0.14	-0.02 ($2.6 \cdot 10^8$)	-2.59
8F-MIA	-0.54 ($4.2 \cdot 10^6$)	0.05	-0.05 ($4.4 \cdot 10^8$)	-2.75
9F-MIA	-0.51 ($6.1 \cdot 10^6$)	0.10	-0.19 ($3.2 \cdot 10^8$)	-2.66

7 Fluorescence

Table S6: Calculated transition dipole moments μ_{S1S0} in Debye of MIA and its fluorinated derivatives 6F-, 7F-, 8F- and 9F-MIA in gas phase as well as aqueous solution.

Flavin	μ_{S1S0}	
	gas phase	H_2O
MIA	4.80	4.54
6F-MIA	4.53	4.24
7F-MIA	4.78	4.65
8F-MIA	5.04	4.81
9F-MIA	4.31	4.09

8 Spin–orbit coupling

For The lowest $(\pi\pi^*)^3$-transitions, T1 and T3, direct couplings do not exceed the size of order 10^{-4} cm^{-2} and a vibronic treatment has to be applied.

8.1 Direct spin–orbit coupling

Table S7: Summary of direct spin-orbit couplings $|\langle\Psi_{S1}|\hat{\mathcal{H}}_{SO}|\Psi_{T2}\rangle|^2_{q0}$ / cm^{-2} at the optimized S1 geometries of MIA and its fluorinated derivatives 6F-, 7F-, 8F- and 9F-MIA in gas phase as well as aqueous solution.

Flavin	$\|\langle\Psi_{S1}\|\hat{\mathcal{H}}_{SO}\|\Psi_{T2}\rangle\|^2$	
	gas phase	H_2O
MIA	77.99	47.78
6F-MIA	109.11	66.01
7F-MIA	66.08	48.49
8F-MIA	74.35	65.94
9F-MIA	71.05	64.24

8.2 Vibronic spin–orbit coupling

The size of derivatives of spin–orbit matrix elements with respect to normal modes Q_k depends on the effectiveness of the respective modes to induce spin–orbit coupling between the involved states. For the investigated transitions, the $^3(\pi\pi^*)$-states (T1, T3) are required to borrow $n\pi^*$-character from triplet states in energetic proximity. Exemplary normal modes for the S1 $\rightsquigarrow$ T3-ISC rate are following a"-modes:

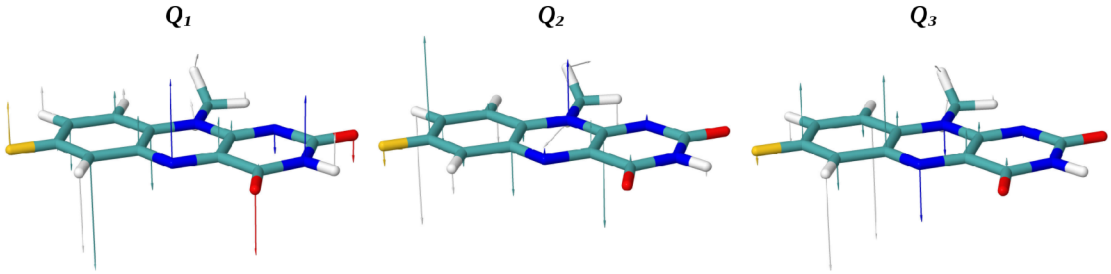

Figure S2: Illustration of three eigenvectors of 7F-MIA.

The depicted eigenvectors induce the biggest derivatives of SOMEs for the considered transition.

Table S8: Biggest derivatives of spin-orbit matrix elements $|\partial\langle\Psi_{S1}|\hat{\mathcal{H}}_{SO}|\Psi_{T3}\rangle|^2_{q0}/\partial Q_k|$ / cm^{-2} in water (model A) at the optimized S1 geometry of 7F-MIA with respect to normal modes Q_k and corresponding frequencies $\tilde{\nu}$ / cm^{-1}.

Q_k	$\tilde{\nu}$	$\|\partial SOME/\partial Q_k\|^2$
Q_1	147.28	0.42
Q_2	572.88	0.38
Q_3	462.54	0.34

9 Dependency of S1 ⇝ T3 ISC in water on energy gap

Table S9: Summary of S1 ⇝ T3 ISC-rate constants in aqueous solution (model A). In the first column rate constants k_{ISC} / $10^8 \cdot s^{-1}$ calculated with the original energy gaps are given. The italic numbers represent rate constants for shifted T3 energies ($k_{ISC}{}^{+0.1\,ev}$ / $10^8 \cdot s^{-1}$). The factors in the last row represent a measure for the sensitivity of the transition on the energy gap.

Flavin	k_{ISC}	$k_{ISC}{}^{+0.1\,ev}$	$\frac{k_{ISC}}{k_{ISC}^{+0.1\,ev}}$
MIA	2.7	*1.4*	1.9
6F	1.6	*0.6*	3.0
7F	2.6	*0.4*	7.4
8F	4.4	*2.3*	1.9
9F	3.2	*1.7*	1.8

10 Vertical absorption spectra

The line styles depict the main orbital contribution (S1 and T1: $\pi_H \rightarrow \pi_L$, T3 and S5: $\pi_{H-1} \rightarrow \pi_L$, T2 and S3: $n_{N2} \rightarrow \pi_L$, S2: $n_{O2} \rightarrow \pi_L$).

Gas phase

For the relaxation paths in vacuum T1, T2, T3 as well as S2 are considered for the deactivation of the populated S1 state.

10.1 S0

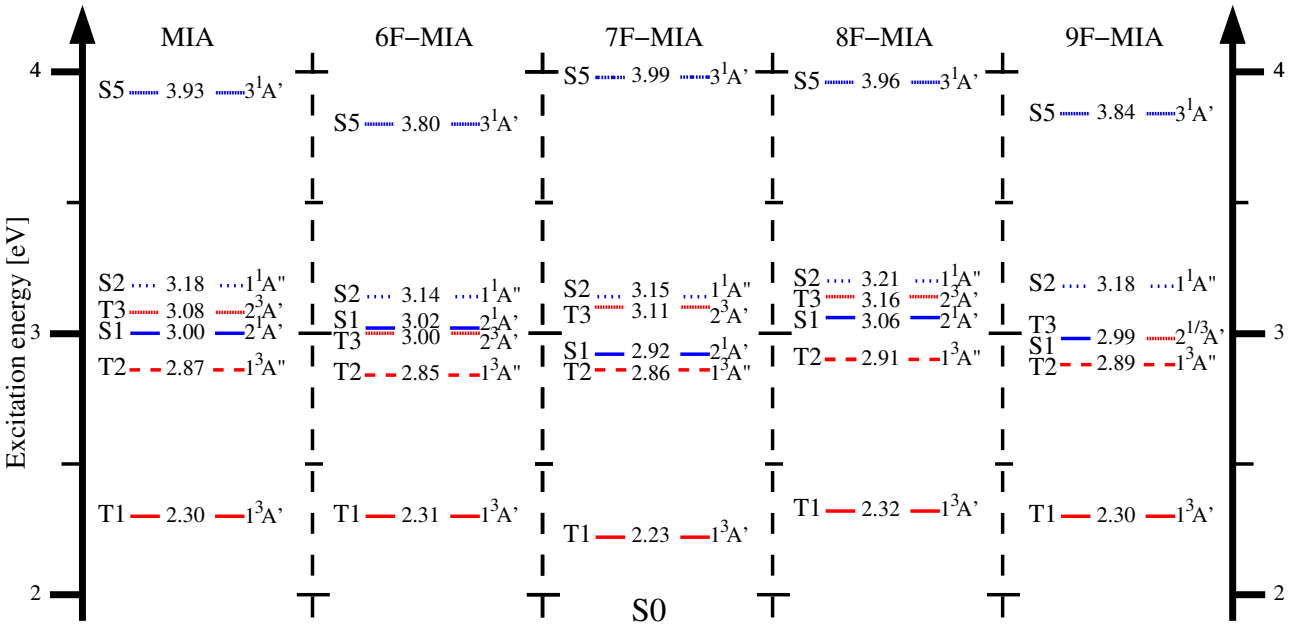

Figure S3: Selected vertical electronic transition energies in eV (DFT/MRCI) at the respective ground state geometries in gas phase.

10.2 S1

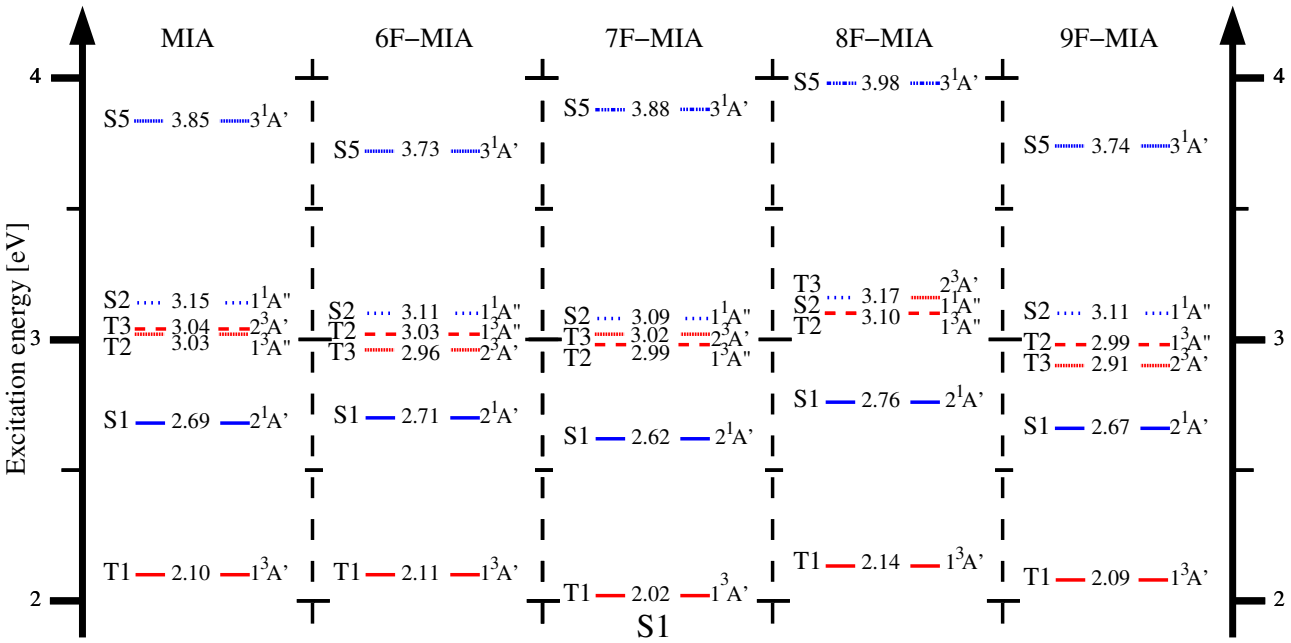

Figure S4: Selected vertical electronic transition energies in eV (DFT/MRCI) at the respective S1 equilibrium geometries in gas phase.

10.3 S2

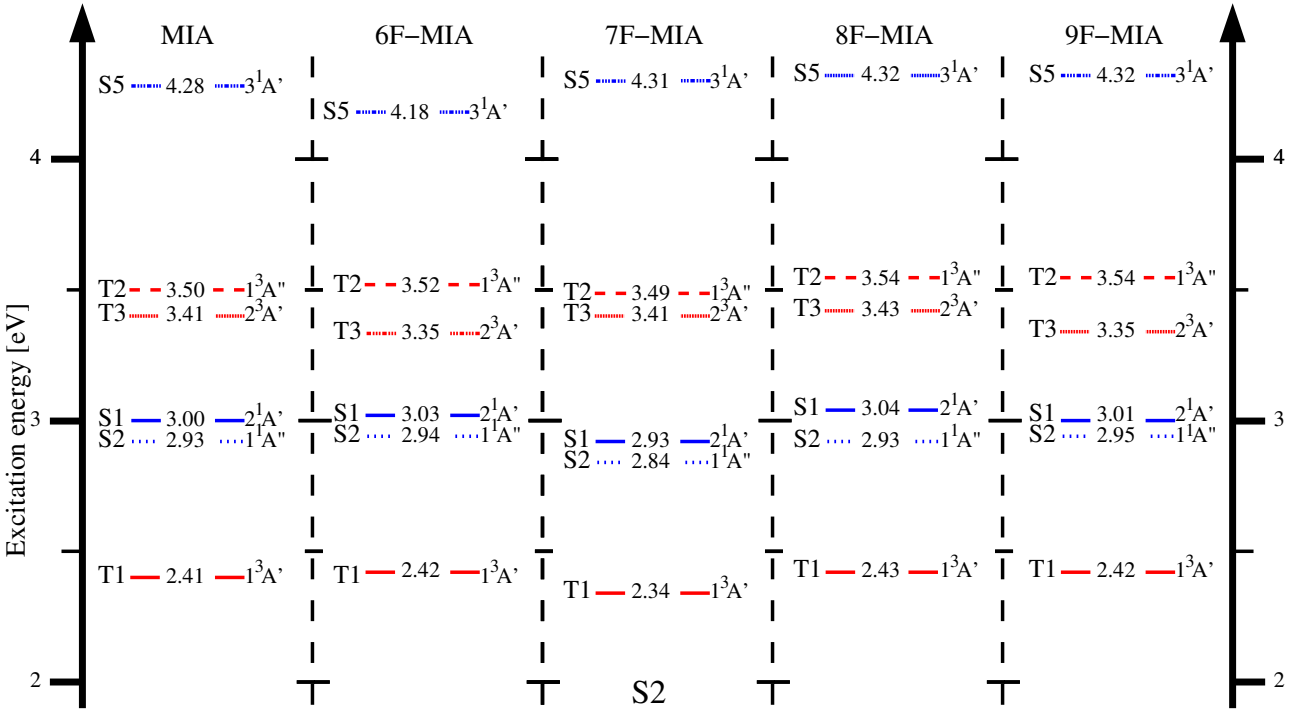

Figure S5: Selected vertical electronic transition energies in eV (DFT/MRCI) at the respective S2 equilibrium geometries in gas phase.

10.4 T1

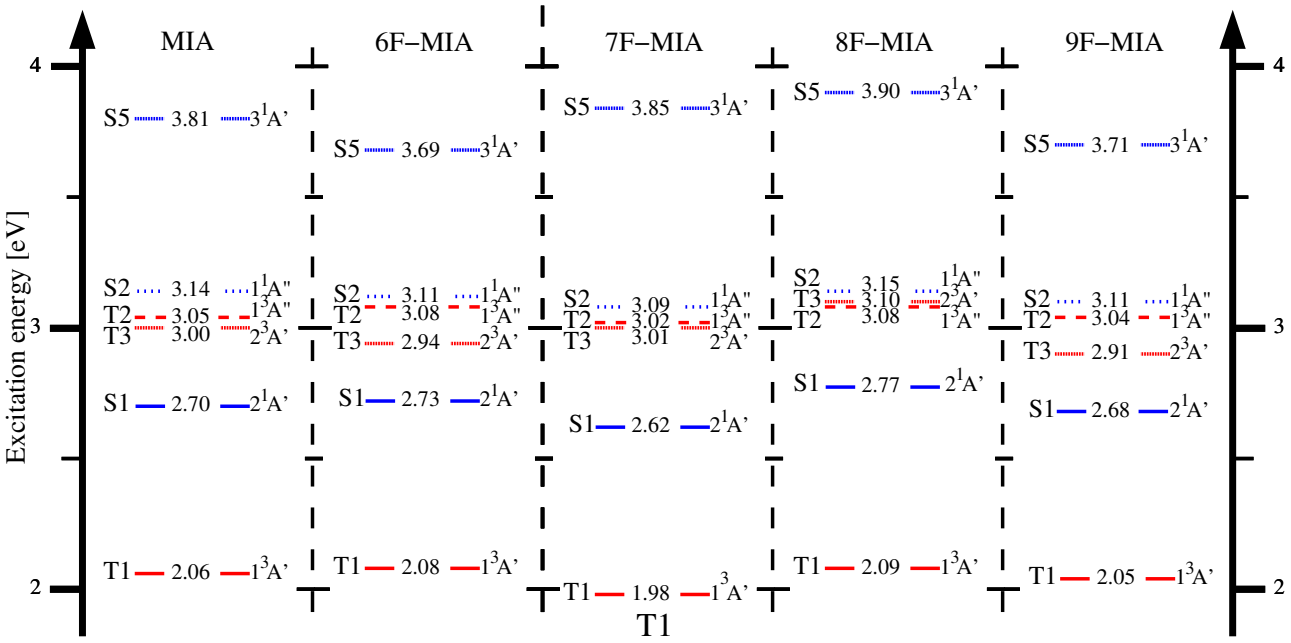

Figure S6: Selected vertical electronic transition energies in eV (DFT/MRCI) at the respective T1 equilibrium geometries in gas phase.

10.5 T2

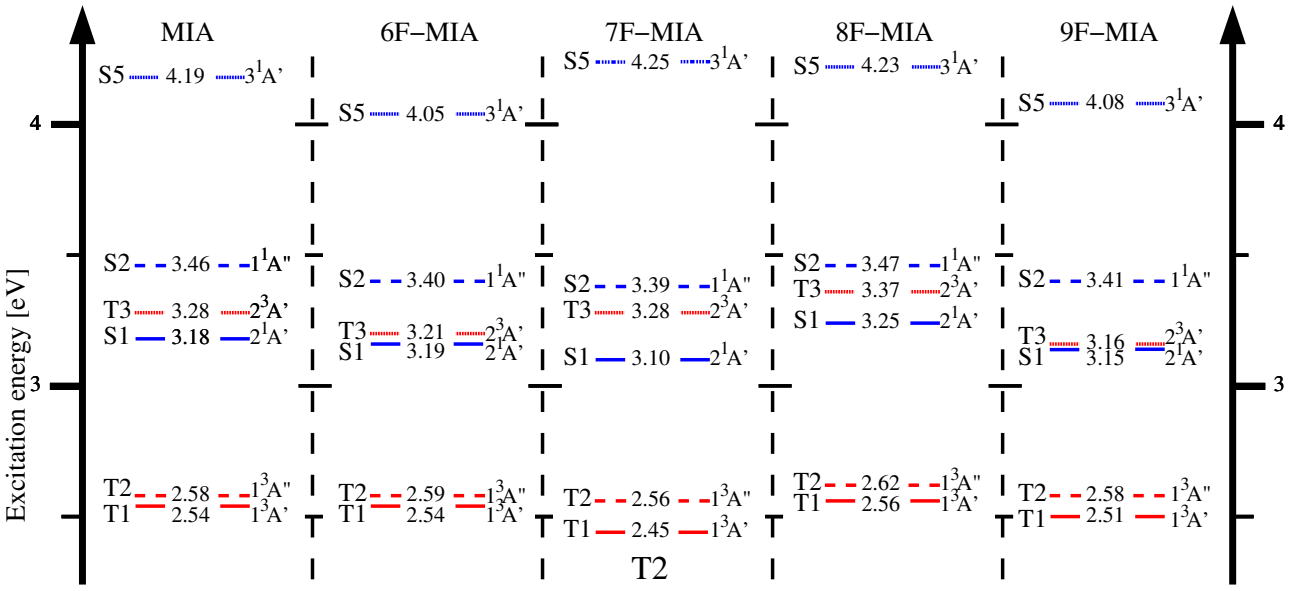

Figure S7: Selected vertical electronic transition energies in eV (DFT/MRCI) at the respective T2 equilibrium geometries in gas phase.

10.6 T3

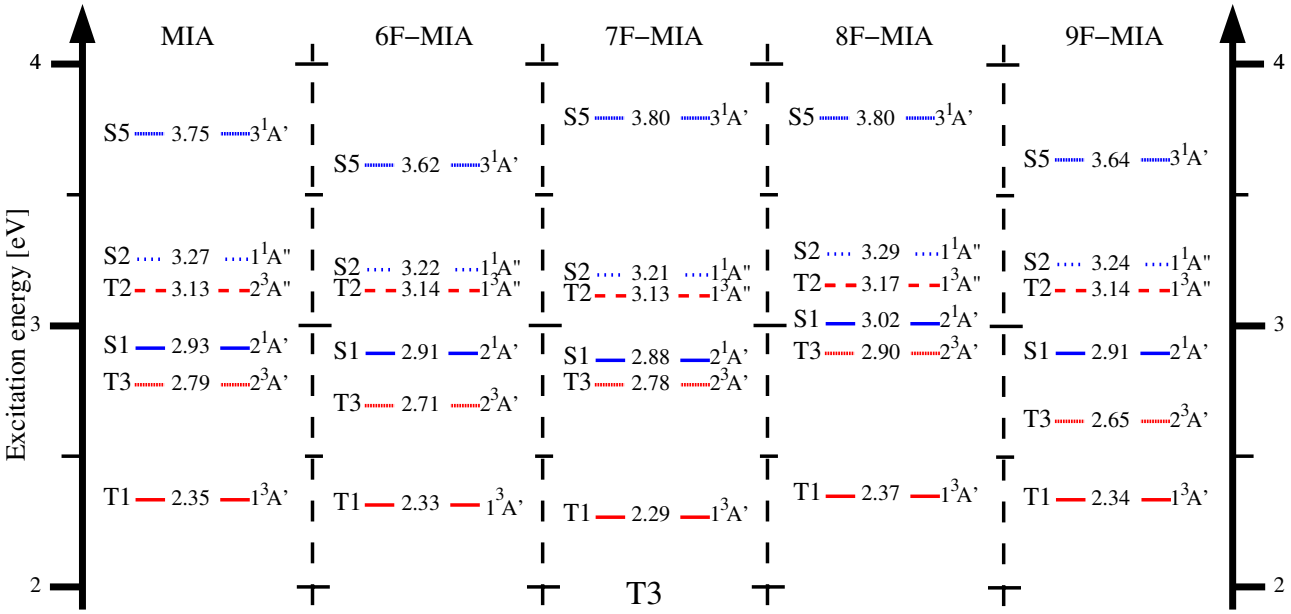

Figure S8: Selected vertical electronic transition energies in eV (DFT/MRCI) at the respective T3 equilibrium geometries in gas phase.

Aqueous medium

$(n\pi^*)^1$-states are strongly blue shifted in aqueous medium, so that the S2 minimum potential is excluded from the investigation.

Model A

10.7 Ground state

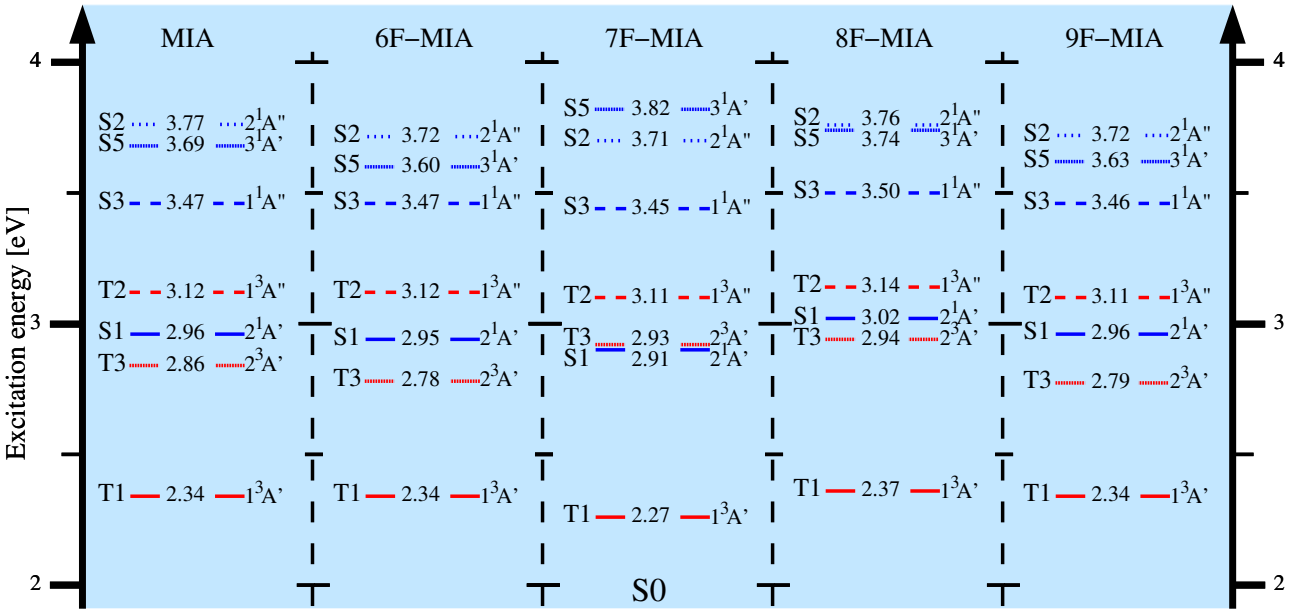

Figure S9: Selected vertical electronic transition energies in eV (DFT/MRCI) at the respective ground state equilibrium geometries in aqueous medium (model A).

10.8 S1

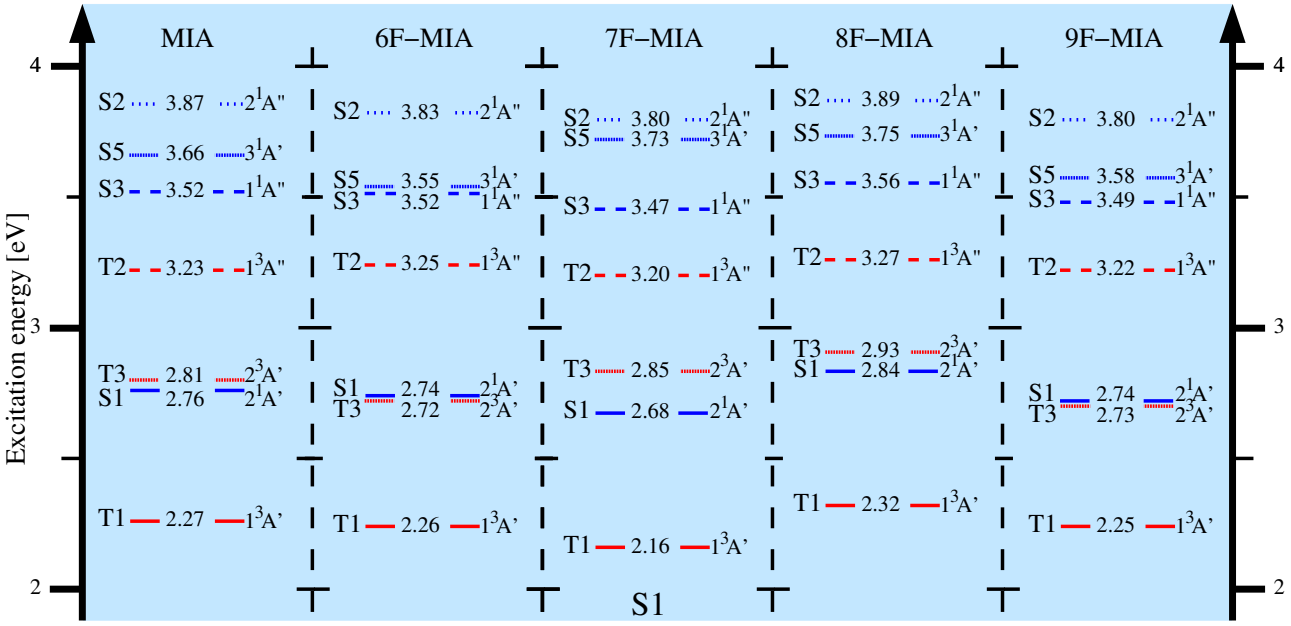

Figure S10: Selected vertical electronic transition energies in eV (DFT/MRCI) at the respective T1 equilibrium geometries in aqueous medium (model A).

10.9 T1

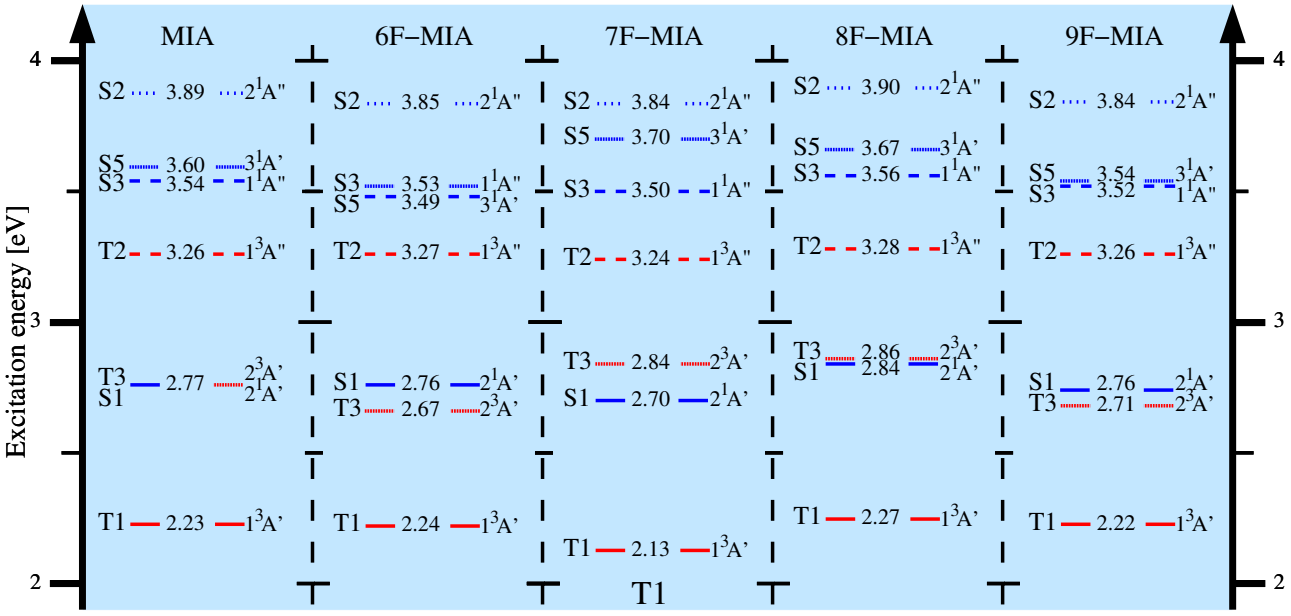

Figure S11: Selected vertical electronic transition energies in eV (DFT/MRCI) at the respective T1 equilibrium geometries in aqueous medium (model A).

10.10 T2

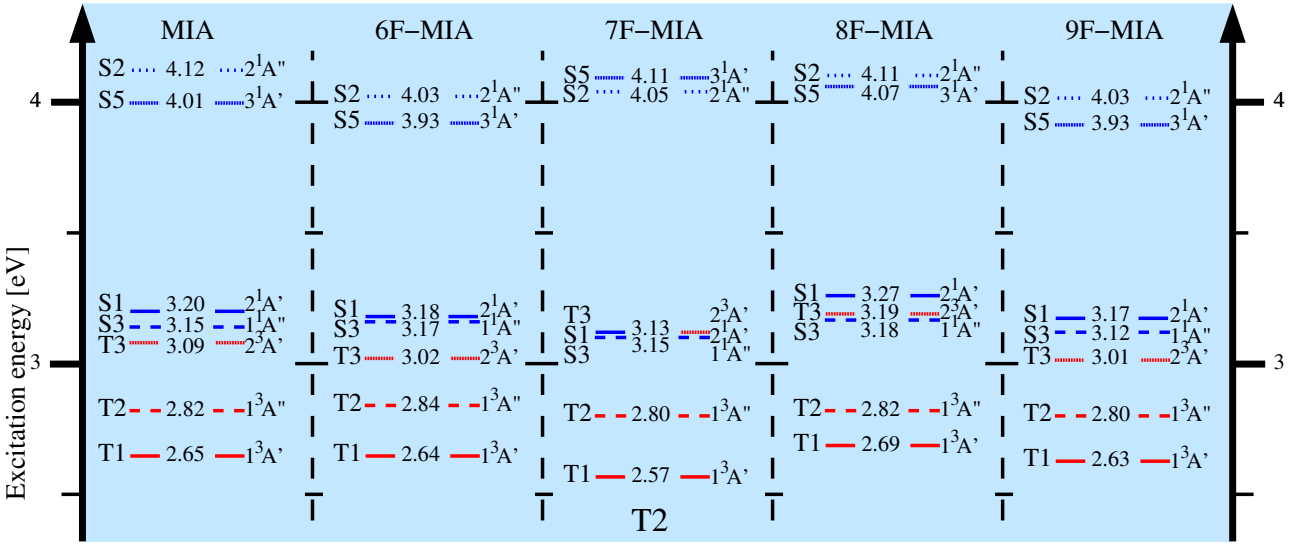

Figure S12: Selected vertical electronic transition energies in eV (DFT/MRCI) at the respective T3 equilibrium geometries in aqueous medium (model A).

10.11 T3

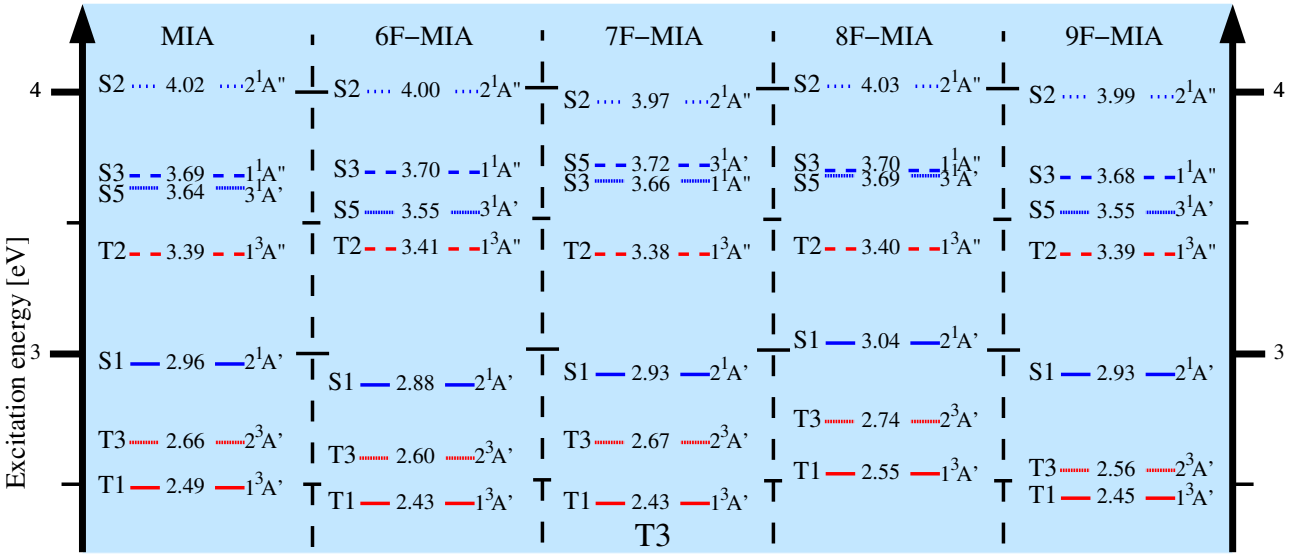

Figure S13: Selected vertical electronic transition energies in eV (DFT/MRCI) at the respective T3 equilibrium geometries in aqueous medium (model A).

Model B

10.12 Ground state

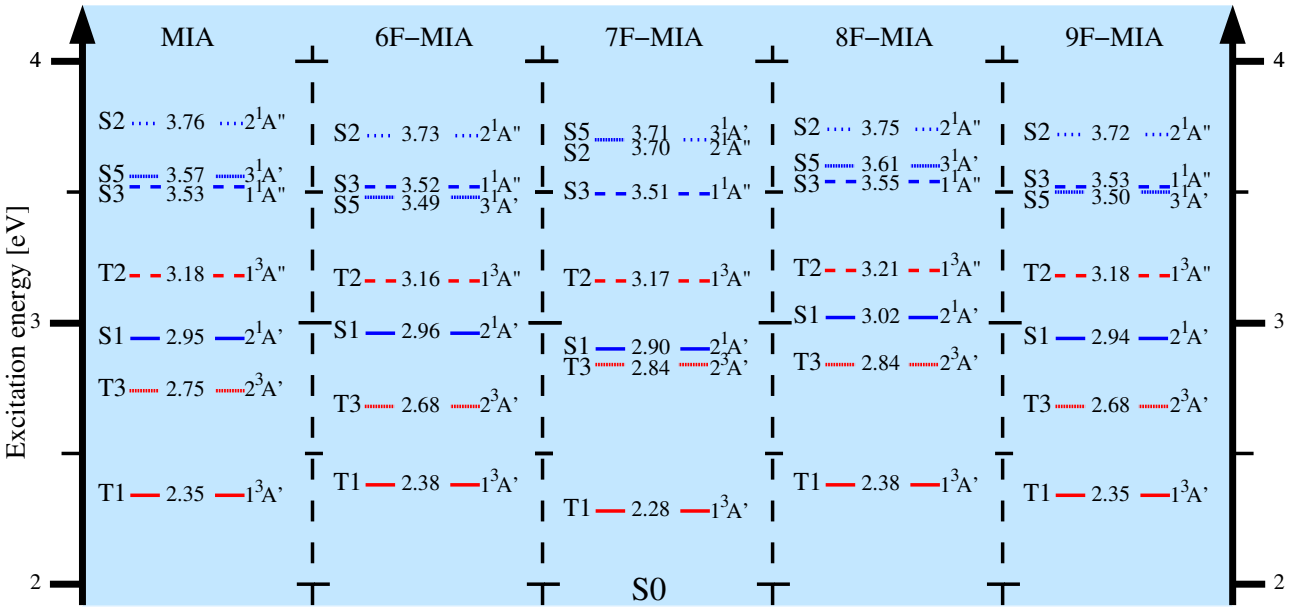

Figure S14: Selected vertical electronic transition energies in eV (DFT/MRCI) at the respective ground state equilibrium geometries in aqueous medium (model B).

ChemPhotoChem

Research Articles
doi.org/10.1002/cptc.202200040

Chemistry Europe
European Chemical Societies Publishing

www.chemphotochem.org

Special Collection

Computer-Aided Design of Fluorinated Flavin Derivatives by Modulation of Intersystem Crossing and Fluorescence

Mario Bracker,[a] Mira K. Kubitz,[b] Constantin Czekelius,[b] Christel M. Marian,[a] and Martin Kleinschmidt*[a]

This study aims at finding fluorinated flavin derivatives with modified intersystem crossing (ISC) and fluorescence properties. In total, photophysical properties of 8 derivatives were investigated computationally using combined density functional theory and multireference configuration interaction methods. On top of a screening procedure, the excited-state decay mechanisms of selected chromophores were investigated in detail. Kinetic schemes including fluorescence, ISC as well as internal conversion (IC) channels were set up to unravel the complex excited-state decay kinetics. We find two chromophores that exhibit promising properties with respect to fluorescence microscopy. Distinctive stabilization of the bright S_1 $\pi\pi^*$ state results in absorption in the green wavelength region and emission of (infra-)red light. The $^1(\pi_H\pi_L)\rightsquigarrow{}^3(\pi_{H-1}\pi_L)$ ISC channel of the flavin chromophore was found to be deactivated upon both modifications, but nonradiative deactivation of the fluorescence by IC appears to be a problem. Alternative modifications of the pteridine dione moiety were found to result in a marked stabilization of $n\pi^*$ states along with activation of El-Sayed allowed ISC channels. For the latter two compounds, we predict fluorescence to be quenched by ISC followed by efficient population of the long-lived T_1 state via IC.

Introduction

Diverse photoreactive proteins carry a flavin moiety.[1–7] Among photoreceptors, phototropins are plasma-membrane-associated proteins mediating primarily phototropic plant movement.[8–10] In phototropins, the optically active flavin mononucleotide (FMN) is incorporated into light, oxygen and voltage sensitive (LOV) domains. Upon characteristic blue-light absorption,[11–13] the photosensing LOV domain undergoes a photocycle: The lowest-lying triplet state of FMN is efficiently populated via intersystem crossing (ISC). Accompanied by another ISC, a metastable adduct between the cofactor and a nearby cysteine residue is formed transducing a structural signal to an effector domain.[13–15] Eventually, the adduct decomposes thermally on the timescale of seconds.[16] Various modified flavins (8-isopropyl,[17] 1- and 5-deaza,[18] 8-bromo and 8-trifluoromethyl,[19] roseoflavin[20,21] as well as methyl substitution patterns[17,22,23] in positions 7 and 8) have been incorporated into LOV domains. Riboflavin-5'-phosphate (FMN) can be divided into two parts: Lumiflavin (LF) and the ribophosphyl chain attached to the nitrogen atom in position 10 of the core ring (see Figure 1). The latter is involved in the signal transduction upon excitation of the LF moiety by blue-light absorption. The photophysics of FMN is dominated by the isoalloxazine core ring and the experimental absorption as well as emission spectra of FMN and LF are found to be very similar.[11,12] LF exhibits two methyl groups in positions 8 and 9 (see Figure 1), which have minor influence on the photophysics.[24]

[a] M. Bracker, Prof. C. M. Marian, Dr. M. Kleinschmidt
Institute of Theoretical and Computational Chemistry, Heinrich-Heine-University Düsseldorf, D-40204 Düsseldorf, Germany
E-mail: Martin.Kleinschmidt@hhu.de
[b] M. K. Kubitz, Prof. C. Czekelius
Institute of Organic and Macromolecular Chemistry, Heinrich-Heine-University Düsseldorf, D-40204 Düsseldorf, Germany

Supporting information for this article is available on the WWW under https://doi.org/10.1002/cptc.202200040

An invited contribution to a Special Collection on Emissive Materials for Organic Light Emitting Diodes

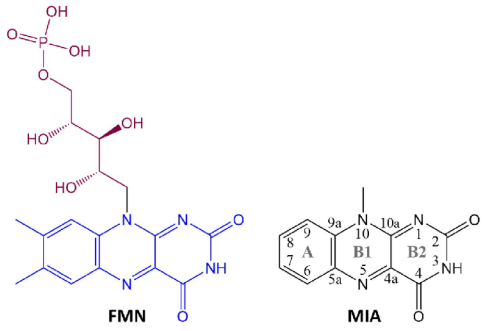

Figure 1. Chemical structures of flavin mononucleotide (FMN) and 10-methylisoalloxazine (MIA). The structure highlighted in blue colour is the lumiflavin (LF) chromophore and the ribophosphyl chain is illustrated in wine-red colour.

Modulation of intersystem crossing

The ISC channels of naturally occurring flavins have been analyzed in several previous studies, either linked to the mechanism of photoreception[13,15,25] or describing the isolated chromophore.[24,26,27] In this study we focus on the core ring (MIA, see Figure 1). Starting from the equilibrium geometry of the S_1 $\pi_H\pi_L$ state of MIA, three triplet states have been found to be decisive for the efficiency of ISC: T_1, T_2 and T_3. The electronic structure of the T_1 state corresponds to the one of the bright S_1 state, the T_2 state exhibits nitrogen-centered [N(1+5)] $n_N\pi^*$ character and the T_3 $\pi_{H-1}\pi_L$ transition is an internal charge transfer (ICT) from the benzene (A) ring to the peridinone (B) rings of MIA (see Figure 1). The role of the latter two states for deactivation strongly depends on the polarity and proticity of the environment: Polar interactions cause a strong blueshift of the $n\pi^*$ states and a stabilization of the ICT state (see Figure 2, middle scheme). As a result, the fast El-Sayed allowed $^1(\pi_H\pi_L)\rightsquigarrow{}^3(n_N\pi_L)$ channel, accessible in vacuum and apolar media, is deactivated and ISC relies on spin–vibronic interactions instead.[24,27] $S_1\rightsquigarrow T_1$ and $S_1\rightsquigarrow T_3$ ISC are promoted by a Herzberg-Teller-like intensity borrowing mechanism:[28–30] Invoking vibrational spin–orbit coupling, the $\pi\pi^*$ states partially adopt $n\pi^*$ character thus increasing the ISC probability. Reiffers et al. determined ISC of MIA in aqueous medium from femtosecond transient absorption and nanosecond laser flash photolysis experiments ($k_{ISC} = \Phi_T/\tau_F$) to take place with a rate constant of about $1\times10^8\ s^{-1}$.[26] With the aid of advanced quantum chemical methods, $^1(\pi_H\pi_L)\rightsquigarrow{}^3(\pi_{H-1}\pi_L)$ ISC was identified as the productive channel featuring a rate constant of $3\times10^8\ s^{-1}$, approximately two orders of magnitude faster than the alternative $^1(\pi_H\pi_L)\rightsquigarrow{}^3(\pi_H\pi_L)$ channel.[24,27] $^3(\pi_{H-1}\pi_L)\rightsquigarrow{}^3(\pi_H\pi_L)$ internal conversion (IC) takes place at the femtosecond timescale ($>10^{13}\ s^{-1}$, see Section S8 in the Electronic Supplementary Information (ESI)). The $^3(\pi_{H-1}\pi_L)$ population is thus rapidly transferred to the T_1 $^3(\pi_H\pi_L)$ state. The experimental triplet quantum yield of MIA amounts to $\Phi_T = 0.5\ (\pm0.1)$ in aqueous solution.[26] With a rate constant of approximately $5\times10^7\ s^{-1}$ and a quantum yield of $\Phi_F = 0.22\ (\pm0.01)$ fluorescence is nearly competitive to ISC in MIA.[26,27] This finding raises the question, whether and how the decay mechanism of MIA following photo excitation could be modified to either increase the fluorescence quantum yield or the triplet quantum yield of the chromophore.

In principle, there are two approaches to modulate the complex ISC mechanism of flavins: a) modify the chromophore itself[18,19,21,27,31,32] or b) adjust the polarity and proticity of the environment.[24,33] This study focuses on the modification of the MIA chromophore in aqueous solution. Activation of an El-Sayed favoured ISC channel is anticipated to result in high Φ_T and deactivation of the $^1(\pi_H\pi_L)\rightsquigarrow{}^3(\pi_{H-1}\pi_L)$ channel is taken as the best-case scenario for raising Φ_F (see Figure 2).

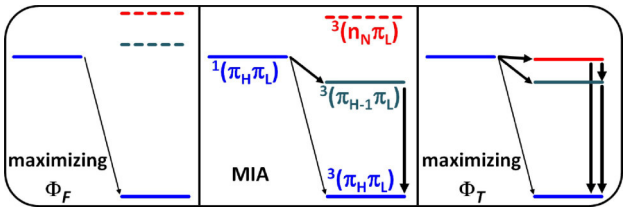

Figure 2. Schematic depiction of adiabatic energies associated with increased fluorescence quantum yield (left) or increased triplet quantum yield (right), respectively. The middle scheme illustrates the adiabatic energies of MIA in aqueous solution. Dashed states are thermodynamically inaccessible from the $^1(\pi_H\pi_L)$ state and the thickness of the arrows correlates with the magnitudes of the rate constants.

Modification of the flavin chromophore

To find potential chromophores suitable for each scenario depicted in Figure 2, we use a screening method that is motivated by our latest work on flavin derivatives fluorinated in the A-ring of MIA.[27] Fluorine is a very potent substituent when it comes to tailoring photophysical properties.[26,27,34–37] For one thing, it is the element with the highest electronegativity and therefore a strong impact on the electronic structure is expected. Secondly, the steric change when substituting hydrogen by fluorine is small.[38,39] A positive side effect is the stabilization with respect to photo-oxidation.[40,41] In the present study, fluorine is incorporated into the B-rings (Figure 3). In particular, the substitution pattern focuses on the carbonyl groups and the nitrogen atoms in positions 1 and 5 of the pteridine dione unit (see Figure 1 for atom labels). The studies address the influence of a single fluorine atom or geminal disubstitution by fluorine. Compounds $2CF_2$-MIA and $4CF_2$-MIA, in which the C=O moiety is replaced by a difluoromethylidene group, incorporate an electron-deficient enamine. In solution, acid-catalyzed tautomerization to the corresponding pteridi-

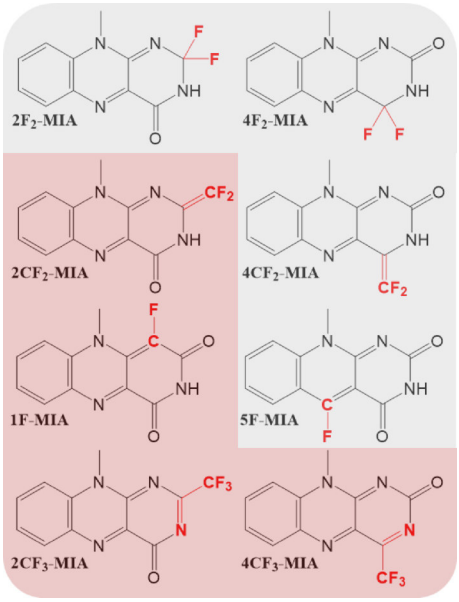

Figure 3. Chemical structures of flavin derivatives investigated in this work. Derivatives highlighted with red background are studied in detail with respect to excited state kinetics.

none may occur, which is prevented e.g. by N-alkylation rendering the depicted compounds suitable models for calculation.

Our previous in-depth study on the fluorination of carbon centers in the A-ring revealed that shifts of vertical electronic energies with respect to the parent compound at the ground-state geometry can be used to estimate adiabatic electronic energies of excited states with reasonable precision.[27] In the present study, we rely on this observation and, in a first step, characterize the derivatives at the ground state geometry. The most promising candidates are then investigated in further detail with respect to their excited state kinetics.

Methods and Computational Details

Ground state geometries were optimized at the density functional theory (DFT) level utilizing the Turbomole 7.3 program package.[42,43] The B3LYP functional[44,45] combined with the TZVP basis set[46] was employed. For excited singlet states, full linear response equations were solved[47] and for triplet states the Tamm–Dancoff approximation[48] was chosen to avoid triplet instabilities. Unless otherwise stated, a C_s symmetry constraint was applied for geometry optimization. Vibrational frequency analyses were carried out using numerical second derivatives with the SNF program.[49] Subsequent DFT/MRCI[50] single-point calculations were performed with the original parametrization established by Grimme and Waletzke.[51] DFT/MRCI is a semi-empirical multireference configuration interaction ansatz based on Kohn-Sham orbitals (BHLYP)[45,52] as a one-particle basis. For the construction of two-electron integrals, the TZVP auxiliary basis set[53] from the Turbomole library was applied for the resolution-of-identity approximation.[54] In the case of singlet states 12 roots were computed and for triplets 8 states were considered. DFT/MRCI computed line spectra were broadened in the cm^{-1} regime using a Gaussian function with a standard deviation of $\sigma = 1500\,cm^{-1}$ and then converted to nm. Environment effects of aqueous solution at ambient temperature were mimicked applying the implicit solvation model COSMO[55] with a relative permittivity of $\varepsilon_r = 80$ to the ground state optimizations as well as DFT/MRCI calculations. Solvation effects at the excited state geometries were included by introducing state-specific energy shifts as described in reference [56]. Wavefunction analysis based on Löwdin orthogonalization of the one-electron density matrix was carried out using the TheoDORE program.[57,58] We computed spin–orbit coupling matrix elements (SOCMEs) at the DFT/MRCI level of theory using the program package SPOCK[59,60] developed in our laboratory. The coupling is described by a spin–orbit mean-field (SOMF) approximation[61,62] of the Breit–Pauli spin–orbit operator. Non-adiabatic coupling matrix elements (NACMEs) were obtained with our newly developed program DELTA.[56] ISC and IC rate constants at ambient temperature were computed via the generating function approach as implemented in the program VIBES.[56,63,64] For all ISC channels, numerical derivatives of the SOCMEs were computed at the respective equilibrium geometries. Corresponding generating functions, G_{ISC} and G_{IC}, can be found in references [64] and [56] respectively.

$$k_{NR}^{a\rightsquigarrow b} = Z^{-1}\int_{-\infty}^{+\infty} G_{NR}\, e^{it\Delta E_{ab}}\, dt \tag{1}$$

$Z = \sum_j e^{-E_{aj}/k_BT}$ is the canonical partition function for vibrational motion in the initial electronic state and ΔE_{ab} is the adiabatic separation of states a and b. Fluorescence rate constants are given by

$$k_F^{a\rightarrow b} = \frac{1}{3\pi\varepsilon_0 \hbar^4 c^3}\Delta E_{ab}^3 |\vec{\mu}_{ab}|^2\,, \tag{2}$$

where $\vec{\mu}_{ab}$ is the transition dipole moment and in this case ΔE_{ab} represents the vertical energy of electronic states a and b. Fluorescence spectra were computed with the program VIBES to include explicit vibrational broadening.

Results and Discussion

Screening of derivatives

Figure 4 illustrates the influence of each modification on the electronic energies of selected states at the ground state geometries in aqueous medium. The depicted shifts refer to the vertical excitation energies of the stem compound MIA. The respective data of MIA is summarized in Table 1. The character of the electronic states is determined by the leading configuration and the values in parentheses represent the squared coefficients of the contribution. The numbering of the n_N orbitals refers to the energetic order of the different linear

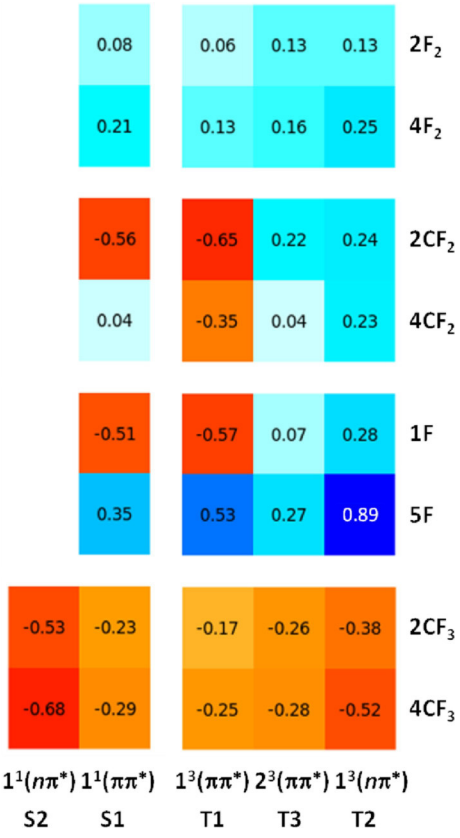

Figure 4. Illustration of the impact of modification on the electronic energies of the S1 as well as T1–T3 states in aqueous medium. For 2/4CF_3-MIA the $^1(n\pi^*)$state is included. The blue-/redshifts in eV are computed at the ground state geometries and refer to the vertical excitation energies of MIA.

Table 1. Excited states properties of MIA in aqueous solution.

State	Electronic structure ($\|c\|^2$)	$\Delta E_{vertical}$ / eV (*f*)
$^1(\pi_H\pi_L)$	$\pi_H \rightarrow \pi_L$(0.83)	2.96 (*0.275*)
$^1(n_N\pi_L)$	$n_{N2} \rightarrow \pi_L$(0.76)	3.47
$^3(\pi_H\pi_L)$	$\pi_H \rightarrow \pi_L$(0.88)	2.33
$^3(\pi_{H-1}\pi_L)$	$\pi_{H-1} \rightarrow \pi_L$(0.81)	2.86
$^3(n_N\pi_L)$	$n_{N2} \rightarrow \pi_L$(0.70) + $n_{N1} \rightarrow \pi_L$(0.14)	3.12

combinations. In the case of the deaza-compounds, only one n_N orbital remains and for $2CF_3$- as well as $4CF_3$-MIA a third n_N orbital is introduced. Corresponding oxygen-centered n_O orbitals are strongly stabilized in polar environment.[24,27] However, the n_{O2} orbital gains significance for the $n\pi^*$ states of the deaza-compounds. The notation of states without subscript (e.g. S1 instead of S_1) refers to the order of the electronic states at the ground-state equilibrium geometry.

For $2CF_3$- as well as $4CF_3$-MIA, the $^1(n_N\pi_L)$ state is added as the $n\pi^*$states are strongly stabilized. For the other molecules, the $^1(n_N\pi_L)$ state is blueshifted and therefore neglected. Molecular orbitals and tables summarizing excited state properties are presented here only for the most interesting derivatives, i.e., 1F-, $2CF_2$, $2CF_3$- as well as $4CF_3$-MIA. Corresponding data for the remaining fluorinated flavins is displayed in Section S1 in the ESI. Fragment-based analysis, absorption spectra, orbital energies, transition dipole moments and additional depictions of molecular orbitals are collected in Sections S2–6 in the ESI.

$2CF_2$-MIA and $4CF_2$-MIA. $2CF_2$-MIA and $4CF_2$-MIA differ from the stem chromophore MIA by an isolobal replacement of the oxygen atom in 2- or 4-position by difluoro-methylidene. Interestingly, these substitutions have vastly different effects on the energetic location of the first excited singlet state. While the S1 state undergoes a small blueshift of 0.04 eV in $4CF_2$-MIA, in the corresponding derivative modified in position 2 the $^1(\pi_H\pi_L)$ state is strongly redshifted by more than half an electronvolt (−0.56 eV). This remarkable difference is not reflected in the main character of the excitation, in both cases the S1 state is described as $\pi_H \rightarrow \pi_L$ transition by about 80 %. The molecular orbitals generally are destabilized upon introduction of CF_2. Whilst the effect is similar for the π_L orbitals, the energetic shift of the π_H orbital is far less pronounced for modification in position 4. To rationalize this finding, the π_H orbitals have to be inspected (compare Figures 5, and S1 in the ESI): In both cases we find a strong electron withdrawing effect diminishing the electron density on the benzene core and for modification in position 2 of the B2-ring, the nodal structure on the B1-ring is changed. The same applies to the T1 state, which is redshifted by −0.65 eV for $2CF_2$-MIA compared to −0.35 eV for modification in position 4. The blueshift of the $^3(n_N\pi_L)$ state is almost the same for both derivatives, whereas the destabilization of the $^3(\pi_{H-1}\pi_L)$ state strongly depends on the position of modification. The more pronounced blueshift of the latter excitation in $2CF_2$-MIA (0.22 eV compared to 0.04 eV) is explained by the remarkably high admixture of the $\pi_{H-2}\pi_L$ excitation to an extent that the main character changes (Table 2). As a consequence, the S1 and T1 states of $2CF_2$-MIA

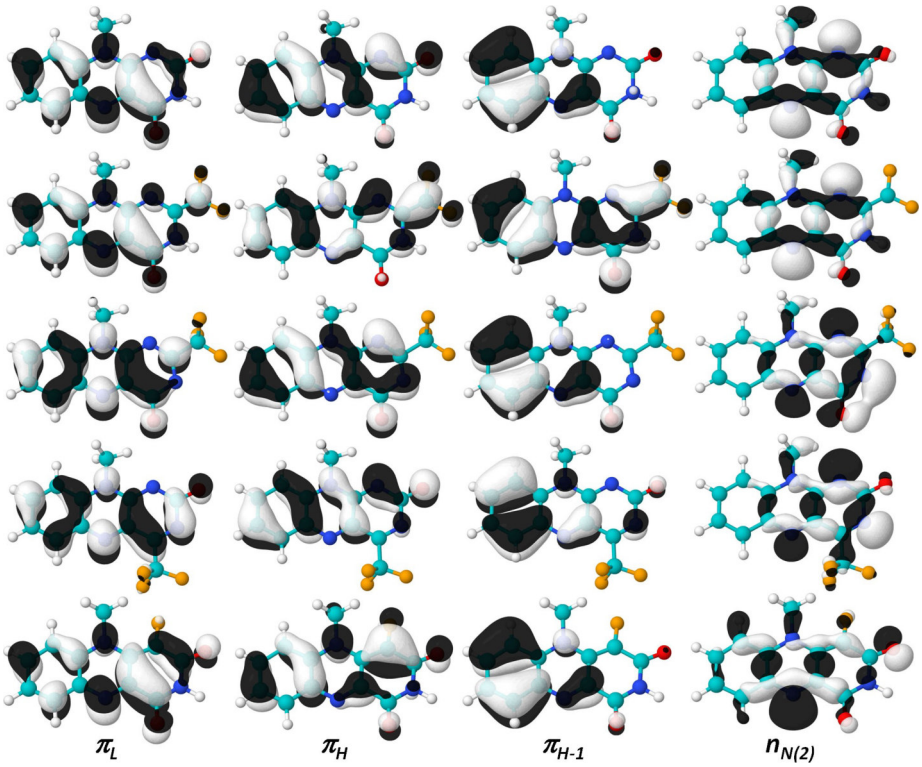

Figure 5. Frontier orbitals (isovalue = 0.03) of MIA, $2CF_2$-MIA, $2CF_3$-MIA, $4CF_3$-MIA, and 1F-MIA in aqueous solution (top to bottom).

Table 2. Excited states properties of $2CF_3$-MIA in aqueous solution.

State	Electronic structure ($\|c\|^2$)	$\Delta E_{vertical}$ / eV (*f*)
$^1(\pi_H\pi_L)$	$\pi_H \rightarrow \pi_L(0.80)$	2.40 *(0.271)*
$^3(\pi_H\pi_L)$	$\pi_H \rightarrow \pi_L(0.85)$	1.69
$^3(\pi_{H-2}\pi_L)$	$\pi_{H-2} \rightarrow \pi_L(0.35) + \pi_{H-1} \rightarrow \pi_L(0.29) + \pi_H \rightarrow \pi_{L+1}(0.16)$	3.08
$^3(n_N\pi_L)$	$n_{N2} \rightarrow \pi_L(0.72) + n_{N1} \rightarrow \pi_L(0.10)$	3.36

are separated energetically from higher lying states and depopulation of the S1 state via ISC is limited to the El-Sayed forbidden $^1(\pi_H\pi_L) \rightsquigarrow {}^3(\pi_H\pi_L)$ channel. In accordance with the mirror image rule, the fluorescence wavelength is predicted to be strongly redshifted by more than half an electronvolt resulting in emission of (infra-)red light. This prediction is confirmed by further studies in Section 3.2. In the case of $4CF_2$-MIA, the impact on the energetics of the $^1(\pi_H\pi_L) \rightsquigarrow {}^3(\pi_{H-1}\pi_L)$ ISC channel is found to be minimal and the $^3(n_N\pi_L)$ state remains inaccessible. Whilst the energetic position of the bright S1 absorption band barely changes, an increase of the transition dipole moment by about 20 % results in an oscillator strength of $f = 0.412$.

$2F_2$- and $4F_2$-MIA. Substitution of the oxygen atom in position 2 by two fluorine atoms results in a weak blueshift of the considered states. The effect ranges from 0.06 eV for the $^3(\pi_H\pi_L)$ state to 0.13 eV for the higher triplets and the S1 state is destabilized by 0.08 eV. The explanation for this uniform effect lies within the electron distribution of the π_L orbital (compare Figures 5 and S1 in the ESI): In the stem compound, MIA, it describes a π-system spanning the whole chromophore. The removal of the oxygen atom interrupts the π-system in position 2 and diminishes delocalisation. $4F_2$-MIA, in all aspects, is very similar to $2F_2$-MIA. Destabilization of the π_L orbital goes hand in hand with blueshifting the considered electronic states. The replacement of the oxygen atom attached to C(4) results in more pronounced shifts (0.13 eV–0.25 eV). Inspecting the π_L orbital of MIA, it is not surprising that the destabilization for $4F_2$-MIA turns out to be stronger: Electron density on the B2-ring is mainly localised in positions 4, 4(a) and 10(a). Contrary to the π_L orbital, the π_{H-1} orbital does not possess a significant amount of electron density in position 2 as well as 4 and consequently modification does not have a marked impact. The picture is similar for the σ-bonds described by the n_{N2} orbitals. In conclusion, the modifications investigated are not expected to have a strongly modulating effect on ISC. The absorption spectra resemble that of MIA aside from the general blueshift. The oscillator strength of the bright $^1(\pi_H\pi_L)$ absorption band is reduced by about 28 % upon replacement of the oxygen atom bound to C(2) by two fluorine atoms, whereas it does not decrease for modification in position 4 as the impairment of the transition dipole moment is much weaker and the increase in energy counteracts the effect. In agreement with the overall trend, the fluorescence wavelengths are predicted to be blueshifted by about 0.1 eV for $2F_2$-MIA and 0.2 eV for $4F_2$-MIA.

$2CF_3$- and $4CF_3$-MIA. $2CF_3$- and $4CF_3$-MIA are modified in positions 2/4 as well as 3. The carbon atoms in positions 2/4 are equipped with trifluoromethyl groups and the hydrogen atom in position 3 is removed, thus introducing an additional double bond in the B2 ring. For $2CF_3$- and $4CF_3$-MIA, all considered states are computed to be stabilized (Tables 3 and 4), regardless whether the state exhibits $\pi\pi^*$ or $n\pi^*$ character. The striking feature here is that the stabilization of $n\pi^*$ states is significantly stronger, which is a direct consequence of removing the hydrogen atom in position 3. As a result, a third nitrogen-centered n_N orbital is introduced and the nitrogen atom N(3) has a significant share in the energetically highest-lying n_{N3} orbital (Figure 5). The general redshift of all excitations is explained by a comparatively strong impact of the modification on the π_L orbital as it is stabilized to a higher extent than the other π orbitals. The principal difference between the π_L orbitals of MIA and those of $2CF_3$- and $4CF_3$-MIA is that the out-of-plane p orbital of the oxygen atom directly contributes to the π-system, whereas the trifluoromethyl group influences the π-system via hyperconjugation. Remarkably, for $4CF_3$-MIA all redshifts are computed to turn out even more pronounced. We attribute this effect to the clear quinoid structure of the π-system in the B-rings. As is to be expected, the stabilization of the considered states is reflected in the absorption spectra of $2/4CF_3$-MIA: The characteristic absorption bands are redshifted by >0.2 eV. Regarding the $^3(n_N\pi_L)$ state of $4CF_3$-MIA, the share of the oxygen lone pair is negligibly small. The enhanced stabilization of $n_N\pi^*$ states for $4CF_3$-MIA is predicted to have profound effects on the excited state kinetics of the chromophore. The $^1(n_N\pi_L)$ and $^1(\pi_H\pi_L)$ minima are estimated to be nearly isoenergetic, so that additional ISC channels are introduced. The El-Sayed allowed $^1(\pi_H\pi_L) \rightsquigarrow {}^3(n\pi^*)$ channel is computed to be activated for both derivatives.

1F- and 5F-MIA. 1F- and 5F-MIA are deaza-compounds in which the corresponding N(1) or N(5) atom was exchanged by a C–F group. Unlike the ground-state geometries of MIA and the modifications discussed previously, the S_0 equilibrium geometry of 1F-MIA is not planar. Steric interaction of the

Table 3. Excited states properties of $2CF_3$-MIA in aqueous solution.

	Electronic structure ($\|c\|^2$)	$\Delta E_{vertical}$ / eV (*f*)
$^1(\pi_H\pi_L)$	$\pi_H \rightarrow \pi_L(0.81)$	2.73 (*0.275*)
$^1(n_N\pi_L)$	$n_{N3} \rightarrow \pi_L(0.75)$	2.94
$^3(\pi_H\pi_L)$	$\pi_H \rightarrow \pi_L(0.90)$	2.17
$^3(\pi_{H-1}\pi_L)$	$\pi_{H-1} \rightarrow \pi_L(0.84)$	2.60
$^3(n_N\pi_L)$	$n_{N3} \rightarrow \pi_L(0.70) + n_{N2} \rightarrow \pi_L(0.13)$	2.74

Table 4. Excited states properties of $4CF_3$-MIA in aqueous solution.

	Electronic structure ($\|c\|^2$)	$\Delta E_{vertical}$ / eV (*f*)
$^1(\pi_H\pi_L)$	$\pi_H \rightarrow \pi_L(0.81)$	2.67 (*0.271*)
$^1(n_N\pi_L)$	$n_{N3} \rightarrow \pi_L(0.81)$	2.80
$^3(\pi_H\pi_L)$	$\pi_H \rightarrow \pi_L(0.89)$	2.09
$^3(\pi_{H-1}\pi_L)$	$\pi_{H-1} \rightarrow \pi_L(0.82)$	2.58
$^3(n_N\pi_L)$	$n_{N3} \rightarrow \pi_L(0.78)$	2.60

methyl group in 10-position and the fluorine atom gives rise to a shallow energy barrier of 0.05 eV (see Section S7 in the ESI).

5F-MIA is the derivative that experiences the strongest blueshifts. The effect ranges from 0.27 eV for the $^3(\pi_H\pi_L)$ state up to preeminent 0.89 eV for the $n\pi^*$ triplet. Comparison of the excitation energies of 1F-MIA and 5F-MIA (Tables 5 and S4 in the ESI) reveals that both chromophores behave fundamentally different. The importance of the position of modification is best demonstrated for the $\pi_H \rightarrow \pi_L$ transition: The electron density distribution in the π_H orbital of 5F-MIA (Figure S1 in the ESI) is almost unchanged with respect to MIA. The corresponding orbital of MIA (Figure 5) does not exhibit density on the N(5) atom at all and therefore modification in this position has no marked effect. By contrast, the same modification in position 1 leads to strong destabilization of the π_H orbital. For 1F-MIA, the largest contribution to the molecular orbital is centered on the C(1) atom and the orbital exhibits antibonding character for the C(1)–F bond (Figure 5). The resulting strong destabilization of the π_H orbital leads to a redshift of the S1 and T1 states (~ 0.5 eV). The blueshift of the $\pi_H\pi_L$ and $\pi_{H-1}\pi_L$ states of 5F-MIA is related to the destabilization of the π_L orbital. In analogy to the π_H orbital of 1F-MIA, the shift of the orbital energy is caused by the pronounced antibonding character of the introduced C–F bond (Figure S4 in the ESI). The stronger destabilization of the $^3(\pi_H\pi_L)$ state compared to the corresponding singlet is explained by the larger weight of the $\pi_H \rightarrow \pi_L$ transition in the triplet wavefunction (Table S4 in the ESI). The effect on the $n\pi^*$ triplet depends on the position of the modification as well. In either case, the energy of the remaing n_N orbital is lowered due to the removal of a nitrogen-centered lone pair. As a result, the n_O orbitals gain significance. While the $n_N\pi_L$ character clearly remains dominant in 1F-MIA, the lowest $n\pi^*$ excitation of 5F-MIA is of $n_{O2}\pi_L$ type.

Table 5. Excited states properties of 1F-MIA in aqueous solution.

	Electronic structure ($\|c\|^2$)	$\Delta E_{vertical}$ / eV (*f*)
$^1(\pi_H\pi_L)$	$\pi_H \rightarrow \pi_L$(0.82)	2.45 (*0.238*)
$^3(\pi_H\pi_L)$	$\pi_H \rightarrow \pi_L$(0.88)	1.76
$^3(\pi_{H-1}\pi_L)$	$\pi_{H-1} \rightarrow \pi_L$(0.73)	2.93
$^3(n_N\pi_L)$	$n_N \rightarrow \pi_L$(0.49) + $n_{O2} \rightarrow \pi_L$(0.11)	3.40

In spite of the fundamental changes in the electronic structure of the 5F-MIA chromophore, two ISC channels remain active because the blueshifts of the S1, T1, and $^3(\pi_{H-1}\pi_L)$ states are rather similar. Nonetheless, the substantial destabilization of the $n\pi^*$ states is expected to have an indirect impact on the El-Sayed forbidden channels as vibronic interaction between the $\pi\pi^*$ and $n\pi^*$ states is handicapped by their larger energy gap. In fact, a fluorescence quantum yield of $\Phi_F = 0.52$ has been observed for a closely related chromophore, 5-deazariboflavin,[31] which might be traced back to this effect. In the case of 1F-MIA, the strong stabilization of the $\pi_H\pi_L$ states is predicted to have profound impact on the ISC channels. Only the El-Sayed forbidden $^1(\pi_H\pi_L) \rightsquigarrow {}^3(\pi_H\pi_L)$ channel remains active and the $n\pi^*$ states are energetically separated from the $\pi_H\pi_L$ states hampering intensity borrowing via vibronic SOC. Previous experimental as well as quantum chemical studies on the related 1-deazariboflavin chromophore revealed a strong bathochromic shift of the S1 absorption maximum.[31]

Relaxation pathways

To get an estimate of the adiabatic energies of the derivatives in aqueous solution, we calculated approximated values by adding the computed blue-/redshifts at the ground-state geometries (see Figure 4) to the adiabatic energies of MIA in water. Deviations of the approximated adiabatic energies and those computed from optimized excited-state geometries of the derivatives are found to be below 0.10 eV. The resulting values for the $^1(\pi_H\pi_L) \rightsquigarrow T_{1-3}$ transitions are listed in Table 6 and enable clear assignment of the molecules to one of the scenarios sketched in Figure 2.

The screening reveals promising derivatives with respect to energetic schemes associated with increased Φ_F or Φ_T, respectively. The strong stabilization of $n\pi^*$ states for $2CF_3$- and $4CF_3$-MIA opens up the El-Sayed allowed $^1(\pi_H\pi_L) \rightsquigarrow {}^3(n_N\pi_L)$ channel. In the cases of $2CF_2$- and 1F-MIA, the S_1 and T_1 states are largely separated from the other excited states resulting in only one remaining El-Sayed-forbidden ISC channel. Therefore, we selected these four derivatives for a detailed examination of their excited state pathways. The application of the harmonic approximation with substantial adiabatic energy gaps of about

Table 6. Adiabatic excitation energies of the lowest triplet states of MIA and screened flavin derivatives with respect to the corresponding $^1(\pi_H\pi_L)$ minimum in aqueous solution. Values in bold print are computed from excited states geometries and the remaining entries are best estimates calculated from the adiabatic energies of MIA and the shifts for the screened derivatives at the ground state geometries (see Figure 4).

	$\Delta E_{adiabatic}$ / eV					
Derivative	$^3(\pi_H\pi_L)$		$^3(\pi_{H-1}\pi_L)$		$^3(n_N\pi_L)$	
MIA	—	**−0.56**	—	**−0.10**	—	**0.16**
$2F_2$-MIA	−0.58		−0.05		0.21	
$4F_2$-MIA	−0.62		−0.15		0.20	
$2CF_2$-MIA	−0.65	**−0.74**	0.68	—[a]	0.96	—[a]
$4CF_2$-MIA	−0.95		−0.10		0.35	
$2CF_3$-MIA	−0.50	**−0.49**	−0.13	**−0.11**	0.01	**0.00**
$4CF_3$-MIA	−0.52	**−0.56**	−0.09	**−0.05**	−0.07	**−0.16**
1F-MIA	−0.62	**−0.65**	0.48	—[a]	0.95	—[a]
5F-MIA	−0.38		−0.18		—[b]	

[a]Geometry of this state not optimized, as it is thermally inaccessible; [b]Energy not estimated due to change of electronic structure.

2 eV is not reliable for computing the nonradiative deactivation of the S_1 state to the ground state. Comparison with an experimentally determined rate constant for IC of MIA in aqueous solution at room temperature (2×10^7 s^{-1})[26] shows, however, that our computed value (5×10^7 s^{-1}) has the right order of magnitude. Information on the nonadiabatic coupling matrix elements $\langle GS|\nabla_R|S1\rangle$ and the most important coupling vibrational modes is provided in Section S8 in the ESI. Electric dipole transition moments are summarized in Table S9 in the ESI.

$2CF_2$- and 1F-MIA. Following green light absorption in the Franck–Condon region at 2.45 eV (**1F-MIA**) or 2.40 eV (**$2CF_2$-MIA**), respectively, relaxation of the geometry to the S_1 minimum mainly results in changes within the pteridine moiety (see Section S7 in the ESI). The S_1 and T_1 minimum geometries (**1F-MIA**) do not exhibit C_s symmetry. Like in the electronic ground state, steric interaction of the fluorine atom in position 1 and the methyl residue in position 10 causes the chromophore to lose planarity with a barrier of about 0.05 eV separating both minima. The S_1 and T_1 geometries are very similar, which can be traced back to the dominant $\pi_H \rightarrow \pi_L$ excitation contributing well above 80 %. In contrast, the geometries of the two $\pi_H \rightarrow \pi_L$ states of **$2CF_2$-MIA** differ markedly due to symmetry breaking of the T_1 state. TDDFT leads to very shallow double minima for symmetry-restrained optimizations of the $\pi_H \rightarrow \pi_L$ states (first-order saddle points). At the DFT/MRCI level of theory, however, the C_s symmetric structure of the S_1 state is lower in energy, which is not the case for the corresponding triplet.

The kinetic schemes in Figure 6 suggest that T_2 and T_3 are thermally not accessible from the S_1 minimum so that $S_1 \rightsquigarrow T_1$ remains as the only reasonable triplet population pathway. For flavins, typically the $S_1 \rightsquigarrow T_1$ ISC rate decreases exponentially with increasing energy difference: The transition is described by the weak coupling case as defined by Englman and Jortner.[65] The adiabatic $S_1 \rightsquigarrow T_1$ energy of **1F-MIA** in aqueous solution is computed to 0.65 eV compared to 0.55 eV for MIA. The efficiency of the vibronic spin–orbit coupling mainly depends on the energetic separation of the $\pi_H\pi_L$ states from the nitrogen-centered $n\pi^*$ states in each domain and the magnitude of the matrix elements $\langle {}^1(\pi_H\pi_L)|\hat{\mathcal{H}}_{SO}|{}^3(n_N\pi_L)\rangle$ as well as $\langle {}^3(\pi_H\pi_L)|\hat{\mathcal{H}}_{SO}|{}^1(n_N\pi_L)\rangle$. Herzberg-Teller-like intensity borrowing is most effective for small energy gaps and strong spin–orbit coupling. Despite the pronounced destabilization of the $n_N\pi_L$ states for **1F-MIA**, we compute the $S_1 \rightsquigarrow T_1$ ISC rate constant to be increased by one order of magnitude. The gain in efficiency can be traced back to stronger SOCMEs in terms of intensity borrowing (see Section S8 in the ESI). Despite the increased rate constant of the $S_1 \rightsquigarrow T_1$ channel, ISC in total is hampered because the productive ${}^1(\pi_H\pi_L) \rightsquigarrow {}^3(\pi_{H-1}\pi_L)$ channel of MIA is deactivated. Overall, the rate constant is decreased by about a factor of 5 to 2×10^7 s^{-1}. Due to the atypical deviation of the S_1 and T_1 geometries of **$2CF_2$-MIA**, the transition does no longer comply with the weak coupling case.[30] As a consequence, the adiabatic energy of 0.78 eV causes more efficient vibrational overlap. In the case of **$2CF_2$-MIA**, overall, ISC is computed to be slowed down to proceed at a rate constant of 3×10^7 s^{-1}.

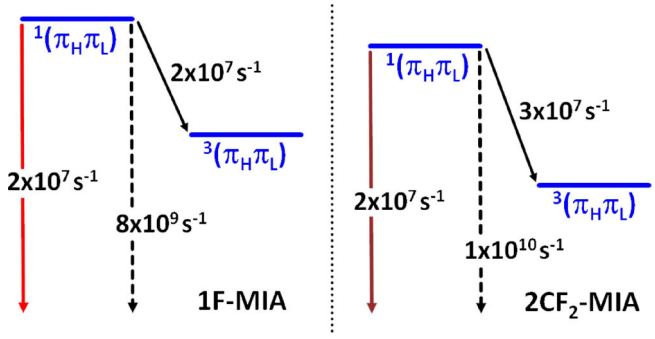

Figure 6. Adiabatic relaxation schemes of 1F- and $2CF_2$-MIA in aqueous medium. The solid vertical arrows originating from the ${}^1(\pi_H\pi_L)$ states refer to fluorescence, the dashed ones to IC.

As described by equation (2), the fluorescence rate constant depends on the transition dipole moment $\vec{\mu}_{S1S0}$ (**1F-MIA**: 4.73 D, **$2CF_2$-MIA**: 5.40 D) as well as the vertical $S_1 \rightarrow S_0$ transition energy (**1F-MIA**: 1.68 eV, **$2CF_2$-MIA**: 1.59 eV). The former enters the expression quadratically and the energy cubically. Hence, the characteristic redshift of the $\pi_H\pi_L$ states results in a decreased fluorescence rate constant as well and we obtain a value of 2×10^7 s^{-1} for both chromophores.

1F-MIA and **$2CF_2$-MIA** exhibit particularly interesting characteristics with respect to fluorescence microscopy. They can be addressed under milder conditions than the stem compound MIA or the related riboflavin which is the core chromophore of many blue-light receptors. Photoexcitation by green light is expected to cause fewer photochemical damages than blue-light irradiation. Furthermore, the wavelength window 650–900 nm is transparent in living tissue because hemoglobin, water and lipids do not absorb at those wavelengths and infrared light scatters much less in living tissue than visible light.[66,67] The unequalled redshift of the S_1 state of **$2CF_2$-MIA** results in an emission spectrum covering mainly near infrared wavelengths. The maximum of the emission spectrum (see Figure 7) is computed at 844 nm and half maximum is reached at 691 as well as 1211 nm. The emission spectrum of **1F-MIA** peaks at 765 nm and covers the wavelength region 640–1020 nm above half maximum.

The energy gap law typically makes nonradiative deactivation a serious competitor of infrared emission.[65,68] The rate constant for the $S_1 \rightsquigarrow S_0$ IC of MIA, computed in harmonic approximation, was found to be about twice as large as the experimental value. Hence, we expect the calculated IC rate constants for the $S_1 \rightsquigarrow S_0$ IC of **1F-MIA** and **$2CF_2$-MIA** to be overestimated as well, but to have roughly the right order of magnitude. Two factors enhance the probability of nonradiative deactivation of the S_1 state by IC to the S_0 state in relation to MIA: a better overlap of the vibrational wavefunctions of the accepting modes due to the smaller energy gap and the nonplanarity of the excited-state geometry resulting in larger NACMEs (see Section S8 in the ESI). While fluorescence and ISC appear to be competitive in both compounds (Figure 6), the computed IC rate constants of $\approx 8 \times 10^8$ s^{-1} (**1F-MIA**) and

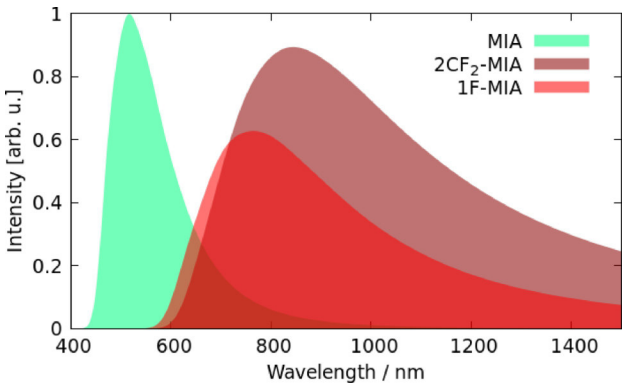

Figure 7. Emission spectra of **1F-MIA** and **2CF$_2$-MIA** as well as the stem compound **MIA** (normalized to intensity = 1) with explicit vibrational broadening. The vibrational overlaps are scaled by the squared transition dipole moments $\vec{\mu}^2_{S1S0}$. The maxima of the computed emission spectra are found at 1.47 eV (2CF$_2$-MIA), 1.62 eV (1F-MIA) and 2.40 eV (MIA).

$\approx 10^{10}$ s^{-1} (**2CF$_2$-MIA**) suggest that nonradiative deactivation is the dominating process. We therefore expect **1F-MIA** and **2CF$_2$-MIA** to emit fluorescence in the (infra-)red spectral range with comparatively small quantum yields. Unfluorinated 1-deaza-flavins have been investigated thoroughly in the past.[18,31,69–71] 1-deazariboflavin does not show triplet quantum yield at all and fluorescence quantum yields have been reported to be well

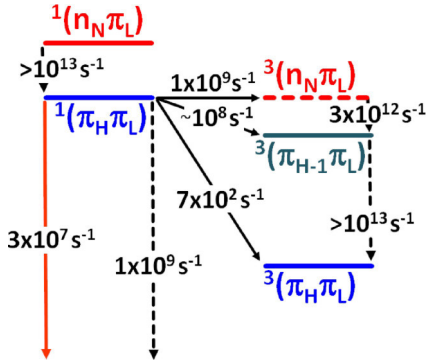

Figure 8. Adiabatic relaxation scheme of **2CF$_3$-MIA** in aqueous medium. The solid vertical arrow originating from the $^1(\pi_H\pi_L)$ state refers to fluorescence, the dashed one to IC.

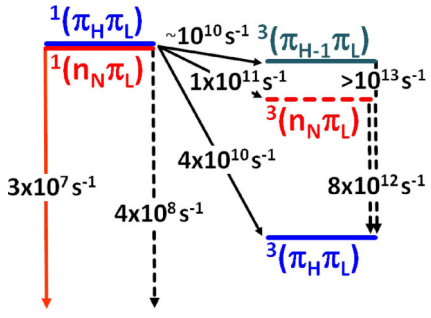

Figure 9. Adiabatic relaxation scheme of **4CF$_3$-MIA** in aqueous medium. The solid vertical arrow on the left side refers to fluorescence of the $^1(\pi_H\pi_L)$ state, the dashed one to IC.

below 1% in aqueous solution and acetonitrile.[13,71] However, the reason for the lack of fluorescence remained unclear and ultrafast spin-allowed nonradiative processes were contemplated to quench spin-allowed radiation. In the case of 1-deaza-FMN incorporated into the LOV domain of the YtvA protein from *Bacillus subtilis*, Silva-Junior et al. proposed a mechanism of internal conversion through a biradicaloid conical intersection of S_1 and S_0.[18] Similar photochemical reactivity of **1F-MIA** or **2CF$_2$-MIA** in the S_1 state cannot be ruled out within this study.

2CF$_3$- and 4CF$_3$-MIA. In the cases of **2CF$_3$-** and **4CF$_3$-MIA**, the $^3(\pi_{H-1}\pi_L)$ state and first singlet and triplet $n\pi^*$ states are energetically accessible after $^1(\pi_H\pi_L)$ absorption and hence are added to the kinetic schemes (Figures 8 and 9). For all states, C_s symmetric geometries are used. Complications arose while searching the minima of the $^1(\pi_H\pi_L)$ and $^3(\pi_{H-1}\pi_L)$ potentials: TDDFT optimization favours C_1-symmetric structures, whereas DFT/MRCI scans along the concerned out-of-plane modes reveal flat potential energy surfaces. Artificial symmetry breaking deformations at the TDDFT level have been observed for various ketones[56,72,73] and have been reported for the flavin chromophore[24,27] as well. In such occasions we replace the imaginary frequency by a real value corresponding to the outer branches of the TDDFT potential energy profile. In case of the S_1 state we utilize the T_1 equilibrium geometry as a proxy: Both states are characterized by the $\pi_H \rightarrow \pi_L$ transition contributing well above 80% and the DFT/MRCI energy for the S_1 state is found to be slightly lower at the T_1 TDDFT minimum.

Following excitation to the Franck–Condon region of the bright $^1(\pi_H\pi_L)$ state (**2CF$_3$-MIA**: 2.73 eV, **4CF$_3$-MIA**: 2.67 eV), relaxation to the equilibrium geometry goes hand in hand with substantial geometrical changes within the pteridine moiety. In the cases of **2CF$_3$-** and **4CF$_3$-MIA**, the C(4)–C(4a) and C(4a)–C(10a) bonds are shortened and the C(4a)–N(5) as well as C(4)–O bonds are elongated considerably (see Section S7 in the ESI). The excited state decay kinetics of both derivatives are strongly influenced by the $n\pi^*$ states.

In the case of **2CF$_3$-MIA**, we compute the $^1(\pi_H\pi_L)$ and $n_N\pi_L$ triplet states to be almost isoenergetic. According to the calculations, the El-Sayed allowed ISC proceeds at a rate constant of 1×10^9 s^{-1}. The direct electronic coupling is increased to 24.9 cm^{-1} compared to 8.8 cm^{-1} for MIA. The enhancement of the spin–orbit interaction can be traced back to the coupling of the out-of plane p orbital at the N(3) center (π_H) with the lone pair that results from removing the hydrogen atom (n_{N3}). In addition to the activation of the $^1(\pi_H\pi_L) \rightsquigarrow {}^3(n_N\pi_L)$ channel, we find $^1(\pi_H\pi_L) \rightsquigarrow {}^3(\pi_{H-1}\pi_L)$ ISC to be efficiently promoted by vibronic interactions. The rate constant of 10^8 s^{-1} is an estimate oriented towards the El-Sayed allowed process, because the $\pi_{H-1}\pi_L$ and $n_N\pi_L$ triplets are almost degenerate at the S_1 geometry resulting in oversized numerical derivatives. Unsurprisingly, the $S_1 \rightsquigarrow T_1$ channel can be neglected as relaxation pathway: The sequential transitions via the T_2 and T_3 states are found to be drastically more efficient. Internal conversion from the $n\pi^*$ triplet to the $^3(\pi_{H-1}\pi_L)$ state is computed to take place on the timescale of 10^{12} s^{-1}. Subsequent IC to the T_1 state is found to be even faster occuring on

the femtosecond timescale. The alternative direct IC channel, $^3(n_N\pi_L)\rightsquigarrow{}^3(\pi_H\pi_L)$, is computed to be slower by almost two orders of magnitude (6×10^{10} s^{-1}). The primary reason for this finding lies in the size of the electronic coupling: The magnitude of NACMEs is antiproportional to the vertical energy difference of the interacting states[56] at the initial geometry and the energy gap for the ultrafast $^3(\pi_{H-1}\pi_L)\rightsquigarrow{}^3(\pi_H\pi_L)$ IC amounts to 0.11 eV, whereas is it about four times as big for the slower channels [$^3(n_N\pi_L)\rightsquigarrow{}^3(\pi_H\pi_L)$: 0.44 eV, $^3(n_N\pi_L)\rightsquigarrow{}^3(\pi_{H-1}\pi_L)$: 0.38 eV]. Nonradiative transition of the initially excited S_1 state by IC to the electronic ground state is estimated to proceed with a rate constant of $\approx 1\times10^9$ s^{-1} and might therefore be competitive deactivation channel. The $^1(n_N\pi_L)$ state lies adiabatically 0.16 eV above the $^1(\pi_H\pi_L)$ minimum and does not play an important role in the triplet population of **2CF$_3$-MIA**.

In contrast, we compute the first $n\pi^*$ and $\pi\pi^*$ singlets to be adiabatically almost isoenergetic for **4CF$_3$-MIA** [E($\pi\pi^*\rightarrow n\pi^*$) = 0.01 eV] in polar environment. Hence, two El-Sayed allowed ISC channels have to be taken into account. $^1(\pi_H\pi_L)\rightsquigarrow{}^1(n_N\pi_L)$ internal conversion and vice versa is computed to $6-7\times10^{11}$ s^{-1}. The reason for the surprisingly slow equilibration is a moderate change in geometry combined with the vanishingly small adiabatic energy difference resulting in small overlap of the nuclear wavefunctions. The transition between the equilibrium geometries causes a substantial change of the C(4)–O coordinate as the $\pi_H\rightarrow\pi_L$ excitation is accompanied by an elongation of the bond by 4.0 pm. Figure 9 depicts the fastest ISC channels starting from either S_1 or S_2. The computed rate constant for the $^1(n_N\pi_L)\rightsquigarrow{}^3(\pi_H\pi_L)$ transition amounts to 4×10^{10} s^{-1}. The rate constant increases to 1×10^{11} s^{-1} for the $^1(\pi_H\pi_L)\rightsquigarrow{}^3(n_N\pi_L)$ channel. Consistently, the direct spin-orbit coupling for the faster channel is stronger: The matrix elements amount to 31.2 cm^{-1} and 12.8 cm^{-1}, respectively. The geometrical changes of both ISC channels are closely related due to the similarity of the $^1(n_N\pi_L)$ and $^3(n_N\pi_L)$ (as well as $\pi_H\pi_L$) geometries (see Section S7 in the ESI). As is the case for **2CF$_3$-MIA**, the depicted rate constant for $^1(\pi_H\pi_L)\rightsquigarrow{}^3(\pi_{H-1}\pi_L)$ ISC is an estimate oriented towards the El-Sayed allowed process. Within the triplet domain, we find the $n_N\pi_L\rightsquigarrow\pi_H\pi_L$ transition to occur with a rate constant of 8×10^{12} s^{-1}. Interestingly, the direct transition from the $\pi_{H-1}\pi_L$ triplet to the T_1 state is computed to be preferred over the cascade via the $n\pi^*$ triplet: The rate determining step, $^3(\pi_{H-1}\pi_L)\rightsquigarrow{}^3(n_N\pi_L)$ IC, turns out to take place with a rate constant of 3×10^{11} s^{-1}. The vertical energy differences of the interacting triplet states amount to 0.2 eV for the productive channels [$^3(n_N\pi_L)\rightsquigarrow{}^3(\pi_H\pi_L)$: 0.20 eV, $^3(\pi_{H-1}\pi_L)\rightsquigarrow{}^3(\pi_H\pi_L)$: 0.23 eV], whereas it is about twice as large (0.42 eV) for the slower IC channel.

As expected, the timescale of fluorescence of the bright $^1(\pi_H\pi_L)$ state (10^7 s^{-1}) does not change for the investigated modifications and the radiative rate constant of the $^1(n_N\pi_L)$ state of **4CF$_3$-MIA** is substantially slower (2×10^4 s^{-1}). Therefore, radiative depopulation cannot compete against the El-Sayed allowed ISC channels. The nonadiabatic coupling at the $^1(\pi_H\pi_L)$ geometries as well as the $^1(n_N\pi_L)$ minimum of **4CF$_3$-MIA** is found to be similar in size to MIA: The couplings of the five most efficient promoting modes vary between 0.05 a_0^{-1} and 0.02 a_0^{-1} (see Section S8 in the ESI). The computed value for the $S_1\rightsquigarrow S_0$ IC rate constant of 4×10^8 s^{-1} is considered an upper estimate showing that IC cannot compete with the much faster ISC in this compound. In summary, we expect the triplet quantum yield to be significantly increased for both derivatives in comparison to MIA.

Summary and Conclusions

In this work, we have investigated various fluorinated flavin derivatives with respect to increasing triplet or fluorescence quantum yield, respectively. Based on shifts of electronic energies of selected states at the ground state geometries, we identified promising chromophores for detailed characterization of excited-state decay mechanisms. We find two derivatives with promising properties concerning fluorescence microscopy: In the case of **1F-MIA** and **2CF$_2$-MIA**, the $\pi_H\pi_L$ transitions are strongly stabilized and separated energetically from higher-lying states. We predict both compounds to absorb in the green wavelength region, redshifted by more than half an electronvolt compared to MIA. Particularly interesting for *in-vivo* fluorescence microscopy, the stabilization of the bright $\pi_H\pi_L$ singlet state is computed to result in emission of (infra-) red light. Using advanced quantum chemical methods, we find fluorescence and ISC to proceed on the same timescale (10^7 s^{-1}) for both compounds. Estimates of the $S_1\rightarrow S_0$ IC rate constants unfortunately suggest that nonradiative deactivation outcompetes the two former processes in **1F-MIA** and **2CF$_2$-MIA**. We therefore expect the photoluminescence quantum yields of these compounds to be low.

Aiming at increased triplet quantum yields, we detected two other promising derivatives: **2CF$_3$-MIA** and **4CF$_3$-MIA**. Removal of the hydrogen atom in position 3 is found to result in a marked stabilization of the $n\pi^*$ states. As a consequence, even in polar environments, El-Sayed allowed ISC channels become accessible and our computations predict fluorescence to be efficiently quenched by those. We have set up kinetic schemes including fluorescence as well as ISC and IC channels of the excited states. In the case of **2CF$_3$-MIA**, we compute $^1(\pi_H\pi_L)\rightsquigarrow{}^3(n_N\pi_L)$ ISC to take place with a rate constant of 1×10^9 s^{-1} in aqueous solution, surpassing fluorescence by almost two orders of magnitude (3×10^7 s^{-1}). For the derivative modified in position 4 we have found the $^1(n_N\pi_L)$ state to exhibit a markedly higher dipole moment resulting in a less distinct destablization by polar environment and ultimately further accessible El-Sayed allowed ISC channels. We compute ISC of **4CF$_3$-MIA** (1×10^{11} s^{-1}) to proceed considerably faster than for MIA or even **2CF$_3$-MIA**, which can be traced back to stronger electronic coupling (direct and vibronic SOC) as well as more efficient vibrational overlap for the $^1(\pi_H\pi_L)\rightsquigarrow{}^3(n_N\pi_L)$ channel. Subsequent to ISC, we compute the long-lived T_1 state to be populated on the picosecond timescale for both derivatives.

Supporting Information

Electronic Supplementary Information (ESI) available: Assessment of the screening protocol, excited-state properties of less promising derivatives, frontier molecular orbitals and their energies, fragment-based wavefunction analysis, transition dipole moments, computed absorption spectra, molecular geometries, spin-orbit and nonadiabatic couplng matrix elements, harmonic vibrational frequencies, selected vibronic coupling modes.

Acknowledgment

We cordially thank Peter Gilch for helpful discussion. This research was funded by the Deutsche Forschungsgemeinschaft (DFG, German Research Foundation) – 396890929/GRK 2482. Open Access funding enabled and organized by Projekt DEAL.

Conflict of Interest

The authors declare no conflict of interest.

Data Availability Statement

The data that support the findings of this study are available from the corresponding author upon reasonable request.

Keywords: ab initio calculations · computational photochemistry · excited states · fluorine · quantum chemistry

[1] L. O. Björn. Photobiology: The Science of Light and Life. Springer, New York, **2015**.
[2] A. Sancar, *Chem. Rev.* **2022**, *103*, 2203–2237.
[3] R. Banerjee, A. Batschauer, *Planta* **2005**, *220*, 498–502.
[4] A. Losi, W. Gärtner, *Annu. Rev. Plant Biol.* **2012**, *63*, 49–72.
[5] J. M. Christie, L. Blackwood, J. Petersen, S. Sullivan, *Plant Cell Physiol* **2014**, *56*, 401–413.
[6] Q. Mei, V. Dvornyk, *PLoS One* **2015**, *10*, e0135940.
[7] P. Parihar, R. Singh, S. Singh, D. K. Tripathi, D. K. Chauhan, V. P. Singh, S. M. Prasad, *J. Photochem. Photobiol. B* **2016**, *162*, 223–231.
[8] W. R. Briggs, C. F. Beck, A. R. Cashmore, J. M. Christie, J. Hughes, J. A. Jarillo, T. Kagawa, H. Kanegae, E. Liscum, A. Nagatani, K. Okada, M. Salomon, W. Rüdiger, T. Sakai, M. Takano, M. Wada, J. C. Watson, *Plant Cell* **2001**, *13*, 993–997.
[9] W. Holzer, A. Penzkofer, P. Hegemann, *Chem. Phys.* **2005**, *308*, 79–91.
[10] J. M. Christie, *Annu. Rev. Plant Biol.* **2007**, *58*, 21–45.
[11] A. Bowd, P. Byrom, J. B. Hudson, J. H. Turnbull, *Photochem. Photobiol.* **1968**, *8*, 1–10.
[12] M. Sun, T. A. Moore, P.-S. Song, *J. Am. Chem. Soc.* **1972**, *94*, 1730–1740.
[13] S. Salzmann, M. R. Silva-Junior, W. Thiel, C. M. Marian, *J. Phys. Chem. B* **2009**, *113*, 15610–156189.
[14] C. Neiß, P. Saalfrank, *Photochem. Photobiol.* **2003**, *77*, 101–109.
[15] S. Nakagawa, O. Weingart, C. M. Marian, *J. Phys. Chem. B* **2017**, *121*, 9583–9596.
[16] B. D. Zoltowski, B. Vaccaro, B. R. Crane, *Nat. Chem. Biol.* **2009**, *5*, 827–834.
[17] M. Mansurova, P. Scheercousse, J. Simon, M. Kluth, W. Gärtner, *Chem. Bio Chem.* **2011**, *12*, 641–646.
[18] M. R. Silva-Junior, M. Mansurova, W. Gärtner, W. Thiel, *Chem. Bio Chem.* **2013**, *14*, 1648–1661.
[19] M. Mansurova, J. Simon, S. Salzmann, C. M. Marian, W. Gärtner, *Chem. Bio Chem.* **2013**, *14*, 645–654.
[20] A. Tyagi, A. Penzkofer, T. Mathes, P. Hegemann, *J. Photochem. Photobiol. B* **2010**, *101*, 76–88.
[21] B. Karasulu, W. Thiel, *J. Phys. Chem. B* **2015**, *119*, 928–943.
[22] S. Richert, J. Chen, N. Pompe, V. Radtke, B. Illarionov, M. Fischer, A. Bacher, S. Weber, *J. Chem. Phys.* **2019**, *151*, 235102.
[23] A. Brosi, B. Illarionov, T. Mathes, M. Fischer, M. Joshi, A. Bacher, P. Hegemann, R. Bittl, S. Weber, E. Schleicher, *J. Am. Chem. Soc.* **2010**, 132, 8935–8944.
[24] S. Salzmann, J. Tatchen, C. M. Marian, *J. Photochem. Photobiol. A* **2008**, *198*, 221–231.
[25] K. Zenichowski, M. Gothe, P. Saalfrank, *J. Photochem. Photobiol.* **2007**, *190*, 290–300.
[26] A. Reiffers, C. Torres Ziegenbein, A. Engelhardt, R. Kühnemuth, P. Gilch, C. Czekelius, *Photochem. Photobiol.* **2018**, *94*, 667–676.
[27] M. Bracker, F. Dinkelbach, O. Weingart, M. Kleinschmidt, *Phys. Chem. Chem. Phys.* **2019**, *21*, 9912–9923.
[28] J. Tatchen, N. Gilka, C. M. Marian, *Phys. Chem. Chem. Phys.* **2007**, *9*, 5209–5221.
[29] T. J. Penfold, E. Gindensperger, C. Daniel, C. M. Marian, *Chem. Rev.* **2018**, *118*, 6975–7025.
[30] C. M. Marian, *Annu. Rev. Phys. Chem.* **2021**, *72*, 617–640.
[31] S. Salzmann, V. Martinez-Junza, B. Zorn, S. E. Braslavsky, M. Mansurova, C. M. Marian, W. Gärtner, *J. Phys. Chem. A* **2009**, *113*, 9365–9375.
[32] C. M. Marian, S. Nakagawa, V. Rai-Constapel, B. Karasulu, W. Thiel, *J. Phys. Chem. B* **2014**, *118*, 1743–1753.
[33] E. Sikorska, I. V. Khmelinskii, D. R. Worrall, J. Koput, M. Sikorski, *J. Fluoresc.* **2004**, *14*, 57–64.
[34] T. Mondal, S. Mahapatra, *J. Chem. Phys.* **2010**, *133*, 084304.
[35] T. Mondal, S. Mahapatra, *J. Chem. Phys.* **2010**, *133*, 084305.
[36] M. A. H. Alamiry, A. C. Benniston, J. Hagon, T. P. L. Winstanley, H. Lemmetyinen, N. V. Tkachenko, *RSC Adv.* **2012**, *2*, 4944–4950.
[37] X. Zhang, J. Wu, D. Wei, Y. Cai, X. Sun, *Dyes Pigm.* **2021**, *187*, 109109.
[38] A. Bondi, *J. Phys. Chem.* **1964**, *68*, 441–451.
[39] J. C. Biffinger, H. W. Kim, S. G. DiMagno, *Chem. Bio Chem.* **2004**, *5*, 622–627.
[40] F. Babudri, G. M. Farinola, F. Naso, R. Ragni, *Chem. Commun.* **2007**, 1003–1022.
[41] A. Calzolari, B. Vercelli, A. Ruini, T. Virgili, M. Pasini, *J. Phys. Chem. C* **2013**, *117*, 26760–26767.
[42] M. von Arnim, R. Ahlrichs, *J. Comput. Chem.* **1999**, *19*, 1746–1757.
[43] TURBOMOLE V7.3 2018, development of University of Karlsruhe and Forschungszentrum Karlsruhe GmbH, 1989–2007, TURBOMOLE GmbH, since 2007; available from http://www.turbomole.com.
[44] A. D. Becke, *J. Chem. Phys.* **1993**, *98*, 5648–5652.
[45] C. Lee, W. Yang, R. G. Parr, *Phys. Rev. B* **1988**, *37*, 785–789.
[46] A. Schäfer, C. Huber, R. Ahlrichs, *J. Chem. Phys.* **1994**, *100*, 5829–5835.
[47] F. Furche, R. Ahlrichs, *J. Chem. Phys.* **2002**, *117*, 7433–7447.
[48] S. Hirata, M. Head-Gordon, *Chem. Phys. Lett.* **1999**, *314*, 291–299.
[49] T. Weymuth, M. P. Haag, K. Kiewisch, S. Luber, S. Schenk, C. R. Jacob, C. Herrmann, J. Neugebauer, M. Reiher, *J. Comput. Chem.* **2012**, *33*, 2186–2198.
[50] C. M. Marian, A. Heil, M. Kleinschmidt, *Wiley Interdiscip. Rev. Comput. Mol. Sci.* **2018**, *9*, e1394.
[51] S. Grimme, M. Waletzke, *J. Chem. Phys.* **1999**, *111*, 5645–5655.
[52] A. D. Becke, *J. Chem. Phys.* **1993**, *98*, 1372–1377.
[53] F. Weigend, M. Häser, H. Patzelt, R. Ahlrichs, *Chem. Phys. Lett.* **1998**, *294*, 143–152.
[54] O. Vahtras, J. Almöf, M. W. Feyereisen, *Chem. Phys. Lett.* **1993**, *213*, 514–518.
[55] A. Klamt, G. Schürmann, *J. Chem. Soc., Perkin Trans. 2* **1993**, 799–805 .
[56] M. Bracker, C. M. Marian, M. Kleinschmidt, *J. Chem. Phys.* **2021**, *155*, 014102.
[57] F. Plasser, H. Lischka, *J. Chem. Theory Comput.* **2012**, *8*, 2777–2789.
[58] F. Plasser, *J. Chem. Phys.* **2020**, *152*, 084108.
[59] M. Kleinschmidt, J. Tatchen, C. M. Marian, *J. Comp. Chem.* **2002**, *23*, 824–833.
[60] M. Kleinschmidt, C. M. Marian, *Chem. Phys.* **2005**, *311*, 71–79.
[61] AMFI is an atomic spin–orbit integral program, B. Schimmelpfennig, University of Stockholm, **1996**.
[62] B. A. Heß, C. M. Marian, U. Wahlgren, O. Gropen, *Chem. Phys. Lett.* **1996**, *251*, 365–371.
[63] M. Etinski, J. Tatchen, C. M. Marian, *J. Chem. Phys.* **2011**, *134*, 154105.
[64] M. Etinski, J. Tatchen, C. M. Marian, *J. Chem. Phys.* **2014**, *140*, 114104.

[65] R. Englman, J. Jortner, *Mol. Phys.* **1970**, *18*, 145–164.
[66] R. Weissleder, V. Ntziachristos, *Nat. Med.* **2003**, *9*, 123–128.
[67] V. Marx, *Nat. Methods* **2014**, *11*, 717–720.
[68] Yu-Chen Wei, Sheng Fu Wang, Yun Hu, Liang-Sheng Liao, Deng-Gao Chen, Kai-Hsin Chang, Chi-Wei Wang, Shih-Hung Liu, Wei-Hsiang Chan, Jia-Ling Liao, Wen-Yi Hung, Tsai-Hui Wang, Po-Ting Chen, Hsiu-Fu Hsu, Yun Chi, Pi-Tai Chou, *Nat. Photonics* **2020**, *14*, 570–577.
[69] R. Spencer, J. Fisher, C. Walsh, **1977**, *16*, 3586–3594.
[70] S. Ghisla, V. Massey, *Biochem. J.* **1986**, *239*, 1–12.
[71] C. Slavov, M. Mansurova, A. R. Holzwarth, W. Gärtner, *Photochem. Photobiol.* **2010**, *86*, 31–38.
[72] K. Tomi'c, J. Tatchen, C. M. Marian, *J. Phys. Chem. A* **2005**, *109*, 8410–8418.
[73] J. Tatchen, C. M. Marian, *Phys. Chem. Chem. Phys.* **2006**, *8*, 2133–2144.

Manuscript received: February 10, 2022
Revised manuscript received: March 21, 2022
Version of record online: ■■, ■■■

RESEARCH ARTICLES

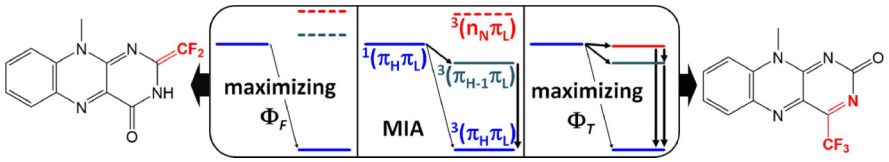

Excited states: In this study, fluorinated flavin derivatives with modified intersystem crossing (ISC) and fluorescence properties are designed and analysed by means of high-level quantum chemical methods. In total, photophysical properties of eight derivatives are investigated. Compounds with promising energetics are examined further with respect to excited-state decay mechanisms. Kinetic schemes of four selected fluorinated flavin derivatives including ISC, fluorescence as well as internal conversion channels are presented.

ChemPhotoChem

Supporting Information

Computer-Aided Design of Fluorinated Flavin Derivatives by Modulation of Intersystem Crossing and Fluorescence

Mario Bracker, Mira K. Kubitz, Constantin Czekelius, Christel M. Marian, and Martin Kleinschmidt*

Contents

S1 Screening

4CF_2-MIA

Table S1: Excited states properties of 4CF_2-MIA in aqueous solution.

State	Electronic structure ($\|c\|^2$)	$\Delta E_{vertical}$ / eV (f)
$^1(\pi_H\pi_L)$	$\pi_H \rightarrow \pi_L(0.81)$	2.99 (*0.412*)
$^3(\pi_H\pi_L)$	$\pi_H \rightarrow \pi_L(0.84)$	1.99
$^3(\pi_{H-1}\pi_L)$	$\pi_{H-1} \rightarrow \pi_L(0.76)$	2.89
$^3(n_N\pi_L)$	$n_{N2} \rightarrow \pi_L(0.72) + n_{N1} \rightarrow \pi_L(0.10)$	3.35

2F_2-MIA

Table S2: Excited states properties of 2F_2-MIA in aqueous solution.

State	Electronic structure ($\|c\|^2$)	$\Delta E_{vertical}$ / eV (f)
$^1(\pi_H\pi_L)$	$\pi_H \rightarrow \pi_L(0.84)$	3.04 (*0.198*)
$^3(\pi_H\pi_L)$	$\pi_H \rightarrow \pi_L(0.85)$	2.39
$^3(\pi_{H-1}\pi_L)$	$\pi_{H-1} \rightarrow \pi_L(0.79)$	2.98
$^3(n_N\pi_L)$	$n_{N2} \rightarrow \pi_L(0.71) + n_{N1} \rightarrow \pi_L(0.12)$	3.25

4F_2-MIA

Table S3: Excited states properties of 4F_2-MIA in aqueous solution.

State	Electronic structure ($\|c\|^2$)	$\Delta E_{vertical}$ / eV (f)
$^1(\pi_H\pi_L)$	$\pi_H \rightarrow \pi_L(0.83)$	3.17 (*0.287*)
$^3(\pi_H\pi_L)$	$\pi_H \rightarrow \pi_L(0.88)$	2.46
$^3(\pi_{H-1}\pi_L)$	$\pi_{H-1} \rightarrow \pi_L(0.80)$	3.01
$^3(n_N\pi_L)$	$n_{N2} \rightarrow \pi_L(0.70) + n_{N1} \rightarrow \pi_L(0.12)$	3.37

5F-MIA

Table S4: Excited states properties of 5F-MIA in aqueous solution.

State	Electronic structure ($\|c\|^2$)	$\Delta E_{vertical}$ / eV (f)
$^1(\pi_H\pi_L)$	$\pi_H \rightarrow \pi_L(0.83)$	3.31 (*0.247*)
$^3(\pi_H\pi_L)$	$\pi_H \rightarrow \pi_L(0.90)$	2.87
$^3(\pi_{H-1}\pi_L)$	$\pi_{H-1} \rightarrow \pi_L(0.83)$	3.13
$^3(n_O\pi_L)$	$n_{O2} \rightarrow \pi_L(0.54)$ + $n_{O1} \rightarrow \pi_L(0.12)$	4.01

S2 Molecular orbitals

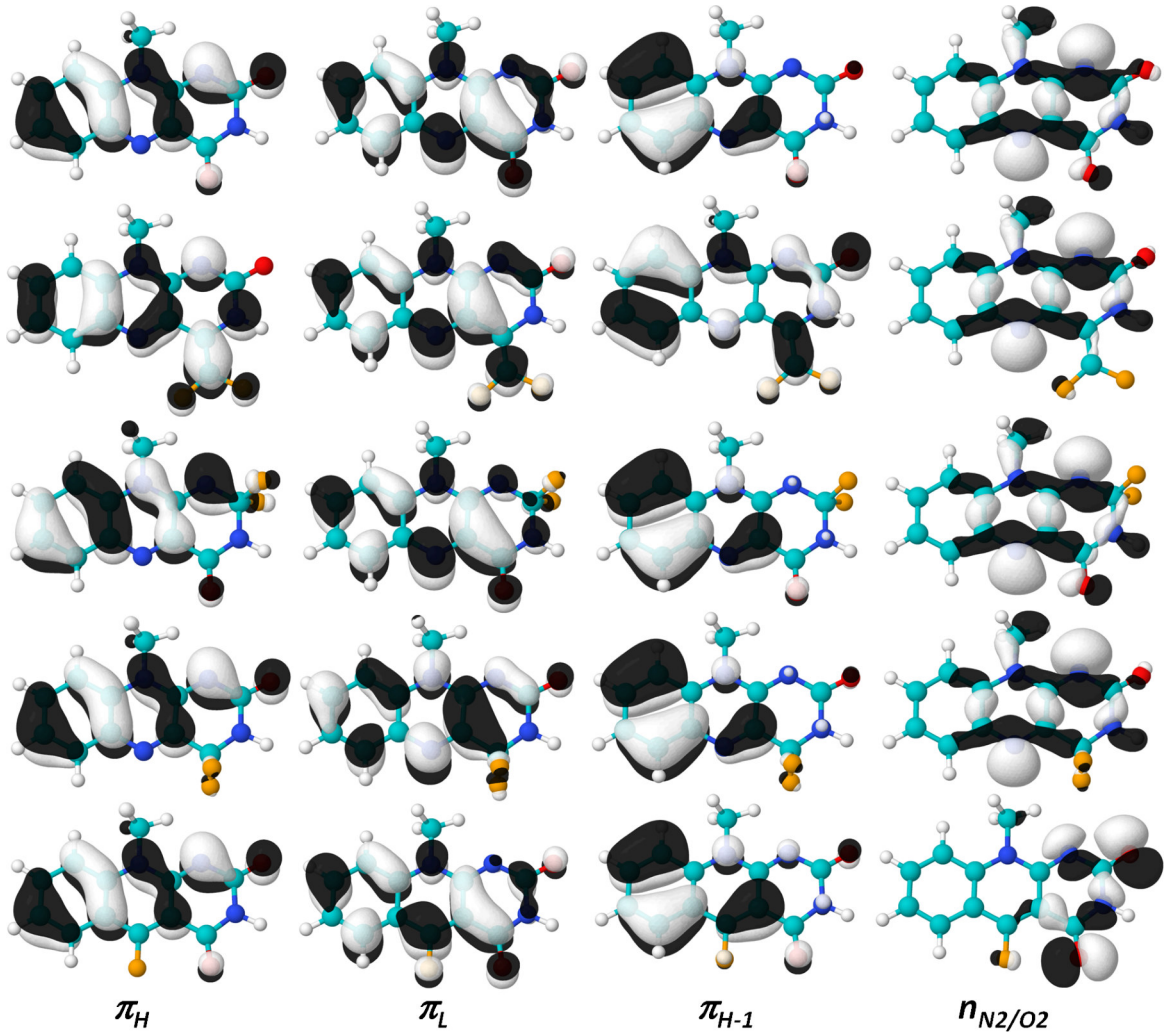

Figure S1: Frontier orbitals (isovalue = 0.03) of MIA, 4CF_2-MIA, 2F_2-MIA, 4F_2-MIA, and 5F-MIA in aqueous solution (top to bottom).

Table S5: Selected molecular orbital energies of screened flavin derivatives at the ground state geometry in aqueous solution. Derivatives studied with respect to excited state kinetics are highlighted in bold print.

Derivative	$E_{orbital}$ / eV			
	n_{N2}	π_{H-1}	π_H	π_L
MIA	-9.633	-8.481	-7.727	-2.281
$2F_2$-MIA	-9.667	-8.427	-7.628	-2.066
$4F_2$-MIA	-9.657	-8.473	-7.699	-2.020
$2CF_2$-MIA	-9.492	-8.179[a]	-6.573	-1.889
$4CF_2$-MIA	-9.380	-7.956	-7.067	-1.841
$2CF_3$-MIA	-9.314[b]	-8.585	-7.945	-2.692
$4CF_3$-MIA	-9.217[b]	-8.511	-7.807	-2.744
1F-MIA	-10.191[c]	-8.359	-6.990	-2.163
5F-MIA	-9.659[d]	-8.431	-7.724	-1.764

[a] π_{H-2}: -8.494
[b] n_{N3} character
[c] n_N character
[d] n_{O2} character

Further illustrations of molecular orbitals corresponding to excitations with contributions exceeding 10 % ($|c|^2 \geq 10$):

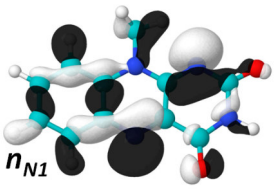

Figure S2: Further frontier orbital of MIA.

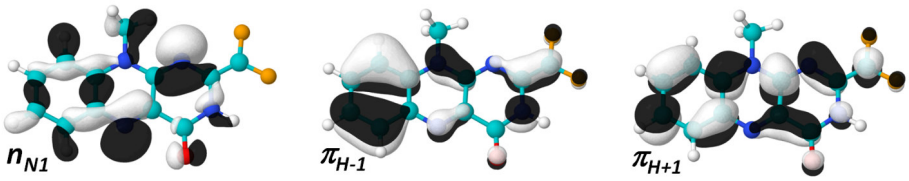

Figure S3: Further frontier orbitals of $2CF_2$-MIA.

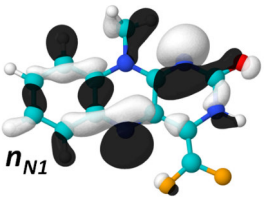

Figure S4: Further frontier orbital of $4CF_2$-MIA.

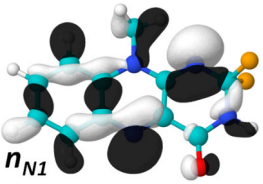

Figure S5: Further frontier orbital of $2F_2$-MIA.

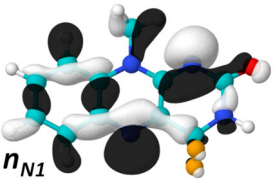

Figure S6: Further frontier orbital of $4F_2$-MIA.

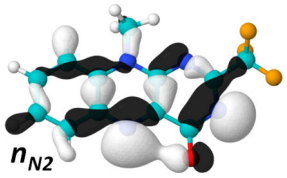

Figure S7: Further frontier orbital of $2CF_3$-MIA.

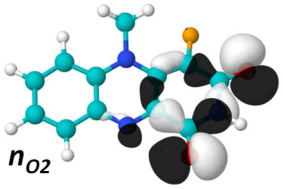

Figure S8: Further frontier orbital of 1F-MIA.

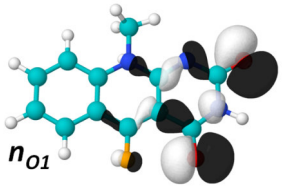

Figure S9: Further frontier orbital of 5F-MIA.

S3 Adiabatic energies and the solvent model

Table 5 summarizes estimated adiabatic energies for the $^1(\pi_H\pi_L)$ state combined with the respective triplets in aqueous solution. The energies are estimated from the computed adiabatic energies of MIA and blue-/redshifts characteristic of the derivatives at the ground state geometries (see Figure 4). The corresponding adiabatic energies of MIA amount to:

- $\mathrm{E}[^1(\pi_H\pi_L) \rightarrow {}^3(\pi_H\pi_L)] = 0.56\,\mathrm{eV}$
- $\mathrm{E}[^1(\pi_H\pi_L) \rightarrow {}^3(\pi_{H-1}\pi_L)] = 0.10\,\mathrm{eV}$
- $\mathrm{E}[^1(\pi_H\pi_L) \rightarrow {}^3(n_N\pi_L)] = -0.16\,\mathrm{eV}$

Adiabatic energies applying implicit solvation (COSMO)[1] to the excited state geometries instead of the stateshift procedure[2] are in excellent agreement for the $^1(\pi_H\pi_L) \rightarrow {}^3(\pi\pi^*)$ transitions and result in a smaller gap for the $^1(\pi_H\pi_L) \rightarrow {}^3(n_N\pi_L)$ transition:[3]

- $\mathrm{E}[^1(\pi_H\pi_L) \rightarrow {}^3(\pi_H\pi_L)] = 0.53\,\mathrm{eV}$
- $\mathrm{E}[^1(\pi_H\pi_L) \rightarrow {}^3(\pi_{H-1}\pi_L)] = 0.11\,\mathrm{eV}$
- $\mathrm{E}[^1(\pi_H\pi_L) \rightarrow {}^3(n_N\pi_L)] = -0.05\,\mathrm{eV}$

The impact of hydrogen bonds on top of implicit solvation was elaborated in our previous study on fluorination of the A-ring.[3] The additional blueshift of the $^3(n_N\pi_L)$ state amounts to 0.06 eV and the stabilization of the $\pi_{H-1}\pi_L$ ICT state was computed to be increased by -0.11 eV. The high sensitivity of the corresponding singlet state to formation of hydrogen bonds has been demonstrated experimentally for related compounds.[4;5] The energies of the S1 and T1 states barely change for additional explicit interactions (S1: -0.01 eV, T1: 0.01 eV).

S4 Fragment-based analysis

Fragment A describes the benzene core (atoms 5a – 9a) and fragment B represents the pteridine moiety (B1+B2, see Figure 1). For the $^3(n\pi^*)$ state, additionally the n_O as well as n_N character is determined: The height of the bars corresponds to the (single-)excitation from the sp^2 hybridised nitrogen/oxygen atoms.

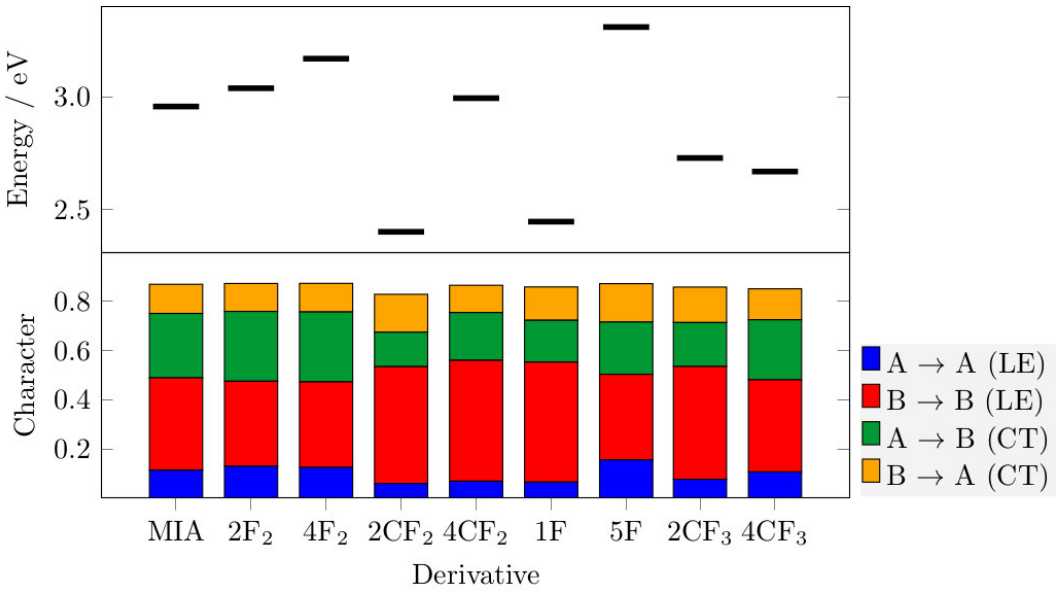

Figure S10: Fragment-based analysis of the $^1(\pi_H\pi_L)$ DFT/MRCI wavefunctions of MIA and derivatives.

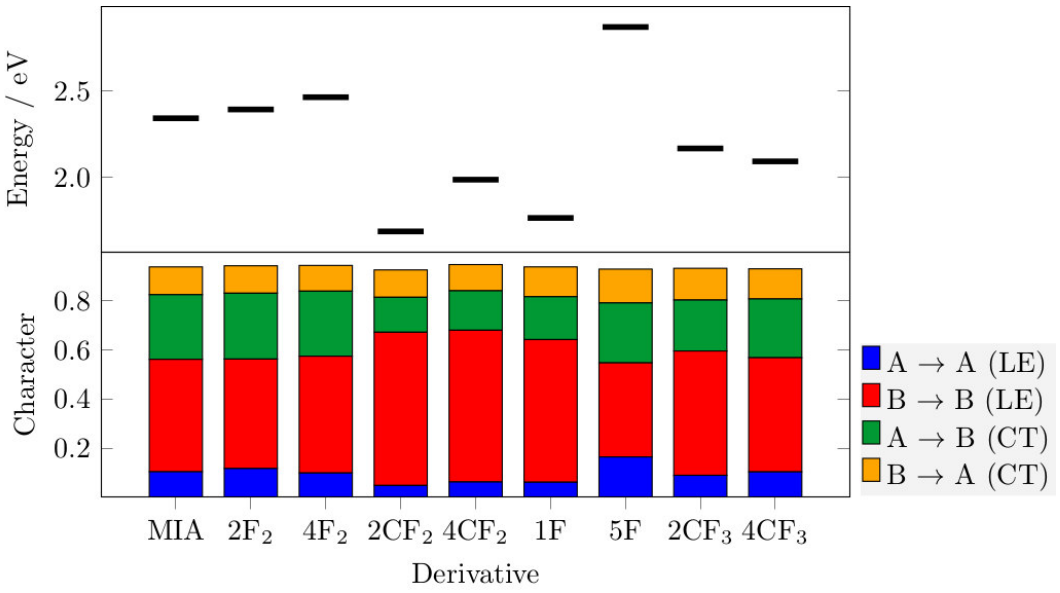

Figure S11: Fragment-based analysis of the $^3(\pi_H\pi_L)$ DFT/MRCI wavefunctions of MIA and derivatives.

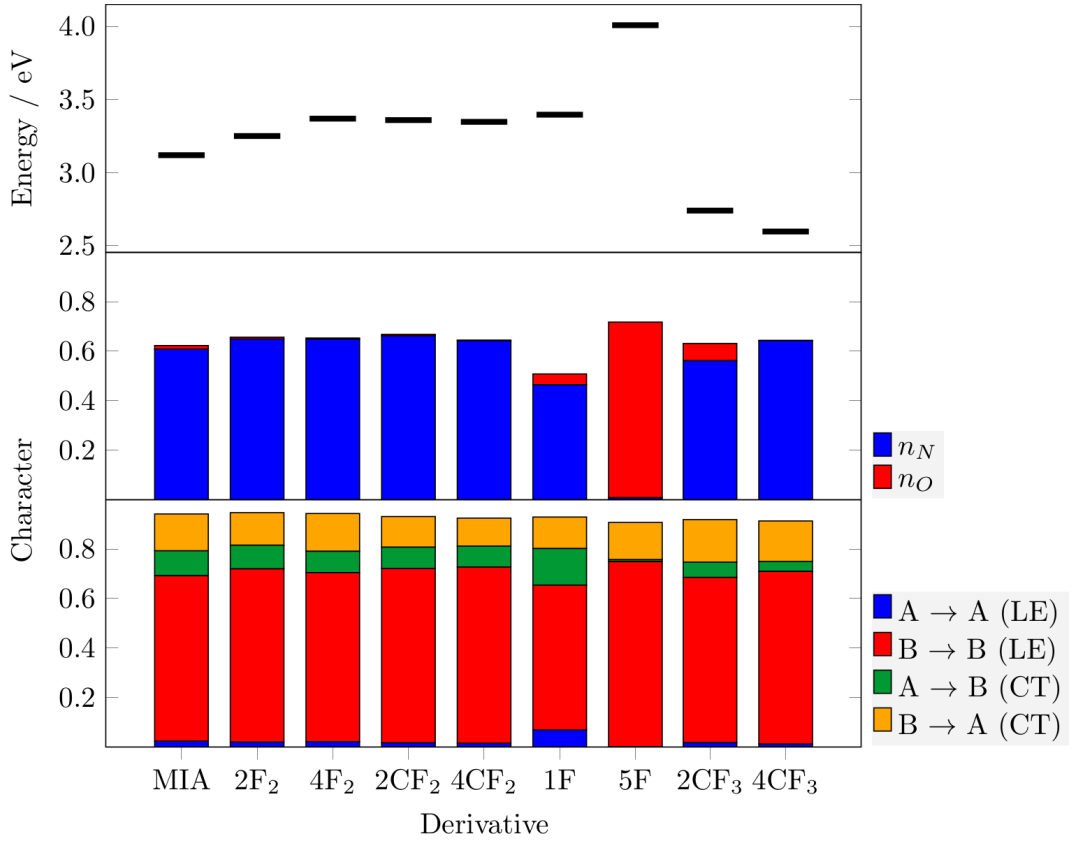

Figure S12: Fragment-based analysis of the $^3(n\pi^*)$ DFT/MRCI wavefunctions of MIA and derivatives.

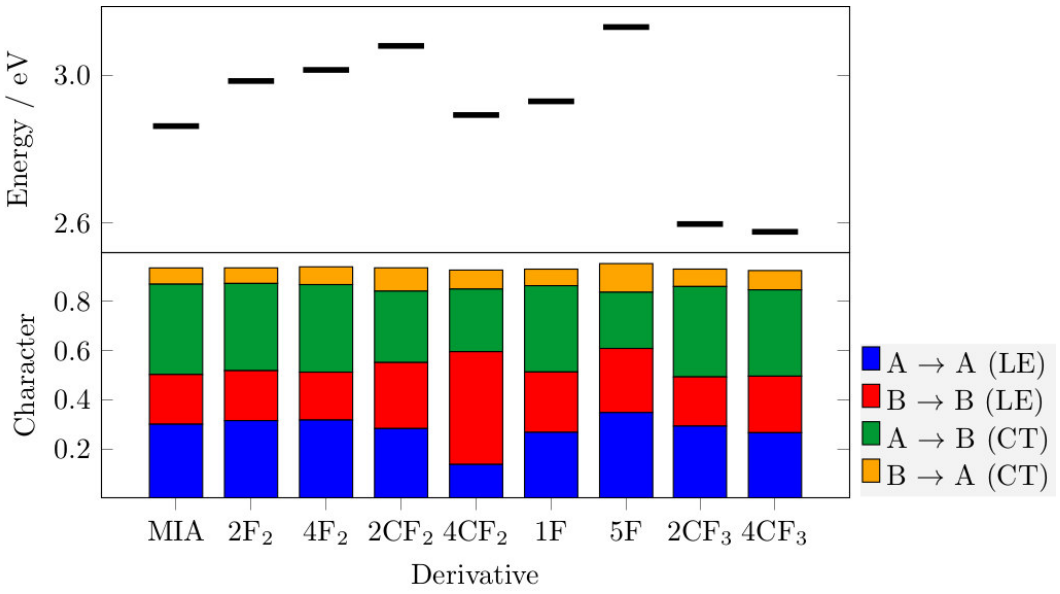

Figure S13: Fragment-based analysis of the $^3(\pi_{H-1}\pi_L)$ DFT/MRCI wavefunctions of MIA and derivatives.

S5 Transition dipole moments

Table S6: GS $\leftrightarrow \pi_H\pi_L$ transition dipole moments of screened flavin derivatives (Absorption: cosmo model, Emission: vacuum). The entries for absorption refer to the S_0 minimum in aqueous medium and the entries for emission refer to the $\pi_H\pi_L$ geometry. Derivatives studied with respect to excited state kinetics are highlighted in bold print.

Derivative	μ / D	
	Abs.	Em.
MIA	4.949	4.800
$2F_2$-MIA	4.147	
$4F_2$-MIA	4.886	
$2CF_2$-MIA	5.451	5.404
$4CF_2$-MIA	6.024	
$2CF_3$-MIA	5.197	5.354
$4CF_3$-MIA	5.175	5.600
1F-MIA	5.066	4.727
5F-MIA	4.435	

S6 Absorption spectra

To illustrate the impact of modification, the spectrum of each derivative is plotted together with the spectrum of MIA. The latter exhibits three pronounced bands in the energy regime up to about 5 eV / 250 nm.[6;7] The one lowest in energy is assigned to the bright $^1(\pi_H\pi_L)$ state. The second absorption band originates from the singlet corresponding to the discussed $^3(\pi_{H-1}\pi_L)$ state. The first and third band are insensitive to environmental effects, whereas the $\pi_{H-1}\pi_L$ states show pronounced solvatochromism due to their ICT character.[4;5]

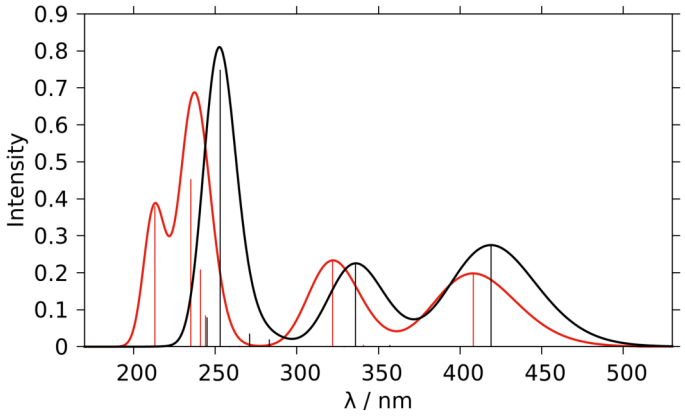

Figure S14: Absorption spectra of $2F_2$-MIA (red) and MIA (black) in aqueous solution.

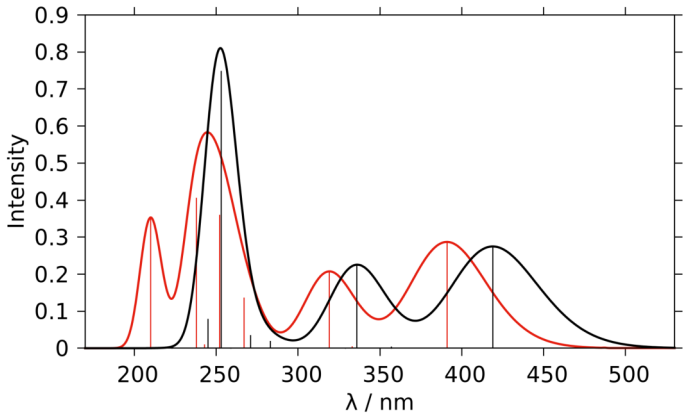

Figure S15: Absorption spectra of $4F_2$-MIA (red) and MIA (black) in aqueous solution.

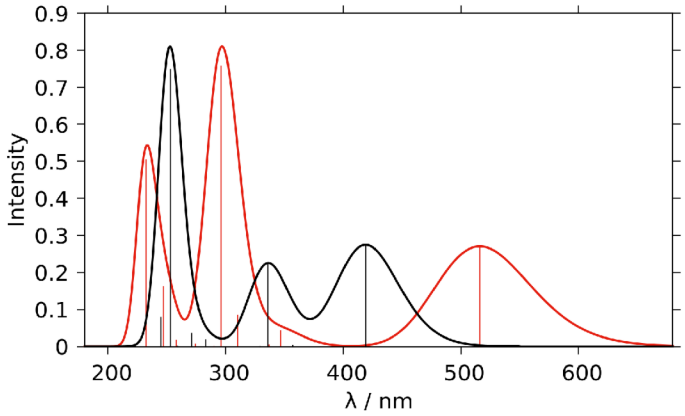

Figure S16: Absorption spectra of $2CF_2$-MIA (red) and MIA (black) in aqueous solution.

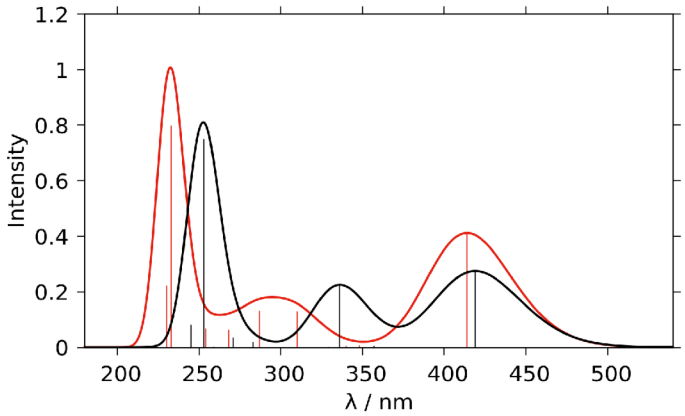

Figure S17: Absorption spectra of $4CF_2$-MIA (red) and MIA (black) in aqueous solution.

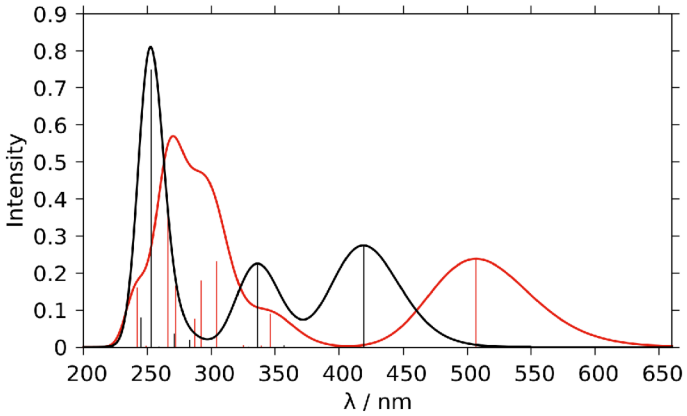

Figure S18: Absorption spectra of 1F-MIA (red) and MIA (black) in aqueous solution.

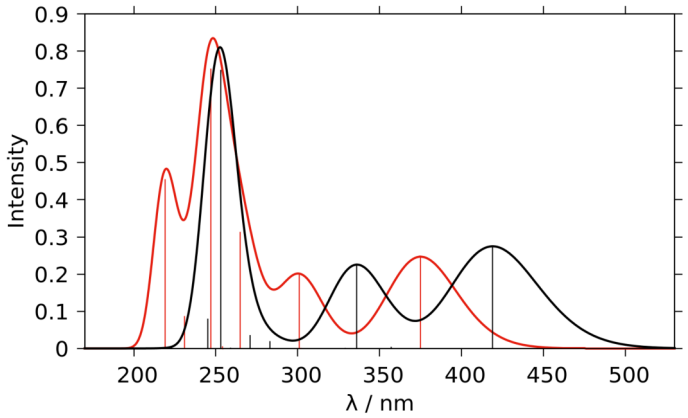

Figure S19: Absorption spectra of 5F-MIA (red) and MIA (black) in aqueous solution.

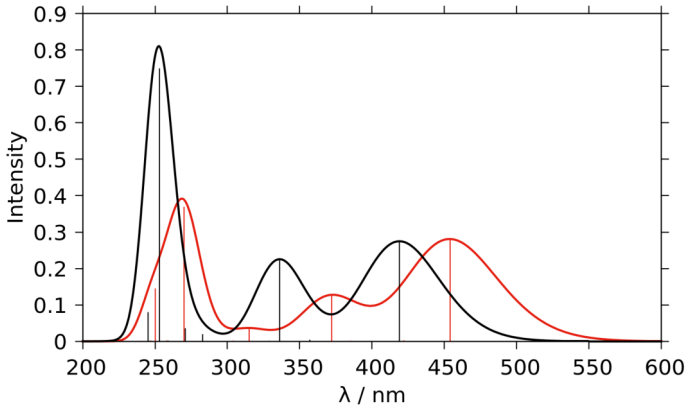

Figure S20: Absorption spectra of $2CF_3$-MIA (red) and MIA (black) in aqueous solution.

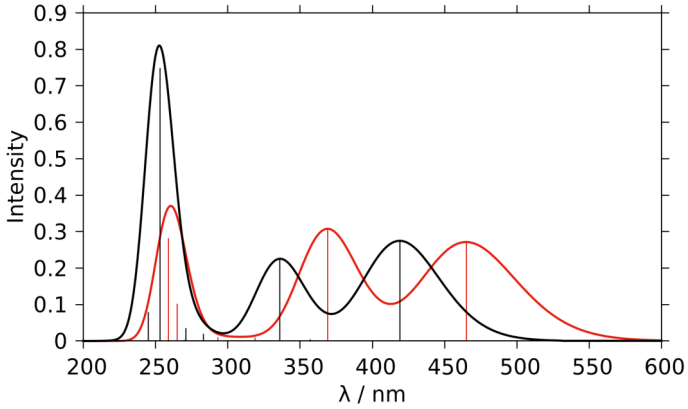

Figure S21: Absorption spectra of $4CF_3$-MIA (red) and MIA (black) in aqueous solution.

S7 Geometries

In general, the ground state geometries of the derivatives are planar as it is the case for MIA. An exception arises from modification in position 1.

Table S7: Selected angles of MIA and 1F-MIA. The numbering of atoms refers to Figure 1.

Angle / °	Flavin MIA	Flavin 1F-MIA
1–10–9	179.6	167.5
4–5–6	177.0	174.4
C(10)–10–5	179.6	169.6
F–1–4		173.6

Substitution of N(1) results in interaction of the methyl group with the additional unit attached to C(1).

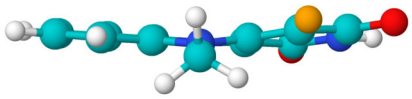

Figure S22: Depiction of the ground state geometry of 1F-MIA.

The barrier between both isomers amounts to 0.05 eV.

Bond lengths

In the following, according to the order of MIA in vacuum, T_2 is used to label the $^3(n_N\pi_L)$ state and T_3 refers to the $^3(\pi_{H-1}\pi_L)$ state. S_2 is assigned to the $^1(n_N\pi_L)$ state.

For the ground state geometries, sets for vacuum as well as aqueous solution (cosmo) are listed. In the cases of $2CF_2$-MIA and $4CF_2$-MIA, the triplet $\pi_H\pi_L$ minimum is used as a proxy for the singlet state.

For the computation of the mean absolute deviations *dev*, the bond lengths of the equilibrium geometry in vacuum are used for the ground state.

Table S8: Bond lengths of MIA at the ground state as well as excited state geometries. Experimental values for the ground state originate from X-ray diffraction experiments.[8]

Derivative	Length / pm						
	S_0(vac)	Exp	S_0(aq)	S_1	T_1	T_2	T_3
N(1)−C(2)	138.1	136.0(5)	136.3	140.0	139.1	137.7	138.1
C(2)−N(3)	141.4	140.8(5)	140.7	137.6	138.4	140.4	140.8
N(3)−C(4)	137.9	135.4(5)	136.9	141.7	139.8	138.8	138.9
C(4)−C(4a)	150.2	148.5(5)	149.1	145.3	147.1	146.0	147.1
C(4a)−N(5)	129.0	129.5(5)	129.7	135.7	136.9	132.3	136.0
N(5)−C(5a)	136.9	136.6(5)	136.1	133.9	133.6	134.7	133.2
C(5a)−C(6)	140.6	141.8(5)	141.0	141.4	142.3	139.9	143.3
C(6)−C(7)	137.8	136.8(6)	137.5	138.2	137.2	138.5	143.3
C(7)−C(8)	140.1	139.5(6)	140.6	140.6	141.1	139.2	135.9
C(8)−C(9)	138.4	138.8(6)	138.2	138.6	138.5	139.3	144.7
C(9)−C(9a)	140.3	139.2(5)	140.4	140.3	139.9	139.4	140.2
C(9a)−N(10)	138.6	139.0(5)	138.4	139.1	139.0	140.0	137.6
N(10)−C(10a)	138.2	136.9(5)	136.9	136.9	139.7	138.8	141.8
C(10a)−N(1)	130.0	131.9(5)	131.5	133.9	132.9	130.0	130.4
C(4a)−C(10a)	146.2	146.6(5)	145.2	142.4	141.0	144.3	142.5
C(5a)−C(9a)	141.9	141.8(5)	142.2	144.6	145.2	142.8	142.7
N(10)−R	146.8	148.8(5)	147.3	147.1	146.3	146.4	146.6
C(2)−O	121.1	121.6(5)	122.8	122.0	122.0	121.3	121.5
C(4)−O	121.0	121.7(5)	122.1	121.6	121.4	121.9	121.8

Table S9: Mean absolute deviations *dev* of bond lengths of MIA.

dev / pm			
S_1S_0	S_1T_1	S_1T_3	T_3T_1
2.1	0.9	2.2	1.9

Table S10: Bond lengths of 1F-MIA at the ground state as well as excited state geometries.

Derivative	Length / pm			
	S_0(vac)	S_0(aq)	S_1	T_1
C(1)−C(2)	145.6	143.7	147.4	145.6
C(2)−N(3)	140.1	139.8	136.5	138.0
N(3)−C(4)	138.2	136.9	143.0	140.5
C(4)−C(4a)	151.1	150.1	144.5	147.3
C(4a)−N(5)	128.6	129.1	134.9	136.0
N(5)−C(5a)	137.7	136.9	133.4	133.9
C(5a)−C(6)	140.1	140.6	142.1	142.0
C(6)−C(7)	138.2	137.9	137.4	137.4
C(7)−C(8)	139.7	140.2	140.8	140.6
C(8)−C(9)	138.8	138.5	138.6	138.6
C(9)−C(9a)	140.1	140.3	139.8	139.7
C(9a)−N(10)	139.2	138.9	141.0	140.0
N(10)−C(10a)	138.9	137.9	135.1	138.3
C(10a)−C(1)	136.3	137.1	140.8	141.5
C(4a)−C(10a)	146.5	146.1	145.8	140.9
C(5a)−C(9a)	141.6	141.9	143.6	143.8
N(10)−C	146.8	147.4	147.7	147.0
C(2)−O	121.5	122.9	122.0	122.2
C(4)−O	120.9	122.1	122.0	121.5
C(1)−F	135.2	135.8	132.8	133.0

Table S11: Mean absolute deviations *dev* of bond lengths of 1F-MIA.

dev / pm	
S_1S_0	S_1T_1
2.5	1.1

Table S12: Bond lengths of $2CF_2$-MIA at the ground state as well as excited state geometries. The fluorine atoms are numbered from top to bottom.

Derivative	Length / pm			
	S_0(vac)	S_0(aq)	S_1	T_1
N(1)−C(2)	136.8	136.8	135.0	131.1
C(2)−N(3)	140.7	140.8	139.1	136.2
N(3)−C(4)	137.6	136.0	142.3	141.9
C(4)−C(4a)	150.5	149.8	144.8	146.7
C(4a)−N(5)	128.8	129.0	134.8	134.9
N(5)−C(5a)	137.8	137.6	132.4	135.0
C(5a)−C(6)	140.1	140.3	143.0	141.5
C(6)−C(7)	138.3	138.2	136.6	137.8
C(7)−C(8)	139.7	140.0	141.9	139.9
C(8)−C(9)	138.8	138.7	137.9	139.0
C(9)−C(9a)	140.1	140.2	140.4	139.6
C(9a)−N(10)	138.9	138.8	138.7	140.0
N(10)−C(10a)	139.0	138.3	135.7	137.7
C(10a)−N(1)	129.6	130.0	132.5	135.8
C(4a)−C(10a)	146.2	145.9	144.8	140.6
C(5a)−C(9a)	141.8	141.8	146.2	143.1
N(10)−C	146.3	146.7	147.2	146.3
C(2)−C	134.3	134.3	137.2	143.7
C(4)−O	121.2	122.5	121.6	121.1
C−F(1)	132.0	132.5	131.4	131.8
C−F(2)	133.5	133.4	132.5	133.5

Table S13: Mean absolute deviations *dev* of bond lengths of $2CF_2$-MIA.

dev / pm	
S_1S_0	S_1T_1
2.4	2.0

Table S14: Bond lengths of $2CF_3$-MIA at the ground state as well as excited state geometries.

Derivative	Length / pm					
	S_0(vac)	S_0(aq)	S_1/T_1	S_2	T_2	T_3
N(1)−C(2)	136.1	133.5	133.3	130.7	131.5	135.7
C(2)−N(3)	129.1	130.8	131.4	131.4	133.1	129.3
N(3)−C(4)	139.9	138.1	138.2	138.9	132.8	140.0
C(4)−C(4a)	151.2	149.5	145.9	151.1	143.3	148.0
C(4a)−N(5)	129.7	130.7	135.4	132.3	134.4	136.2
N(5)−C(5a)	136.3	135.2	134.5	135.4	135.2	133.6
C(5a)−C(6)	140.9	141.5	141.7	141.0	141.4	142.7
C(6)−C(7)	137.5	137.1	137.5	138.1	137.8	142.6
C(7)−C(8)	140.4	141.1	140.6	139.7	140.0	136.1
C(8)−C(9)	138.2	137.8	138.5	139.1	138.8	144.0
C(9)−C(9a)	140.4	140.6	140.0	139.5	139.8	139.8
C(9a)−N(10)	138.3	137.7	138.8	139.9	139.5	137.7
N(10)−C(10a)	137.3	136.0	138.6	137.6	137.3	141.0
C(10a)−N(1)	131.1	133.1	134.3	135.3	134.1	131.3
C(4a)−N(10a)	145.2	143.9	140.3	140.8	141.1	141.7
C(5a)−C(9a)	142.2	142.9	144.4	142.9	143.4	142.7
N(10)−C	147.0	147.6	146.4	146.3	146.4	146.4
C(4)−O	120.9	122.6	124.5	120.5	129.9	122.1
C(2)−C	153.7	153.6	153.1	152.7	153.3	153.2
C−F(oop)	135.2	135.1	135.1	134.4	135.0	135.4
C−F(ip)	133.2	133.9	133.2	133.8	133.4	133.3

Table S15: Mean absolute deviations *dev* of bond lengths of $2CF_3$-MIA.

dev / pm						
S_1S_0	S_1T_2	S_1T_3	S_2S_1	T_2T_1	T_3T_1	T_3T_2
1.8	1.2	1.9	1.3	1.2	1.9	2.7

Table S16: Bond lengths of $4CF_3$-MIA at the ground state as well as excited state geometries.

Derivative	Length / pm					
	S_0(vac)	S_0(aq)	S_1/T_1	S_2	T_2	T_3
N(1)−C(2)	139.1	136.7	138.6	139.6	139.2	140.3
C(2)−N(3)	144.5	143.2	137.4	139.0	139.6	141.4
N(3)−C(4)	127.3	127.8	131.0	130.1	130.6	130.5
C(4)−C(4a)	146.4	145.1	142.1	142.2	142.1	141.9
C(4a)−N(5)	129.7	130.6	135.7	132.4	131.8	136.0
N(5)−C(5a)	136.6	135.2	134.0	135.4	135.7	133.9
C(5a)−C(6)	140.8	141.5	141.9	141.1	140.9	142.2
C(6)−C(7)	137.6	137.1	137.3	138.0	138.0	142.2
C(7)−C(8)	140.3	141.0	141.0	139.7	139.7	136.2
C(8)−C(9)	138.3	138.0	138.2	139.2	139.0	143.7
C(9)−C(9a)	140.4	140.5	140.3	139.3	139.4	139.6
C(9a)−N(10)	138.3	137.9	138.4	140.7	140.7	138.1
N(10)−C(10a)	138.3	137.0	138.9	136.2	136.3	141.1
C(10a)−N(1)	129.6	131.3	131.5	130.6	130.3	129.1
C(4a)−C(10a)	145.7	144.6	142.7	144.5	145.2	143.8
C(5a)−C(9a)	142.3	142.9	144.7	142.8	142.6	142.6
N(10)−C	146.8	147.4	146.6	146.5	146.5	146.4
C(2)−O	120.8	122.8	124.8	120.3	120.2	121.5
C(4)−C	153.8	153.5	153.1	153.2	152.7	153.3
C−F(oop)	134.9	134.8	135.0	134.5	134.5	135.2
C−F(ip)	133.2	134.0	133.5	133.7	133.9	133.4

Table S17: Mean absolute deviations *dev* of bond lengths of $4CF_3$-MIA.

dev / pm						
S_1S_0	S_1T_2	S_1T_3	S_2S_1	T_2T_1	T_3T_1	T_3T_2
1.9	1.4	1.7	1.3	1.4	1.7	1.7

S8 Coupling matrix elements

In the following, according to the order of MIA in vacuum, T2 is used to label the $^3(n_N\pi_L)$ state and T3 refers to the $^3(\pi_{H-1}\pi_L)$ state. S2 is assigned to the $^1(n_N\pi_L)$ state.

Direct SOCMEs

Table S18: Squareroots of sums of squared spin–orbit coupling matrix elements (SOCMEs; x-, y- and z-components) of the El-Sayed allowed inter-system crossings at the $^1(\pi_H\pi_L)$ or $^1(n_N\pi_L)$ geometry, respectively.

Derivative	SOCME / cm^{-1}		
	S1T2	S2T1	S2T3
MIA	8.83132	-	-
$2CF_3$-MIA	24.90745	-	-
$4CF_3$-MIA	31.15968	12.74860	7.32867

The corresponding S1T1 matrix element of 1F-MIA amounts to $1.09035\,cm^{-1}$. The comparatively high direct spin–orbit coupling occurs due to the loss of planarity (MIA: $0.00897\,cm^{-1}$).

Table S19: Squareroots of sums of squared spin–orbit coupling matrix elements (SOCMEs; x-, y- and z-components) of the El-Sayed allowed inter-system crossings at the $^1(\pi_H\pi_L)$ geometry.

Derivative	SOCME / cm^{-1}	
	S1T2	T1S2
MIA	8.83132	17.08080
$2CF_2$-MIA	5.68489	13.71751
1F-MIA	9.50673	23.51324

Table S19 summarizes SOCMEs of the S1 and T1 states with the $^{3/1}(n_N\pi_L)$ states at the S_1 equilibrium geometries. The listed couplings are essential for the vibrational spin–orbit interaction. Neglecting electronic coupling (SOC $\stackrel{!}{=} 1\,cm^{-1}$), the rate constant computed from the Franck–Condon overlaps amounts to $3\,x\,10^6\,s^{-1}$ for MIA. For 1F- and $2CF_2$-MIA, the constants are increased to $5\,x\,10^6\,s^{-1}$ or $4\,x\,10^7\,s^{-1}$, respectively.

Promoting modes of IC and ISC

For each transition, the five biggest couplings are highlighted in red and the corresponding modes are illustrated. Only totalsymmetric normal modes exhibit nonvanishing nonadiabatic coupling matrix elements for the $S_1 \rightsquigarrow S_0$ and $T_3 \rightsquigarrow T_1$ transitions of the planar flavins. Internal conversion between A′- and A″-symmetric states ($S_2 \rightsquigarrow S_0$, $S_2 \leftrightsquigarrow S_1$, $T_3 \leftrightsquigarrow T_2$ as well as $T_2 \rightsquigarrow T_1$) is promoted by oop-modes. Vibronic SOCMEs of $S_1 \rightsquigarrow T_3$ are not listed because the $\pi_{H-1}\pi_L$ and $n_N\pi_L$ triplets are almost degenerate at the S_1 geometries resulting in oversized numerical derivatives.

MIA

Table S20: Harmonic frequencies ν (cm^{-1}) and NACMEs (a_0^{-1}) of MIA at the equilibrium geometries of the $^1(\pi_H\pi_L)$ and $^3(\pi_{H-1}\pi_L)$ states.

Mode	$\nu(S_1)$	S1S0	$\nu(T_3)$	T3T1
1	52.5	0.00000	41.1	0.00000
2	60.7	0.00000	57.3	0.00000
3	114.7	0.00000	92.3	0.00000
4	134.5	0.00000	131.9	0.00000
5	205.1	0.00125	159.7	0.00000
6	211.8	0.00000	162.4	0.00000
7	213.5	0.00000	206.1	0.03264
8	225.7	0.00000	215.2	0.00000
9	269.9	0.00000	270.8	0.00000
10	329.2	-0.00337	315.3	0.00000
11	344.5	0.00708	326.3	0.01446
12	359.4	0.00000	335.6	0.00905
13	383.3	0.00337	348.5	0.00000
14	428.4	0.00000	388.0	-0.04374
15	429.0	0.00883	419.2	0.00000
16	481.4	0.00000	428.5	-0.00242
17	511.2	0.01601	507.5	-0.02868
18	532.6	0.00335	539.2	0.06658
19	539.0	0.00000	540.6	0.00000
20	550.7	0.00000	545.0	0.04154
21	596.3	0.00042	603.7	-0.00701
22	622.2	0.00000	620.4	0.00000
23	636.8	-0.01182	633.7	-0.08040
24	637.1	0.00000	677.5	0.00000
25	698.0	0.00000	682.5	0.00000
26	709.3	0.00281	715.1	0.00000
27	719.8	0.00000	720.3	-0.04589
28	739.1	0.00000	734.1	0.00000
29	772.9	0.00529	762.8	0.00000
30	835.2	-0.00635	783.5	0.00284
31	839.2	0.00000	822.2	0.04422
32	893.8	0.00324	831.4	0.00000
33	905.9	0.00000	892.0	-0.01624
34	948.3	0.00000	925.3	0.00000
35	992.8	-0.00809	981.7	-0.07727

Mode	$\nu(S_1)$	S1S0	$\nu(T_3)$	T3T1
36	1004.5	-0.00601	1012.1	0.03884
37	1042.5	0.00001	1020.2	-0.05349
38	1081.2	0.00397	1038.7	-0.03577
39	1105.7	0.03494	1098.5	-0.02742
40	1141.4	0.00000	1138.0	0.00000
41	1148.4	0.00722	1159.9	-0.00735
42	1182.8	0.01938	1177.4	0.03038
43	1200.9	0.02125	1207.6	-0.07944
44	1221.7	-0.01350	1267.0	-0.03785
45	1290.3	-0.00085	1291.9	-0.05752
46	1298.5	0.00658	1313.9	0.04134
47	1323.1	0.01110	1324.7	0.04612
48	1373.5	0.01092	1382.7	0.08378
49	1378.7	-0.04262	1398.3	0.09780
50	1387.6	0.00725	1414.7	0.04190
51	1406.8	-0.01073	1422.3	-0.13038
52	1434.7	0.00985	1439.0	0.02324
53	1452.9	-0.01682	1445.7	0.11185
54	1496.8	0.01541	1491.8	-0.02610
55	1500.1	0.00000	1511.7	0.00000
56	1504.2	0.02348	1512.7	-0.03141
57	1520.7	0.01132	1563.9	0.15172
58	1547.3	-0.00412	1604.3	-0.04365
59	1593.0	0.00756	1691.3	-0.14902
60	1652.0	0.00515	1747.1	-0.19631
61	1744.7	-0.01120	1774.4	0.40051
62	3051.6	-0.00252	3041.6	0.02425
63	3113.2	0.00000	3104.6	0.00000
64	3182.7	0.00026	3170.2	-0.00671
65	3197.5	-0.00136	3194.0	0.01519
66	3200.1	-0.00088	3208.7	0.00542
67	3209.7	-0.00079	3213.8	0.00696
68	3220.2	0.00164	3222.0	0.00156
69	3593.1	-0.00400	3587.1	-0.00359

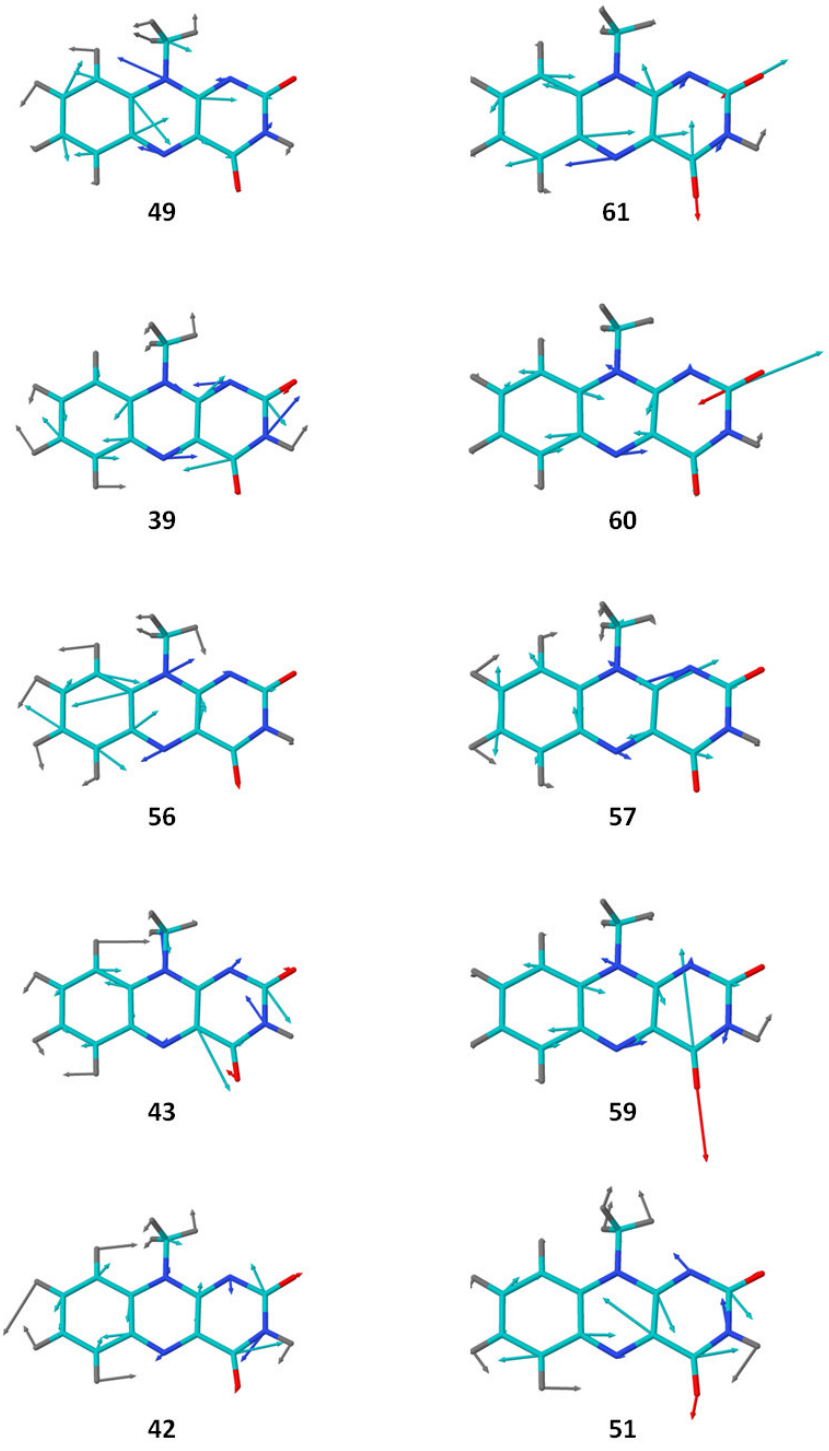

Figure S23: Illustration of the most effective promoting modes of MIA for $S_1 \rightsquigarrow S_0$ (left) and $T_3 \rightsquigarrow T_1$ (right) IC.

$2CF_2$-MIA

Table S21: Harmonic frequencies ν (cm^{-1}), NACMEs (a_0^{-1}) as well as component-averaged absolute values of derivatives of SOCMEs ($cm^{-1}a_0^{-1}$) of $2CF_2$-MIA at the equilibrium geometry of the $^1(\pi_H\pi_L)$ state.

Mode	$\nu(S_1)$	S1S0	S1T1
1	44.5	0.00000	0.10432
2	65.7	0.00000	0.01490
3	105.9	0.00000	0.02453
4	113.2	0.00000	0.04362
5	118.0	-0.00735	0.06391
6	183.3	0.00000	0.00210
7	197.6	0.00000	0.04033
8	203.5	0.00000	0.04246
9	225.3	0.00000	0.04394
10	228.8	-0.00394	0.00010
11	279.6	0.00000	0.07753
12	288.8	0.00239	0.00070
13	313.0	0.00000	0.06109
14	344.7	-0.00626	0.00080
15	355.2	0.00051	0.00208
16	355.2	0.00000	0.07882
17	406.5	0.00000	0.04102
18	430.9	0.00287	0.00361
19	465.1	0.00000	0.02374
20	479.2	-0.00304	0.00014
21	517.3	0.00000	0.15301
22	519.1	0.00179	0.00173
23	538.6	-0.00137	0.00324
24	566.2	0.00685	0.00052
25	577.6	0.00000	0.10293
26	609.1	0.00223	0.00028
27	629.1	0.00000	0.11200
28	637.1	-0.01339	0.00017
29	681.4	0.00000	0.07048
30	697.2	0.00367	0.00434
31	706.4	0.00000	0.11771
32	740.8	0.00000	0.06703
33	750.1	0.00481	0.00137
34	832.2	-0.00681	0.00141
35	837.3	0.00000	0.02209
36	886.2	0.00850	0.00071
37	918.6	0.00000	0.14798
38	953.7	0.00912	0.00119

Mode	$\nu(S_1)$	S1S0	S1T1
39	969.5	0.00000	0.09502
40	1001.0	0.01248	0.00244
41	1031.3	-0.00431	0.00021
42	1100.9	-0.00606	0.00180
43	1120.9	0.01170	0.00069
44	1145.7	0.00000	0.04337
45	1150.8	0.01612	0.00306
46	1162.1	0.00131	0.00353
47	1187.3	0.00514	0.00153
48	1205.3	0.00138	0.00548
49	1276.9	0.00435	0.00113
50	1308.5	0.01872	0.00158
51	1320.9	0.00483	0.00629
52	1342.9	-0.00673	0.00764
53	1359.3	0.00109	0.00509
54	1396.6	-0.01005	0.00027
55	1424.5	0.01014	0.00412
56	1435.0	-0.00165	0.00650
57	1447.3	0.00418	0.00131
58	1456.6	0.01027	0.00052
59	1472.1	0.00733	0.00152
60	1505.7	0.00000	0.10214
61	1507.5	0.00448	0.00074
62	1534.7	-0.01088	0.00004
63	1555.5	-0.01663	0.00049
64	1609.6	-0.03064	0.00111
65	1629.6	0.00282	0.00013
66	1740.9	-0.00355	0.00952
67	1785.4	-0.10255	0.00348
68	3061.3	0.00338	0.00075
69	3125.8	0.00000	0.06898
70	3179.6	0.00168	0.00167
71	3194.7	0.00107	0.00086
72	3200.2	0.00166	0.00031
73	3206.5	0.00001	0.00042
74	3215.2	0.00169	0.00045
75	3624.2	-0.00626	0.00331

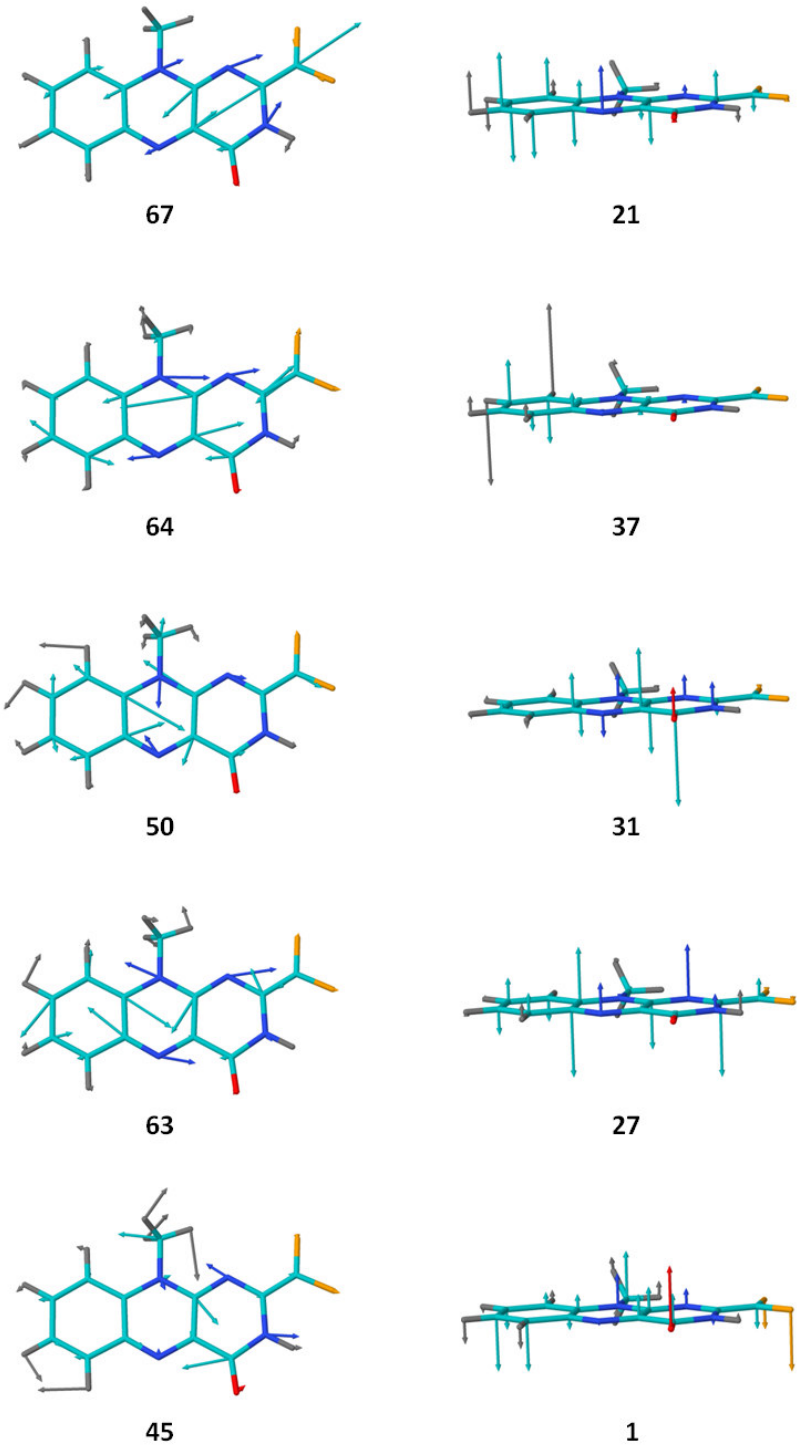

Figure S24: Illustration of the most effective promoting modes of $2CF_2$-MIA for $S_1 \rightsquigarrow S_0$ IC (left) and $S_1 \rightsquigarrow T_1$ ISC (right).

1F-MIA

Table S22: Harmonic frequencies ν (cm^{-1}), NACMEs (a_0^{-1}) as well as component-averaged absolute values of derivatives of SOCMEs ($cm^{-1}a_0^{-1}$) of 1F-MIA at the equilibrium geometry of the $^1(\pi_H\pi_L)$ state.

Mode	$\nu(S_1)$	S1S0	S1T1
1	51.3	-0.00449	0.07726
2	59.7	0.00193	0.04193
3	91.6	0.00645	0.08165
4	117.2	-0.00179	0.03753
5	140.5	0.00179	0.01084
6	166.4	0.00135	0.02822
7	209.2	-0.00412	0.01391
8	238.6	0.00229	0.09568
9	258.4	0.00464	0.10131
10	316.9	-0.00510	0.05207
11	327.3	-0.00676	0.14447
12	338.8	0.00450	0.03606
13	355.9	0.00446	0.03471
14	393.6	-0.00246	0.07808
15	406.0	-0.01817	0.03576
16	424.4	0.00649	0.03773
17	458.7	-0.00658	0.03557
18	474.4	0.01040	0.00828
19	510.2	-0.00554	0.03272
20	518.4	-0.00273	0.02140
21	537.7	-0.00423	0.02605
22	581.8	0.00516	0.03699
23	602.2	0.00360	0.03802
24	628.5	0.00584	0.03316
25	632.5	-0.00023	0.03341
26	671.6	-0.00053	0.11000
27	692.0	-0.00532	0.11315
28	723.8	0.00757	0.04333
29	728.6	-0.00031	0.06616
30	739.1	0.00652	0.03381
31	742.7	-0.00194	0.03181
32	769.6	-0.00109	0.00366
33	845.5	0.00033	0.01809
34	895.6	0.00571	0.05600
35	912.7	-0.00113	0.05125
36	964.4	-0.00811	0.02182

Mode	$\nu(S_1)$	S1S0	S1T1
37	966.3	-0.00428	0.03375
38	1027.99	0.00587	0.03863
39	1047.19	-0.00461	0.01734
40	1102.91	-0.01615	0.03532
41	1135.55	-0.00314	0.03708
42	1144.17	-0.01399	0.02021
43	1163.94	0.00386	0.01078
44	1179.46	0.00852	0.06262
45	1201.18	0.00094	0.04993
46	1229.32	-0.00390	0.05587
47	1273.34	0.00461	0.04702
48	1303.52	-0.00279	0.01718
49	1322.96	0.02525	0.01400
50	1340.61	0.01856	0.05900
51	1382.91	-0.00894	0.04344
52	1402.44	0.00544	0.01615
53	1423.65	0.00452	0.05608
54	1447.81	0.01350	0.01623
55	1462.08	0.00421	0.03336
56	1478.31	0.00177	0.04098
57	1505.55	-0.01050	0.03977
58	1513.81	-0.00464	0.02338
59	1523.61	0.00481	0.06700
60	1552.54	0.02206	0.03176
61	1577.71	-0.05563	0.06321
62	1613.58	0.01176	0.03647
63	1727.10	0.01814	0.14291
64	1732.91	-0.02053	0.04163
65	3069.24	0.00257	0.02123
66	3156.23	-0.00019	0.03953
67	3180.56	0.00005	0.00976
68	3197.24	0.00011	0.01620
69	3206.02	0.00318	0.03126
70	3208.14	0.00229	0.05805
71	3214.59	-0.00166	0.01176
72	3581.55	0.00086	0.01070

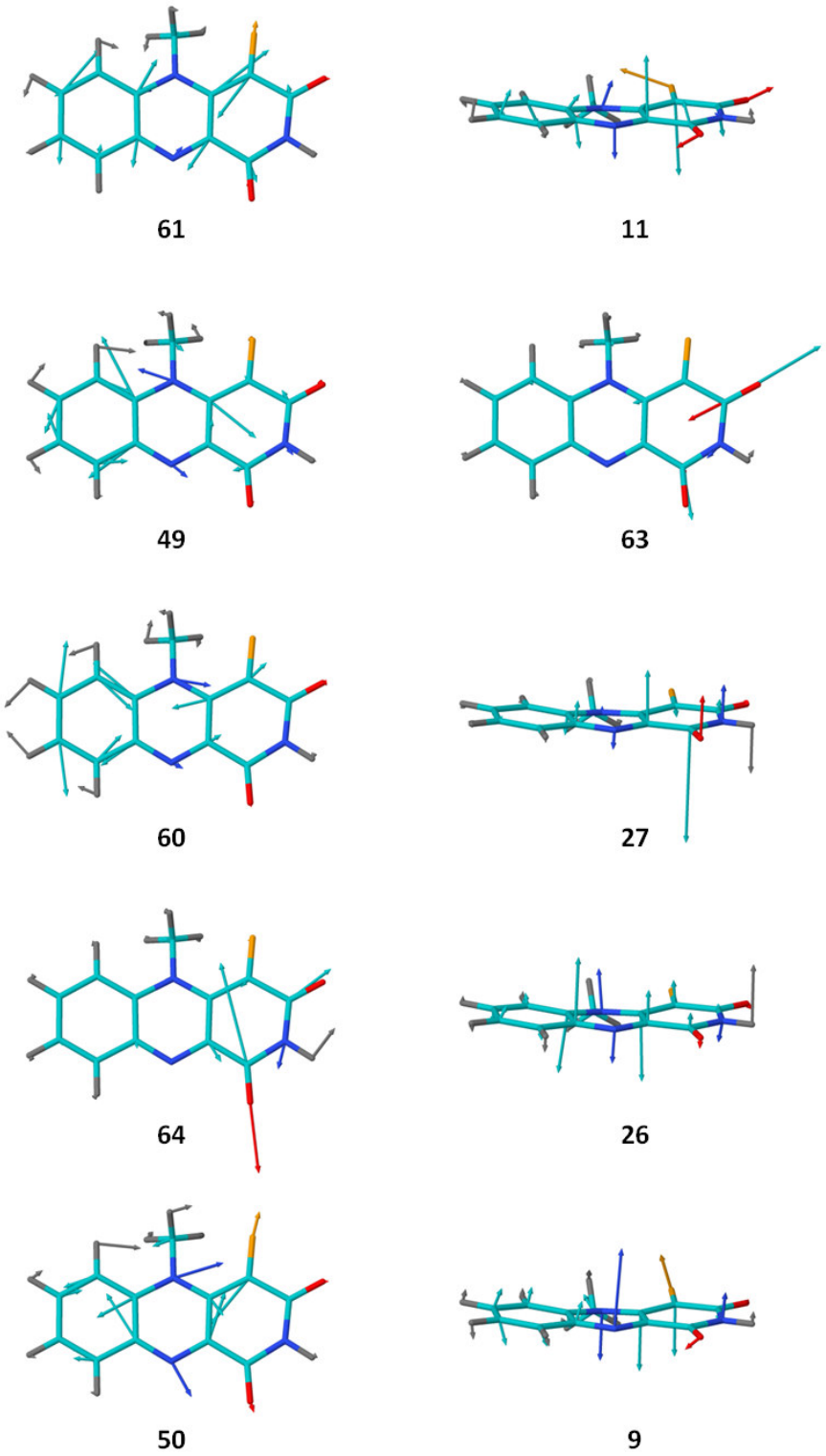

Figure S25: Illustration of the most effective promoting modes of 1F-MIA for $S_1 \rightsquigarrow S_0$ IC (left) and $S_1 \rightsquigarrow T_1$ ISC (right).

2CF$_3$-MIA

Table S23: Harmonic frequencies ν (cm^{-1}), NACMEs (a$_0^{-1}$) as well as component-averaged absolute values of derivatives of SOCMEs (cm^{-1}a$_0^{-1}$) of 2CF$_3$-MIA at the equilibrium geometry of the $^1(\pi_H\pi_L)$ state.

Mode	ν(S$_1$)	S1S0	S1T1	S1T2
1	8.2	0.00000	0.13490	0.19144
2	34.6	0.00000	0.65024	0.12364
3	66.7	0.00000	0.68196	0.15230
4	108.7	0.00000	0.49721	0.66675
5	117.1	0.00018	0.00369	0.19817
6	129.5	0.00000	0.05474	0.08829
7	175.2	0.00000	1.00411	0.77976
8	197.1	0.00000	0.56949	0.53675
9	226.9	-0.00470	0.00291	0.24935
10	239.4	0.00000	0.17936	0.14841
11	265.1	-0.00378	0.00080	0.32816
12	266.6	0.00000	0.36091	0.63556
13	326.2	-0.00651	0.00332	0.24806
14	340.6	-0.00750	0.00108	0.23362
15	343.1	0.00000	0.27121	0.26838
16	401.0	-0.00103	0.00031	0.22088
17	403.8	0.00000	0.25893	0.15780
18	472.6	0.00351	0.00575	0.28718
19	473.9	0.00000	0.45094	0.34322
20	499.6	0.00000	0.14243	0.29362
21	507.8	-0.01042	0.00143	0.44858
22	514.0	0.00000	0.71340	0.33084
23	534.2	0.01416	0.00028	0.44673
24	564.0	-0.00922	0.00071	0.17628
25	576.1	0.00000	0.64050	0.27254
26	587.2	-0.01313	0.00292	0.15216
27	630.4	0.00934	0.00139	0.05676
28	656.7	0.00000	0.77547	0.78314
29	677.2	0.00000	0.83082	0.45730
30	698.4	-0.00806	0.01026	0.99416
31	716.4	-0.00167	0.00597	0.68298
32	753.0	0.00000	0.05207	0.05922
33	757.6	0.00000	0.07859	0.03691
34	762.8	-0.00644	0.03541	0.24648
35	843.3	0.00000	0.14148	0.06967
36	850.2	-0.00124	0.03800	0.87592
37	880.3	-0.00192	0.00022	0.57588
38	927.0	0.00000	0.12770	0.10856

Mode	$\nu(S_1)$	S1S0	S1T1	S1T2
39	950.4	0.00104	0.03250	0.35165
40	961.4	0.00000	0.05645	0.05609
41	1013.9	0.01234	0.00691	0.76725
42	1046.7	-0.00151	0.00007	0.71655
43	1077.1	0.00846	0.02750	2.74991
44	1088.9	-0.00548	0.04783	0.62500
45	1130.5	0.00000	0.15347	0.07190
46	1144.4	0.00000	0.51173	0.12374
47	1144.7	-0.00603	0.04850	0.27699
48	1177.1	-0.00868	0.00221	0.55875
49	1186.6	0.01324	0.03714	0.62922
50	1206.6	-0.00612	0.01017	0.05771
51	1218.8	-0.01140	0.00749	0.18527
52	1250.7	-0.00554	0.00945	0.97781
53	1284.0	0.01045	0.00627	0.67480
54	1316.2	-0.04293	0.04223	0.61685
55	1326.5	0.00506	0.00291	0.96469
56	1339.4	0.03307	0.03522	0.98260
57	1350.7	-0.00225	0.00543	0.28667
58	1375.6	0.00941	0.04406	0.45392
59	1384.1	-0.02224	0.03732	0.83164
60	1443.3	-0.01085	0.04075	0.42630
61	1460.6	-0.01873	0.04011	0.17064
62	1475.9	0.00146	0.00216	0.35631
63	1506.5	0.00000	0.01560	0.09483
64	1510.6	-0.00165	0.03874	0.14287
65	1517.1	0.01079	0.03425	0.60927
66	1539.5	0.01017	0.00252	0.61514
67	1574.1	0.01296	0.00290	0.35539
68	1615.2	-0.00581	0.03745	0.02868
69	3044.7	-0.00318	0.00506	0.01869
70	3102.7	0.00000	0.08237	0.09277
71	3184.2	0.00016	0.00108	0.07625
72	3193.0	0.00099	0.03862	0.24476
73	3198.3	0.00054	0.03992	0.28447
74	3211.2	-0.00041	0.00066	0.09788
75	3219.8	-0.00130	0.00101	0.06384

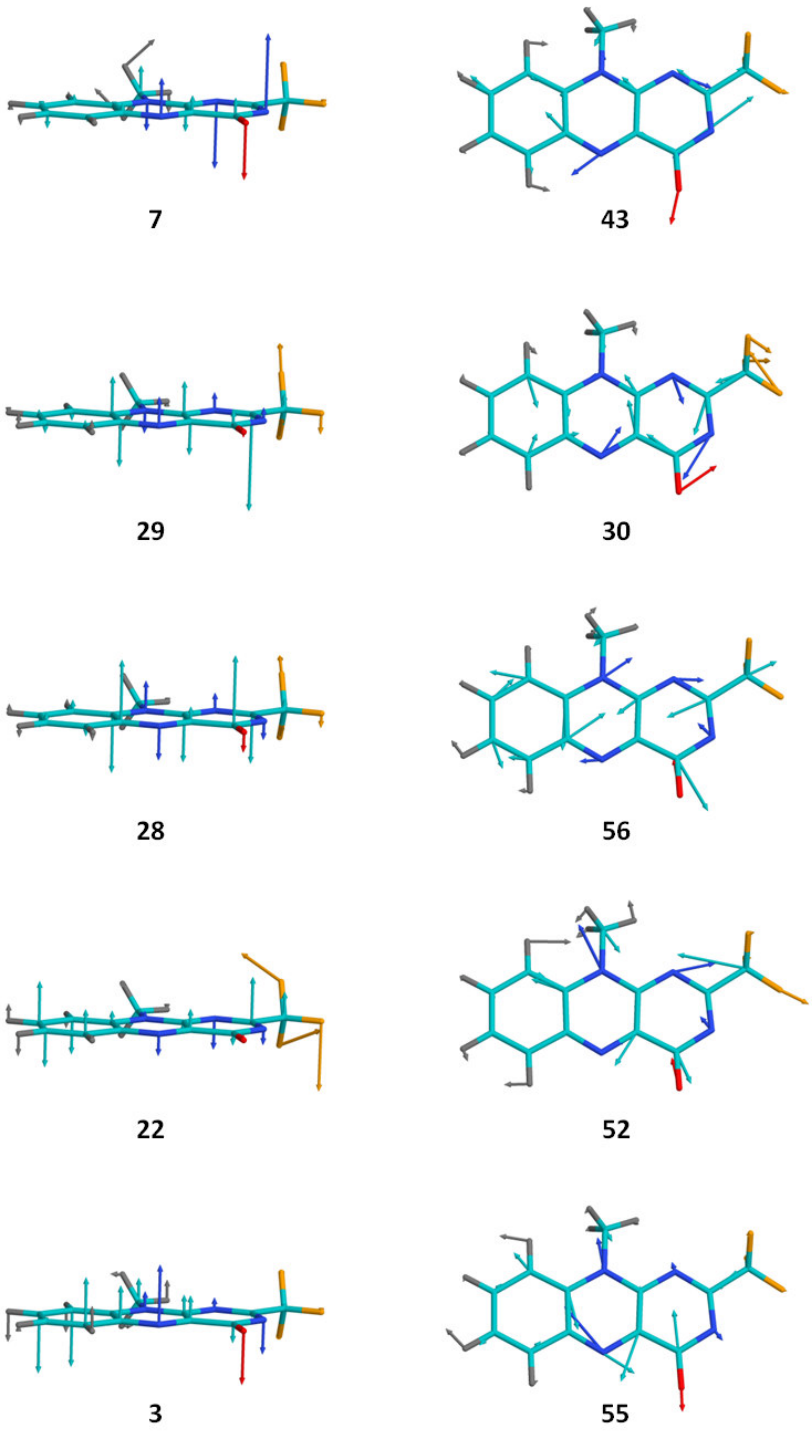

Figure S26: Illustration of the most effective promoting modes of $2CF_3$-MIA for $S_1 \rightsquigarrow T_1$ (left) and $S_1 \rightsquigarrow T_2$ ISC (right).

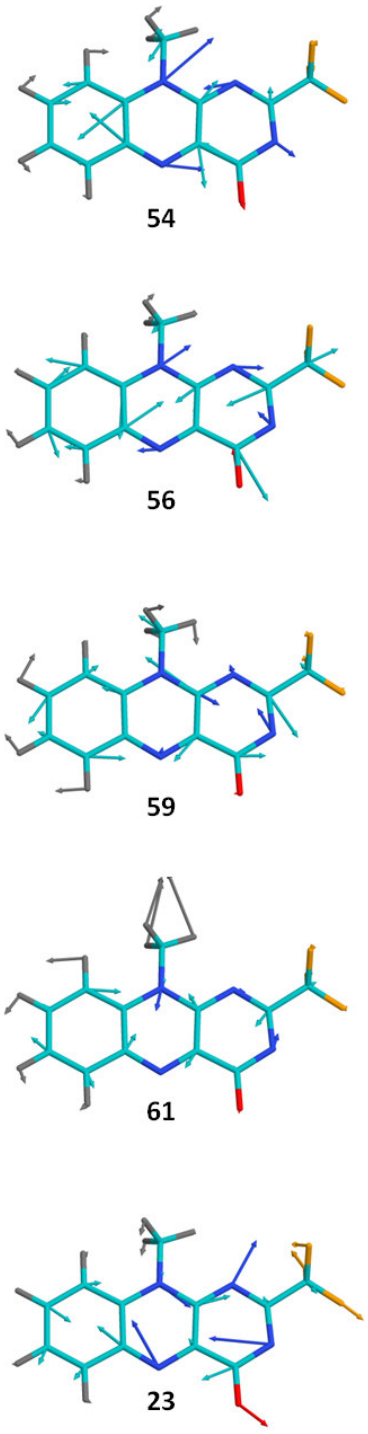

Figure S27: Illustration of the most effective promoting modes of $2CF_3$-MIA for $S_1 \rightsquigarrow S_0$ IC.

Table S24: Harmonic frequencies ν (cm^{-1}) and NACMEs (a_0^{-1}) of $2CF_3$-MIA at the equilibrium geometries of the $^1(n_N\pi_L)$, $^3(\pi_{H-1}\pi_L)$ and $^3(n_N\pi_L)$ states.

Mode	$\nu(S_2)$	S2S1	$\nu(T_3)$	T3T1	$\nu(T2)$	T2T3	T2T1
1	37.7	-0.05338	21.2	0.00000	36.2	0.01614	-0.04546
2	72.7	-0.14628	35.7	0.00000	73.8	0.01604	-0.05299
3	92.3	-0.49083	75.9	0.00000	113.8	0.00557	0.00086
4	109.1	0.00000	109.5	0.00000	119.2	0.00000	0.00000
5	135.6	-0.25519	119.8	0.01660	134.7	0.00122	0.02546
6	172.6	0.46502	137.3	0.00000	189.4	0.02977	0.04056
7	185.0	-0.21496	162.0	0.00000	197.2	0.03078	0.07429
8	187.8	0.04461	198.6	0.00000	214.9	0.00000	0.00000
9	215.0	0.00000	228.7	-0.04625	201.2	-0.00040	0.00064
10	250.4	0.00000	252.8	0.00000	246.0	-0.02592	0.05896
11	261.2	0.49806	266.4	-0.02581	263.8	0.00000	0.00000
12	270.3	-0.22758	281.1	0.00000	269.8	-0.01588	-0.03628
13	319.0	0.00000	323.7	-0.01422	307.9	0.00000	0.00000
14	333.7	0.00000	334.5	-0.00170	332.9	0.00000	0.00000
15	343.7	0.27236	340.8	0.00000	349.5	-0.01854	-0.03647
16	391.5	0.00000	360.5	0.00000	400.5	0.00000	0.00000
17	424.3	0.00000	399.8	0.02764	413.8	0.04624	-0.04276
18	445.3	0.01621	423.8	0.00000	465.7	0.00000	0.00000
19	476.8	0.22640	444.8	0.00000	483.0	0.02009	0.00454
20	506.0	0.00000	468.0	0.08227	495.0	0.00000	0.00000
21	509.5	0.42808	506.2	0.08157	505.6	-0.00922	0.04611
22	517.7	0.00000	517.5	0.00000	531.8	0.00372	-0.02615
23	532.8	0.11940	528.8	-0.02352	537.9	0.00000	0.00000
24	542.7	0.00000	556.4	0.00000	558.1	0.00000	0.00000
25	575.3	0.00000	557.8	-0.08149	585.5	0.00000	0.00000
26	602.5	0.07353	586.8	0.03303	617.2	-0.02758	0.02106
27	607.1	0.00000	619.3	0.08974	633.6	0.00000	0.00000
28	659.0	0.19277	631.0	0.00000	659.0	0.00000	0.00000
29	670.1	0.00000	700.1	-0.04284	669.2	0.02962	0.04690
30	691.4	0.64863	706.4	0.00000	680.5	-0.05393	0.01897
31	700.4	0.00000	719.2	0.06357	714.9	0.00000	0.00000
32	713.5	-0.77015	728.9	0.00000	760.7	-0.01885	-0.01644
33	753.7	0.00000	742.6	0.00000	762.6	0.00000	0.00000
34	757.6	0.03131	761.5	-0.01250	768.2	-0.00453	-0.03794
35	825.7	0.00000	789.2	0.00000	847.2	0.00408	-0.00421
36	842.1	0.00877	830.8	-0.04340	868.2	0.00000	0.00000
37	882.2	0.00000	868.9	0.00000	885.9	0.00000	0.00000
38	913.0	0.00000	884.9	-0.08264	933.1	0.00401	-0.00117

Mode	$\nu(S_2)$	S2S1	$\nu(T_3)$	T3T1	$\nu(T_2)$	T2T3	T2T1
39	923.1	0.01070	935.3	0.00000	950.1	0.00000	0.00000
40	952.6	0.00000	937.7	-0.10847	959.9	0.00361	0.00260
41	955.5	0.01784	1003.5	0.05923	1018.2	0.00000	0.00000
42	1009.9	0.00000	1034.8	-0.01352	1057.6	0.00000	0.00000
43	1059.2	0.00000	1049.5	0.10221	1108.9	0.00000	0.00000
44	1112.3	0.00000	1094.5	0.03211	1133.0	0.00201	-0.00259
45	1143.7	0.00000	1115.6	-0.05646	1147.8	-0.01896	-0.01262
46	1145.8	-0.07691	1119.7	0.00000	1148.5	0.00000	0.00000
47	1155.7	-0.13193	1139.4	0.00000	1164.2	0.00000	0.00000
48	1182.4	0.00000	1188.0	-0.08011	1189.6	0.00000	0.00000
49	1188.5	0.00000	1191.6	0.05044	1207.7	0.00000	0.00000
50	1206.3	0.00000	1197.5	-0.05756	1221.1	0.00000	0.00000
51	1225.7	0.00000	1233.7	-0.09348	1271.4	0.00000	0.00000
52	1251.2	0.00000	1268.9	0.13340	1283.5	0.00000	0.00000
53	1280.7	0.00000	1320.3	0.06446	1300.0	0.00000	0.00000
54	1314.7	0.00000	1326.7	-0.01198	1316.3	0.00000	0.00000
55	1324.5	0.00000	1344.5	0.22394	1337.8	0.00000	0.00000
56	1350.4	0.00000	1392.4	-0.40497	1351.0	0.00000	0.00000
57	1368.7	0.00000	1405.6	0.13600	1378.9	0.00000	0.00000
58	1390.2	0.00000	1430.6	0.19610	1423.4	0.00000	0.00000
59	1460.6	0.00000	1435.4	-0.06225	1450.7	0.00000	0.00000
60	1474.2	0.00000	1444.2	-0.14496	1465.5	0.00000	0.00000
61	1485.1	0.00000	1484.2	0.01234	1472.5	0.00000	0.00000
62	1499.2	0.00000	1503.8	-0.14839	1501.1	0.00000	0.00000
63	1503.2	0.02790	1505.1	0.00000	1508.1	0.00222	0.00486
64	1519.9	0.00000	1519.6	-0.20754	1517.3	0.00000	0.00000
65	1547.2	0.00000	1526.8	-0.00021	1531.5	0.00000	0.00000
66	1595.5	0.00000	1598.8	-0.20296	1570.1	0.00000	0.00000
67	1620.2	0.00000	1622.7	-0.11877	1599.0	0.00000	0.00000
68	1726.0	0.00000	1720.6	-0.28163	1628.1	0.00000	0.00000
69	3041.5	0.00000	3039.4	0.02518	3045.7	0.00000	0.00000
70	3097.2	0.00395	3100.6	0.00000	3104.5	0.00174	-0.00158
71	3182.1	0.00000	3173.6	-0.00493	3183.1	0.00000	0.00000
72	3190.1	0.00000	3197.2	-0.01976	3186.1	0.00000	0.00000
73	3196.0	0.00000	3209.1	-0.00020	3196.2	0.00000	0.00000
74	3209.9	0.00000	3214.3	0.00849	3209.0	0.00000	0.00000
75	3220.3	0.00000	3221.6	-0.00167	3220.3	0.00000	0.00000

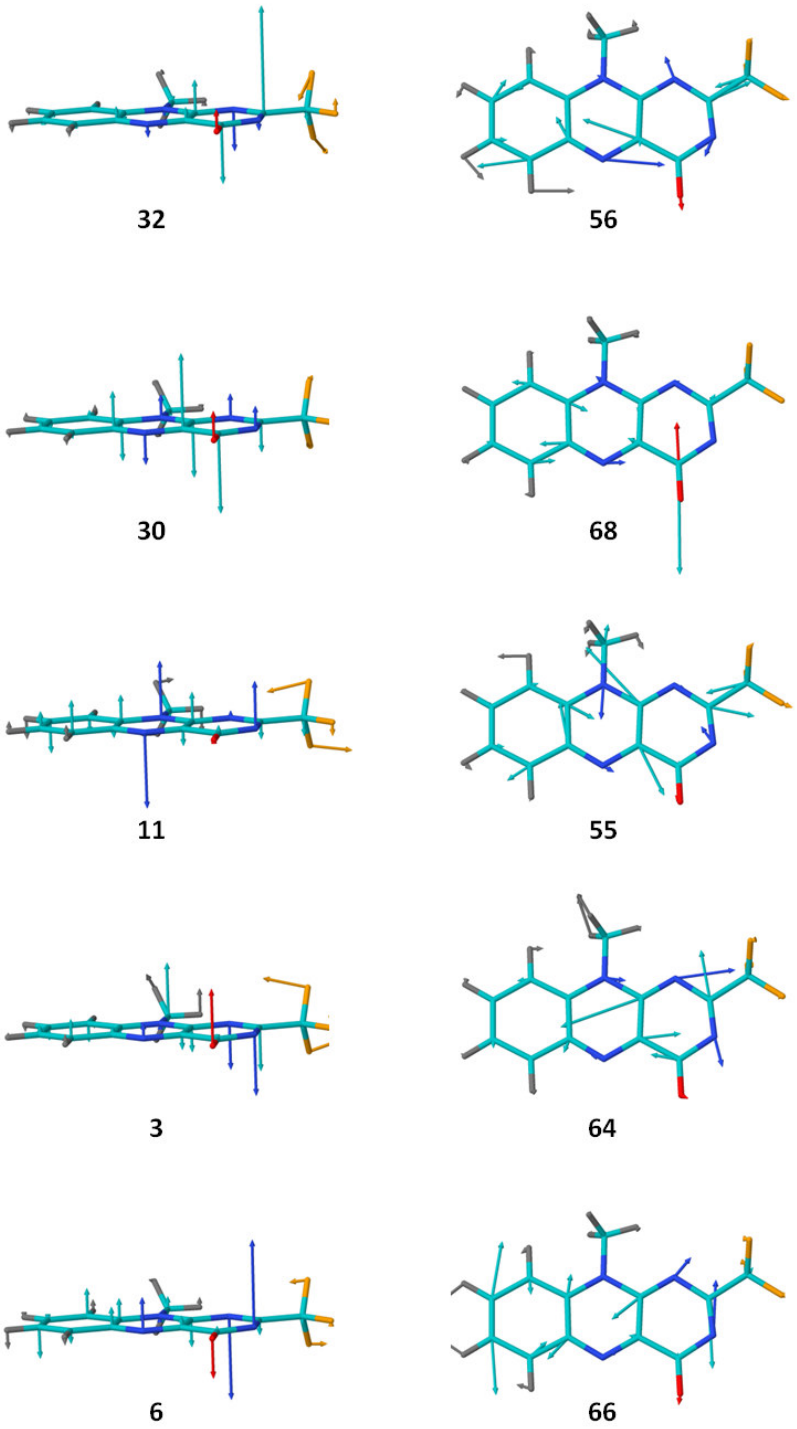

Figure S28: Illustration of the most effective promoting modes of $2CF_3$-MIA for $S_2 \rightsquigarrow S_1$ IC (left) and $T_3 \rightsquigarrow T_1$ ISC (right).

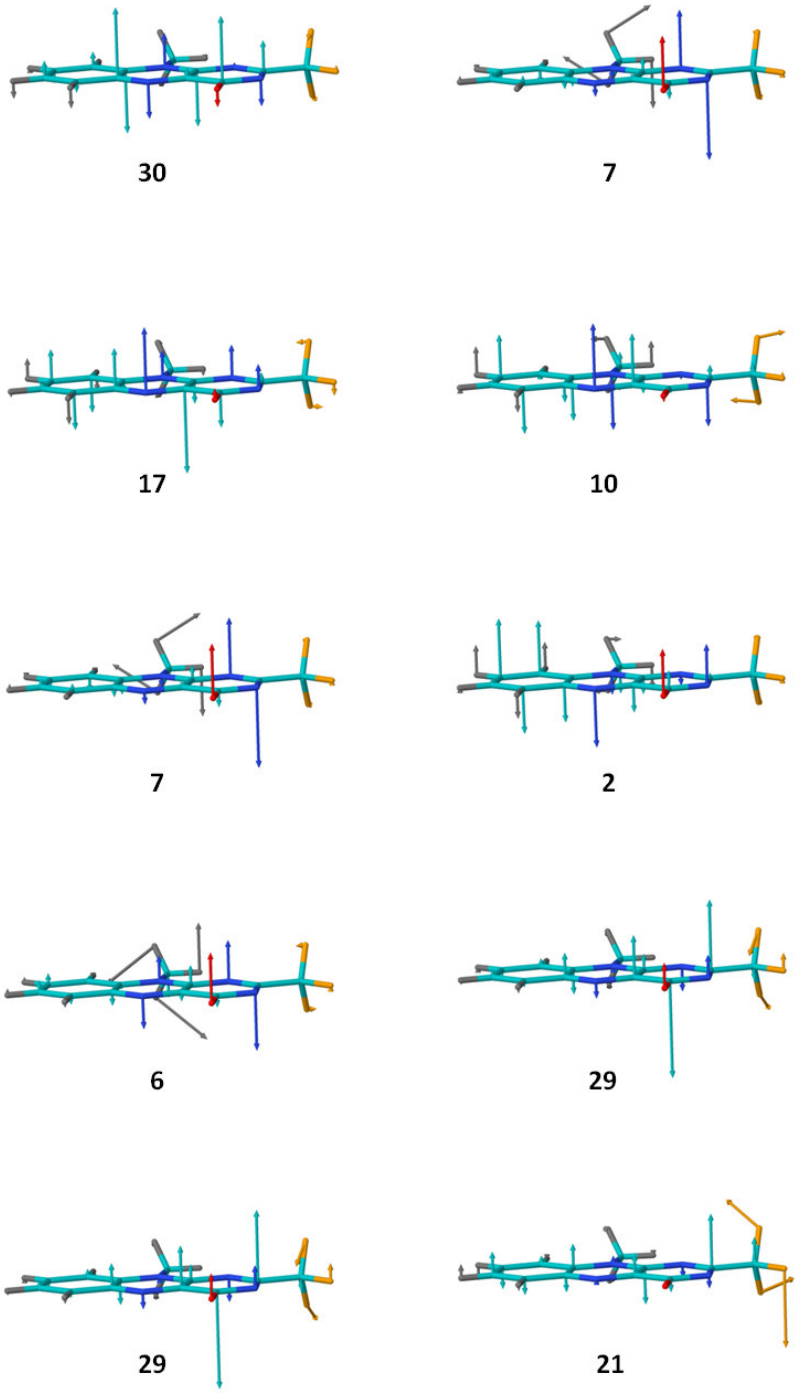

Figure S29: Illustration of the most effective promoting modes of $2CF_3$-MIA for $T_2 \rightsquigarrow T_3$ (left) and $T_2 \rightsquigarrow T_1$ IC (right).

4CF$_3$-MIA

Table S25: Harmonic frequencies ν (cm^{-1}), NACMEs (a$_0^{-1}$) as well as component-averaged absolute values of derivatives of SOCMEs (cm^{-1}a$_0^{-1}$) of 4CF$_3$-MIA at the equilibrium geometry of the $^1(\pi_H\pi_L)$ state.

Mode	ν(S$_1$)	S1S2	S1S0	S1T1	S1T2
1	32.6	-0.25971	0.00000	3.34497	0.73711
2	50.7	-0.00959	0.00000	0.30730	0.17643
3	65.8	-0.02369	0.00000	0.39175	0.27890
4	109.3	0.10732	0.00000	1.49482	0.47467
5	117.2	0.00000	-0.00869	0.00012	0.06007
6	128.2	-0.43081	0.00000	5.27239	0.81229
7	152.6	-0.14157	0.00000	2.39617	0.51130
8	195.1	0.10534	0.00000	1.20166	0.15641
9	234.9	-0.05376	0.00000	0.27269	0.04241
10	240.5	0.00000	0.00584	0.00037	0.37374
11	279.1	0.00000	-0.00435	0.00046	0.17798
12	285.5	0.15679	0.00000	1.62404	0.15565
13	301.9	-0.25793	0.00000	3.62569	0.57933
14	315.5	0.00000	-0.00460	0.00110	0.53959
15	333.4	0.00000	-0.00442	0.00023	0.11399
16	400.0	0.05466	0.00000	0.99584	0.15923
17	407.3	0.00000	-0.00370	0.00207	0.52090
18	455.7	0.00000	0.00225	0.00258	0.58405
19	463.6	0.10037	0.00000	1.27379	0.02116
20	491.2	0.08732	0.00000	1.08751	0.09261
21	510.5	-0.04693	0.00000	0.49631	0.04964
22	516.0	0.00000	-0.00573	0.00047	0.41791
23	537.9	0.00000	0.00090	0.00078	0.43024
24	562.7	0.00000	-0.00185	0.00033	0.59145
25	568.5	0.16739	0.00000	2.26493	0.40548
26	605.2	0.00000	0.00991	0.00104	0.92414
27	623.5	0.00000	0.01157	0.00119	0.68220
28	644.2	-0.05677	0.00000	0.53869	0.08239
29	707.4	0.00000	0.00953	0.00313	0.23956
30	712.8	0.09488	0.00000	1.28081	0.54501
31	732.2	0.00000	-0.00128	0.00263	0.62627
32	752.6	0.00819	0.00000	0.27945	0.04147
33	772.2	0.00000	-0.00260	0.00130	0.65365
34	784.0	-0.01068	0.00000	0.54811	0.48542
35	834.6	0.00000	-0.00701	0.00204	1.80319
36	842.6	-0.00959	0.00000	0.19631	0.16307
37	881.7	0.00000	0.01150	0.00262	1.43317
38	912.0	0.00000	0.01396	0.00291	1.45876

Mode	$\nu(S_1)$	S1S2	S1S0	S1T1	S1T2
39	928.6	-0.00651	0.00000	0.09437	0.08796
40	962.8	-0.00523	0.00000	0.09552	0.04179
41	998.3	0.00000	-0.01445	0.00142	2.93094
42	1043.6	0.00000	0.01011	0.00310	0.19811
43	1059.6	0.00000	-0.00270	0.00050	0.70163
44	1101.6	0.00000	-0.03296	0.00425	3.57019
45	1135.2	0.00549	0.00000	0.14814	0.11830
46	1144.2	0.00000	0.02596	0.00226	0.63956
47	1144.3	0.00802	0.00000	0.12455	0.05199
48	1161.9	0.00000	-0.00788	0.00278	0.50287
49	1188.6	0.00000	0.00311	0.00296	0.14550
50	1194.8	0.00000	0.01500	0.00295	0.19482
51	1221.8	0.00000	0.01748	0.00185	3.79783
52	1257.6	0.00000	-0.00009	0.01041	1.57094
53	1273.3	0.00000	0.01545	0.00405	0.58144
54	1308.4	0.00000	-0.02448	0.00746	0.62536
55	1320.3	0.00000	0.03890	0.00092	0.32705
56	1349.0	0.00000	-0.02500	0.00018	1.29686
57	1369.4	0.00000	0.00998	0.00322	0.14242
58	1390.0	0.00000	-0.00002	0.00545	0.86325
59	1401.4	0.00000	0.00446	0.00650	1.54338
60	1443.7	0.00000	-0.00049	0.00083	1.00037
61	1460.9	0.00000	0.01501	0.00192	1.09596
62	1480.2	0.00000	-0.01725	0.00316	0.39622
63	1508.2	-0.01981	0.00000	0.17871	0.17270
64	1509.4	0.00000	0.00406	0.00058	0.23287
65	1522.0	0.00000	0.02392	0.00630	0.25493
66	1559.0	0.00000	-0.00976	0.00110	0.33816
67	1581.8	0.00000	-0.00709	0.00307	0.61245
68	1618.7	0.00000	0.00533	0.00318	0.11638
69	3049.6	0.00000	0.00598	0.00294	0.16785
70	3111.2	0.00431	0.00000	0.11558	0.11010
71	3184.3	0.00000	0.00023	0.00068	0.01095
72	3188.5	0.00000	-0.00217	0.00130	0.01768
73	3199.2	0.00000	-0.00060	0.00018	0.01655
74	3211.5	0.00000	0.00060	0.00032	0.01491
75	3221.8	0.00000	0.00229	0.00147	0.01849

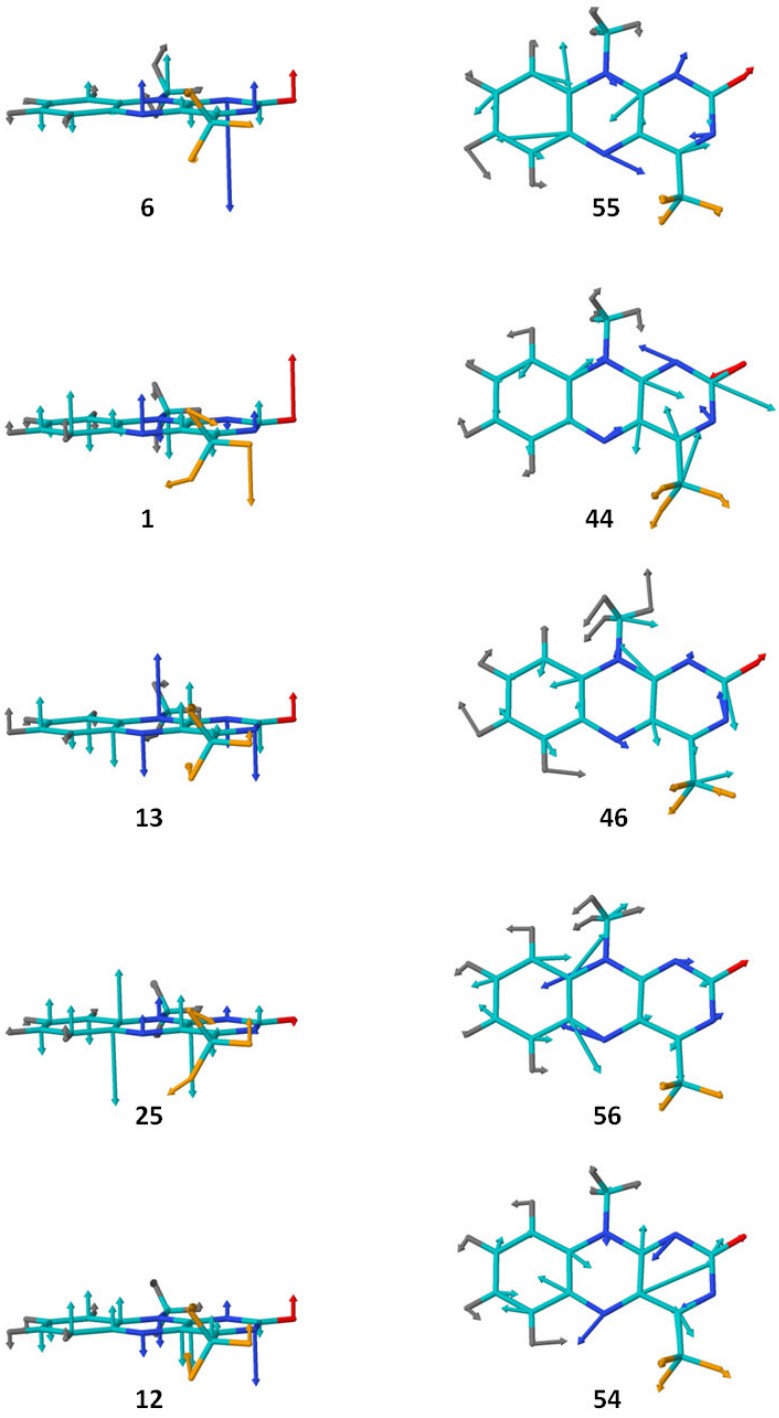

Figure S30: Illustration of the most effective promoting modes of $4CF_3$-MIA for $S_1 \rightsquigarrow S_2$ (left) and $S_1 \rightsquigarrow S_0$ IC (right).

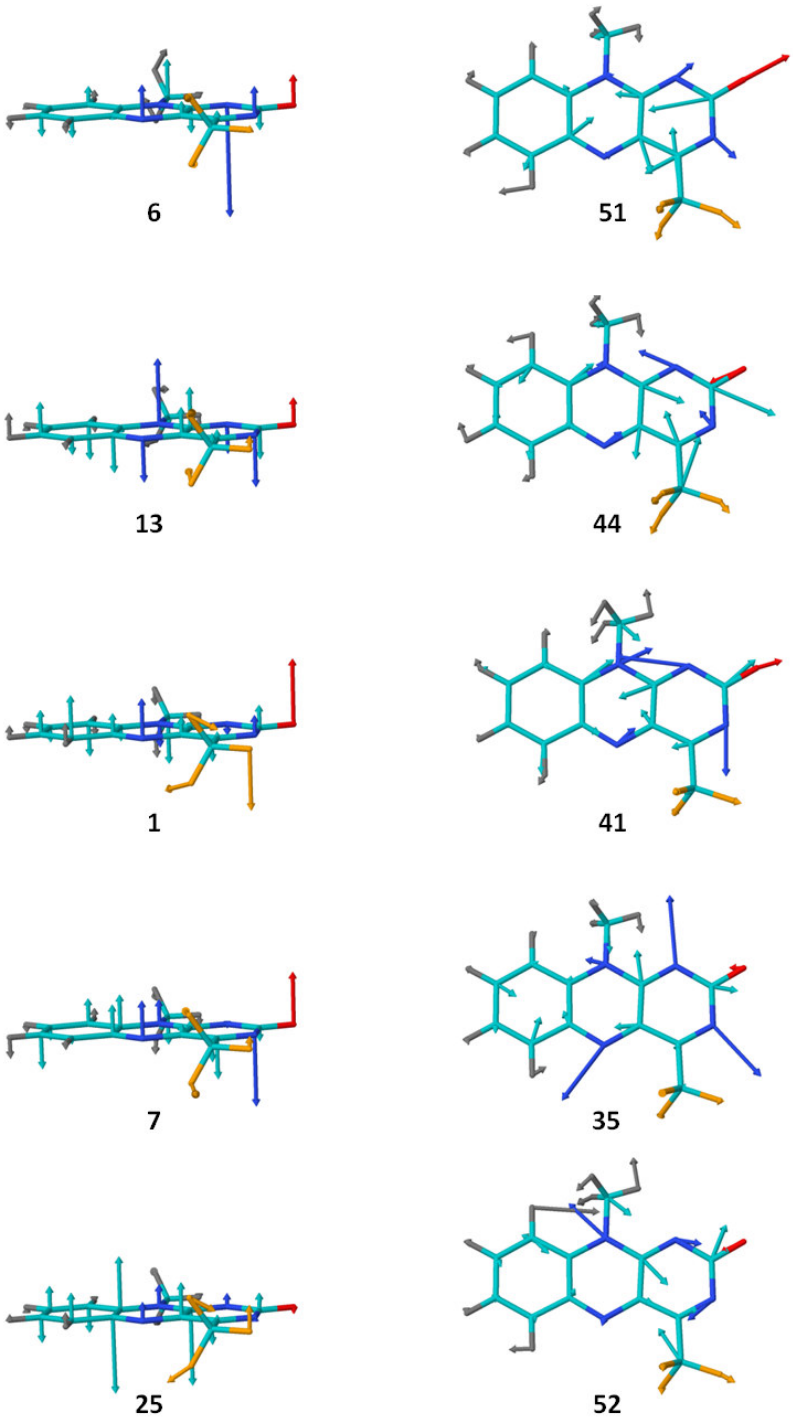

Figure S31: Illustration of the most effective promoting modes of $4CF_3$-MIA for $S_1 \rightsquigarrow T_1$ (left) and $S_1 \rightsquigarrow T_2$ ISC (right).

Table S26: Harmonic frequencies ν (cm^{-1}) and NACMEs (a_0^{-1}) of $4CF_3$-MIA at the equilibrium geometries of the $^3(\pi_{H-1}\pi_L)$ and $^3(n_N\pi_L)$ states.

Mode	$\nu(S_2)$	S2S1	S2S0	$\nu(T_3)$	T3T2	T3T1	$\nu(T_2)$	T2T1
1	46.2	0.00425	0.00340	35.4	0.00738	0.00000	43.4	-0.15736
2	49.8	0.04400	-0.00739	53.0	0.01770	0.00000	44.7	-0.00405
3	61.7	-0.06621	-0.01393	69.8	0.04162	0.00000	61.1	-0.06935
4	98.3	0.02981	-0.00655	105.5	0.01780	0.00000	94.9	-0.05569
5	110.3	0.00000	0.00000	117.3	0.00000	0.00000	109.3	0.00000
6	153.1	0.06058	-0.01792	143.4	-0.01095	0.00800	144.6	-0.14350
7	163.7	0.01598	0.00101	173.3	-0.04986	0.00000	159.7	-0.08464
8	173.2	-0.10455	0.01908	210.2	0.08313	0.00000	165.2	-0.13449
9	230.4	0.00000	0.00000	218.0	0.04143	0.00000	231.6	0.00000
10	264.9	0.01804	-0.03312	241.0	0.00000	0.02713	260.3	0.03625
11	270.5	0.00000	0.00000	248.9	0.04224	0.00000	269.5	0.00000
12	293.8	-0.02192	0.01033	276.4	0.00000	0.00397	273.6	-0.13793
13	303.5	0.00000	0.00000	302.8	-0.04921	0.00000	303.9	0.00000
14	319.7	-0.06367	-0.00283	313.2	0.00000	-0.00865	313.4	0.18554
15	323.2	0.00000	0.00000	327.0	0.00000	-0.00567	324.0	0.00000
16	405.1	0.00000	0.00000	346.2	-0.00089	0.00000	405.4	0.00000
17	408.5	0.05330	0.00261	382.8	-0.05701	0.00000	405.9	-0.07847
18	420.0	0.00000	0.00000	403.5	0.00000	-0.04337	423.8	0.00000
19	474.3	-0.04340	0.00901	445.5	0.08702	0.00000	464.8	-0.19651
20	506.5	0.00000	0.00000	457.5	0.00000	0.04679	496.4	-0.20279
21	513.3	-0.06018	-0.01324	508.2	0.02799	0.00000	505.4	0.00000
22	533.4	-0.02892	-0.01777	512.4	0.00000	-0.02270	531.7	0.05925
23	536.8	0.00000	0.00000	537.3	0.00000	-0.00514	533.4	0.00000
24	541.2	0.00000	0.00000	553.6	0.06473	0.00000	540.8	0.00000
25	583.4	0.00000	0.00000	561.0	0.00000	0.00110	581.7	0.00000
26	599.2	0.15365	0.02137	606.2	0.00000	0.04120	584.3	0.31302
27	621.7	0.00000	0.00000	613.0	0.00000	-0.08284	620.8	0.00000
28	652.3	-0.16941	-0.01314	651.8	0.07836	0.00000	627.9	-0.20769
29	695.4	-0.00549	0.01397	693.0	0.00262	0.00000	679.2	-0.15044
30	706.6	0.00000	0.00000	703.6	0.00000	0.00143	693.2	-0.02535
31	711.9	0.05627	-0.04861	713.1	-0.03134	0.00000	704.1	0.00000
32	721.6	0.00000	0.00000	740.4	0.00000	-0.02882	721.6	0.00000
33	758.1	-0.02117	0.00926	771.1	-0.00757	0.00000	758.7	-0.03535
34	770.0	0.00000	0.00000	773.6	0.00000	-0.00008	769.6	0.00000
35	804.3	0.00000	0.00000	819.5	-0.16519	0.00000	810.9	0.00000
36	845.0	0.00633	-0.00102	821.5	0.00000	-0.04240	846.3	-0.01026
37	882.5	0.00000	0.00000	880.1	-0.01032	0.00000	881.3	0.00000
38	885.1	0.00000	0.00000	881.6	0.00000	-0.01940	898.4	0.00000

Mode	$\nu(S_2)$	S2S1	S2S0	$\nu(T_3)$	T3T2	T3T1	$\nu(T_2)$	T2T1
39	925.5	0.00992	-0.00417	908.6	0.00000	0.00937	928.7	0.01016
40	932.5	0.00000	0.00000	935.6	-0.00546	0.00000	932.5	0.00000
41	957.1	-0.00409	-0.00071	969.4	0.00000	-0.04303	957.8	0.00119
42	1028.0	0.00000	0.00000	1041.1	0.00000	-0.04137	1039.1	0.00000
43	1060.6	0.00000	0.00000	1046.6	0.00000	0.04395	1061.6	0.00000
44	1066.5	0.00000	0.00000	1084.4	0.00000	-0.00096	1065.2	0.00000
45	1133.5	0.00000	0.00000	1104.2	0.00000	0.00733	1136.0	0.00000
46	1145.4	-0.04127	-0.00024	1128.0	0.00077	0.00000	1145.5	0.06786
47	1150.6	0.00000	0.00000	1139.8	0.00000	0.07330	1148.3	0.01057
48	1152.9	0.01656	0.01402	1142.6	-0.04014	0.00000	1151.7	0.00000
49	1179.1	0.00000	0.00000	1177.7	0.00000	-0.00703	1175.0	0.00000
50	1190.7	0.00000	0.00000	1191.9	0.00000	-0.07523	1191.7	0.00000
51	1221.7	0.00000	0.00000	1237.2	0.00000	-0.03061	1215.8	0.00000
52	1273.8	0.00000	0.00000	1275.1	0.00000	-0.06963	1278.2	0.00000
53	1307.2	0.00000	0.00000	1296.0	0.00000	0.06789	1304.6	0.00000
54	1321.3	0.00000	0.00000	1314.4	0.00000	-0.00457	1323.7	0.00000
55	1331.4	0.00000	0.00000	1337.6	0.00000	0.10516	1326.7	0.00000
56	1357.6	0.00000	0.00000	1396.0	0.00000	0.10917	1360.4	0.00000
57	1389.1	0.00000	0.00000	1407.3	0.00000	-0.13356	1381.5	0.00000
58	1435.9	0.00000	0.00000	1435.6	0.00000	0.06367	1444.9	0.00000
59	1460.4	0.00000	0.00000	1444.4	0.00000	-0.00858	1460.7	0.00000
60	1479.2	0.00000	0.00000	1452.9	0.00000	0.03529	1472.8	0.00000
61	1487.0	0.00000	0.00000	1464.2	0.00000	-0.15558	1487.1	0.00000
62	1496.7	0.02629	-0.00395	1497.7	0.00000	0.01250	1498.7	-0.04407
63	1515.0	0.00000	0.00000	1513.1	0.02824	0.00000	1514.4	0.00000
64	1534.3	0.00000	0.00000	1524.4	0.00000	-0.01961	1533.6	0.00000
65	1579.1	0.00000	0.00000	1580.6	0.00000	-0.23425	1570.4	0.00000
66	1590.8	0.00000	0.00000	1596.4	0.00000	0.07828	1593.5	0.00000
67	1634.4	0.00000	0.00000	1649.8	0.00000	-0.12578	1636.6	0.00000
68	1778.4	0.00000	0.00000	1735.1	0.00000	0.03276	1777.5	0.00000
69	3047.1	0.00000	0.00000	3038.2	0.00000	0.01746	3048.5	0.00000
70	3109.0	0.00393	-0.00057	3100.0	0.00370	0.00000	3110.5	-0.00021
71	3165.0	0.00000	0.00000	3166.4	0.00000	-0.00413	3170.3	0.00000
72	3183.5	0.00000	0.00000	3196.6	0.00000	0.00971	3183.4	0.00000
73	3196.5	0.00000	0.00000	3208.4	0.00000	-0.00375	3196.3	0.00000
74	3208.2	0.00000	0.00000	3213.7	0.00000	-0.00469	3208.1	0.00000
75	3218.4	0.00000	0.00000	3221.6	0.00000	0.00103	3219.3	0.00000

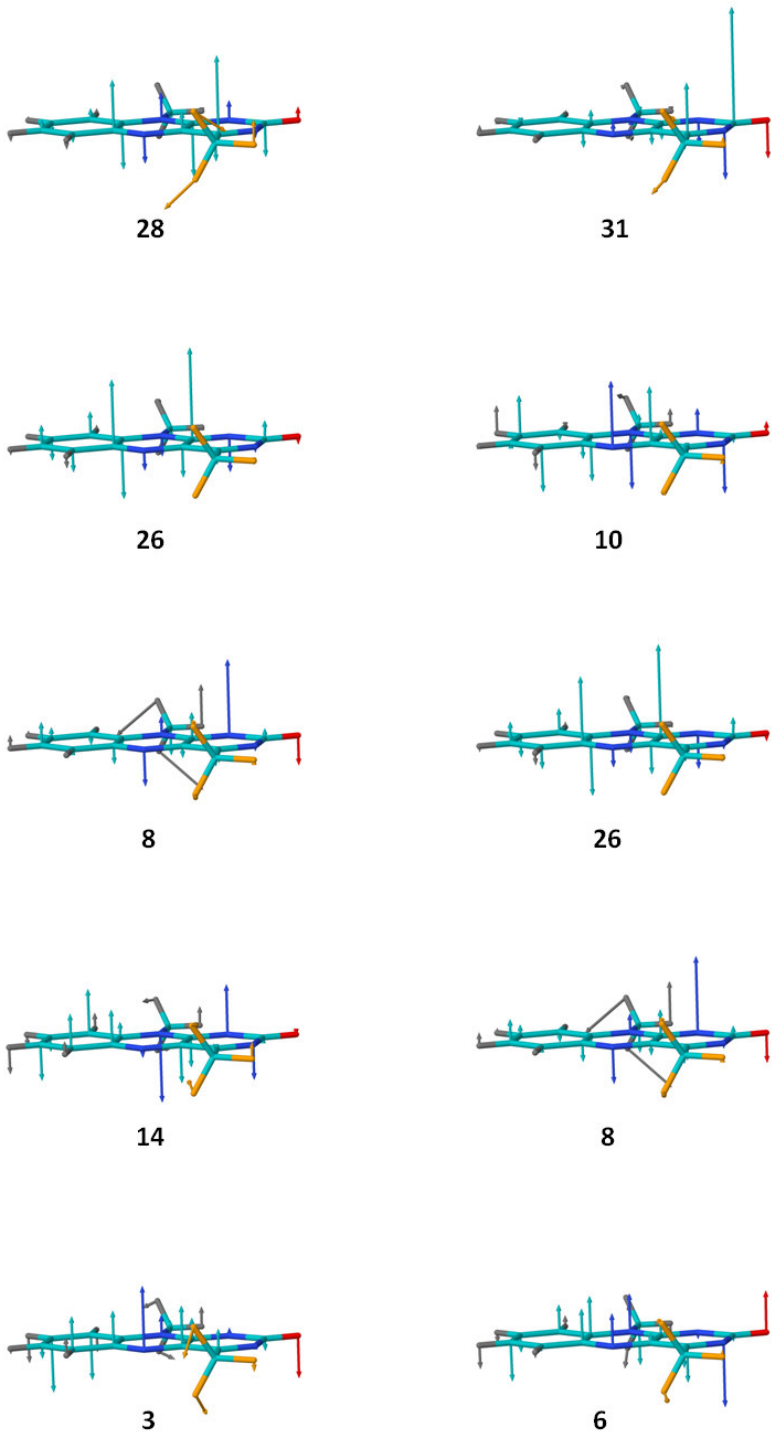

Figure S32: Illustration of the most effective promoting modes of $4CF_3$-MIA for $S_2 \rightsquigarrow S_1$ (left) and $S_2 \rightsquigarrow S_0$ IC (right).

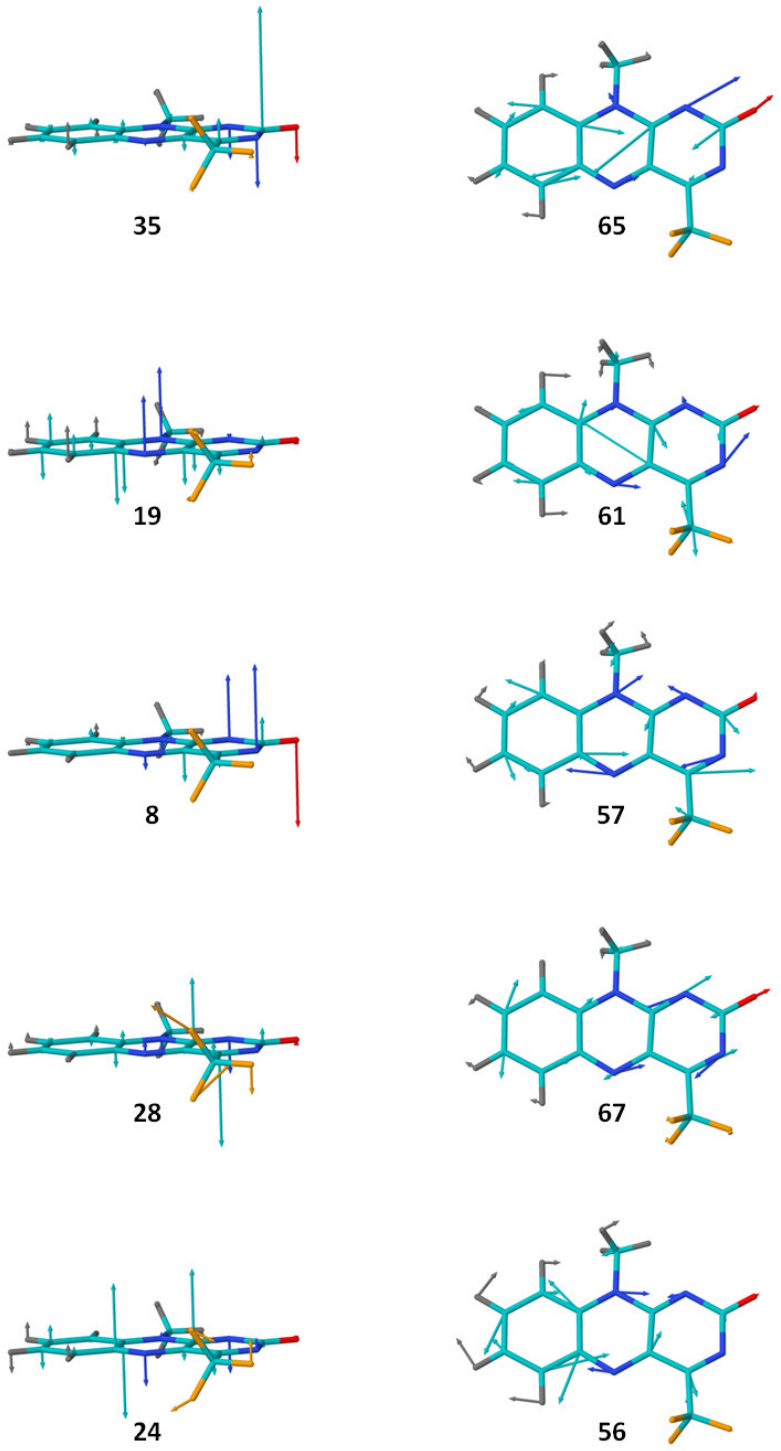

Figure S33: Illustration of the most effective promoting modes of 4CF_3-MIA for $T_3 \rightsquigarrow T_2$ (left) and $T_3 \rightsquigarrow T_1$ IC (right).

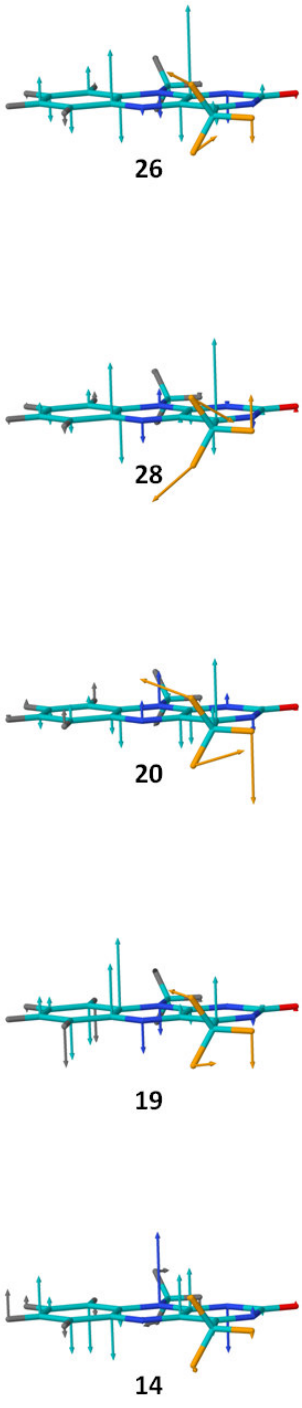

Figure S34: Illustration of the most effective promoting modes of $4CF_3$-MIA for $T_2 \rightsquigarrow T_1$ IC.

References

[1] A. Klamt and G. Schüürmann. COSMO: A New Approach to Dielectric Screening in Solvents with Explicit Expressions for the Screening Energy and its Gradient. *J. Chem. Soc., Perkin Trans. 2*, pages 799–805, 1993.

[2] M. Bracker, C. M. Marian, and M. Kleinschmidt. Internal conversion of singlet and triplet states employing numerical DFT/MRCI derivative couplings: Implementation, tests, and application to xanthone. *J. Chem. Phys.*, 155:014102, 2021.

[3] M. Bracker, F. Dinkelbach, O. Weingart, and M. Kleinschmidt. Impact of fluorination on the photophysics of the flavin chromophore: a quantum chemical perspective. *Phys. Chem. Chem. Phys.*, 21:9912–9923, 2019.

[4] A. Weigel, A. L. Dobryakov, M. Veiga, and J. L. Pérez Lustres. Photoinduced Processes in Riboflavin: Superposition of $\pi\pi^* - n\pi^*$ States by Vibronic Coupling, Transfer of Vibrational Coherence, and Population Dynamics under Solvent Control. *J. Phys. Chem. A*, 112:12054–12065, 2008.

[5] M. Insińska-Rak, E. Sikorska, J. R. Herance, J. L. Bourdelande, I. V. Khmelinskii, M. Kubicki, W. Prukała, I. F. Machado, A. Komasa, L. F. V. Ferreirae, and M. Sikorski. Spectroscopy and photophysics of flavin-related compounds: 3-benzyl-lumiflavin. *Photochem. Photobiol. Sci.*, 4:463–468, 2005.

[6] M. Sun, T. A. Moore, and P.-S. Song. Molecular Luminescence Studies of Flavins. I. The Excited States of Flavins. *J. Am. Chem. Soc.*, 94:1730–1740, 1972.

[7] S. Salzmann, J. Tatchen, and C. M. Marian. The photophysics of flavins: What makes the difference between gas phase and aqueous solution? *J. Photochem. Photobiol. A*, 198:221–231, 2008.

[8] M. Wang and C. J. Fritchie Jr. Geometry of the unperturbed flavin nucleus. the crystal structure of 10-methylisoalloxazine. *Acta Cryst.*, B29:2040–2045, 1973.

THE JOURNAL OF PHYSICAL CHEMISTRY A
A JOURNAL OF THE AMERICAN CHEMICAL SOCIETY

pubs.acs.org/JPCA Article

Large Inverted Singlet–Triplet Energy Gaps Are Not Always Favorable for Triplet Harvesting: Vibronic Coupling Drives the (Reverse) Intersystem Crossing in Heptazine Derivatives

Fabian Dinkelbach, Mario Bracker, Martin Kleinschmidt, and Christel M. Marian*

Cite This: J. Phys. Chem. A 2021, 125, 10044–10051 Read Online

ACCESS | Metrics & More | Article Recommendations | Supporting Information

ABSTRACT: Heptazine derivatives are promising dopants for electroluminescent devices. Recent studies raised the question whether heptazines exhibit a small regular or an inverted singlet–triplet (IST) gap. It was argued that the $S_1 \leftarrow T_1$ reverse intersystem crossing (RISC) is a downhill process in IST emitters and therefore does not require thermal activation, thus enabling efficient harvesting of triplet excitons. Rate constants were not determined in these studies. Modeling the excited-state properties of heptazine proves challenging because fluorescence and intersystem crossing (ISC) are symmetry-forbidden in first order. In this work, we present a comprehensive theoretical study of the photophysics of heptazine and its derivative HAP-3MF. The calculations of electronic excitation energies and vibronic coupling matrix elements have been conducted at the density functional theory/multireference configuration interaction (DFT/MRCI) level of theory. We have employed a finite difference approach to determine nonadiabatic couplings and derivatives of spin–orbit coupling and electric dipole transition matrix elements with respect to normal coordinate displacements. Kinetic constants for fluorescence, phosphorescence, internal conversion (IC), ISC, and RISC have been computed in the framework of a static approach. Radiative $S_1 \leftrightarrow S_0$ transitions borrow intensity mainly from optically bright E′ $\pi \rightarrow \pi^*$ states, while $S_1 \leftrightarrow T_1$ (R)ISC is mediated by E″ states of n $\rightarrow \pi^*$ character. Test calculations show that IST gaps as large as those reported in the literature are counterproductive and slow down the $S_1 \leftarrow T_1$ RISC process. Using the adiabatic DFT/MRCI singlet–triplet splitting of −0.02 eV, we find vibronically enhanced ISC and RISC to be fast in the heptazine core compound. Nevertheless, its photo- and electroluminescence quantum yields are predicted to be very low because $S_1 \rightarrow S_0$ IC efficiently quenches the luminescence. In contrast, fluorescence, IC, ISC, and RISC proceed at similar time scales in HAP-3MF.

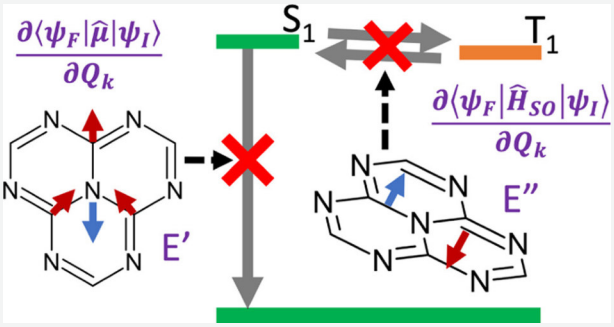

INTRODUCTION

Organic light-emitting diodes (OLEDs), which are based on thermally activated delayed fluorescence (TADF), require the singlet–triplet splitting ΔE_{ST} to be not too large versus thermal energy. If the spin–orbit coupling (SOC) strength is sufficient, $S_1 \leftarrow T_1$ reverse intersystem crossing (RISC) may compete against nonradiative deactivation of the triplet state at room temperature and triplet excitons can be harvested in addition to the singlet excitons.[1]

The energy difference ΔE_{ST} between a singlet and triplet-coupled open-shell configuration depends on the exchange interaction of the unpaired electrons. This interaction is small when the density distributions of the orbitals involved in the excitation do not overlap substantially. Typically, this requirement is fulfilled by charge-transfer (CT) states of donor–acceptor compounds whose unpaired electrons are spatially far apart. Very small singlet–triplet splittings can also be achieved in molecular systems where the electron density distributions in the half-occupied orbitals peak at different atoms and hence are disjunct. Such a situation occurs, for example, in electronically excited nonalternant conjugated hydrocarbons, with pentalene and azulene as well-known representatives.[2−4] One might therefore suppose that, in addition to donor–acceptor compounds, organic molecules with disjunct π-electron distributions in the highest occupied molecular orbital (HOMO) and the lowest unoccupied molecular orbital (LUMO) are well-suited dopants for TADF-based OLEDs. Unfortunately, the spatial overlap of the electron density distributions in the initial and final states plays a decisive role for the magnitudes of the electronic SOC and the electric dipole transition moment as well. The electronic couplings are

Received: October 21, 2021
Published: November 10, 2021

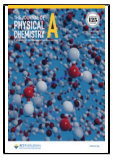

https://doi.org/10.1021/acs.jpca.1c09150
J. Phys. Chem. A 2021, 125, 10044−10051

typically very small in CT compounds, but vibronic interactions with nearby locally excited states can enhance (R)ISC and fluorescence rate constants appreciably.[5,6]

Very recently, triangle-shaped compounds with inverted singlet−triplet (IST) gap such as cycl[3.3.3]azine or heptazine (1,3,4,6,7,9,9*b*-heptaazaphenalene) and derivatives thereof were proposed as promising molecular OLED emitters for efficient triplet harvesting.[7−9] It was argued that the $S_1 \leftarrow T_1$ RISC is a downhill process in IST emitters due to the inversion of the energy gap and therefore does not require thermal activation. Indeed, heptazine-based π-conjugated materials such as HAP-3MF (2,5,8-tris(4-fluoro-3-methylphenyl)-1,3,4,6,7,9,9*b*-heptaazaphenalene) have been used as OLED emitters with high triplet harvesting capabilities.[10−15] Unfortunately, an experimental value for its ΔE_{ST} was not reported. One peculiarity of HAP-3MF is the spatial orientation of the peripheral substituents in relation to the heptazine core. In contrast to most organic CT emitters, their π-systems are not perpendicular or twisted but co-planar.

The frontier molecular orbitals of heptazine and HAP-3MF are π orbitals with spatially disjunct electron density distributions (Figure 1). Therefore, one might expect ΔE_{ST}

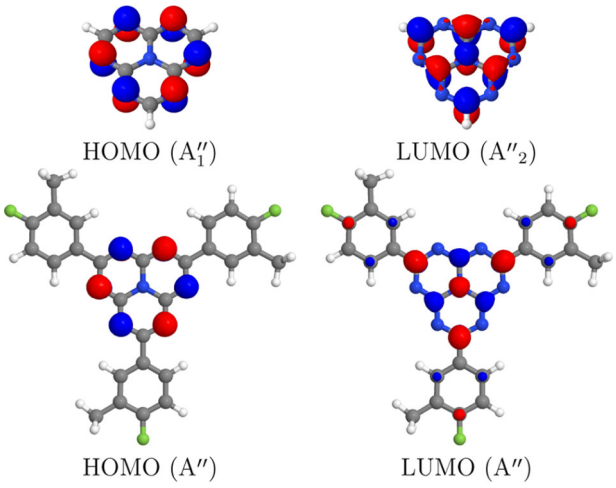

Figure 1. Frontier molecular orbitals of heptazine (top) and HAP-3MF (bottom).

in the HOMO → LUMO excited S_1 and T_1 states to be small, but not negative. The inversion of the regular order of open-shell singlet and triplet states with equal orbital occupation can be brought about by spin polarization.[2,16] In spin-restricted calculations, the effect only shows up in wavefunction-based excited-state correlation methods such as ADC(2), CC2, EOM-CCSD, or CASPT2, which explicitly include doubly excited configurations or if double-hybrid functionals are employed in time-dependent density functional theory (TDDFT).[7,8,17,18] The combined density functional theory (DFT) and multireference configuration interaction (MRCI) method,[19,20] utilized in this work, has this capability as well. In contrast, conventional TDDFT using a frequency-independent kernel yields a regular singlet−triplet energy splitting.[18]

Irrespective of the question whether the triangle-shaped π-chromophores are TADF or IST systems, a problem arises in the highly symmetric cyclazine, heptazine, and HAP-3MF systems because their S_1−T_1 spin−orbit and S_1−S_0 electric dipole couplings vanish due to point-group symmetry selection rules in Franck−Condon (FC) approximation. One way to lift the restrictions on the electric dipole coupling is the asymmetric substitution of the azaphenalene core, which was shown to result in small but non-negligible oscillator strengths for the $S_1 \rightarrow S_0$ emissions.[8] Still, the S_1−T_1 SOC and hence the (R)ISC processes remain forbidden in first order, even in those compounds. For ISC and RISC between a singlet and triplet state with equal orbital occupation to occur, the inclusion of spin−vibronic interactions is mandatory.[6] In the present work, we therefore move past the FC approximation and investigate the details of the radiative and nonradiative transitions by explicitly including vibronic interactions in our model, employing Herzberg−Teller (HT) expansions of the electric dipole couplings for absorption and emission, HT expansions of the spin−orbit coupling matrix elements (SOCMEs) for ISC and RISC, and nonadiabatic coupling matrix elements of the S_1 and S_0 potentials to get an estimate of the internal conversion (IC) rate constants.

COMPUTATIONAL METHODS

Ground- and excited-state geometries were optimized using the DFT and TDDFT methods, respectively, implemented in TURBOMOLE.[21] For triplets, the Tamm−Dancoff approximation (TDDFT-TDA)[22] was employed in addition. Throughout, the PBE0 density functional[23,24] was used in combination with a valence triple zeta basis set with polarization functions (TZVP).[25] Stationary points were verified to be minima by frequency analyses performed with GAUSSIAN.[26] To account for systematic errors, the harmonic frequencies were scaled by 0.9944.[27]

Note that TDDFT methods were employed solely for the optimization of the nuclear coordinates and the vibrational frequencies of the potentials. In these calculations, the full point-group symmetry, namely, D_{3h} (heptazine) and C_{3h} (HAP-3MF), was applied. The electronic excitation energies of 20 singlet and triplet states as well as all coupling matrix elements were based on MRCI wavefunctions utilizing the DFT/MRCI method[19,20] in conjunction with the R2016 Hamiltonian.[28] For heptazine, we used the standard parameter set with a selection threshold of 1.0 E_h and an initial active space of double excitations of 12 electrons in 10 orbitals. The short parameter set paired with a selection threshold of 0.8 E_h and an initial active space of single excitations of 20 electrons in 20 orbitals was used for HAP-3MF. Due to technical reasons, the DFT/MRCI calculations were performed in the Abelian subgroups C_{2v} and C_s.

The DFT/MRCI wavefunctions were employed to compute SOCMEs with the spin−orbit coupling kit (SPOCK).[29,30] SPOCK uses an effective one-electron spin−orbit mean-field Hamiltonian[31] in conjunction with the atomic mean-field integral (AMFI)[32] approximation. Phosphorescence rate constants were computed at the level of quasi-degenerate perturbation theory.

Vibronic contributions to the ISC ($\hat{O} = \hat{H}_{SO}$) and electric dipole transitions ($\hat{O} = \hat{\mu}$) between an initial molecular state Ψ_{Ia} and a set of final molecular states Ψ_{Fb} were treated within the HT approximation,[33] where the coupling matrix element is expanded about a reference point (Q_0) as a function of the normal mode coordinates Q_k.

https://doi.org/10.1021/acs.jpca.1c09150
J. Phys. Chem. A 2021, 125, 10044−10051

$$\sum_b \langle \Psi_{Fb}|\hat{O}|\Psi_{Ia}\rangle = \langle \psi_F|\hat{O}|\psi_I\rangle\Big|_{Q_0} \sum_b \langle v_{Fb}|v_{Ia}\rangle + \sum_k^N \frac{\partial\langle \psi_F|\hat{O}|\psi_I\rangle}{\partial Q_k}\Big|_{Q_0} \sum_b \langle v_{Fb}|Q_k|v_{Ia}\rangle + \ldots \quad (1)$$

Herein, ψ_I and ψ_F denote the electronic parts and v_{Ia} and v_{Fb} denote the vibrational parts of the molecular wavefunctions. For IC, only the linear coupling terms of the nonadiabatic corrections

$$\sum_k^N \langle \Psi_{Fb}|\frac{\partial^2}{\partial Q_k^2}|\Psi_{Ia}\rangle = \sum_k^N \langle \psi_F|\frac{\partial}{\partial Q_k}|\psi_I\rangle|_{Q_0}\langle v_{Fb}|\frac{\partial}{\partial Q_k}|v_{Ia}\rangle + \ldots \quad (2)$$

were taken into account. The gradients of the matrix elements and the derivative couplings were obtained by distorting the nuclear framework along dimensionless normal modes using a step size of 0.5 units, utilizing averaged two-point finite difference techniques.[34,35] The phases of these gradients are arbitrary and need to be aligned properly by relating the phases of the molecular orbitals and of the DFT/MRCI wavefunctions to a reference calculation as performed in earlier work.[36] Evaluation of nonradiative rate constants in the energy domain according to

$$k_{nr} = \frac{2\pi}{\hbar}\sum_b |\langle \Psi_{Fb}|\hat{O}|\Psi_{Ia}\rangle|^2 \delta(E_{Fb} - E_{Ia}) \quad (3)$$

is not practicable for molecules as large as those investigated here because the density of vibrational states is too high. A way to avoid the explicit summation over all final vibrational states b is to transform Fermi's golden rule into the Heisenberg picture. To this end, the Dirac δ function is expressed as the Fourier integral

$$\delta(E_{Fb} - E_{Ia}) = \frac{1}{2\pi}\int_{-\infty}^{+\infty} e^{i(E_{Fb}-E_{Ia})/\hbar}\mathrm{d}t \quad (4)$$

In the harmonic oscillator approximation, analytical expressions for the generating functions of ISC and IC rate transitions including a Duschinsky transformation of the respective normal coordinates can be derived.[35,37−42] In the VIBES program, correlation functions were implemented, which use the normal coordinates of the initial state as a common basis for evaluating the FC factors and the nuclear coupling terms.[35,40−42] ISC, RISC, and IC rate constants are then obtained by numerically integrating the resulting correlation functions in the time domain. A further advantage of the Fourier transform approach is that it is easily extended to include temperature effects by assuming a Boltzmann population of the vibrational levels in the initial electronic state.[35,41,42] To speed up the numerical integration, a Gaussian damping function is introduced. The width of the damping function, the integration interval, and the number of grid points are technical parameters that have to be chosen with great care. For ISC and RISC rate constants, we used an integration time of 25 ps, a grid of 2^{16} points, and a damping of 1 cm^{-1} full width at half-maximum (FWHM). Because of the higher fluctuation of the correlation function of the $S_1 \rightarrow S_0$ IC, the number of grid points was increased to 2^{18} (heptazine) and 2^{19} (HAP-3MF) in the evaluation of IC rate constants. To make sure that the calculated rate constants are converged, the width of the damping function was varied between 0.1 and 10 cm^{-1}. For the weaker damping functions, the integration parameters had to be adapted. Technical details of these calculations are given in the Supporting Information, where also the shapes of the correlation functions are displayed. Vibrationally resolved spectra were obtained with the VIBES[40,41] program at 300 K with an integration time of 300 fs, a grid of 2^{14} points, and a Gaussian damping function of 50 cm^{-1} FWHM. Additional calculations were performed for stronger damping functions with 100 and 200 cm^{-1} FWHM. HT fluorescence rate constants were computed by integrating the HT spectrum $I^{HT}(\omega)$.[43,44] Since the spectral density $S(\omega)$ is not properly normalized in the VIBES program, it has to be renormalized making use of the closure relation for the FC spectral density $S^{FC}(\omega)$.

$$k_F^{HT} = \int I^{HT}(\omega)\mathrm{d}\omega = \frac{4}{3\hbar c_0^3}\frac{\int \omega^3 S^{HT}(\omega)\mathrm{d}\omega}{\int S^{FC}(\omega)\mathrm{d}\omega} \quad (5)$$

RESULTS AND DISCUSSION

We find heptazine and HAP-3MF to be D_{3h} and C_{3h} symmetric, respectively, in their electronic ground states. TDDFT lowers the symmetry in the first excited singlet and triplet states. At this level of theory, the D_{3h} and C_{3h} structures represent first-order transition states where the minima are reached by lifting the central nitrogen atom out of the heptazine core plane, thus breaking the horizontal mirror plane in the process. In contrast, scans along the imaginary frequency mode at the DFT/MRCI level show minima at the higher-symmetry points. Therefore, we will concentrate on the D_{3h}- and C_{3h}-symmetric structures in our analysis. The frequency of the imaginary mode was approximated by its harmonic force constant fitted to the curvature of the outer branches of a TDDFT scan along the normal mode. The fits yield frequencies of 131 cm^{-1} for the S_1 state and 178 cm^{-1} for the T_1 state in heptazine. For HAP-3MF, we obtained 232 and 253 cm^{-1}, respectively.

Electronic excitation energies of heptazine and HAP-3MF and the oscillator strengths of the electric dipole-allowed transitions at the ground-state and first excited-state geometries are given in Tables S1−S6, respectively. Difference densities illustrating the characters of the most important excited states are displayed in Figures 2 and S1−S6. They reveal that the S_1 and T_1 states originate from $\pi \rightarrow \pi^*$ excitations shifting electron density from the nitrogen atoms on the rim of the heptazine ring to the carbon atoms and the central nitrogen atom. In HAP-3MF, additionally, small CT contributions are visible, moving electron density from the heptazine core to π orbitals on the phenyl rings. This is remarkable because heptazine is typically considered an electron acceptor, not a donor. Substantial CT from the peripheral substituents to the heptazine core is observed in the optically very bright E′-symmetric S_2 state, which lies about 0.9 eV above the S_1 state in HAP-3MF and has the proper symmetry to lend intensity to the electric dipole-forbidden S_1-S_0 transitions via vibronic coupling.

In our DFT/MRCI calculations, the S_1 and T_1 states (A_2') of heptazine are located vertically at 2.59 and 2.60 eV, respectively, at the D_{3h}-symmetric ground-state geometry, corroborating the inversion of the typical singlet−triplet order reported by Sobolewski, Domcke, and co-workers[9,17] in

https://doi.org/10.1021/acs.jpca.1c09150
J. Phys. Chem. A 2021, 125, 10044−10051

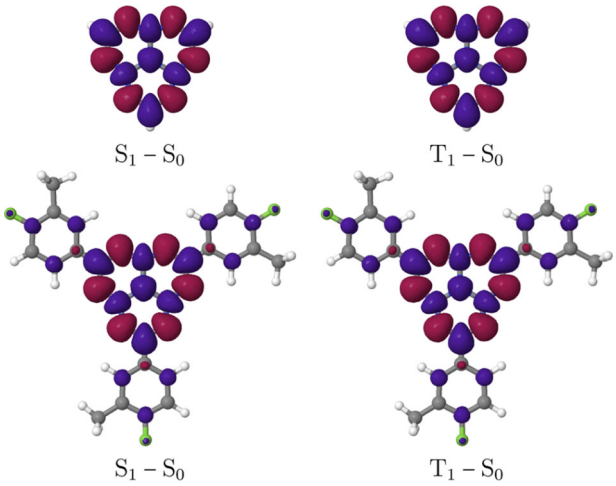

Figure 2. Differences of the electron density distributions in the S_1 and T_1 states of heptazine (top) and HAP-3MF (bottom) with regard to the density distribution in the respective S_0 states. Areas losing electron density upon excitation from the electronic ground state are shown in dark red, and areas gaining electron density are shown in violet.

principle. The highest-intensity peaks in the absorption spectrum of heptazine (Figure 3) correspond to E′-symmetric $\pi \rightarrow \pi^*$ transitions to the S_4 state at 4.32 eV (287 nm) and to the S_{10} state at 5.73 eV (216 nm). Besides the bright $\pi \rightarrow \pi^*$ states, we find dark n $\rightarrow \pi^*$ states, which are of particular interest for vibronically enhanced ISC. In heptazine, the lowest n $\rightarrow \pi^*$ states are the A_1''-symmetric T_3 and S_2 states, located at 3.76 and 3.86 eV, respectively. Their leading configuration is the HOMO-1 → LUMO excitation. The HOMO-2 → LUMO and HOMO-3 → LUMO excitations together form the lowest E″-symmetric triplet (T_4) and singlet (S_3) states, which are essential promotors of the symmetry-forbidden $S_1 \leftrightarrow T_1$ ISC and RISC as will become apparent below. Interactions of the n orbitals with the peripheral ligands lead to a blue shift of the corresponding n $\rightarrow \pi^*$ states by about 0.20 eV in HAP-3MF in comparison to heptazine. Comparing the difference densities of the bright states in heptazine and HAP-3MF reveals that the S_4 state in heptazine corresponds to the S_8 state in HAP-3MF, which is slightly red-shifted due to the extension of the π system. Additional $\pi \rightarrow \pi^*$ CT states appear in the low-energy region of the HAP-3MF spectrum, of which the $S_2 \leftarrow S_0$ transition is the brightest. Compared to the experimental UV–vis spectrum with maximum at 331 nm in toluene solution,[13] the calculations underestimate the excitation energy of the first intense CT band by about 0.15 eV, whereas the position of the first very weak absorption band matches its experimental counterpart perfectly (Figure 3). Due to its low oscillator strength, Li et al. assigned an n $\rightarrow \pi^*$ excitation to this $S_1 \leftarrow S_0$ transition, at variance with our results. We find the S_1 and T_1 states (A′) to have $\pi \rightarrow \pi^*$ character, in accordance with the results of the ADC(2) calculations by Sobolewski and Domcke.[9] Symmetry selection rules forbid absorption into the S_1 state in FC approximation, but vibrations of E′ ($A_2' \otimes E'_{vib} = E'[x, y]$) and A_1'' ($A_2' \otimes A''_{1,vib} = A_2''[z]$) can break the symmetry constraints and render the vibronic transition weakly allowed. The gradients of the dipole transition moments (Table S16) show that mainly E′ normal modes in the wavenumber range between approximately 1400 and 1700 cm^{-1} drive the absorption by borrowing intensity from the bright E′ states. The vibrational progression in the HT absorption spectrum is in good agreement with the experimentally resolved vibrational fine structure of the $S_1 \leftarrow S_0$ transition, thus lending support to our computational model.

Geometry relaxation in the excited states of heptazine and HAP-3MF entails only small changes in the vertical excitation energies, due to the strong geometric constraints imposed by the annelated rings. We find the S_1 and T_1 states adiabatically at 2.50 and 2.52 eV, respectively, in heptazine and at 2.66 and 2.65 eV, respectively, in HAP-3MF. Thus, the small energy gap and the singlet–triplet order found at the ground-state nuclear arrangement are maintained upon geometry relaxation. Zero-point vibrational energy (ZPVE) corrections change the picture and restore the typical singlet–triplet order of the S_1 and T_1 states. In our computational setup, the first vibrational level of the S_1 state of heptazine is located 0.06 eV above the vibrational ground state of the T_1 state in the D_{3h} symmetry. A similar energy separation of the zero vibrational levels (0.07 eV) of the S_1 and T_1 potentials is obtained for HAP-3MF in the C_{3h} symmetry. As we will see below, the question whether heptazines are IST or TADF systems plays a minor role for the interconversion of their singlet and triplet populations.

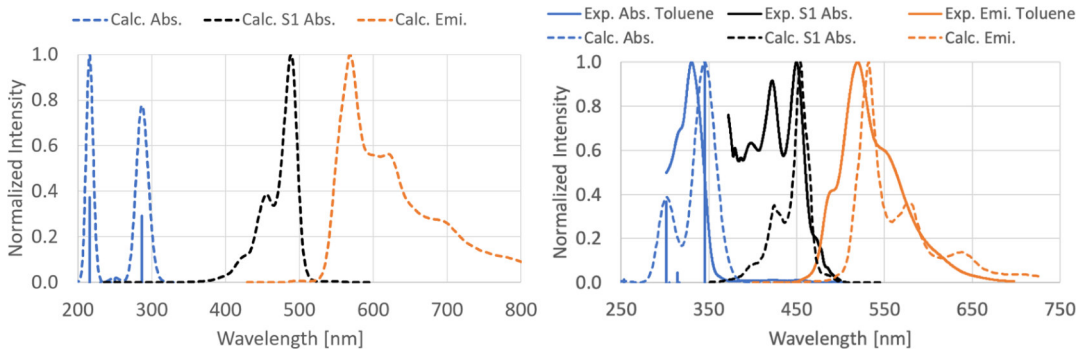

Figure 3. Absorption and emission spectra of heptazine (left) and HAP-3MF (right). Vibronic spectra were computed only for the S_1 absorption (black) and emission (orange) transitions. Their HT spectra are not drawn to scale but were normalized separately. The spectral lines of the electric dipole-allowed electronic transitions in the shorter-wavelength regime (blue) were broadened with Gaussian functions of 1000 cm^{-1} FWHM. Digitized experimental spectra were read from Figure 2 of an article by Li et al.,[13] where the S_1 absorption intensity was magnified by a factor of 100. The measurements were conducted in toluene by these authors, while our computational results are obtained in vacuum.

https://doi.org/10.1021/acs.jpca.1c09150
J. Phys. Chem. A 2021, 125, 10044–10051

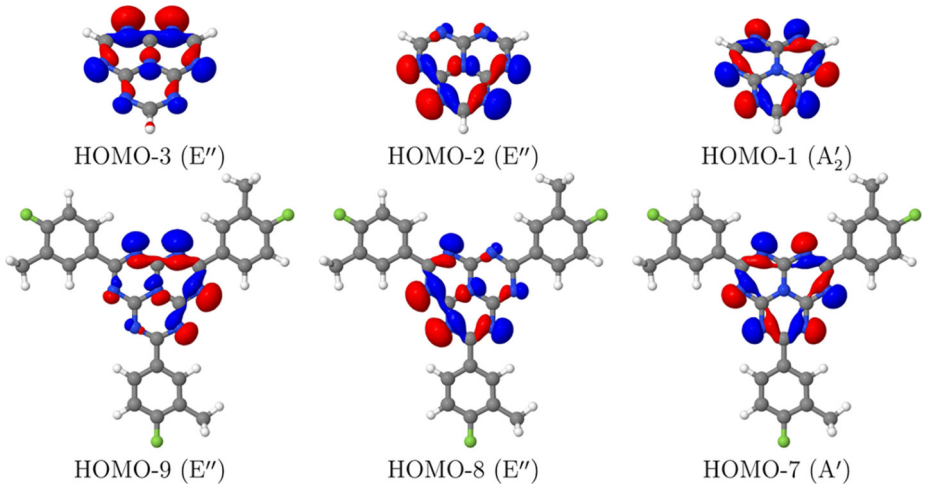

Figure 4. Nonbonding lone-pair molecular orbitals of heptazine (top) and HAP-3MF (bottom).

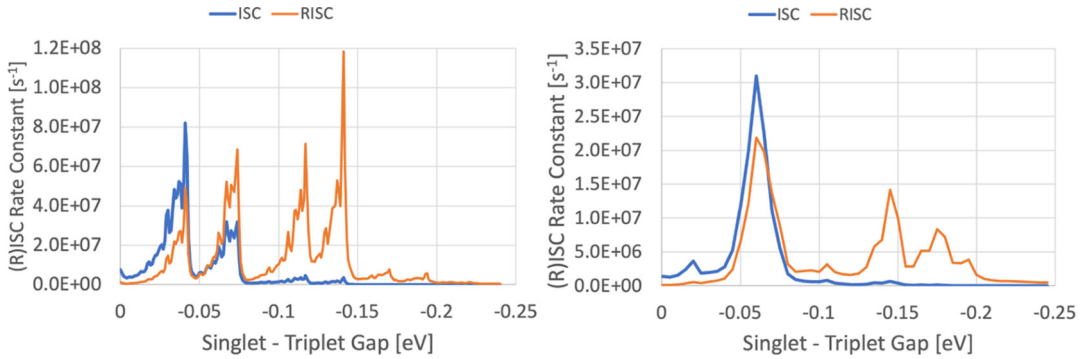

Figure 5. Rate constants for $S_1 \leftrightarrow T_1$ (R)ISC in heptazine (left) and HAP-3MF (right) computed in HT approximation for various singlet−triplet energy gaps ΔE_{ST}. The scan of the energy splitting was performed with a resolution of 0.001 eV for heptazine and of 0.005 eV for HAP-3MF. A negative ΔE_{ST} value indicates that the triplet state is located adiabatically above the singlet state. For 0−0 energies, ZPVE energy corrections (+0.08 eV for heptazine, +0.06 eV for HAP-3MF) have to be added.

Application of heptazine and its derivatives in OLEDs requires an efficient luminescence of the emitter in conjunction with fast (R)ISC to harvest all possible singlet and triplet excitons. However, direct ISC and RISC are forbidden by symmetry selection rules. S_1 and T_1 exhibit A_2' spatial symmetry in heptazine, and there is no component of the angular momentum operator coupling these states, as $\hat{\mathcal{L}}_z$ is A_2' symmetric and $\hat{\mathcal{L}}_x$ and $\hat{\mathcal{L}}_y$ transform according to the E″ irreducible representation. For ISC to be fast, El-Sayed's rules[6,45] need to be satisfied, which requires states to be singly excited with respect to each other and to involve a change of orbital type. Both requirements appear to be fulfilled for states of n → π^* type. HOMO, HOMO-1, HOMO-2, and HOMO-3 are MOs with large contributions from 2p atomic orbitals on the outer ring of N atoms. While HOMO is a linear combination of $2p_z$ orbitals perpendicular to the molecular plane (Figure 1), HOMO-1, HOMO-2, and HOMO-3 are linear combinations of in-plane $2p_x$ and $2p_y$ orbitals on the same centers (Figure 4). In the local one-particle picture underlying El-Sayed's rule, $2p_z$ and $2p_x$ or $2p_y$ can strongly interact via the angular momentum operators contained in $\hat{\mathcal{H}}_{SO}$. A closer look at the character table of D_{3h} reveals, however, that the local contributions to the orbital angular momentum coupling matrix element of HOMO-1 and HOMO cancel each other because HOMO is of A_1'' symmetry, HOMO-1 transforms according to A_2' and their direct product representation $A_1'' \otimes A_2' = A_2''$ does neither contain A_2' nor E″, which are the proper irreducible representations for $\hat{\mathcal{L}}$. In contrast, the orbital angular momentum coupling between HOMO and HOMO-2 or HOMO-3 is symmetry-allowed, and so are $\langle T_4|\hat{\mathcal{H}}_{SO}|S_1\rangle$, $\langle T_4|\hat{\mathcal{H}}_{SO}|T_1\rangle$, and $\langle S_3|\hat{\mathcal{H}}_{SO}|T_1\rangle$.

Vibrational SOC is therefore solely promoted by E″-symmetric modes in heptazine (Tables S9 and S10). For HAP-3MF, the mutual SOC between S_1 and T_1 is symmetry-allowed in principle but vanishes at the minima. Irrespective of the molecular point-group symmetry, SOCMEs between orbitally nondegenerate singlet and triplet states with equal orbital occupations are zero because the angular momentum operator has purely imaginary cartesian components.[46] Non-vanishing SOC between them can only be brought about by multiconfiguration effects or by spin−vibronic interactions. In HAP-3MF, the HOMO-7 → LUMO excitation gives rise to the A″-symmetric S_3 and T_7 states, which do not interact with S_1 and T_1 via SOC, whereas the E″-symmetric S_6 and T_8 states, dominated by the HOMO-8 → LUMO and HOMO-9 → LUMO excitations, have the appropriate spatial symmetry. It is therefore not surprising that the largest SOCME gradients arise along E″-symmetric distortions of the nuclear framework

https://doi.org/10.1021/acs.jpca.1c09150
J. Phys. Chem. A 2021, 125, 10044−10051

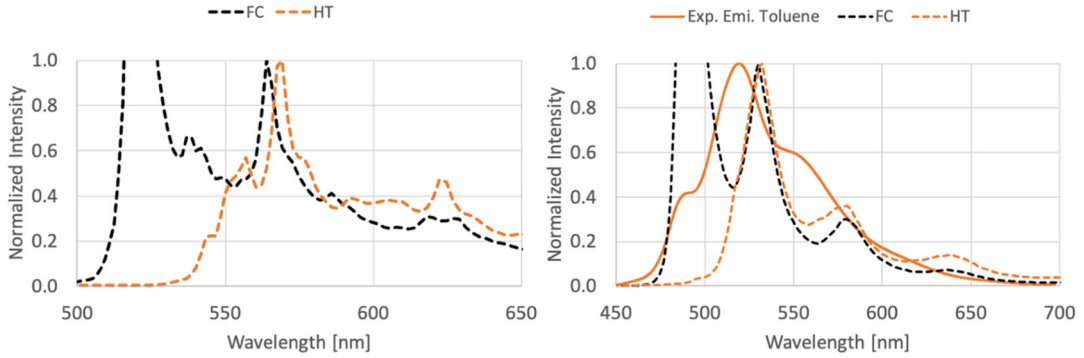

Figure 6. Overlay of the computed HT emission spectra of heptazine (left) and HAP-3MF (right) with the corresponding FC spectral density. Note that the emission is forbidden in FC approximation in full point-group symmetry, i.e., D_{3h} (heptazine) and C_{3h} (HAP-3MF). For HAP-3MF, the experimental emission spectrum, recorded by Li et al.[13] in toluene solution, is depicted as well.

(Tables S18 and S19). We obtain ISC and RISC rate constants of $k_{ISC} = 1 \times 10^7$ s^{-1} and $k_{RISC} = 3 \times 10^6$ s^{-1} for heptazine at 300 K. Somewhat smaller but still sizeable rate constants of $k_{ISC} = 7 \times 10^6$ s^{-1} and $k_{RISC} = 3 \times 10^5$ s^{-1} are determined for HAP-3MF at 300 K if our computed S_1−T_1 energy separation is employed.

The ISC and RISC rate constants do hardly change if the technical parameters for their evaluation are varied (Tables S21 and S22), but they are sensitive with respect to the energy separation between the initial and final states. Because the magnitude of our adiabatic DFT/MRCI singlet−triplet gap (−0.02 eV) differs markedly from values reported in various other theoretical works,[8,9,17,18] we recomputed the HT R(ISC) rate constants for ΔE_{ST} values ranging from 0 to −0.24 eV. The results of these scans are displayed in Figure 5. The ISC and RISC transition probabilities peak at several maxima indicating energies, where the S_1 and T_1 vibrational wavefunctions optimally overlap. The scans also show that a large negative singlet−triplet energy gap is not necessarily favorable for a spin population transfer between the T_1 and S_1 states of heptazine: The constants decrease to $k_{ISC} = 3 \times 10^2$ s^{-1} and $k_{RISC} = 5 \times 10^5$ s^{-1} if the ADC(2) value (−0.24 eV), reported by Sobolewski and Domcke,[9] is employed. In HAP-3MF, the optimum for the interconversion of singlet and triplet population lies at $\Delta E_{ST} = -0.06$ eV.

Emission from the S_1 state follows the same selection rules as the absorption and is therefore enhanced vibronically by the same normal modes. The 0−0 transition is absent in the computed HT spectra of heptazine and HAP-3MF (Figure 6) as it should be the case for molecules with a first-order symmetry-forbidden dipole transition in harmonic oscillator approximation. Obviously, HAP-3MF does not fully comply with the restrictions of the harmonic oscillator model in reality so that a 0−0 transition becomes weakly allowed and is visible as a shoulder in the experimental spectra. Moreover, the experimental peaks are broader than the computed ones and the peak positions are slightly shifted, but otherwise, the vibrational progressions are very similar. They can be assigned to totally symmetric C−N bond stretching modes of the heptazine core.

With a rate constant of $k_F = 3 \times 10^5$ s^{-1}, fluorescence is 1 to 2 orders of magnitudes slower in heptazine than ISC and RISC and 3 orders of magnitude slower than IC to the ground state (Table 1). We therefore expect the photo- and electroluminescence quantum yields to be very low for the heptazine core compound. IC is mainly driven by the A_2'-symmetric

Table 1. Rate Constants of Radiative and Nonradiative Transitions in Heptazine and Hap-3MF Calculated Including Vibronic Interactions at 300 K

rate constant [s^{-1}]	process	heptazine	HAP-3MF
k_F	$S_1 \rightarrow S_0$	3×10^5	9×10^5
k_P	$T_1 \rightarrow S_0$	2×10^0	
k_{IC}	$S_1 \rightarrow S_0$	3×10^8	9×10^5
k_{ISC}	$S_1 \rightarrow T_1$	1×10^7	7×10^6
k_{RISC}	$S_1 \leftarrow T_1$	3×10^6	3×10^5

coupling mode 39 (Figure S9), which entails torsional motions about the central C_3 axis. The $S_1 \rightarrow S_0$ IC rate constant, listed in Table 1, should be considered only a rough estimate: Due to the large energy splitting of the S_1 and S_0 states, the harmonic oscillator model underlying the calculations is far from being ideal. Vibronic interactions also enhance the T_1 phosphorescence probability. However, with a rate constant of about $k_P = 2$ s^{-1} in HT approximation, the process is too slow to compete against other triplet deactivation channels such as RISC or triplet−triplet annihilation.

The ratios of the radiative and nonradiative decay constants are more favorable in the case of HAP-3MF. Replacement of the heptazine hydrogen atoms by fluorinated toluene substituents appears to slow down the nonradiative deactivation of the first excited singlet state to the electronic ground state. IC is promoted by A′-symmetric torsion modes in HAP-3MF, the most dominant coupling mode being mode 135 with a vibrational frequency of 1598 cm^{-1} (Figure S14). According to our calculations, IC and fluorescence proceed approximately at the same time scale at 300 K (Table 1). The rate-determining process for the prompt fluorescence decay following photoexcitation appears to be the ISC to the T_1 state. Our computed fluorescence rate constant of $k_F = 9 \times 10^5$ s^{-1} is in good agreement with the findings by Li et al.,[13] who estimated an emissive rate constant of 1×10^6 s^{-1} for this compound based on a measured fluorescence lifetime of 252 ns and a photoluminescence quantum yield of 0.26 in toluene at room temperature. RISC is somewhat slower than ISC and fluorescence ($k_{RISC} = 10^5$ s^{-1}), suggesting both prompt and delayed fluorescence to take place, as seen by Li et al.[13] who observed a delayed component in addition to the prompt fluorescence in oxygen-free toluene and in solid films of HAP-3MF. The computed rate constants cannot explain the experimentally determined ratios of delayed vs prompt and luminescence components following photoexcitation (4%) and

https://doi.org/10.1021/acs.jpca.1c09150
J. Phys. Chem. A 2021, 125, 10044−10051

electric excitation (71%) in 6 wt %-doped DPEPO film, however.

CONCLUSIONS

Summarizing the discussion of the excited-state processes (Figure 7), we find that ISC and RISC allow efficient singlet−triplet interconversion in heptazine and HAP-3MF. These processes are solely enabled by vibronic coupling, where E″-symmetric modes enhance ISC and RISC transitions between the S_1 and T_1 states while vibrations of the E′ symmetry boost the radiative transitions. However, fluorescence cannot compete against nonradiative deactivation of the S_1 state by IC in the parent heptazine compound. We therefore expect its electroluminescence quantum yield to be very small, despite the fact that heptazine appears to be an IST system with slightly negative ΔE_{ST}. ZPVE corrections are found to restore the regular singlet−triplet energetic order in this compound. A regular singlet−triplet energy separation does not impair the potential of heptazine derivatives as OLED emitters. On the contrary, test calculations show that IST gaps as large as the ones reported in recent quantum chemical works[8,9,17,18] substantially reduce the rate constant of a $T_1 \rightarrow S_1$ spin−vibronic transition in heptazine.

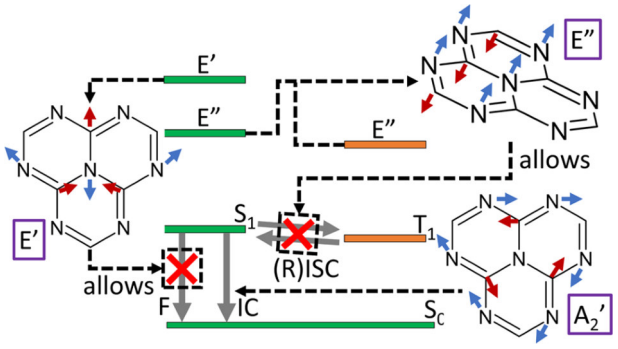

Figure 7. Schematic of the fluorescence, IC, and (R)ISC processes in heptazine. Modes of E′ symmetry enable intensity borrowing from bright E′ states and mediate fluorescence, while E″-symmetric modes mix E″ states of n → π^* character into the S_1 and T_1 wavefunctions. IC is promoted by A_2' normal modes.

Due to the heavier peripheral substituents, the IC process is slowed down in HAP-3MF in comparison to the parent heptazine molecule so that light emission occurs with a higher probability and singlet as well as triplet excitons can be harvested efficiently in electroluminescent devices. For HAP-3MF, the DFT/MRCI picture of a TADF emitter with nearly degenerate S_1 and T_1 states and vibronically enhanced ISC, RISC, and electric dipole transitions is in good agreement with the experimental observations,[13] where delayed fluorescence on the microsecond time scale is seen in oxygen-free toluene solutions and in solid HAP-3MF films.

ASSOCIATED CONTENT

Supporting Information

The Supporting Information is available free of charge at https://pubs.acs.org/doi/10.1021/acs.jpca.1c09150.

Vertical and adiabatic excitation energies of heptazine and HAP-3MF utilizing the DFT/MRCI method; difference densities of the most important electronic states; pictures of most relevant vibrational coupling modes; gradients and derivative couplings along normal mode displacements for vibronic absorption, fluorescence, IC, ISC, and RISC; correlation functions and rate constants for varying technical parameters of the VIBES calculations; FC and HT spectra for different damping functions (PDF)

AUTHOR INFORMATION

Corresponding Author

Christel M. Marian − *Institute of Theoretical and Computational Chemistry, Heinrich-Heine-University Düsseldorf, 40225 Düsseldorf, Germany;* orcid.org/0000-0001-7148-0900; Phone: +49 (0)211 8113210; Email: christel.marian@hhu.de

Authors

Fabian Dinkelbach − *Institute of Theoretical and Computational Chemistry, Heinrich-Heine-University Düsseldorf, 40225 Düsseldorf, Germany*

Mario Bracker − *Institute of Theoretical and Computational Chemistry, Heinrich-Heine-University Düsseldorf, 40225 Düsseldorf, Germany*

Martin Kleinschmidt − *Institute of Theoretical and Computational Chemistry, Heinrich-Heine-University Düsseldorf, 40225 Düsseldorf, Germany*

Complete contact information is available at: https://pubs.acs.org/10.1021/acs.jpca.1c09150

Notes

The authors declare no competing financial interest.

ACKNOWLEDGMENTS

This research was funded by the Deutsche Forschungsgemeinschaft (DFG, German Research Foundation)—396890929/GRK 2482. The authors thank Prof. Wolfgang Domcke for bringing the heptazine singlet−triplet inversion to their attention.

REFERENCES

(1) Yersin, H. *Highly Efficient OLEDs, Materials Based on Thermally Activated Delayed Fluorescence*; Wiley-VCH, 2018.

(2) Koseki, S.; Nakajima, T.; Toyota, A. Violation of Hund's multiplicity rule in the electronically excited states of conjugated hydrocarbons. *Can. J. Chem.* **1985**, *63*, 1572−1579.

(3) Klan, P.; Wirz, J. *Photochemistry of Organic Compounds: From Concepts to Practice*, John Wiley & Sons, Weinheim, 2009; p 151.

(4) Vosskötter, S.; Konieczny, P.; Marian, C. M.; Weinkauf, R. Towards an understanding of the singlet−triplet splittings in conjugated hydrocarbons: azulene investigated by anion photoelectron spectroscopy and theoretical calculations. *Phys. Chem. Chem. Phys.* **2015**, *17*, 23573−23581.

(5) Penfold, T. J.; Gindensperger, E.; Daniel, C.; Marian, C. M. Spin-Vibronic Mechanism for Intersystem Crossing. *Chem. Rev.* **2018**, *118*, 6975−7025.

(6) Marian, C. M. Understanding and Controlling Intersystem Crossing in Molecules. *Annu. Rev. Phys. Chem.* **2021**, *72*, 616−640.

(7) Sanz-Rodrigo, J.; Ricci, G.; Olivier, Y.; Sancho-García, J. C. Negative Singlet−Triplet Excitation Energy Gap in Triangle-Shaped Molecular Emitters for Efficient Triplet Harvesting. *J. Phys. Chem. A* **2021**, *125*, 513−522.

(8) Pollice, R.; Friederich, P.; Lavigne, C.; dos Passos Gomes, G.; Aspuru-Guzik, A. Organic molecules with inverted gaps between first excited singlet and triplet states and appreciable fluorescence rates. *Matter* **2021**, *4*, 1654−1682.

https://doi.org/10.1021/acs.jpca.1c09150
J. Phys. Chem. A 2021, 125, 10044−10051

(9) Sobolewski, A. L.; Domcke, W. Are Heptazine-Based Organic Light-Emitting Diode Chromophores Thermally Activated Delayed Fluorescence or Inverted Singlet−Triplet Systems? *J. Phys. Chem. Lett.* **2021**, *12*, 6852−6860.
(10) Li, J.; Tao, L.; Wang, Y.; Yao, Y.; Guo, Q. Heptazine-Based π-Conjugated Materials for Light-Emitting. *Front. Chem.* **2021**, *9*, No. 717569.
(11) Kim, J. H.; Han, S. H.; Lee, J. Y. Concentration quenching resistant donor-acceptor molecular structure for high efficiency and long lifetime thermally activated delayed fluorescent organic light-emitting diodes via suppressed non-radiative channel. *Chem. Eng. J.* **2020**, *395*, No. 125159.
(12) Li, J.; Nomura, H.; Miyazaki, H.; Adachi, C. Highly efficient exciplex organic light-emitting diodes incorporating a heptazine derivative as an electron acceptor. *Chem. Commun.* **2014**, *50*, 6174−6176.
(13) Li, J.; Zhang, Q.; Nomura, H.; Miyazaki, H.; Adachi, C. Thermally activated delayed fluorescence from $^3n\pi^*$ to $^3n\pi^*$ up-conversion and its application to organic light-emitting diodes. *Appl. Phys. Lett.* **2014**, *105*, No. 013301.
(14) Li, J.; Nakagawa, T.; MacDonald, J.; Zhang, Q.; Nomura, H.; Miyazaki, H.; Adachi, C. Highly Efficient Organic Light-Emitting Diode Based on a Hidden Thermally Activated Delayed Fluorescence Channel in a Heptazine Derivative. *Adv. Mater.* **2013**, *25*, 3319−3323.
(15) Bala, I.; Gupta, S. P.; Kumar, S.; Singh, H.; De, J.; Sharma, N.; Kailasam, K.; Pal, S. K. Hydrogen-bond mediated columnar liquid crystalline assemblies of C3-symmetric heptazine derivatives at ambient temperature. *Soft Matter* **2018**, *14*, 6342−6352.
(16) Kollmar, H.; Staemmler, V. Violation of Hundas rule by spin polarization in molecules. *Theor. Chim. Acta* **1978**, *48*, 223−239.
(17) Ehrmaier, J.; Rabe, E. J.; Pristash, S. R.; Corp, K. L.; Schlenker, C. W.; Sobolewski, A. L.; Domcke, W. Singlet-triplet inversion in heptazine and in polymeric carbon nitrides. *J. Phys. Chem. A* **2019**, *123*, 8099−8108.
(18) de Silva, P. Inverted Singlet-Triplet Gaps and Their Relevance to Thermally Activated Delayed Fluorescence. *J. Phys. Chem. Lett.* **2019**, *10*, 5674−5679.
(19) Grimme, S.; Waletzke, M. A combination of Kohn-Sham density functional theory and multi-reference configuration interaction methods. *J. Chem. Phys.* **1999**, *111*, 5645−5655.
(20) Marian, C. M.; Heil, A.; Kleinschmidt, M. The DFT/MRCI method. *WIREs Comput. Mol. Sci.* **2019**, *9*, No. e1394.
(21) TURBOMOLE V7.5, a development of University of Karlsruhe and Forschungszentrum Karlsruhe GmbH, 1989-2007, TURBOMOLE GmbH, since 2007. 2020, https://www.turbomole.org.
(22) Hirata, S.; Head-Gordon, M. Time-dependent density functional theory within the Tamm−Dancoff approximation. *Chem. Phys. Lett.* **1999**, *314*, 291−299.
(23) Perdew, J. P.; Burke, K.; Ernzerhof, M. Generalized Gradient Approximation Made Simple. *Phys. Rev. Lett.* **1996**, *77*, 3865−3868.
(24) Adamo, C.; Barone, V. Toward reliable density functional methods without adjustable parameters: The PBE0 model. *J. Chem. Phys.* **1999**, *110*, 6158−6170.
(25) Schäfer, A.; Huber, C.; Ahlrichs, R. Fully optimized contracted Gaussian basis sets of triple zeta valence quality for atoms Li to Kr. *J. Chem. Phys.* **1994**, *100*, 5829−5835.
(26) Frisch, M. J.; Trucks, G. W.; Schlegel, H. B.; Scuseria, G. E.; Robb, M. A.; Cheeseman, J. R.; Scalmani, G.; Barone, V.; Petersson, G. A.; Nakatsuji, H. et al.*Gaussian 16*. revision C.01, Gaussian Inc., Wallingford CT 2016.
(27) Kesharwani, M. K.; Brauer, B.; Martin, J. M. L. Frequency and Zero-Point Vibrational Energy Scale Factors for Double-Hybrid Density Functionals (and Other Selected Methods): Can Anharmonic Force Fields Be Avoided? *J. Phys. Chem. A* **2015**, *119*, 1701−1714.
(28) Lyskov, I.; Kleinschmidt, M.; Marian, C. M. Redesign of the DFT/MRCI Hamiltonian. *J. Chem. Phys.* **2016**, *144*, No. 034104.
(29) Kleinschmidt, M.; Tatchen, J.; Marian, C. M. Spin-orbit coupling of DFT/MRCI wavefunctions: Method, test calculations, and application to thiophene. *J. Comput. Chem.* **2002**, *23*, 824−833.
(30) Kleinschmidt, M.; Marian, C. M. Efficient generation of matrix elements for one-electron spin−orbit operators. *Chem. Phys.* **2005**, *311*, 71−79.
(31) Heß, B. A.; Marian, C. M.; Wahlgren, U.; Gropen, O. A mean-field spin-orbit method applicable to correlated wavefunctions. *Chem. Phys. Lett.* **1996**, *251*, 365−371.
(32) Schimmelpfennig, B. *AMFI is an Atomic Spin-Orbit Integral Program*, University of Stockholm, 1996.
(33) Herzberg, G.; Teller, E. Schwingungsstruktur der Elektronenübergänge bei mehratomigen Molekülen. *Z. Phys. Chem.* **1933**, *21B*, 410−446.
(34) Tatchen, J.; Gilka, N.; Marian, C. M. Intersystem crossing driven by vibronic spin−orbit coupling: a case study on psoralen. *Phys. Chem. Chem. Phys.* **2007**, *9*, 5209−5221.
(35) Bracker, M.; Marian, C. M.; Kleinschmidt, M. Internal conversion of singlet and triplet states employing numerical DFT/MRCI derivative couplings: Implementation, tests, and application to xanthone. *J. Chem. Phys.* **2021**, *155*, No. 014102.
(36) Dinkelbach, F.; Marian, C. M. Vibronic and spin−orbit coupling effects in the absorption spectra of pyrazine: A quantum chemical approach. *J. Serb. Chem. Soc.* **2019**, *84*, 819−836.
(37) Islampour, R.; Miralinaghi, M. Dynamics of Radiationless Transitions: Effects of Displacement-Distortion-Rotation of Potential Energy Surfaces on Internal Conversion Decay Rate Constants. *J. Phys. Chem. A* **2007**, *111*, 9454−9462.
(38) Peng, Q.; Yi, Y.; Shui, Z.; Shao, J. Excited State Radiationless Decay Process with Duschinsky Rotation Effect: Formalism and Implemantation. *J. Chem. Phys.* **2007**, *126*, No. 114302.
(39) Niu, Y.; Peng, Q.; Deng, C.; Gao, X.; Shuai, Z. Theory of excited state decays and optical spectra: Application to polyatomic molecules. *J. Phys. Chem. A* **2010**, *114*, 7817−7831.
(40) Etinski, M.; Tatchen, J.; Marian, C. M. Time-dependent approaches for the calculation of intersystem crossing rates. *J. Chem. Phys.* **2011**, *134*, No. 154105.
(41) Etinski, M.; Rai-Constapel, V.; Marian, C. M. Time-dependent approach to spin-vibronic coupling: Implementation and assessment. *J. Chem. Phys.* **2014**, *140*, No. 114104.
(42) Etinski, M.; Tatchen, J.; Marian, C. M. Thermal and solvent effects on the triplet formation in cinnoline. *Phys. Chem. Chem. Phys.* **2014**, *16*, 4740−4751.
(43) Banerjee, S.; Baiardi, A.; Bloino, J.; Barone, V. Temperature Dependence of Radiative and Nonradiative Rates from Time-Dependent Correlation Function Methods. *J. Chem. Theory Comput.* **2016**, *12*, 774−786.
(44) Lyskov, I.; Etinski, M.; Marian, C. M.; Russo, S. P. Exciton energy transfer in organic light emitting diodes with thermally activated delayed fluorescence dopants. *J. Mater. Chem. C* **2018**, *6*, 6860−6868.
(45) El-Sayed, M. A. Triplet state. Its radiative and nonradiative properties. *Acc. Chem. Res.* **1968**, *1*, 8−16.
(46) Marian, C. *Reviews in Computational Chemistry*;Lipkowitz, K.; Boyd, D., Eds.; Wiley-VCH, Weinheim, 2001; Vol. *17*, pp 99−204.

https://doi.org/10.1021/acs.jpca.1c09150
J. Phys. Chem. A 2021, 125, 10044−10051

Supporting Information for: Large Inverted Singlet–Triplet Energy Gaps Are Not Always Favorable for Triplet Harvesting: Vibronic Coupling Drives the (Reverse) Intersystem Crossing in Heptazine Derivatives

Fabian Dinkelbach, Mario Bracker, Martin Kleinschmidt, and Christel M. Marian*

Institute of Theoretical and Computational Chemistry, Heinrich-Heine-University Düsseldorf, Düsseldorf, Germany

E-mail: christel.marian@hhu.de

Phone: +49 (0)211 8113210

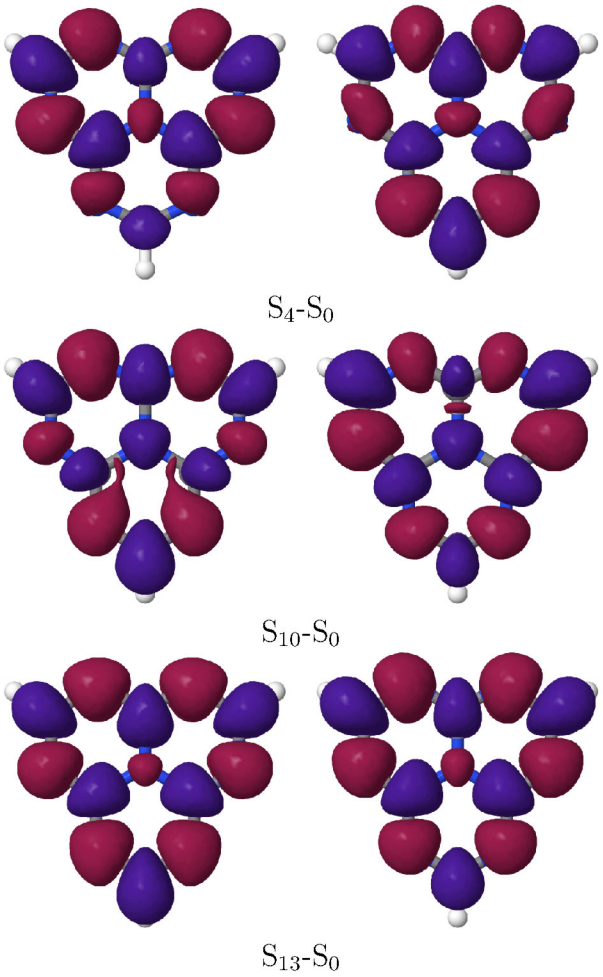

Figure S1: Difference densities of E′ symmetric singlet states contributing to vibronic fluorescence in heptazine. Areas losing electron density in comparison to the electronic ground state are shown in red, areas gaining electron density in blue.

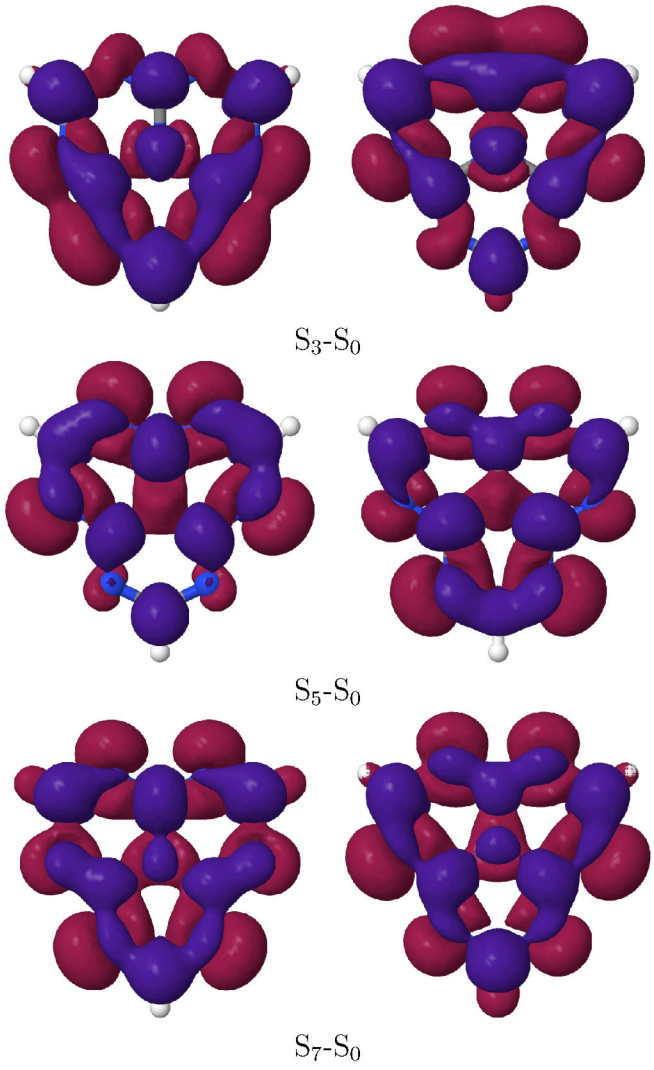

Figure S2: Difference densities of E″ symmetric singlet states contributing to vibronic SOC in heptazine. For color codes, see Figure S1.

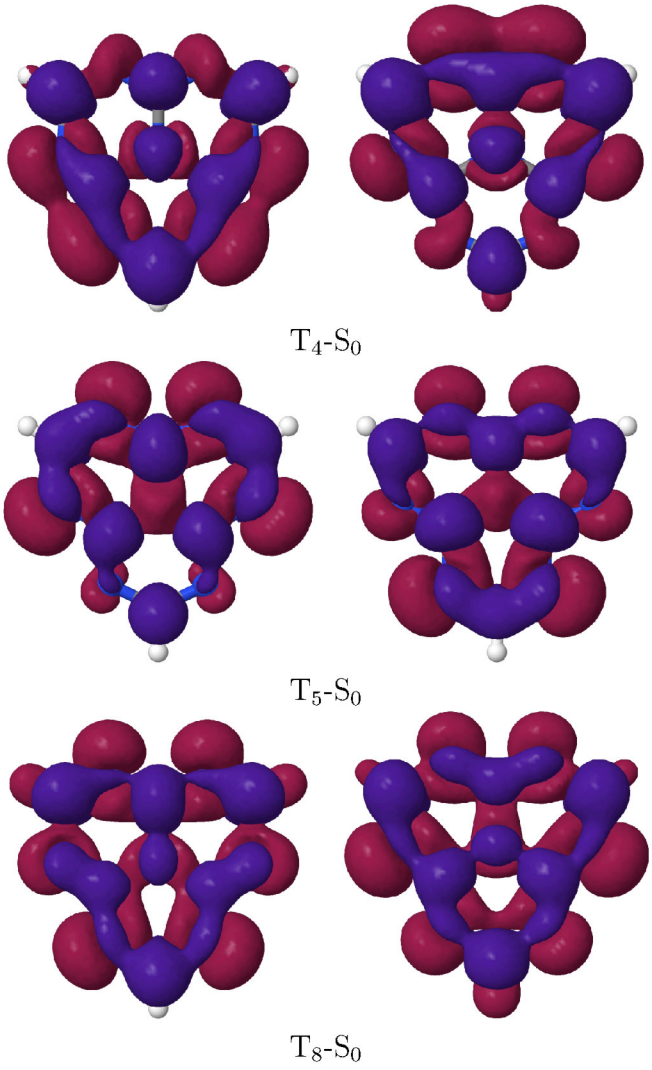

Figure S3: Difference densities of E″ symmetric triplet states contributing to vibronic SOC in heptazine. For color codes, see Figure S1.

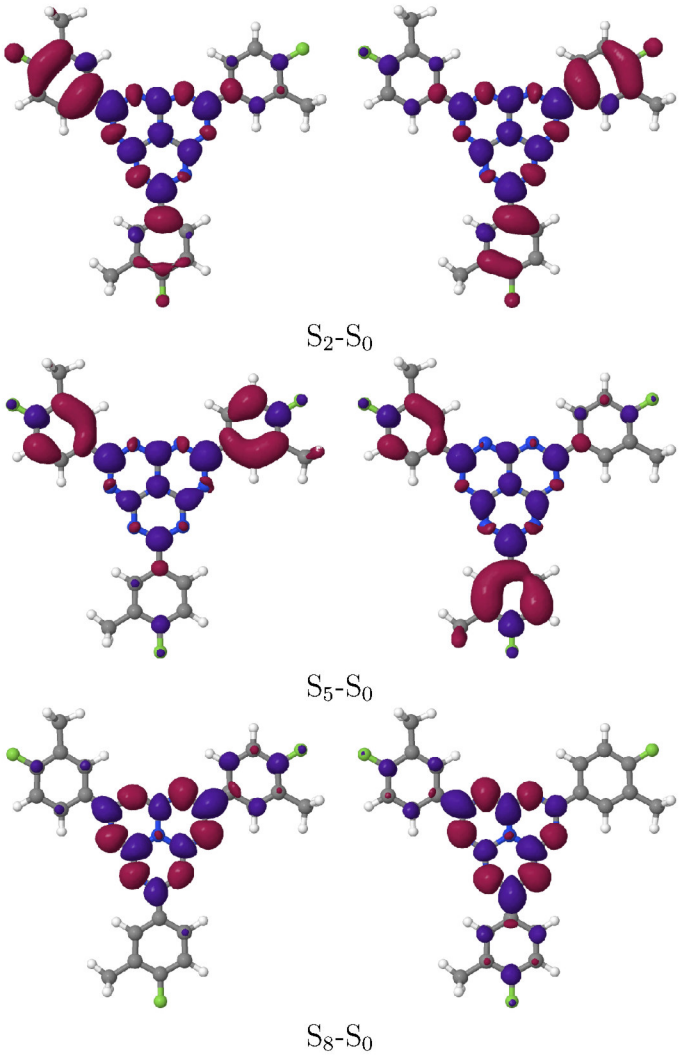

Figure S4: Difference densities of E′ symmetry singlet states contributing to vibronic fluorescence in HAP-3MF. For color codes, see Figure S1.

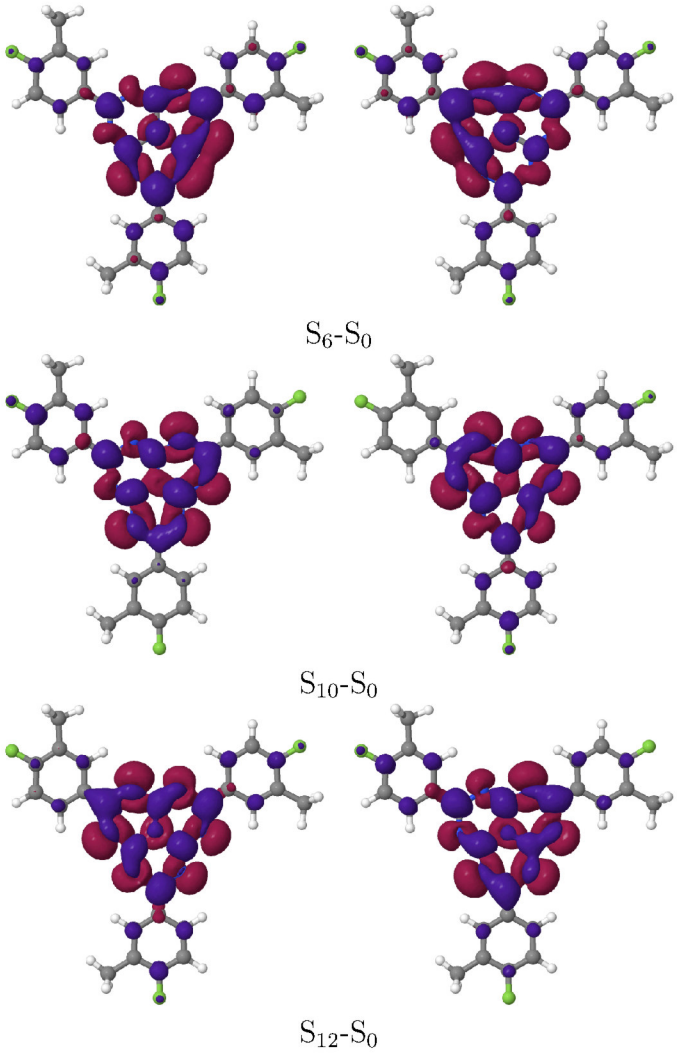

Figure S5: Difference densities of E″ symmetric singlet states contributing to vibronic SOC in HAP-3MF. For color codes, see Figure S1.

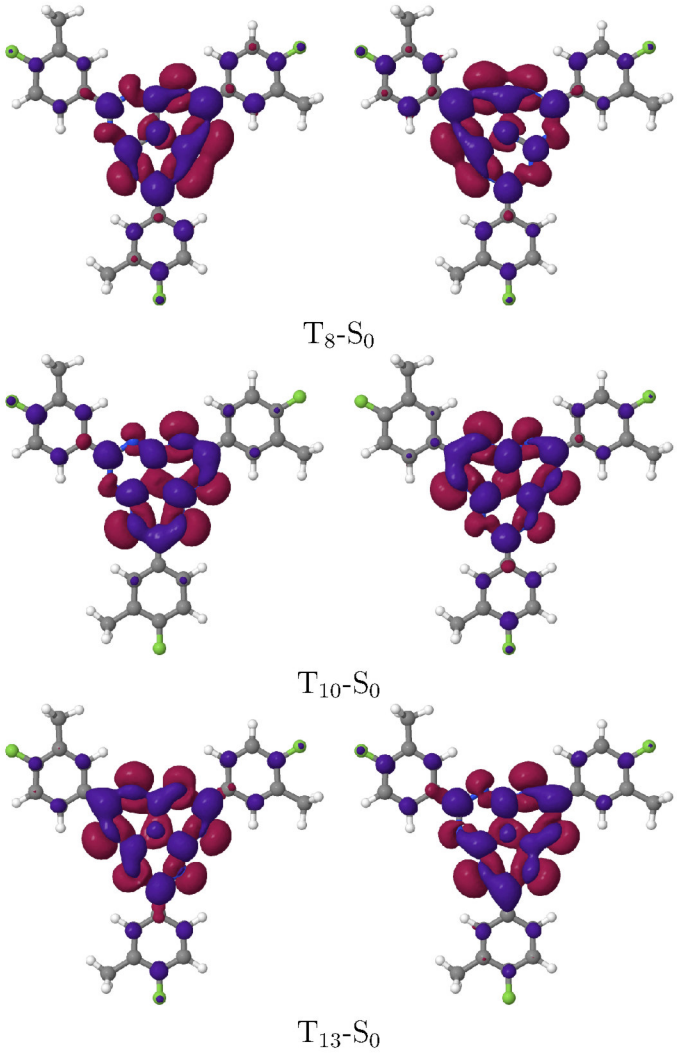

Figure S6: Difference densities of E″ symmetric triplet states contributing to vibronic SOC in HAP-3MF. For color codes, see Figure S1.

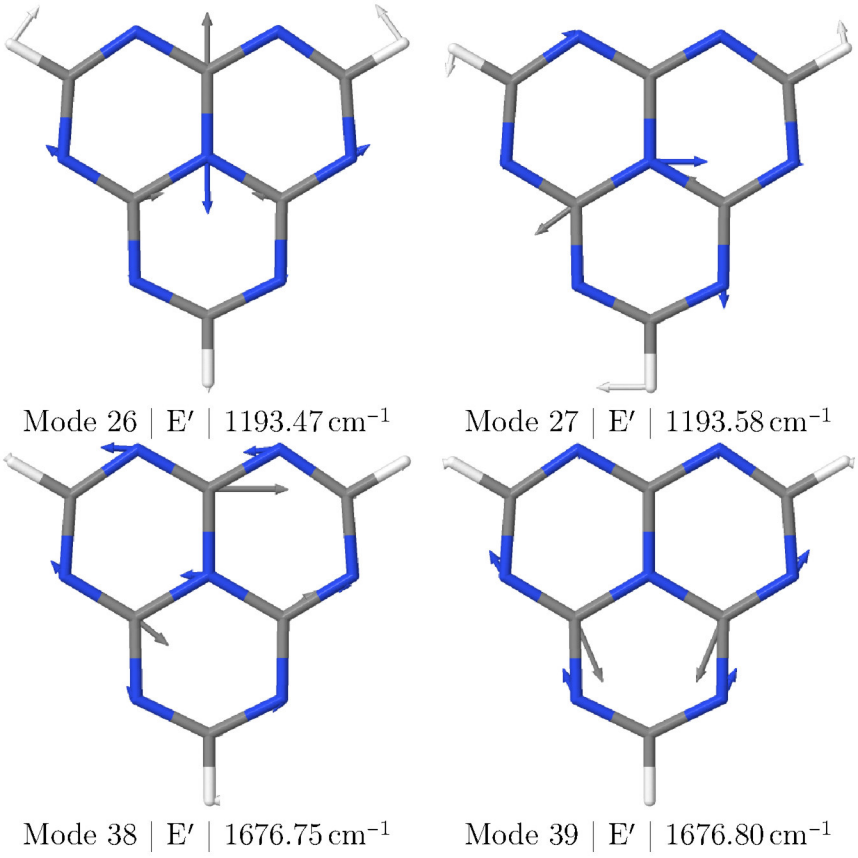

Figure S7: Vibrational modes at the S_0 minimum contributing to vibronic absorption in heptazine.

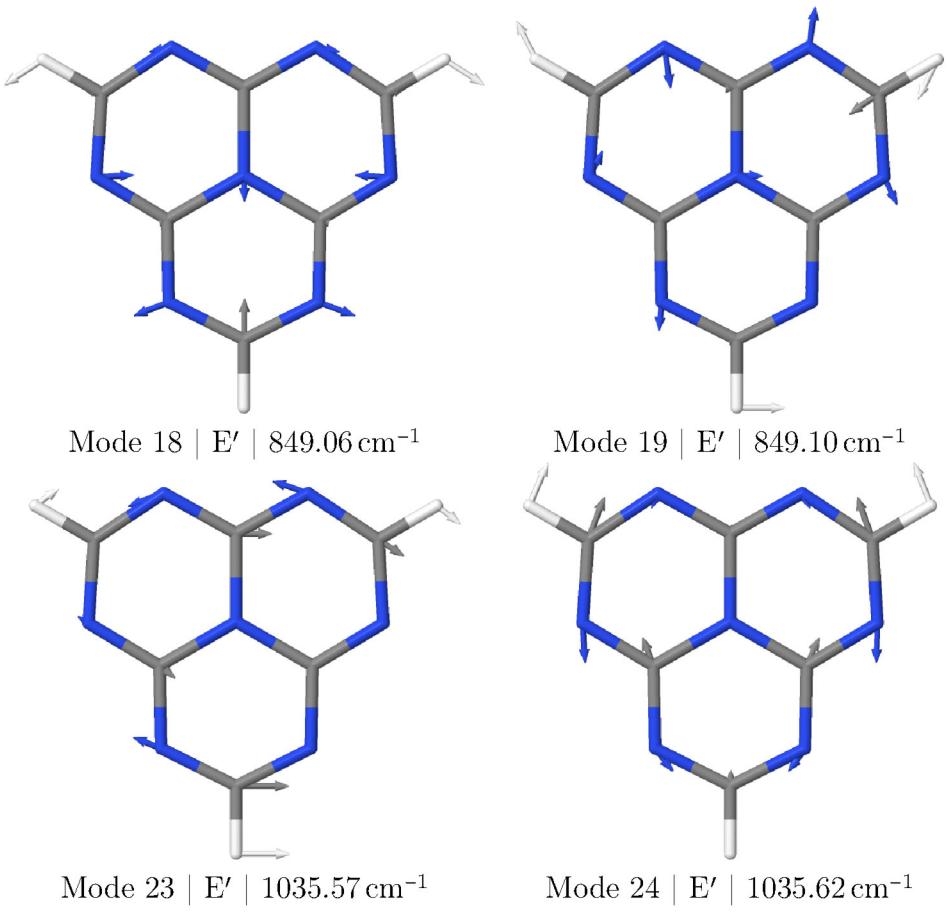

Mode 18 | E′ | 849.06 cm^{-1} Mode 19 | E′ | 849.10 cm^{-1}

Mode 23 | E′ | 1035.57 cm^{-1} Mode 24 | E′ | 1035.62 cm^{-1}

Figure S8: Vibrational modes at the S_1 minimum contributing to vibronic fluorescence in heptazine.

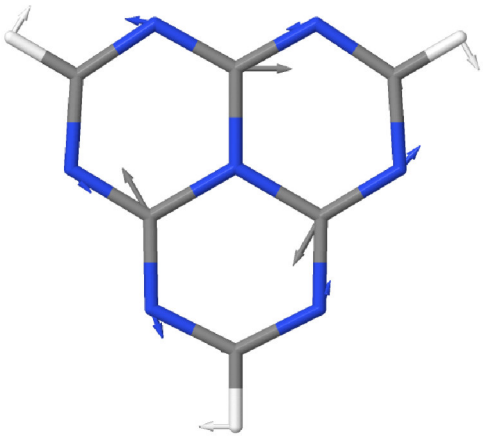

Mode 39 | A_2' | 1652.45 cm^{-1}

Figure S9: Vibrational modes at the S_1 minimum contributing to IC in heptazine.

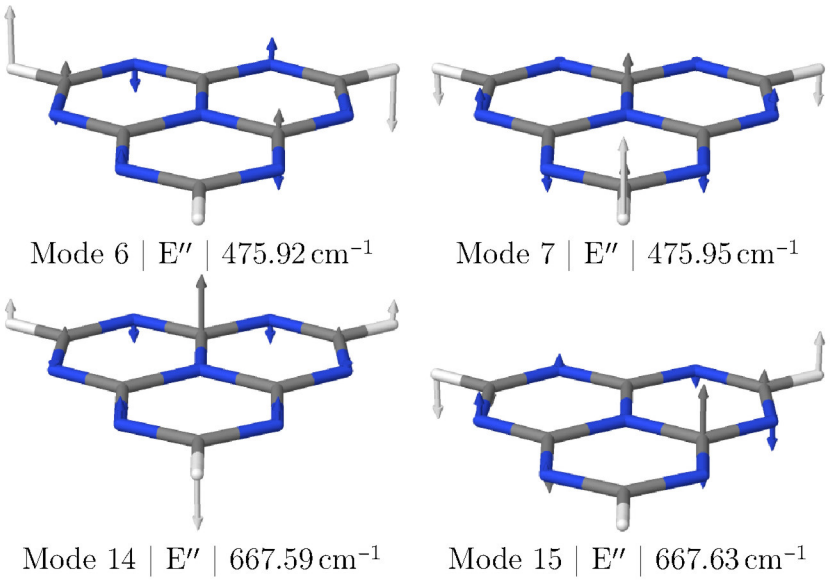

Figure S10: Vibrational modes at the S_1 minimum contributing to vibronic SOC in heptazine.

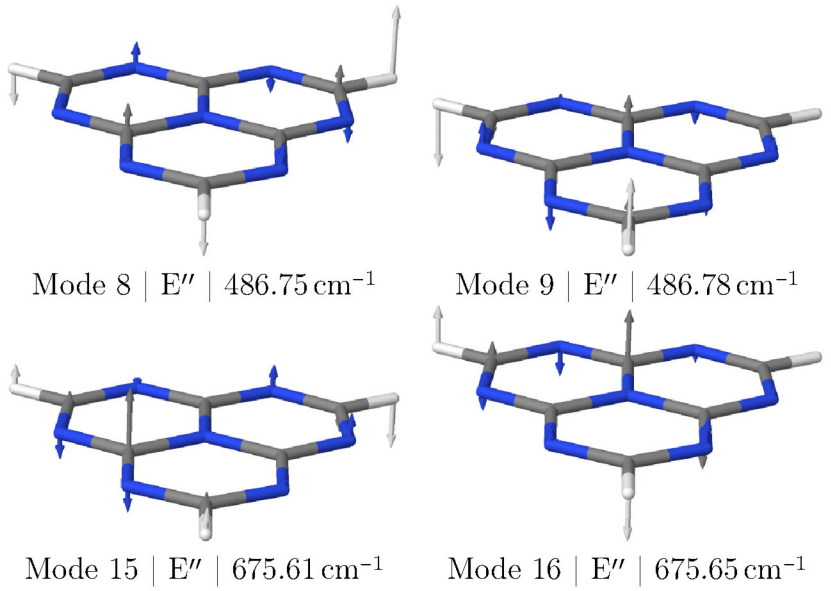

Figure S11: Vibrational modes at the T_1 minimum contributing to vibronic SOC in heptazine.

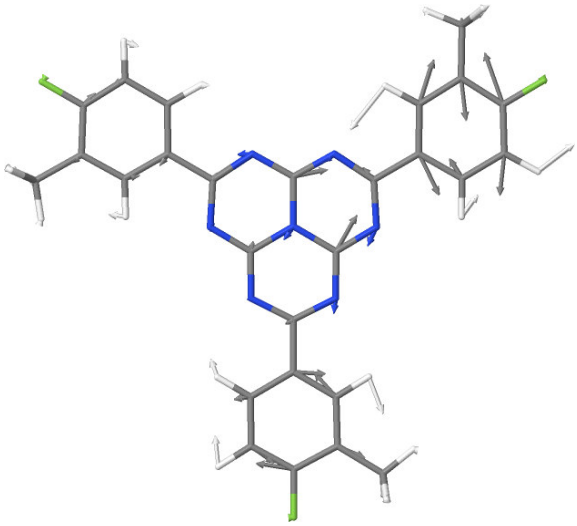

Mode 137 | E′ | 1660.40 cm^{-1}

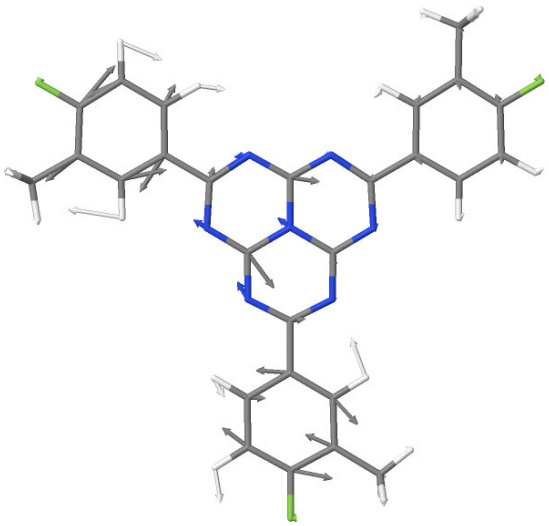

Mode 138 | E′ | 1660.42 cm^{-1}

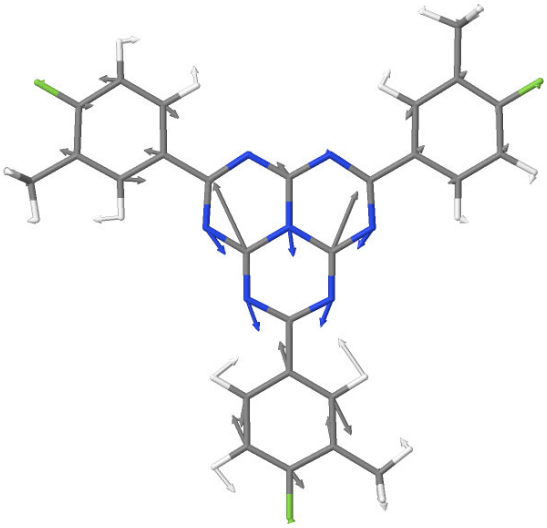

Mode 140 | E′ | 1682.87 cm^{-1}

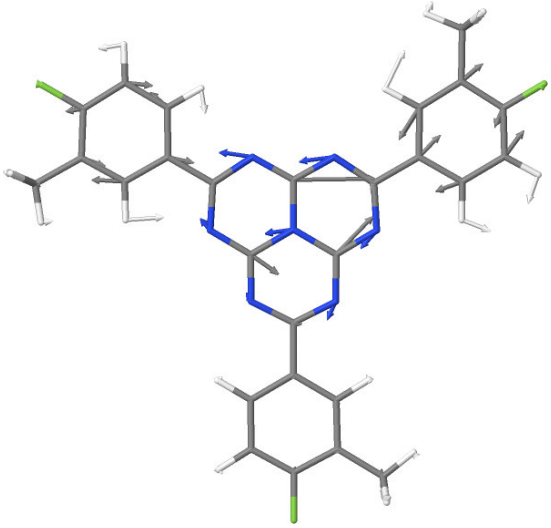

Mode 141 | E′ | 1682.92 cm^{-1}

Figure S12: Vibrational modes at the S_0 minimum contributing to vibronic absorption in HAP-3MF.

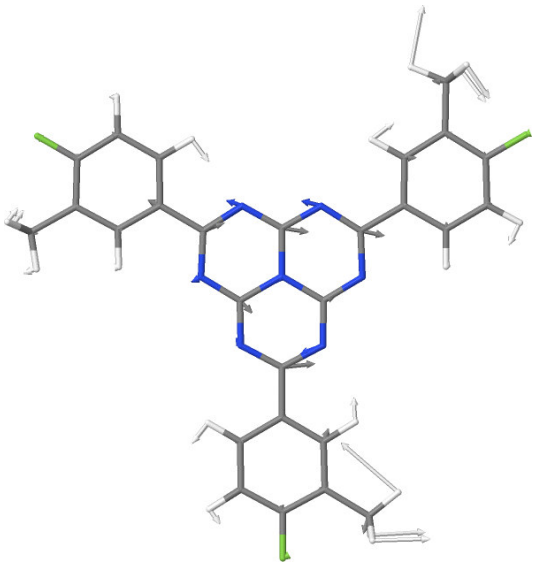

Mode 85 | E′ | 1020.43 cm^{-1}

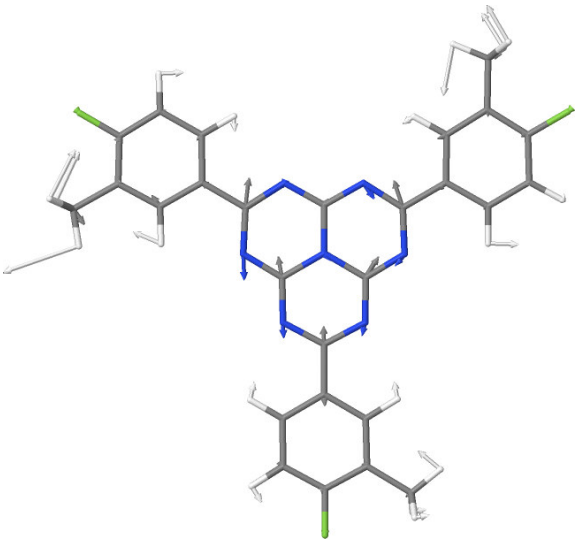

Mode 86 | E′ | 1020.52 cm^{-1}

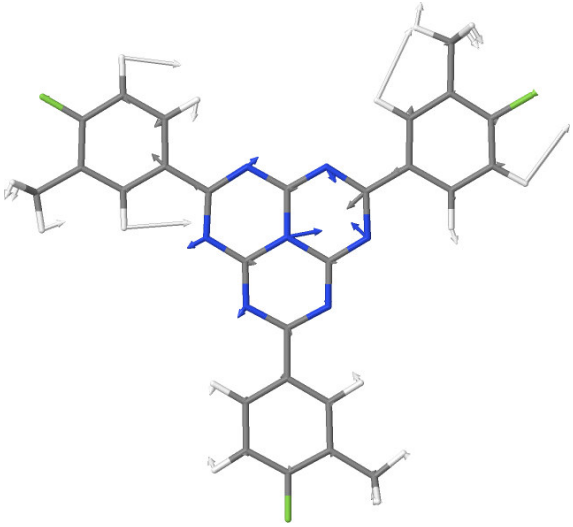

Mode 91 | E′ | 1084.36 cm^{-1}

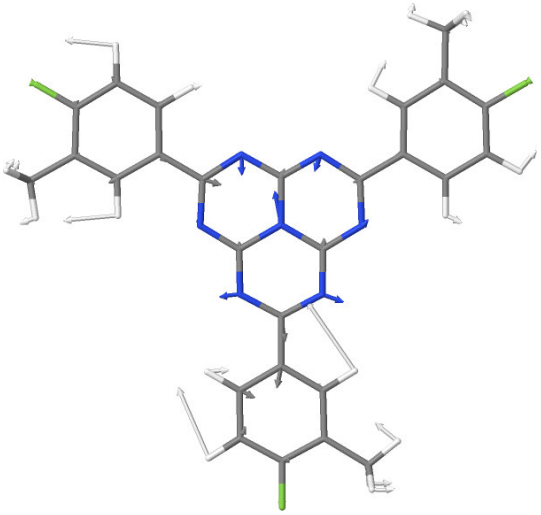

Mode 92 | E′ | 1084.38 cm^{-1}

Figure S13: Vibrational modes at the S_1 minimum contributing to vibronic fluorescence in HAP-3MF.

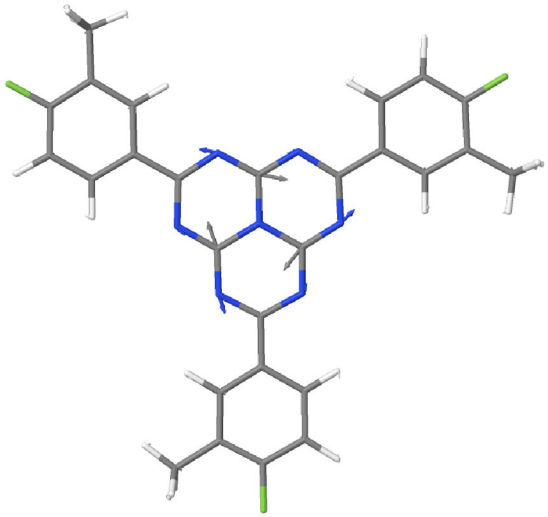

Mode 135 | A′ | 1598.29 cm^{-1}

Figure S14: Vibrational modes at the S_1 minimum contributing to IC in HAP-3MF.

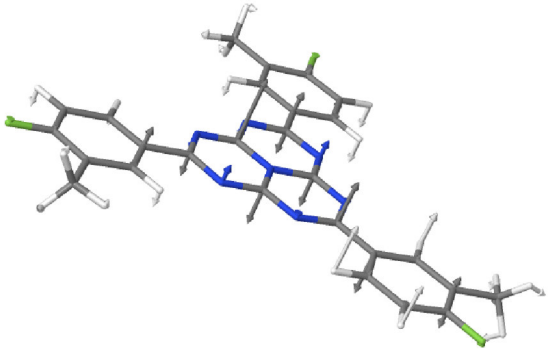

Mode 50 | E″ | 583.84 cm^{-1}

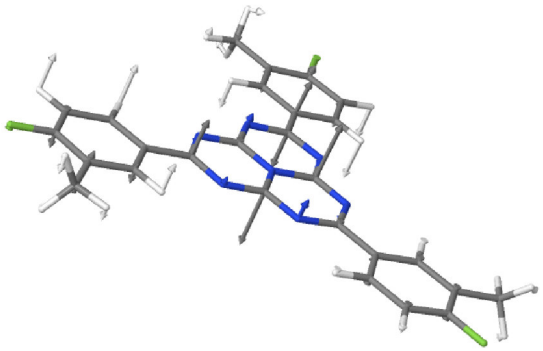

Mode 51 | E″ | 583.87 cm^{-1}

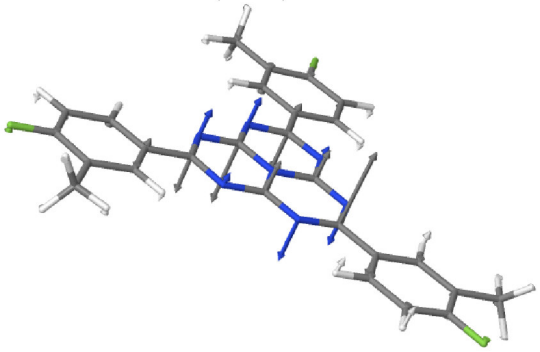

Mode 60 | E″ | 676.72 cm^{-1}

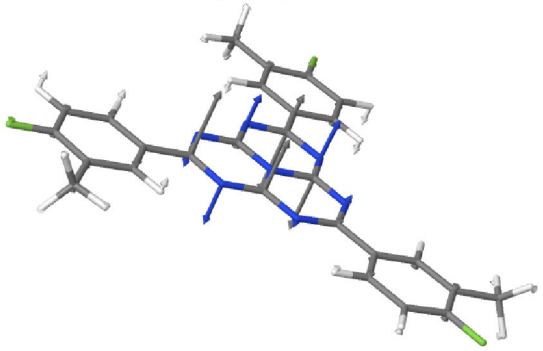

Mode 61 | E″ | 676.75 cm^{-1}

Figure S15: Vibrational modes at the S_1 minimum contributing to vibronic SOC in HAP-3MF.

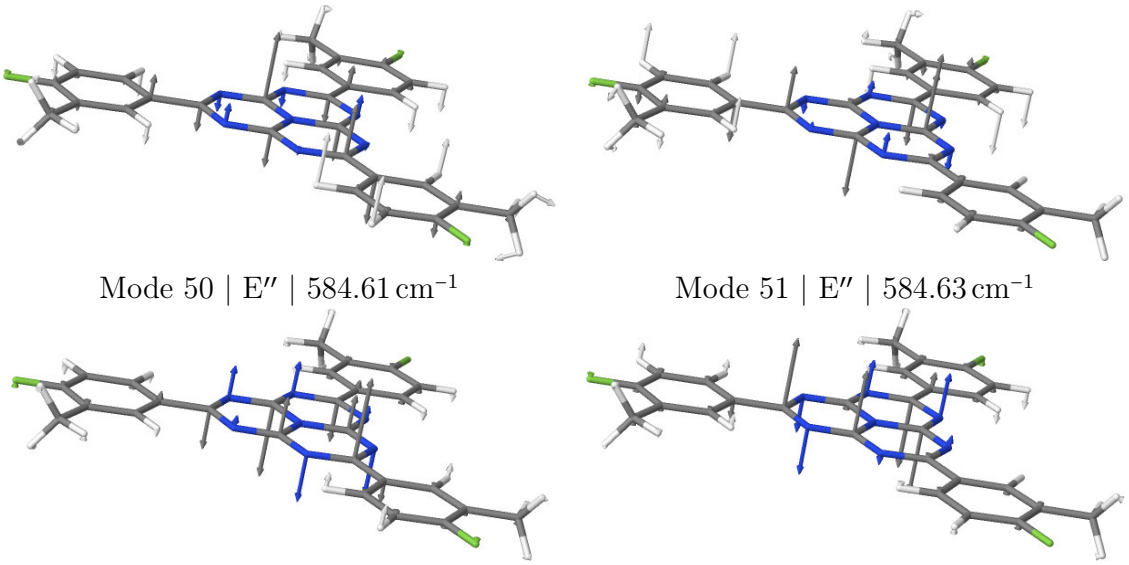

Mode 50 | E″ | 584.61 cm^{-1} Mode 51 | E″ | 584.63 cm^{-1}

Mode 62 | E″ | 677.04 cm^{-1} Mode 63 | E″ | 677.07 cm^{-1}

Figure S16: Vibrational modes at the T_1 minimum contributing to vibronic SOC in HAP-3MF.

Table S1: Vertical DFT/MRCI excitation energies of heptazine at the S_0 minimum.

State	D_{3h}	C_{2v}	ΔE [eV]	Osc. Strength f(L)
S_0	A_1'	A_1	0.00	
S_1	A_2'	B_1	2.59	0.00000
T_1	A_2'	B_1	2.60	
T_2	E′	A_1	3.35	
	E′	B_1	3.35	
T_3	A_1''	A_2	3.76	
T_4	E″	A_2	3.81	
	E″	B_2	3.81	
S_2	A_1''	A_2	3.86	0.00000
S_3	E″	A_2	3.92	0.00000
	E″	B_2	3.92	0.00000
S_4	E′	A_1	4.32	0.29062
	E′	B_1	4.32	0.28927
T_5	E″	A_2	4.63	
	E″	B_2	4.64	
T_6	A_2''	B_2	4.77	
T_7	E′	B_1	4.82	
	E′	A_1	4.82	
S_5	E″	A_2	4.87	0.00000
	E″	B_2	4.88	0.00001
T_8	E″	A_2	4.95	
	E″	B_2	4.96	
S_6	A_2''	B_2	4.97	0.01530
T_9	A_1''	A_2	4.98	
S_7	E″	A_2	5.04	0.00000
	E″	B_2	5.05	0.00002
S_8	A_1''	A_2	5.10	0.00000
T_{10}	A_1'	A_1	5.21	
T_{11}	A_2''	B_2	5.22	
S_9	A_2''	B_2	5.36	0.00006
T_{12}	E′	A_1	5.69	
	E′	B_1	5.70	
S_{10}	E′	B_1	5.73	0.37346
	E′	A_1	5.73	0.37348
T_{13}	A_1'	A_1	5.89	
S_{11}	A_1'	A_1	6.05	0.00000
T_{14}	A_2'	B_1	6.15	
S_{12}	A_2'	B_1	6.26	0.00000
S_{13}	E′	B_1	6.51	0.03363
	E′	A_1	6.52	0.02905
S_{14}	E′	A_1	6.53	0.00339

Table S2: Vertical DFT/MRCI excitation energies of heptazine at the S_1 minimum relative to S_0 minimum.

State	D_{3h}	C_{2v}	ΔE [eV]	Osc. Strength f(L)
S_0	A_1'	A_1	0.08	
S_1	A_2'	B_1	2.50	0.00000
T_1	A_2'	B_1	2.53	
T_2	E′	A_1	3.39	
	E′	B_1	3.39	
T_3	A_1''	A_2	3.63	
T_4	E″	A_2	3.70	
	E″	B_2	3.70	
S_2	A_1''	A_2	3.74	0.00000
S_3	E″	A_2	3.81	0.00000
	E″	B_2	3.81	0.00000
S_4	E′	A_1	4.35	0.27737
	E′	B_1	4.35	0.27652
T_5	E″	A_2	4.65	
	E″	B_2	4.66	
T_6	E′	B_1	4.73	
	E′	A_1	4.73	
T_7	A_2''	B_2	4.81	
S_5	E″	A_2	4.88	0.00000
	E″	B_2	4.89	0.00000
T_8	E″	A_2	4.91	
	E″	B_2	4.91	
T_9	A_1''	A_2	4.95	
S_6	A_2''	B_2	5.00	0.01334
S_7	E″	A_2	5.00	0.00000
	E″	B_2	5.02	0.00025
T_{10}	A_1'	A_1	5.06	
S_8	A_1''	A_2	5.08	0.00000
T_{11}	A_2''	B_2	5.19	
S_9	A_2''	B_2	5.31	0.00000
S_{10}	E′	B_1	5.64	0.37613
	E′	A_1	5.65	0.37707
T_{12}	E′	A_1	5.67	
	E′	B_1	5.68	
S_{11}	A_1'	A_1	5.86	0.00000
T_{13}	A_1'	A_1	5.87	
T_{14}	A_2'	B_1	6.17	
S_{12}	A_2'	B_1	6.25	0.00000
S_{13}	E′	B_1	6.47	0.02152
	E′	A_1	6.49	0.01898
S_{14}	E′	A_1	6.48	0.00183

Table S3: Vertical DFT/MRCI excitation energies of heptazine at the T_1 minimum relative S_0 minimum.

State	D_{3h}	C_{2v}	ΔE [eV]	Osc. Strength f(L)
S_0	A_1'	A_1	0.08	
S_1	A_2'	B_1	2.50	0.00000
T_1	A_2'	B_1	2.52	
T_2	E′	A_1	3.39	
	E′	B_1	3.39	
T_3	A_1''	A_2	3.62	
T_4	E″	A_2	3.70	
	E″	B_2	3.70	
S_2	A_1''	A_2	3.73	0.00000
S_3	E″	A_2	3.81	0.00000
	E″	B_2	3.81	0.00000
S_4	E′	A_1	4.35	0.27714
	E′	B_1	4.35	0.27628
T_5	E″	A_2	4.65	
	E″	B_2	4.65	
T_6	E′	B_1	4.72	
	E′	A_1	4.72	
T_7	A_2''	B_2	4.81	
S_5	E″	A_2	4.88	0.00000
	E″	B_2	4.89	0.00000
T_8	E″	A_2	4.90	
	E″	B_2	4.91	
T_9	A_1''	A_2	4.95	
S_6	A_2''	B_2	5.00	0.01316
S_7	E″	A_2	5.00	0.00000
	E″	B_2	5.01	0.00030
T_{10}	A_1'	A_1	5.07	
S_8	A_1''	A_2	5.08	0.00000
T_{11}	A_2''	B_2	5.19	
S_9	A_2''	B_2	5.30	0.00002
S_{10}	E′	B_1	5.64	0.37729
	E′	A_1	5.65	0.37753
T_{12}	E′	A_1	5.67	
	E′	B_1	5.67	
S_{11}	A_1'	A_1	5.85	0.00000
T_{13}	A_1'	A_1	5.88	
T_{14}	A_2'	B_1	6.17	
S_{12}	A_2'	B_1	6.25	0.00000
S_{13}	E′	B_1	6.47	0.02205
	E′	A_1	6.48	0.01330
S_{14}	E′	A_1	6.48	0.00803

Table S4: Vertical DFT/MRCI excitation energies of HAP-3MF at the S_0 minimum.

State	C_{3h}	C_s	ΔE [eV]	Osc. Strength f(L)
S_0	A′	A′	0.00	
T_1	A′	A′	2.70	
S_1	A′	A′	2.72	0.00000
T_2	E′	A′	3.00	
	E′	A′	3.01	
T_3	A′	A′	3.05	
T_4	E′	A′	3.32	
	E′	A′	3.32	
T_5	E′	A′	3.59	
	E′	A′	3.59	
S_2	E′	A′	3.60	1.00453
	E′	A′	3.60	1.00442
T_6	A′	A′	3.61	
T_7	A″	A″	3.82	
T_8	E″	A″	3.90	
	E″	A″	3.90	
S_3	A″	A″	3.92	0.00000
S_4	A′	A′	3.92	0.00160
S_5	E′	A′	3.95	0.04609
	E′	A′	3.95	0.04604
S_6	E″	A″	4.00	0.00000
	E″	A″	4.00	0.00000
T_9	A′	A′	4.04	
S_7	A′	A′	4.06	0.00038
S_8	E′	A′	4.12	0.36871
	E′	A′	4.12	0.36922
S_9	A′	A′	4.56	0.00065
T_{10}	E″	A″	4.60	
	E″	A″	4.60	
T_{11}	A″	A″	4.72	
S_{10}	E″	A″	4.80	0.00000
	E″	A″	4.80	0.00000
T_{12}	A″	A″	4.87	
T_{13}	E″	A″	4.88	
	E″	A″	4.88	
S_{11}	A″	A″	4.90	0.01353
S_{12}	E″	A″	4.95	0.00000
	E″	A″	4.95	0.00000
S_{13}	A″	A″	4.99	0.00001
T_{14}	E″	A″	5.43	
S_{14}	E″	A″	5.52	0.00000

Table S5: Vertical DFT/MRCI excitation energies of HAP-3MF at the S_1 minimum relative to S_0 minimum.

State	C_{3h}	C_s	ΔE [eV]	Osc. Strength f(L)
S_0	A′	A′	0.09	
T_1	A′	A′	2.65	
S_1	A′	A′	2.66	0.00000
T_2	E′	A′	3.02	
	E′	A′	3.02	
T_3	A′	A′	3.07	
T_4	E′	A′	3.32	
	E′	A′	3.32	
S_2	E′	A′	3.61	1.04103
	E′	A′	3.62	1.04104
T_5	E′	A′	3.62	
	E′	A′	3.62	
T_6	A′	A′	3.64	
T_7	A″	A″	3.70	
S_3	A″	A″	3.80	0.00000
T_8	E″	A″	3.80	
	E″	A″	3.81	
S_4	E″	A″	3.91	0.00000
	E″	A″	3.91	0.00000
S_5	A′	A′	3.95	0.00115
S_6	E′	A′	3.98	0.02872
	E′	A′	3.98	0.02890
S_7	A′	A′	4.10	0.12909
S_8	E′	A′	4.10	0.34830
	E′	A′	4.10	0.24979
T_9	A′	A′	4.10	
T_{10}	E″	A″	4.58	
	E″	A″	4.59	
S_9	A′	A′	4.59	0.00052
T_{11}	A″	A″	4.74	
S_{10}	E″	A″	4.76	0.00000
	E″	A″	4.77	0.00000
T_{12}	E″	A″	4.78	
	E″	A″	4.79	
T_{13}	A″	A″	4.81	
S_{11}	E″	A″	4.88	0.00000
	E″	A″	4.89	0.00001
S_{12}	E″	A″	4.90	0.00771
	E″	A″	4.92	0.00420
T_{14}	A″	A″	5.38	
S_{13}	A″	A″	5.47	0.00000

Table S6: Vertical DFT/MRCI excitation energies of HAP-3MF at the T_1 minimum relative S_0 minimum.

State	C_{3h}	C_s	ΔE [eV]	Osc. Strength f(L)
S_0	A′	A′	0.09	
T_1	A′	A′	2.65	
S_1	A′	A′	2.66	0.00000
T_2	E′	A′	3.02	
	E′	A′	3.03	
T_3	A′	A′	3.07	
T_4	E′	A′	3.32	
	E′	A′	3.32	
T_5	E′	A′	3.62	
	E′	A′	3.62	
S_2	E′	A′	3.62	1.04111
	E′	A′	3.62	1.04105
T_6	A′	A′	3.64	
T_7	A″	A″	3.69	
S_3	A″	A″	3.80	0.00000
T_8	E″	A″	3.80	
	E″	A″	3.80	
S_4	E″	A″	3.91	0.00000
	E″	A″	3.91	0.00000
S_5	A′	A′	3.95	0.00118
S_6	E′	A′	3.98	0.02893
	E′	A′	3.98	0.02915
S_7	E′	A′	4.10	0.32906
	E′	A′	4.10	0.36092
T_9	A′	A′	4.10	
S_8	A′	A′	4.10	0.03749
T_{10}	E″	A″	4.58	
	E″	A″	4.58	
S_9	A′	A′	4.59	0.00002
T_{11}	A″	A″	4.74	
S_{10}	E″	A″	4.76	0.00000
	E″	A″	4.76	0.00000
T_{12}	E″	A″	4.78	
	E″	A″	4.79	
T_{13}	A″	A″	4.80	
S_{11}	E″	A″	4.87	0.00000
	E″	A″	4.89	0.00001
S_{12}	E″	A″	4.90	0.00799
	E″	A″	4.91	0.00398
T_{14}	A″	A″	5.38	
S_{13}	A″	A″	5.47	0.00000

Table S7: Transition dipole moment gradients above 0.01 ea_0 **per displacement along dimensionless normal mode for the** $S_0 \rightarrow S_1$ **transition in heptazine at the** S_0 **minimum.**

Mode	Symmetry D_{3h}	Frequency [cm^{-1}]	x	y	z
10	E′	529.41	0.011887	-0.000001	0.000001
11	E′	529.47	0.000000	0.012795	-0.000000
18	E′	880.06	0.056349	0.000000	-0.000011
19	E′	880.10	0.000000	0.056545	0.000001
23	E′	1089.89	0.000000	-0.070317	-0.000002
24	E′	1089.89	0.070596	0.000005	0.000002
26	E′	1193.47	-0.000001	-0.081889	-0.000002
27	E′	1193.58	0.082462	-0.000000	-0.000009
29	E′	1312.15	-0.075081	-0.000003	0.000000
30	E′	1312.15	-0.000010	0.074846	-0.000004
32	E′	1437.77	0.011774	0.000000	-0.000003
33	E′	1437.79	-0.000004	-0.011792	0.000013
36	E′	1601.53	-0.026703	-0.000003	-0.000002
37	E′	1601.54	-0.000015	0.026817	0.000003
38	E′	1676.75	-0.115710	0.000002	-0.000010
39	E′	1676.80	-0.000000	0.114856	-0.000000
40	E′	3177.84	0.027071	0.000001	-0.000008
41	E′	3177.84	-0.000000	-0.027109	-0.000005

Table S8: Transition dipole moment gradients above 0.01 ea_0 per displacement along dimensionless normal mode for the $S_1 \rightarrow S_0$ transition in heptazine at the S_1 minimum.

Mode	Symmetry D_{3h}	Frequency [cm^{-1}]	x	y	z
10	E′	515.92	0.014603	0.000001	0.000000
11	E′	515.98	-0.000001	0.016257	-0.000000
18	E′	849.06	-0.084349	-0.000000	-0.000001
19	E′	849.10	-0.000001	0.082111	0.000000
23	E′	1035.57	-0.106727	-0.000005	0.000002
24	E′	1035.62	0.000010	0.108133	-0.000000
25	E′	1075.34	0.000002	-0.079176	0.000001
26	E′	1075.35	0.081727	0.000003	-0.000000
28	E′	1255.07	0.000001	-0.061916	0.000000
29	E′	1255.17	0.063576	0.000002	0.000001
31	E′	1310.83	0.030800	0.000002	0.000002
32	E′	1310.87	0.000005	0.033557	0.000000
33	E′	1450.88	0.000128	-0.052916	0.000000
34	E′	1450.88	0.053776	0.000137	0.000003
36	E′	1508.25	-0.047447	-0.000007	-0.000001
37	E′	1508.29	-0.000002	0.047263	-0.000000
40	E′	3210.66	-0.000005	-0.026335	0.000000
41	E′	3210.67	0.025920	0.000002	-0.000000

Table S9: SOCME gradients above 0.01 cm^{-1} per displacement along dimensionless normal mode for the $S_1 \rightarrow T_1$ transition in heptazine at the S_1 minimum.

Mode	Symmetry D_{3h}	Frequency [cm^{-1}]	x	y	z
2	E″	127.02	0.059280	-0.000070	0.000000
3	E″	127.03	0.000300	0.055460	0.000000
6	E″	475.92	0.000090	-0.054300	0.000000
7	E″	475.95	0.070810	-0.000010	0.000000
14	E″	667.59	-0.000300	0.074200	0.000000
15	E″	667.63	0.082460	0.000340	0.000000
21	E″	886.02	-0.000030	0.005460	0.000000
22	E″	886.14	-0.012210	0.000020	0.000000

Table S10: SOCME gradients above 0.01 cm^{-1} per displacement along dimensionless normal mode for the $T_1 \rightarrow S_1$ transition in heptazine at the T_1 minimum.

Mode	Symmetry D_{3h}	Frequency [cm^{-1}]	x	y	z
2	E″	130.56	0.053180	0.000110	0.000000
3	E″	130.58	0.000380	0.052140	0.000000
8	E″	486.75	-0.000170	-0.055650	0.000010
9	E″	486.78	-0.084070	0.000130	0.000000
15	E″	675.61	0.000030	0.076770	0.000000
16	E″	675.65	0.082210	0.000240	0.000000

Table S11: NACMEs above 0.01 a_0^{-1} per displacement along dimensionless normal mode for the $S_1 \rightarrow S_0$ transition in heptazine at the S_1 minimum.

Mode	Symmetry D_{3h}	Frequency [cm^{-1}]	NACME
30	A_2'	1301.79	0.030724
35	A_2'	1459.45	-0.044209
39	A_2'	1652.45	-0.125802

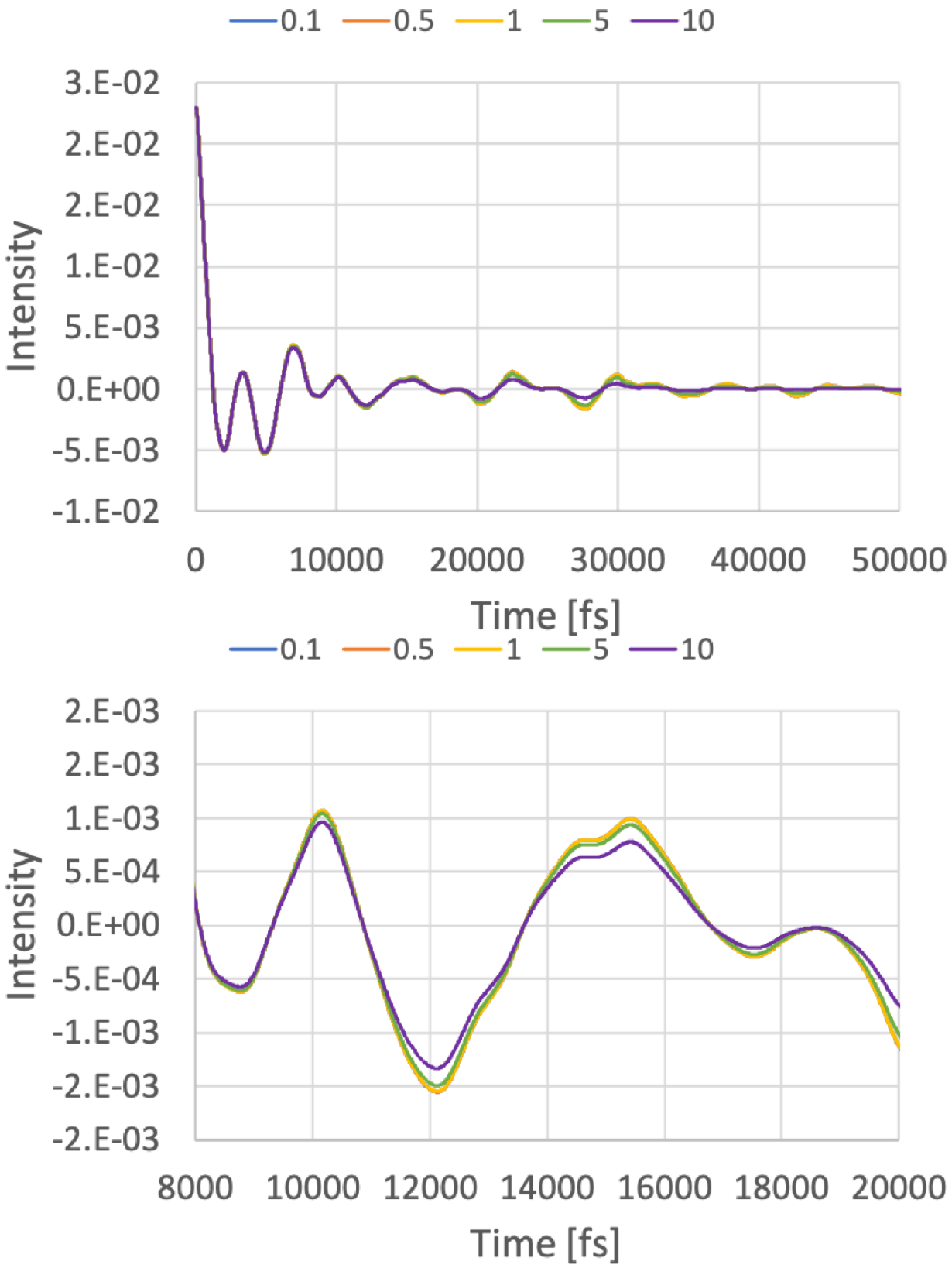

Figure S17: Correlation function of the $S_1 \rightsquigarrow T_1$ ISC transition of heptazine computed with different correlation function dampings in the time interval 0-50 ps (upper panel) and 8-20 ps (lower panel).

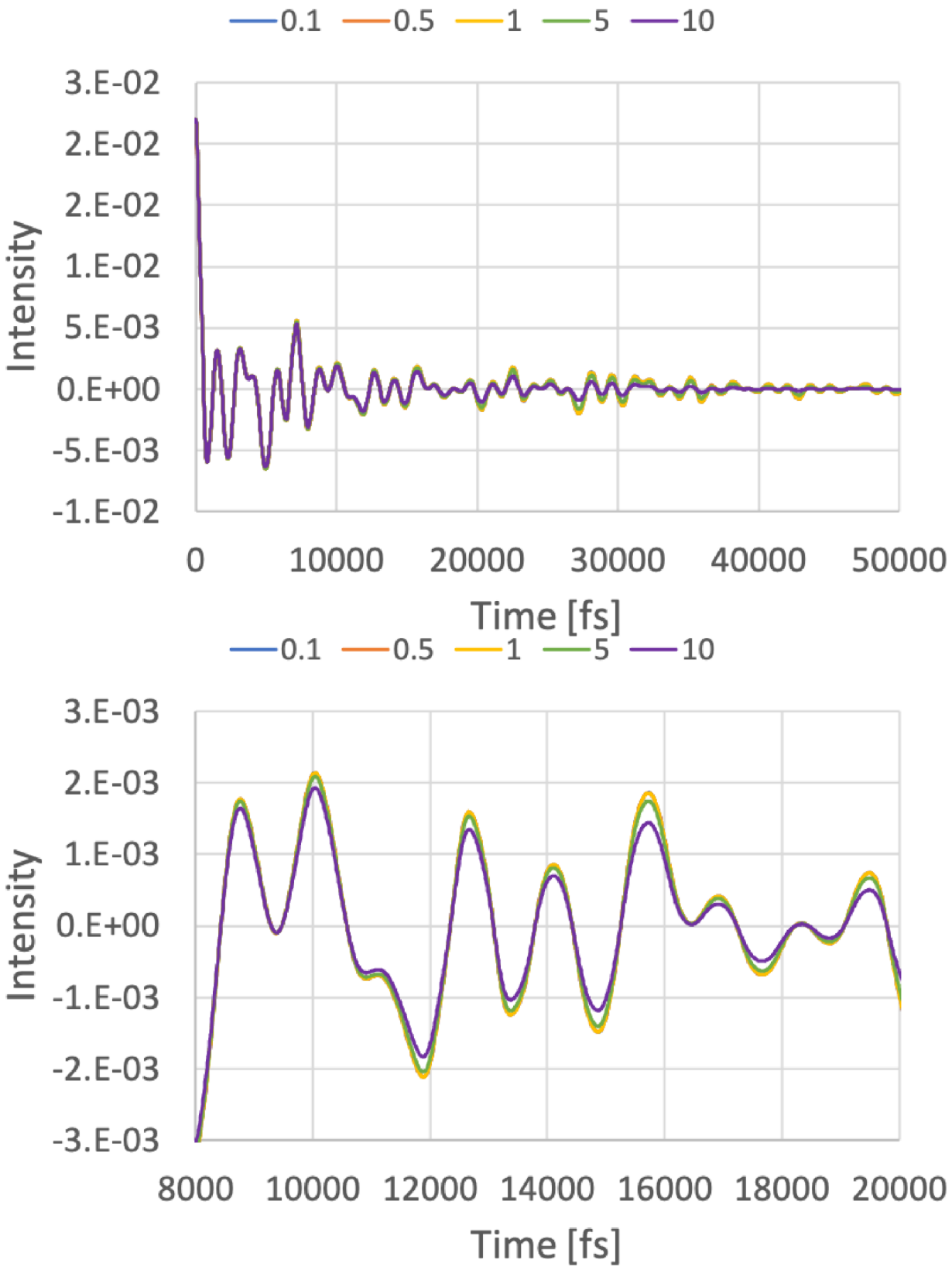

Figure S18: Correlation function of the $S_1 \rightsquigarrow T_1$ RISC transition of heptazine computed with different correlation function dampings in the time interval 0-50 ps (upper panel) and 8-20 ps (lower panel).

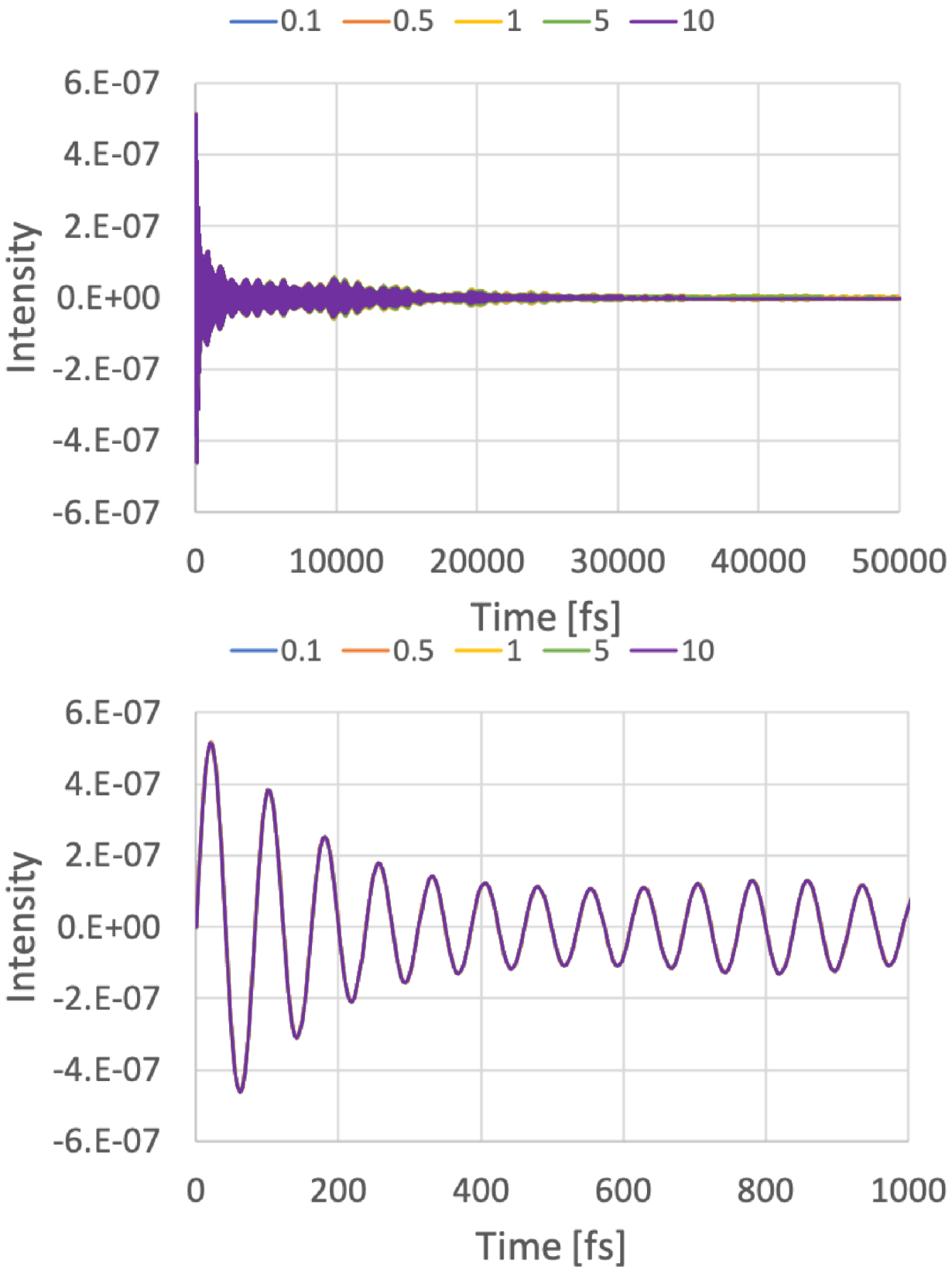

Figure S19: Correlation function of the $S_1 \rightsquigarrow S_0$ IC transition of heptazine computed with different correlation function dampings in the time interval 0-50 ps (upper panel) and 0-1 ps (lower panel).

Table S12: ISC rate constants of heptazine computed with different correlation function dampings.

Damping [cm^{-1}]	Rate Constant [s^{-1}]	Points	Time [fs]
10	1.10×10^7	65536	25000
5	1.07×10^7	65536	25000
1	1.05×10^7	65536	25000
0.5	1.05×10^7	262144	250000
0.1	1.58×10^7	262144	250000

Table S13: RISC rate constants of heptazine computed with different correlation function dampings.

Damping [cm^{-1}]	Rate Constant [s^{-1}]	Points	Time [fs]
10	2.93×10^6	65536	25000
5	2.85×10^6	65536	25000
1	2.77×10^6	65536	25000
0.5	2.76×10^6	262144	250000
0.1	4.11×10^6	262144	250000

Table S14: IC rate constants of heptazine computed with different correlation function dampings.

Damping [cm^{-1}]	Rate Constant [s^{-1}]	Points	Time [fs]
10	3.29×10^8	262144	25000
5	3.29×10^8	262144	25000
1	3.29×10^8	262144	25000
0.5	3.29×10^8	2097152	250000
0.1	3.33×10^8	2097152	250000

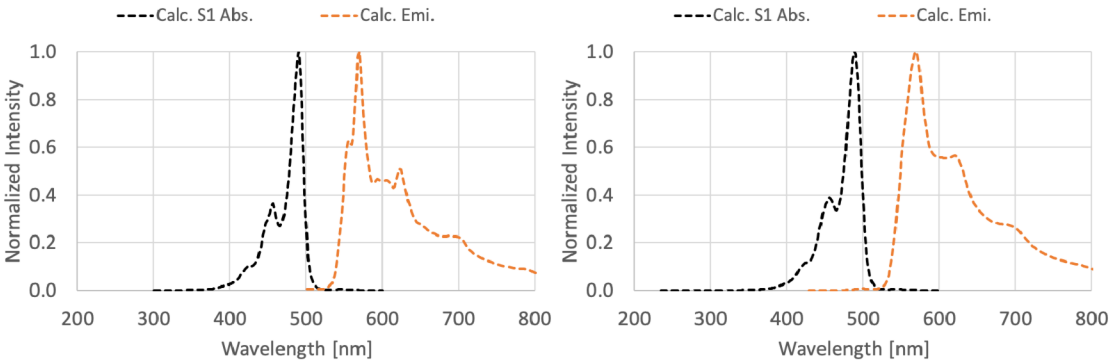

Figure S20: Herzberg–Teller $S_1 \leftarrow S_0$ absorption (black) and $S_1 \rightarrow S_0$ emission spectra (orange) of heptazine computed with damping functions of 100 cm^{-1} (left) and 200 cm^{-1} (right) FWHM.

Table S15: Fluorescence rate constants of heptazine computed with different correlation function dampings utilizing a grid of 16384 points and a integration time of 300 fs.

Damping [cm^{-1}]	Rate Constant [s^{-1}]
200	3.38×10^5
100	3.38×10^5
50	3.37×10^5

Table S16: Transition dipole moment gradients above 0.03 ea_0 per displacement along dimensionless normal mode for the $S_0 \rightarrow S_1$ transition in HAP-3MF at the S_0 minimum.

Mode	Symmetry C_{3h}	Frequency [cm^{-1}]	x	y	z
47	E′	576.42	0.019965	-0.004847	0.000000
48	E′	576.44	-0.003987	-0.020305	0.000000
72	E′	886.86	0.005433	0.036192	0.000000
73	E′	886.88	-0.035720	0.005195	0.000000
89	E′	1095.94	0.044478	-0.046685	0.000000
90	E′	1095.96	0.047719	0.043983	-0.000000
91	E′	1133.59	-0.034098	0.002810	-0.000000
92	E′	1133.61	0.003384	0.034064	0.000000
95	E′	1168.12	0.042855	-0.052048	0.000000
96	E′	1168.14	-0.049546	-0.045109	0.000000
98	E′	1216.24	-0.030173	0.004750	-0.000000
99	E′	1216.26	-0.005066	-0.029560	0.000000
101	E′	1258.07	-0.019202	0.050103	0.000000
102	E′	1258.12	0.050579	0.017673	0.000000
107	E′	1295.54	-0.046228	-0.021871	-0.000000
108	E′	1295.55	0.022149	-0.045843	-0.000000
116	E′	1414.99	-0.095684	0.075514	0.000000
117	E′	1415.01	0.078282	0.093569	0.000000
119	E′	1454.68	-0.094077	0.034328	-0.000000
120	E′	1454.70	0.033754	0.093096	0.000000
129	E′	1543.01	0.020205	-0.083653	0.000000
130	E′	1543.04	0.081213	0.018791	-0.000000
131	E′	1568.29	-0.053025	0.019623	0.000000
132	E′	1568.30	0.025369	0.051186	0.000000
134	E′	1635.64	0.073614	0.076834	-0.000000
135	E′	1635.67	-0.078274	0.072094	0.000000
137	E′	1660.40	-0.136477	0.062325	-0.000000
138	E′	1660.42	-0.063430	-0.131732	0.000000
140	E′	1682.87	-0.008610	0.160439	0.000000
141	E′	1682.92	-0.153660	-0.006416	0.000000

Table S17: Transition dipole moment gradients above 0.03 ea_0 per displacement along dimensionless normal mode for the $S_1 \rightarrow S_0$ transition in HAP-3MF at the S_1 minimum.

Mode	Symmetry C_{3h}	Frequency [cm^{-1}]	x	y	z
62	E′	682.38	-0.005935	0.030365	0.000000
63	E′	682.38	-0.031854	-0.005643	0.000001
72	E′	875.87	0.025089	0.066125	0.000000
73	E′	875.89	0.066319	-0.024701	0.000000
80	E′	953.51	0.020998	0.042101	0.000000
81	E′	953.52	0.043011	-0.020569	-0.000001
83	E′	1001.19	0.034578	0.085011	-0.000000
84	E′	1001.29	-0.093650	0.036575	-0.000000
85	E′	1020.43	0.059134	0.095785	-0.000000
86	E′	1020.52	-0.103727	0.064975	-0.000000
91	E′	1084.36	0.039720	-0.109463	-0.000002
92	E′	1084.38	0.108221	0.039233	-0.000000
97	E′	1167.77	-0.046567	0.077512	0.000001
98	E′	1167.80	0.078278	0.046128	-0.000000
100	E′	1217.64	-0.034896	0.005579	-0.000000
101	E′	1217.65	-0.005969	-0.034952	-0.000000
118	E′	1423.43	0.061657	-0.032615	-0.000000
119	E′	1423.47	0.032420	0.061856	0.000000
120	E′	1443.26	-0.065747	0.024752	0.000000
121	E′	1443.29	0.025576	0.064032	0.000001
129	E′	1499.37	0.002231	0.045185	0.000000
130	E′	1499.41	-0.045225	0.001456	-0.000000
136	E′	1636.58	0.007133	-0.034717	0.000002
137	E′	1636.59	0.033706	0.010540	0.000001

Table S18: SOCME gradients above 0.02 cm^{-1} per displacement along dimensionless normal mode for the $S_1 \rightarrow T_1$ transition in HAP-3MF at the S_1 minimum.

Mode	Symmetry C_{3h}	Frequency [cm^{-1}]	x	y	z
3	E″	22.21	0.010060	0.009240	0.000000
4	E″	22.36	-0.008640	0.009840	0.000000
10	A″	94.23	0.002460	0.006500	0.000000
11	E″	94.54	0.007540	-0.010680	0.000000
12	E″	95.72	-0.007980	-0.005280	0.000000
32	E″	344.14	0.006460	0.011150	0.000000
33	E″	344.17	-0.012830	0.006260	0.000000
50	E″	583.84	-0.018440	-0.002480	0.000000
51	E″	583.87	-0.002100	0.019560	0.000000
60	E″	676.72	-0.040940	0.007660	0.000000
61	E″	676.75	0.005340	0.035510	0.000000
69	E″	823.19	-0.010920	-0.012900	0.000000
70	E″	823.24	0.013600	-0.008500	0.000000
74	A″	897.15	-0.009000	0.012740	0.000000
75	E″	897.30	-0.007340	-0.014830	0.000000
76	E″	897.34	0.017820	0.001140	0.000000
78	E″	942.86	-0.016080	0.009220	0.000000
79	E″	942.93	-0.007240	-0.015600	0.000000
88	E″	1050.48	-0.015660	-0.002440	0.000000
89	E″	1050.49	-0.000700	-0.013390	0.000000

Gradients along mode 10 and 74 arise due to mixing with close lying E″ modes.

Table S19: SOCME gradients above 0.01 cm^{-1} per displacement along dimensionless normal mode for the $T_1 \rightarrow S_1$ transition in HAP-3MF at the T_1 minimum.

Mode	Symmetry C_{3h}	Frequency [cm^{-1}]	x	y	z
11	E″	94.00	0.008320	-0.010740	0.000000
12	E″	95.23	-0.007820	-0.007300	0.000000
32	E″	344.74	0.006200	0.009270	0.000000
33	E″	344.77	-0.010280	0.005800	0.000000
50	E″	584.61	-0.019140	0.000780	0.000000
51	E″	584.63	0.000770	0.019270	0.000000
62	E″	677.04	-0.035120	0.006500	0.000000
63	E″	677.07	0.006140	0.034360	0.000000
71	E″	823.15	-0.007640	-0.011040	0.000000
72	E″	823.20	0.012620	-0.010800	0.000000
76	A″	896.30	-0.008700	0.013080	0.000000
77	E″	896.44	-0.004090	-0.016620	0.000000
78	E″	896.48	0.018480	0.003740	0.000000
80	E″	942.23	-0.016640	0.010970	0.000000
81	E″	942.30	-0.010100	-0.014780	0.000010
88	E″	1050.29	-0.015540	-0.003170	0.000000
89	E″	1050.30	0.001710	-0.013480	0.000000

Gradients along mode 76 arise due to mixing with close lying E″ modes.

Table S20: NACMEs above 0.01 a_0^{-1} per displacement along dimensionless normal mode for the $S_1 \rightarrow S_0$ transition in HAP-3MF at the S_1 minimum.

Mode	Symmetry C_{3h}	Frequency [cm^{-1}]	NACME
13	A′	107.57	-0.016199
34	A′	373.94	0.016374
41	A′	500.39	0.011468
47	A′	568.81	0.010195
59	A′	651.91	-0.011899
110	A′	1324.66	-0.041613
114	A′	1375.71	-0.029828
122	A′	1450.45	0.012254
134	A′	1592.89	0.026079
135	A′	1598.29	-0.104239
138	A′	1636.67	-0.023678
139	A′	1659.98	0.013319

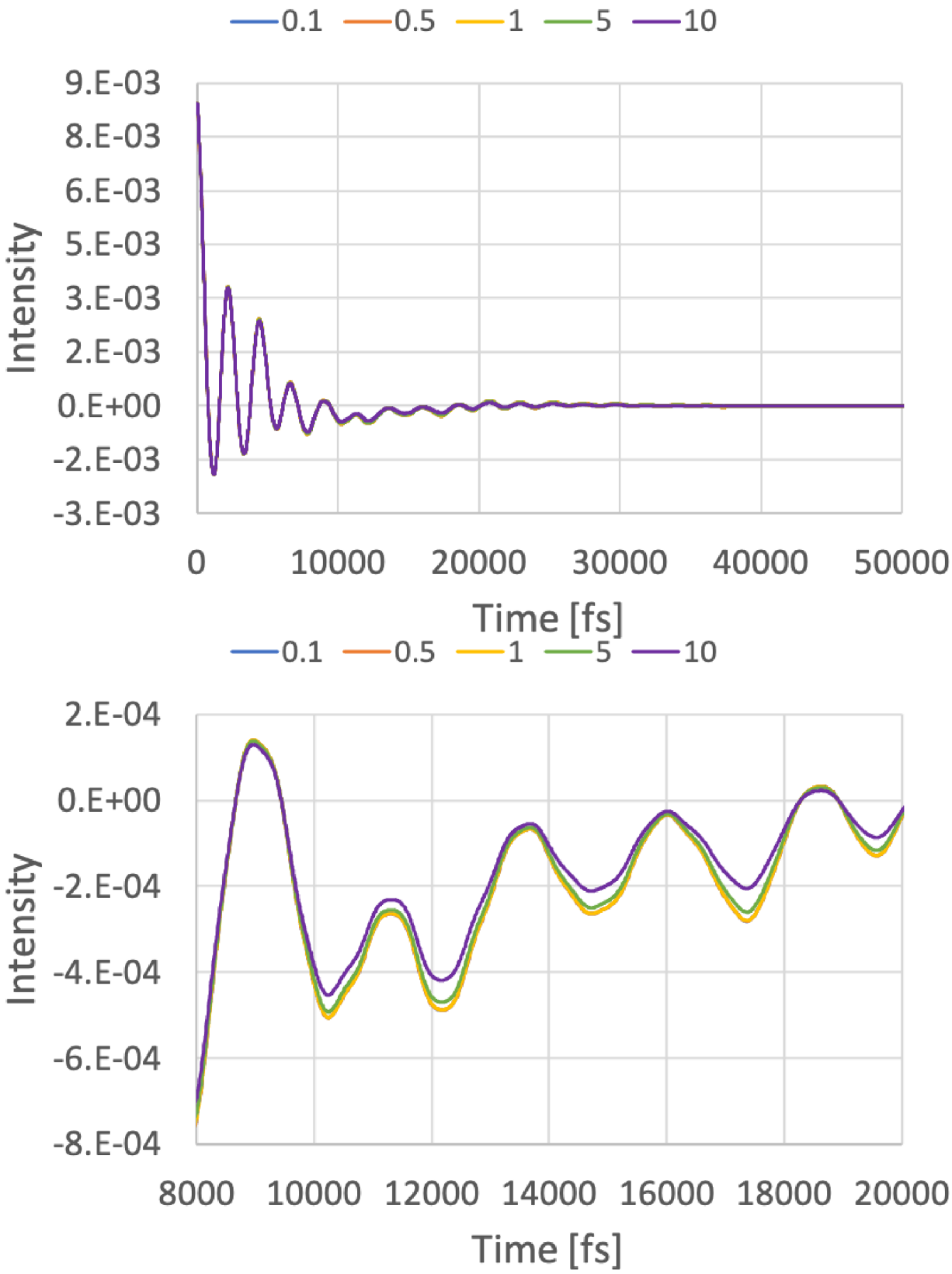

Figure S21: Correlation function of the $S_1 \rightsquigarrow T_1$ ISC transition of HAP-3MF computed with different correlation function dampings in the time interval 0-50 ps (upper panel) and 8-20 ps (lower panel).

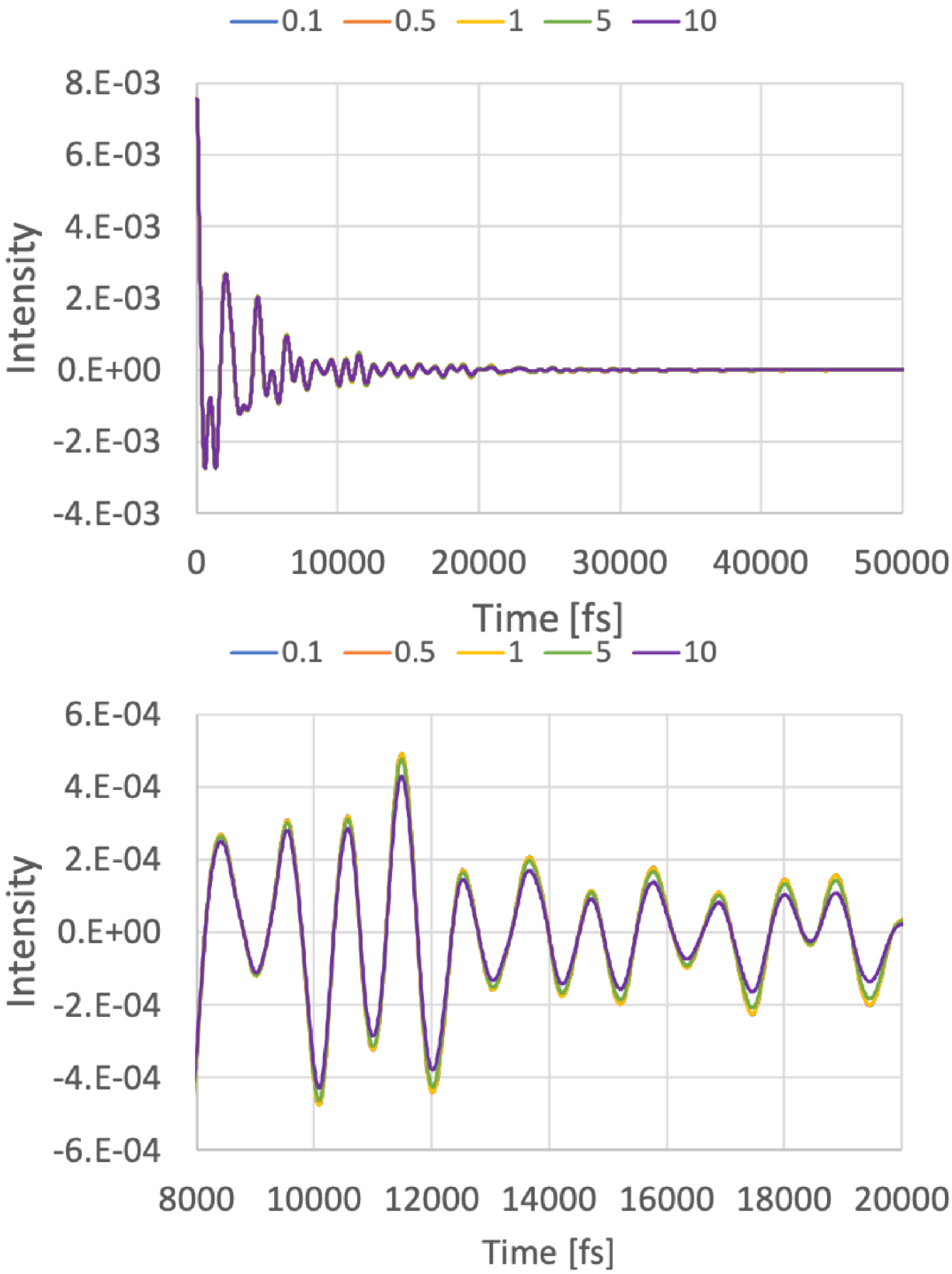

Figure S22: Correlation function of the $S_1 \backsim T_1$ RISC transition of HAP-3MF computed with different correlation function dampings in the time interval 0-50 ps (upper panel) and 8-20 ps (lower panel).

Table S21: ISC rate constants of HAP-3MF computed with different correlation function dampings.

Damping [cm^{-1}]	Rate Constant [s^{-1}]	Points	Time [fs]
10	7.68×10^6	65536	25000
5	7.42×10^6	65536	25000
1	7.33×10^6	65536	25000
0.5	7.33×10^6	262144	250000
0.1	7.33×10^6	262144	250000

Table S22: RISC rate constants of HAP-3MF computed with different correlation function dampings.

Damping [cm^{-1}]	Rate Constant [s^{-1}]	Points	Time [fs]
10	3.25×10^5	65536	25000
5	3.16×10^5	65536	25000
1	3.13×10^5	65536	25000
0.5	3.13×10^5	262144	250000
0.1	3.13×10^5	262144	250000

Table S23: IC rate constants of HAP-3MF computed with different correlation function dampings.

Damping [cm^{-1}]	Rate Constant [s^{-1}]	Points	Time [fs]
10	8.61×10^5	524288	25000
5	8.61×10^5	524288	25000
1	8.61×10^5	524288	25000
0.5	8.61×10^5	524288	25000
0.1	8.61×10^5	524288	25000

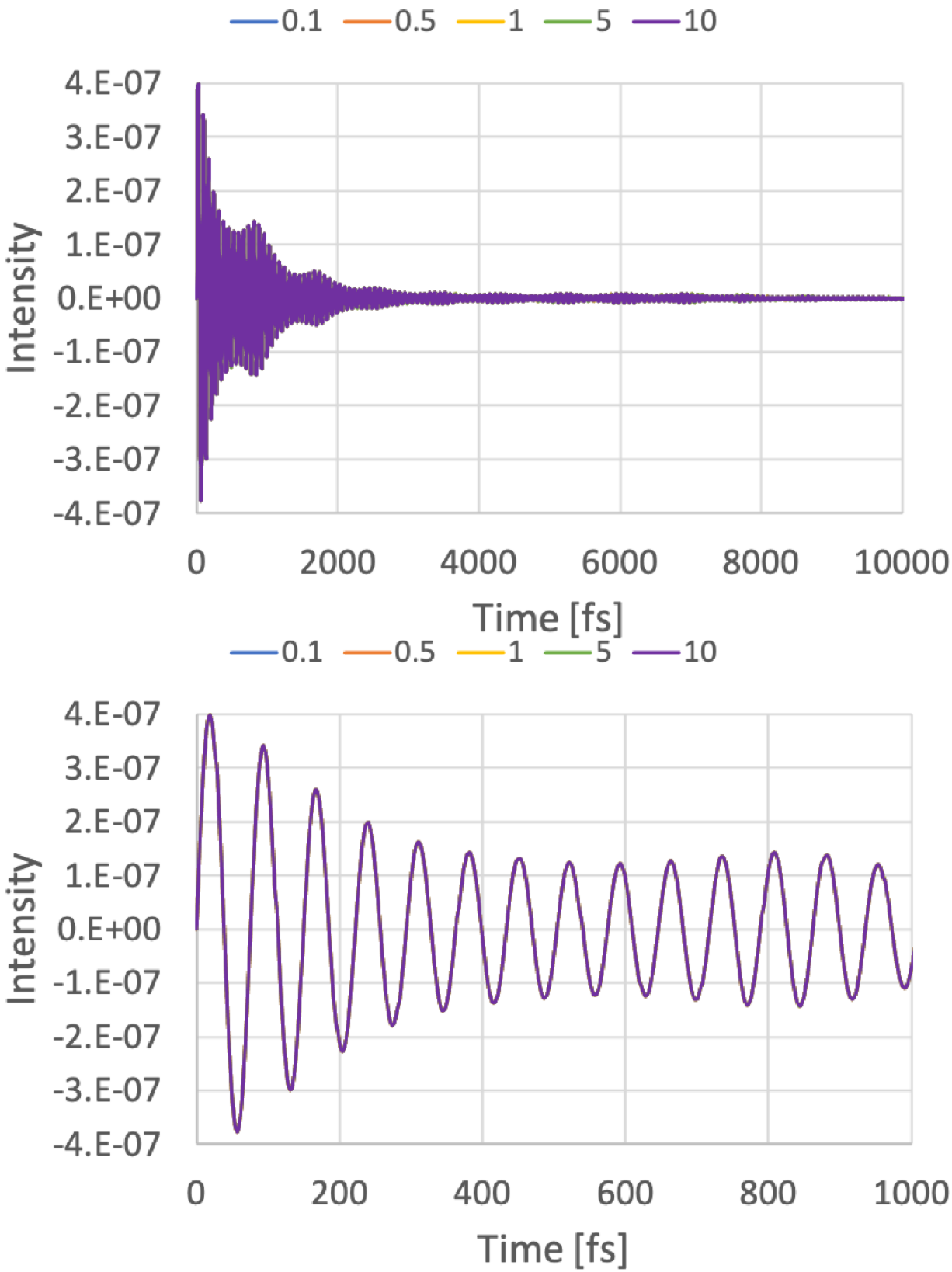

Figure S23: Correlation function of the $S_1 \rightsquigarrow S_0$ IC transition of HAP-3MF computed with different correlation function dampings in the time interval 0-10 ps (upper panel) and 0-1 ps (lower panel).

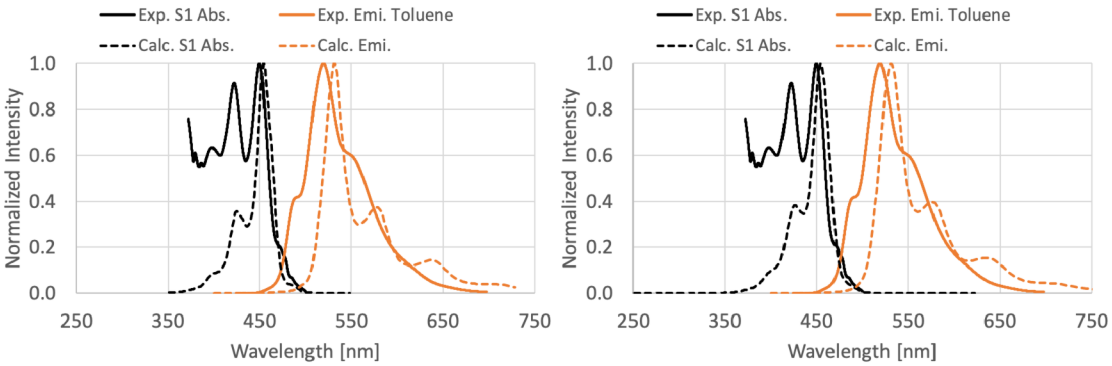

Figure S24: Herzberg–Teller $S_1 \leftarrow S_0$ absorption (black) and $S_1 \rightarrow S_0$ emission spectra (orange) of HAP-3MF computed with damping functions of 100 cm^{-1} (left) and 200 cm^{-1} (right) FWHM.

Table S24: Fluorescence rate constants of HAP-3MF computed with different correlation function dampings utilizing a grid of 16384 points and a integration time of 300 fs.

Damping [cm^{-1}]	Rate Constant [s^{-1}]
200	9.11×10^5
100	9.11×10^5
50	9.11×10^5

THE JOURNAL OF PHYSICAL CHEMISTRY LETTERS
A JOURNAL OF THE AMERICAN CHEMICAL SOCIETY

pubs.acs.org/JPCL

Letter

Acridones: Strongly Emissive HIGHrISC Fluorophores

Kristoffer A. Thom, Felix Wieser, Kevin Diestelhorst, Anna Reiffers, Constantin Czekelius, Martin Kleinschmidt, Mario Bracker, Christel M. Marian, and Peter Gilch*

Cite This: *J. Phys. Chem. Lett.* 2021, 12, 5703−5709

Read Online

ACCESS | Metrics & More | Article Recommendations | Supporting Information

ABSTRACT: An acridone derivative (*N*-methyl-difluoro-acridone, NMA-dF) is characterized with respect to its utility as an emitter in organic light emitting diodes (OLEDs). Using steady-state and time-resolved spectroscopy as well as quantum chemistry, its ability to convert singlet and triplet excitons into light was scrutinized. NMA-dF emits in the deep blue range of the visible spectrum. Its fluorescence emission occurs with quantum yields close to 1 and a radiative rate constant of $\approx 5 \times 10^8$ s^{-1}. So, it processes singlet excitons very efficiently. Using 1,4-dichlorobenzene as a sensitizer, it is shown that NMA-dF also converts triplet excitons into light. With the aid of quantum chemistry, this is related to a reverse intersystem crossing starting from a higher triplet state (HIGHrISC).

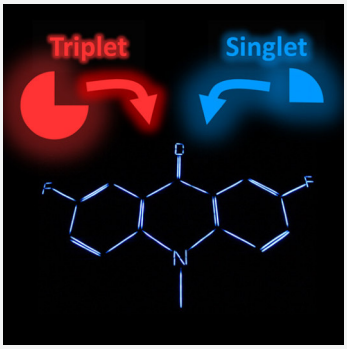

Present organic light emitting diodes (OLEDs) for the red and green regions of the visible spectrum mostly contain iridium complexes as emitters.[1,2] In an OLED, these complexes are excited via electron−hole recombination. Thereafter, they emit phosphorescence. They do so for excitation by triplet correlated electron−hole pairs (3/4 of all pairs) as well as singlet ones (1/4). In the latter case, the initial singlet excitation of the complex is rapidly converted to a triplet one by intersystem crossing (ISC). The large spin−orbit coupling in the iridium ion enables efficient ISC to this triplet state as well as phosphorescence originating from it. Phosphorescent complexes for the deep blue region of the visible spectrum (≈470 nm) have been described.[3] However, their chemical instability presently hampers their applications in OLEDs.[1,4,5] This as well as cost and environmental concerns[2] motivate the quest for alternative emitters.

These alternative emitters commonly make use of E-type delayed fluorescence[6] now often referred to as thermally activated delayed fluorescence (TADF).[7−9] TADF requires molecules with first excited singlet (S_1) and triplet (T_1) states in close energetic vicinity. Their energy gap ought to be of the order of the thermal energy k_bT. Further, provisions have to be made for rapid ISC transitions among these states.[10−12] Under these circumstances, population of the T_1 state by electron−hole recombination will be followed by reverse ISC (rISC) to the S_1 state. This state will then emit fluorescence. A small energy gap between the S_1 and the T_1 states, i.e., a small exchange interaction, requires a large separation of electron and hole densities in the excited state.[13] The relevant excited states of OLED emitters are, thus, charge transfer or charge shift ones. A consequence of that is commonly small radiative rate constants k_{rad} (cf. Figure 1a). Therefore, a trade-off is necessary between an energy gap small enough to allow for efficient rISC and for a high radiative rate constant. Efforts on this issue have already been made, and some emitters representing a good compromise have been reported.[13,14] However, another disadvantage of the TADF approach remains. The long lifetime of the delayed fluorescence in the microsecond range[15] renders deteriorating competing processes likely and limits the brightness of the emitter.

With molecules undergoing rISC starting from a *higher* triplet state $T_{n>1}$ (HIGHrISC) to the emissive S_1 state, which lies below the T_n one in terms of energy, no compromise between large rISC and radiative rate constants is necessary. In this approach, one may in principle select molecules with the largest possible radiative rate constants as emitters (Figure 1b). Additionally, the rISC process will be much faster than the following radiative decay and not lead to a delayed fluorescence. HIGHrISC emitters, thus, do not feature long lifetimes, which could give rise to nonradiative decay pathways. However, this immediately poses two challenges: (i) Can the HIGHrISC process compete with the internal conversion (IC) between the triplet states? (ii) Can a preferential population of the T_n state be achieved? Concerning challenge (i), from the 1960s onward there are sporadic indications in the literature that rISC from upper triplet states may lead to an enhanced

Received: April 28, 2021
Accepted: June 9, 2021
Published: June 14, 2021

https://doi.org/10.1021/acs.jpclett.1c01381
J. Phys. Chem. Lett. 2021, 12, 5703−5709

The Journal of Physical Chemistry Letters pubs.acs.org/JPCL Letter

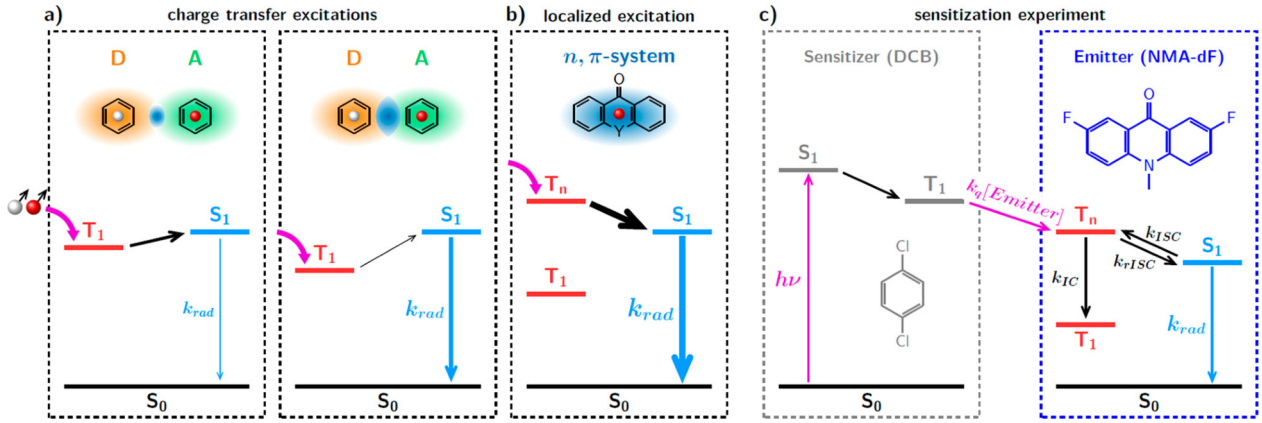

Figure 1. Scheme illustrating the potential advantage of emitters with HIGHrISC over TADF ones. The curved violet arrows symbolize the population of triplet states by electron hole pair recombination. (a) In a TADF emitter one aims at a small spatial overlap (marked in blue) of the hole density at the donor (D, orange) and the electron density at the acceptor (A, green). A small overlap results in a small singlet−triplet energy gap but commonly also in small radiative rate constants k_{rad}. (b) For locally excited emitters relying on rISC starting from a higher triplet state T_n the rate constant k_{rad} and the pertinent energy gap are not correlated. Such emitters ought to be studied by direct and sensitized excitation since the involvement of a T_n state might not be observable by direct excitation. (c) Jablonksi scheme of the sensitization experiment conducted. Photoexcitation of the sensitizer DCB is followed by efficient ISC. The energy of the DCB triplet state is transferred to the emitter. If HIGHrISC is possible, fluorescence emission can be observed.

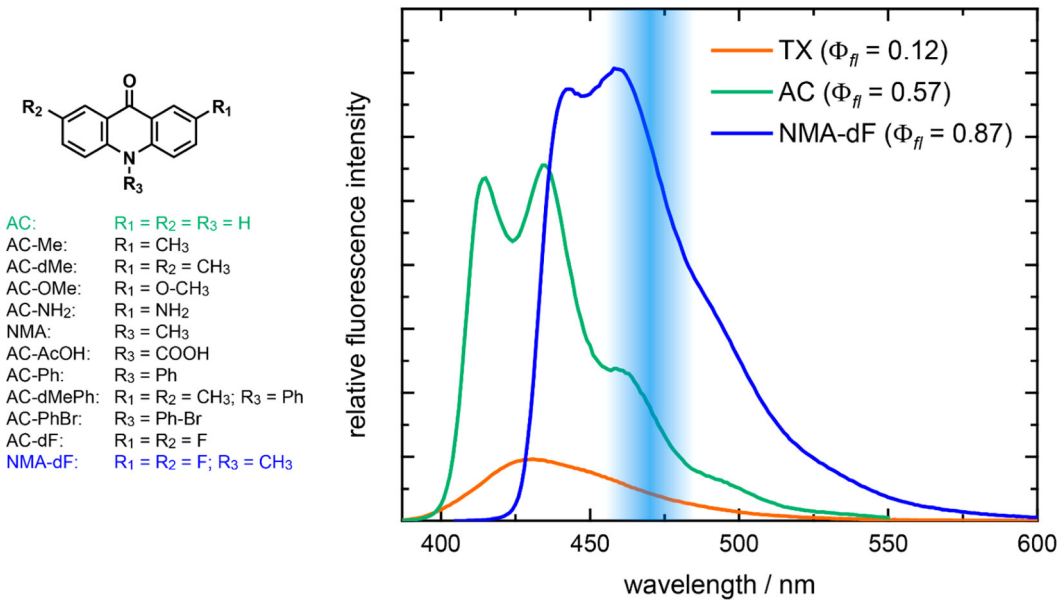

Figure 2. Acridones screened for their fluorescence properties. Fluorescence spectra in methanol for the parent compounds TX (orange) and acridone (AC, green) as well as for NMA-dF (blue) are compiled on the right. They are scaled to match their respective fluorescence quantum yields Φ_{fl}. The deep blue region is highlighted in blue.

fluorescence emission.[16,17] Yet, the relevant rate constants were not quantified. While in these studies molecules in solution were investigated, D. Hu et al. reported on emitters in OLEDs making use of HIGHrISC.[18,19] Their studies imply that both challenges can be coped with.

In a series of studies, we have shown that a simple ketone, namely, thioxanthone (TX), dissolved in protic solvents features interesting properties in that context.[20−23] By means of steady-state and time-resolved spectroscopy as well as quantum chemistry, the following photophysical behavior was revealed. The S_1 state of TX is a $^1\pi\pi^*$ one. In protic solvents, a $^3n\pi^*$ state (T_2) is isoenergetic with the S_1 one within k_bT.[22] Since the ISC transition and thereby also the rISC one are Elsayed allowed, the two states equilibrate within picoseconds.[21] The equilibration persists for nanoseconds. The depletion of the equilibrated states occurs via fluorescence, nonradiative ground state recovery, and IC to the lowest triplet state T_1. The validity of this model was checked by direct excitation[21] into the $^1\pi\pi^*$ state as well as by sensitized one[23] (cf. Figure 1c). The triplet excited sensitizer can be seen as a surrogate for the triplet correlated electron hole pair in an OLED. It should be stressed that the sensitizer is *not* supposed to play a role in an actual device. Instead, the upper triplet state is supposed to be populated by excitons directly. In the experiments described here, 1,4-dichlorobenzene (DCB) served as a triplet sensitizer. The photoexcitation of DCB results in a nearly quantitative

https://doi.org/10.1021/acs.jpclett.1c01381
J. Phys. Chem. Lett. 2021, 12, 5703−5709

population of its triplet state. In a diffusional process the energy of the DCB triplet can be transferred to the T_2 state of TX. Via the aforementioned equilibrium fluorescence emission results. The results have clearly shown that TX can convert singlet and triplet excitations into light. However, two molecular properties of TX render it not optimal as an OLED emitter. Its fluorescence quantum yield Φ_{fl} is way below of the maximal value of 1. In methanol, for instance, it amounts to ≈0.1.[21,24] Further, its emission occurs at around 430 nm and is thus outside the deep blue range.

Acridones are structurally closely related to TX. Yet, their fluorescence quantum yields are reported to be commonly higher. In particular, for *N*-methylacridone (NMA), Siegmund and Bendig reported a fluorescence quantum yield close to 1 in methanol solutions.[25] Furthermore, a quantum chemical study by Rai-Constapel and Marian[26] suggests that in acridones ISC and rISC occur on the picosecond time scale. A screening of several acridone derivatives (see below) revealed that the difluorinated compound, *N*-methyl-difluoro-acridone (NMA-dF), is a very promising chromophore regarding the fluorescence quantum yield and emission range. To connect with earlier studies on TX, for the present study we have selected this compound dissolved in methanol. In the following spectroscopic experiments comparison will be made between direct and sensitized excitation of NMA-dF. Experiments will be accompanied by quantum chemical computations. The results will show that this compound qualitatively behaves as TX. Yet, for acridone derivatives like NMA-dF, the photophysical parameters are more in favor for an OLED application.

The starting point of our investigation was a study by Siegmund and Bendig[25] on NMA. They report a fluorescence quantum yield Φ_{fl} close to 1 in methanol solutions. Our determination of the NMA quantum yield Φ_{fl} afforded somewhat smaller values (0.87 in methanol as opposed to 0.99 and 0.37 in acetonitrile as opposed to 0.55). These quantum yields were determined independently with coumarin 102 as well as POPOP as references. Furthermore, fluorescence lifetimes in combination with radiative rate constants retrieved via Strickler−Berg analysis could be successively used to crosscheck our values. We therefore assume a systematic error in the previous study based on the reference used.[27] However, NMA still features a much higher fluorescence quantum yield Φ_{fl} than TX as well as a small redshift of the emission band. Further screening was therefore undertaken on various commercially available as well as synthesized acridone derivatives (for structures see Figure 2). Inspired by a recent study on the impact of fluorination on the photophysics of the flavine chromophore,[28,29] fluorine-substituted acridone derivatives such as NMA-dF were synthesized as described in the Supporting Information (SI). Regarding fluorescence quantum yields and emission ranges, it turned out that NMA-dF is the most promising chromophore tested (Figure 2, right). In the following its photophysics will be investigated in depth.

The absorption band of NMA-dF in methanol (Figure 3) lowest in energy features a pronounced vibronic progression with peaks at 400 and 420 nm. The absorption is rather strong with absorption coefficients around 10 000 M^{-1} cm^{-1}. Emission occurs in the range between 400 and 550 nm with maxima at 443 and 459 nm, featuring CIE coordinates of (0.15, 0.10). The absorption and fluorescence spectra obey the mirror image rule. From the spectra a 0−0 energy of 23 148 cm^{-1} (2.87 eV) and a Stokes shift of 1180 cm^{-1} are retrieved. Via a Strickler−Berg analysis,[30,31] the radiative rate constant is estimated to be $k_{rad} \approx 5.4 \times 10^7$ s^{-1}.

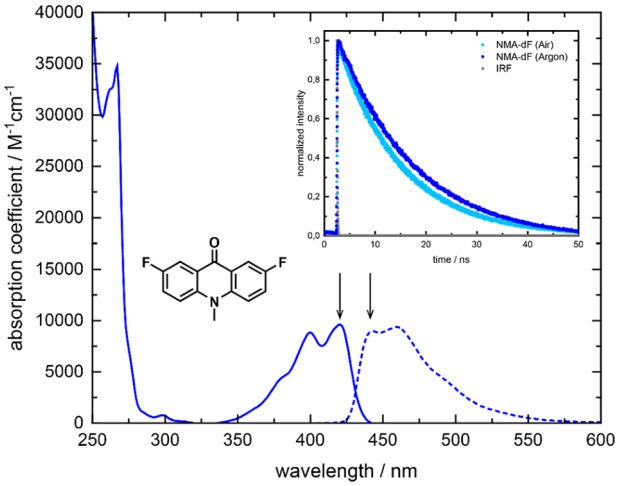

Figure 3. Absorption (coefficients, solid line) and fluorescence (constant wavelength bandpass, dashed line) spectra of NMA-dF in methanol. Inset: Fluorescence decay traces recorded by TCSPC. Excitation and detection wavelengths are marked in the spectra.

The fluorescence quantum yield Φ_{fl} of NMA-dF in methanol was measured with coumarin 102 (Φ_{fl} = 0.8 in ethanol[32,33]) as well as POPOP (0.85 in ethanol[34]) as references. Yields of 0.87 and 0.66 resulted in deoxygenized and air-saturated solutions, respectively. The fluorescence lifetime τ_{fl} of NMA-dF was determined by time-correlated single photon counting (TCSPC, Figure 3, inset) to be 15.0 ns in deoxygenized and 12.2 ns in air-saturated solution. With the measured lifetimes and the radiative rate constant determined via Strickler−Berg (see above) quantum yields, the Φ_{fl} values were crosschecked using eq 1.

$$\Phi_{fl} = k_{rad} \cdot \tau_{fl} \tag{1}$$

These yields are 0.81 for deoxygenized conditions and 0.66 for air. They are very close to the values obtained using the references. A dependence on the excitation wavelength was not found.

The fluorescence quantum yield Φ_{fl} being somewhat smaller than 1 indicates that nonradiative processes compete with the fluorescence emission. The quantum yield of the lowest triplet Φ_T as determined by nanosecond transient absorption spectroscopy (Figure S4, Supporting Information) amounts to 0.11 ± 0.03. Thus, nonradiative decay is mostly due to ISC.

For TX in methanol, it was shown by femtosecond transient absorption spectroscopy that the primarily excited S_1 state (a $^1\pi\pi^*$ one) equilibrates with the T_2 state (a $^3n\pi^*$ one) within picoseconds.[21] This equilibration results in a reduction of the spectrally integrated stimulated emission (see Figure 4; note the stimulated emission is a negative signal) on the picosecond time scale. The nanosecond decay later on is due to a concerted depletion of the equilibrated states. Conducting the same experiment on NMA-dF did not show any indications for the equilibration of the S_1 and a T_n state (Figure 4). The early increase in stimulated emission seen here is presumably due to dielectric relaxation.[35] This could either be caused by a much longer time constant for the equilibration or by a larger energetic spacing between the S_1 and T_n states in NMA-dF.

https://doi.org/10.1021/acs.jpclett.1c01381
J. Phys. Chem. Lett. 2021, 12, 5703−5709

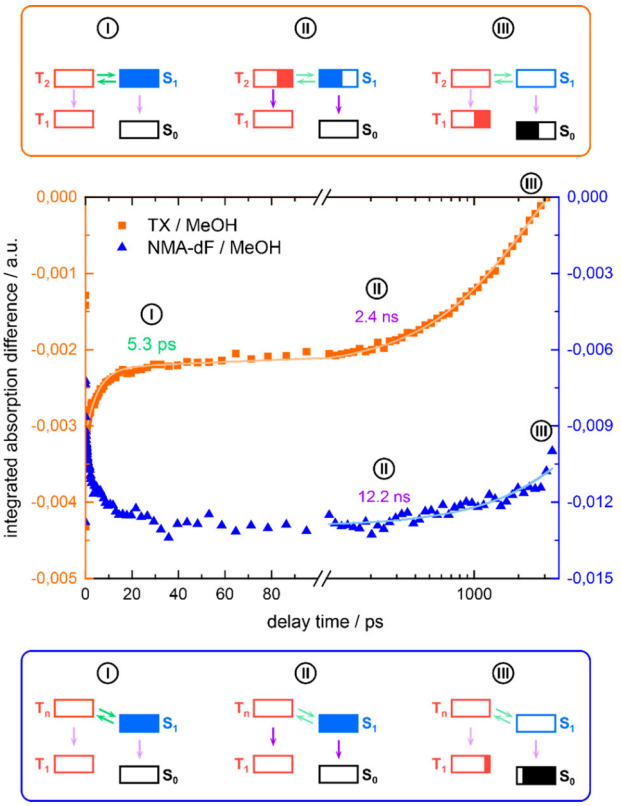

Figure 4. Decay of the stimulated emission of TX (orange) and NMA-dF (blue) dissolved in methanol. The solutions were excited at 400 nm by femtosecond laser pulses. Transient absorption spectra were spectrally integrated over ranges covering the stimulated emission (TX: 420 to 490 nm, NMA-dF: 450 to 520 nm) to obtain the depicted time traces. Boxes at the top and bottom illustrate the relative population of the lowest excited states.

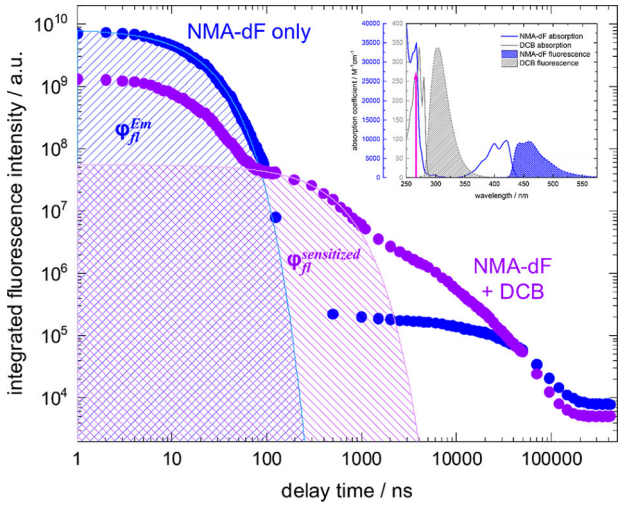

Figure 5. Triplet energy transfer between the sensitizer DCB and the emitter NMA-dF dissolved in methanol as evidenced by time-resolved emission spectroscopy. The spectrally integrated NMA-dF emission (integration range 410−625 nm) is plotted versus the delay time after excitation with 266 nm laser pulses. Note the bilogarithmic representation. Blue dots mark a measurement on an NMA-dF (0.24 mM) only solution, and purple dots represent the behavior after the addition of 0.3 M DCB. Filled areas below the solid lines are proportional to quantum yields φ_{fl}^{Em} and $\varphi_{fl}^{sensitized}$ entering the determination of the efficiency η (see text). Inset: Steady-state absorption and emission spectra. Emission spectra were scaled to match the height of the respective absorption band. The excitation wavelength at 266 nm is indicated.

The quantum chemical computations described below favor the latter interpretation.

The direct excitation experiment suggests that the T_n state of NMA-dF is not in energetic reach from the S_1 one. In an experiment with sensitized excitation, the T_n state can be accessible provided that the T_1 state of the sensitizer is energetically above the T_n state of the emitter. As outlined in ref 23, DCB is a promising sensitizer in that respect. Its T_1 0−0 energy amounts to 3.47 eV.[36] The S_1 0−0 energy of NMA-dF was determined to be 2.87 eV (see above). Therefore, provided that the T_n state of NMA-dF is located a couple of 0.1 eV above its S_1 state, a triplet energy transfer from DCB to this state should be exergonic. Evidence for this transfer is given by time-resolved emission spectroscopy. In this experiment, deoxygenated sample solutions were excited with 266 nm laser pulses. At this wavelength the DCB absorption lowest in energy is located. This band overlaps with a higher absorption band of the emitter NMA-dF. Thus, an exclusive excitation of the sensitizer is not possible (cf. Figure 5, inset). The emission induced by the laser pulses was traced by a gated CCD camera (Figure 5). The respective time traces represent spectral integrals covering the range of the NMA-dF fluorescence. This emission does not overlap with the one of the sensitizer (Figure 5, inset). The respective time trace for the NMA-dF only solution shows a decay at shorter delay times. Taking the instrumental response function into account, the decay may be fitted single-exponentially with a time constant of 16 ns. The value is in very good agreement with the TCSPC result (see above). It is attributed to the prompt NMA-dF fluorescence due to direct excitation. A second component with a lifetime of 12.4 μs is also observed. With reference to the respective behavior of TX,[23] this component is attributed to triplet−triplet annihilation (TTA). For TTA weakly contributing to the T_1 depletion the measured time constant ought to be half of the triplet lifetime τ_T.[6] So, the measured value implies a triplet lifetime of 24.8 μs. Nanosecond transient absorption measurements predict a lifetime of 29.5 μs for the concentration employed (cf. Figure S4, Supporting Information). Adding DCB to the NMA-dF solution reduces the amplitude of the prompt component due to the inner filter effect. From 100 ns onward, the emission in the presence of DCB is higher than the one in absence. An exponential fit of the additional component yielded a lifetime τ_{EET} of 390 ns for the energy transfer. At even longer times the signal remains higher compared to the NMA-dF only solution. As will be discussed later, this can be explained by an enhanced TTA. Spectra recorded after 100 ns and those recorded earlier are identical in shape to each other and to the stationary fluorescence spectra of NMA-dF (Figure S5, Supporting Information). Thus, NMA-dF holds responsible for the "early" and "late" emission. Since the S_1 lifetime of DCB (≈ 500 ps[23]) is much shorter, a singlet energy transfer can safely be excluded.

Instead, a triplet energy transfer starting from DCB followed by HIGHrISC must be operative. With reference to Figure 1c, the transfer time τ_{EET} can be related to the intrinsic T_1 decay of

https://doi.org/10.1021/acs.jpclett.1c01381
J. Phys. Chem. Lett. 2021, 12, 5703−5709

the sensitizer DCB, rate constant k_0^{Sens}, and the quenching constant k_q multiplied by the emitter concentration $[Emitter]$

$$\frac{1}{\tau_{EET}} = k_0^{Sens} + k_q \cdot [Emitter] \tag{2}$$

The rate constant k_0^{Sens} was determined by nanosecond transient absorption to be 4.5×10^5 s^{-1} ($\hat{=}$ 2.1 μs). No indications for concentration quenching were observed. Probing the T_1 state of NMA-dF, a rise component is observable (Figure S6, Supporting Information) in the transient absorption experiment. From the dependence of these time traces on the emitter concentration $[Emitter]$, a quenching constant $k_q = 9.8 \times 10^9$ M^{-1} s^{-1} is extracted. As this quenching process relies on the diffusional encounter of emitter and sensitizer, it is limited by the second-order diffusional rate constant k_{diff}. In methanol, the constant k_{diff} equals 1.1×10^{10} M^{-1} s^{-1}.[36] The measured value of k_q is close to that limit. Entering this value and the emitter concentration $[Emitter]$ = 0.24 mM employed in the time-resolved emission experiment into eq 2, an energy transfer time τ_{EET} of 360 ns is predicted. This is in good agreement with the experimental value (390 ns).

From the time traces in Figure 5, an efficiency $\eta < 1$ can be estimated. This efficiency relates the number of photons released by the emitter N_{Em}^{Em} upon energy transfer to the ones absorbed by the sensitizer N_{abs}^{Sens},

$$\eta = \frac{N_{Em}^{Em}}{N_{abs}^{Sens}} \tag{3}$$

An effective quantum yield of emitted photons due to the energy transfer $\varphi_{fl}^{Sensitized}$ can be determined from the fraction of light absorbed by the sensitizer (the absorptions of NMA-dF and DCB are denoted as A^{Em} and A^{Sens}, respectively) and the efficiency η, as well as the fluorescence quantum yield of the emitter φ_{fl}^{Em}:

$$\varphi_{fl}^{Sensitized} = \frac{A^{Sens}}{A^{Em} + A^{Sens}} \cdot \eta \cdot \varphi_{fl}^{Em} \tag{4}$$

The quantum yields φ_{fl}^{Em} and $\varphi_{fl}^{Sensitized}$ are proportional to the integrals marked in Figure 5. These integrals are given by the product of the respective amplitudes and lifetimes derived from fits. Entering these values into eq 4 yields an efficiency η of 0.17. A determination based on steady-state fluorescence spectra yields the same magnitude (cf. SI, Figure S7).

According to the kinetic scheme given in Figure 1c, the following equation can be derived for the efficiency η:

$$\eta = \Phi_T^{Sens} \cdot \frac{k_q[Emitter]}{k_0^{Sens} + k_q[Emitter]} \cdot \eta_\infty \tag{5}$$

The triplet quantum yield Φ_T^{Sens} of the sensitizer DCB amounts to 0.95.[36] The second term parametrizes the branching between the triplet decay of the sensitizer by quenching, rate constant $k_q[Emitter]$, and its intrinsic decay, rate constant k_0^{Sens}. The efficiency η_∞ is the efficiency measured for infinitely high emitter concentrations $[Emitter]$ and is thus independent of the diffusional process. It quantifies the fraction of quenching events resulting in an S_1 excitation of the emitter NMA-dF. This efficiency η_∞ amounts to ≈0.25. The increased TTA amplitude observed in the sensitization experiment (cf. Figure 5) and a rise component in the respective transient absorption experiment (see Figure S6, Supporting Information) indicate that the fraction $1 - \eta_\infty$ ends up in the T_1 state of NMA-dF.

Two limiting scenarios may explain why η_∞ is smaller than 1 (Figure 6): (i) All energy transfer events end up in T_n states of the emitter. The rISC process to the emissive S_1 state would then occur in competition with the IC process populating the T_1 state. Therefore, a part of the population would be lost for emission due to this IC process. In scenario (ii), a branching occurs during the energy transfer processes starting in the T_1 state of the sensitizer. A part of the population (fraction η_∞) ends up in the T_n states and the rest (fraction $1 - \eta_\infty$) in the T_1 state of NMA-dF. Quantum chemical computations (for details, see the SI) on NMA-dF dissolved in methanol favor scenario (i). The computations place the 0−0 energy of the S_1 ($^1\pi\pi^*$) state at 2.93 eV. This compares favorably with the experimental values of 2.87 eV. For its radiative decay a rate constant of 5.4×10^7 s^{-1} (oscillator strength of 0.1466) was computed, in good agreement to the experimental one. The T_1 ($^3\pi\pi^*$) origin lies at 2.28 eV. The T_1 state can therefore not contribute to a delayed fluorescence. Two higher triplet states are accessible from the T_1 state (3.47 eV)[36] of the sensitizer DCB. One ($^3\pi\pi^*_2$) is a higher $^3\pi\pi^*$ state with a 0−0 energy of 3.17 eV. The other one is the lowest $^3n\pi^*$ state. Its 0−0 energy amounts to 3.38 eV. These energies are in accordance with the experimental finding that upon S_1 excitation no equilibration between the S_1 and higher triplet states is observable. The computation separates the two upper triplet states energetically by only 0.2 eV. In view of the confidence interval of the DFT/MRCI method (±0.2 eV) and the crude solvent model

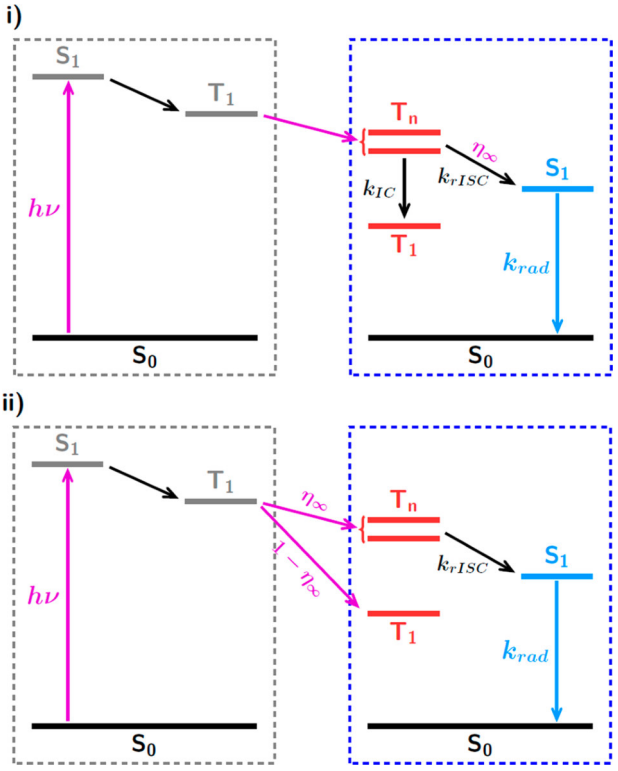

Figure 6. Scenarios explaining why the efficiency η_∞ is smaller than 1. In scenario (i), the T_n states of the emitter decay via IC and ISC. In scenario (ii), the T_n and T_1 states of the emitter are populated during the energy transfer from the sensitizer.

https://doi.org/10.1021/acs.jpclett.1c01381
J. Phys. Chem. Lett. 2021, 12, 5703−5709

employed (see the SI for details), a different ordering (the $^3n\pi^*$ state being the lower one) cannot be excluded. The computed rate constant k_{rISC} for the El-Sayed forbidden transition $^3\pi\pi^*_2 \rightarrow S_1$ equals 6×10^9 s^{-1}. The competing IC process $^3\pi\pi^*_2 \rightarrow {}^3\pi\pi^*$ has a rate constant k_{IC} of 5×10^{12} s^{-1}. So, only a fraction of 10^{-3} of the population in the $^3\pi\pi^*_2$ state ought to end up in the S_1 state. For the $^3n\pi^*$ state, the El-Sayed allowed transition $^3n\pi^* \rightarrow S_1$ occurs with a rate constant k_{rISC} of 7×10^{10} s^{-1}. The IC process $^3n\pi^* \rightarrow {}^3\pi\pi^*$ has a rate constant k_{IC} of 4×10^{10} s^{-1}. Here, a fraction of ≈0.6 of the population in the $^3n\pi^*$ state is expected to transition to the S_1 state. This fraction is of similar magnitude as the efficiency η_∞. Note, however, that the $^3n\pi^*$ state is predicted to decay to the $^3\pi\pi^*_2$ state at the subpicosecond time scale in the case that the $^3n\pi^*$ state is the upper state. These finding contradict the experimental observation that the S_1 state is populated from one of the upper triplet states. Within scenario (i), the value of the efficiency η_∞ is rationalized as follows. In the course of the energy transfer from the sensitizer, the $^3\pi\pi^*_2$ and $^3n\pi^*$ states of NMA-dF get populated. These two states equilibrate on the femtosecond time scale. Provided that the $^3n\pi^*$ state is the lower one of the two, a branching ratio close to the experimental value is obtained. From this we infer that the T_2 state is indeed a $^3n\pi^*$ one. A direct population of the T_1 state of NMA-dF in the course of the energy transfer (scenario (ii)) might also play a certain role. It seems to be less relevant than in TX.[23,37] For TX, the respective energy gap between the DCB T_1 state and TX T_1 state is smaller and has therefore more favorable Franck−Condon factors.

Concerning the application of NMA-dF as an emitter in OLEDs, the present study has shown that the chromophore can convert singlet and triplet excitons into light. If NMA-dF accepts energy from a singlet-correlated electron−hole pair, its S_1 state will emit photons efficiently (fluorescence quantum yield Φ_{fl} of ≈0.9) and rapidly (fluorescence lifetime of $\tau_{fl} \approx 15$ ns). If a triplet-correlated electron−hole pair provides the energy and T_n states are accessed, some (a fraction of ≈0.5) of the excitations will be converted into photons. For a transfer to the T_1 state, however, the excitation energy will be lost. If and how OLED host materials may be designed to ensure predominant transfer to the "right" T_n state remains to be seen (for a recent overview on our understanding of transfer processes to the host and emitter, see ref 38). OLED applications aside, NMA-dF might also serve as a potent intracellular triplet sensor. Presently, derivatives of 9,10-dibromoanthracene serve this purpose.[39,40] NMA-dF lacking the bromines of 9,10-dibromoanthracene might feature a higher photostability.

■ ASSOCIATED CONTENT

Supporting Information

The Supporting Information is available free of charge at https://pubs.acs.org/doi/10.1021/acs.jpclett.1c01381.

Experimental procedures, characterization data, computational details, and supplementary figures (PDF)

■ AUTHOR INFORMATION

Corresponding Author

Peter Gilch − *Institut für Physikalische Chemie, Heinrich-Heine-Universität Düsseldorf, 40225 Düsseldorf, Germany;* orcid.org/0000-0002-6602-9397; Email: gilch@hhu.de

Authors

Kristoffer A. Thom − *Institut für Physikalische Chemie, Heinrich-Heine-Universität Düsseldorf, 40225 Düsseldorf, Germany*

Felix Wieser − *Institut für Physikalische Chemie, Heinrich-Heine-Universität Düsseldorf, 40225 Düsseldorf, Germany*

Kevin Diestelhorst − *Institut für Physikalische Chemie, Heinrich-Heine-Universität Düsseldorf, 40225 Düsseldorf, Germany*

Anna Reiffers − *Institut für Physikalische Chemie, Heinrich-Heine-Universität Düsseldorf, 40225 Düsseldorf, Germany*

Constantin Czekelius − *Institut für Organische Chemie und Makromolekulare Chemie, Heinrich-Heine-Universität Düsseldorf, 40225 Düsseldorf, Germany;* orcid.org/0000-0002-2814-8686

Martin Kleinschmidt − *Institut für Theoretische Chemie und Computerchemie, Heinrich-Heine-Universität Düsseldorf, 40225 Düsseldorf, Germany*

Mario Bracker − *Institut für Theoretische Chemie und Computerchemie, Heinrich-Heine-Universität Düsseldorf, 40225 Düsseldorf, Germany*

Christel M. Marian − *Institut für Theoretische Chemie und Computerchemie, Heinrich-Heine-Universität Düsseldorf, 40225 Düsseldorf, Germany;* orcid.org/0000-0001-7148-0900

Complete contact information is available at: https://pubs.acs.org/10.1021/acs.jpclett.1c01381

Notes

The authors declare no competing financial interest.

■ ACKNOWLEDGMENTS

We thank our former bachelor student Abdulrahman Mohabbat for experimental support. Financial support by the Deutsche Forschungsgemeinschaft (396890929/GRK 2482) is gratefully acknowledged.

■ REFERENCES

(1) Lee, J.-H.; Chen, C.-H.; Lee, P.-H.; Lin, H.-Y.; Leung, M.-k.; Chiu, T.-L.; Lin, C.-F. Blue Organic Light-Emitting Diodes: Current Status, Challenges, and Future Outlook. *J. Mater. Chem. C* **2019**, *7*, 5874−5888.

(2) Volz, D.; Wallesch, M.; Fléchon, C.; Danz, M.; Verma, A.; Navarro, J. M.; Zink, D. M.; Bräse, S.; Baumann, T. From Iridium and Platinum to Copper and Carbon: New Avenues for More Sustainability in Organic Light-Emitting Diodes. *Green Chem.* **2015**, *17*, 1988−2011.

(3) Minaev, B.; Baryshnikov, G.; Agren, H. Principles of Phosphorescent Organic Light Emitting Devices. *Phys. Chem. Chem. Phys.* **2014**, *16*, 1719−1758.

(4) Miao, Y.; Tao, P.; Gao, L.; Li, X.; Wei, L.; Liu, S.; Wang, H.; Xu, B.; Zhao, Q. Highly Efficient Chlorine Functionalized Blue Iridium-(III) Phosphors for Blue and White Phosphorescent Organic Light-Emitting Diodes with the External Quantum Efficiency Exceeding 20%. *J. Mater. Chem. C* **2018**, *6*, 6656−6665.

(5) Wong, M. Y.; Zysman-Colman, E. Purely Organic Thermally Activated Delayed Fluorescence Materials for Organic Light-Emitting Diodes. *Adv. Mater.* **2017**, *29*, 1605444.

(6) Klán, P.; Wirz, J. *Photochemistry of Organic Compounds: From Concepts to Practice*; Wiley-Blackwell: Chichester, 2009.

(7) Endo, A.; Sato, K.; Yoshimura, K.; Kai, T.; Kawada, A.; Miyazaki, H.; Adachi, C. Efficient up-Conversion of Triplet Excitons into a Singlet State and Its Application for Organic Light Emitting Diodes. *Appl. Phys. Lett.* **2011**, *98*, 083302.

https://doi.org/10.1021/acs.jpclett.1c01381
J. Phys. Chem. Lett. 2021, 12, 5703−5709

(8) Uoyama, H.; Goushi, K.; Shizu, K.; Nomura, H.; Adachi, C. Highly Efficient Organic Light-Emitting Diodes from Delayed Fluorescence. *Nature* **2012**, *492*, 234−238.
(9) Dias, F. B; Penfold, T. J; Monkman, A. P Photophysics of Thermally Activated Delayed Fluorescence Molecules. *Methods Appl. Fluoresc.* **2017**, *5*, 012001.
(10) dos Santos, P. L.; Etherington, M. K.; Monkman, A. P. Chemical and Conformational Control of the Energy Gaps Involved in the Thermally Activated Delayed Fluorescence Mechanism. *J. Mater. Chem. C* **2018**, *6*, 4842−4853.
(11) Penfold, T. J.; Gindensperger, E.; Daniel, C.; Marian, C. M. Spin-Vibronic Mechanism for Intersystem Crossing. *Chem. Rev.* **2018**, *118*, 6975−7025.
(12) Marian, C. M. Mechanism of the Triplet-to-Singlet Upconversion in the Assistant Dopant ACRXTN. *J. Phys. Chem. C* **2016**, *120*, 3715−3721.
(13) Shizu, K.; Tanaka, H.; Uejima, M.; Sato, T.; Tanaka, K.; Kaji, H.; Adachi, C. Strategy for Designing Electron Donors for Thermally Activated Delayed Fluorescence Emitters. *J. Phys. Chem. C* **2015**, *119*, 1291−1297.
(14) Miwa, T.; Kubo, S.; Shizu, K.; Komino, T.; Adachi, C.; Kaji, H. Blue Organic Light-Emitting Diodes Realizing External Quantum Efficiency over 25% Using Thermally Activated Delayed Fluorescence Emitters. *Sci. Rep.* **2017**, *7*, 284.
(15) Dias, F. B. Kinetics of Thermal-Assisted Delayed Fluorescence in Blue Organic Emitters with Large Singlet-Triplet Energy Gap. *Philos. Trans. R. Soc., A* **2015**, *373*, 20140447.
(16) Keller, R. A. Excited Triplet−Singlet Intersystem Crossing. *Chem. Phys. Lett.* **1969**, *3*, 27−29.
(17) Catalani, L. H.; Wilson, T. Energy Transfer from Triplet Acetophenones to 9,10-Dibromoanthracene (S1): Role of Its Tn State. *J. Am. Chem. Soc.* **1987**, *109*, 7458−7462.
(18) Hu, D.; Yao, L.; Yang, B.; Ma, Y. Reverse Intersystem Crossing from Upper Triplet Levels to Excited Singlet: A 'Hot Excition' Path for Organic Light-Emitting Diodes. *Philos. Trans. R. Soc., A* **2015**, *373*, 20140318.
(19) Xu, Y.; Xu, P.; Hu, D.; Ma, Y. Recent Progress in Hot Exciton Materials for Organic Light-Emitting Diodes. *Chem. Soc. Rev.* **2021**, *50*, 1030.
(20) Wöll, D.; Laimgruber, S.; Galetskaya, M.; Smirnova, J.; Pfleiderer, W.; Heinz, B.; Gilch, P.; Steiner, U. E. On the Mechanism of Intramolecular Sensitization of Photocleavage of the 2-(2-Nitrophenyl)Propoxycarbonyl (NPPOC) Protecting Group. *J. Am. Chem. Soc.* **2007**, *129*, 12148−12158.
(21) Villnow, T.; Ryseck, G.; Rai-Constapel, V.; Marian, C. M.; Gilch, P. Chimeric Behavior of Excited Thioxanthone in Protic Solvents: I. Experiments. *J. Phys. Chem. A* **2014**, *118*, 11696−11707.
(22) Rai-Constapel, V.; Villnow, T.; Ryseck, G.; Gilch, P.; Marian, C. M. Chimeric Behavior of Excited Thioxanthone in Protic Solvents: II. *J. Phys. Chem. A* **2014**, *118*, 11708−11717.
(23) Torres Ziegenbein, C.; Fröbel, S.; Glöß, M.; Nobuyasu, R. S.; Data, P.; Monkman, A.; Gilch, P. Triplet Harvesting with a Simple Aromatic Carbonyl. *ChemPhysChem* **2017**, *18*, 2314−2317.
(24) Dalton, J. C.; Montgomery, F. C. Solvent Effects on Thioxanthone Fluorescence. *J. Am. Chem. Soc.* **1974**, *96*, 6230−6232.
(25) Siegmund, M.; Bendig, J. Die Temperatur-und Lösungs-mittel abhängigkeit der Fluoreszenzquantenausbeuten von N-substituierten Acridonen. *Ber. Bunsenges. Phys. Chem.* **1978**, *82*, 1061−1068.
(26) Rai-Constapel, V.; Marian, C. M. Solvent Tunable Photophysics of Acridone: A Quantum Chemical Perspective. *RSC Adv.* **2016**, *6*, 18530−18537.
(27) This difference might have its cause in the references used. Siegmund and Bendig used 0.83 as the quantum yield of 9,10-diphenylanthracene in hexane. Unfortunately, the cited reference does not mention this value; instead several divergent values published earlier are compiled and concluded that 9,10-diphenylanthracene "does not suit as a reference".
(28) Reiffers, A.; Torres Ziegenbein, C.; Engelhardt, A.; Kühnemuth, R.; Gilch, P.; Czekelius, C. Impact of Mono-Fluorination on the Photophysics of the Flavin Chromophore. *Photochem. Photobiol.* **2018**, *94*, 667−676.
(29) Bracker, M.; Dinkelbach, F.; Weingart, O.; Kleinschmidt, M. Impact of Fluorination on the Photophysics of the Flavin Chromophore: A Quantum Chemical Perspective. *Phys. Chem. Chem. Phys.* **2019**, *21*, 9912−9923.
(30) Strickler, S.; Berg, R. Relationship between Absorption Intensity and Fluoresence Lifetime of Molecules. *J. Chem. Phys.* **1962**, *37*, 814−822.
(31) Parson, W. W. *Modern Optical Spectroscopy*, Student edition; Springer: Dordrecht, Heidelberg, London, New York, 2009.
(32) Dobek, K.; Karolczak, J.; Kubicki, J. Temperature Effects on Excitation and Deactivation Processes of Coumarin 102. A Comparison with Coumarin 153. *Dyes Pigm.* **2014**, *100*, 222−231.
(33) Rurack, K.; Spieles, M. Fluorescence Quantum Yields of a Series of Red and near-Infrared Dyes Emitting at 600−1000 Nm. *Anal. Chem.* **2011**, *83*, 1232−1242.
(34) Mardelli, M.; Olmsted, J. Calorimetric Determination of the 9,10-Diphenyl-Anthracene Fluorescence Quantum Yield. *J. Photochem.* **1977**, *7*, 277−285.
(35) Bagchi, B.; Jana, B. Solvation Dynamics in Dipolar Liquids. *Chem. Soc. Rev.* **2010**, *39*, 1936−1954.
(36) Montalti, M.; Credi, A.; Prodi, L.; Gandolfi, T. *Handbook of Photochemistry*, 3rd ed.; Taylor & Francis: Boca Raton, FL, 2006.
(37) Northey, T.; Keane, T.; Eng, J.; Penfold, T. J. Understanding the Potential for Efficient Triplet Harvesting with Hot Excitons. *Faraday Discuss.* **2019**, *216*, 395−413.
(38) Eng, J.; Penfold, T. J. Understanding and Designing Thermally Activated Delayed Fluorescence Emitters: Beyond the Energy Gap Approximation. *Chem. Rec.* **2020**, *20*, 831−856.
(39) Catalani, L. H.; Wilson, T.; Bechara, E. J. H. Two Water-Soluble Fluorescence Probes for Chemiexcitation Studies: Sodium 9,10-Dibromo- and 9, 10-Diphenylanthracene-2-Sulfonate. Synthesis, Properties and Application to Triplet Acetone and Tetramethyldioxetane. *Photochem. Photobiol.* **1987**, *45*, 273−281.
(40) Premi, S.; Wallisch, S.; Mano, C. M.; Weiner, A. B.; Bacchiocchi, A.; Wakamatsu, K.; Bechara, E. J. H.; Halaban, R.; Douki, T.; Brash, D. E. Chemiexcitation of Melanin Derivatives Induces DNA Photoproducts Long after UV Exposure. *Science* **2015**, *347*, 842−847.

https://doi.org/10.1021/acs.jpclett.1c01381
J. Phys. Chem. Lett. 2021, 12, 5703−5709

Acridones: Strongly Emissive HIGHrISC Fluorophores

Supporting Information

Kristoffer A. Thom,[1] Felix Wieser,[1] Kevin Diestelhorst,[1] Anna Reiffers,[1] Constantin Czekelius,[2] Martin Kleinschmidt,[3] Mario Bracker,[3] Christel M. Marian,[3] and Peter Gilch[1*]

[1]Institut für Physikalische Chemie, Heinrich-Heine-Universität Düsseldorf, Universitätsstr. 1, 40225 Düsseldorf, Germany

[2]Institut für Organische Chemie und Makromolekulare Chemie, Heinrich-Heine-Universität Düsseldorf, Universitätsstr. 1, 40225 Düsseldorf, Germany

[3]Institut für Theoretische Chemie und Computerchemie, Heinrich-Heine-Universität Düsseldorf, Universitätsstr. 1, 40225 Düsseldorf, Germany

*E-mail: gilch@hhu.de

Contents

1. Experimental procedures

Samples

NMA, TX (97%) and thymidine (≥ 99.0%) were purchased from Sigma-Aldrich. DCB (> 99.0%) and AC (> 98.0%) were supplied by TCI. Coumarin 102 and 1,4-bis(5-phenyloxazol-2-yl)-benzene (POPOP) were purchased from Radiant Dyes Laser. The solvents used for spectroscopic experiments were of HPLC gradient grade. All commercially available chemicals were used as received.

Common conditions

All measurements were carried out at room temperature (≈ 20 °C). Except for steady-state absorption and femtosecond transient absorption spectra all sample solutions were deoxygenized by purging them prior to and during the experiments with argon or nitrogen (Air Liquide, 99.999 %). Gases were saturated with the corresponding solvent to prevent concentration changes of the sample solutions. Unless stated otherwise fused silica cells (Hellma Analytics) with d = 1 cm path length were used. Sample solutions were pumped through flow cells to avoid signal contributions of photo-products.

Steady-state spectroscopy

Absorption spectra were recorded with a two-beam Lambda 19 spectrometer (Perkin Elmer). Steady-state fluorescence spectra were obtained on a FluoroMax-4 from HORIBA Scientific. All spectra were corrected for the spectral sensitivity of the instruments.

Fluorescence data on DCB were acquired using a home-build Kerr-setup[1] due to its higher sensitivity in the UV region. The sample was excited at 267 nm and pumped through a 1 mm flow cell. The fluorescence light passed the Kerr gate in its open state (parallel polarizers) in 180° geometry. The spectral sensitivity of the instrument was corrected for. To determine the fluorescence quantum yield of DCB, thymidine served as reference (Φ_{fl} = 10^{-4} in water[2]).

CIE coordinates were determined using a Qmini Wide VIS spectrometer (RGB Photonics) while irradiating the sample with a hand-held UV lamp at 385 nm.

Correction of steady-state fluorescence spectra

In the steady-state sensitization experiments described in this study, absorptions were employed for which a linear relation between fluorescence and absorption breaks down. Therefore, a calibration curve was recorded with the same instrumental settings (λ_{exc} = 266 nm, spectral bandpass of 1 nm for both, excitation and emission) as in the actual experiments. The calibration curve was acquired by measuring various solutions with different absorptions and plotting the spectrally integrated fluorescence signals S_{int} as a function of the absorption A. For solutions with A/d < 0.1 / cm the signal increases almost linear with the absorption while for higher optical densities the signal grows slower showing a peak intensity for optical densities ≈ 0.9 / cm. For even higher values the fluorescence signal decreases due to the inner filter effect. This behavior was fitted with a trial function adapted from ref. [3].

$$S_{int}(A) = f \cdot \left[10^{-\frac{A}{d}\left(x_m - \frac{\Delta x}{2}\right)} - 10^{-\frac{A}{d}\left(x_m + \frac{\Delta x}{2}\right)}\right] \quad \text{(S1)}$$

Herein, f is a scaling factor and A the absorption of the solution for complete light passage of a cuvette with thickness d = 1 cm. For the right-angle geometry employed here, fluorescence emission originating from the center of the cuvette located at x_m ought to dominate the signal. The width of the region contributing is denoted Δx. The fit yields 0.49 cm and 0.16 cm for x_m and Δx, respectively. Fluorescence spectra obtained in the sensitization experiments were corrected by dividing them by the right-hand side of eq. S1. Hereby, the total absorption given by the sum of NMA-dF and DCB contributions was inserted as A.

Time-resolved fluorescence spectroscopy

Time-correlated single photon counting was performed on a FluoTime 300 (PicoQuant) with a supercontinuum picosecond laser (SuperK Extreme and SuperK Extend-UV, NKT Photonics) as excitation source running at 19.5 MHz. Emission was detected under magic angle conditions until a peak value of 10 000 counts was achieved. The sample solution featured an optical density of < 0.1 / cm at the excitation wavelength.

Time-resolved fluorescence data on longer time scales were obtained with a home-built setup. A pulsed Nd:YAG laser (Spitlight 600, Innolas) tuned to 266 nm served as excitation source, providing pulses of 12 ns FWHM at a repetition rate of 10 Hz. At the sample location the laser light featured an energy per pulse of 125 µJ and a diameter of 0.5 mm. The emitted fluorescence light was collected at 54° before being dispersed in a spectrograph (SpectraPro 308, Acton Research) with a custom grating blazed at 410 nm (121.6 l/mm) and detected by a gated iCCD camera (PI-MAX, Princeton Instruments). The delay between excitation and detection was controlled electronically (PTG, Princeton Instruments) and enabled delay times from the nanosecond to millisecond regime. To achieve proper signal intensities even at long delay times the integration time of the detector as well as the number of accumulations were increased for longer delay times. Furthermore, signals were amplified by raising the gain voltage of the microchannel plate. The signals of those pixel rows of the CCD chip on which the fluorescence light impinged on were added up (200 rows) and the resulting spectra were spectrally integrated over the emission band of interest. To correct for different baselines the integrated signals recorded at another 200 pixel rows of the CCD chip where no fluorescence light impinged onto were subtracted from the raw data points. Finally, the pre-corrected data points were divided by the number of accumulations and by the integration time applied. Compensation for different gain voltage was accomplished by acquiring a calibration curve with same instrumental settings at different gain voltages U_{MCP}. An exponential dependence according to eq. S2 between the fluorescence intensity S_{int} and the amplification was found.

$$S_{int}(U_{MCP}) = a \cdot e^{b \cdot U_{MCP}} \tag{S2}$$

For NMA-dF in methanol a = 1 041 263 and b = 0.01564 resulted with U_{MCP} ranging from 0 to 255. Correction of this dependence was achieved by dividing each data point by the right-hand-side of eq. S2.

Nanosecond flash photolysis

Nanosecond transient absorption data were acquired with a LKS.60 spectrometer from Applied Photophysics in a right-angle geometry. A Nd:YAG laser (Spitlight 600, Innolas) with a repetition rate of 1 Hz and a pulse duration of 12 ns (FWHM) served as the excitation source. The output wavelength was frequency-quadrupled to 266 nm. The average pulse energy amounted to ≈ 3 mJ. Probe light was provided by a flashed xenon lamp (L2273, Hamamatsu). After passing the flow cell (2 mm path length in pump and 10 mm path length in probe direction), the light was dispersed in a grating monochromator and detected by a photomultiplier (1P28, Hamamatsu). To obtain transient spectra, time traces were collected from 250 to 620 nm in 5 nm steps and averaged 10 times. For sensitization experiments time traces at selected wavelengths were averaged 100 times.

Femtosecond transient absorption

The setup is described in detail elsewhere.[4] Pump pulses were tuned to 400 nm by second harmonic generation of the fundamental of a Ti:Sa amplifier system featuring a repetition rate of 1 kHz and a pulse width of 150 fs. The energy of a pump pulse amounted to 1.2 µJ. Transient absorption was probed by a supercontinuum generated in CaF_2. Relative polarization of pump and probe beams was set to magic angle conditions. At the sample location their respective diameters amounted to 280 µm and 30 µm. Solutions were pumped through a 0.5 mm flow cell having an optical density at the excitation wavelength of 1.75 / mm. For every position of the delay line ranging from -1 ps to about 3.4 ns 2000 spectra were accumulated and averaged over four scans. Raw data were corrected for the chirp and solvent contributions.

Data analysis

For the determination of 0-0 energies and Stokes shifts fluorescence spectra were converted from constant wavelength bandpass to constant wavenumber bandpass by multiplying with λ^2.[5] Absorption and fluorescence spectra were further corrected for their intrinsic frequency dependence by multiplying by $\tilde{\nu}^{-1}$ and $\tilde{\nu}^{-3}$, respectively.[6] 0-0 energies were then obtained as the intersection of the corrected absorption and fluorescence spectra normalized to their maxima. Strickler-Berg analysis was performed according to ref. [7-8], in which only the bands lowest in energy entered the analysis.

2. Synthesis and characterization

Reagents and solvents were purchased from Acros, Sigma-Aldrich, Fisher Scientific, or Fluorochem. Chemicals were used without further purification or purified according to standard laboratory methods. Solvents were dried using the solvent purification system MP-SPS 800 from M.Braun.

Reactions were monitored by thin-layer chromatography (TLC) using Macherey-Nagel silica gel plates ALUGRAM® Xtra SIL G/UV_{254} (0.20 mm thickness) and visualized by UV light. Chromatographic purification of products was performed on Macherey-Nagel 60 M (0.04 - 0.063 mm) silica gel.

^{1}H-, ^{13}C-, and ^{19}F-NMR spectra were recorded on Bruker Avance III 300 and 600 NMR spectrometer. Chemical shifts are reported in parts per million (ppm) with respect to TMS using the residual solvent signal as reference. The order of citation in parentheses is a) multiplicity (s = singlet, d = doublet, m = multiplet), b) coupling constants, c) number of protons, and d) assignment. Coupling constants (*J*) were reported in Hertz (Hz). If not described differently the NMR-spectra were measured at 298 K.

IR spectra were recorded using a Jasco FT/IR-6200 spectrometer. Samples were measured as KBr pellets. The absorption bands were given in wavenumbers (cm^{-1}). High-resolution mass spectra (HRMS) were measured with a Bruker Daltonics UHR-QTOF maXis 4G. Melting points were recorded on a Büchi B-540.

2,7-Difluoroacridin-9(10*H*)-one (**AC-dF**) was prepared by Ullmann-type coupling from 4-fluoro-aniline and 2-bromo-5-fluoro-benzoic acid, followed by intramolecular Friedel-Crafts acylation according to literature precedence.[9-10]

2,7-Difluoro-10-methylacridin-9(10*H*)-one (NMA-dF)

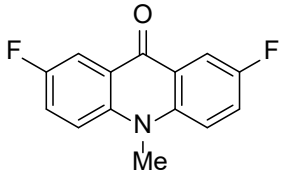

N-Alkylation of the acridone was done following a modified protocol by Inagaki and coworkers.[11]

2,7-Difluoroacridin-9(10*H*)-one (**AC-dF**, 260 mg, 1.12 mM) was suspended in dry DMF (10 mL) and sodium hydride (60% in mineral oil, 113 mg, 2.83 mM) added in portions at RT. Methyl iodide (175 µL, 399 mg, 2.81 mM) was added to the bright yellow suspension and stirring at RT continued for 6 h. Saturated $NaHCO_3$-Solution (50 mL) was carefully added to the green solution and the mixture extracted with dichloromethane (3 x 50 mL). The combined organic layers were washed with water (50 mL) and brine (50 mL). After drying over sodium sulfate, all volatiles were removed in vacuo. Flash column chromatography (silica gel, hexane/ethyl acetate 1:1 to 1:2) gave the product as a canary yellow solid (235 mg, 0.958 mmol, 86%).

Mp = 245 °C. **^{1}H-NMR** (600 MHz, DMSO-d_6): δ [ppm] = 7.88 (m, 4 H, C(1/8)-*H* and C(3/6)-*H*); 7.70 (m, 2 H, C(4/5)-*H*); 3.91 (s, 3 H, *Me*). **^{13}C-NMR** (151 MHz, DMSO-d_6): δ [ppm] = 175.1, 156.9 (d, *J* = 241.0 Hz); 138.9; 122.5 (d, *J* = 24.8 Hz); 121.4 (d, *J* = 6.1 Hz); 119.2 (d, *J* = 7.7 Hz); 110.1 (d, *J* = 22.0 Hz); 34.4. **^{19}F-NMR** (564 MHz, DMSO-d_6): δ [ppm] = - 121.3. **IR** (film), $\tilde{\upsilon}$ [cm^{-1}]: 3061, 2923, 1606, 1584, 1503, 1277, 1176, 1163, 926, 808, 779. **HRMS** (ESI): *m/z* calculated for $C_{14}H_{10}F_2NO$ $[M+H]^+$: 246.0725; found: 246.0730.

NMR Spectra

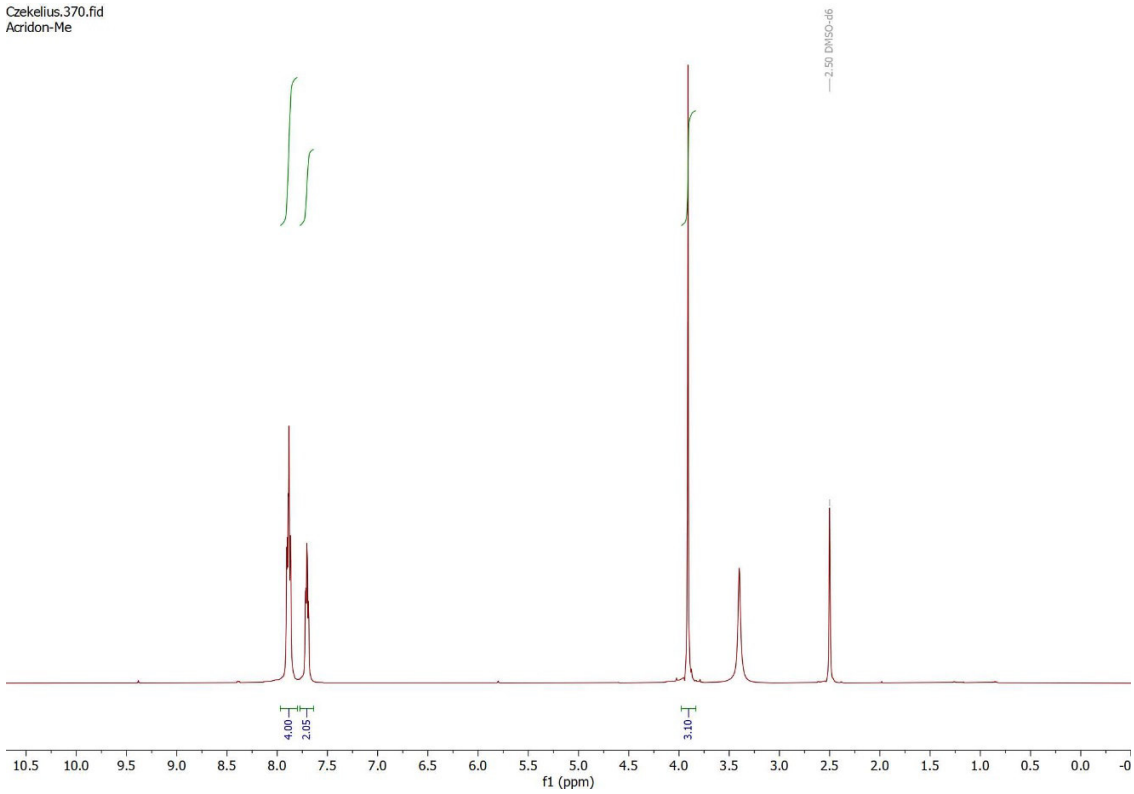

Figure S1: ^{1}H NMR spectrum (298K, 600 MHz, DMSO-d_6) of 2,7-difluoro-10-methylacridin-9(10*H*)-one (**NMA-dF**).

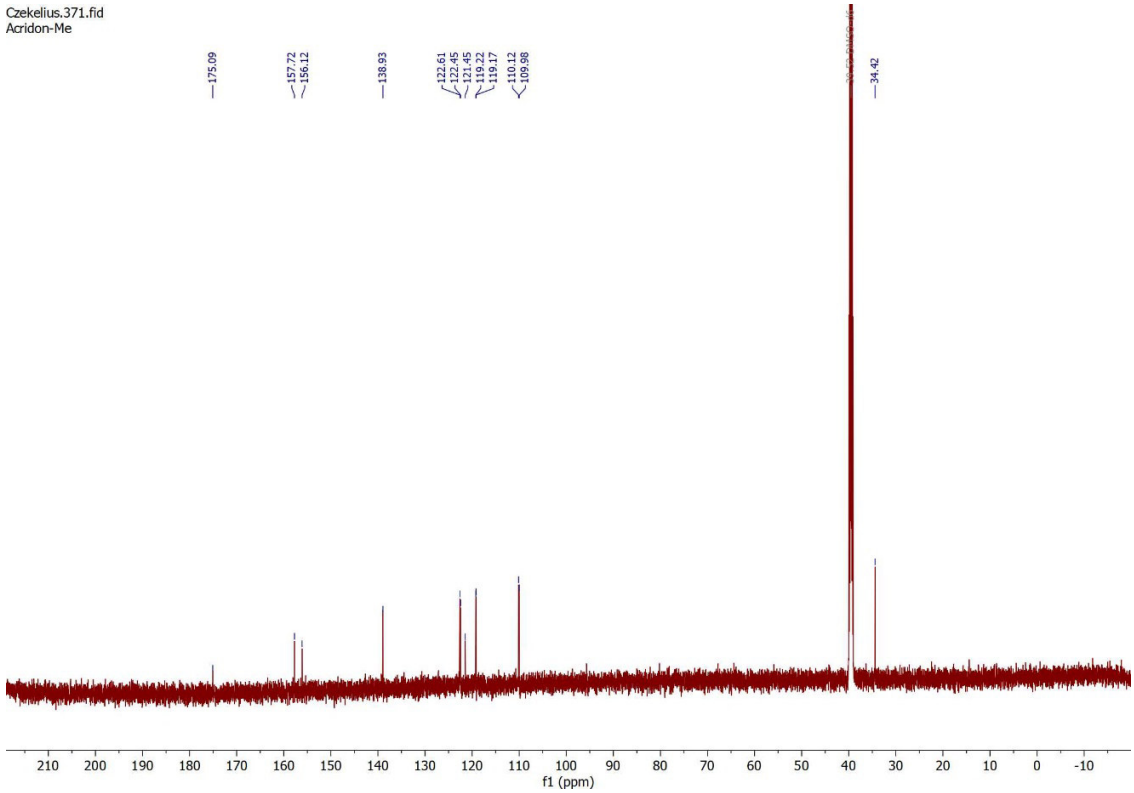

Figure S2: ^{13}C NMR spectrum (298K, 151 MHz, DMSO-d_6) of 2,7-difluoro-10-methylacridin-9(10*H*)-one (**NMA-dF**).

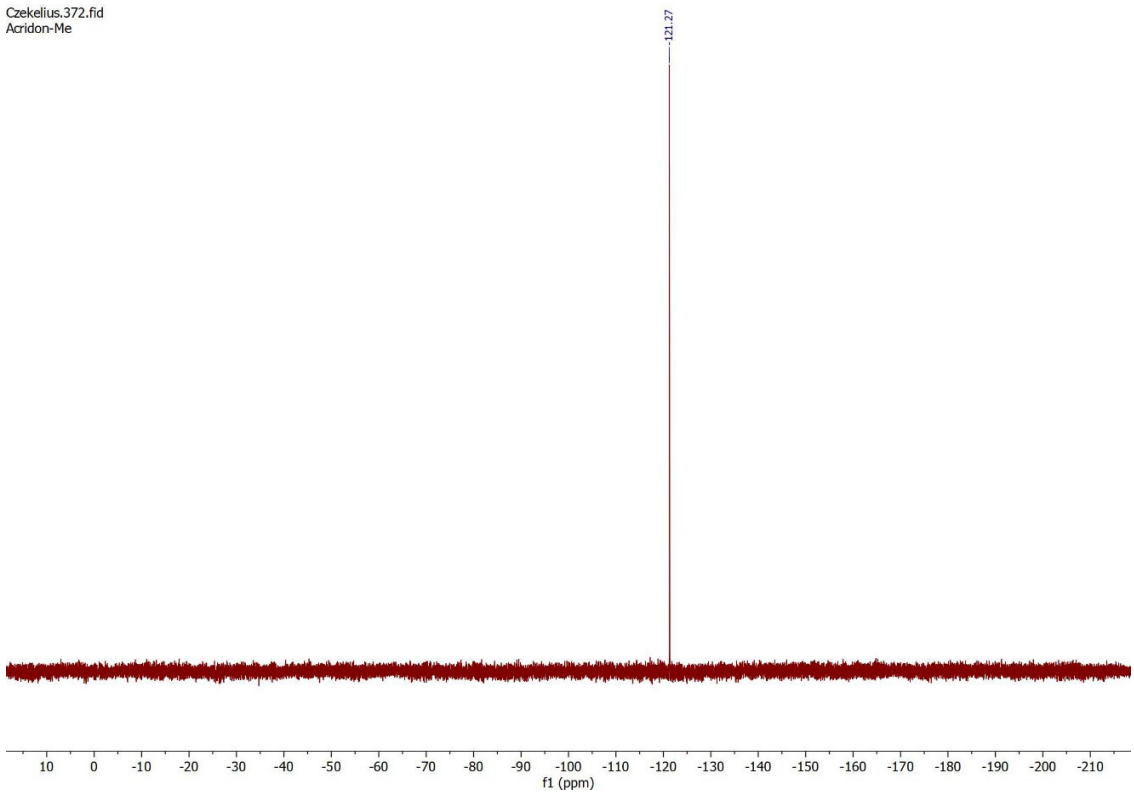

Figure S3: ^{19}F NMR spectrum (298K, 564 MHz, DMSO-d_6) of 2,7-difluoro-10-methylacridin-9(10*H*)-one (**NMA-dF**).

3. Nanosecond transient absorption on NMA-dF

The triplet quantum yield of NMA-dF in methanol was retrieved from nanosecond transient absorption spectra as described in ref. [8]. The spectrum (Figure S4) features two transient absorption bands peaking at 575 nm and around 280 nm. Between 375 nm and 430 nm a ground state bleach is discernable. To determine the triplet quantum yield, the stationary ground state spectrum was scaled into the GSB of the transient spectrum to receive a scaling factor, which relates the molar absorption coefficient to the amplitude of the transient spectra. A difference absorption coefficient of the triplet absorption at 575 nm of around 20 000 $M^{-1}cm^{-1}$ was estimated.

Based on the modified Lambert-Beer law

$$\Delta A = \Phi_T \cdot \Delta\varepsilon \cdot c^* d \qquad \text{(S3)}$$

the triplet yield Φ_T was calculated from the measured signal amplitude ΔA and the difference absorption coefficient $\Delta\varepsilon$. The latter one was derived from the amplitude of the ground state bleach. c^* represents the concentration of initially excited molecules and d the (effective) pathlength. The product $c^* d$ was determined by measuring thioxanthone ($\Phi_T = 0.6$, $\Delta\varepsilon = 26000\ M^{-1}cm^{-1}$)[12-13] in methanol as reference under the same conditions. For NMA-dF a triplet yield of Φ_T^{NMA} = 0.11 (± 0.03) as the average of two independent runs resulted.

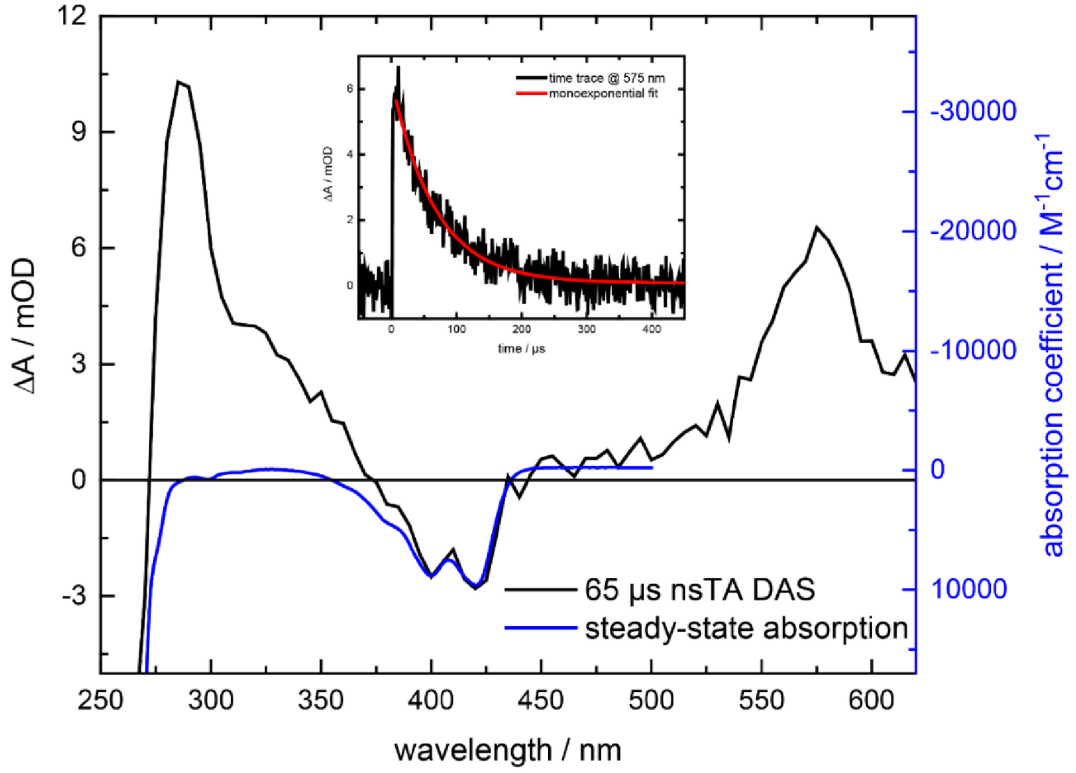

Figure S4: Nanosecond transient absorption spectrum of NMA-dF in methanol (0.02 mM, black). The steady-state absorption (blue) was inverted, shifted, and scaled to fit into the ground state bleach. Inset: time trace at 575 nm.

From measurements at different concentrations of NMA-dF covering two orders of magnitude the intrinsic rate constant k_0^{Em} and the selfquenching constant k_{self}^{Em} were obtained from a linear fit of the observed triplet lifetime τ_T against the concentration [Emitter].

$$\frac{1}{\tau_T} = k_0^{Em} + k_{self}^{Em} \cdot [\text{Emitter}] \tag{S4}$$

The T_1 state of NMA-dF exhibits an intrinsic lifetime of 74 µs (k_0 = 1.3·10^4 s^{-1}) and a selfquenching rate constant k_{self} of approximately 8.1·10^7 M^{-1}s^{-1}.

4. Time-resolved emission spectra of NMA-dF + DCB mixtures

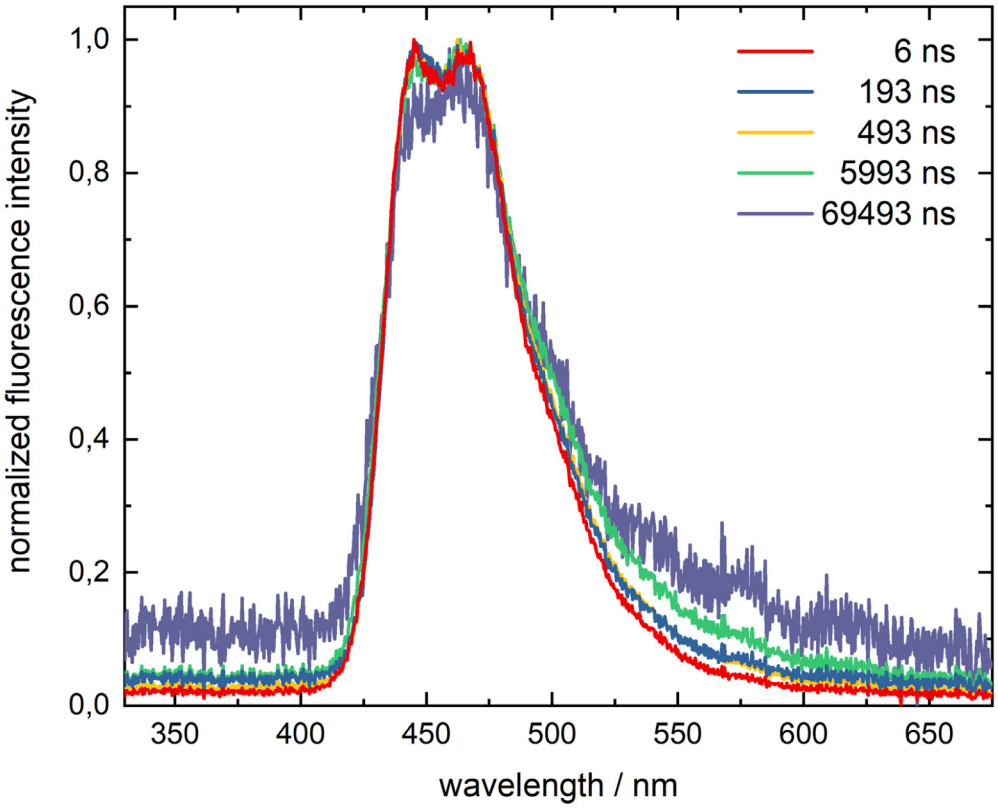

Figure S5: Emission spectra of NMA-dF in presence of DCB at various delay times as received from the time-resolved experiment. The sample solutions (nitrogen-purged methanol) were excited with 266 nm laser pulses.

5. Nanosecond transient absorption on NMA-dF + DCB mixtures

Time traces for NMA-dF and NMA-dF + DCB solutions are compared in Figure S6. Time traces are given for a probe wavelength of 575 nm where the T_1 absorption of the emitter peaks (cf. Figure S4). In absence of the sensitizer, a single-exponential decay with a time constant of 34 µs is observed. After adding DCB to the solution this decay remains unaffected while a delayed rise featuring a time constant of 550 ns becomes discernable. According to eq. 2 of the main text this corresponds to a quenching constant of $9.8 \cdot 10^9$ $M^{-1}s^{-1}$ in good agreement to the one obtained from the nsFl experiment.

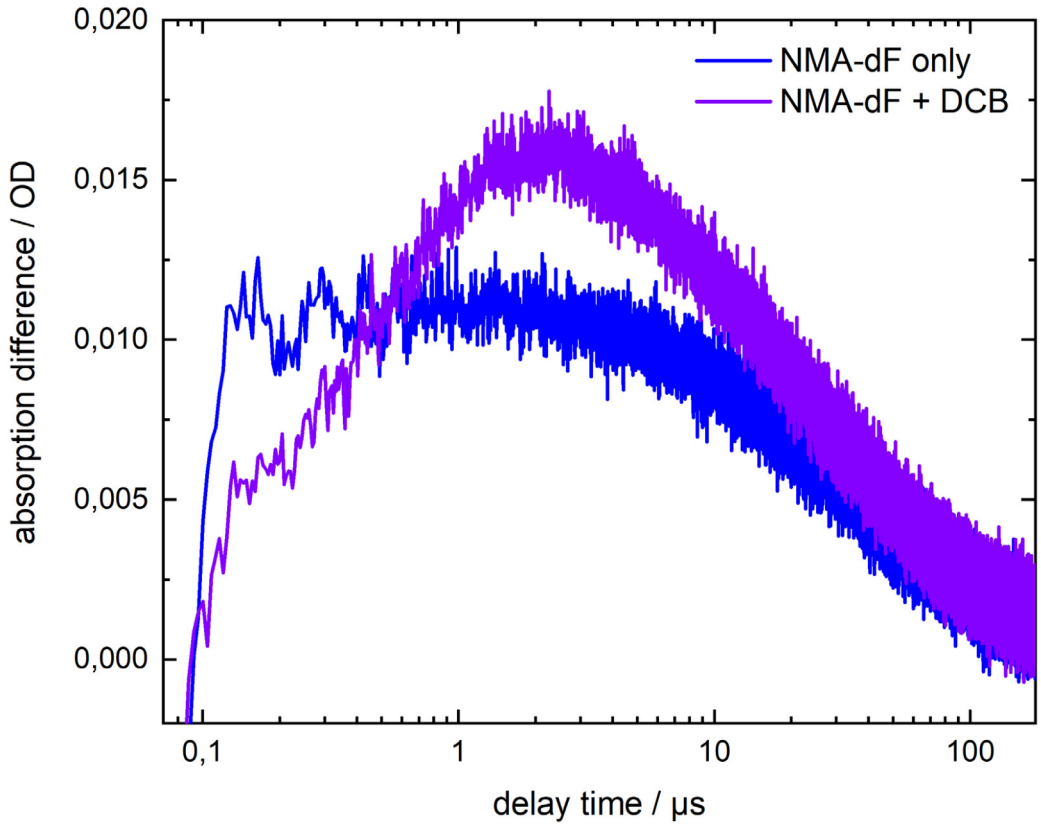

Figure S6: Nanosecond transient absorption time traces of NMA-dF (0.14 mM) in absence (blue) and presence of DCB (purple) dissolved in nitrogen purged methanol. The sample solutions were excited with 266 nm laser pulses and the absorption change probed at 575 nm.

6. Steady-state fluorescence experiments on NMA-dF + DCB mixtures

In the steady-state experiments, argon-purged solutions of NMA-dF were excited at 266 nm (Figure S7, left). When adding DCB to the solution, the fluorescence signal of NMA-dF corrected for the absorbed light flux (cf. Experimental Procedures) decreases. This decrease is a consequence of the inner filter effect of DCB. If no energy transfer between DCB and NMA-dF occurred at all, the fractional decrease of the NMA-dF emission would be given by the part of light flux absorbed by DCB. However, the signal decrease actually observed is less pronounced than the fraction of light absorbed implies. This shows that a part of the energy absorbed by DCB is transferred to NMA-dF and causes fluorescence emission of this compound.

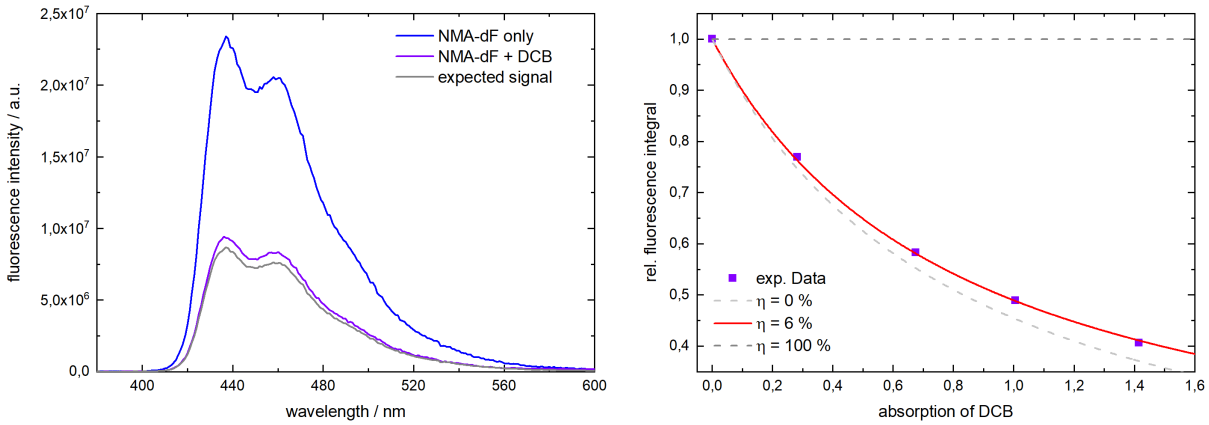

Figure S7: Steady-state sensitization experiment. Left: Steady-state fluorescence spectra of NMA-dF (0.025 mM) in absence (blue) and presence of DCB (purple) dissolved in argon purged methanol. The gray dashed spectrum represents the expected fluorescence signal based on the fraction of light absorbed by NMA-dF within the NMA-dF + DCB mixture without considering an energy transfer. Right: Spectrally integrated fluorescence of NMA-dF + DCB mixtures as a function of the absorption of DCB (purple dots) and a fit according to eq. S6 for η = 0.06 (red line). Simulations for η = 0.0 and η = 1 are shown as well (dashed lines). Spectra depicted on the left correspond to the data point for A^{DCB} = 1.42 in the right graph.

For a quantitative assessment the following procedure was used: The fluorescence quantum yield $\varphi_{fl}^{Em+Sens}$ of an NMA-dF + DCB mixture can be separated into a direct and a sensitized part (eq. S5). The first term contains the fraction of light absorbed by the emitter and its fluorescence quantum yield φ_{fl}^{Em}. In the second term, one finds the fraction of light absorbed by the sensitizer, the quantum yield φ_{fl}^{Em} and the efficiency η for an energy transfer populating the emitting state of NMA-dF.

$$\varphi_{fl}^{Em+Sens} = \underbrace{\frac{A^{Em}}{A^{Em}+A^{Sens}} \cdot \varphi_{fl}^{Em}}_{\text{direct}} + \underbrace{\frac{A^{Sens}}{A^{Em}+A^{Sens}} \cdot \eta \cdot \varphi_{fl}^{Em}}_{\text{sensitized}} \qquad \text{(S5)}$$

Rearranging eq. S5 yields the expression used for the steady-state analysis of the HIGHrISC behavior. The left hand side of this expression equals the spectrally integrated fluorescence signal of the emitter in presence of the sensitizer divided by the respective emitter only integral.

$$\frac{\int S^{Emitter+Sens}}{\int S^{Emitter}} = \frac{\varphi_{fl}^{Emitter+Sens}}{\varphi_{fl}^{Emitter}} = \frac{A^{Emitter}}{A^{Emitter} + A^{Sens}} + \frac{A^{Sens}}{A^{Emitter} + A^{Sens}} \cdot \eta \qquad \text{(S6)}$$

The efficiency η may be determined by conducting a set of experiments in which $A^{Emitter}$ is kept constant, whereas A^{Sens} is varied by successively adding DCB to the solution (Figure S7, right). Hereby, η was the only variable parameter. The resulting fit describes the experimental behavior well. For an NMA-dF concentration of 0.025 mM an efficiency of 0.064 (± 0.004) results. All experimental values are well above the limit for η = 0, stressing that indeed an energy transfer takes place.

Note that the efficiency η depends on the emitter concentration (see main text). The value of 0.064 given here refers to a rather low concentration. An extrapolation to high concentrations based on eq. 5 (main text) yields an efficiency η_∞ of 0.18, which matches the value determined by time-resolved spectroscopy.

7. Quantum chemical calculations

Geometry optimizations were conducted with the Turbomole program[14] using density functional theory (DFT) with the B3LYP functional for the ground state and time-dependent DFT (TDDFT) for the excited states, additionally applying the Tamm-Dancoff approximation (TDDFT-TDA) in the triplet manifold. The TZVP basis set from the Turbomole library was used throughout.

For the numerical computation of vibrational frequencies, the SNF program was used.[15] Vibrational overlaps for emission and absorption spectra, as well as for intersystem crossing (ISC) rate constants were obtained by the Vibes program in its time-dependent version.[16]

Vertical excitation energies at fixed geometries were computed with the DFT/MRCI program.[17-18] The original Hamiltonian of Grimme and Waletzke was used with standard parameters and a selection threshold of 1.0 Hartree. The core electrons were kept frozen, the initial reference space comprised all single and double excitations of 12 electrons in 12 orbitals and was subsequently optimized to contain the most important configurations of all roots. Spin–orbit matrix elements (SOMEs) were obtained from DFT/MRCI wavefunctions by the SPOCK program[19] applying the spin–orbit operator in mean-field approximation.[20] Derivatives of the SOMEs were obtained numerically and used for the calculation of the El-Sayed forbidden T_2-S_1 ISC.

Internal conversion (IC) rate constants, were obtained by a code recently developed in our group, computing non-adiabatic coupling matrix elements (NACMEs) by taking numerical derivatives of the wave function overlaps and subsequently calculating the IC rates via a modified version of the Vibes program.[21]

Molecular geometries of the ground state and the two lowest excited singlet and three triplet states were calculated in vacuum. All of these correspond to true minima on the potential energy

surface (PES). The influence of solvation in methanol was estimated by computing the ground state geometry in an implicit solvation environment (Conductor Like Screening Model (COSMO) as implemented in Turbomole) and adding two explicit methanol molecules as hydrogen-bridge donors at the carbonyl group. The vertical DFT/MRCI excitation spectrum obtained this way was compared to the corresponding spectrum in vacuum and the solvation shift of the states of interest subsequently applied to the corresponding states at the other (vacuum) geometries (Table 1). These shifts were also applied in the numerical derivation of the wavefunction overlaps for the NACMEs.

Table 1: Vertical excitation energies at different geometries. Energies for the ground state refer to the optimized vacuum geometries. Energies given for excited states are estimated based on the solvent shifts between vacuum and MeOH. Values are given in eV.

	vac	MeOH		MeOH				
Geometry	S_0	S_0	shift	S_1	S_2	T_1	T_2	T_3
S_0	0	0		0.14	0.41	0.14	0.43	0.44
S_1 ($^1\pi\pi^*$)	3.30	3.17	-0.13	3.06	3.32	3.07	3.33	3.36
S_2 ($^1n\pi^*$)	3.37	3.90	+0.53	3.84	3.55	3.71	3.53	3.90
T_1 ($^3\pi\pi^*$)	2.71	2.51	-0.20	2.46	2.49	2.39	2.50	2.72
T_2 ($^3n\pi^*$)	3.23	3.80	+0.57	3.74	3.48	3.63	3.46	3.83
T_3 ($^3\pi\pi^*_2$)	3.57	3.59	+0.02	3.55	3.59	3.53	3.61	3.31
T_4 ($^3\pi\pi^*_3$)	3.60	3.54	-0.05	3.58	3.77	3.76	3.81	3.85
T_5 ($^3\pi\pi^*_4$)	3.73	3.69	-0.04	3.67	3.97	3.69	4.00	3.98

Table 2: Adiabatic and 0-0 energies of the relevant states. Values are given in eV.

	S_1 ($^1\pi\pi^*$)	S_2 ($^1n\pi^*$)	T_1 ($^3\pi\pi^*$)	T_2 ($^3n\pi^*$)	T_3 ($^3\pi\pi^*_2$)
adiabatic energy	3.06	3.55	2.39	3.46	3.31
0-0 energy	2.93	3.46	2.28	3.38	3.17

References

1. Mundt, R.; Villnow, T.; Ziegenbein, C. T.; Gilch, P.; Marian, C.; Rai-Constapel, V., Thioxanthone in Apolar Solvents: Ultrafast Internal Conversion Precedes Fast Intersystem Crossing. *Phys. Chem. Chem. Phys.* **2016**, 6637-6647.
2. Onidas, D.; Markovitsi, D.; Marguet, S.; Sharonov, A.; Gustavsson, T., Fluorescence Properties of DNA Nucleosides and Nucleotides: A Refined Steady-State and Femtosecond Investigation. *J. Phys. Chem. B* **2002**, *106*, 11367-11374.
3. Kubista, M.; Sjöback, R.; Eriksson, S.; Albinsson, B., Experimental Correction for the Inner-Filter Effect in Fluorescence Spectra. *Analyst* **1994**, *119*, 417-419.
4. Fröbel, S.; Buschhaus, L.; Villnow, T.; Weingart, O.; Gilch, P., The Photoformation of a Phthalide: A Ketene Intermediate Traced by FSRS. *Phys. Chem. Chem. Phys.* **2015**, *17*, 376-386.
5. Mooney, J.; Kambhampati, P., Get the Basics Right: Jacobian Conversion of Wavelength and Energy Scales for Quantitative Analysis of Emission Spectra. *J. Phys. Chem. Lett.* **2013**, *4*, 3316-3318.
6. Parson, W. W., *Modern Optical Spectroscopy, with Exercises and Examples from Biophysics and Biochemistry, Student Edition*; Springer: Dordrecht, Heidelberg, London, New York, 2009.
7. Strickler, S.; Berg, R., Relationship between Absorption Intensity and Fluoresence Lifetime of Molecules. *J. Chem. Phys.* **1962**, *37*, 814-822.
8. Reiffers, A.; Torres Ziegenbein, C.; Engelhardt, A.; Kühnemuth, R.; Gilch, P.; Czekelius, C., Impact of Mono-Fluorination on the Photophysics of the Flavin Chromophore. *Photochem. Photobiol.* **2018**, *94*, 667-676.
9. Zhou, W.; Yang, Y.; Liu, Y.; Deng, G.-J., Copper-Catalyzed C–C Bond Cleavage and Intramolecular Cyclization: An Approach toward Acridones. *Green Chem.* **2013**, *15*, 76-80.
10. Andronico, L. A.; Quintavalla, A.; Lombardo, M.; Mirasoli, M.; Guardigli, M.; Trombini, C.; Roda, A., Synthesis of 1,2-Dioxetanes as Thermochemiluminescent Labels for Ultrasensitive Bioassays: Rational Prediction of Olefin Photooxygenation Outcome by Using a Chemometric Approach. *Chem. Eur. J.* **2016**, *22*, 18156-18168.
11. Maegawa, Y.; Mizoshita, N.; Tani, T.; Inagaki, S., Transparent and Visible-Light Harvesting Acridone-Bridged Mesostructured Organosilica Film. *J. Mater. Chem.* **2010**, *20*, 4399-4403.
12. Villnow, T.; Ryseck, G.; Rai-Constapel, V.; Marian, C. M.; Gilch, P., Chimeric Behavior of Excited Thioxanthone in Protic Solvents: I. Experiments. *J. Phys. Chem. A* **2014**, *118*, 11696-11707.
13. Carmichael, I.; Helman, W. P.; Hug, G. L., Extinction Coefficients of Triplet--Triplet Absorption Spectra of Organic Molecules in Condensed Phases: A Least-Squares Analysis. *J. Phys. Chem. Ref. Data* **1987**, *16*, 239-260.
14. Turbomole V7.5 2020, a Development of University of Karlsruhe and Forschungszentrum Karlsruhe GmbH, Turbomole GmbH, since 2007; Available from https://www.turbomole.org. 1989-2007.
15. Neugebauer, J.; Reiher, M.; Kind, C.; Hess, B. A., Quantum Chemical Calculation of Vibrational Spectra of Large Molecules - Raman and IR Spectra for Buckminsterfullerene. *J. Comput. Chem.* **2002**, *23*, 895-910.
16. Etinski, M.; Tatchen, J.; Marian, C. M., Time-Dependent Approaches for the Calculation of Intersystem Crossing Rates. *J. Chem. Phys.* **2011**, *134*, 154105.
17. Grimme, S.; Waletzke, M., A Combination of Kohn−Sham Density Functional Theory and Multi-Reference Configuration Interaction Methods. *J. Chem. Phys.* **1999**, *111*, 5645-5655.
18. Marian, C. M.; Heil, A.; Kleinschmidt, M., The DFT/MRCI Method. *WIREs Comput. Mol. Sci.* **2019**, *9*, e1394.
19. Kleinschmidt, M.; Tatchen, J.; Marian, C. M., Spin-Orbit Coupling of DFT/MRCI

Wavefunctions: Method, Test Calculations, and Application to Thiophene. *J. Comput. Chem.* **2002**, *23*, 824-833.
20. Heß, B. A.; Marian, C. M.; Wahlgren, U.; Gropen, O., A Mean-Field Spin-Orbit Method Applicable to Correlated Wavefunctions. *Chem. Phys. Lett.* **1996**, *251*, 365-371.
21. Bracker, M; Marian, C. M.; Keinschmidt, M., Internal conversion of singlet and triplet states employing numerical DFT/MRCI derivative couplings: Implementation, tests and application to xanthone. *Submitted to J. Chem. Phys.*